ASSESSMENT OF POTENTIAL AERODYNAMIC BENEFITS FROM SPANWISE BLOWING AT THE WING TIP

By

Raymond Edward Mineck

Bachelor of Science, June 1970

Rensselaer Polytechnic Institute

Master of Science, May 1975

The George Washington University

A Dissertation submitted to

The Faculty of

The Graduate School of Engineering and Applied Science

of The George Washington University in partial satisfaction

of the requirements for the degree of

Doctor of Science

May 1992

Dissertation directed by

Dr. John L. Whitesides

Professor of Engineering and Applied Science

ASSESSMENT OF POTENTIAL AERODYNAMIC BENEFITS FROM SPANWISE BLOWING AT THE WING TIP

By

Raymond E. Mineck

ABSTRACT

A comprehensive set of experimental and analytical investigations have been conducted to assess the potential aerodynamic benefits from spanwise blowing at the tip of a moderate aspect ratio, swept wing. An analytical model has been developed to simulate a jet exhausting from the wing tip. The model demonstrated that vorticity added to the flowfield by the jet near the wing tip tends to diffuse the tip vortex and displace it outwards. The diffused and displaced vortex should induce a smaller downwash at the wing and, consequently, the wing should have increased lift and decreased induced drag. An experimental study of a subsonic jet exhausting from the wing tip was conducted to investigate the effect of spanwise blowing from the tip on the aerodynamic characteristics of a moderate aspect ratio, swept wing. Special attention was given to obtaining accurate balance measurements in the presence of the air supply lines. Wing force and moment data and surface pressure data were measured at Mach numbers up to 0.72. Results indicated that small amounts of blowing from small jets increase the lift curve slope a small amount but have little effect on drag. Larger amounts of blowing from longer jets blowing increase lift near the tip and reduce drag at low Mach numbers. These benefits become smaller and vanish as the Mach number increased to 0.5. A Navier-Stokes solver with modified boundary conditions at the tip was used to extrapolate the results to a Mach number of 0.72. Calculations indicated that lift increases with increasing jet momentum coefficient and that a separated flow region develops near the tip which is consistent with the experimental trend that the drag benefit vanishes. With current technology and conventional wing shapes, spanwise blowing at the wing tip does not appear to be a practical means of reducing drag of moderate aspect ratio wings at high subsonic Mach numbers.

ACKNOWLEDGMENTS

The author wishes to express his appreciation to the NASA Langley Research Center for supporting him in this work. The Center provided the resources to design and fabricate the model and conduct the experiments. It also provided the computer resources to perform the needed computations.

The author wishes to express his thanks to Dr. John L. Whitesides for serving as his faculty advisor and as his committee chairman. His guidance, suggestions, and thought provoking questions led to the successful completion of this task.

Thanks are extended to Mr. Dennis M. Bushnell for suggesting this research topic. The author also wishes to thank Mr. L. Elwood Putnam, former head of the Transonic Aerodynamics Branch. Mr. Putnam provided Branch resources to design, fabricate, and calibrate the model. He also allocated test time in the 7- by 10-foot High Speed Tunnel to perform the needed experiments. The author wishes to extend his appreciation to the operations staff of the 7- by 10-foot High Speed Tunnel who helped perform the experiments, especially Ms. Shirley M. Jones, Ms. Patricia Christian, Mr. Charles H. Fox, Mr. Jarrett K. Huffman, and Mr. A. Bruce Graham. Ms. Jones helped with the initial assembly of the model, adapted the shop air supply to the model airlines, and modified the air supply lines to fit within the body without interference and to reduce the pressure losses. Ms. Christian performed the weight loading to calibrate the airline stiffness effects and operated the air supply system when calibrating the tip jet momentum. Mr. Fox and Mr. Huffman assisted with the calibration of the instrumentation, setting up the data acquisition system, and acquisition of the wind tunnel data. Mr. Graham wrote the interface software to convert the data tapes from the new data acquisition system into a format compatible with the standard data reduction program.

The author wishes to express his thanks to Dr. James M. Luckring, present head of the Transonic Aerodynamics Branch, for allocating Branch resources to support the needed computations. An expression of thanks is also extended Mr. Bruce W. Wedan for his suggestions during the generation of the computational grids. Special thanks are extended to Dr. Veer N. Vatsa for his patience,

suggestions, and guidance when learning about and modifying the Navies-Stokes solver. The author wishes to thank Mr. Brent Bates for his help in generating grids, manipulating the various grid and solution files, and plotting the Navier-Stokes results.

Most importantly, the author wishes to thank his family: Linda, his wife, and Jennifer, Christine, and John, his children, for their patience and sacrifices while persuing this degree.

CONTENTS

APPENDICES

LIST OF FIGURES

LIST OF TABLES

SYMBOLS

Symbol

A	Influence coefficient
A_j	jet area, ft.^{2}
AR	wing aspect ratio, $\frac{b^2}{S}$
b	wing span, ft.
c	local wing chord, ft.
$\bar{c}$	mean aerodynamic chord, ft.
c_j	length of jet, ft.
C_b	wing root bending moment coefficient, $\frac{2\ M_X}{q_\infty\ S\ b}$
C_{b_L}	slope of wing root bending moment curve, $\frac{d\ C_b}{d\ C_L}$
C_{b_0}	wing root bending at zero lift
C_D	wing drag coefficient, $\frac{D}{q_\infty\ S}$
C_{D_μ}	slope of wing drag coefficient versus momentum coefficient curve, $\frac{d\ C_D}{d\ C_\mu}$
$C_{D_{cor.}}$	total drag coefficient, $\frac{D+\dot{m}_j V_\infty}{q_\infty\ S}$
C_{D_i}	induced drag coefficient, $\frac{C_L^2}{\pi\ AR\ e}$
C_L	wing lift coefficient, $\frac{L}{q_\infty\ S}$
C_{L_α}	wing lift curve curve, $\frac{d\ C_L}{d\ C_\alpha}$
C_{L_μ}	slope of wing lift coefficient versus momentum coefficient curve, $\frac{d\ C_L}{d\ C_\mu}$
c_l	section lift coefficient, $\frac{l}{q_\infty\ c}$, ft.$^{-1}$

c_{l_α} section lift curve slope, $\frac{d\, c_l}{d\alpha}$, ft.$^{-1}$deg.$^{-1}$

C_m wing pitching moment coefficient, $\frac{2\, M_Y}{q_\infty\, S\, \bar{c}}$

C_{m_L} slope of wing pitching moment curve, $\frac{d\, C_m}{d\, C_L}$

C_{m_0} wing pitching moment at zero lift

C_P local static pressure coefficient, $\frac{p - p_\infty}{q_\infty}$

c_t wing tip chord, ft.

C_{μ} wingtip jet total momentum coefficient, $\frac{\dot{m}_j\, V_j}{q_\infty\, S}$

C_{μ_1} front wingtip jet momentum coefficient, $\frac{(\dot{m}_j\, V_j)_{front}}{q_\infty\, S}$

C_{μ_2} rear wingtip jet momentum coefficient, $\frac{(\dot{m}_j\, V_j)_{rear}}{q_\infty\, S}$

D force in the drag direction, lbf.

d_e effective jet diameter, ft., $\sqrt{\frac{4\, A_j}{\pi}}$

e Oswald efficiency factor

F force, lbf.

f function defining the lift curve slope in terms of aspect ratio. (See Reference 23.)

G integral of vorticity. (See eq. 3.25)

h_j half-spacing of the jet counter-rotating vortices. (See figure 6.)

L total force in the lift direction, lbf.

l section lift per unit span, $\frac{\text{lbf.}}{\text{ft.}}$

M_X total measured moment about the X-axis resolved about the origin, ft.-lbf.

M_Y	total measured moment about the Y-axis resolved about the 0.25 $\bar{c}$, ft.-lbf.
M_∞	free stream Mach number
$\dot{m}_j$	jet mass flow rate, $\frac{\text{slugs}}{\text{sec.}}$
p	local static pressure, $\frac{\text{lbf.}}{\text{ft.}^2}$
p_∞	free stream static pressure, $\frac{\text{lbf.}}{\text{ft.}^2}$
$\bar{q}$	complex conjugate of the velocity induced by a vortex sheet
q_j	jet dynamic pressure at jet exit, psf, $\frac{1}{2}\rho_j \bar{V}_j^2$
q_∞	free stream dynamic pressure, psf, $\frac{1}{2}\rho_\infty V_\infty^2$
R	Unit Reynolds number per foot, $\frac{\rho_\infty V_\infty}{\mu}$
S	wing reference area, ft.^{2}
s	distance from the control point to the segment endpoint
t	airfoil local thickness, ft.
V	velocity, $\frac{\text{ft.}}{\text{sec.}}$
V_e	effective jet velocity ratio, $\frac{V_j}{V_\infty}$
V_j	jet velocity at the jet exit, $\frac{\text{ft.}}{\text{sec.}}$
V_x	component of local velocity in streamwise direction, $\frac{\text{ft.}}{\text{sec.}}$
V_∞	free stream velocity, $\frac{\text{ft.}}{\text{sec.}}$
u,v,w	velocity components in X, Y, Z directions, $\frac{\text{ft.}}{\text{sec.}}$
X,Y,Z	axis system with origin at the wing root leading edge, (See figure 29.)
x	chordwise distance, positive measured aft from the leading edge, ft.

y	spanwise distance, positive measured out the right wing, ft.
z	vertical distance, positive measured up from the wing reference plane, ft.
	or position on the complex plane
α	wing angle of attack, positive leading edge up, deg.
α_i	induced angle of attack, $\tan^{-1}\left(\frac{w_i}{V_\infty}\right)$, deg.
α_0	wing angle of zero lift, deg.
Γ	circulation, $\frac{\text{ft.}}{\text{sec.}}$
γ	vorticity
Δ	change in a parameter
δ_j	jet dihedral (deflection in the Y-Z plane), deg. (See figure 22)
η	fraction of wing semi-span, $\frac{y}{b/2}$
θ	slope at a control point (See equation 3.5) or argument of a complex number
θ_{twist}	wing twist
Λ	leading edge sweep, deg.
μ	free stream viscosity, $\frac{\text{slugs}}{\text{ft. sec.}}$
ρ_j	density of the jet, $\frac{\text{slugs}}{\text{ft.}^3}$
ρ_∞	free stream density, $\frac{\text{slugs}}{\text{ft.}^3}$
σ	distance from a pivot point
ψ_j	jet sweep (deflection in the X-Y plane), deg. (See figure 22)
ξ	dummy variable

Subscripts and superscripts

b	bound vortex
e	end
i	induced
j	jet
$( )^{(p)}$	p^{th} derivative
root	wing root
R	resultant
tip	wing tip
w	wake
∞	free stream
$'$	(prime), first derivative of the function with respect to its argument

Abbreviations:

AFOSR	U. S. Air Force Office of Scientific Research
AFWAL	U. S. Air Force Wright Aeronautical Laboratories
AIAA	American Institute of Aeronautics and Astronautics
ARP	Airfoil Reference Plane
HST	High Speed Tunnel
JIAA	Joint Institute for Aeronautics and Acoustics
NACA	National Advisory Committee for Aeronautics
NASA	National Aeronautics and Space Administration

CHAPTER I

INTRODUCTION

Aerodynamic efficiency is an important factor in the marketing of subsonic, commercial transport aircraft. Efficiency can be improved by increasing the maximum lift to drag ratio at the cruise flight condition. Improvements are frequently aimed at reducing the drag at the cruise lift coefficient. For a subsonic transport with subcritical flow, drag can be divided into pressure drag, skin friction drag, and induced drag. Since induced drag is often the largest component of drag at cruise, it is frequently the target of drag reduction efforts. At a constant angle of attack, the wing lift increases and the induced drag decreases as the wing effective aspect ratio increases. Subscale experiments with spanwise blowing from the tips of low aspect ratio wings suggest that spanwise blowing from the wing tip increases the effective aspect ratio. This paper presents the results of a comprehensive investigation to assess the potential aerodynamic benefits from spanwise blowing at the tip of a moderate aspect ratio, swept wing.

This chapter will review the origination of induced drag, review its reduction by wing shape modifications, and propose spanwise blowing as a means of reducing induced drag based on published test results. The three major sources of drag on a subsonic transport are reviewed first. Since induced drag can be the largest component of total drag, it will be discussed in greater detail than the other components. A description of attempts to reduce induced drag by modifications to the shape of the wing follows. Practical modifications to the wing shape have led to small reductions in induced drag. Spanwise blowing at the wing tip is then proposed as an alternate means to improve the wing efficiency. Published results are reviewed to determine that further investigation of spanwise blowing is needed to assess its potential aerodynamic benefits at cruising flight conditions.

Pressure drag comes from regions of separated flow or from the unclosed surface formed by

the aircraft and its wake. To reduce pressure drag, regions of separated flow must be reduced. Aerodynamicists can use design tools to predict regions of adverse pressure gradient where separation would be likely to occur and then modify the design to eliminate the separation. Devices such as vortex generators or the application of suction or tangential blowing can eliminate separation on an existing design. For a good design, that is, one with little separation, only small reductions in drag are expected by reducing the pressure drag.

Skin friction drag comes from the viscous forces arising from the no-slip condition at the surface. Skin friction is larger in turbulent boundary layers than in laminar boundary layers, and at large Reynolds numbers, the boundary layer quickly transitions from laminar to turbulent. To reduce skin friction drag, transition from a laminar to a turbulent boundary layer should be delayed. Transition can be delayed by active means such as suction or cooling at the surface. It can also be delayed by maintaining very smooth surfaces and favorable pressure gradients. An overview of current work in viscous drag reduction is presented in reference 1. Tests of recent airfoil designs have demonstrated long runs of laminar boundary layers at large Reynolds numbers and high subsonic Mach numbers. Where laminar flow cannot be maintained, passive devices such as riblets or large eddy break up devices can be used to reduce the turbulent skin friction. For a design which uses natural laminar flow, laminar flow control, or turbulent drag reduction devices, further reductions in skin friction drag using current technology are expected to be small.

Induced Drag

Induced drag or drag due to lift comes from the downwash induced at the wing by the vorticity in the wing wake. Most of the downwash is induced by vorticity which typically rolls up into two wing tip vortices. These tip vortices produce another detrimental effect when aircraft encountering these trailing vortices are subjected to hazardous flowfields capable of overwhelming the control power of the aircraft. Reference 2 describes the trailing vortex wake problem and some of the techniques applied to try to alleviate the problem.

The concept of induced drag can be explained using Prandtl's lifting line theory. The wing span is assumed to be much larger than the wing chord. Wing lift is represented by a lifting line or bound vortex. The wake is assumed to lie in a plane of the lifting line and the free stream velocity. A sketch of this flowfield is presented in figure 1. For an infinite span wing with constant bound circulation, Γ, no vorticity is shed in the wake. From the Kutta-Joukowski theorem, the resultant force is perpendicular to the local velocity vector. With no vorticity in the wake, no downwash, $w_i(y)$, is induced at the wing. The local velocity vector, V_R, is the same as the free stream vector, V_∞. Thus, there is no component of the resultant force, F_R, in the drag direction. For a finite span wing, the circulation goes to zero at the tips and vorticity is shed in the wake. By Helmholtz's theorem, vorticity shed from the wing extends downstream to infinity (or the starting vortex). The shed vortex wake induces a downwash on the bound vortex. Using the Biot-Savart law, the induced downwash can be expressed as

$$w_i(y) = -\frac{1}{4\pi} \int_{-\frac{b}{2}}^{+\frac{b}{2}} \frac{\Gamma'(\xi)}{y - \xi}\, d\xi \tag{1.1}$$

This downwash rotates the local velocity vector downward. Since the resultant force is perpendicular to this direction, it has a component in the drag direction, $D_i(y)$, as shown in figure 1. From the Kutta-Jukowski theorem, the lift and induced drag are:

$$L = \int_{-\frac{b}{2}}^{+\frac{b}{2}} \rho_\infty V_\infty \Gamma(y)\, dy \tag{1.2}$$

$$D_i = \int_{-\frac{b}{2}}^{+\frac{b}{2}} \rho_\infty w_i(y)\, \Gamma(y)\, dy \tag{1.3}$$

Monk, assuming a planar vortex wake, proved in reference 3 that induced drag is a minimum if the

downwash across the span is constant. For an elliptical circulation distribution, such as

$$\Gamma(y) = \Gamma_{root} \sqrt{1 - \left(\frac{y}{b/2}\right)^2} \tag{1.4}$$

the downwash, lift, and induced drag are:

$$w_i(y) = -\frac{\Gamma_{root}}{2\,b} = \text{constant} \tag{1.5}$$

$$L = \frac{\pi}{4}\rho_\infty V_\infty \Gamma_{root}\, b \tag{1.6}$$

$$D_i = -\frac{w_i}{V_\infty} L = \frac{\Gamma_{root}\, L}{2\,b\,V_\infty} \tag{1.7}$$

Since an elliptical circulation distribution produces a constant downwash, it also produces a minimum induced drag. These expressions do not address how the elliptical circulation distribution is to be achieved. The spanwise distribution of lift for an elliptical circulation distribution can be written as follows:

$$\begin{aligned} l(y) &= c_{l_\alpha}(y)\ \ \alpha(y)\ \tfrac{1}{2}\ \rho_\infty\ V_\infty^2\ c(y) \\ &= \rho_\infty\ V_\infty\ \Gamma_{root} \sqrt{1 - \left(\frac{y}{b/2}\right)^2} \end{aligned} \tag{1.8}$$

Collecting the terms dependent on the spanwise position, the following result is obtained

$$c(y)\ \alpha(y)\ c_{l_\alpha}(y) = \frac{2\Gamma_{root}}{V_\infty} \sqrt{1 - \left(\frac{y}{b/2}\right)^2} \tag{1.9}$$

Thus, an elliptical circulation distribution can be obtained by varying the local wing chord, twist, and lift curve slope (or airfoil section).

Combining the expressions from equations 1.5, 1.6, and 1.7 for downwash, lift, and induced drag, the relationship of induced drag to lift is

$$C_{D_i} = \frac{C_L^2}{\pi\ AR\ e} \tag{1.10}$$

where the Oswald efficiency factor, e, has been added for wings without an elliptical load distribution. This factor is 1.0 for an elliptical span load distribution. As stated above, these results were derived assuming a flat lifting surface and a planar wake.

Cone extended this analysis to a nonplanar lifting surface and trailing wake in reference 4. He noted that the induced downwash in equation 1.1 and the induced drag will be reduced if the spanwise derivative of the circulation, $\Gamma'(\xi)$, is reduced or if the distance between the control point on the wing and the shed vorticity, $(y\text{-}\xi)$, is increased. Both of these conditions are achieved for an increase in wing span. If an increase in span is not possible, the length of the lifting surface can be increased by extending the wing into the vertical plane. The derivative of the circulation with respect to arc length along the wing span is reduced because the length of the lifting surface (or arc length) is increased and the distance from most of the wing to the tip, where the derivative is largest, is increased. Cone found that the Oswald efficiency factor increases for circular arc lifting lines up to a value of 1.50 for a semicircle with a diameter equal to the reference wing span. It should be noted that the surface area has increased by $\frac{\pi}{2}$ (to about 1.57 times the original area). Profile drag would be expected to increase to about 1.57 times the original level and the induced drag would be expected to decrease to about .67 times the original level. Thus, a circular arc span line will reduce the total drag if the reduction in induced drag more than offsets the increase in profile drag.

Induced Drag Reduction

Induced drag is typically 30 to 50 percent of the total drag on a subsonic commercial passenger transport in cruising or climbing flight. Reducing the strength of the wing tip vortices, diffusing them, or displacing them outboard should reduce the induced drag because of the increase in effective aspect ratio. Several types of planform modifications have been investigated to reduce induced drag. Early attempts to reduce the induced drag involved placing endplates at the wing tips. More recent modifications include winglets, wing tip sails, tip turbines, and tip vanes. An

alternative technique for reducing the induced drag which uses one or more jets exhausting spanwise from the wing tip will be proposed.

Induced drag can be reduced by modifications to the wing planform both in and out of the wing plane. Modifications have generally been directed out of the plane of the wing because Monk's stagger theorem indicates that in-plane modifications of an elliptical circulation distribution would not change the induced drag. Out of plane modifications have included devices such as endplates, winglets, and tip sails. Monk's stagger theorem assumed a planar wake. If the planar wake assumption is relaxed, in-plane planform modifications can reduce the induced drag. Recent in-plane modifications have focused on sheared wing tips and crescent shaped planforms. Induced drag can also be reduced by modifying the flowfield near the tip to reduce the intensity of the wing tip vortex. Devices tested to diffuse the tip vortex include wing tip mounted turbines and vanes and air injection (or blowing) at the tip. Wing planform modifications and spanwise wing tip blowing will be discussed in the following sections.

Planform modifications

Much of the early experimental work aimed at reducing induced drag involved planform modifications out of the wing plane. Some of these planform modifications are shown in figure 2. The modifications first took the form of endplates at the wing tips. References 5 and 6 are examples of early and modern endplate research. In general, end plates increase the lift curve slope, reduce the induced drag, and increase the maximum lift coefficient. Benefits decrease as the wing aspect ratio increases. However, end plates also increase the profile drag because of the additional wetted area. The net result is often a small increase in the lift to drag ratio over a small range of lift coefficients but a decrease in the maximum lift to drag ratio. Analytical studies indicated that an extension of the wing span by placing the area of the endplate in the plane of the wing is more effective in reducing the induced drag. These early endplates were not designed with the flowfield at the tip in mind. Development of analytical wing design techniques and research

involving the wing tip trailing vortex hazard have led to a better understanding of the flowfield near the wing tip. New devices such as winglets and wing tip sails were designed using these techniques with the tip flowfield in mind.

Winglets are small, nearly vertical, winglike surfaces mounted at the wing tips. The primary surface is mounted from the aft part of the tip and extends upward. The secondary surface is mounted forward of the primary surface and extends downward. Winglets are designed to provide a larger reduction in drag than would be obtained by extending the span with the same weight penalty. The design approach used to develop winglets is described in reference 7. Winglets reduce the induced drag coefficient and can provide a small increase in lift coefficient. They increase the section lift coefficient near the wing tip. Tests of winglets on a model of a transport wing in reference 8 showed changes in the pressure distribution over the outer 10 percent of the span, or about one tip chord. Winglets increase the wing root bending moment slightly. Flow surveys behind a wing with and without winglets showed that winglets diffuse the tip vortex. Crossflow velocities, as well as the wing downwash, were significantly reduced at the measurement station. The net result is that winglets provide an increase in the lift to drag ratio near the design condition. However, similar to the effect of endplates, the drag on a wing with winglets is usually larger than the drag without winglets at off design conditions.

Wing tip sails are a series of small chord wings staggered along the length of the wing tip. The incidence of each of these wings is set to produce a component of resultant force in the free stream direction, much like the sails on a yacht. Sails are staggered to form a cascade in which the induced effect of the forward sail reduces the local angle of attack on the following sail to prevent stall or separation. Details of the development of tip sails are presented in references 9 and 10. Experimental results indicated that wing tip sails increase the drag at zero lift, reduce the induced drag, and increase the wing root bending moment. Increasing the number of sails reduces the induced drag by diminishing amounts and increases the profile drag.

In-plane modifications to the wing planform can reduce the induced drag if the wake is not planar. One such modification is the sheared wing tip shown at the bottom of figure 2. This modification shifts the lifting elements in the plane of the wing without changing the area of the lifting surface. Thus, it would not be expected to incur much of a change in the profile drag if the effects of the increased spanwise flow in the boundary layer are small. A reduction in the induced drag would be expected to increase the maximum lift to drag ratio. An analytical investigation of the effect of shearing the wing tip using a nonplanar wake analysis is presented in reference 11. Analysis showed that shearing the wingtip increased the Oswald efficiency factor, e, up to 5 percent while increasing the wing root bending moment less than 1 percent. The associated experimental investigation in reference 11 showed that shearing the wing tip has no measurable effect on the lift but that drag was reduced at all lifts tested and the Oswald efficiency factor was increased up to 3 percent. There is no drag penalty at the off design conditions. The measured increase in the maximum lift to drag ratio was 4.6 percent. As expected, moving the lifting surface aft by shearing the wing tip improves the longitudinal static stability. Shearing the wing tips increases the torsional moment at the wing root and increases the structural complexity of the wing.

Modifications to the wing planform often involve an increase in wing root bending moment and an increase in the structural weight. Wing modifications such as winglets are designed to be effective over a small part of the operating envelope of the aircraft. Extension of the benefits to a wider range of flight conditions would involve the additional complication of variable geometry winglets. However, this is not cost effective with current technology. The winglet study cited above (reference 8) indicated that the winglet diffused the wing tip vortex. Other techniques which diffuse the wing tip vortex could provide a reduction in induced drag. One such technique is spanwise blowing at the wing tip. An advantage of using a jet is that the jet configuration (exit size, velocity, and direction) can be changed relatively easily for different flight conditions so that the benefits would not be restricted to a small part of the operating envelope. Development work on this concept is described in the following section.

Spanwise blowing at the wing tip

Wing tip blowing entails exhausting one or more jets of air from the wing tip in a generally spanwise direction as shown in figure 3. The parameter used to characterize the jet blowing magnitude is the jet momentum coefficient, C_μ, which is defined in this paper as:

$$C_\mu = \frac{\dot{m}_j V_j}{q_\infty S} \tag{1.11}$$

The jet can be one continuous sheet or be several smaller, discrete jets. Air for the jet can be air bled from the propulsion system, removed from the flow by a laminar flow control system, or ducted from the region of the stagnation line along the wing leading edge as shown in figure 4. If engine bleed air is used, the ram drag of the extra air must be included when evaluating the results. Use of air ducted from the leading edge would provide a passive system with the effect of ram drag already included. However, only relatively small mass flow rates would be available from such a system. Early work in wing tip blowing involved large jet momentum coefficients and jet chords which were a large fraction of the wing chord like the continuous jet in figure 3. Resulting required mass flow rates were quite large. Recent studies have addressed smaller jet momentum coefficients and multiple, shorter chord jets. This section outlines the development of wing tip blowing which was usually aimed at augmenting the lift of low aspect ratio wings. Almost all of the experimental investigations used semispan wings. Characteristics of the models used are found in table I.

The first published work to evaluate spanwise blowing at the wing tip was reference 12, published by Ayers and Wilde of the Cranfield College of Aeronautics in England in 1956. This experimental study used a swept, constant chord wing with an aspect ratio of 1.4. Measurements included the total forces and moments, chordwise pressure distributions at several spanwise stations, and flow visualization on and above the model surface. Results showed that spanwise blowing increases the lift curve slope, reduces the drag at a given lift, and changes the span load

distribution of the wing. These results are consistent with an increase in the effective aspect ratio. Blowing helped keep the boundary layer from separating so that the maximum lift coefficient increased with blowing. It significantly increased the wing loading near the tip although the effect of blowing could be seen across the span of the low aspect ratio wing. Flow visualization demonstrated that the wing tip vortex moves outboard when blowing is applied. Two counter-rotating vortices associated with the tip jet flow were discovered. The strength of the upper vortex increased whereas the strength of the lower vortex decreased as the angle of attack increased. The upper jet vortex would merge with the wing tip vortex and the combined vortex moved in a spanwise direction away from the wing tip as the strength of the blowing increased.

In 1957, Smith and Simpson conducted a similar investigation of spanwise blowing at the wing tip. This investigation, described in reference 13, used a rectangular, aspect ratio 3.0 wing. Three jet dihedral angles were tested: 0°, -60°, and -90°. For the -60° jet deflection, two different jet exit heights were tested. Four chordwise rows of model surface pressures were integrated to determine the section normal force coefficient at each station. Normal force was resolved into the lift and drag directions and a smooth line faired through the data and extrapolated to the root and the tip. Extrapolation of the results to the tip is questionable and leads to optimistic results. Aerodynamic results are similar to those of Ayers and Wilde above. A tuft grid was placed one chord downstream of the trailing edge to determine the effect of blowing on the tip vortex location. As was found above, increasing the tip blowing with the jet dihedral set to 0° moved the tip vortex outboard and upward. Increasing the tip blowing with the jet dihedral set to -60° moved the tip vortex outboard and slightly downward. Limited data with the reduced jet height showed only a small effect.

White, in 1960, investigated spanwise blowing on a wing with a 20 percent chord flap. Jet momentum coefficient was varied from 0.0 to about 1.0. Results, reported in 1963 in reference 14, showed trends similar to those of Ayers and Wilde. Trends were the same for the flap retracted and for the flap deflected. Moderate blowing moved the center of lift outboard. Increasing C_μ

above 0.50 did not change the aerodynamic coefficients. Such large values of jet blowing are not practical for drag reduction because of the large amount of power required to generate them.

In 1962, Carafoli developed a simple theory to model spanwise blowing along the full length of the chord at the wing tip. Details of the method are presented in reference 15. The jet was divided into strips in the spanwise direction. Assuming a simple force distribution on the strip, the radius of curvature of the jet was determined using the law of conservation of momentum. A fictitious wing was defined which combined the actual wing with a fluidic spanwise extension at the wing tip equal to the jet radius of curvature to determine the circulation distribution. Wing lift was determined from the bound circulation between the actual wing tips. The theory was compared to experimental results from an aspect ratio 2.0 wing. No details of the wing or the experimental setup are available. Agreement was fair over an angle of attack range up to stall and jet momentum coefficients from .25 to 1.75. Results from the experiments are consistent with previous research in that blowing increases the lift curve slope and increases the maximum lift coefficient. The calculated component of the jet in the lift direction was subtracted from the total lift to determine the wing lift. The increment in wing lift due to blowing was nearly the same for the 0° and the -45° jet dihedral angles. When the direct component of the jet momentum in the lift direction is included, the total increment in lift is greater for the -45° jet dihedral. The success of these studies led to additional experimental studies on wings with aspect ratios of 0.6, 1.0, 1.5, and 2.0. Results, published in 1969 in reference 16, were similar to those obtained at Cranfield. Tests showed that the increases in lift became larger as the aspect ratio decreases. The theory, refined in reference 17 to remove some of the simplifying assumptions, followed the trends of the experimental results but did not match the levels very well. Extended to include the effects of jet dihedral in reference 18, the theory predicts a small increase in wing lift when the jets are deflected downward.

Lloyd presented results from a full span, low aspect ratio wing at large jet momentum coefficients in reference 19. Results for lift were consistent with previously published works.

Increasing the blowing at a constant lift was found to reduce the drag. The maximum lift to drag ratio increased with increasing jet momentum coefficient. Effects of the air supply line crossing the balance were not discussed and the ram drag associated with the formation of the high jet momentum coefficients was not considered.

Scheiman and Shivers tested a cylinder with a blowing slot mounted on the tip of a rectangular wing to determine the effect of tip blowing on the wing tip trailing vortex. Results, presented in reference 20, are not consistent with most of the previously published results. Small amounts of blowing had no discernible effect on the lift and drag. Moderate blowing increased both the lift and the drag. The addition of blowing did not have a significant effect on the tip vortex location. No reason is given why these results are not in general agreement with the previously published results.

These works comprise the early, exploratory studies on the effects of wing tip blowing. In general, the aspect ratio was small, the jet extended across most of the length of the wing tip chord, and the tests were conducted at large jet momentum coefficients. Spanwise blowing increases the loading across the span of a low aspect ratio wing, with the largest increases occurring near the tip. It moves the tip vortex outboard, increases the lift curve slope, and increases the maximum lift coefficient. Little faith is placed in drag measurements computed from chordwise pressure distributions in reference 13. Conflicting results were reported for the effect of tip blowing on drag. Accurate measurement of drag requires using a balance and special attention to the effects of the airline stiffness and the airline pressure which apparently were not adressed in these investigations. These early studies were followed by more detailed studies described below, most of which were conducted in the 1980's.

Tavella et al. at Stanford University tested a rectangular wing with spanwise blowing at the wing tip. The wing had a movable endplate to vary the aspect ratio. Model surface pressures and flowfield data in the wake are presented in references 21 and 22. Blowing increased the suction

on the upper surface with the most pronounced effect near the wing tip. These and other published results were used to develop scaling laws to predict the effect of jet momentum coefficient, angle of attack, jet dihedral angle, and aspect ratio on the increment in lift. Development of these scaling laws is presented in references 23 and 24. Assuming the jet extended the full length of the chord and using the mathematical definition of radius of curvature, a second-order, ordinary differential equation for the jet path was developed. The equation was integrated until the direction of the jet path reached vertical. This distance was considered to be the effective wing span. The scaling law predicted the following expression for the increment in lift coefficient:

$$\Delta C_L \propto f(AR) \left[C_\mu \left(1 - \sin \delta_j \right) \right]^{\frac{2}{3}} \alpha^{\frac{1}{3}} - \frac{C_\mu}{AR} \sin \delta_j \cos \alpha \qquad (1.12)$$

Results from references 16 and 21 were used to assess this expression. Reasonable agreement was obtained for the dependence on the jet momentum coefficient and angle of attack; however, the agreement for the aspect ratio dependence was only fair. The scaling law suggests that downward deflected jets (negative values of δ_j) improve the lift through both terms of the above expression.

Additional experiments using the same model were carried out to look at other jet configurations. The jet was displaced upward from the tip centerline, deflected downward, and both displaced downward and deflected upward. Results, presented in references 25 and 26, showed that displacing the jet towards the upper surface increases the increment in lift above that found for the jet on the centerline. As before, the effect is seen across the span with the largest increase occurring in the region of the wing tip. These results were in good agreement with the above scaling law. Deflecting the jet downward also produced a larger increment in lift than that produced by the undeflected jet. The improvement was not as great as that which was obtained for the upward displaced jet. These experimental results were only in fair agreement with the scaling laws. Experimental results for the combination downward displaced and upward deflected jet showed a deterioration in lift and did not follow the scaling laws. The flowfields behind the undeflected jet, displaced jet, and deflected jet were surveyed with a five-hole, flow angularity

probe and the results are presented in reference 27. At lower angles of attack and higher jet momentum coefficients, a second vortex rotating in the direction opposite to the wing tip vortex was found. This second vortex is attributed to the pair of counter-rotating vortices formed when a jet exhausts into a cross flow. The size of the primary vortex increases with angle of attack. Addition of a small amount of blowing increases the size of the primary vortex. Further increases in blowing do not have an effect on the vortex size. Strength of the primary vortex increases with increasing jet momentum coefficient and increasing angle of attack. The secondary vortex increases in strength with blowing coefficient and decreases in strength with angle of attack until it eventually cannot be detected. The wing tip vortex moves outboard and upward with blowing and inboard with angle of attack. Spanwise movement of the vortex with increasing jet momentum follows the scaling law reasonably well for the undeflected jet but only fairly for the deflected jet.

Briggs and Schwind undertook an experimental investigation of wing tip blowing on eight low aspect ratio, tapered wings which were representative of fighter wing planforms. Only the total forces and moments were measured. Results, presented in references 28 and 29, showed that the increment in lift associated with small amounts of blowing is significantly reduced as the taper ratio increases.

The above investigations primarily studied the effect of spanwise blowing on the lift of low aspect ratio wings. Values of jet momentum coefficient were typically quite large, ranging from about 0.1 to 1.75. Such values are probably larger than the thrust required to overcome the vehicle drag and are not practical for drag reduction studies. Jet momentum coefficient can be reduced by reducing the jet exit area or the jet exit velocity. Jet exit area can be reduced by replacing a single, continuous jet with a series of discrete jets with much shorter chords, as shown at the bottom of figure 3.

In 1982, Wu et al. proposed in reference 30 the use of several, small discrete jets rather than the single, long, continuous jet. The combined exit area of the discrete jets is smaller than

the area for a single, full chord jet. Experiments were run at lower blowing coefficients, typically between 0.001 and 0.008, using a rectangular, aspect ratio 3.4 wing with three discrete jets. Although not obvious from the data presented, the authors reported that the discrete jets increased the lift distribution across the wing span. Test results with discrete jets indicated that the effect of blowing is strongly dependent on the location and the orientation of the jet exhaust. A significant improvement in the wing normal force coefficient was obtained for a single discrete jet located near the trailing edge and operating at C_μ= 0.0008.

These preliminary tests were followed by additional wind tunnel tests reported in references 31 and 32 and water tunnel tests reported in references 33 and 34. The wind tunnel tests used two interchangable wing tips, each with three discrete jets. Results were similar to those obtained in the preliminary tests. Water tunnel tests used colored dyes for flow visualization to study the flowfield near the wing tip and the wing tip vortex. Spanwise wing tip blowing with discrete jets was found to displace the wing tip vortex upward and outward. The middle and rear jets were more effective in displacing the wing tip vortex outward. The rear jet was most effective in raising the wing tip vortex. Flow visualization showed the two counter-rotating vortices associated with the tip jet. At increasing angles of attack, one of the counter-rotating vortices would merge with the wing tip vortex. Other secondary vortices appeared in the wing tip region depending on the jet configuration, an indication of the complexity of the combined jet and wing flowfields. Discrete jets produce the same types of effects as long continuous jets, although the magnitude of the effects are smaller.

A mathematical model was developed and described in reference 34 to study the effect of the counter-rotating jet vortices on the wake roll up. The wake was represented by discrete vortices extending to infinity in both directions. Jet counter-rotating vortices were represented by two infinite, straight vortex filaments located symetrically with respect to the tip. The discrete vortices were allowed to be convected by the local velocity field. The mathematical model showed that the presence of the two counter-rotating vortices reduced the downwash inboard, reduced the

strength of the rolled up tip vortex, and moved the tip vortex outboard.

Smith, et al. conducted a flow visualization study, described in reference 35, in a water tunnel to investigate the effect of blowing on the wing tip vortex on an aspect ratio 6 wing. Problems with making the wing tip vortex visible limited the usefulness of the study. The path of the jet was visible and was used to surmise the effect of blowing on the wing tip vortex location.

Tip blowing increases the suction on the upper surface, increases the lift near the tip, increases the total lift and the lift curve slope, displaces the rolled up tip vortex outward, and diffuses the rolled up tip vortex. These effects suggest an increase in the effective aspect ratio of the wing. An increased effective aspect ratio will result in a reduced induced downwash on the wing. At a given angle of attack, the reduced downwash will lead to an increase in lift and a decrease in induced drag. Thus, spanwise blowing has the potential to increase the wing aerodynamic efficiency.

Most previous tip blowing experiments investigated lift augmentation of low aspect ratio, rectangular wings. Efficiency of such wings is poor so relatively small changes will lead to large improvements in efficiency. Benefits from blowing should become smaller as the aspect ratio increases and the taper ratio decreases. Jet momentum coefficients used in the experiments with continuous jets are too large to be of practical use on the moderate aspect ratio wings found on a commercial subsonic transport. However, jet momentum coefficients used in the experiments with discrete jets are much more practical. For a typical transport with a drag coefficient of 0.0300, the total engine thrust (momentum) coefficient would be 0.0300. Discrete blowing with a jet momentum coefficient of 0.0030 would be an acceptable fraction of the total installed engine momentum if the drag reduction exceeded 30 counts. Experiments indicated the benefits from blowing are dependent on the jet exhaust location and orientation. Discrete blowing can be a practical means of improving the aerodynamic efficiency of wings.

The goal of this investigation is to systematically investigate the potential aerodynamic

benefits from spanwise blowing at the tip of a wing representative of one found on a commercial transport. The following tasks were identified to accomplish this goal:

(1) Develop and apply a simple analytical model to investigate the importance of different discrete jet parameters.

(2) Use published results and results from the simple analytical model to select parameters to be investigated in the wind tunnel experiments.

(3) Design the wind tunnel experiments to measure the wing forces and moments accurately.

(4) Conduct wind tunnel experiments to systematically vary the selected jet parameters

(5) Extend the wind tunnel data base for information not measured through computations using a Navier-Stokes solver.

CHAPTER II

APPROACH

Spanwise blowing has been shown to increase the lift across the span of low aspect ratio wings and to alter the roll up of the wing tip vortex. These benefits were relatively large since low aspect ratio wings are relatively inefficient. Test results suggest that spanwise blowing increases the effective aspect ratio of the wing. Spanwise blowing can possibly increase the lift and reduce the induced drag on larger aspect ratio wings. This chapter describes the approach taken to assess the potential aerodynamic benefits from spanwise blowing at the wing tip of a moderate aspect ratio wing. Since the baseline, moderate aspect ratio wing was more efficient than the previously tested wings, the benefits may not be as large as in previous tests. A mathematical model of a wing with spanwise blowing at the tip was developed and used to investigate the effect of several jet blowing parameters on the roll up of the wing tip vortex. Mathematical model results were used to select the parameters to be used in the wind tunnel experiments. Experiments were designed and conducted on a transport type wing with blowing at the wing tip. Special care was taken to obtain accurate balance measurements with air supply lines crossing the balance. The longer chord jets were not tested at the higher Mach numbers because the air supply line could not provide large enough mass flow rates to produce practical jet momentum coefficients. Therefore, a Navier-Stokes solver was modified to simulate a wing with spanwise blowing at transonic Mach numbers and used to extend the results for the longer chord jets from the wind tunnel experiments to a higher Mach number.

No complete mathematical model for spanwise blowing from discrete jets at the wing tip was identified in the literature survey. A simple, inexpensive model was needed to assess the importance of different discrete jet parameters. Mathematical models of the flowfield of a wing and of a jet exhausting into a cross flow were extended and combined to simulate a wing with blowing from discrete jets at the tip. Development of this model is described in Chapter III. The

model is implemented as a FORTRAN computer program. Application of the model is presented in Chapter IV. Various options of the program are tested and the parameters for the wake integration selected. The program demonstrated some of the published experimental trends. The effects of different jet parameters on the wake were assessed using the program. The results were were used to select those parameters to be used in the wind tunnel investigation.

An experimental investigation was conducted to study the the effect of spanwise blowing on the aerodynamic characteristics of a moderate aspect ratio, swept wing. A semispan wing with two separate air channels was designed and fabricated. Seven interchangable tip sections were built to study the effects of momentum, length, location, and orientation. The wing was suspended on a semispan strain gage balance. Special attention was given to the effects of the airline on the balance calibration. Five chordwise rows of pressure orifices were installed in the wing. The wing was tested in the NASA Langley 7- by 10-foot High Speed Tunnel at Mach numbers up to 0.72. Details of the model, the instrumentation, and the wind tunnel are presented in Chapter V. Experimental results are presented and analysed in Chapter VI.

To expand the experimental data base, a Navier-Stokes solver for moderate aspect ratio wings moving at subsonic or transonic Mach numbers was modified to simulate a wing with spanwise blowing at the tip. A special grid was generated to accommodate the region of large velocity gradients along the jet path. The modified solver was validated using the experimental results from Chapter VI as well as flow visualization photographs from a water tunnel test conducted to support this project. The validated solver was used to supplement the experimental results. These efforts are described in Chapter VII.

The experimental results from Chapter VI and the analytical results from Chapter VII form the basis for the conclusions presented in Chapter VIII.

CHAPTER III

SIMPLIFIED MATHEMATICAL MODEL

A mathematical model was needed to investigate the effects of jet momentum, length, location, and orientation on the wing aerodynamic characteristics. These results were used to select the more promising configurations for wind tunnel testing. The model needed to be quick and inexpensive to use since there were many reasonable combinations of parameters. No mathematical model for spanwise blowing from a discrete jet at the wing tip was identified in the literature survey. When these calculations were being performed, Navier-Stokes solvers were not sufficiently developed, computer speeds were not sufficiently fast, and computer costs were very high. Navier-Stokes solvers were not practical for preliminary design and analysis of tip blowing configurations. A simple mathematical model which predicts the proper trends and is quick and inexpensive to use was needed. The vortex lattice model has been developed for a thin wing, the segmented vortex sheet has been developed for the rollup of the wing wake, and an empirical, discrete vortex model has been developed for a jet in a cross wind. These three models have been modified and combined into a single model to represent a wing and its wake with discrete blowing at the wing tip. This chapter describes each of the three models and their combination into a simple mathematical model for spanwise blowing at the wing tip.

Results from several experiments, such as those of references 27 and 34, indicated that the counter-rotating vortices associated with the tip jet flow field interact with the wing tip vortex. A mathematical model of the vorticity of the wing and its wake combined with a model of the vorticity of the jet was formulated. The model uses a vortex lattice to represent the wing and a pair of counter-rotating vortices to represent each jet. The sheet of vorticity shed from the wing and the path of the counter-rotating vortices are allowed to deform as they are convected by the local flow field. This chapter describes the development of this mathematical model.

Wing Model

The wing model is a lattice of horseshoe vortices in which the wing is divided into trapezoidal panels with the parallel sides of each panel aligned with the free stream velocity and the other sides aligned along lines which are a constant fraction of the local wing chord. A horseshoe vortex is placed on each panel with the bound vortex on the quarter chord line of the panel and the trailing vortices extending downstream. A sketch of the assumed layout is presented in figure 5. The initial wake shape is flat. No flow passes through the lift control points, which are located at the midspan position of the three quarter chord line of each panel. The downwash induced by all the horseshoe vortices at a control point is cancelled by the component of the free stream velocity in the normal direction. At the control point on panel m, the downwash, w_m, from the horseshoe vortex with a circulation strength, Γ_k, on panel k can be expressed as:

$$w_m = A_{m,k}\,\Gamma_k \qquad \text{(no sum on k)} \tag{3.1}$$

The influence coefficient, $A_{m,k}$, is a simple function of the corner points of the horseshoe vortex, k, and the location of the control point, m. Derivation of the influence coefficient, $A_{m,k}$, may be found in reference 36. Summing the contribution from each horseshoe vortex, the downwash at control point, m, from the wing can be expressed as:

$$w_m = \sum_{k=1}^{n} A_{m,k}\,\Gamma_k \tag{3.2}$$

where n is the number of panels on the wing. Downwash induced by the jet counter-rotating vortices also must be included. At the control point, m, the total downwash is the sum of the downwash from the wing and the downwash from the jet.

$$w = w_m + w_j = \sum_{k=1}^{n} A_{m,k}\,\Gamma_k + w_j \tag{3.3}$$

The method to determine the downwash from the jet, w_j, is discussed in the section describing the

jet model. After dividing both sides of equation 3.3 by the free stream velocity, the left hand side, $\frac{w}{V_\infty}$, must equal the local slope of the airfoil, θ_m, at the control point m.

$$\theta_m = \frac{w}{V_\infty} = \sum_{k=1}^{n} A_{m,k} \frac{\Gamma_k}{V_\infty} + \frac{w_j}{V_\infty} \tag{3.4}$$

The local slope, θ_m, is the sum of the wing root angle of attack, local wing twist, and the slope of the airfoil camber line.

$$\theta_m = \alpha + \theta_{twist} + \frac{dz}{dx} \tag{3.5}$$

The result is a system of n nonhomogeneous, linear, algebraic equations

$$\sum_{k=1}^{n} A_{m,k} \frac{\Gamma_k}{V_\infty} = \theta_m - \frac{w_j}{V_\infty} \tag{3.6}$$

which can be solved by Gaussian elimination for $\frac{\Gamma_k}{V_\infty}$.

Jet Model

Previous studies of wings with spanwise blowing from the wing tip indicate that the effects of blowing are dependent on the jet momentum. Different definitions for the nondimensional jet momentum coefficient have been used by different authors. In this paper, the jet momentum coefficient will be defined using the free stream dynamic pressure and the wing reference area (exposed planform area) as follows:

$$C_\mu = \frac{\dot{m}_j V_j}{q_\infty S} \tag{3.7}$$

Previous studies of a jet exhausting into a cross flow have shown that two counter-rotating vortices are associated with the jet as shown in figure 6. The path, separation, and strength of the

counter-rotating vortices are functions of the effective jet velocity ratio defined as follows:

$$V_e = \frac{V_j}{V_\infty} \tag{3.8}$$

However, induced effects from spanwise blowing at the tip depend on the jet momentum coefficient, C_μ, not the velocity ratio, V_e. If the jet and free stream densities are assumed to be equal, the jet momentum coefficient is related to the jet velocity ratio by:

$$C_\mu = \frac{2\,A_j}{S} V_e^{\,2} \tag{3.9}$$

In the mathematical model, the effect of the jet will be represented by two continuous, segmented vortex filaments. A sketch of the flowfield associated with a jet in a cross wind is shown in figure 6. An empirical model was used to determine the path, separation, and strength of the two vortices. Fearn and Weston published experimental results in reference 37 for a round jet exhausting in a direction normal to the free stream. This was extended to include other exhaust directions in reference 38. Thames and Weston tested aspect ratio 4, rectangular jets at various injection angles and reported the results in reference 39. These authors used a power law to represent the experimental results. Expressions for the nondimensional vortex path $\left(\frac{y_j}{d_e}\right)$, separation $\left(\frac{h_j}{d_e}\right)$, and strength $\left(\frac{\Gamma_j}{2\,V_\infty\,d_e}\right)$ as a function of the jet velocity ratio as shown in equations 3.10, 3.11, and 3.12.

$$\frac{y_j}{d_e} = .9201\ V_e^{.8821} \left(\frac{x_j}{d_e}\right)^{.3367} \tag{3.10}$$

$$\frac{h_j}{d_e} = 0.305\ V_e^{.6667} \left(\frac{x_j}{d_e}\right)^{.3333} \tag{3.11}$$

$$\frac{\Gamma_j}{2\,V_\infty\,d_e} = 1.420 \left(\frac{x_j}{d_e}\right)^{-.6666} \tag{3.12}$$

Counter-rotating vortices from the tip jet induce a downwash at each control point. The

nondimensional vortex strength, path, and spacing are first determined in a jet axis system as shown in figure 6 using the proper empirical constants and velocity ratio. The jet path and spacing are then rotated for the specified jet dihedral angle, δ_j, and multiplied by the effective jet diameter, d_e, to obtain the location of the discrete vortex segments in the wing axis system. The nondimensional jet downwash at each control point on the wing, $\left(\frac{w_j}{V_\infty}\right)$, for equation 3.6 is computed by applying the Biot-Savart law for each segment of the jet counter-rotating vortices.

Wake Roll Up

The sheet of vorticity shed from a wing will self-deform with most of the vorticity rolling up into a well defined pair of wing tip vortices as shown in figure 7(a). Addition of vorticity from the tip jets will alter the roll up of the wing tip vortex. Previous attempts to model the roll up of the vorticity in the wake have represented the vorticity by multiple, infinite, discrete vortex filaments extending from the bound vortex as shown in figure 7(b). Filaments, initially placed in the wing plane, are convected by the local velocity field. The position of a vortex filament is found by integrating the induced velocity at that point with time. As filaments near the tip roll up in a spiral, they can come so close to each other that the induced velocity becomes very large. The resulting large displacement of the outermost filament often causes that filament to cross the line connecting the other vortex filaments which represent the vortex sheet as shown in figure 7(b). Once the sheet is pierced, the model no longer represents a self-deforming vortex sheet. An alternate approach is needed which delays this instability. Fink and Soh showed in reference 40 that the motion of an infinitely long sheet of vorticity cannot be represented by the motion of multiple discrete vortices. The self-induced velocity at a control point should be determined by integrating the vorticity distribution across the sheet. A technique for integrating the induced effect of the continuous vorticity distribution across an infinitely long sheet was developed in reference 40. That technique was modified to calculate the induced effect across a semi-infinite vortex sheet behind a wing. The derivation of the modified technique, presented below, follows the

derivation presented in reference 40.

Deformation of the vortex sheet at a given position in the wake is treated as a two-dimensional problem. The complex conjugate of the local velocity induced by the wake, $\bar{q}_w$, at a point z_j, is the integral of the vorticity distribution over the contour C, as shown in the top of figure 8.

$$\bar{q}_w(z_j) = \frac{1}{4\pi i} \int_C \frac{\gamma(s)\, ds}{z_j - z(s)} \tag{3.13}$$

The initial wake shape is flat, extending from wing tip to wing tip. The initial vorticity distribution, $\gamma(s)$, is obtained by numerically differentiating the bound circulation distribution on the wing. The motion of the vortex sheet is determined by integrating the local velocity at a set of n pivot points on contour C. The contour is simplified to n straight segments with a pivot point within each segment as shown in figure 8. From the Biot-Savart law, the conjugate of the complex velocity at the pivot point z_j, induced by a vortex sheet located on the contour C may be written

$$\bar{q}_w(z_j) \approx \sum_{k=1}^{n} \frac{1}{4\pi i} \int_{seg\ k} \frac{\gamma_k(\sigma)\, d\sigma}{z_j - z(\sigma)} \tag{3.14}$$

The vorticity distribution along a segment, γ_k, may be written as a Maclauren series with the origin selected to coincide with the pivot point

$$\gamma_k(\sigma) = \sum_{p=0}^{\infty} \frac{\gamma_k^{(p)} \sigma^p}{p!} \tag{3.15}$$

where σ is the distance along the segment from the pivot point z_k and $\gamma_k^{(p)}$ is the p^{th} derivative of the vorticity evaluated at the pivot point (σ=0). The denominator may also be written as a Taylor series about z_k

$$\frac{1}{z_j - z(\sigma)} = \frac{1}{z_j - z_k} + \sum_{m=1}^{\infty} \frac{(z_k - z(\sigma))^m}{(z_j - z_k)^{m+1}} \tag{3.16}$$

The segment k has an inclination of θ_k with respect to the real axis. The complex expression

z_k - $z(\sigma)$ has a magnitude σ and an argument θ_k and can be represented by $\sigma\, e^{i\theta_k}$. Substituting this expression into the series of equation 3.16 and then substituting equations 3.15 and 3.16 into equation 3.14 yields

$$\bar{q}_w(z_j) = \sum_{k=1}^{n} \frac{1}{4\pi i} \left[\int_{-\Delta s_{k_l}}^{\Delta s_{k_u}} \frac{\gamma_k(\sigma)\, d\sigma}{z_j - z_k} + \int_{-\Delta s_{k_l}}^{\Delta s_{k_u}} \sum_{m=1}^{\infty} \frac{\sigma^m e^{im\theta_k}}{(z_k - z_j)^{m+1}} \times \sum_{p=0}^{\infty} \frac{\gamma_k^{(p)} \sigma^p}{p!}\, d\sigma \right] \tag{3.17}$$

where Δs_{k_u} and Δs_{k_l} are the distances to the upper and lower endpoints of the segment respectively. The integrals in the above expression can be easily evaluated for all segments where $j \neq k$. The integral of the vorticity strength along the segment is the change in circulation along the segment. The resulting expression, after defining a new summation index l where $l = m+p-1$, for $j \neq k$ is

$$\bar{q}_w(z_j) = \sum_{k=1}^{n} \frac{1}{4\pi i} \left[\frac{\Gamma_k}{z_j - z_k} + \sum_{m=1}^{\infty} \frac{e^{im\theta_k}}{(z_k - z_j)^{m+1}} \times \sum_{l=m+1}^{\infty} \frac{\gamma_k^{(l-m-1)}}{l(l-m-1)!} \left[\Delta s_{k_u}^l - (-1)^l \Delta s_{k_l}^l \right] \right] \tag{3.18}$$

For j=k, the Cauchy principal value of equation 3.17 is

$$\bar{q}_w(z_j) = \frac{-e^{-i\theta_k}}{2\pi i} \left[\gamma_k^{(0)} \ln\left(\frac{\Delta s_{k_u}}{\Delta s_{k_l}}\right) + \sum_{p=1}^{\infty} \frac{\gamma_k^{(p)}}{p \cdot p!} \left(\Delta s_{k_u}^p - (-1)^p \Delta s_{k_l}^p\right) \right] \tag{3.19}$$

The total velocity induced at point z_j is simply the sum of expressions in equations 3.18 and 3.19. Note that if the pivot point is at the midpoint of the segment ($\Delta s_{k_u} = \Delta s_{k_l}$), the logrithmic term is zero and the contribution to the velocity of the even powers of Δs_k is zero. The first order approximation (the p summation ranges from 0 to 1) was chosen to compute the local velocity, resulting in

$$\bar{q}_w(z_j) = \frac{1}{2\pi i} \sum_{k \neq j} \frac{\Gamma_k}{z_j - z_k} - \frac{e^{i\theta_j}}{2\pi i} \left[\gamma_k^{(0)} \ln\left(\frac{\Delta s_{k_u}}{\Delta s_{k_l}} \right) + \gamma_k^{(1)} \left(\Delta s_{k_u} + \Delta s_{k_l} \right) \right] \tag{3.20}$$

Dividing both sides by the freestream velocity, V_∞, yields the non-dimensional induced velocity from the wake.

$$\frac{\bar{q}_w(z_j)}{V_\infty} = \frac{1}{2\pi i}\sum_{k\neq j}\frac{\Gamma_k}{V_\infty}\left[\frac{1}{z_j - z_k} - \frac{e^{i\theta_j}}{2\pi i}\left[\frac{\gamma_k^{(0)}}{V_\infty}\ln\left(\frac{\Delta s_{k_u}}{\Delta s_{k_l}}\right) + \frac{\gamma_k^{(1)}}{V_\infty}(\Delta s_{k_u} + \Delta s_{k_l})\right]\right] \tag{3.21}$$

The total velocity is the sum of the induced velocities from the wake, the bound vortex, and the jet.

$$\frac{\bar{q}(z_j)}{V_\infty} = \frac{\bar{q}_w(z_j)}{V_\infty} + \frac{\bar{q}_b(z_j)}{V_\infty} + \frac{\bar{q}_j(z_j)}{V_\infty} \tag{3.22}$$

The change in position of the pivot point is found by integrating the total velocity.

$$\Delta z_j = \int \frac{\bar{q}(z_j)}{V_\infty} V_\infty \, dt = \int \frac{\bar{q}(z_j)}{V_\infty} \, dx \tag{3.23}$$

Note that if the angle between the segments changes drastically, the model no longer accurately represents the vortex sheet as shown in figure 7(c). The numerical instabilities generally appear when the angle change between segments becomes large. As this equation is numerically integrated, the pivot points no longer lie at the midpoint of the segment and the sheet stretches. To correct for this, the segment end points and pivot points are repositioned whenever the sheet has stretched to allow the inclusion of another original length segment. To accomplish this, an arclength is defined with the origin at one endpoint of the contour as shown in figure 8. The arclength to each segment endpoint and to each pivot point is determined assuming that each segment is a straight line. The position of any point on the contour is dependent on the arc length.

$$z = f(s) \tag{3.24}$$

Similarly, the integral of the vorticity from the endpoint of the contour to any point on the

contour is also dependent on the arclength.

$$G = \int_0^s \gamma(\xi)\, d\xi = g(s) \tag{3.25}$$

To compute the new position and sheet strength, the sheet is divided in the desired number of equal length segments. The arc length to each segment pivot point and end point is then computed. The new pivot point and end point locations are determined by interpolating the complex function f(s) and the new sheet strength is determined by interpolating the derivative of the function g(s).

CHAPTER IV

APPLICATION OF THE SIMPLIFIED MATHEMATICAL MODEL

Benefits from blowing with discrete jets are sensitive to the location and the orientation of the jet. The simple mathematical model will be used to predict the benefits from blowing with the discrete jet for various combinations of jet location and orientation. Those combinations with the larger benefits will be used in the wind tunnel experiments. Computations without blowing were used to determine the minimum initial number of spanwise control points and the integration step size so that these two parameters would not have a significant effect on the results. Using these values, the mathematical model was used to predict the effects of jet chordwise location, vertical location, in plane deflection (sweep), and out of plane deflection (dihedral) on the wake rollup.

The simplified mathematical model was used to simulate the flowfield with and without wing tip blowing behind the wing used in references 26 and 27 since that work contains the only surveys of the wake behind a wing with and without wing tip blowing. The wing had a rectangular planform and an aspect ratio of 3.1. The mathematical model allows the initial number of spanwise control points across the wake and the streamwise integration step size to be varied. A suitable value of integration step size and initial number of spanwise control points across the wake was determined first. The wake roll up behind the wing was computed using several different chordwise integration step sizes with initially 80 control points distributed across the wake. The results at one chord behind the wing trailing edge are presented in figure 9. Reducing the integration step size leads to a smoother rollup of the ends of the vortex sheet with an increased number of spirals. As the spiral winds up tightly at the end of the sheet, large angle changes occur between adjacent segments. This violates one of the assumptions used in developing the model. When a large angle change occurs, the sheet will cross itself, invalidating the results there. The large angle change can be reduced by increasing the initial number of segments, and hence, the segment length. Large differences in the wake shape when the step size is reduced from

0.10 to 0.05 chords indicate that the solution is not numerically converged for a step size of 0.10 chords. Wake shapes for the outer portion of the spirals step sizes of 0.05 and 0.02 are similar; only the innermost portions are different. Reducing the initial spacing of the control points should eliminate the differences in the innermost portion of the spirals. Thus, a step size of 0.05 chords should be adequate for calculations with this mathematical model.

The wake roll up behind the wing was computed for several different numbers of control points across the wake with a constant integration step size of 0.05 chords. Results, presented in figure 10, show very small changes as the number of control points is increased above 100. Thus, for the remaining computations using this simple mathematical model, the integration step size will be 0.05 chords and the number of wake control points will be 100.

The mathematical model was used to show how the path of the rolled up vortex sheet changes with angle of attack. The results at one chord downstream of the trailing edge are presented in figure 11 for two angles of attack. As the angle of attack increases, the vorticity in the outer portion of the sheet is stronger. Higher vorticity leads to larger self-induced velocities. The center portion of the sheet is convected downward a larger distance for the larger angle of attack. Spirals at the ends of the sheet represent the roll up of the vortex sheet into two wing tip vortices. The ends of the sheet have rolled up more turns for the higher angle of attack, concentrating more vorticity in the wing tip vortices. These spirals are centered about a more inboard station at the higher angle of attack. The model predicts that the wing tip vortices move inboard with angle of attack which is consistent with the results from reference 26.

The model was then used to investigate the effect of wing tip blowing from a single, discrete jet located at the quarter chord. A jet with a length to height ratio of 4 was positioned on the chordline. The ratio of the jet exit area to the wing area was 0.00535. Results at several locations downstream of the trailing edge are presented in figure 12. With no blowing, the ends of the vortex sheet move upward and inboard with increasing downstream distance as shown in

figure 12(a). The central portion of the sheet, where the strength of the sheet is low, is convected down by the downwash from the bound vortex as well as the higher strength of the vorticity near the ends of the sheet. The center of the spiral moves inboard. At about two chords downstream (not shown), the center of the spiral stops its upward movement and begins to move down, crossing the plane of the wing at about four chords downstream. The centers of the spirals continue to move inboard.

With blowing, two pairs of counter-rotating vortices are added to the flowfield. The location of these vortices is noted on the plots of the vortex sheet roll up by the circle and the square. The spanwise position, vertical separation, and strength of the jet vortices increase as the jet to freestream velocity ratio, V_e, increases. With moderate blowing ($V_e = 1$), the spanwise location of the jet vortices is relatively close to the wing tip. The jet vortices will distort the roll up of the ends of the sheet. At all downstream locations, the center of the spiral has been displaced outboard and the spiral is distorted over a larger vertical distance as shown in figure 12(b). There are fewer turns of the spiral with blowing, indicating less vorticity located there. Spreading the spiral over a larger area and fewer turns of the spiral are indications that the vorticity is less concentrated. The jet vortices are convected around the spiral by the concentrated vorticity there. The upper vortex of each counter-rotating pair is being drawn into the spiral and the wing tip vortex. These results are similar to those found in reference 27. Results presented therein indicated that blowing displaced the wing tip vortex upward and outward and diffused the wing tip vortex. At an increased level of blowing, ($V_e = 2$), the spiral at the end is again displaced outboard as shown in figure 12(c) but the vertical distortion is reduced. The upper vortex does not show signs of being drawn into the rolled up wing tip vortex. At the higher levels of blowing that were investigated, ($V_e = 3$ or 4), the model predicts that the the sheet does not wind up as many turns so that the vorticity is less concentrated there and that the wing tip vortices are displaced outboard as shown in figures 12(d) and 12(e). The vortices from the jet do not come near the wing tip vortex.

Results from reference 27 indicated that displacing the jet above the chord line displaces the wing tip vortex further outboard and upward compared to the wing tip vortex location for a jet located on the chord line. The single, discrete jet was relocated 0.15 chords above the wing chord. Roll up of the vortex sheet with the vertically displaced jet is shown in figure 13. Comparing the results in figure 12 with those for the jet above the chord line shows that displacing the jet vertically spreads the spiral laterally and inhibits the inward spiral.

Directing the exhaust downward has been found to displace the wing tip vortex a small distance downward and outboard when compared to an undeflected jet. The shape of the roll up of the wing wake with the discrete jet deflected downward 30° is shown in figure 14. When compared with the results for the undeflected jet in figure 12, deflecting the jet downward did not change the spanwise position of the spiral but it did displace it downward slightly. The shape of the wake with the deflected jet is stretched laterally. Since the jet counter-rotating vortices start below the plane of the wing, the upper vortex does not roll around and into the wing tip vortex at the downstream locations shown.

Redirecting the jet exhaust downstream in the plane of the wing (jet sweep) creates a component of thrust opposite the drag direction and produces a direct reduction in drag. The discrete jet located on the chordline was deflected streamwise 30° and the calculated shape of the vortex sheet is shown in figure 15. There is very little difference between the results for the unswept jet in figure 12 and the 30° jet sweep results in figure 15. This suggests that it might be possible to obtain the same effect on the roll up of the vortex sheet with the additional benefit of reducing the drag by the component of the jet momentum in the free stream (or drag) direction.

Moving the jet exhaust aft from the quarter chord location should bring the jet counter-rotating vortices closer to the wing tip vortex. The effect of relocating the jet aft was investigated with the mathematical model by moving the discrete jet from the 25 percent to the 85 percent chord location. The calculated shape of the vortex sheet is presented in figure 16. Compared to

the results at the 25 percent chord location in figure 12, moving the jet rearward moves the rolled up portion of the sheet upward and outward. It also elongates the shape of the rolled up wake. The distortion of the wake for the rearward displaced jets is much larger at moderate levels of blowing ($V_e = 2$).

This mathematical model of a wing with a discrete jet duplicates many of the experimental trends reported in reference 27. Without blowing, the model indicated that the tip vortices move inboard with increasing angle of attack. With spanwise blowing from the chordline, the model shows that blowing displaces the tip vortices outboard and makes them more diffused. The model did not duplicate the upward and outward movement of the tip vortex when the jet is displaced vertically nor did it predict the outward movement when the jet is deflected downward. The results suggest that jets located in the rear portion of the tip and jets deflected rearward may have additional benefits above those found with jets located in the center of the tip and directed spanwise. Discrete jets located near the trailing edge or directed aft may have increased benefits over jets located at the quarter chord and exhausting spanwise. Water tunnel studies described in the literature also indicate benefits associated with aft located, discrete jets. Therefore, the jet configurations to be tested in the wind tunnel will include the jets at different chordwise locations and jets with the exhaust directed downstream.

CHAPTER V

DESCRIPTION OF THE EXPERIMENT

This chapter presents a description of the experiments conducted to investigate the effects of spanwise blowing from the wing tip on the wing aerodynamic characteristics. The description is divided into sections describing the wind tunnel, semispan wing model and wing tip jets, instrumentation and data acquisition, test procedures, and data reduction and corrections.

Wind Tunnel

The experimental portion of this study was performed in the NASA Langley 7- by 10-foot High Speed Tunnel (HST). Descriptions of the tunnel and its support equipment can be found in reference 41. A photograph of the exterior of the tunnel is presented in figure 17, and a sketch of the test section internal components is presented in figure 18. The 7- by 10-foot HST is a single return, closed-circuit, fan-driven wind tunnel which operates at ambient temperature and pressure. All four test section walls are solid. Wooden fairings on the side walls provide a uniform longitudinal Mach number distribution along the centerline of the test section. The test section is 6.58 feet high and 9.57 feet long with a usable length of 10.83 feet. Four anti-turbulence screens are located just upstream of the 17:1 contraction section to provide good flow quality. A 14,000 horsepower variable-speed motor drives the fan to provide a continuous Mach number range from near 0 to 0.94 with the test section empty. The nominal operating envelope of the tunnel is presented in figure 19.

The tunnel has a sting model support system for full span testing and a side wall turntable on the left wall for semispan testing as shown in figure 18. For this investigation, the model was mounted on the side wall turntable with the sting model support system stowed along the floor of the test section to minimize any interference.

Two shop air supply sources (110 psia), located outside of the test section, were used as independent air sources for the two jets on the wing tip. Air pressure was manually controlled.

Semispan Wing Model

The model used in this investigation was designed to represent the wing of a business jet or the outer portion of the wing of a subsonic passenger transport. Planforms of several commercial passenger transports were scaled so that each had a wing span of unity. Comparison of the scaled planforms showed that the leading edge sweep, the location of the break in the chord distribution, and the taper in the outboard region were similar for many types of subsonic passenger transports. Values of these parameters, typical of those of the scaled planforms, that were selected for this investigation were: leading edge sweep of 33°, break in the wing chord at the 40 percent semispan location, and a taper ratio of 0.4 outboard of the break in the wing chord distribution.

The model was designed for testing in a pressure wind tunnel with a test section configured for airfoil testing. The half span wing model was to be mounted from one of the turntables normally used to mount an airfoil model. A rake of flow angularity probes was to be installed in place of the airfoil wake rake. After model design and construction were completed, research priorities at the airfoil tunnel changed so that testing of the model would be delayed several years. Test time was obtained in the 7- by 10-foot High Speed Tunnel, a large subsonic, atmospheric wind tunnel with a semispan model support system. The balance support hardware would not fit within the semispan model support system so that it had to be mounted on the flow side of the turntable. A body was designed and fabricated to cover the balance and its support hardware. Details of the design of the model and the support hardware to mount the model in the test section of the large, subsonic wing tunnel are presented below.

The model was designed for a test section 36 inches wide by 89 inches tall. This placed constraints on the size of the wing that could be tested. Model wing tip chord had to be

sufficiently large to allow the tip jets to be machined to reasonable tolerances. Model span should not exceed about 60 percent of the width of the test section to minimize any artificial restraint from the test section side wall on the flowfield near the wing tip or the path of the tip jet flow. Only the outer 60 percent of a typical transport wing is modeled since the induced effects from the tip jets are expected to be very small near the wing root. These constraints led to a selection of a tip chord of 4.0 inches and a semispan of 20.0 inches. A thick airfoil section was desirable to allow for the installation of two, internal high pressure air passages. The wing has no twist so that a straightforward installation of the air passages was possible. A photograph of the wing is found in figure 20. Details of the model are presented in figure 21 and various design and reference parameters are listed in table II. The wing root airfoil reference plane (ARP), which corresponded to the line z=0, was located on the horizontal centerline of the body.

Several factors influenced the selection of the airfoil section used for the wing. The airfoil should be representative of those used on business jets or commercial transports with low drag at moderate lift coefficients and high subsonic Mach numbers. It should be a state of the art design with long runs of natural laminar flow and be relatively thick to provide two air passages to supply the tip jets. The HSNLF(1)-0213 airfoil section came closest to meeting these criteria. It is designed for a Mach number of 0.70 and a lift coefficient of 0.20 at a Reynolds number of 11 x 10^6. At the design conditions, 50 percent of the upper surface and 70 percent of the lower surface boundary layers are laminar. Details of the aerodynamic characteristics of the airfoil section may be found in reference 42. The airfoil is 13 percent thick with sufficient height in the center portion for installation of the air passages. A sketch of the airfoil cross section is presented in figure 21(c) and the airfoil ordinates are listed in table III.

Although designed for a test section 36 inches wide, the wing was tested in the relatively large 7- by 10-foot HST. The wing must be tested in a uniform free stream flow but the test section sidewall boundary layer can be up to 4 inches thick at the sidewall turntable. The wing root must be displaced from the sidewall so that the wing is immersed in a uniform flow. A body

and mounting structure were designed to support the balance and wing. The body height (or diameter) was 6.50 inches, which was the smallest possible diameter to enclose the balance with sufficient clearence to avoid interference. The body radius was not large enough to position the wing root outside the sidewall boundary layer so flat panels, 6.78 inches wide, were used to extend the body. With the clearance between the body and the side wall, the wing root was displaced 10.00 inches from the sidewall.

The body, shown in figure 21(a), was formed in three parts: a forward section, a center section, and an aft section. The forward section, which was 8.00 inches long, consisted of a half body of revolution outboard with 6.78 inch flat panels inboard. Ordinates of the forward section are listed in table IV. The center section of the body, which was 32.50 inches long, consisted of semicircle with a diameter of 6.50 inches outboard with 6.78 inch flat panels inboard. The opening for the wing was rectangular and slightly larger than the wing root. Soft, foam rubber was bonded to the wing within the fuselage to form a seal to prevent flow into or out of the body. The aft section of the body, which was 10.00 inches long, consisted of a half body of revolution 6.50 inches in diameter with 6.78 inch flat panels. Ordinates of the aft section of the body are listed in table IV.

Different tip jet parameters could be tested by using removable wing tip sections as shown in figure 21(b). The same airfoil section used for the wing was also used for the wing tip sections. The tipcap on the end of the wing was defined by revolving a radius equal to one half the airfoil local thickness about the camber line. Each wing tip section had a forward plenum and an aft plenum and each plenum was supplied high pressure air by a separate air passage in the wing. A 0.020 inch inside diameter tube was routed through each air passage and ended in a hook or "J" located in the plenum to measure the total pressure at the tip. Each wing tip section was fastened to the wing by two screws: one just aft of the leading edge and the other at about the 40 percent chord location. Alignment was maintained by two dowels, one in front of the forward plenum and the other behind the aft plenum. With the exception of tip 4, each plenum supplied high pressure

air to a single jet. By using separate plenums, each jet could be tested separately.

The semispan wing was mounted on a five component, strain gage balance. No measurement capability was provided in the side force direction and the accuracy of the measurement of the yawing moment direction was very low. The strain gage balance was mounted to the model support turntable by a balance support block within the body as shown in figure 21(b). The airlines were connected to the balance support block and the wing root. Flexible hoses could have been used to bring high pressure air across the balance. Although such an arrangement would yield only a small effect on the balance calibration, previous experience indicated that the effect of a flexible hose with pressure was not repeatable. Therefore, two thin-walled, stiff tubes were bent into coils looping back and forth within the body. Coils provide extra length to make a more flexible connection between the non-metric balance support block and the metric wing root. Experiences with such an arrangement have produced repeatable data. Techniques used to determine the effect of the airline stiffness on the balance calibration are described in Appendix A along with the results from the airline stiffness calibration.

Previous experiments showed that the tip jet increases the lift over much of the wing. These wings had small aspect ratios so that, for an aspect ratio 2 wing, the effect was monitored for about 1 chord inboard from the wing tip. The effect of tip blowing on the local lift several wing tip chords from the tip should be small. Therefore, chordwise rows of pressure orifices were concentrated over the outer portion of the wing. Five rows of pressure orifices were installed in the model at $\eta = 0.25$, 0.50, 0.70, 0.80, and 0.90. The orifices in each row were located at the same nominal nondimensional chordwise locations. Actual locations of the orifices are listed in table V. Each orifice had a diameter of 0.010 inches and was drilled normal to the wing surface. A sketch of the orifice locations is presented in figure 21(c). Each chordwise row consisted 20 orifices on the upper surface extending from the leading edge back to 90 percent chord and 19 orifices on the lower surface extending from 2 percent chord back to 90 percent chord. The wing was too thin aft of the 90 percent chord position to locate any orifices there. Results from two-dimensional tests of this

airfoil section in reference 42 indicate that there is little loading on the rear portion of the airfoil when the flow is attached. Assuming little or no trailing edge separation, omitting these orifices should not effect the computation of the section lift coefficient.

Accurate and repeatable drag measurements on a wing with tip blowing were crucial to the success of this investigation. Viscous drag on the wing will change if the boundary layer transition point changes. To prevent the transition point and the drag from changing as the model surface finish changes during the test, the transition location was fixed using carborundum grit. Grit location was determined using the method of reference 43. Different grit sizes were used on the inboard and the outboard section as shown in figure 21(d) because of the different boundary layer characteristics.

Seven interchangeable wing tip sections were built to investigate the effect of jet vertical location, chordwise location, in-plane deflection (sweep), out of plane deflection (dihedral), and length. Conventions used to define these parameters are presented in figure 22. A sketch of each of the wing tip sections is presented in figure 23. Design characteristics of each tip jet are presented in table VI.

Since the literature survey indicated that blowing from discrete jets produces the same type of benefits as blowing from continuous jets, the wing tip sections were designed to allow a systematic variation of the jet location and exhaust direction for a common jet exit size. Each discrete jet was 0.062 inches high and 0.25 inches wide. Effects of jet chordwise location could be determined by comparing the results from the jets positioned at five locations along the airfoil reference plane as shown figure 24(a) Jets were centered at nominally the 20, 30, 50, 60, and 70 percent chord locations. Note that each jet location could be tested independently because of the interchangeable tips and the separate air passages. Each jet exhausted in a spanwise direction. Effect of jet vertical location could be determined by comparing the results from jets positioned at the 30 and 50 percent chord locations as shown in figure 24(b). One tip was fabricated with long

jets, as shown in figure 24(c), to approach the continuous jets used in many of the exploratory experiments. Length of the forward jet was 0.62 inches and the length of the aft jet was 1.25 inches. Jet height was 0.062 inches and both jets exhausted in a spanwise direction. Effect of jet sweep could be determined by comparing the results from jets positioned at the 30 and 60 percent chord locations and the jet exhaust directed in a spanwise direction and 30° downstream from the spanwise direction as shown in figure 24(d). Effect of jet dihedral could be determined by comparing the results from jets positioned at the 30 percent chord location with the jet exhaust directed in a spanwise direction and directed 20° downward as shown in figure 24(e).

Instrumentation and Data Acquisition

Measurements of the wing forces and moments, wing surface static pressures, jet mass flow rate and momentum, and test conditions were required. Wing forces and moments were measured by a five component, strain gage balance. There were no gages to measure the wing side force. Also, the very low sensitivity of the gages in the yawing moment direction prevented making accurate measurements in that direction. All balance strain gages are temperature compensated and the balance has been calibrated for the first and second order interactions. Effects of the airlines have been included in the balance calibration. The body was not supported by the strain gage balance. Thus, the balance measures the forces transmitted to only the exposed portion of the wing.

Wing surface static pressures were measured by an electronically-scanned, pressure measurement system with a transducer dedicated to each orifice. Each transducer measured a differential pressure. A common reference pressure was used for all the static pressure measurements. All wing pressures were measured at virtually the same time that the rest of the data was measured.

Pressure and temperature instrumentation were used with the air supply system to

determine the jet momentum and to correct the balance data for the effect of pressure in the airlines. A schematic of the air supply system and of the associated instrumentation is presented in figure 25. Differential pressure transducers were connected to each airline just upstream of the rigid attachment to the balance support block. These airline pressures were used to correct the balance data for the effect of airline pressure as described in appendix A. Differential pressure transducers were connected to the "J" tubes installed in the two tip plenum chambers. These jet total pressures and the free stream static pressure were used to determine the jet momentum using the procedures described in appendix B. The mass flow rate to each jet and the free stream velocity were needed to determine the ram drag associated with each jet. Mass flow rate was determined from the density of the high pressure air and the volume flow rate to each jet. Volume flow rate to each of the two tip jets was measured by separate, turbine flowmeters. Static pressure and temperature at the inlet of the flowmeters were measured to determine the gas density. Inlet static pressure was measured with a strain gage differential pressure transducer referenced to the common reference pressure. Inlet temperature was measured with a thermocouple.

Tunnel static and total pressures were measured by quartz bourdon tube pressure transducers. This same type of transducer was used to measure the common reference pressure used for the electronically scanned pressure modules and the differential pressure transducers. These quartz pressure transducers were referenced to a vacuum to provide absolute pressure measurements.

The model angle of attack was measured with an accelerometer mounted on the wing root as shown in figure 20. This provided the actual wing angle of attack so that no corrections for bending were required.

The 7- x 10-foot HST data acquisition system was used to measure, display, and record the data. The data acquisition system, controlled by a mini-computer, has both analog and digital data acquisition units and a pressure measurement system. The analog data acquisition unit has

192 analog channels with six possible analog ranges: ±4, ±8, ±16, ±32, ±64, and ±128 mv. All analog channels have a 2 hertz low pass filter. The digital data acquisition unit has 16 channels. The pressure measurement system can measure pressures from 256 orifices. The transducers are grouped in 32 port modules which can be calibrated on demand, including when the tunnel is running. An average of 10 samples from each channel are used in the final data reduction.

Calibration of the Airline Stiffness and the Wing Tip Jets

Presence of the airlines provides additional load paths for the wing forces and moments as shown in the sketch of figure 26. Effects of airline stiffness and pressure must be determined so that they can be removed from the balance data. The stiffness of the airline can change with pressure. In addition, coils in the airline will tend to unwind as they are pressurized. The wing tip section was removed and a loading bar attached to the end of the wing as shown in the sketch of figure 26 and the photograph in figure 27. The airlines were disconnected from the wing root and known loads were applied to the wing and balance. The airlines were then connected to the wing root and the loadings repeated with and without pressure in the airlines. The difference in the measured results is the effect of the airline on the balance calibration. Pressures used in this investigation, which were generally less than 110 psi, were too small to have a measurable effect on the airline stiffness and the balance measurements. Each airline was then pressurized separately to determine the effect of pressure on the static loads on the balance by unwinding the airline coils. Details of the airline stiffness calibration procedures and the results may be found in Appendix A.

Momentum of the tip jets could not be measured in all three directions because there was no side force measurement from the balance. An alternate means of determining the jet momentum was used. Five total pressure probes spaced over the width of the jet exhaust were used to survey completely across the jet exhaust as shown in figure 28. Ambient pressure, jet total temperature, and five jet total pressures were measured at multiple positions normal to the plane of the jet exhaust. Jet momentum per unit width of jet was determined by integrating the profile

normal to the jet for each of the five total pressure tubes. Thrust or jet momentum was computed by integrating the variation of the jet momentum per unit width over the width of the jet exhaust. This process was repeated for either two or three different plenum pressures. Jet thrust was calibrated as a function of the difference between the total pressure measured in the jet plenum and the ambient static pressure. Details of the calibration procedures, derivation of the equations used to compute the jet momentum, and the calibration measurements are presented in Appendix B.

Test Procedures

Each tip was first tested without blowing at angles of attack from -2° to 11° at a Mach number of 0.3. This established a baseline for each tip to eliminate the effects of any minor manufacturing differences among the tips. Then, each tip was tested at the same Mach number and angles of attack with blowing from the front jet, aft jet, and both jets. Each tip except tip 8 was tested at a constant angle of attack and the jet momentum coefficient varied from zero to the maximum value available. These additional tests were conducted at Mach numbers of 0.5 and 0.7 with blowing from both jets. The jet exit Mach number was restricted to 0.9 to avoid noise problems associated with a supersonic jet. Tip 8 was tested at Mach numbers from 0.2 to 0.5 at a constant angle of attack and the jet momentum coefficient varied from 0 to the maximum value available. These tests were done with blowing from the forward jet, the rear jet, and both jets. At each test condition, the balance forces and moments, the wing surface static pressures, the test conditions, and the plenum pressure, airline pressure, flowmeter turbine rotational speed, flowmeter temperature, and flowmeter pressure for each jet were recorded.

Data Reduction and Corrections

Wing balance data have been corrected for weight tares, first and second order interactions, and stiffness and pressure of the airlines. Data are resolved about a moment reference center at the quarter chord of the mean geometric chord as shown in figure 21(a). The moment reference center

was 7.61 inches aft of the wing root leading edge on the airfoil reference plane. Note that the wing root bending moment reference point was at the edge of the fuselage. Wing root bending moment is resolved in the model axis system and the wing lift, drag, and pitching moment are resolved in the stability axis system as shown in figure 29. All data have been converted to coefficient form. Wall interference corrections were computed using the technique of reference 44 and found to be negligible.

Wing pressure data have been referenced to the free stream static pressure and nondimensionalized by the free stream dynamic pressure. Pressures at the rearmost two pressure orifices were used to extrapolate to the pressure at the wing trailing edge. The nondimensional data have been integrated in the chordwise and the normal directions to obtain the section normal force and chord force coefficients. These coefficients were used to obtain the section lift coefficients at each chordwise row of orifices.

Jet momentum coefficient as well as the jet contributions to the lift, drag, root bending moment, and pitching moment were computed from the jet calibration. These direct thrust effects were subtracted from the balance results to obtain the thrust removed results.

CHAPTER VI

DISCUSSION OF THE EXPERIMENTAL RESULTS

This chapter presents the results from the tip blowing experiments. The experimental apparatus was designed to minimize the effects of the airline on the balance measurements, especially drag. Two wing tips were retested without blowing to determine the repeatability of the wing force and moment data, chordwise pressure distributions, and span load distributions with the airlines present. Each wing tip was tested without blowing as a reference for determining the effects of spanwise blowing at the wing tip and with blowing from the front jet, rear jet, and both jets. All results presented herein have transition grit installed on both surfaces of the wing. This chapter will discuss three areas: data accuracy and repeatability, reference aerodynamic characteristics of the wing without blowing, and effect of blowing on the wing aerodynamic characteristics.

Data Accuracy and Repeatability

Accuracy of the wing force and moment data depends on the accuracy of the balance and angle of attack measurements. Balance accuracy is 0.5 percent of the full scale balance load, which equates to 2.0 lbf normal force, 0.15 lbf axial force, 10.0 in-lbf pitching moment, and 5.0 in-lbf rolling moment. The inaccuracy of the measurement generally increases as the load increases. It is largest when several balance components are highly loaded. In general, these tests were limited by the balance rolling moment capacity. Since only one component was highly loaded, the accuracy of the measurements is probably better than the quoted accuracy. However, the quoted balance accuracy will be used to determine the accuracy of the measured coefficients. Accuracy of the angle of attack measurement is about 0.02°. For small angles of attack, the drag accuracy depends primarily on the axial force measurement and the lift accuracy depends primarily on the normal force measurement. At a Mach number of 0.3 and small angles of attack, the lift coefficient

accuracy is 0.016, the drag coefficient accuracy is 0.0012, the pitching moment coefficient accuracy is 0.011, and the wing root bending moment coefficient (rolling moment) accuracy is 0.002. Accuracy is better at the higher Mach numbers and slightly worse at the lower Mach number.

Repeatability of the wing force and moment data is affected by problems associated with the two airlines that cross the balance. Problems with mechanical connections, nonuniform expansion and contraction with temperature, changes in the static loads with airline pressure, and hysteresis make it difficult to obtain good drag measurements. The design of the air supply system used in these tests minimized these effects. Repeatability of the wing data was investigated by retesting two of the wing tip sections.

Repeatability of the wing drag data without blowing is presented in figure 30 for tip 2 and tip 8 at a Mach number of 0.3. These tests were conducted with the airlines attached so that the results would be representative of those obtained with tip blowing. Tip 2 was tested two times and tip 8 was tested three times. Different sets of measurements for each tip will be referred to by a Run number. Runs 2 and 3 for tip 8 were measured sequentially in the test program without stopping the tunnel flow. For tip 2, the difference in the drag coefficient between the curves at low lift coefficients is about 0.0010 and the difference decreases as the angle of attack increases. The lower drag for Run 2 is not consistent with the drag obtained on other tips without blowing. Results for tip 8 that were measured sequentially, Runs 2 and 3, are in very good agreement, especially at the lower lift coefficients. However, results obtained earlier in the test, Run 1, show larger differences in the drag as the lift increases. Sequentially measured results from tip 8 are in good agreement with those measured for Run 1 with tip 2. Examination of the raw data indicates that the model was probably not at 0° angle of attack when the reference readings were recorded for Run 1 with tip 8. However, these differences are still within the quoted balance accuracy. Differences that appear in the results are larger for runs that were not measured sequentially. Whenever practical, the effect of tip blowing will be determined by the difference between results with and without tip blowing measured sequentially in order to minimize these differences. From

the limits of data accuracy and data repeatability, differences in the drag that are less than 0.0010 should not be considered significant.

Repeatability of the wing lift data without blowing is presented in figure 31 for the same two wing tip sections. Results for tip 2 and the sequentially measured results for tip 8 are in excellent agreement. The sequentially measured results for tip 8 differ from the results for tip 8 obtained earlier in the test in Run 1. The difference is probably attributable to an error of about 0.1° in positioning the model when recording the reference conditions. However, the difference in lift coefficient at the same angle of attack is about 0.015 which is also within the balance accuracy of 0.016. A linear, least-squares curve was fitted to the linear portion of each set of data to obtain the angle of zero lift, α_0, and the lift curve slope, C_{L_α}, and the results are presented in Table VII. Except for Run 1 for tip 8, repeatability of the results is excellent. The angles of zero lift as well as the lift curve slopes over the linear part of the curve are virtually identical for tip 2. For tip 8, the angles of zero lift and the lift curve slopes for the sequentially acquired data, Runs 2 and 3, are also in excellent agreement.

Variation of the wing root bending moment with lift is presented in figure 32 for the same two tip sections without blowing. For the untwisted wing tested in this investigation, the section lift coefficient at each spanwise station will approach zero as the angle is attack is reduced to the angle of zero lift. With no lift across the wing, the wing root bending moment should also be zero. As the angle of attack increases, the lift at each spanwise station increases linearly with the angle of attack. Wing root bending moment should also vary linearly with angle of attack and lift since the moment is just the integral of the product of the section lift and the spanwise location on the wing. The variation should be linear as long as the flow is attached. Repeatability of the results from tip 2 and the sequentially measured results from tip 8 is very good. Again, Run 1 for tip 8 does not agree very well with the other two runs. A linear, least-squares curve was fitted to the linear portion of each data set to obtain the slope, C_{b_L}, and intercept, C_{b_0}, and the results are presented in Table VII. For tip 2 and the sequentially measured data from tip 8, the repeatability

is excellent. Results from Run 1 for tip 8 differ slightly from the other results presented. This is additional evidence that the reference model attitude for Run 1 for tip 8 was incorrect. For each tip, the repeatability of the computed slopes of the bending moment curves is very good. As before, the sequentially acquired results for tip 8 are slightly different from the results acquired earlier but the are still within the balance accuracy of 0.002. With no lift on the wing, the wing root bending moment was virtually zero for all the results presented except for Run 1 of tip 8.

Repeatability of the pitching moment results is presented in figure 33 for tip 2 and tip 8. For tip 2, there is some scatter in the results at the lower lifts but the curves are in reasonable agreement. The sequentially acquired results for tip 8 are in good agreement but the results for Run 1 are shifted. All results are well within the quoted balance accuracy. A linear, least-squares fit was applied to the results over the same linear portion of the curve to determine the moment at zero lift, C_{m_0}, and the the slope, C_{m_L}, and the results are presented in Table VII. The moment reference center was located at the quarter chord of the mean geometric chord which should be close to the aerodynamic center. Thus, the slopes of the curves are small until separation begins. Repeatability of the slopes is very good although there is a small shift in pitching moment between the runs. Differences only appear at low lift coefficients where the flow is attached. The shift is extremely small for tip 2 with a value of about 0.001 and slightly larger for tip 8 with a value of about 0.003. Both these values are well within the balance accuracy of 0.011.

Repeatability of the chordwise pressure distributions at each of the five spanwise stations is presented in figure 34 for tip 2 at nominal angles of attack of 4° and 8°. The accuracy of the transducers in the electronically scanned pressure modules is 0.15 percent of the transducer full scale rating. At a Mach number of 0.3 and dynamic pressure of 125 psf, the accuracy of the pressure coefficient is better than 0.01. As can be seen from the plots, such accuracy would not even show up on the scales used. For all five wing stations, the chordwise pressure coefficient distributions are in excellent agreement with each other. Any small differences are attributed to leaking pressure tubing connections or foreign matter obstructing the orifice or the tubing.

The chordwise pressure distributions from figure 34 were integrated to obtain the section lift coefficient at each spanwise station. These integrated results are presented in figure 35 for tip 2 at the same two angles of attack of 4° and 8°. The repeatability of the span load distribution is excellent.

Wing Aerodynamic Characteristics Without Blowing

Each tip was tested on the wing at a Mach number of 0.3 without blowing. The results from all the tips were compared and found to be similar although small differences exist as was noted in the section describing the data repeatability. Results from tip 8 will be discussed as being representative of the aerodynamic characteristics without blowing.

Balance data include only the loads imposed on the wing. Loads on the body do not pass through the balance but are transmitted directly to the model support system. However, the elongated body acts as a low aspect ratio lifting surface next to the wing. Blockage of the body leads to a local increase in the velocity which is largest near the body and decreases as the distance from the body increases. Similarly, as the angle of attack increases, the lift on the body increases. Flow goes from the lower surface to the upper surface inducing an upwash field across the wing. This upwash is largest near the body and decreases rapidly as the distance from the body increases and is opposite the downwash field induced across the wing by the vorticity shed in the wake. Thus, the local angle of attack is different from the angle which would result if the body were not present.

The airfoil section used for the semispan wing was designed to achieve long runs of laminar flow on both surfaces at a section lift coefficient of 0.2 and a Mach number of 0.7. Two-dimensional test results of the airfoil section at a Mach number of about 0.3 indicate that the airfoil lift curve is linear up to about 6° angle of attack where trailing edge separation begins. Separation moves forward with increasing angle of attack. At stall, leading edge suction is still

present.

Chordwise pressure distributions at a Mach number of 0.3 are presented in figure 36 with no blowing at angles of attack from about 0° to 10° for all five spanwise stations. At an angle of attack of -0.1°, the measured chordwise pressure distributions generally show a favorable pressure gradient back to at least the 55 percent chord location on both surfaces of the airfoil. The acceleration over the upper surface of the leading edge has been reduced so that there is no large suction peak followed by an adverse pressure gradient. At this angle of attack, the region aft of the 65 percent chord location is providing little, if any, lift. Flow on both surfaces decelerates over the rear portion of the airfoil and appears to be attached to at least the aftmost measurement station at the 90 percent chord location. At 2.1° angle of attack, a much more rapid acceleration occurs around the leading edge of the upper surface followed by a region with a small adverse pressure gradient. The rear portion of the airfoil is providing very little lift. Leading edge suction at the most inboard station is reduced compared to the other stations. As the angle of attack increases to about 4.0°, a suction peak develops which is followed by a region of adverse pressure gradient on the upper surface. The boundary layer is subjected to a much larger pressure gradient than at the lower angles of attack. There is a slight indication of separation at the 90 percent chord location on the lower surface for the outermost chordwise row. This is supported by the break in the lift and pitching moment curves at about 4°. Separation occurs at a lower angle of attack in these tests primarily because of the lower local Reynolds number. At about 6° angle of attack, there are signs of separation on both the upper and lower surfaces between the 80 percent and 90 percent chord locations in that the pressures are no longer tending towards a positive pressure coefficient. Separation probably began at a lower angle of attack but the absence of pressure orifices aft of the 90 percent chord position prevented its detection. At angles of attack of 8° and 10°, the leading edge suction continues to increase and the location of the trailing edge separation moves farther forward. The leading edge suction peak was maintained to the maximum angle tested.

The spanload distribution associated with these chordwise pressure distributions was

computed and the results are presented in figure 37. As the angle of attack increases, the section lift coefficient increases across the wing span. The inboard portion of the wing is strongly influenced by the upwash field induced by the body so the lift increases uniformly with increasing angle of attack. The outboard portion of the wing is influenced more by the vorticity shed in the wake so the increase in lift becomes smaller with increasing angle of attack. Thus, the center of lift moves inboard as the lift increases.

Typical results of the wing aerodynamic characteristics without wing tip blowing are presented in figures 30 to 33. Some of the more important aerodynamic characteristics of the wing with each tip section are summarized in Table VII. Average wing drag coefficient at zero lift is about 0.0104. The change in drag is relatively small for lift coefficients up to about 0.4 but increases rapidly as the lift increases above that level because the profile drag increases due to increasing separation and because the induced drag increases with the square of the lift coefficient. The lift curve is linear with angle of attack up to at least 4° angle of attack (lift coefficient of about 0.55) with a slope of 0.104 per degree and an angle of zero lift of -1.4°. At higher angles of attack, the slope is reduced from that obtained over the linear portion because of trailing edge separation. Maximum lift coefficient was not determined because the maximum angle of attack tested was below the stall angle. Wing root bending moment curves are linear for lift coefficients up to about 0.55 with a slope of 0.42. At higher lift coefficients, the ratio of bending moment to lift coefficient is reduced. The change in the ratio occurs at about the same lift coefficient at which the change in lift curve slope occurred. Over the linear portion of the curve, the equivalent point lift is centered at the 42 percent semispan location. At higher lift coefficients, the ratio is reduced, indicating that the equivalent point lift moves inboard. This is consistent with the span load distributions which showed that, as the lift increased, the loading outboard does not increase as much as the loading inboard. Wing root bending moment is zero for zero lift. The moment reference center is located at the quarter chord of the mean geometric chord which should be close to the wing aerodynamic center. The variation of pitching moment coefficient with lift coefficient

is linear up to lift coefficients of 0.55, with a slope of about 0.005. The pitching moment at zero lift is -0.013 which is very close to the value obtained in the two-dimensional airfoil tests at slightly different test conditions. The smaller increase in lift outboard with the onset of trailing edge separation leads to a positive increment in pitching moment. Results from the lift, bending moment, and pitching moment all indicate that attached flow is maintained up to a lift coefficient of about 0.55 and that the separation begins at the trailing edge.

Effect of Spanwise Blowing on the Wing Aerodynamic Characteristics

Each wing tip was tested on the wing at a Mach number of 0.3 without blowing and with blowing from the forward jet, aft jet, and both jets. The angle of attack for each of these four conditions was varied from -2° to 11°. Each tip except tip 8 was tested at a constant angle of attack and the jet momentum coefficient varied from zero to the maximum value available. These additional tests were conducted at Mach numbers of 0.5 and 0.7 with blowing from both jets. The jet exit Mach number was restricted to 0.9 to avoid noise problems associated with a supersonic jet. Tip 8 was tested at Mach numbers from 0.2 to 0.5 with blowing from the forward jet, the rear jet, and both jets. This section will discuss the effect of blowing on the wing aerodynamic characteristics.

The effect of spanwise blowing from the wing tip on the drag polars for the different tips is presented in figure 38. The baseline jet exit, which was 0.25 inches long and 0.06 inches high, was used on all tips except tip 8. Blowing from the baseline jets had a very small effect on the drag, generally smaller than the accuracy of the drag measurement. Results for tip 1 show a very small decrease in the drag coefficient of about 0.0005 at a given lift when there is blowing from either the forward or aft jets. However, the reduction is within the drag measurement accuracy and should be treated only as a possible trend. For tip 2, blowing had very little effect at low lift coefficients with a possible small decrease in drag coefficient with blowing at a lift coefficient just over 0.8.

Again, the changes were within the accuracy of the drag measurement. Results for tip 3 were mixed with small changes. Blowing from the forward jet of tip 4 had little effect on the drag but blowing from the two aft jets increased the drag. Results for tip 6 indicate a small decrease in drag coefficient of about 0.0006 at low lift coefficients with the addition of blowing but the reduction is within the drag measurement accuracy. The jets on tip 9 are directed rearward 30° so that there is a component of the jet momentum in the negative drag direction equal to $C_\mu \sin 30^\circ \cos \alpha$. As shown, with the direct effects of the jet momentum included, blowing leads to a significant decrease in drag. However, after subtracting the direct effect of the jet momentum, the wing drag is found to increase with blowing (not shown).

The jet exit Mach number was restricted to a value of 0.9. With the exit Mach number and velocity fixed, the maximum jet momentum coefficient available for tests at free stream Mach numbers of 0.5 and 0.7 was smaller than that available at the Mach number of the data presented, that is 0.3. The change in drag coefficient with blowing was very small at these two higher Mach numbers. Thus, the results at the higher Mach numbers are not presented herein.

The effects of blowing should increase with increasing jet momentum coefficient. The momentum coefficient of the baseline length jets cannot be increased by increasing the exit velocity since it was limitted to a Mach number of 0.9. Hovever, the momentum can be increased by increasing the exit area. The length of the front and rear jets on tip 8 was increased to 0.62 inches and 1.25 inches respectively. Each jet exit was 0.06 inches high. With the larger momentum available, larger changes in drag are expected. Results for tip 8 show a measurable reduction in drag with wing tip blowing. Drag reductions range from about .0012 to about .0022 depending on the blowing configuration. The reduction with two jets operating is larger than the reduction with only one jet operating. These are the only measured drag reductions that are larger than the drag measurement accuracy.

The effect of spanwise blowing on the lift curves, presented in figure 39, is small. There is

an indication that the lift increases when blowing is present. For most of the tips, blowing slows the decrease of the lift curve slope with increasing lift coefficient. This indicates that blowing retards separation and leads to a higher loading near the tip at the higher lift coefficients. Because the change in lift due to blowing is small compared to the total lift, it is difficult to determine the effect of blowing from plots of the results. To eliminate any bias, slopes of the linear portions of the lift curves were computing using a linear, least-squares curve fit and the results are presented in figure 40. With the exception of tip 4, all the tips show an increase in the lift curve slope with blowing. Most of the increases are small and there is some scatter in the results. Tip 8 shows a significant increase in the lift curve slope because the longer length jets leads to a larger loading over a longer portion of the tip. It is interesting that the change in lift curve slope with jet momentum coefficient is similar for most of the tips.

The effect of spanwise blowing on the wing root bending moment, presented in figure 41, is small. Blowing increases the slope of the curves, indicating that the center of lift has moved outboard, due to the increased loading near the wing tip. As was done for the lift curves, the slopes of the bending moment curves were determined for the linear portion of the curves and the results are presented in figure 42. For all tips, the slope increases with increasing jet momentum coefficient. Slope increases ranged from about 0.006 to 0.013 indicating that equivalent point lift has moved outboard by 0.6 to 1.3 percent of the semispan. This is consistent with previous research which indicated that spanwise blowing increases the lift primarily in the wing tip region.

The effect of spanwise blowing on the wing pitching moment is presented in figure 43. At low lift coefficients, where the flow is attached, the effect of blowing is very small. In general, blowing increases the longitudinal static stability and provides a small nose down increment in pitching moment. For tip 8, the slope of the linear portion of the pitching moment curve was changed from .003 without blowing to -.015 with both jets operating. This is consistent with the increase in lift curve slope with blowing in that the lift at the tip, which is aft of the moment reference center, increases more rapidly with blowing than without blowing. At the larger lift

coefficients, after the trailing edge separation begins, the reduction in nose up pitching moment is easily seen. The reduction is generally larger at the higher jet momentum coefficients where both jets are operating.

Spanwise blowing from tip 8 showed the largest benefits in reducing drag and increasing lift on the wing. When applied to an aircraft, a source for the high pressure air for the blowing must be identified. If high pressure air is available from a laminar flow control system using suction, the work required to generate the high pressure air would be charged against the laminar flow control system. Without such a system, high pressure air would be bled from the propulsion system. Such engine bleed air would create a ram drag penalty equal to the product of the mass flow rate required by the jet and the free stream velocity. Results for tip 8, adjusted for this ram drag penalty, are presented in figure 44. Drag reduction with blowing from the front jet is counteracted by the ram drag penalty. A small drag reduction remains for the aft jet when the ram drag penalty is included. Differences between the drag without blowing and the total drag with the jets operating (wing drag with the ram drag penalty) are small and mixed. They are about the same magnitude as the accuracy of the drag measurement. The jet configuration should be refined to improve these results so that there is a drag benefit even when the ram drag penalty is included.

Results presented for the baseline chord jets (0.25 in.) were obtained using a high subsonic jet Mach number, typically about 0.9 and a free stream Mach number of 0.3. None of the results indicated a reduction in wing drag larger than the accuracy of the balance measurement. Tests at higher Mach numbers with blowing from both the front and rear jets did not yield any reduction in drag.

The decrease in drag and increase in lift for tip 8 due to spanwise blowing were large enough to warrant additional tests at several different Mach numbers. For these additional tests, the angle of attack was fixed at about 2° and the plenum pressure for the jet varied to investigate

the effect of jet momentum coefficient. Variation of the wing lift and drag coefficients with jet momentum coefficient for tip 8 is presented in figure 45 at a constant angle of attack for the front jet, rear jet, and both jets operating for several different Mach numbers. At a Mach number of 0.2, lift increases with increasing jet momentum coefficient for all three jet operating conditions. Drag decreases with increasing jet momentum coefficient for the rear jet alone and both jets operating blowing condition but increases slightly for the forward jet alone condition. At Mach numbers of 0.3 and 0.4, the lift increased and the drag decreased with increasing jet momentum for both the front and rear jet operating conditions. There appears to be virtually no effect of jet momentum coefficient on the lift or drag at a Mach number of 0.5. The small change in jet momentum coefficient makes it difficult to determine the effects of blowing magnitude. Changes in the lift and drag coefficients with blowing are small and it is difficult to determine the trends because of the scatter in the data. The variation of both the lift and drag coefficients with jet momentum coefficient was determined by fitting a linear least-squares curve through the results. Blowing effectiveness, as measured by the rate of change of lift and drag with jet momentum, is presented in figure 46. The rate of decrease in drag with increasing jet momentum becomes larger as the Mach number increases from 0.2 to 0.4. The rate of change of drag with jet momentum is about three times larger for the rear jet than the front jet. However, at a Mach number of 0.5, the rate of change falls to near zero. Similar trends are found for the increase in lift coefficient in that the rate of increase of lift with jet momentum increases as the Mach number increases to 0.4 and then falls towards zero as the Mach number approached 0.5.

Span load distributions and chordwise pressure distributions can provide additional information about the flowfield near the wing tip with blowing. The effect of blowing on the span load distribution is presented in figure 47 for Mach numbers of 0.2, 0.3, 0.4, and 0.5 at an angle of attack of about 2°. Without blowing, the section lift coefficient increases across the wing to the 70 percent semispan location and then decreases towards the tip. In general, blowing does not have a measurable effect on the lift at spanwise stations out to the 80 percent semispan location.

Increasing the jet momentum coefficient increases the section lift coefficient at the 90 percent semispan location. Increases are largest at the lowest Mach number where the jet momentum coefficient was the largest. The section lift coefficient at the 90 percent span location was plotted against the jet momentum coefficient for each Mach number and the results are presented in figure 48. Results show that, at all four Mach numbers, the lift near the tip increases with jet momentum coefficient and that similar increases occur for similar jet momentum coefficients. Trends are the same for all three blowing configurations.

The effect of spanwise blowing on the chordwise pressure distribution is very small. Changes are difficult to discern with the scales used for the plots of the chordwise pressure distributions. Therefore, the change in pressure coefficient due to blowing will be plotted rather than the pressure coefficient itself. Data were recorded at a constant angle of attack without blowing followed immediately by data with blowing. The difference in the local pressure coefficient with and without blowing, ΔC_p, was computed at $\eta=0.9$ and the results are presented in figure 49. Spanwise blowing increases the suction on the upper surface (negative ΔC_p) and increases the the pressure on the lower surface (positive ΔC_p). The magnitude of the change in the pressure coefficient becomes larger as the jet momentum coefficient increases. Blowing from the front jet produces a larger change in the leading edge suction peak than blowing from the aft jet. In general, the effect of blowing is larger on the upper surface than on the lower surface. Also, the effect of the front jet on the pressure coefficients is larger than the effect of the aft jet. The front jet increases the suction across most of the chord; however, the aft jet tends to have most of its effect on the aft portion of the pressure distribution at the 90 percent spanwise position.

The experimental results indicate that the drag benefit decreases as the maximum momentum coefficient decreases at the higher Mach numbers. The maximum mass flow rate through the airlines was insufficient for testing at a Mach number of 0.7. Additional information is needed to support the contention that there is no measurable drag reduction with blowing at high subsonic Mach numbers. This information will be supplied by a Navier-Stokes solver.

CHAPTER VII

NAVIER-STOKES CALCULATIONS

The maximum mass flow rate to the jets was limited by the air supply system, thus limiting the maximum momentum available from the jets. As dynamic pressure increases with Mach number, the maximum available jet momentum coefficient decreases. The maximum available jet momentum coefficient at Mach numbers above 0.5 was too small for practical experiments. Results indicated that the drag reduction vanishes as the Mach number increased to 0.5. This trend probably continues as the Mach number is increased further. Since no experimental results were available at the higher Mach numbers, results from a Navier-Stokes solver will be used to back up the contention that there is not a drag reduction at a Mach number of 0.72.

This chapter will present a brief description of an existing Navier-Stokes solver and of the modifications to the boundary conditions to simulate the spanwise blowing at the tip. Steps used to develop the grid of control points follow. Results from calculations with different numbers of control points in the three generalized coordinate directions are then used to select a suitable grid for the final calculations. Experimental results at two Mach numbers without blowing are used to validate the Navier-Stokes simulation and the grid. Results at a Mach number of 0.3 are then used to validate the modifications to the numerical simulation for spanwise blowing. Finally, the validated simulation is used to predict the effects of spanwise blowing at a Mach number of 0.72.

Navier-Stokes Solver

Results from previous experimental investigations and from the analytical model described in Chapter III indicated that spanwise blowing from the wing tip altered the roll up of the vortex

wake. The analytical model showed that vorticity of the jet interacts with vorticity shed in the wake of the wing. Previous experiments demonstrated that blowing can also delay separation. A Navier-Stokes simulation is needed to model adequately all these effects. An existing Navier-Stokes solver, TLNS3D, which has been demonstrated to realistically simulate the flowfield about moderate aspect ratio wings at transonic Mach numbers, was selected for use in the study. The computer code, described in references 45 and 46, solves the unsteady Navier-Stokes equations numerically on a grid of control points until steady state conditions are obtained. A finite volume representation of the equations is written in discrete form in general, curvilinear coordinates. This representation makes it easier to treat arbitrary shapes for different types of grid topology. A thin layer assumption is used to simplify the equations since most of the viscous diffusion is normal to the wing surface. A body fitted coordinate system was selected with the three coordinate directions in approximately chordwise, normal, and spanwise directions. The solution is advanced to steady state using a modified, five-stage Runge-Kutta time stepping scheme developed by Jameson in reference 47. Decoupling of the spatial and the temporal terms makes the solution independent of the CFL number. Acceleration techniques, such as use of local time stepping and use of multigrids, are employed to improve the numerical convergence. By using a local time step, a larger time step than the global minimum can be used at each point on the grid. A multigrid scheme is used to reduce the computational time required since roughly the same overall number of iterations is required to achieve a given level of convergence but less work is needed on the coarser meshes. These coarse grids resolve what are low frequency errors on the finer grids. Also, the equations can be vectorized so that full advantage can be taken of the vector operations of supercomputers.

The system of equations is closed with the addition of an eddy viscosity and an eddy conductivity for the momentum and energy equations and the algebraic turbulence model of Baldwin and Lomax (reference 48). This turbulence model works well for attached flows but should not be used for massively separated flows.

Artificial dissipation is added to the momentum equations to prevent oscillations in the solution near the stagnation point and near shocks and to suppress even/odd point decoupling in the numerical solution. The artificial dissipation is a blend of second and fourth order differences with the coefficients dependent on the local pressure gradient.

Five flow variables must be specified on all boundaries in the computational domain. All computations are performed at the cell centers. Ghost cells are created at the plane of symmetry, the downstream boundary, and at the wing surface. Ghost cells are not needed at the farfield boundary. Values for cells at the farfield boundary are based on the Riemann invariants for one-dimensional flow normal to the boundary as outlined by Thomas and Salas in reference 49. Symmetry is imposed on all variables in the plane of symmetry except for the spanwise component of momentum which is antisymmetric. At the downstream boundary, a zero order extrapolation is used to determine the values of the variables at the ghost cell. On the wing surface, no slip and no injection conditions are imposed everywhere except at the jet exit where the three components of momentum are specified. Zero normal pressure and density gradients are assumed on the wing surface. Values at the center of the ghost cell are determined from the values at the center of the cell tangent to the surface and the value specified at the boundary (common cell face). Unless starting from a previous solution, all (non-ghost) cells are initialized to the free stream values.

Grid Generation

The grid topology must be able to capture the rapidly changing features in the flowfield near the wing surface, the wing tip, and across the trailing wake. A "C" type grid was selected to resolve the viscous effects near the surface and across the downstream wake. An "O" type grid was selected to capture the features near the wing tip since a previous study on a similar planform wing (reference 50) indicated that an "H" type grid with a similar number of spanwise grid points would not resolve the features of the flow as well as an "O" type grid. Grid points are laid out in the chordwise, normal, and spanwise directions. In the chordwise direction, grid points extend

from the downstream boundary along the lower surface around the leading edge and continue back along the upper surface to the downstream boundary. Grid points extend in the normal direction from the wing surface out to the outer boundary. In the spanwise direction, grid points extend from the wing root to the wing tip.

Grid generation involved four steps: (1) generating a surface grid of the wing with a squared-off, open wing tip, (2) closing the open wing tip with a round tip cap, (3) expanding the surface grid into a volume grid, and (4) eliminating any collapsed points in the volume grid. A sketch of the development of the surface grid is presented in figure 50(a). The surface grid of the wing should have grid points clustered near the leading and trailing edges of the wing and the near wing tip to resolve the gradients at those locations. Development of the surface grid with the open wing tip is shown in the top part of figure 50(a). Polynomial stretching was used to locate the chordwise rows of grid points closer to each other near the wing tip. The number of points in each chordwise row was divided between the wing surface and the wake. Polynomial stretching was used to cluster the desired number of wing surface grid points near the leading and trailing edges. The same nondimensional chordwise locations were used for each row. The downstream boundary was chosen to be 5 semispans, or 10 root chords, downstream of the wing root leading edge. The distance from the wing trailing edge to the downstream boundary differed from the wing root to the wing tip. Polynomial stretching was also used to cluster the wake grid points near the wing trailing edge for each chordwise row in the wake.

A round tip cap was added to the wing surface grid. A sketch showing the development of the tip cap is presented in the middle part of figure 50(a). At each chordwise station on the wing tip, the location of the camber line and the airfoil thickness were determined from the locations of the grid points on the upper and lower surface of the open wing tip. The sweep of the line with a constant chordwise location was determined from the two chordwise rows of grid points closest to the wing tip. Grid points were spaced at equal angular intervals by rotating a line, with a radius equal to one half of the airfoil local thickness, about a point on the camber line in a plane which

contains the lines at the constant chordwise location. The resulting complete surface grid is shown at the bottom of figure 50(a).

Outer boundaries for the computational space were defined so that the farfield boundary was located 5 semispans upstream of the wing root leading edge and 5 semispans from the plane of symmetry. As noted previously, the downstream boundary was 5 semispans downstream of the wing root leading edge. A sketch of these outer boundaries is shown in the top part of figure 50(b). Transfinite interpolation (reference 51) was used to fill in the volume grid between the wing surface grid and the outer boundaries. Grid points were clustered near the wing surface to capture the large velocity gradients there. These grid points were placed on lines normal to the wing surface and normal to the outer boundary. Points near the farfield were smoothly connected to points near the surface.

Points on the leading and trailing edges of the wing tip collapse onto a single point as shown in the sketch in the center portion of figure 50(b). These collapsed points extend from the tip leading edge to the farfield boundary and from the tip trailing edge to the downstream boundary. Collapsed points lead to cells which have faces with zero surface area. Cells with collapsed faces are not easily handled by the TLNS3D code so the collapsed points must be spread apart. These cells have a very small height to resolve the large velocity gradient in the normal direction near the wing surface. Collapsed points are uniformly spread inboard across a distance equal to the local cell height.

Grid Convergence Study

The number of cells in each coordinate direction should be sufficiently large such that increasing the number of cells in any of the three coordinate directions does not have a significant effect of the wing lift, drag, or pressure distributions. A systematic study of the effect of varying

the number of cells in each direction has been completed to determine the number of cells to be used for the final Navier-Stokes calculations with spanwise blowing. As the number of cells in a given direction was increased, the spacing of the cells was decreased proportionately. Farfield and downstream boundaries remained the same for all grids. The Navier-Stokes solver was run on each grid at a Mach number of 0.311 and an angle of attack of 3.03° until the residual error was reduced by at least four orders of magnitude. Using three levels of multigrid, this typically required 50 cycles on the coarse grid, 50 cycles on the intermediate grid, and 200 cycles on the fine grid. The effect of the number of chordwise cells was studied for three different numbers of normal cells: 32, 48, and 64. Results of these calculations are presented in figure 51(a). There is a significant increase in lift coefficient and decrease in the drag coefficient as the number of chordwise cells increases from 96 to 128 to 192. As the number of cells increases from 192 to 256 for either 48 or 64 normal cells, there is less than a .001 increase in the computed lift coefficient and about a .0002 decrease in the computed drag coefficient. These values are smaller than the accuracy of the experimental measurements. Thus, 192 cells in the chordwise direction will have an error due to grid size that is smaller than that of the experiments of Chapter VI and should be sufficient for this study.

Results from figure 51(a) are cross-plotted in figure 51(b) to determine the required number of normal cells. For 192 chordwise cells, the change in drag coefficient is about .0035 as the number of normal cells increases from 32 to 48 and about .0005 as the number of cells increases from 48 to 64. Increasing the number of cells above 64 should change the drag by a small fraction of the change of .0005 between the last two grids. Thus, 64 cells in the normal direction will provide adequate numerical accuracy and will be used for the final grid for this study.

Using the established number of streamwise and normal cells, the number of spanwise cells was varied from 32 to 48 and the results are presented in figure 51(c). Increasing the number of spanwise cells from 32 to 40 decreases the lift coefficient by .001 and the drag coefficient by .0003. However, increasing the number of cells from 40 to 48 produced less than a .001 change in lift

coefficient and a virtually no change in drag coefficient. Therefore, the number of spanwise cells for the final grid will be 40.

A sketch of the final wing surface grid with the rounded tip cap is presented at the bottom of figure 50(a). Note that every other grid line has been omitted for clarity. The number of chordwise cells on the wing surface is 128 and the number in the wake is 64 for a total of 192. Because of the "C" grid topology, 64 cells are used on each of the upper and lower surfaces and 32 cells are used in the wake from the wing trailing edge to the downstream boundary. Cells at the wing leading edge were spaced 0.2 percent chord apart and cells at the trailing edge were spaced 0.6 percent chord apart. There were 40 cells in the spanwise direction with 8 cells for the upper half and 8 cells for the lower half of the rounded tip cap.

The wing surface grid was extended into the volume grid shown at the bottom of figure 50(b). Note that many of the grid lines have been omitted, especially near the wing surface and the wake. The farfield and downstream boundaries were about 5 semispans from the wing root leading edge. Note that the cells are clustered near the wing surface in the normal direction. Clustering of cells near the trailing edge is manifested by the smaller spacing of the lines extending from the trailing edge on the plane of symmetry to the upper and lower farfield boundaries. There were 64 cells in the normal direction with a height at the wing surface ranging from 0.00005 semispans at the wing root to 0.00002 semispans at the wing tip.

Validation of the Navier-Stokes Solver

The Navier-Stokes code solves the equations on a single grid, usually representing a wing alone. The experimental setup utilized a wing-body combination. Presence of the body modifies the local flowfield about the wing. The wing balance measured the forces and moments on the wing which included induced effects from the body. Comparison of experimental data from the wing-body combination with results from the Navier-Stokes solution for the wing alone would not

be valid. Effects of the body on the wing flowfield must be included in the calculations.

The body blocks the approaching flow leading to a local increase in the velocity in the plane of the wing. It also acts as a low aspect ratio lifting surface inducing an upwash in the plane of the wing. Both of these effects are largest near the body and decrease rapidly with increasing distance from the body. Effects of the body on the local flowfield were computed using the panel method code, VSAERO, described in reference 52. The body alone with a fixed wake was represented using 880 panels. The program provided three components of velocity at user defined points in the flowfield. Vertical and streamwise components of velocity along the quarter chord line of the wing were used to predict the change in local Mach number and angle of attack induced by the body at several different free stream Mach numbers and angles of attack. The increase in velocity and local angle of attack due to the presence of the body are plotted at appropriate spanwise locations on the wing, if it was present, in figure 52. On the quarter chord line, the induced angle of attack was largest near the wing root and decreased rapidly out to the wing tip. Variation of the induced angle is strongly dependent on the body angle of attack and only weakly dependent on the free stream Mach number. The correction factor for the Mach number was largest near the root and decreased toward the wing tip. It was strongly dependent on the free stream Mach number and only weakly dependent on the body angle of attack.

Induced upwash from the body is equivalent to a twist across the wing. The angle distribution from figure 52 was used to define the wing twist at five equally spaced stations across the wing. This wing twist was incorporated into the wing surface grid definition. A separate wing surface grid was defined and used to create a different volume grid for each of the nominal angles of attack used in the numerical study: 0°, 1°, 2°, and 4°.

Induced streamwise flow from the body is equivalent to a spanwise change in the free stream Mach number. To simplify the calculations, an average change in the free stream Mach number will be used as an approximation. Since most of the change occurs near the wing root and

the change is fairly constant on the outer portion of the wing, the use of an average approximation is reasonable. The free stream Mach number for the Navier-Stokes calculations was increased by change in the local Mach number at the 42 percent semispan position since the center of lift is located there. Navier-Stokes calculations are performed on the appropriate grid for the desired angle of attack at the adjusted free stream Mach number and the root angle of attack adjusted for the wing twist. Pressure coefficients are corrected back to the experimental Mach number by multiplying by the ratio of the dynamic pressures and shifting the pressure coefficient by the difference in the free stream static pressures. Section lift and drag coefficients are rotated back into the the untwisted wing axis system and corrected for the change in the free stream dynamic pressure. Corrected section properties are integrated across the span to obtain the corrected wing lift and drag coefficients.

Computed results are compared to experimental results at Mach numbers of 0.3 and 0.7 to demonstrate the ability of the code to predict the aerodynamic characteristics without blowing. The computations were performed at the Reynolds number from the wind tunnel tests: 1.9×10^6 for a Mach number of 0.3 and 3.5×10^6 for a Mach number of 0.72. The start of the turbulent boundary layer calculations began at the experimental location of the transition strip. All computed results have been corrected for the induced effects of the body. Comparisons of computed and experimental results for several spanwise stations at a Mach number of 0.306 and an angle of attack of 2.07° are presented in figure 53. In general, the agreement is very good. There is some scatter in the experimental results. The code generally underpredicts the upper surface suction at all spanwise stations and the peak leading edge suction at the outboard stations. The change with span is probably due to a small error in the twist in the grid and due to the application of a global correction to the Mach number rather than one that varied across the span. The code does a good job predicting the magnitude and location of the rapid compression on the aft portion of the upper surface. However, it tends to overpredict the rapid compression on the lower surface. The difference is largest at the inboard stations. Although the flow is subsonic, the

code treats this compression in the same manner that it would treat a shock. Also, minor manufacturing differences between the measured check points could lead to this overshoot.

Effect of angle of attack on the comparison of experimental and computed chordwise pressure distributions is presented in figure 54 at the 50 percent spanwise location. Again, the computed results are in very good agreement with the experimental results. The leading edge suction peak and the pressures on both surfaces back to the rapid compression agree very well. Agreement improves with increasing angle of attack. The experimental scatter is reduced at the higher angles because the the signal to noise ratio increases as the pressure and the signal increase with angle of attack. The overshoot in the rapid compression region on the lower surface appears for all three angles of attack. Computed results show virtually no trailing edge separation at angles of attack up to 4°, which is consistent with experimental results. The small amount of trailing edge separation in the computed solution is due to the sudden change in the wing surface angle required to close the trailing edge to a point.

Spanload distributions for these three angles of attack were computed and the results are presented in figure 55. Agreement is very good at the two lower angles of attack although there is some scatter in the experimental result. At the larger angle, the agreement is only fair. Comparison of the computed and measured lift and drag is presented in figure 56. In general, the lift curve slopes are in very good agreement but the computed lift is slightly less than the experimental value at a given angle of attack. The difference in lift coefficient ranges from 0.006 to 0.016. Computed drag is greater than the measured drag but follows the trend of the experiment well with a difference in drag coefficient ranging from 0.0004 to 0.0008. Thus, at a Mach number of 0.306, the Navier-Stokes solver does a very good job predicting the pressure distributions everywhere but on a small portion of the lower surface, a good job predicting the span load distributions at the lower angles of attack, and a good job predicting the total lift and drag.

Computed results are compared with experimental results at a Mach number of 0.719

where there is supercritical flow over the wing. Chordwise pressure distributions are compared at several spanwise stations in figure 57 at the highest angle of attack tested, 0.95°. At the inboard station, $\eta = 0.25$, the code tends to overpredict the suction on the central portion of the airfoil. Since the difference is not apparent at the other spanwise stations, a likely cause is interference from the body. At transonic conditions, the use of a global correction to the Mach number may not be adequate. Since the tip region is most important in this study, this minor difference at the inboard station is acceptable. The code predicts the compression region very well. The lower surface is in very good agreement with only a slight overshoot at the end of the rapid compression. Agreement of the results at the two middle stations, $\eta = .50$ and $\eta = .70$, which are farther away from the influence of the body, is excellent. At the most outboard station, η=0.90, the prediction agrees very well with the experiment except for a small region on the upper surface where the flow is decelerating. The start of this small region is very close to the location of the transition strip which suggests that the difference is due to a small region of separation at the transition strip. The code will be used to predict the changes due to blowing so that small differences in the actual values will be subtracted out. The code does a good job in the tip region, which is most important to this study, so that small differences at the inboard stations are acceptable.

Effect of angle of attack on the comparison of the chordwise pressure distributions is presented in figure 58 at the 50 percent spanwise location. At the lower angle of attack, there is only a small region of supersonic flow on the upper surface. However, at an angle of attack of 0.95°, supersonic flow extends from about 10 to 60 percent chord. Computed and the experimental results are in very good agreement. The Navier-Stokes solver tends to overpredict the upper surface suction slightly. The code does a good job predicting the location of the compression region on both surfaces and the magnitude of the pressure rise. The results on the lower surface are in excellent agreement. The code does a very good job predicting the results for conditions which result in regions with supercritical flow.

Computed and experimental spanload distributions for these two angles of attack are

compared in figure 59. As noted previously, the code overpredicts the suction on the upper surface at $\eta = .25$ which leads to an overprediction of the section lift coefficient there. The agreement between $\eta = .70$ and $\eta = .90$ is very good. Since blowing from the wing tip is not expected to have a measurable effect at the inboard portion of the wing, the differences between the calculations and the experiment are acceptable. Comparison of the wing lift and drag are presented in figure 60. Calculations match the experimental results very well. The computed lift differs from the measured lift by 0.005 and the computed drag differs from the measured drag by 0.0005.

From these results without blowing, the Navier-Stokes solver with the correction for the induced effect of the body does a satisfactory job predicting the wing lift, drag, and pressure distributions at Mach numbers of 0.30 and 0.72. Experimental data from this test and flow visualization results from reference 35 will be used to demonstrate that the solver with the modified boundary conditions for blowing does a satisfactory job in predictiong the effects of blowing at a Mach number of 0.30. Validation of the boundary conditions used in the code to simulate blowing is presented below.

Validation of the Boundary Conditions Used to Simulate Tip Blowing

Modifications to the Navier-Stokes solver to simulate spanwise blowing from the wing tip are validated by comparing calculated results with blowing with experimental results. Experimental results from Chapter VI are used to demonstrate that the code predicts the effects of blowing on the surface pressures, span load distribution, lift, and drag. Flow visualization results from reference 35 are used to demonstrate that the computed flow near the surface matches the experimental trends. Computed solutions of flow in the wake are used to demonstrate that the solver predicts the expected trends of blowing on the rollup of the wake behind the wing.

The most significant modification to the code involved changes to the boundary conditions

used for the cells tangent to the wing surface that are used to simulate blowing. Three components of momentum, density, and pressure characterize the jet. The jet exit static pressure is equal to the local static pressure for a fully expanded jet. These physical characteristics at the jet exit are used to determine the mathematical boundary conditions.

To model the jet characteristics, density and the three components of momentum were specified at the exit and the pressure was specified at the ghost cell. Values of the density and momentum for the ghost cells were determined from values at the surface (or exit) and from values for the cells tangent to the surface. The value of the pressure for the ghost cell was obtained from the solution without blowing for the cell tangent to the ghost cell on the wing surface. These boundary conditions led to a converged solution with realistic values of density and pressure near the wing tip. They were used for calculations simulating blowing from the front and rear jets of tip 8 to determine how well the calculations match the experimental results.

The boundary conditions for selected cells were modified to simulate spanwise blowing from the jets of tip 8. Boundaries of cells with blowing do not match the experimental jet boundaries exactly because of the technique used to define the surface grid. The rounded wing tip was formed by spacing grid points at equal angular increments. Such spacing led to cells with changing heights so that the cell boundaries were not aligned with lines of constant height. Cells with boundary conditions modified for blowing were selected by overlaying the outlines of the front and rear jet exits on the sketch of the rounded tip as shown in figure 61. Those cells with more than half of the face area within the jet exit, identified by the shading, had the boundary conditions modified for jet blowing. In general, the jet exhaust was only two cells high. The ratio of the jet exit area to the wing area for the experiment and the calculations are similar. For the front jet, the ratios were 2.8×10^{-4} for the experiment and 2.5×10^{-4} for the computations. For the rear jet, the ratios were 6.7×10^{-4} for the experiment and 7.2×10^{-4} for the computations. Modifications to the boundary conditions to simulate blowing were validated by demonstrating that the code predicts the effects of blowing on the chordwise pressure distribution, span load

distribution, wing lift and drag, particle paths near the wing tip and jet, and streamwise vorticity downstream of the wing tip.

Comparison of Wing Pressures and Loads

The Navier-Stokes solver was used to compute the flowfield with and without tip blowing using the final grid at a Mach number of 0.307 and an angle of attack of 2.07°. All results were corrected for the induced effects from the body. The effect of blowing from the front and rear jets on the chordwise pressure distributions at $\eta = 0.90$ is presented in figure 62. As was found in the experiments, blowing has only a small effect on the pressure coefficients. For the front jet, blowing increases the suction on the upper surface and reduces the pressure slightly on the lower surface. The increase in suction is largest over the central portion of the chord and increases with increasing jet momentum coefficient. Blowing has little effect on the pressures across the rapid compression on the aft portion of the airfoil. For the rear jet, blowing increases the suction on the aft portion of the upper surface and increases the pressure on the lower surface. The region on the upper surface influenced by the jet extends from the central portion of the chord back to the trailing edge. As was the case with the front jet, changes due to blowing increase with increasing jet momentum coefficient. Except for the loss of pressure on the lower surface with blowing from the front jet, these same trends were found in the experiments described in Chapter VI.

Effects of blowing on the pressures are very small when viewed using scales to show the pressure distribution across the wing. Therefore, the change in pressure coefficient due to blowing will be used to compare the calculated and experimental pressure coefficients. Comparison of the results for the front jet and the rear jet at $C_\mu = 0.0066$ is presented in figure 63. For the front jet, the calculated and the experimental increase in suction (negative ΔC_p) on the upper surface are in very good agreement with both showing similar changes at similar locations along the chord. Both the experiment and the calculations show a small positive change in pressure on most of the lower surface but the calculated results show a reduced pressure along the rear portion of the chord. The

trailing edge pressure becomes less positive with blowing. Differences on the aft portion of the airfoil will effect the computed change in lift and drag. For the rear jets, both the calculated and the experimental results show an increase in suction on the upper surface. Both show the largest increases over the aft portion of the chord and a small increase in the suction peak. Calculations underpredict the suction on the forward portion of the chord and overpredict it on the rear portion. On the lower surface, the calculations overpredict the increase in pressure on the front portion of the chord. These small differences will lead to errors in the prediction of the pressure component of the drag. The effect of blowing should increase at locations closer to the tip. Additional experimental data is needed closer to the jet exit to determine better how well the code predicts the effects of blowing.

Changes in the chordwise pressure distributions will be reflected in the span load distributions. Effects of blowing from the front and the rear jets on the computed spanload distributions are presented in figure 64. Similar trends are found for both jets. Blowing increases the loading near the wing tip but the effect becomes small as the distance from the tip increases. Loading near the tip increases with jet momentum coefficient. The increase is larger and extends farther inboard for the rear jet than for the front jet. These trends are similar to the experimental results.

The section lift coefficient near the wing tip increases with increasing jet momentum coefficient. Comparison of the change in the computed and the experimental section lift coefficients at the 90 percent semispan location is presented in figure 65. For the front jet, computations show the proper trend but the predicted increase in lift is too low. Differences between the prediction and the experiment become worse as the blowing increases. For the rear jet, the computations are in reasonable agreement with the experiments. Small differences noted in the change in the chordwise pressure distributions lead to these moderate differences in the section lift coefficients.

Computed changes in the wing lift and drag coefficients are compared to the experimental results in figure 66. For the front jet, the computations match the experiment well at the lower jet momentum coefficients. There were no computations at the highest experimental jet momentum coefficient because a supersonic exhaust velocity was required due to the smaller computational jet exit area. However, the trends are correct. For the rear jet, changes in the computed and experimental lift coefficients are in good agreement. Computed drag increases slightly with increasing jet momentum coefficient, which is opposite of the effect found in the experiments. Although the trend is the opposite of that expected, the change is still very small, on the order of the accuracy of the drag computations. The increase in computed drag is due to the increase in suction on the aft part of the airfoil. Drag calculations are divided into viscous and pressure components. Calculations show that the viscous drag is the same with or without blowing. Pressure drag increases with blowing. This is caused by the increase in suction due to blowing on the rear half of the chord. Since the surface has an aft facing component, increased suction leads to increased drag. Surface pressure coefficients, span load distributions, and the wing lift and drag coefficients predicted by the Navier-Stokes solver are in good agreement with the experimental results.

Comparison of Particle Paths

The solver should also predict other trends described in the literature but not measured in the wind tunnel experiments described herein. The code should predict the entrainment of flow into the jet as well as the outward displacement and diffusion of the wing tip trailing vortex. Water tunnel flow visualization studies, reported in reference 35, were conducted by the author and others to study the effect of blowing on the flow near the surface of the wing tip and the path of the jet exhaust. The studies were conducted in the Langley 16- by 22-Inch Water Tunnel on a 55 percent scale model of the wing used in the experiments presented herein. One of the tips tested, tip B, was the same as tip 8 used in the wind tunnel tests except that the length of the rear jet was

reduced from 0.31 c_t to 0.29 c_t to provide clearance for the attachment screw. The wing and tip were mounted on a splitter plate. Free stream velocity was either 0.25 ft./sec. or 0.375 ft./sec. with the corresponding Reynolds numbers of 0.9×10^4 and 1.3×10^4. The jet to free stream velocity ratio was varied from 0 to 6. Colored dye was injected into the jet supply lines and injected into the flow from three orifices on the upper part of the front of the tip. Flow visualization photographs were recorded of the jet paths and the paths of the flow starting at the three dye orifice locations. A well defined, rolled up wing tip vortex could not be located.

Paths of the jet exhaust depend primarily on the jet velocity ratio (or jet momentum coefficient). For attached flow, particle paths near the tip depend on the wing lift and jet momentum. The photographs showed that the jets penetrate a greater distance into the free stream as the jet momentum coefficient increases and a smaller distance as the angle of attack (or wing lift) increases. Flow over the tip moves inboard with increasing lift and is entrained out towards the jet with increasing jet momentum coefficient. Both of these trends should be present at the higher Mach number and Reynolds number used in the wind tunnel experiments and, consequently, should be predicted by the Navier-Stokes solver.

Flow visualization photographs from reference 35 will be compared with particle paths predicted by the Navier-Stokes solver to demonstrate that the code predicts the observed type of flow patterns. The Navier Stokes code was used to predict the effects of blowing on the flow near the surface of the tip and the path of the jet exhaust as well as the effect of blowing on the rollup of the wing tip vortex. An untwisted grid was used for these calculations because there was no body present for the water tunnel tests. Also, different cells were used to simulate the jet since the rear jet was slightly shorter than the scaled length for tip 8. The angle of attack of the water tunnel model was estimated to be about 5° above the angle of zero lift. Calculations were performed at a Mach number of 0.3 and a Reynolds number of 3.3×10^6 from the wind tunnel experiments and at the estimated angle of attack of 3.6° from the water tunnel tests.

A-2

Comparison of flow visualization photographs with computed particle paths starting at the location of the dye orifices and along the centerline of the jet exit are presented in figure 67. Results without blowing, shown in figure 67(a), are similar on the forward portion of the airfoil. Because of the low Reynolds number and the laminar boundary layer in the water tunnel tests, flow separated from the model just aft of the point of maximum thickness. Particles move inboard as they move downstream. In the water tunnel tests, flow separated from the upper surface at about the 40 percent chord because of the low Reynolds number. Particle traces no longer move inboard but tend to move downstream. Computed results, at a much higher Reynolds number, show the same inboard movement over the forward portion of the tip. They do not show separation and the particles continue to move inboard over the aft portion of the airfoil until the rapid compression region where the flow turns outboard. Experimental and computed jet paths for the front jet, shown in figure 67(b), are very similar. In both cases, blowing inhibits the inboard movement of the particle paths. Particles injected at the rear two dye orifices are entrained directly into the jet. Width of the jet spreads as the jet flow moves downstream with the inboard portion of the jet crossing the tip trailing edge. This inward movement is due to the local flowfield with lift in which flow swirls around the wing tip. Results for the rear jet, shown in figures 67(c) to 67(e), are similar to those of the front jet. At the lowest blowing coefficient tested, the particle paths move inboard and are then entrained into the jet. Poor prediction of the jet path at the lowest momentum coefficient, in figure 67(c), is probably due to an incorrect wing lift since the angle of attack was not accurately known. At low velocity ratios, small changes in the wing lift lead to large changes in the flow swirling around the tip. Jet paths at the two larger jet momentum coefficients are in better agreement.

Computations of Wake Vorticity

Experimental results, published in reference 27, indicated that blowing diffuses the rolled up vortex wake and displaces it outboard. Streamwise vorticity was computed at several locations

downstream of the wing tip trailing edge with and without blowing from the front jet and the results are presented in figure 68 as contours of constant streamwise vorticity. Lift with blowing is only slightly larger than without blowing. Thus, similar amounts of vorticity would be present in each wake. Without blowing, the vorticity just downstream of the wing tip is concentrated in a small area centered just outboard of the wing tip. As it is convected downstream, the vorticity diffuses generally in an upward and outward direction. With blowing, vorticity just downstream of the wing tip is spread over a larger area. The peak level of vorticity has been reduced compared to the no blowing case. At the three most downstream stations shown, the peak level of vorticity without blowing is higher as shown by the additional contour line for the no blowing case. Computations correctly predict that blowing diffuses and displaces the tip vortex.

The pair of counter-rotating vortices did not show up on the contours of streamwise vorticity with blowing present. For these cases, the jet exit was one or two cells thick. Finer resolution of the jet and the region around and downstream of the tip are needed to resolve these two vortices. However, with a structured grid, increasing the resolution increases the number of cells to such an extent that the computer memory capacity is exceeded.

The effect of blowing intensity on the distribution of streamwise vorticity is shown in figure 69 for the rear jet, just downstream of the wing tip, at $\frac{x}{c_t} = 1.4$. Without blowing, vorticity is centered at the wing tip and is concentrated over a small area. With increasing blowing, the center of the vorticity moves outboard and is displaced over a wider area. These trends are consistent with the trends reported in reference 27.

Calculations using the Navier-Stokes solver with modified boundary conditions to simulate blowing from the wing tip demonstrate almost all of the published experimental trends. Generally, computations are in good agreement with experimental results. Computations showed that blowing increases the suction on the upper surface of the wing near the tip, the loading near the wing tip, and the wing lift. The code also predicts similar jet paths and particle paths near the

wing tip. Computations also successfully predicted that blowing displaces and diffuses the wing tip vortex. The only trend not always predicted correctly by the Navier Stokes solver is drag. However, the difference is very small and within the accuracy of the drag measurements. Thus, the code can be used to predict most of the effects of spanwise blowing from the wing tip.

Effect of Blowing at a Cruise Mach Number

The Navier Stokes solver was used to compute the flowfield about the wing with tip 8 at a Mach number of 0.72 at an angle of attack of 1.0°. Jet exhaust velocity was limited to a Mach number of 0.9 since a supersonic jet would probably not be acceptable from standpoints of noise and structural fatigue. This effectively determined the maximum jet momentum coefficient at each Mach number for the fixed jet exit areas of tip 8. Initial computations were performed without blowing and with blowing at the maximum exit velocity for the front jet, rear jet, and both jets. For these initial cases, the jet exhausted in the spanwise direction. Additional computations for both jets were performed at the maximum jet exit velocity but deflected downward 30°.

The effect of blowing from the front jet on the chordwise pressure distributions is presented in figure 70 for three spanwise stations: $\eta = 0.90$, $\eta = 0.95$, and $\eta = 0.98$. Because of the small exit area, the jet momentum coefficient was only 0.0012. At $\eta = 0.90$, blowing reduces the suction on forward portion of the upper surface and increases the suction on the rear portion of the upper surface. Blowing generally increases the pressures on the front portion of the lower surface and reduces the trailing edge pressure. At $\eta = 0.95$, the effects of blowing described for the $\eta = 0.90$ case are accentuated, especially the trailing edge pressure coefficient. Close to the tip, at $\eta = 0.98$, blowing induces large changes in the pressure distribution, especially over the forward portion of the airfoil. It reduces the suction on the upper and lower surfaces at stations ahead of the jet. Suction increases on both surfaces across the jet. Higher suction pressures are maintained aft of the jet on the upper surface. The trailing edge pressure becomes less positive as the tip is approached.

The effect of blowing from the rear jet on the chordwise pressures is presented in figure 71 at the same three spanwise stations. At $\eta = 0.90$, blowing reduces the suction on the upper surface back to the start of the rapid compression. From the start of the compression region and continuing aft, blowing increases the suction on the upper surface. Blowing generally increases the pressures on the lower surface up to the rapid compression region and reduces the trailing edge pressure coefficient. At $\eta = 0.95$, the effects of blowing described for the $\eta = 0.90$ case are accentuated, especially the trailing edge pressure coefficient. Also, the upper surface suction increases on the aft part of the airfoil. Close to the tip, at $\eta = 0.98$, blowing induces large changes in the pressure distribution, especially over the aft portion of the airfoil. This is similar to the effect of blowing from the front jet. Suction is reduced ahead of the jet and increased along the length of the jet, with separation on the aft portion of the upper surface. The strong compression region on the upper surface is diminished and the trailing edge pressure coefficient is greatly reduced.

The effect of blowing with both jets operating on the chordwise pressure distributions is presented in figure 72. Effects of the rear jet, which is longer, predominate at the inner two stations, $\eta = 0.90$ and $\eta = 0.95$. Suction on the front part of the upper surface is reduced and the suction on the rear half is increased by blowing. Blowing also increases the pressure coefficient on the front half of the lower surface. The trailing edge pressure coefficient and the pressure coefficients over the aft portion of the airfoil indicate a thickened boundary layer. Near the tip, at $\eta = 0.98$, effects from both jets can be seen. On the forward portion of the airfoil, the front jet reduces the suction on the upper surface and increases the pressure on the lower surface. The rear jet reduces the rapid pressure recovery on the upper surface as well as the trailing edge pressure coefficient.

The particle paths on the upper surface with and without blowing are presented in figure 73. Without blowing, particle paths starting from the leading edge region on the upper surface move inboard as they are convected downstream until the rapid compression is reached

where they move outboard. Particles released along the tip move inboard along the forward portion of the chord and are eventually drawn to the trailing edge of the tip. With blowing from the front jet, shown by the dashed lines, flow swirls around the tip. At this low velocity ratio of 1.3, the jet blocks the flow leading to a large, triangular shaped, separation region, shown by the absence of particle paths. Blowing has little effect on the particle paths starting from the leading edge. With blowing from the rear jet, the jet swirls over the tip leading to a stagnant region near the surface on the aft part of the tip. At the start of the compression region, the flow turns sharply outboard.

Span load distributions with and without blowing for the front jet, rear jet, and both jets are presented in figure 74. The small momentum from the front jet leads to little change in the span load distribution. For the rear jet, blowing increases the load over the outboard 10 percent of the wing. Results for both jets are practically the same as for the rear jets.

Changes in the section lift coefficient at $\eta = 0.90$ and wing lift and drag coefficient with blowing are presented in figure 75. For the front jet, the momentum is too small to have an impact on the section lift coefficient or the total wing lift coefficient. Drag increases by about 3 counts because of the separated region created by the blockage of the jet. For the rear jet, both the section lift and wing lift coefficients increase by about 1 percent and the drag increases by about 7 counts with the addition of blowing. Results for both jets are roughly just the combination of the changes from the front and rear jets: about a 1 percent increase in lift and about 10 counts increase in drag. The region of separated flow is relatively small so that use of the Baldwin-Lomax turbulence model is still acceptable. Although the actual drag increase might differ from the calculated increase, the existance of the separated flow region supports the contention that there is a small drag increase with blowing from the wing tip.

Blowing from the front jet leads to a large separated region near the tip. The extent of the separated region can be reduced by preventing the jet flow from swirling around the tip. To

counteract this, either the jet momentum coefficient can be increased or the jet exhaust deflected down to oppose the local velocity. Increasing the jet momentum probably would not yield a drag reduction greater the the jet momentum and is probably not practical. Therefore, effect of redirecting the exhaust velocity will calculated. For these calculations, the jet exit Mach number was maintained at 0.9. Chordwise pressure distributions near the tip are presented in figure 76. Deflecting the jet down 30° increased the suction on the upper surface, increased the pressure on the lower surface, and increased the trailing edge pressure coefficient. At $\eta = 0.98$, deflecting the jet down reduced the extent of the separated region on the upper surface. Particle paths for the deflected jet, shown in figure 77, show that the front jet does not swirl around the tip as much as it did for the undeflected jet, although the traingular shaped separation region is still present. The spanload distribution, shown in figure 78, shows an increase in the loading near the tip, which was expected from the pressure distributions. Deflecting the jets down increases the lift from 0.297 to 0.299 without changing the drag from the value obtained with the undeflected jet.

Calculations indicate that spanwise blowing at transonic Mach numbers increases the section lift coefficient near the tip and the wing lift coefficient and increases the drag slightly.

CHAPTER VIII

CONCLUSIONS

The following conclusions can be drawn from the literature survey, the application of the simple mathematical model, the experiments at low Mach number, and the Navier-Stokes calculation at a cruise Mach number.

Published studies were restricted to low aspect ratio wings with lift augmentation, not drag reduction as the main thrust of the research. The studies indicated that blowing increases the suction on the upper surface of the wing, increases the lift near the tip, increases the lift curve slope and possibly the maximun lift coefficient, displaces the tip vortex outboard, and diffuses the tip vortex. These effects are indicative of an increase in the effective aspect ratio. Blowing also entrains flow outboard into the jet. An increase in the effective aspect ratio of a moderate aspect ratio wing could lead to a small increase in the lift and a decrease in the induced drag.

The simple, mathematical model successfully predicted that the wake moves down with increasing lift coefficient and the rolled up vorticity moves inboard with increasing lift (or angle of attack). It showed that blowing displaces the tip vortex outboard and that the outward displacement increases with increasing jet momentum. The stretched spiral with a reduced number of turns indicated that less vorticity is spread over a larger area. The upper counter-rotating vortex from the pair of vortices associated with the jet can be absorbed by the tip vortex for certain flow conditions. Directing the jet downward displaced the tip vortex down slightly. Directing the jet rearward produces the same benefits found with the spanwise directed jet with the additional benefit of a direct component of momentum in the drag direction. Displacing the jet aft leads to a larger modification of the rolled up wake than locating the jet near the quarter chord.

The experiments showed that blowing had little measurable effect on drag for the jets with the baseline exits (0.25 inches by 0.06 inches) when the exit Mach number was restricted to about

0.9. Only tip 8, with the long jets, showed drag reductions that were larger than the balance accuracy. The reductions ranged from .0012 to .0022, which is a significant part of the estimated total drag coefficient of 0.0300. Most tips showed an increase in the lift curve slope with blowing and the linear portion of the curve extended to a higher angle of attack, which is an indicator that blowing possibly delays separation. Blowing increased the slope of the wing root bending moment curves indicating that the center of lift is moved outboard by .6 to 1.3 percent of the semispan. Blowing generated a small negative increment in the pitching moment coefficient.

Additional tests with tip 8 indicated that with the ram drag penalty there is little, if any, total drag reduction with blowing. For moderate lift and Mach numbers ranging from .2 to .4, wing lift increases and drag decreases with blowing for tip 8. At a Mach number of 0.5, blowing has little effect on the drag because the available jet momentum coefficient is too small to be effective. For the long jets of tip 8, blowing increases the section lift coefficient at stations outboard of $\eta = 0.8$. The increase is largest for the largest blowing coefficient. Spanwise blowing increases the suction on the upper surface at $\eta = 0.9$ and the positive pressure on the lower surface. The changes become larger with increasing blowing. Blowing from front jet increases leading edge suction more than blowing from the aft jet.

Water tunnel tests of a subscale model of the wing indicated that the jet penetrates farther into the flow as the jet momentum increases. The penetration is reduced as the wing lift increases. Blowing from the jet entrains flow towards the jet.

Calculations using the Navier-Stokes solver with modified boundary conditions to simulate blowing from the wing tip are consistent with almost all of the published experimental trends. Generally, computations are in good agreement with experimental results. Computations showed that blowing increases the suction on the upper surface of the wing near the tip, the loading near the wing tip, and the wing lift. The code also predicts similar jet paths and particle paths near the wing tip. Computations also successfully predicted that blowing displaces and diffuses the wing tip

vortex. The only quantity not always predicted correctly by the Navier Stokes solver is drag. However, the difference is very small and within the accuracy of the drag computations.

Limiting the jet exhaust to a Mach number of 0.9 severely limits the maximum jet momentum available from the jets. Blowing reduces the suction ahead of the jet on the upper surface, increases the suctions across the jet, and makes the trailing edge pressure less positive. Blockage from the jet leads to a separated region at the tip. The region is larger for the front jet than the rear jet.

Deflecting the jet downward increases the suction on the upper surface and the pressures on the lower surface. It reduces the region of the jet blanketing the upper surface, yielding an increase in lift with no additional increase in drag over that of the undeflected jet.

Both the experiments at low subsonic Mach number and calculations at transonic Mach numbers indicate that spanwise blowing increases the loading near the wing tip and the wing lift coefficient. Experiments showed a small drag reduction with blowing at a low Mach number but the reduction vanished as the maximum jet momentum available decreased. Calculations at transonic Mach numbers indicated a region of separation near the tip with blowing that is consistent with a drag increase. With current technology and conventional wing shapes, subsonic spanwise blowing at the wing tip does not appear to be a practical means of reducing drag of moderate aspect ratio wings at transonic Mach numbers.

REFERENCES

1. anon.; Special Section on Drag Reduction. Aerospace America, January, 1988.

2. Vortex Wake Minimization. NASA SP-409. February 1976.

3. Munk, Max M,: The Minimum Induced Drag of Aerofoils. NACA TR 121.

4. Cone, Clarence D.: The Theory of Induced Lift and Minimum Induced Drag of Nonplanar Lifting Systems. NACA TR R-139. February 1962.

5. Reid, Elliott G.: The Effects of Shielding the Tips of Airfoils. NACA Report 201, 1924.

6. Riley, Donald R.: Wind-Tunnel Investigation and Analysis of the Effects of End Plates on the Aerodynamic Characteristics of an Unswept Wing. NACA TN 2440. May 1951.

7. Whitcomb, Richard T.: A Design Approach and Selected Wind-Tunnel Results at High Subsonic Speeds for Wing-tip Mounted Winglets. NASA TN D-8260, 1976.

8. Flechner, Stuart G.; Jacobs, Peter F.; and Whitcomb, Richard T.: A High Subsonic Speed Wind-Tunnel Investgation of Winglets on a Representative Second-Generation Jet Transport Wing. NASA TN D-8264, July 1976.

9. Spillman, J. J.: Wing Tip Sails; Progress to Date and Future Developments. Aeronautical Journal. December, 1987. pp. 445 - 453.

10. Spillman, J. J.: The Use of Wing Tip Sails to Reduce Vortex Drag. Aeronautical Journal. September 1978. pp. 387 - 395.

11. Vijgen, P. M. H. W.; Van Dam, C. P.; and Holmes, B. J.: Sheared Wing-Tip Aerodynamics: Wind-Tunnel and Computational Investigations of Induced Drag Reductions. AIAA 5th Applied Aerodynamics Conference, AIAA-87-2481, August, 1987.

12. Ayers, R. F.; and Wilde, M. R.: Aerodynamic Characteristics of a Swept Wing with Spanwise Blowing. Cranfield College of Aeronautics Note 57, September 1956.

13. Smith, V. J.; and Simpson, G. J.: A Preliminary Investigation of the Effect of a Thin High Velocity Tip Jet on a Low Aspect Ratio Wing. Australia Department of Supply, Research and Development Branch, Aeronautical Research Laboratories, Aerodynamics Note 163, June 1957.

14. White, Herbert E.: Wind-Tunnel Investigation of the Use of Wing-Tip Blowing to Reduce Drag for Take-Off and Landing. U. S. Navy David W. Taylor Model Basin Aerodynamics Laboratory Report 1043, January 1963.

15. Carafoli, Elie: The Influence of Lateral Jets, Simple or Combined with Longitudinal Jets, upon the Wing Lifting Characteristics. Proceedings of the International Council of the Aeronautical Sciences, pp. 257-262, 1962.

16. Carafoli, E.; and Camarasescu, N.: New Researches on Small Span-Chord Ratio Wings with Lateral Jets. U. S. Air Force Foreign Technology Division Translation FTD-HC-23-319-71, June 1969. (Translated from Studii si Cercetari de Mecanica Aplicata, 1970, Vol. 29, No. 4, pp. 947-962)

17. Carafoli, Elie; and Neamtu, Mihai: New Theoretical Developments on the Wings with Lateral Jets. Presented in "In Honor of Carlo Ferrari", Turin, Libreria Editrice Universitaria Levrotto e Bella. pp. 87-114. December 1974.

18. Carafoli, E.; and Neamtu, M.: Flow Around Wings With Inclined Lateral Jets. Mechanics Research Communications, Vol. 3, No. 3, pp. 163-168. 1976.

19. Lloyd, Adrian: The Effect of Spanwise Blowing on the Aerodynamic Characteristics of a Low Aspect Ratio Wing. von Karman Institute for Fluid Dynamics Project Report 1963-90. 1963.

20. Scheiman, James ; and Shivers, James P.: Exploratory Investigation of the Structure of the Tip Vortex of a Semispan Wing for Several Wing-tip Modifications. NASA TN D-6101, February 1971.

21. Tavella, D. A.; Wood, N. J.; and Harrits, P.: Influence of Tip Blowing on Rectangular Wings. AIAA 3rd Applied Aerodynamics Conference, AIAA-85-5001, October, 1985.

22. Tavella, D.; Wood, N.; and Harrits, P.: Measurements on Wing-Tip Blowing, NASA CR-176930, June 1985. (Also published as Joint Institute for Aeronautics and Acoustics report JIAA TR-64, Stanford University)

23. Tavella, D. A.; and Roberts, L.: The Concept of Lateral Blowing, AIAA 3rd Applied Aerodynamics Conference, AIAA-85-5000, October 1985.

24. Tavella, D.; and Roberts, L: A Theory for Lateral Wing-Tip Blowing, NASA CR-176931, June 1985. (Also published as Joint Institute for Aeronautics and Acoustics report JIAA TR-60, Stanford University)

25. Tavella, D.; Lee, C. S.; and Wood, N.: Influence of Wing Tip Configuration on Lateral Blowing Efficiency. AIAA 24th Aerospace Sciences Meeting, AIAA-86-0475, January 1986.

26. Tavella, D. A.; Wood, N. J.; Lee, C. S.; and Roberts, L.: Two Blowing Concepts for Roll and Lateral Control of Aircraft. NASA CR-180478. October, 1986. (Also published as Joint Institute for Aerodynamics and Acoustics Report No. JIAA-TR-75, Stanford University.)

27. Lee, C. S.; Tavella, D.; Wood, N. J.; and Roberts, L.: Flow Structure of Lateral Wing-Tip Blowing, AIAA-86-1810. 1986.

28. Briggs, M. M.; and Schwind, R. G.: Augmentation of Fighter Aircraft Lift and STOL Capability by Blowing Outboard from the Wing Tips. AIAA 21st Aerospace Sciences Meeting, AIAA-83-0078, January, 1983.

29. Schwind, R. G.; and Briggs, M. M.: Effects of Blowing Spanwise from the Tips of Low Aspect Ratio Wings of Varying Taper Ratio with Application to Improving STOL Capability of Fighter Aircraft. AFOSR-TR-83-1045. February, 1983.

30. Wu, J. M.; Vakili, A.; and Chen, Z. L.: Wing-Tip Jets Aerodynamic Performance. Proceedings of the International Council of the Aeronautical Sciences, paper ICAS-82-5.6.3, pp. 1115-1121, 1982.

31. Wu, J. M. and Vakili, A. D.: Aerodynamic Improvements by Discrete Wing Tip Jets. AFWAL-TR-84-3009, March 1984.

32. Wu, J. M.; Valili, A. D.; and Gilliam, F. T.: Aerodynamic Interactions of Wingtip Flow with Discrete Wingtip Jets. AIAA 2nd Applied Aerodynamics Conference, AIAA-84-2206, August 1984.

33. Wu. J. M.; Vakili, A.; Chen, Z. L.; and Gilliam, F. T.: Investigation on the Effects of Discrete Wingtip Jets, AIAA 21st Aerospace Sciences Meeting, AIAA-83-0546, January 1983.

34. Gilliam, F. T.: An Investigation of the Effects of Discrete Wing Tip Jets on Wake Vortex Roll Up. Ph. D. Dissertation, The University of Tennessee Space Institute, August, 1983.

35. Smith, Jeanette W.; Mineck, Raymond E.; and Neuhart, Dan H.: Flow Visualization Studies of Blowing From the Tip of a Swept Wing. NASA TM-4217. November, 1990.

36. Margason, Richard, J.; and Lamar, John E.: Vortex Lattice Fortran Program For Estimating Subsonic Aerodynamic Characteristics of Complex Planforms. NASA TN D-6142. February 1971.

37. Fearn, Richard L. and Weston, Robert P.: Vorticity Associated with a Jet in a Cross Flow. AIAA Journal, Vol. 12, #12, December, 1974.

38. Krausche, Dolores; Fearn, Richard L; and Weston, Robert P.: Round Jet in a Cross Flow: Influence of Injection Angle on Vortex Properties. AIAA Journal Vol. 16, #6, June, 1978.

39. Thames, F. C. and Weston, R. P.: Properties of Aspect Ratio 4.0 Rectangular Jets in a Subsonic Crossflow. AIAA 78-1508. August 1978.

40. Fink, P. T.; and Soh, W. K.: A New Approach to Roll-up Calculations of Vortex Sheets. Procedings of the Royal Society of London, A. 362, pp. 195-209, 1978.

41. Fox, Charles H. Jr.; and Huffman, Jarrett K.: Calibration and Test Capabilities of the Langley 7- by 10-Foot High Speed Tunnel. NASA TM X-74027. May 1977.

42. Sewall, William G.; McGhee, Robert J.; Viken, Jeffery K.; Waggoner, Edgar J.; Walker, Betty S.; Millard, Betty F.: Wind Tunnel Results for a High Speed, Natural Laminar Flow Airfoil Designed for General Aviation Aircraft. NASA TM 87602. November 1985.

43. Braslow, Albert L.; and Knox, Eugene C.: Simplified Method for Determination of Critical Height of Distributed Roughness Particles for Boundary-Layer Transition at Mach Numbers from 0 to 5. NACA TN 4363. September 1958.

44. Gillis, Clarence L.; Polhamus, Edward C.; and Gray, Joseph L. Jr.: Charts for Determining Jet-boundary Corrections for Complete models in 7- by 10-foot Closed Rectangular Wind Tunnels. NACA WR L-123, 1945. (formerly NACA ARR L5G31.)

45. Vatsa, V. N.: Accurate Numerical Solutions for Transonic Viscous Flow Over Finite Wings. Journal of Aircraft, Vol. 24, June, 1987, pp.377-385.

46. Vatsa, Veer N.; and Wedan, Bruce W.: Development of an Efficient Multigrid Code for 3-D Navier-Stokes Equations. AIAA Paper 89-1791. June, 1989.

47. Jameson, A.; Schmidt, W.; and Turkel, E.: Numerical Solutions of the Euler Equations by Finite Volume Methods Using Runge-Kutta Time-Stepping Schemes. AIAA Paper 81-1259, June, 1981.

48. Baldwin, B. S.; and Lomax, H.: Thin Layer Approximation and Algebraic Model for Separated Turbulent Flows. AIAA Paper 78-257, January 1978.

49. Thomas, J. L.; and Salas, M. D.: Far-field Boundary Conditions for Transonic Lifting Solutions to the Euler Equations. AIAA Paper 85-20. January, 1985.

50. Vatsa, V. N.: Accurate Soultions for Transonic Viscous Flow in Finite Wings. AIAA Paper 86-1052. May, 1986.

51. Eriksson, Lars-Erik: Transfinite Mesh Generation and Computer-Aided Analysis of Mesh Effects. Ph. D. dissertation. Uppsala University, Sweden. March 1984.

52. Maskew, B.: Prediction of Subsonic Aerodynamic Characteristics - A Case for Low-Order Panel Methods. Journal of Aircraft, Vol. 19, No. 2, February 1982, pp.157-163.

Table I

Characteristics of Models Used in Spanwise Wing Tip Blowing Experiments

Author	Ref.	$\frac{c_{tip}}{c_{root}}$	AR	$\frac{c_{jet}}{c_{tip}}$	Λ (deg)	C_μ
Ayers	12	1.0	1.4	.45	50	0-.14
Carafoli	15	?	2.0	?	?	1-1.75
Carafoli	16	1.0	.6 to 2.0	2.0	0	0-1.00
White	14	.5	2.7	.82	6	0-1.00
Smith	13	1.0	3.0	.80	0	0-.80
Scheiman	20	1.0	3.4	.50	0	0-.05
Lloyd*	19	1.0	2.0	.80	0	0-2.50
Briggs	28	.5-1.0	.6 to 4.0	.77-.85	0-26	0-.20
Tavella	21	1.0	3.0	.73	0	0-1.00
Wu	31	1.0	3.4	.10-.15	0	0-.05

*Tests used full span model.

Table II

Characteristics of the Semispan Wing

Twist:	0°
Taper ratio:	0.4
Chord	
root:	10.0 inches
tip:	4.0 inches
Airfoil section:	HSNLF(1)-0213
Sweep	
leading edge:	33°
Reference quantities	
semispan:	20.26 inches
chord:	7.394 inches
area:	140.80 inches^2

Table III

Ordinates of the HSNLF(1)-0213 Airfoil

x/c	y/c upper	y/c lower
0.00000	0.00000	0.00000
0.00025	0.00301	-0.00160
0.00050	0.00428	-0.00230
0.00075	0.00526	-0.00286
0.00100	0.00609	-0.00335
0.00150	0.00747	-0.00419
0.00200	0.00863	-0.00492
0.00250	0.00964	-0.00556
0.00500	0.01351	-0.00796
0.01000	0.01867	-0.01120
0.02000	0.02524	-0.01551
0.04000	0.03400	-0.02155
0.06000	0.04049	-0.02602
0.08000	0.04573	-0.02977
0.10000	0.05015	-0.03308
0.15000	0.05878	-0.03997
0.20000	0.06498	-0.04535
0.25000	0.06936	-0.04971
0.30000	0.07223	-0.05327
0.35000	0.07375	-0.05610
0.40000	0.07400	-0.05817
0.45000	0.07301	-0.05947
0.50000	0.07069	-0.05998
0.55000	0.06678	-0.05980
0.60000	0.06078	-0.05857
0.65000	0.05219	-0.05594
0.70000	0.04132	-0.05093
0.75000	0.02954	-0.04106
0.80000	0.01829	-0.03313
0.85000	0.00810	-0.02695
0.90000	-0.00058	-0.02188
0.95000	-0.00761	-0.01752
0.97500	-0.01066	
0.98000		-0.01555
0.99000	-0.01224	-0.01503
1.00000	-0.01322	-0.01456

Table IV

Ordinates of the Forward and Aft Portions of the Body

(All dimensions in inches)

Forward	
x sta. in.	height in.
0.00	0.00
0.05	0.27
0.10	0.37
0.15	0.30
0.20	0.33
0.25	0.35
0.30	0.38
0.35	0.40
0.40	0.43
0.45	0.45
0.50	0.48
0.60	0.53
0.70	0.58
0.80	0.63
0.90	0.68
1.00	0.73
1.50	0.98
2.00	1.24
2.50	1.48
3.00	1.72
3.50	1.95
4.00	2.17
4.50	2.38
5.00	2.56
5.50	2.73
6.00	2.87
6.50	2.98
7.00	3.06
7.50	3.11
8.00	3.12

Aft	
x sta. in.	height in.
40.50	3.12
41.00	3.12
41.50	3.09
42.00	3.04
42.50	2.98
43.00	2.89
43.50	2.79
44.00	2.68
44.50	2.55
45.00	2.40
45.50	2.25
46.00	2.08
46.50	1.90
47.00	1.71
47.50	1.51
48.00	1.30
48.50	1.09
49.00	0.88
49.50	0.65
49.60	0.61
49.70	0.56
49.80	0.52
49.90	0.47
50.00	0.43
50.05	0.41
50.10	0.38
50.15	0.36
50.20	0.34
50.25	0.32
50.30	0.29
50.35	0.27
50.40	0.25
50.45	0.27
50.50	0.00

Table V
Wing Pressure Orifice Chordwise Locations

(nondimensionalized by the local wing chord)

upper surface				
$\eta = .25$	$\eta = .50$	$\eta = .70$	$\eta = .80$	$\eta = .90$
0.000	0.000	0.000	0.000	0.000
.019	.019	.018	.019	.018
.049	.049	.049	.050	.049
.099	.099	.099	.100	.099
.149	.149	.149	.150	.149
.199	.199	.199	.200	.200
.249	.249	.249	.250	.249
.299	.299	.299	.299	.299
.349	.349	.349	.350	.349
.399	.399	.399	.400	.399
.449	.449	.449	.450	.449
.499	.499	.499	.500	.499
.549	.549	.549	.550	.550
.599	.599	.599	.600	.600
.649	.649	.649	.651	.649
.699	.699	.699	.701	.698
.749	.749	.749	.750	.749
.799	.800	.799	.800	.799
.850	.849	.849	.851	.849
.899	.899	.899	.899	.899

Table V
Concluded

lower surface				
$\eta = .25$	$\eta = .50$	$\eta = .70$	$\eta = .80$	$\eta = .90$
0.000	0.000	0.000	0.000	0.000
.020	.020	.019	.020	.019
.050	.050	.049	.050	.049
.100	.100	.099	.101	.099
.150	.150	.150	.151	.149
.200	.200	.199	.201	.200
.250	.250	.250	.250	.250
.300	.299	.299	.300	.300
.350	.349	.349	.350	.350
.399	.400	.400	.400	.400
.449	.450	.450	.451	.450
.499	.500	.499	.501	.499
.550	.550	.549	.551	.549
.600	.600	.599	.601	.600
.650	.650	.650	.651	.652
.700	.700	.700	.701	.700
.750	.750	.750	.751	.750
.800	.800	.800	.801	.800
.849	.850	.850	.851	.850
.899	.900	.900	.895	.886

Table VI

Tip Jet Characteristics

Tip	x_j inches	z_j inches	c_j inches	δ_j deg	ψ_j deg
1	.825	-.031	.25	0	0
	1.975	-.031	.25	0	0
2	1.195	-.031	.25	0	0
	2.415	-.031	.25	0	0
3	1.195	-.031	.25	20	0
	2.855	-.031	.25	0	0
4	1.195	-.093	.25	20	0
	1.975	-.031	.25	0	0
	3.225	-.031	.25	0	0
6	1.195	.093	.25	0	0
	1.975	.093	.25	0	0
8	1.010	-.031	.62	0	0
	2.475	-.031	1.25	0	0
9	1.195	-.031	.25	0	30
	2.415	-.031	.25	0	30

Table VII

Wing Aerodynamic Characteristics for Each Tip Without Blowing

Tip	C_{L_α}	α_0	C_{D_0}	C_{b_L}	C_{b_0}	C_{m_L}	C_{m_0}
1	.1010	-1.457	.0104	.4166	-.0037	.0050	-.011
2	.1016	-1.382	.0103	.4162	.0017	.0054	-.013
2	.1019	-1.389	.0099	.4168	-.0003	.0061	-.012
3	.1003	-1.411	.0102	.4151	-.0001	.0057	-.013
4	.1013	-1.405	.0107	.4113	.0003	.0071	-.014
6	.1006	-1.307	.0110	.4160	.0028	.0048	-.014
8	.1008	-1.287	.0103	.4188	.0052	.0039	-.014
8	.1010	-1.419	.0112	.4171	-.0009	.0050	-.012
8	.1009	-1.423	.0112	.4174	-.0013	.0052	-.011
9	.1014	-1.344	.0098	.4134	.0003	.0072	-.013
Ave.	.1011	-1.382	.0104	.4159	.0004	.0055	-.013

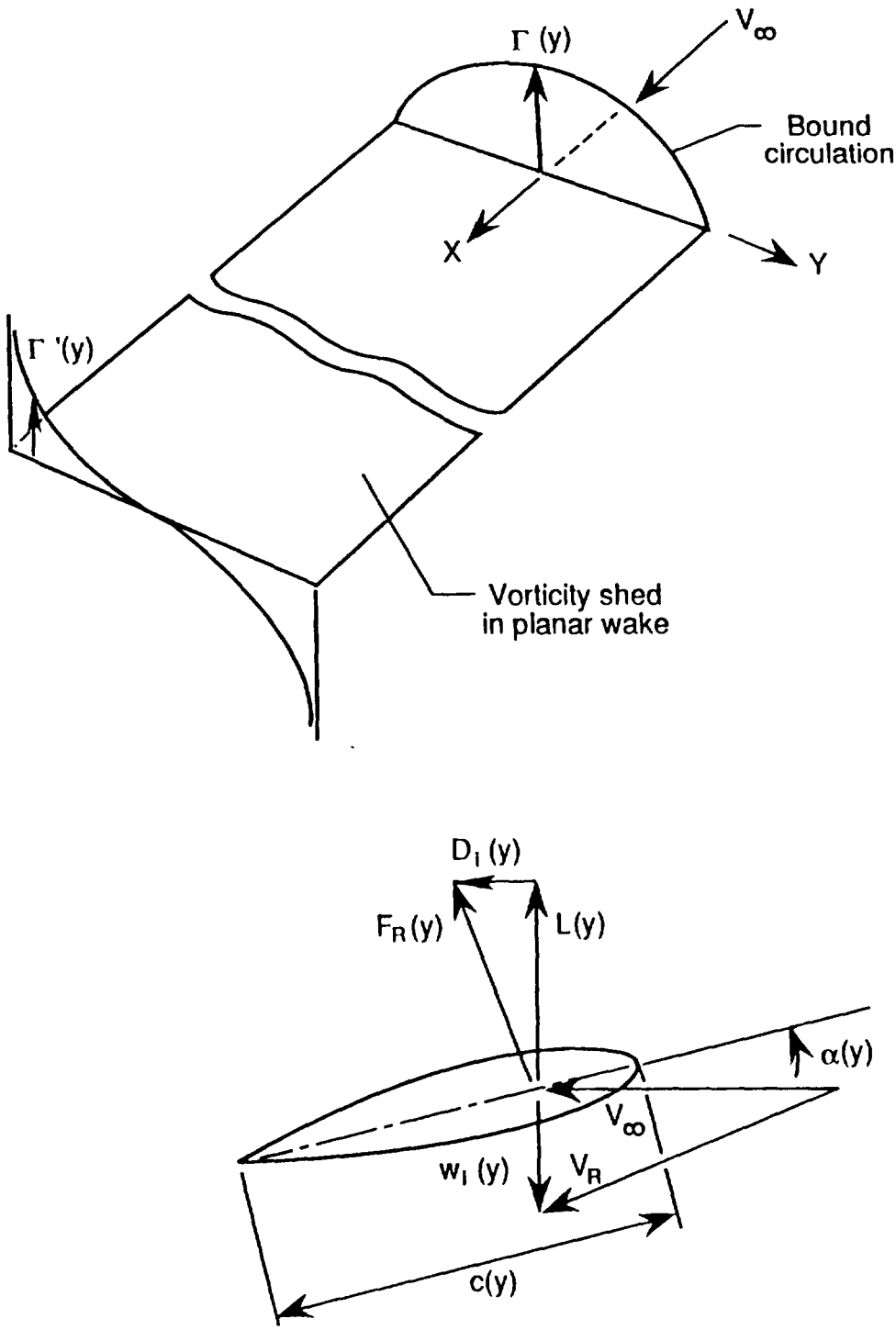

Figure 1. Flowfield assumed in the development of lifting line theory.

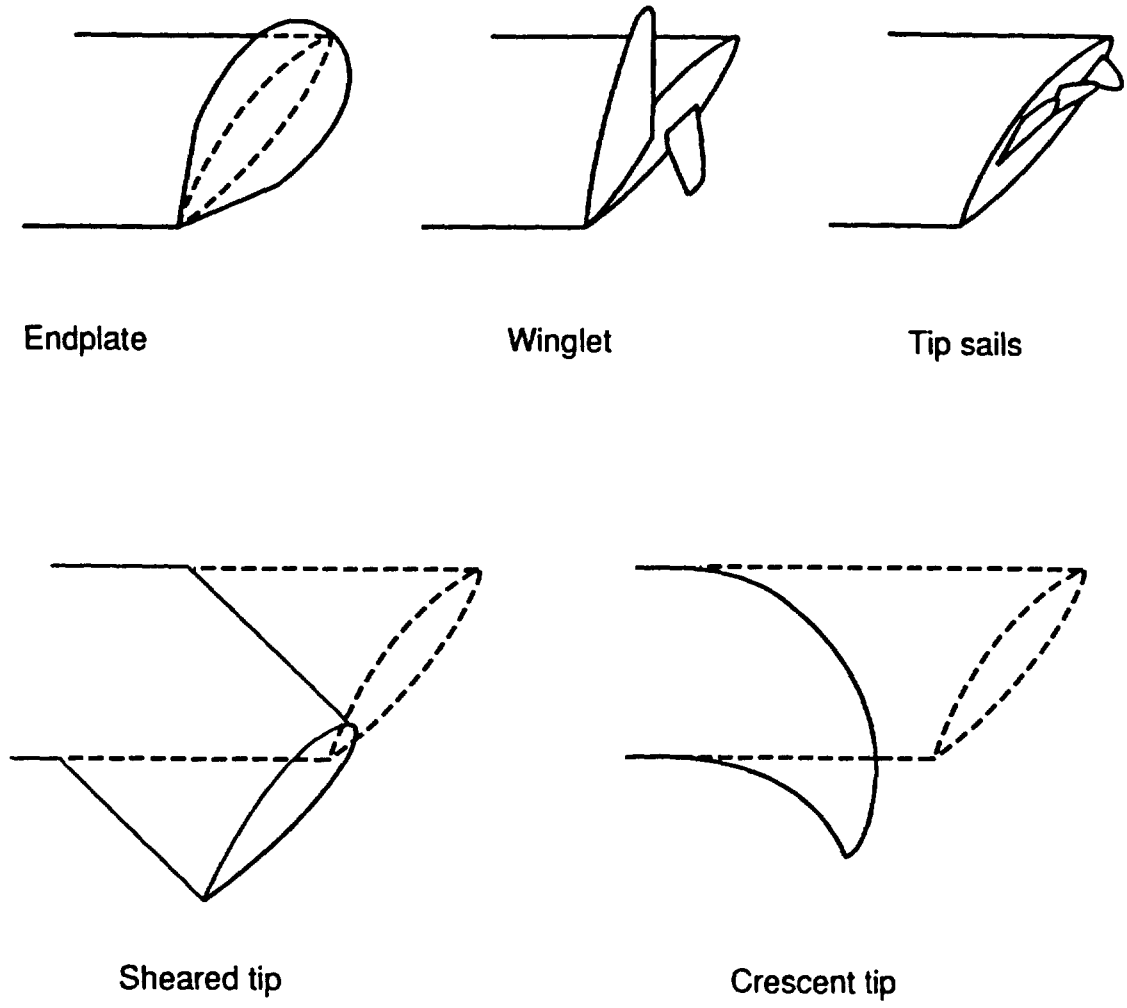

Figure 2. Wing planform modifications to reduce induced drag.

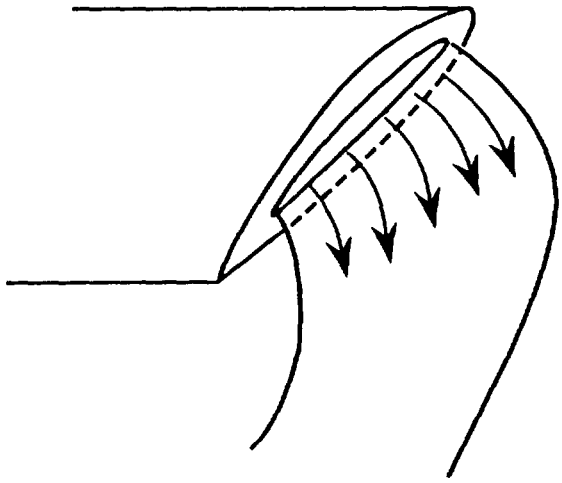

Continuous jet

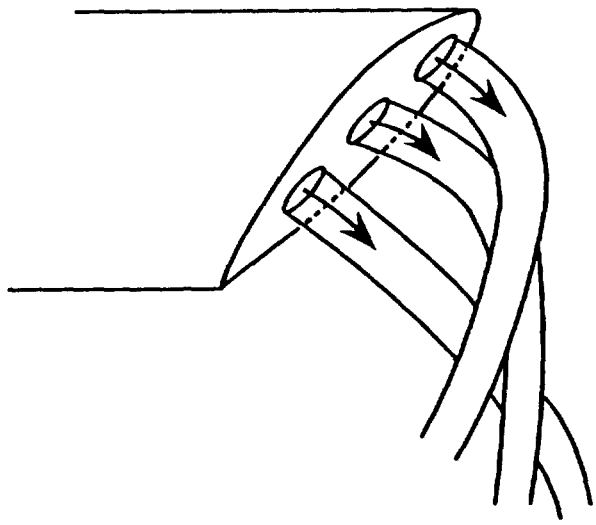

Discrete jet

Figure 3. Spanwise wing tip blowing concepts.

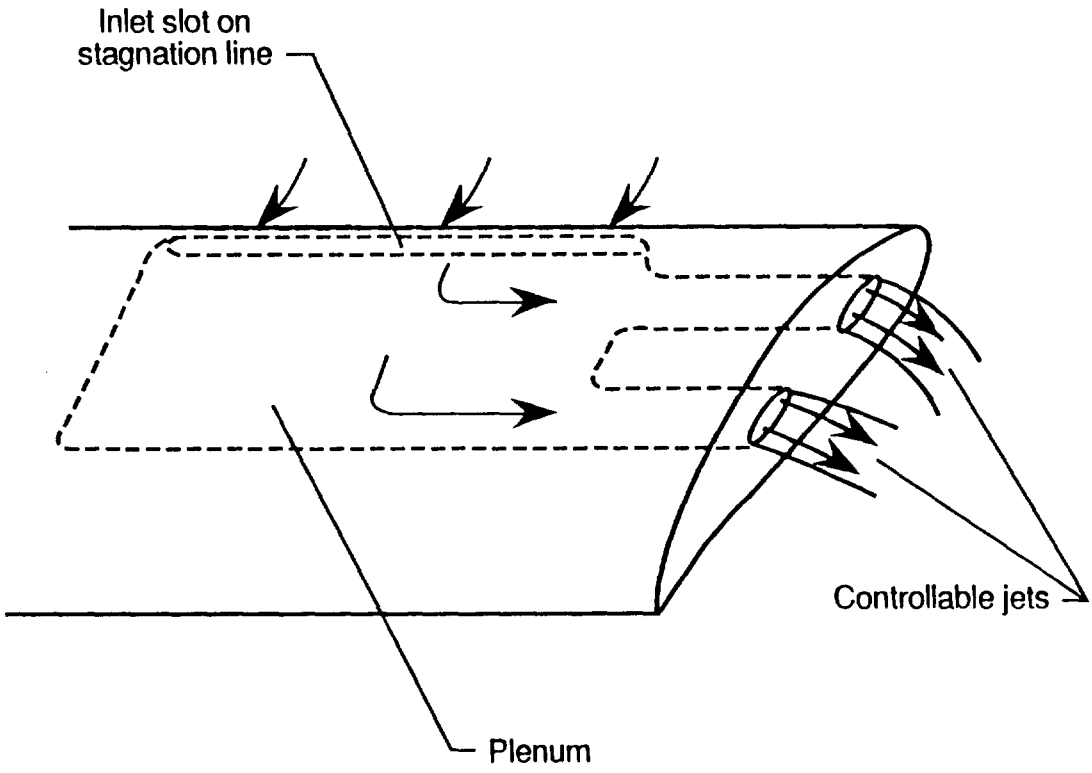

Figure 4. Passive wing tip blowing system

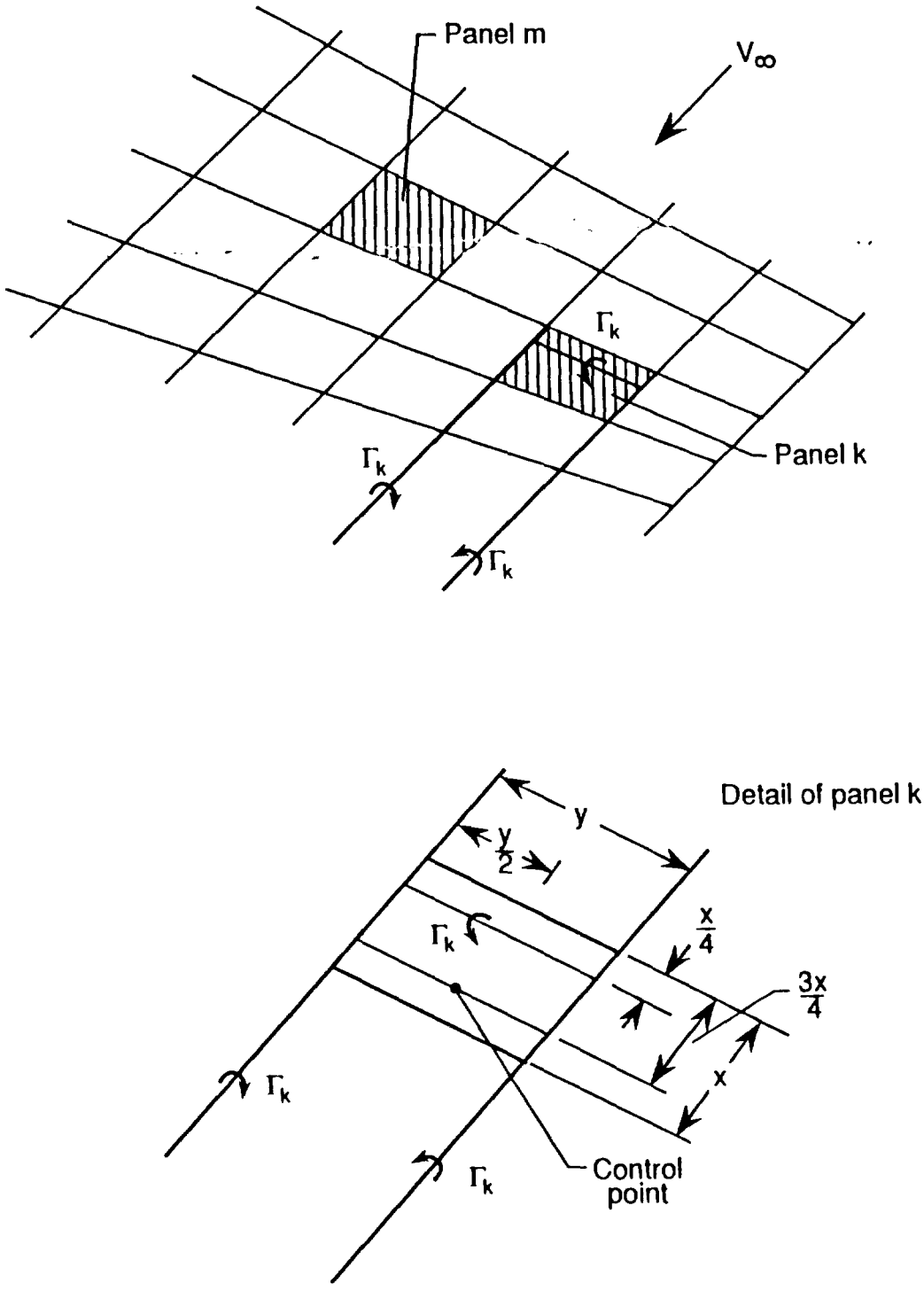

Figure 5. Layout of the horseshoe vortices for the wing model.

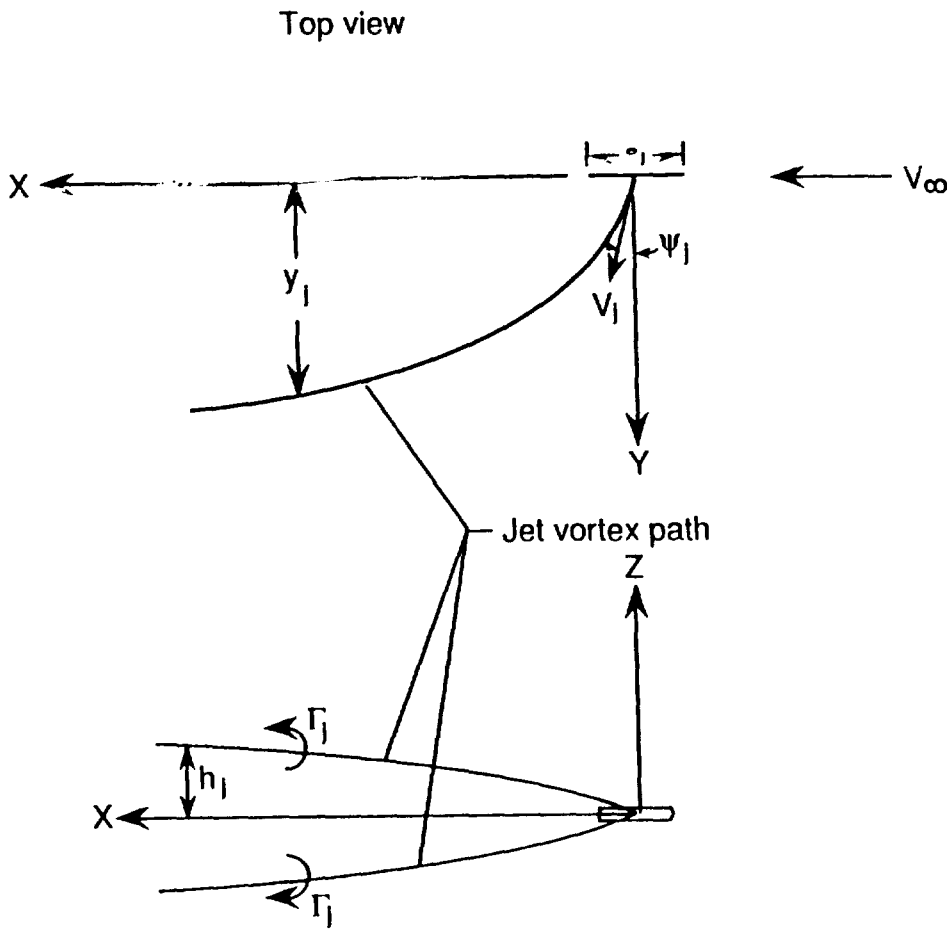

Figure 6. Layout of the jet counter-rotating vortex pair for the jet model.

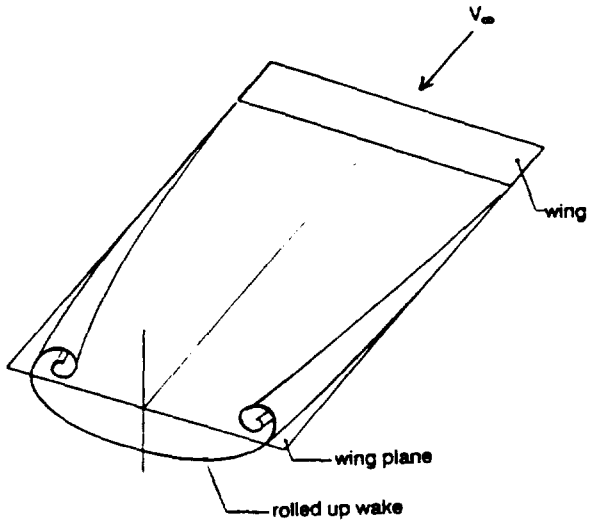

(a) Continuous sheet of vorticity.

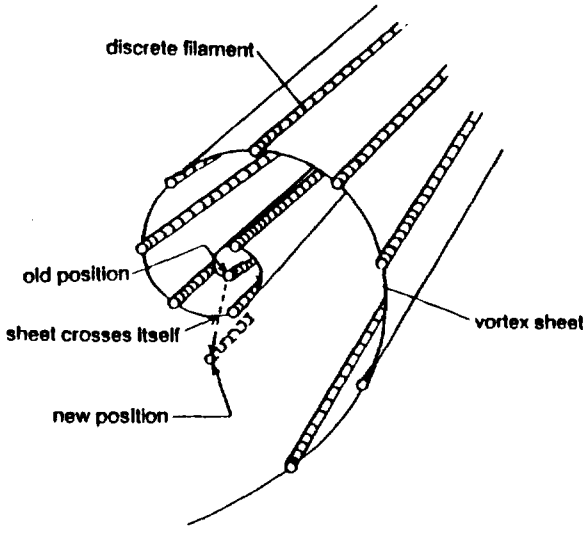

(b) Discrete vortex representation.

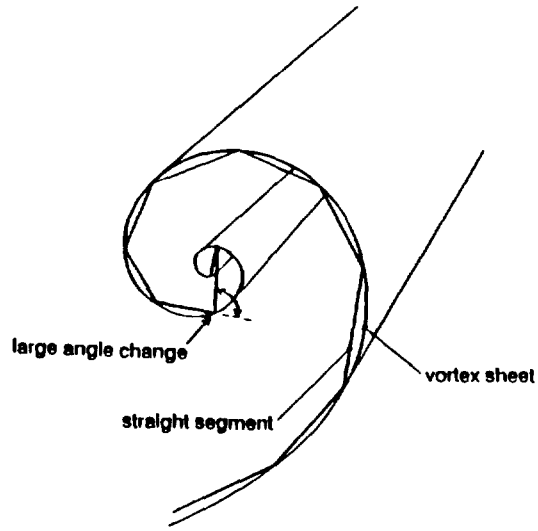

(c) Segmented sheet representation.

Figure 7. Rollup of a vortex sheet.

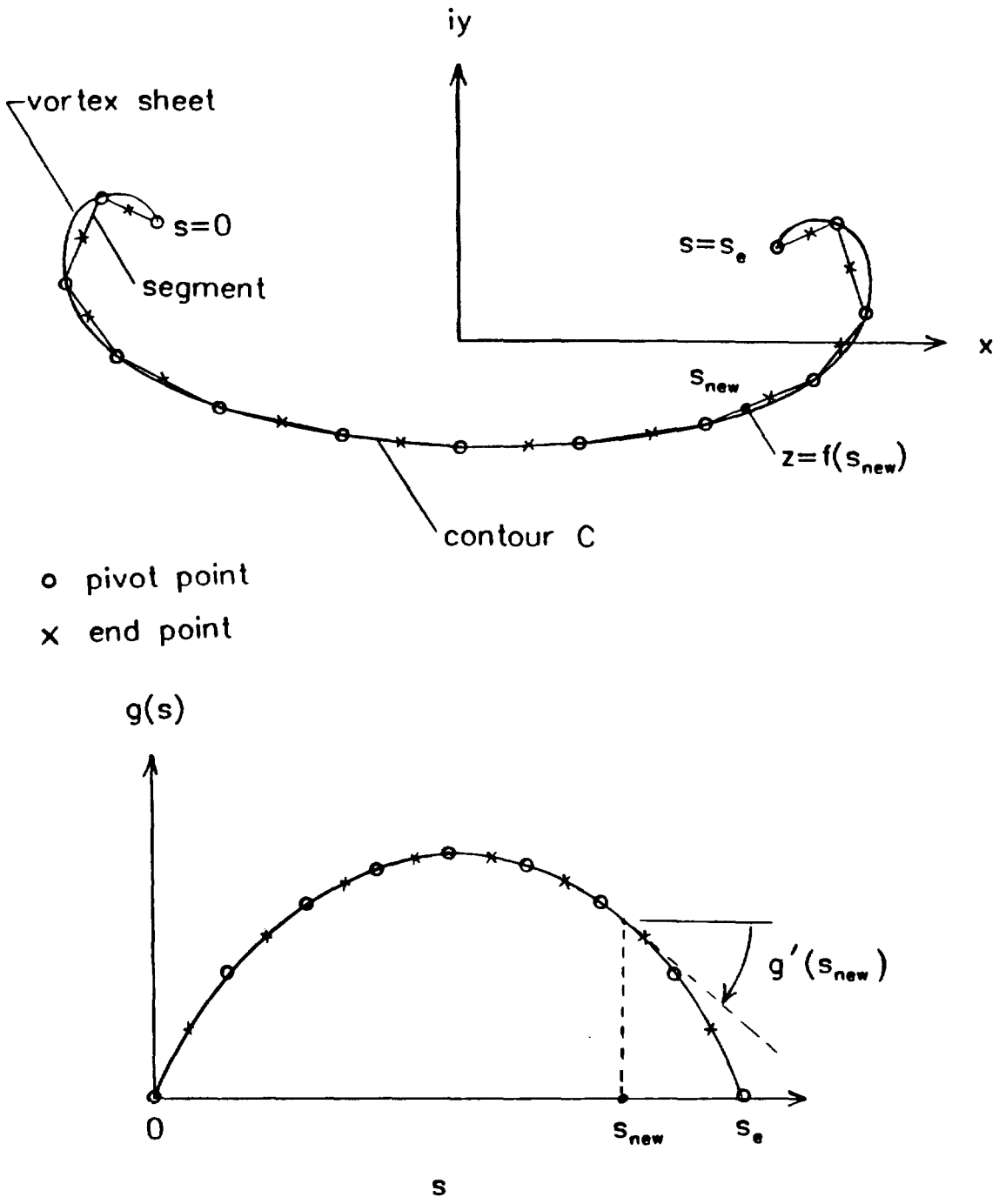

Figure 8. Redistribution of control points on a vortex sheet.

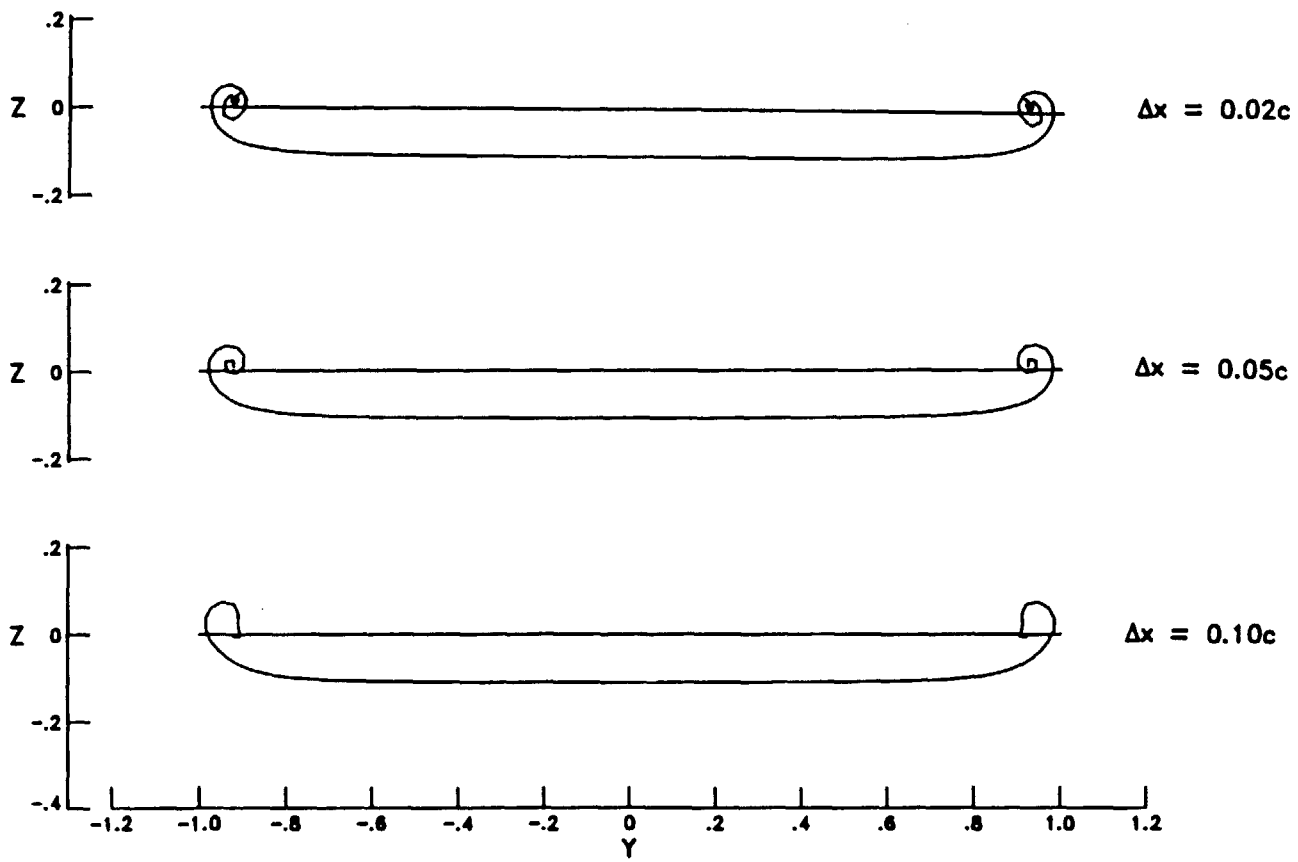

Figure 9. Effect of integration step size on the roll up of the wing wake.

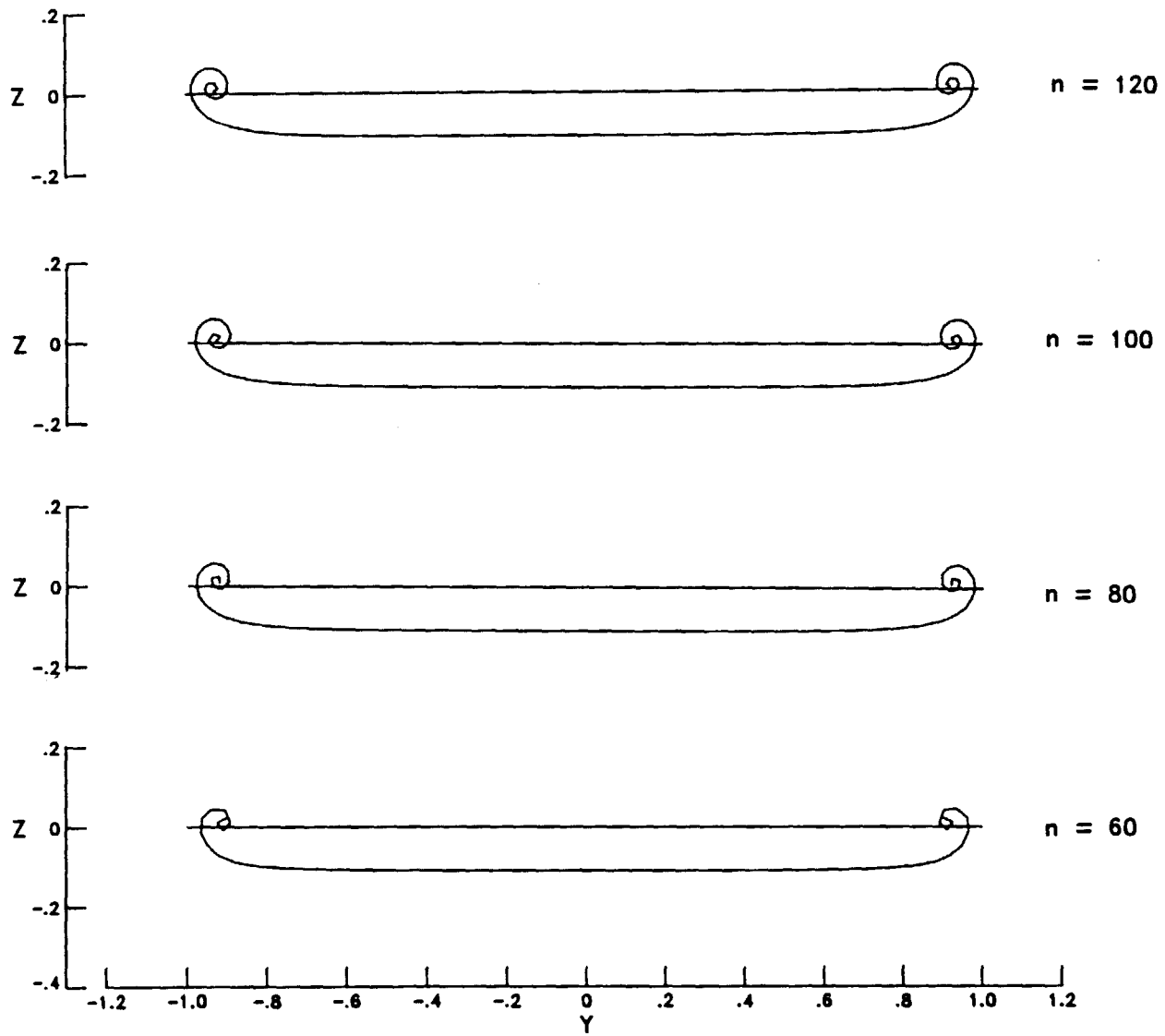

Figure 10. Effect of the number of wake control points on the roll up of the wing wake.

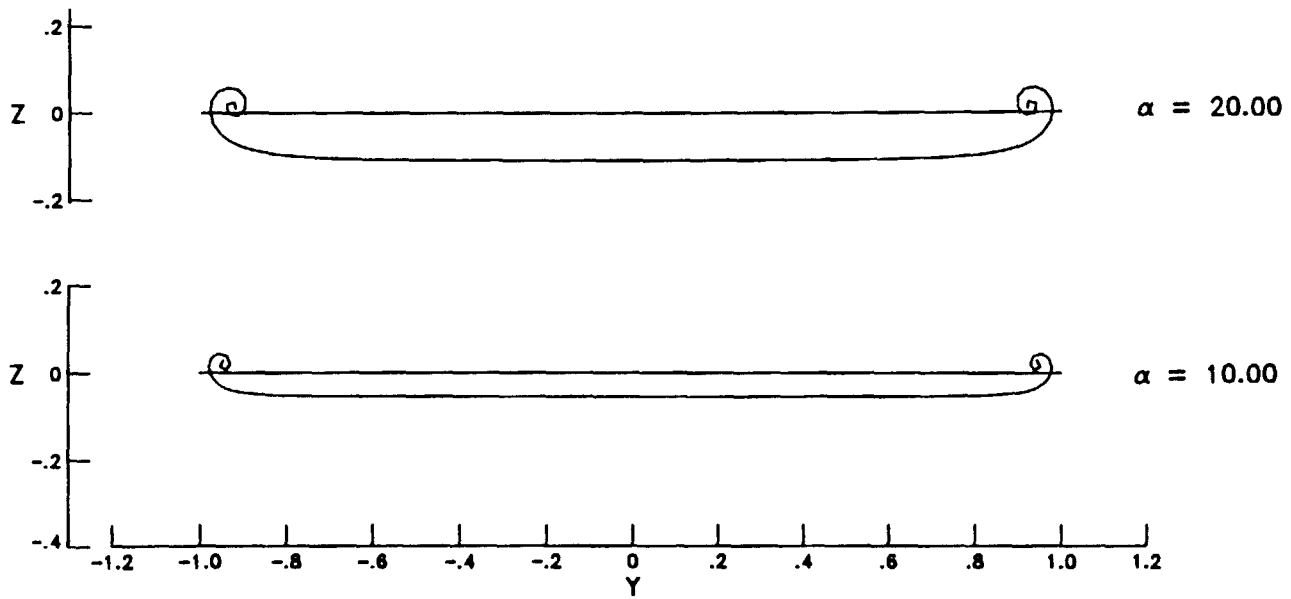

Figure 11. Effect of angle of attack on the roll up of the wing wake without blowing.

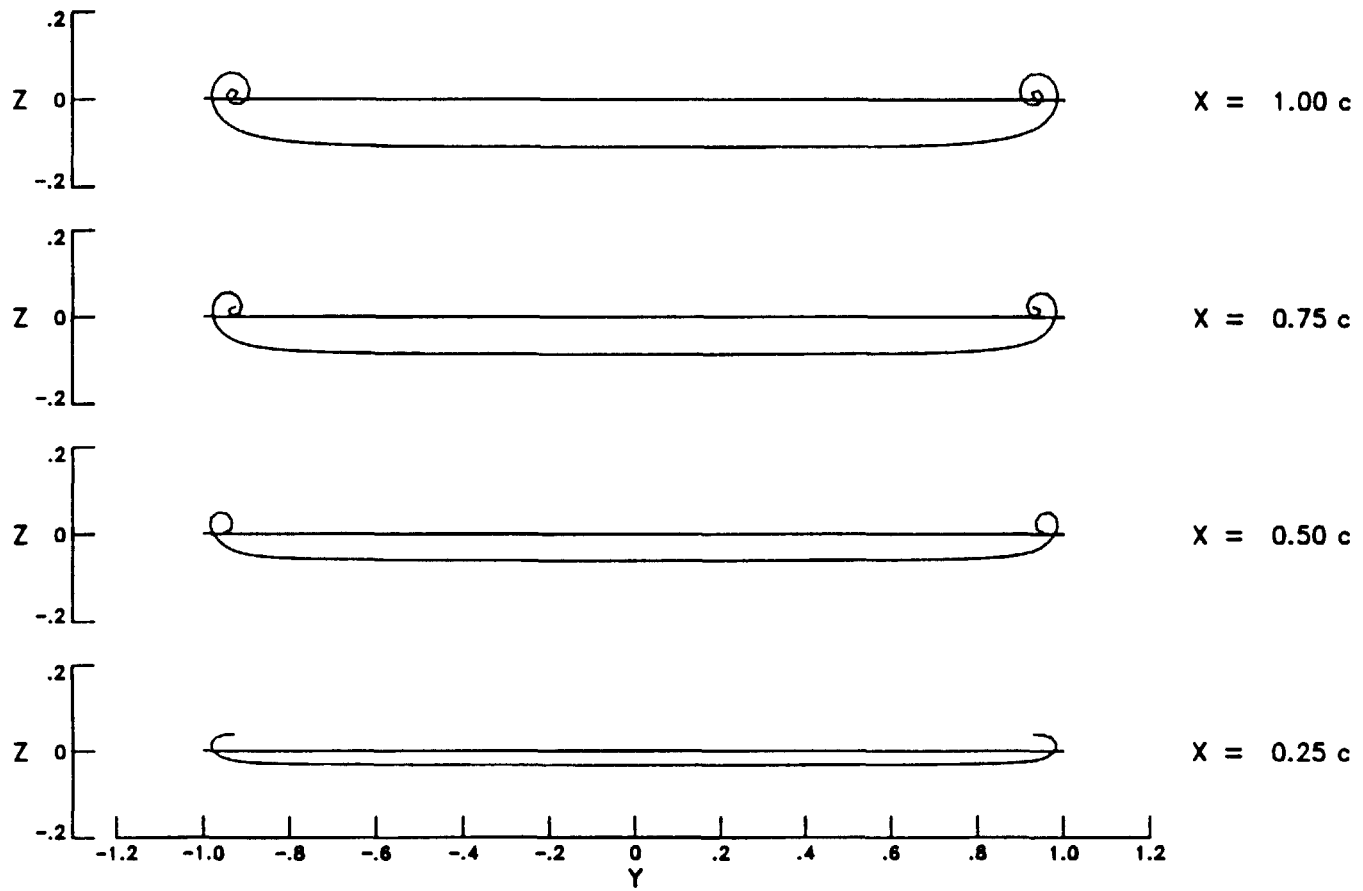

(a) $V_e = 0$ $(C_\mu = 0.0)$.

Figure 12. Roll up of the wing wake at several velocity ratios. $x_j = 0.25c$, $\alpha = 20^\circ$.

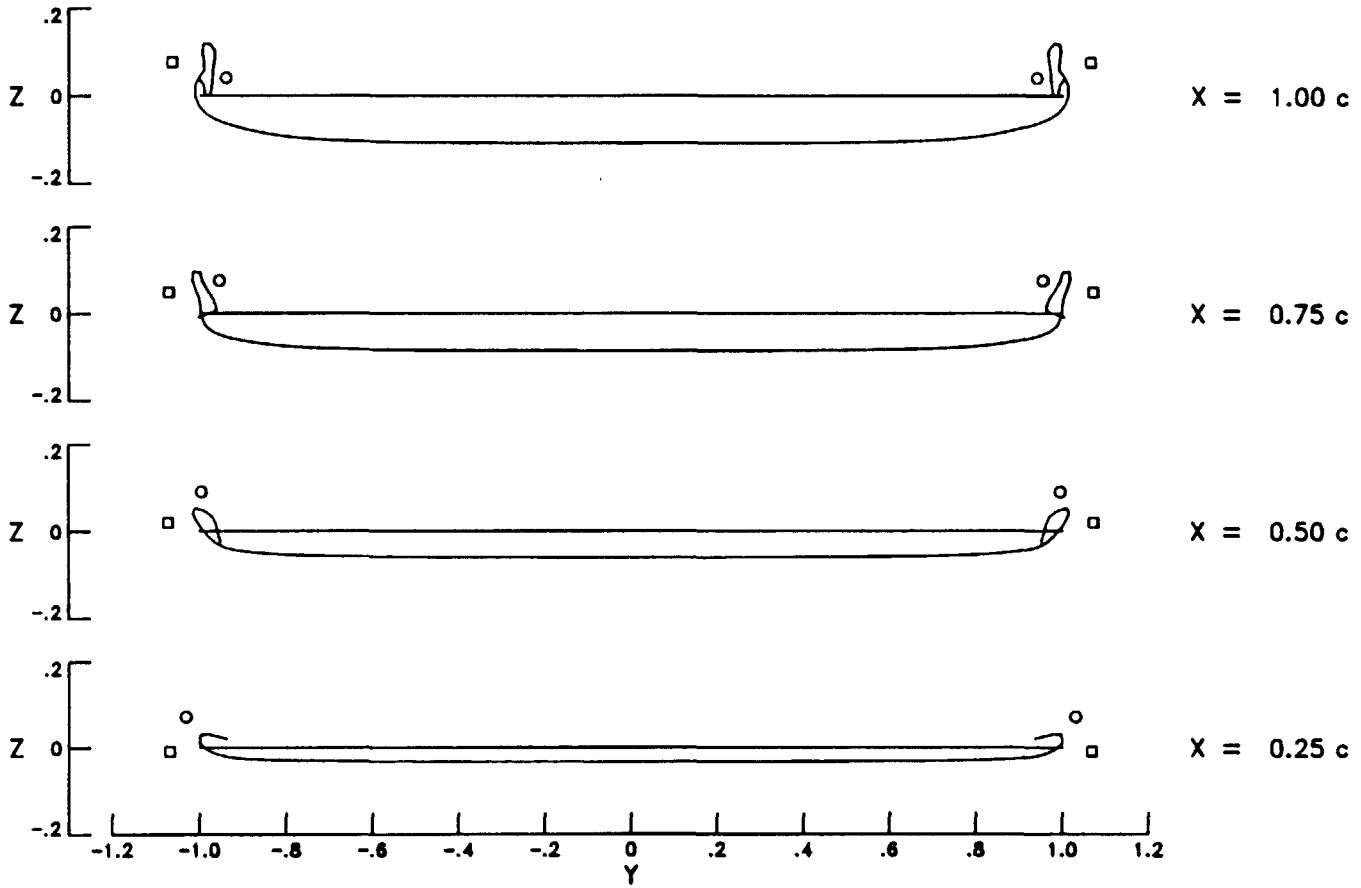

(b) $V_e = 1$ ($C_\mu = 0.005$).

Figure 12. Continued.

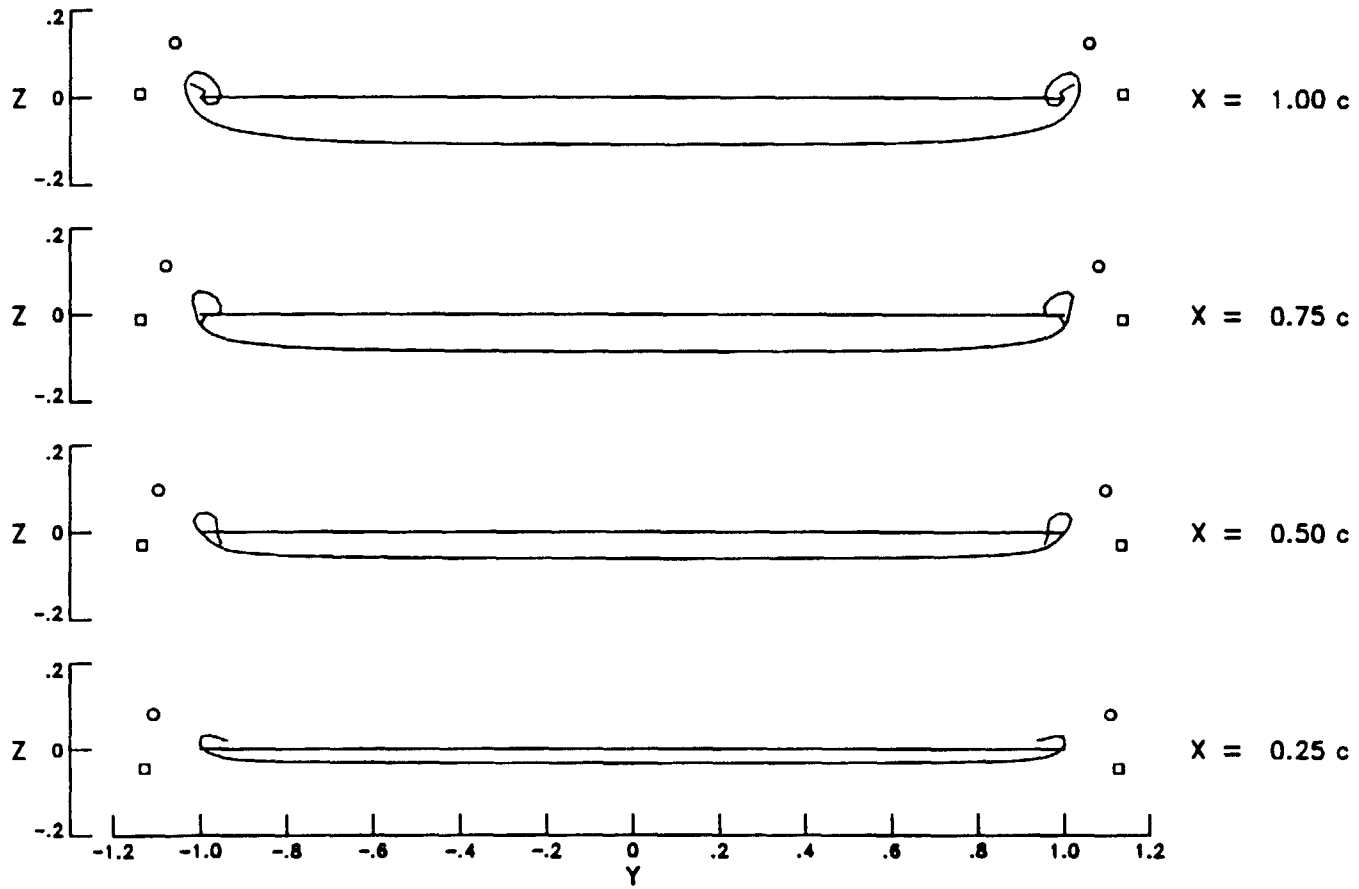

(c) $V_e = 2$ ($C_\mu = 0.021$).

Figure 12. Continued.

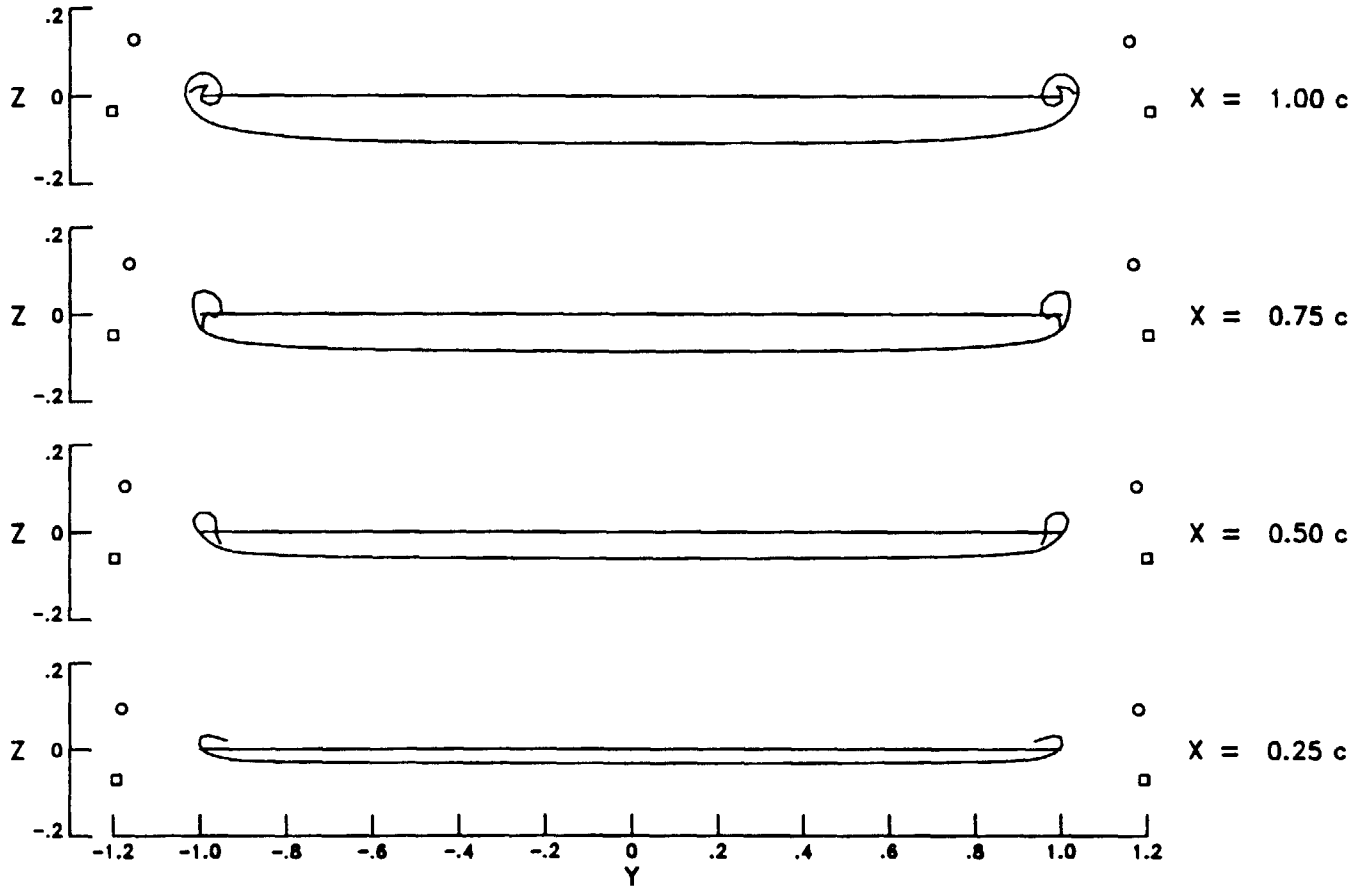

(d) $V_e = 3$ ($C_\mu = 0.048$)

Figure 12. Continued.

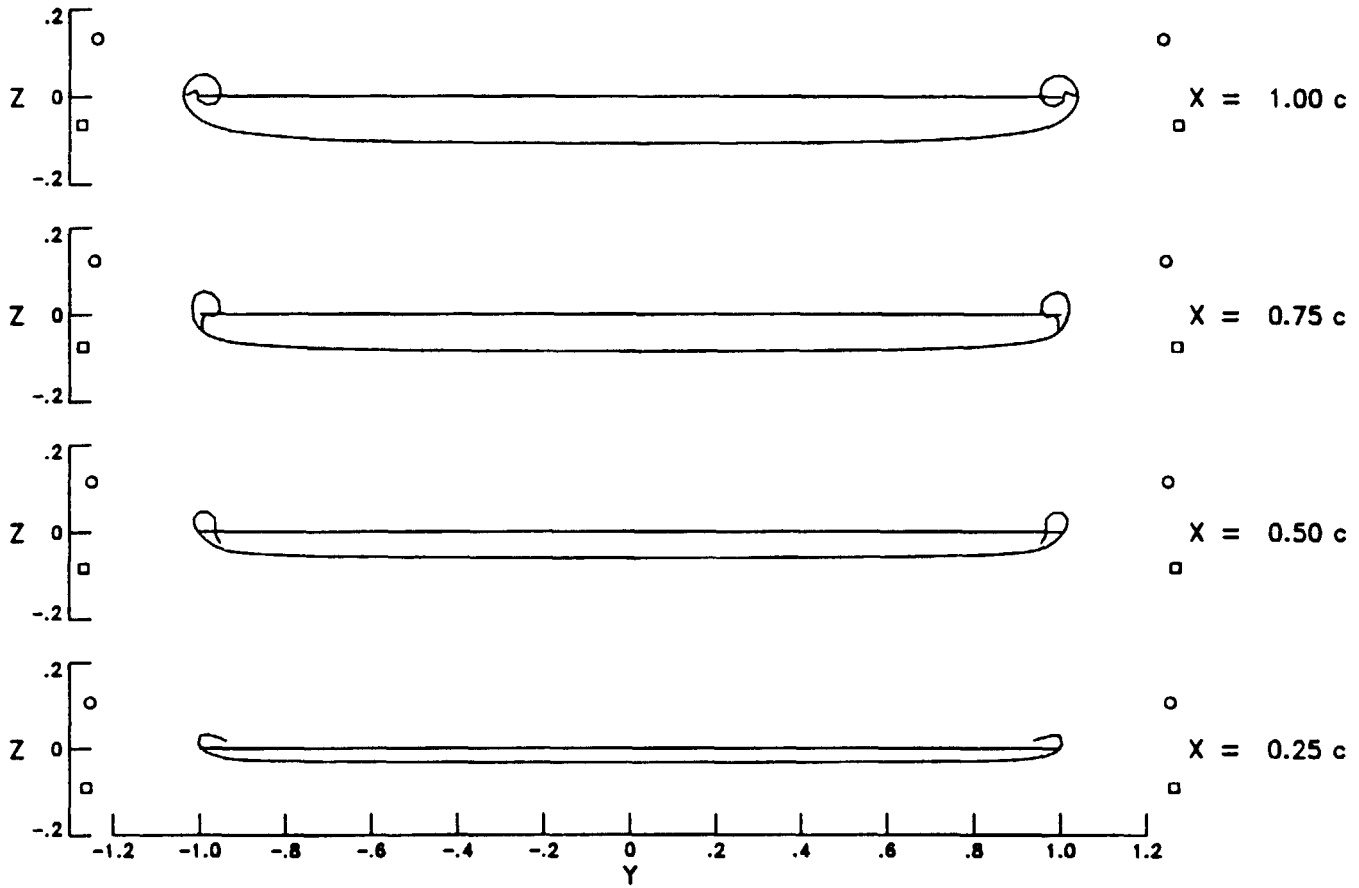

(e) $V_e = 4$ ($C_\mu = 0.086$).

Figure 12. Concluded.

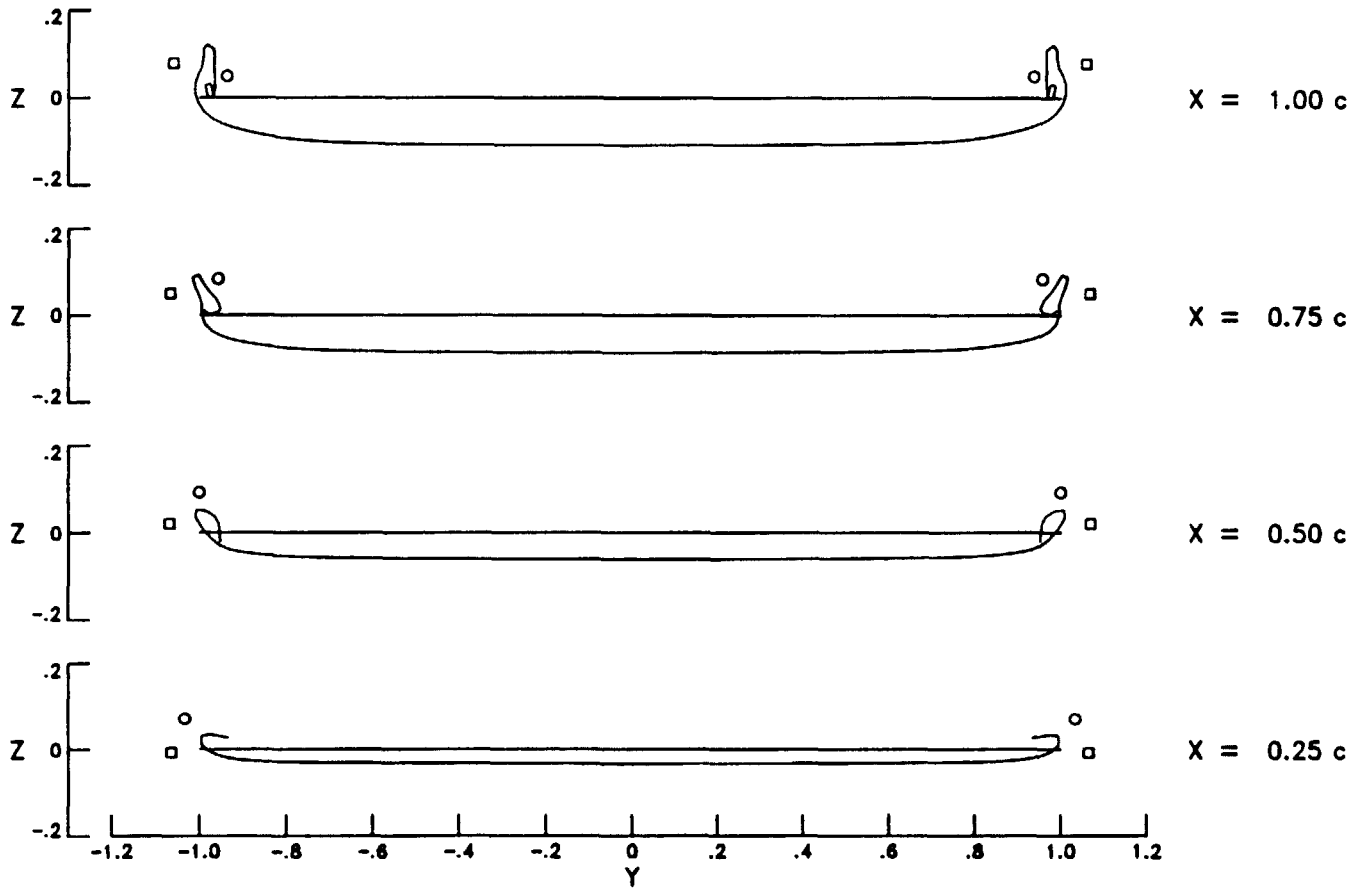

(a) $V_e = 1$ ($C_\mu = 0.005$)

Figure 13. Roll up of the wing wake at several velocity ratios with the jet displaced above the chord line. $z_j = 0.15c$, $x_j = .25c$, $\alpha = 20^\circ$.

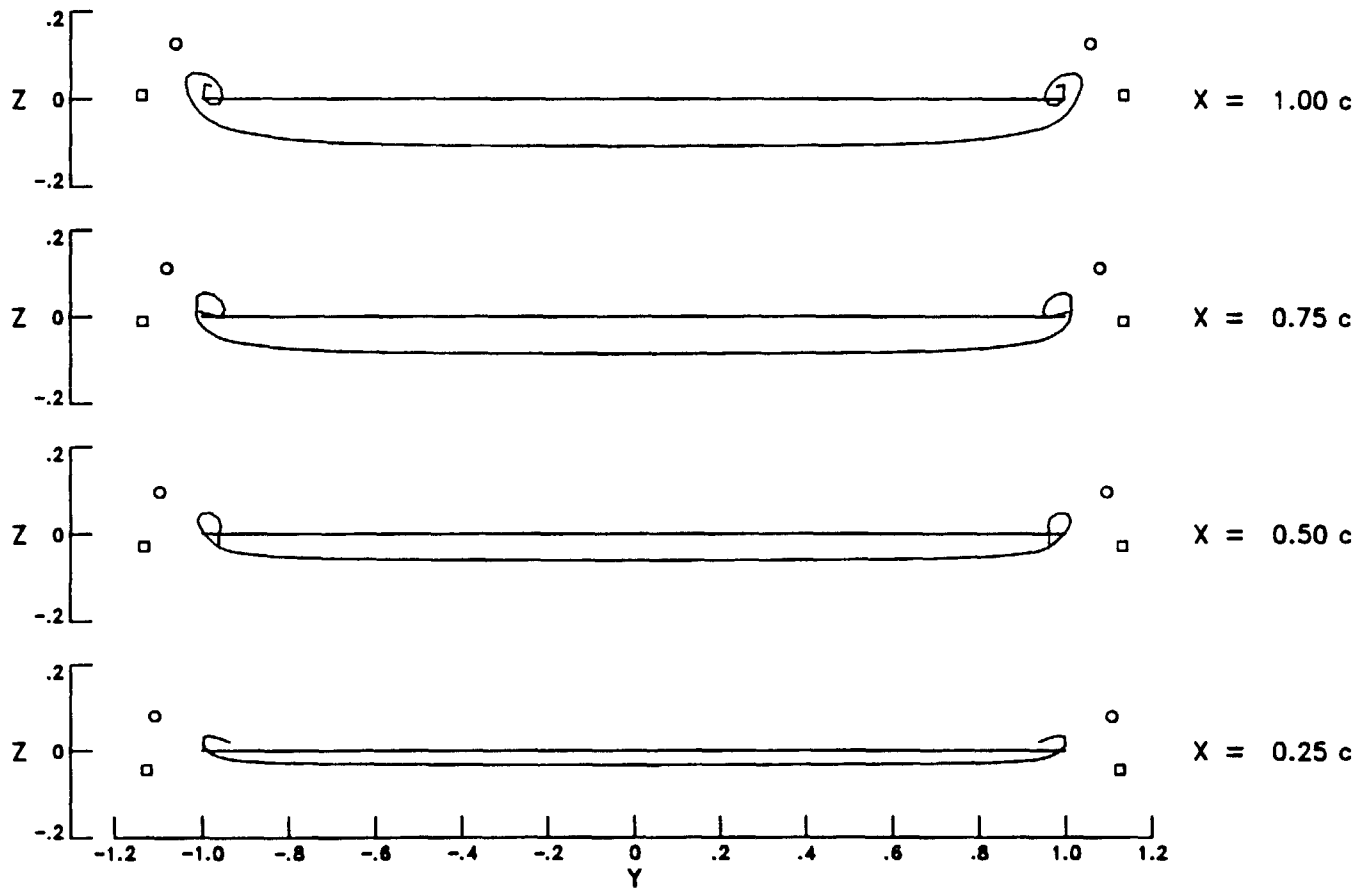

(b) $V_e = 2$ ($C_\mu = 0.021$).

Figure 13. Concluded.

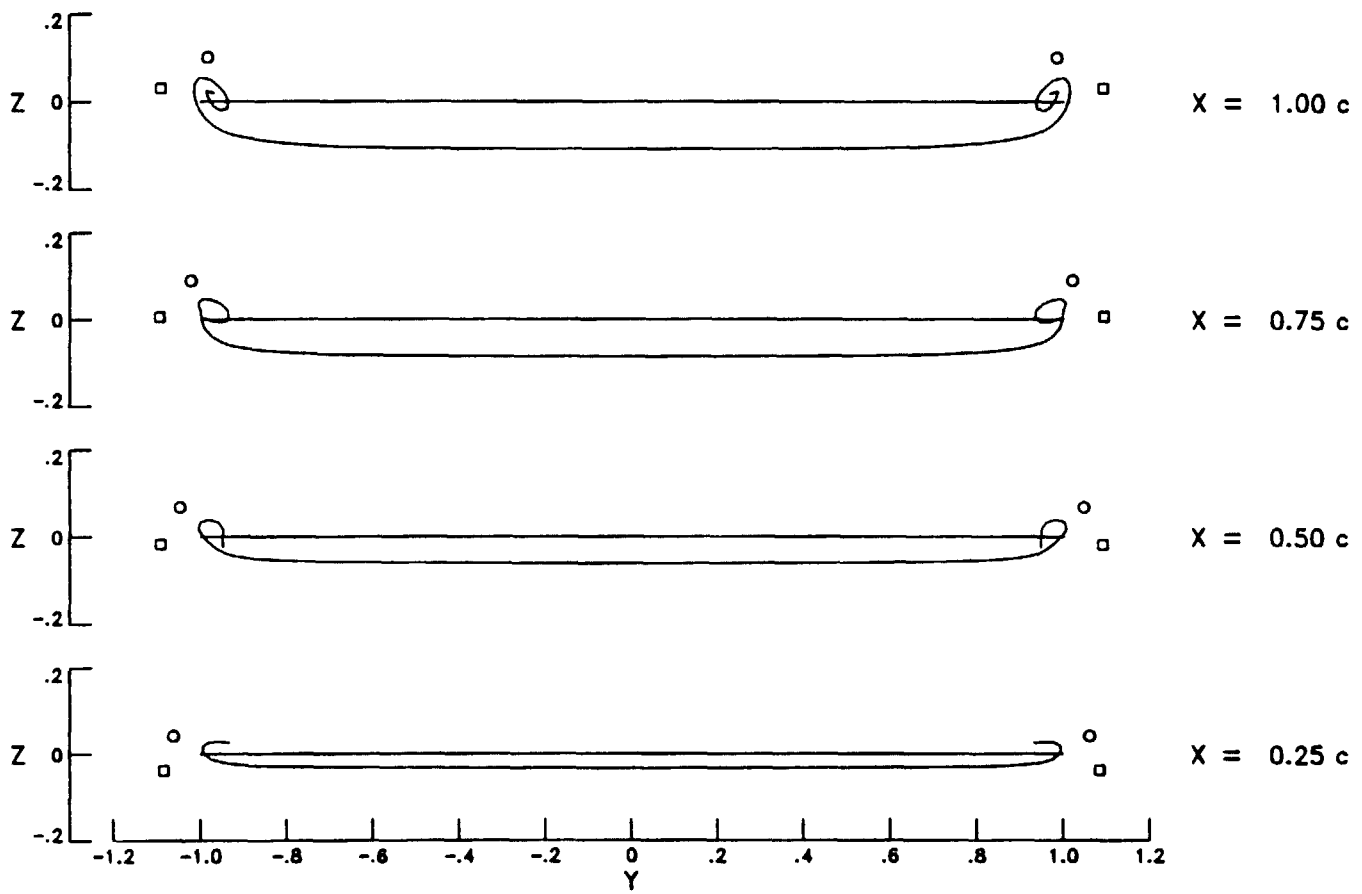

(a) $V_e = 1$ ($C_\mu = 0.005$).

Figure 14. Roll up of the wing wake at several velocity ratios with the jet directed downward 30°. $x_j = 0.25c$, $\alpha = 20°$.

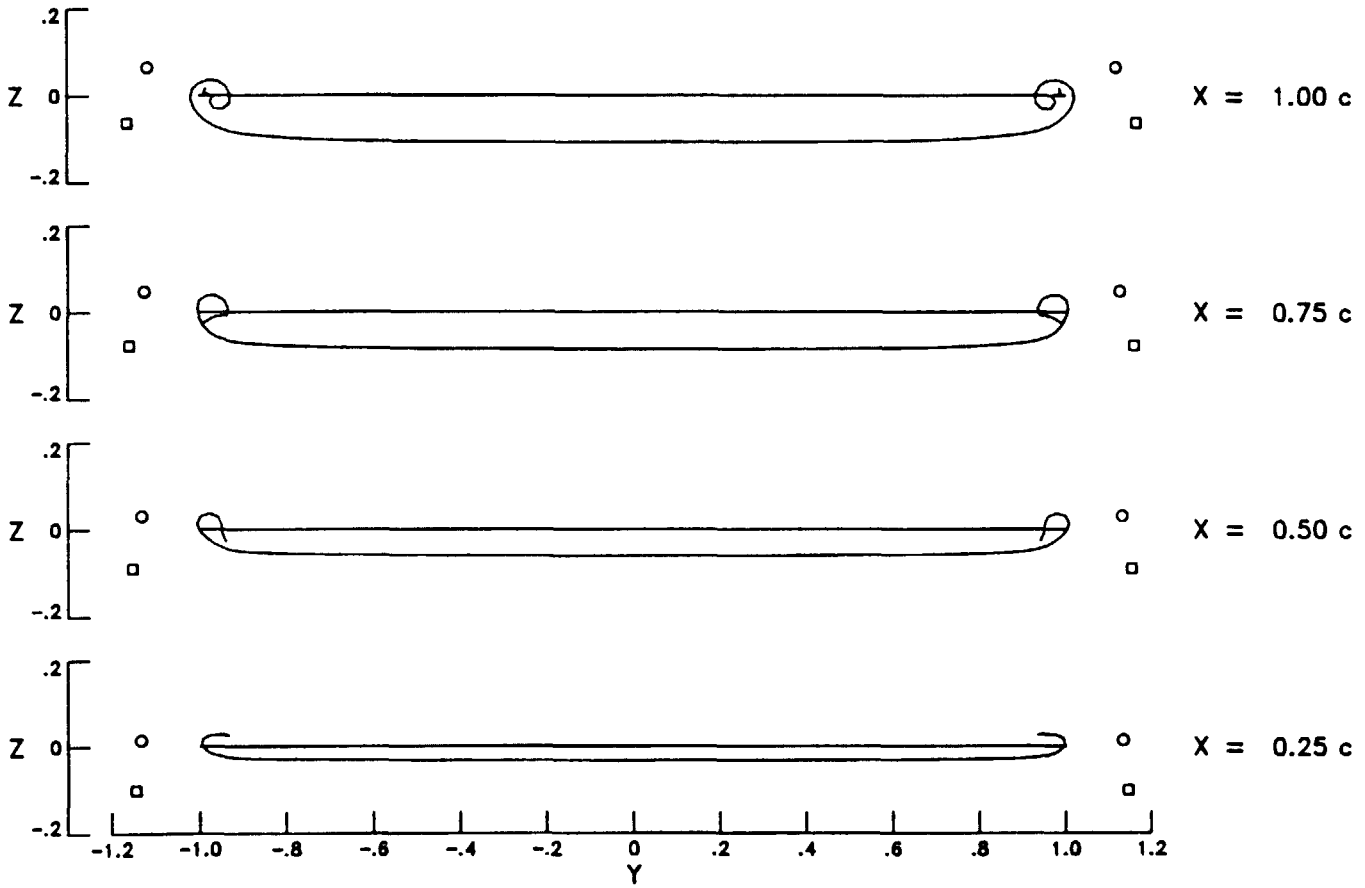

(b) $V_e = 2$ ($C_\mu = 0.021$).

Figure 14. Concluded.

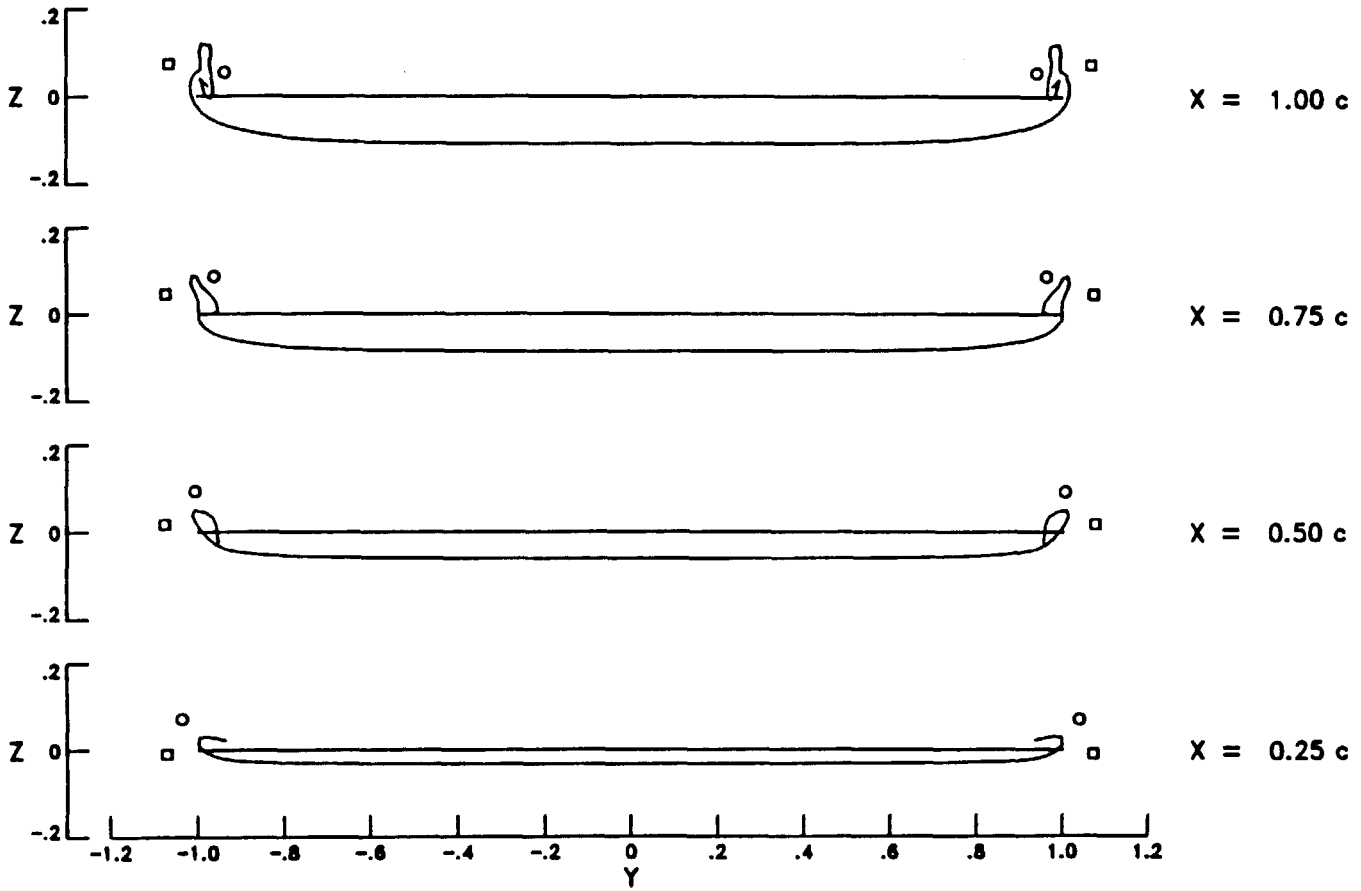

(a) $V_e = 1$ ($C_\mu = 0.005$).

Figure 15. Roll up of the wing wake at several velocity ratios with the jet directed rearward 30°. $x_j = 0.25c$, $\alpha = 20°$.

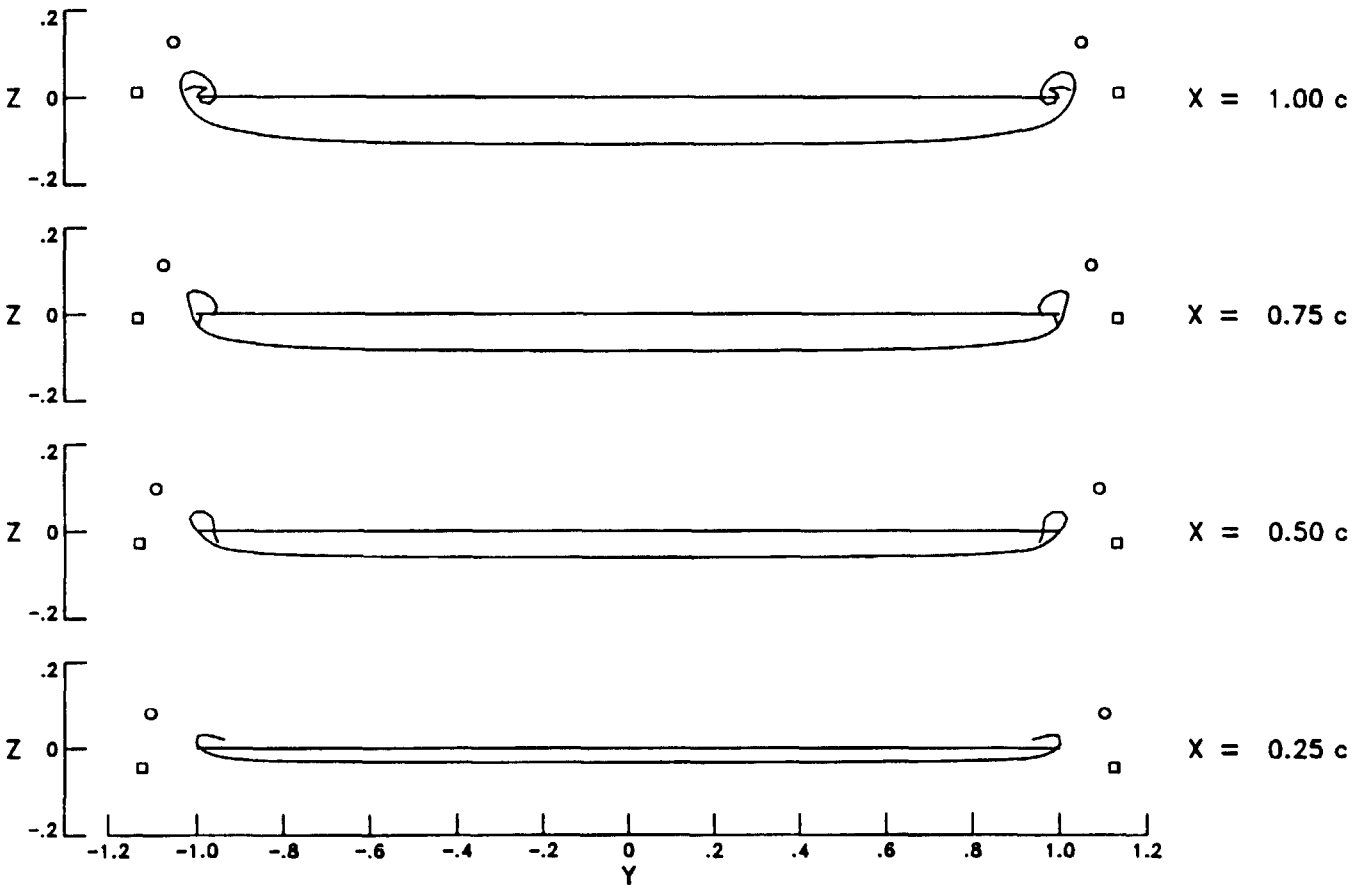

(b) $V_e = 2$ ($C_\mu = 0.021$).

Figure 15. Concluded.

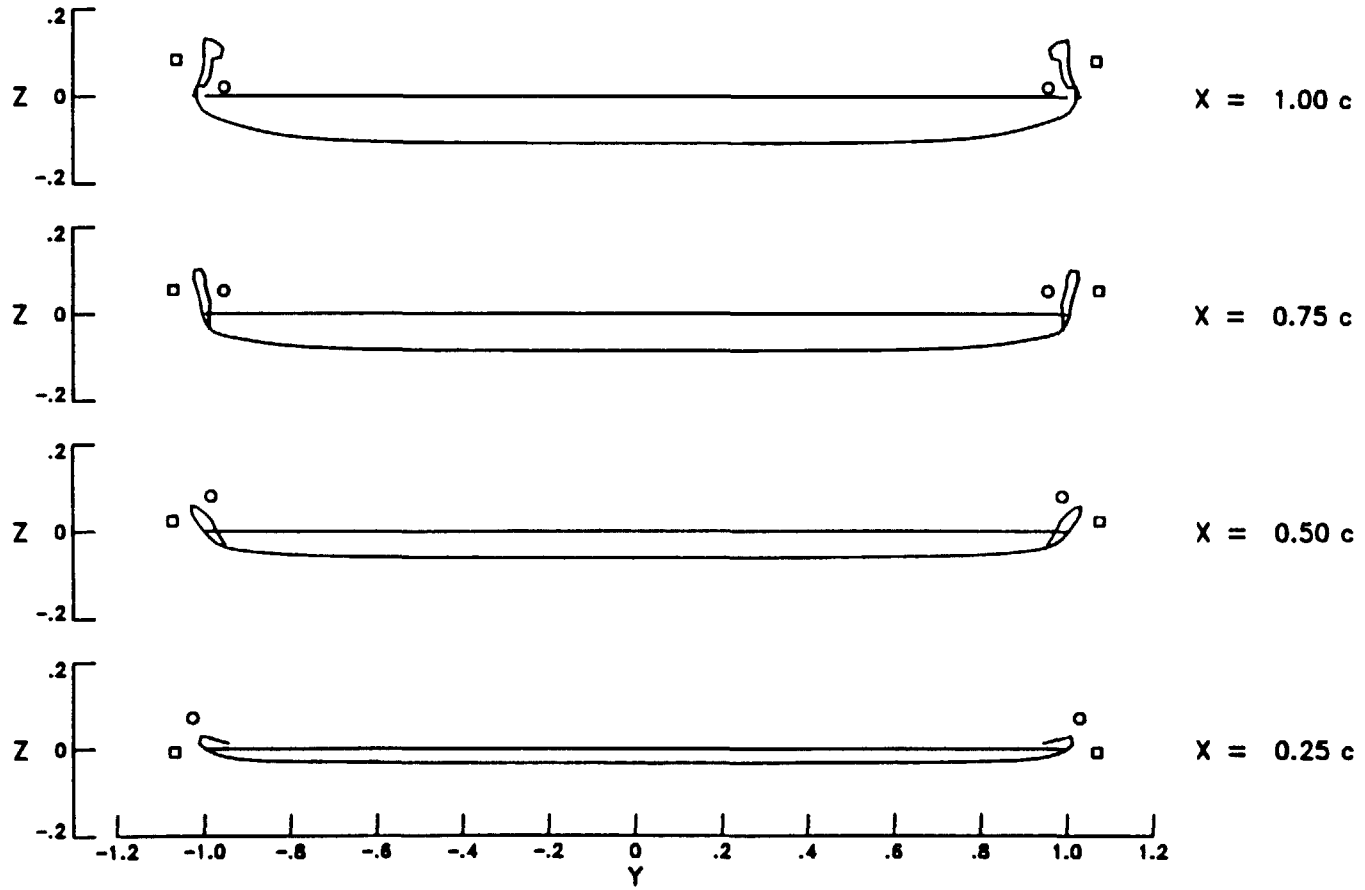

(a) $V_e = 1$ ($C_\mu = 0.005$).

Figure 16. Roll up of the wing wake at several velocity ratios with the jet displaced aft $x_j = 0.85c$, $\alpha = 20^\circ$.

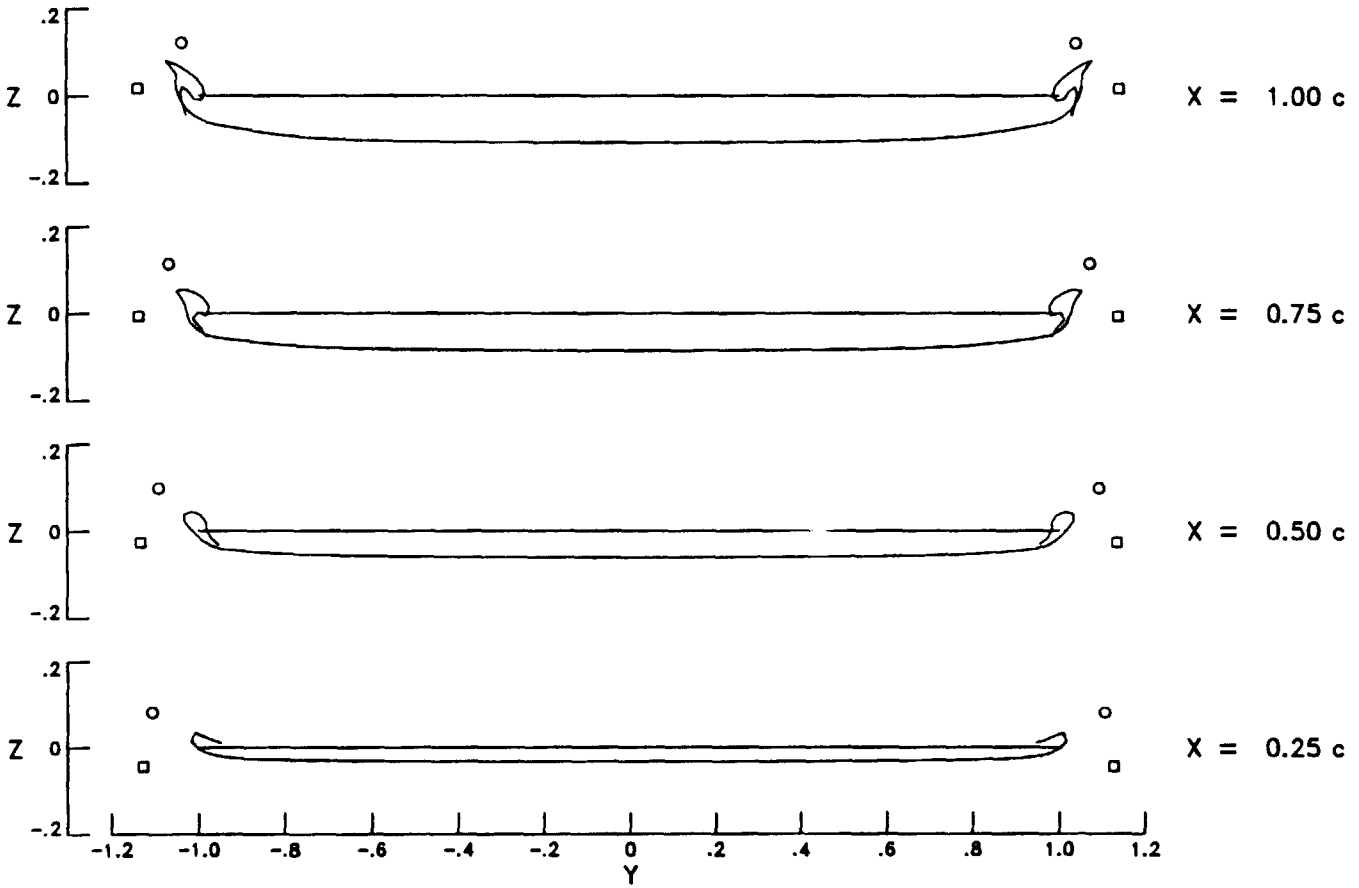

(b) $V_e = 2$ ($C_\mu = 0.021$).

Figure 16. Concluded.

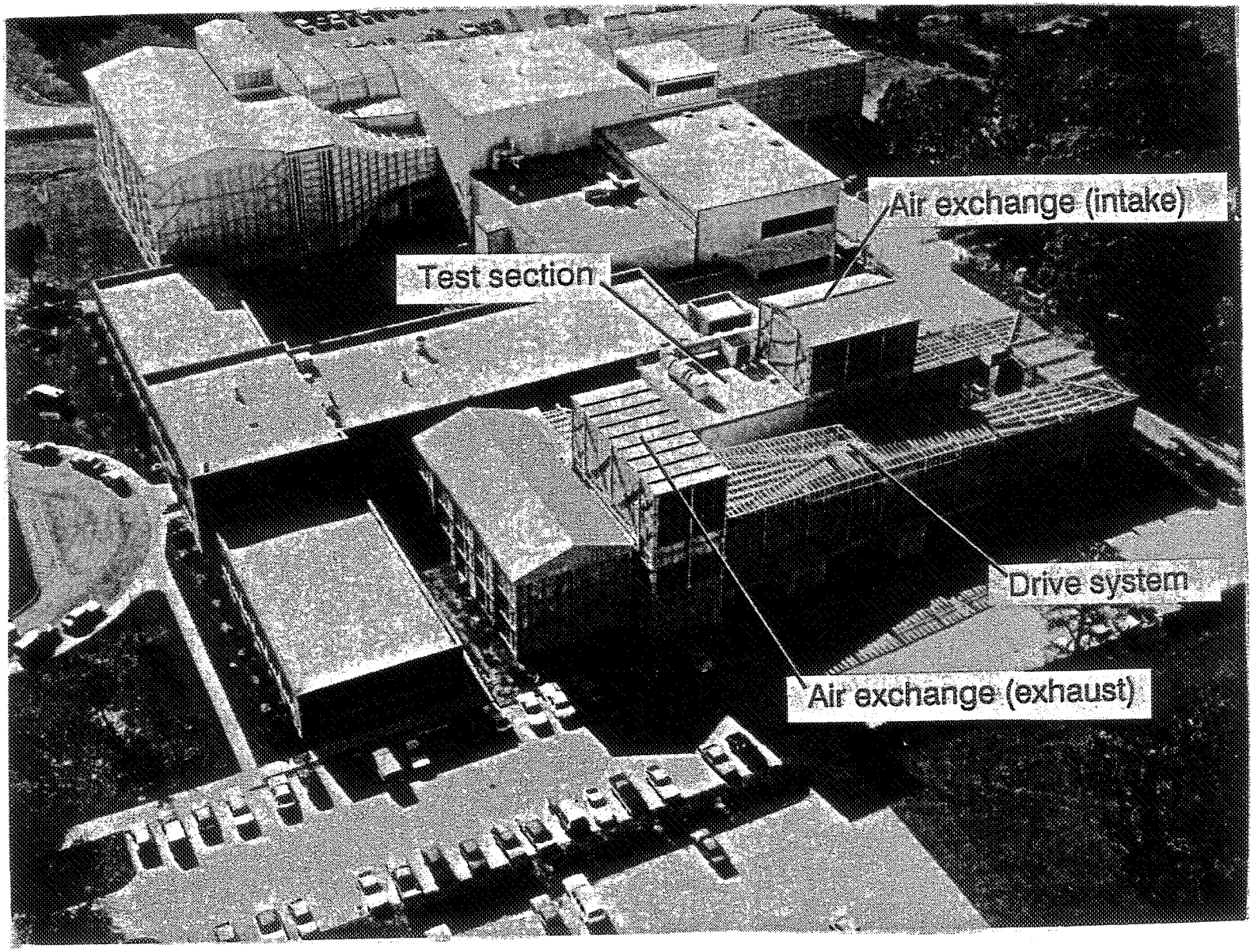

Figure 17. Photograph of the 7- by 10-foot High Speed Tunnel.

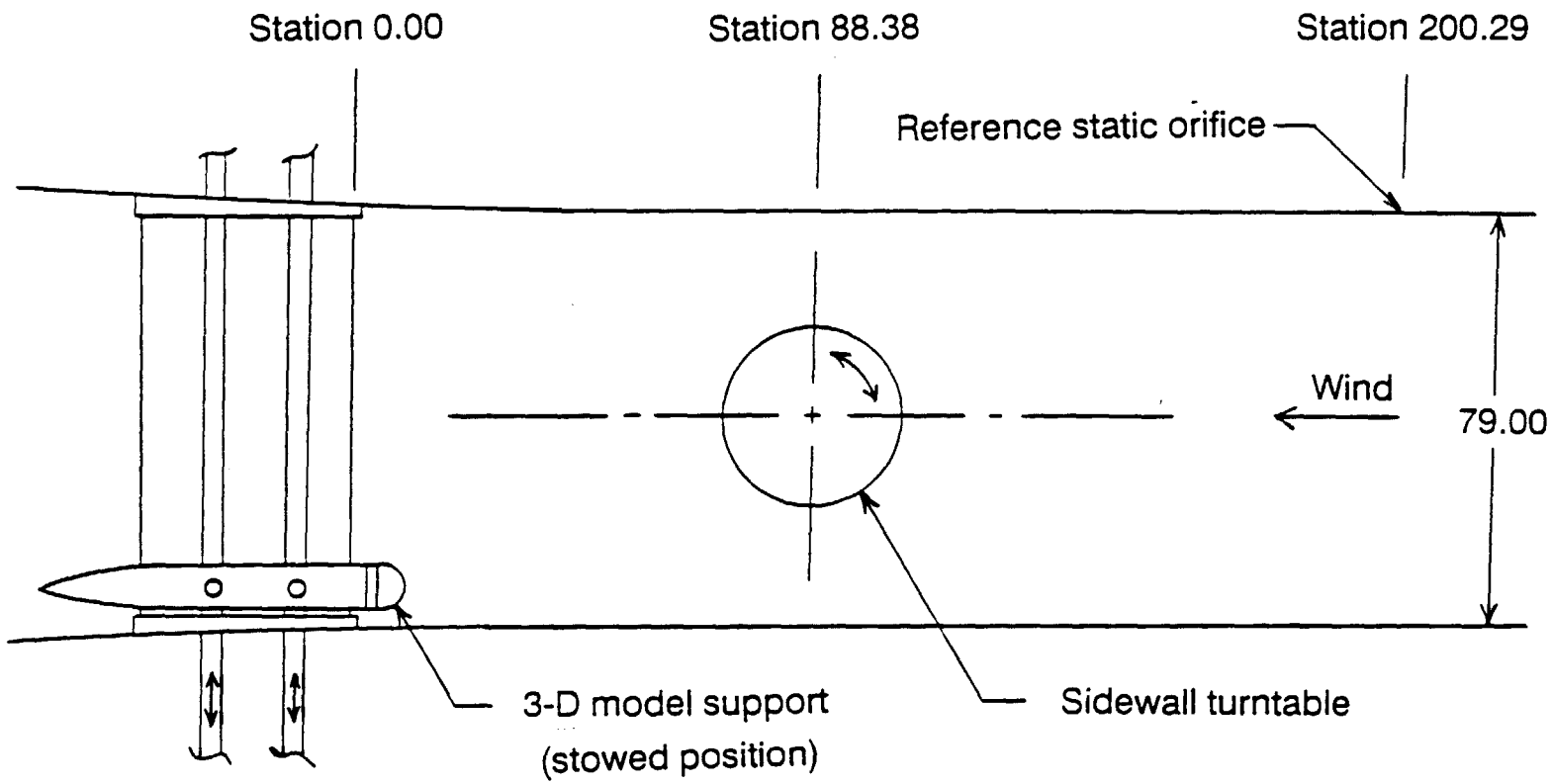

Figure 18. Sketch of the internal components of the 7- by 10-foot High Speed Tunnel test section.

(All dimensions and stations in inches.)

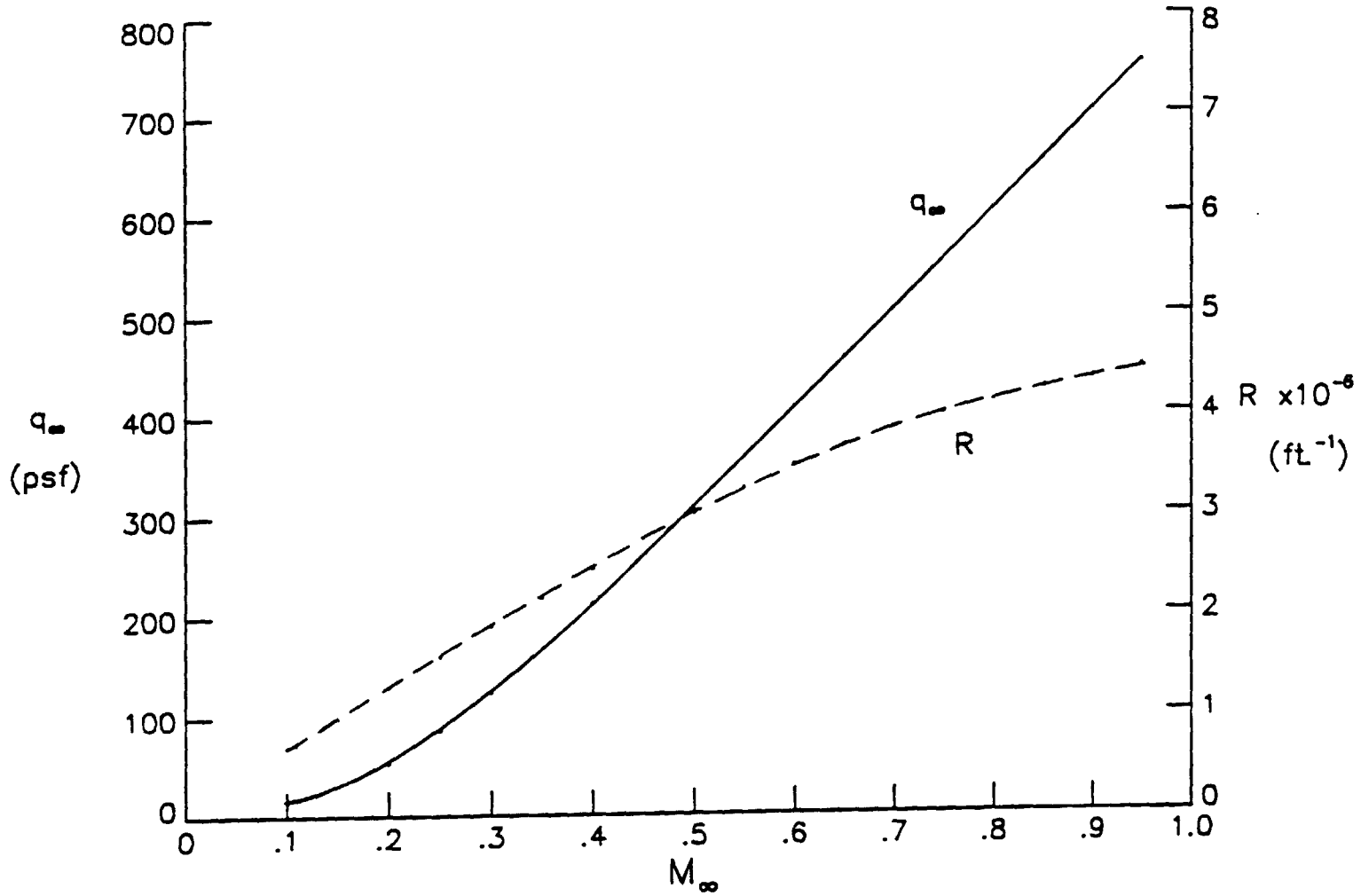

Figure 19. Operating envelope of the 7- by 10-foot High Speed Tunnel.

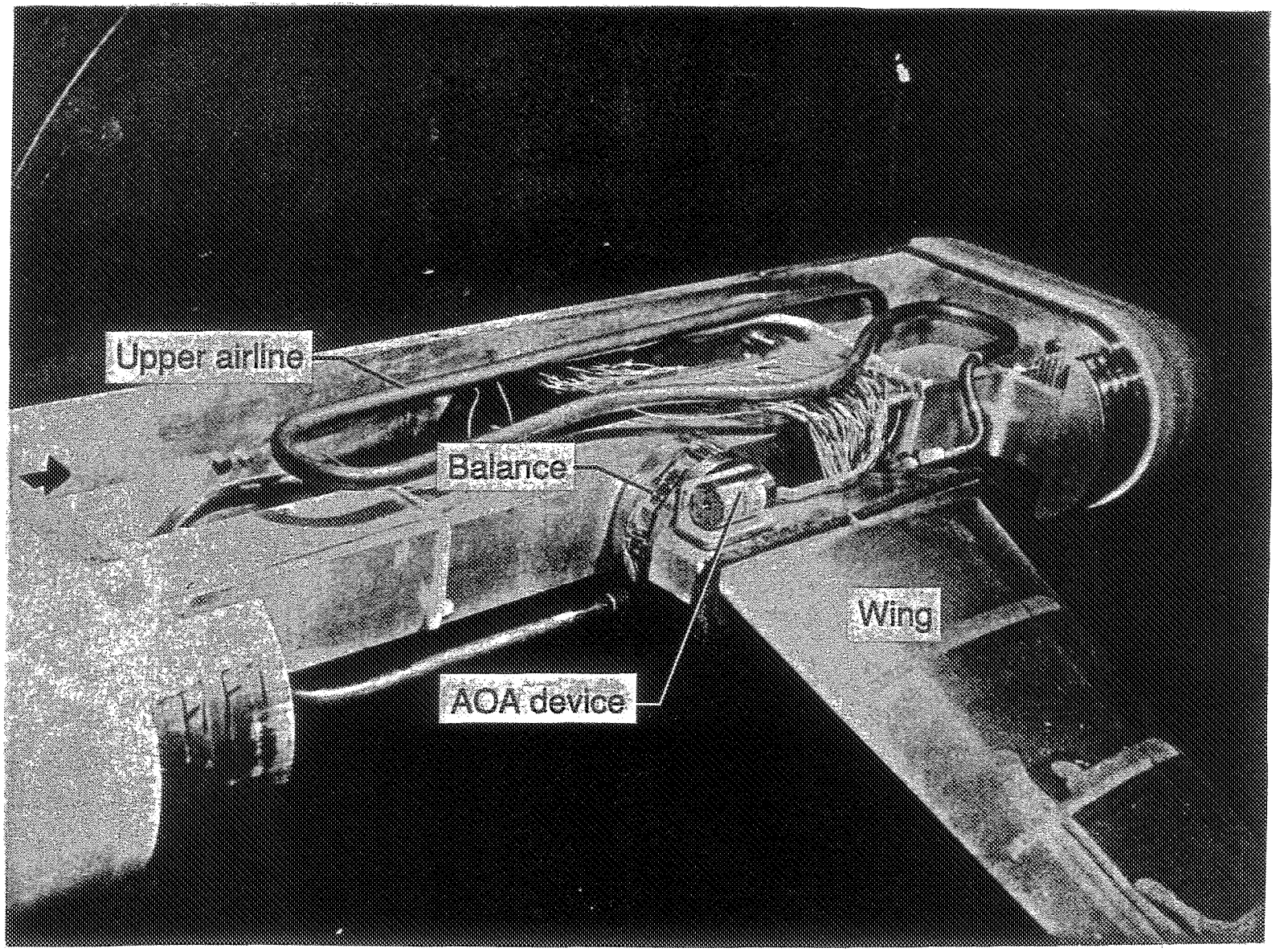

Figure 20. Photograph of the model mounted on the sidewall turntable in the 7- by 10-foot High Speed Tunnel.

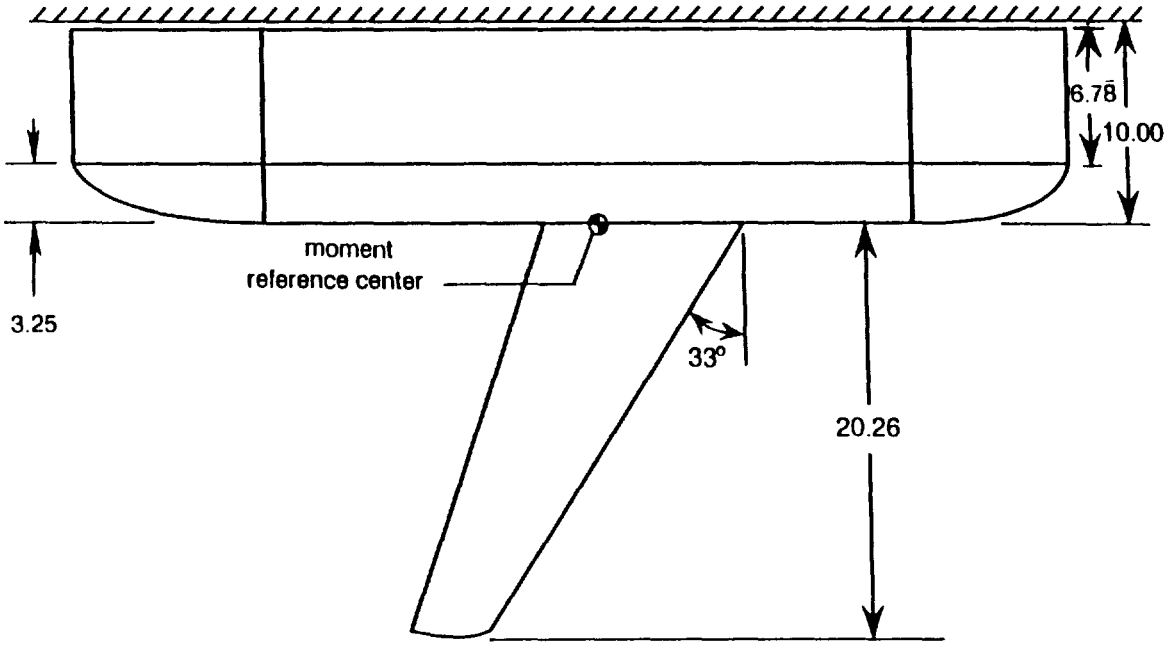

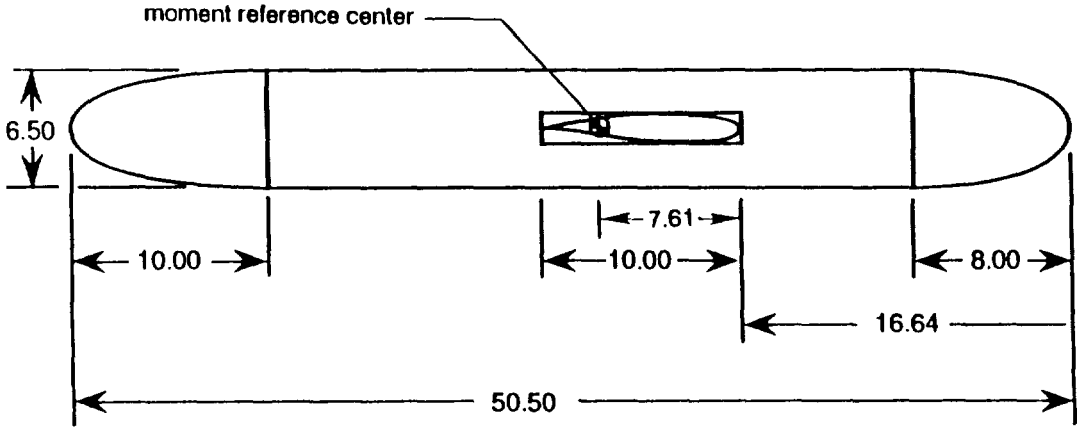

(a) Wing and body details.

Figure 21. Details of the model and the experimental setup.

(All dimensions and stations in inches.)

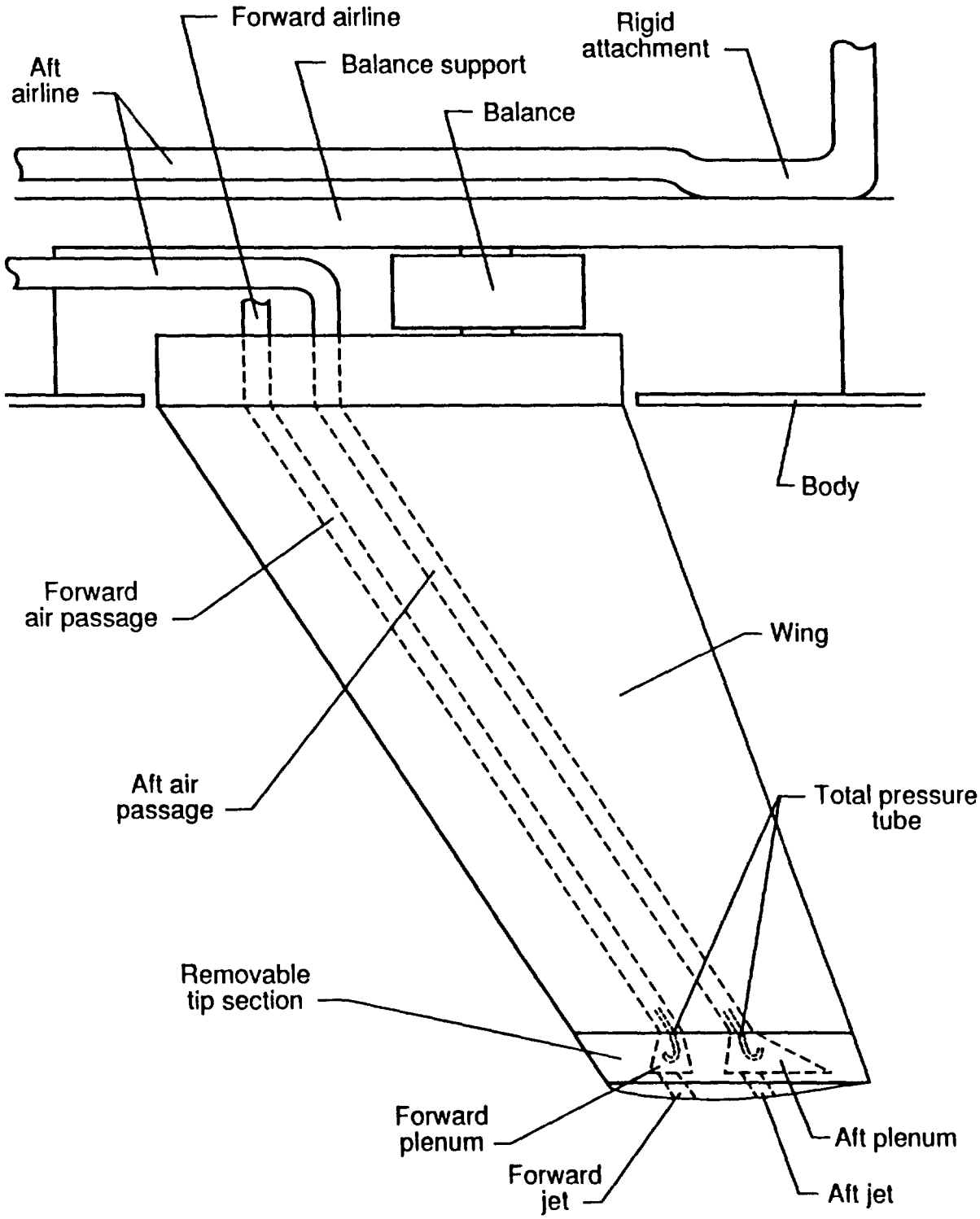

(b) Model components and experimental setup.

Figure 21. Continued.

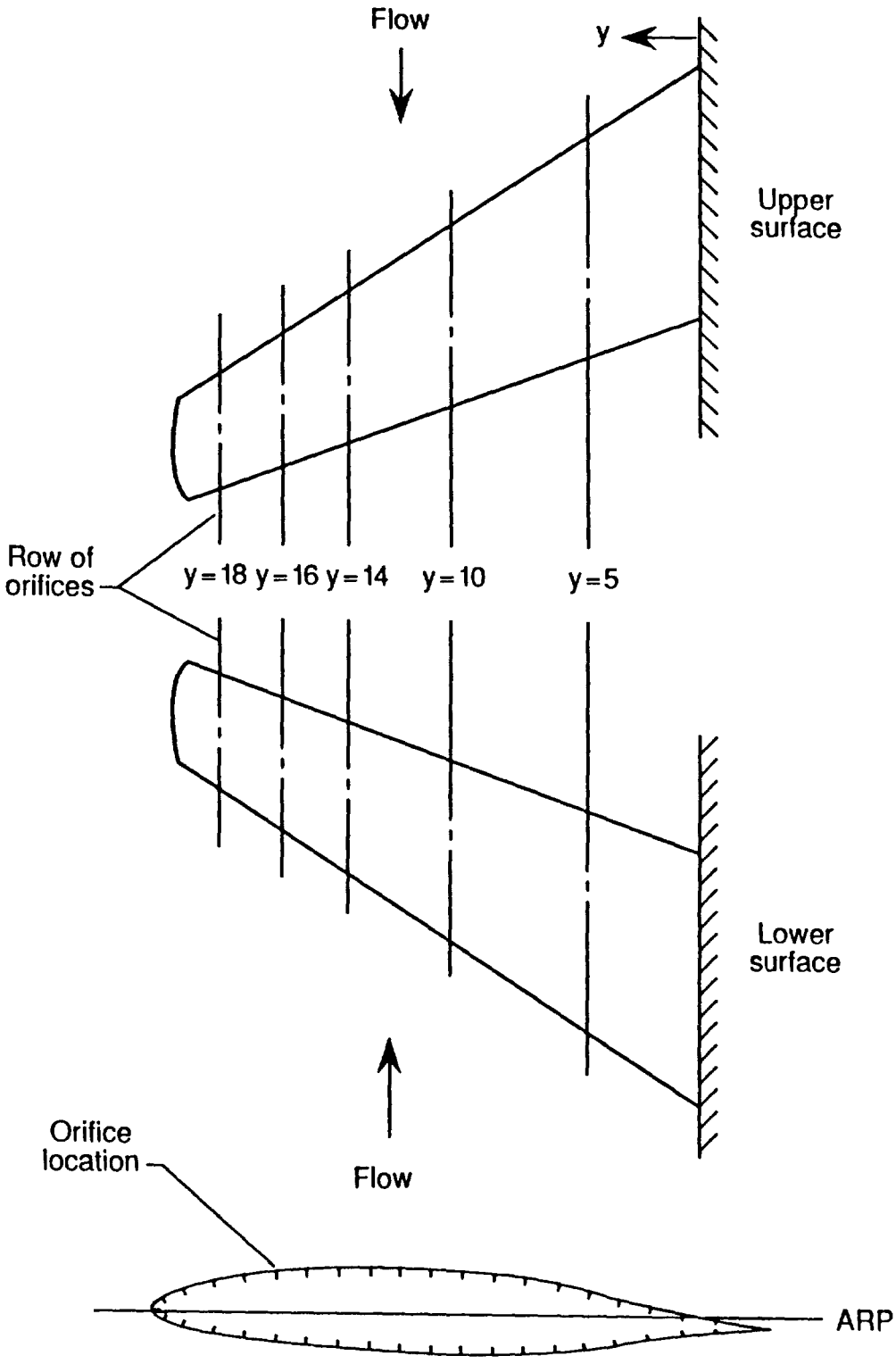

(c) Model static pressure orifice locations.

Figure 21. Continued.

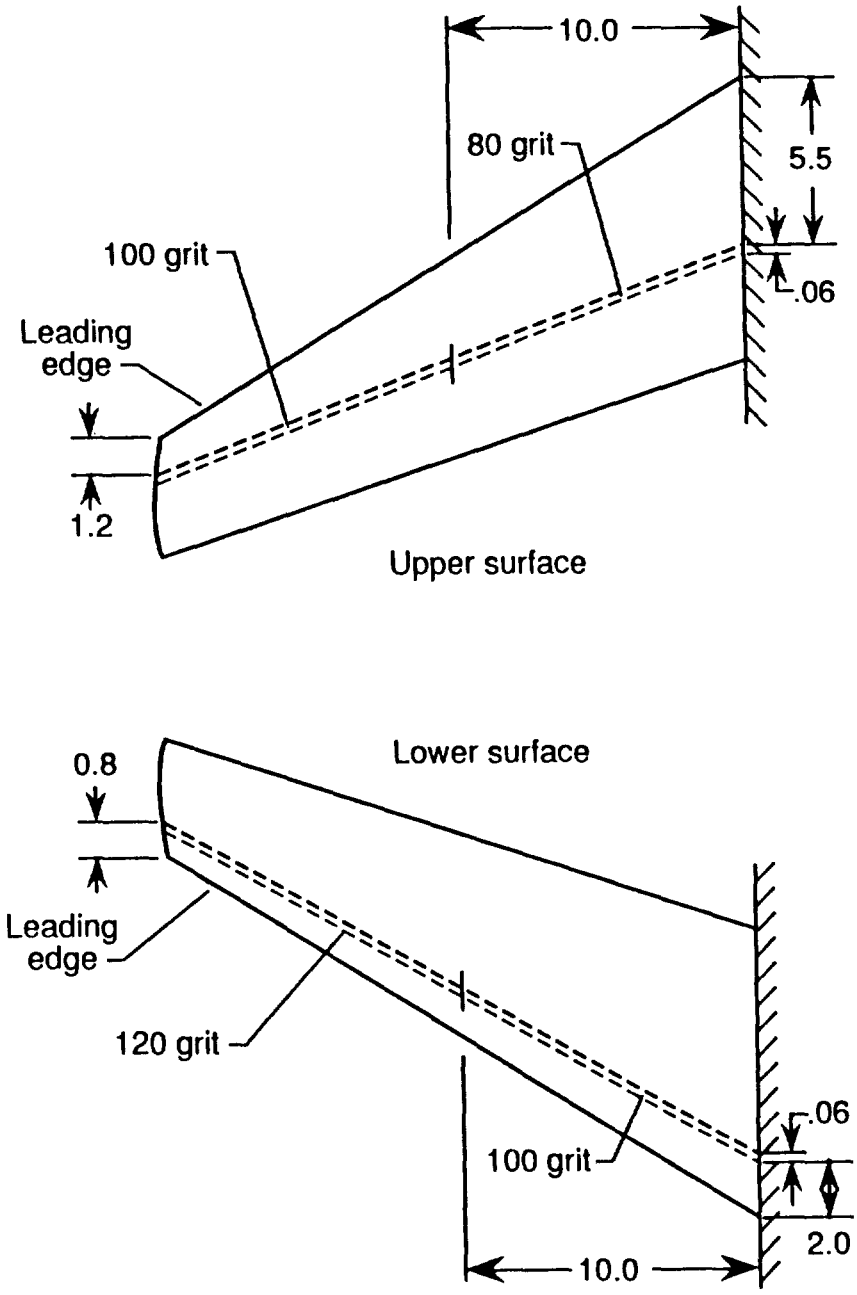

(d) Transition grit size and location.

Figure 21. Concluded.

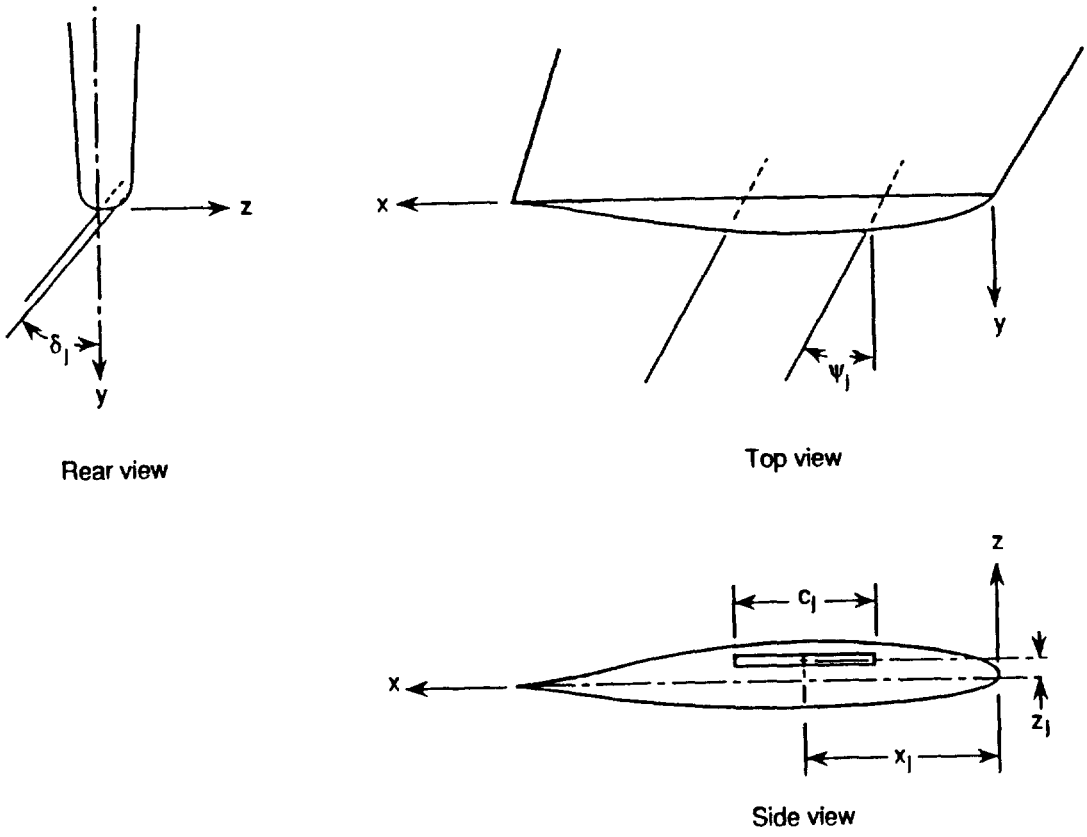

Figure 22. Parameters and sign conventions used to describe the tip jet.

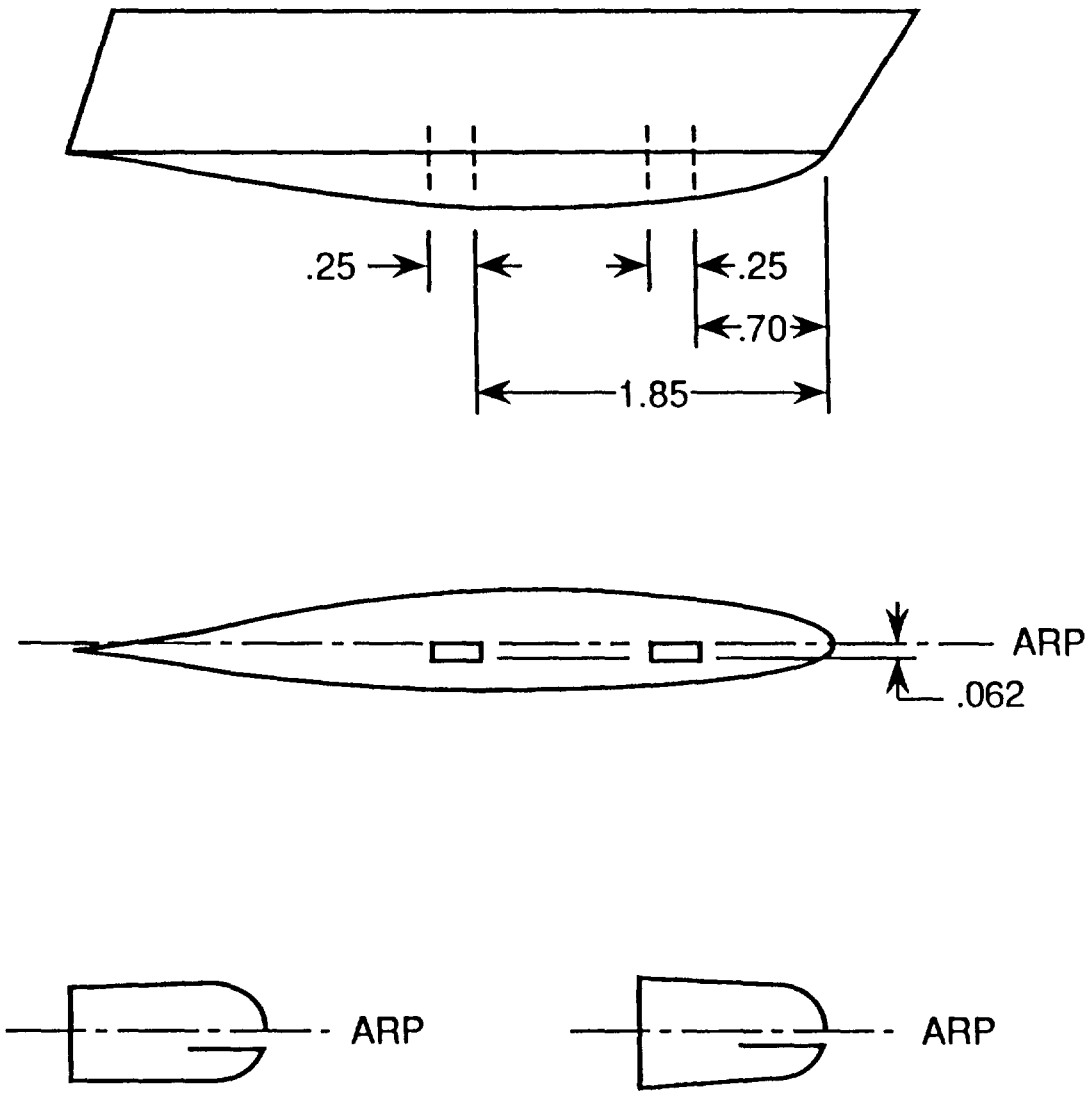

(a) Tip 1.

Figure 23. Sketch of the tip jets.

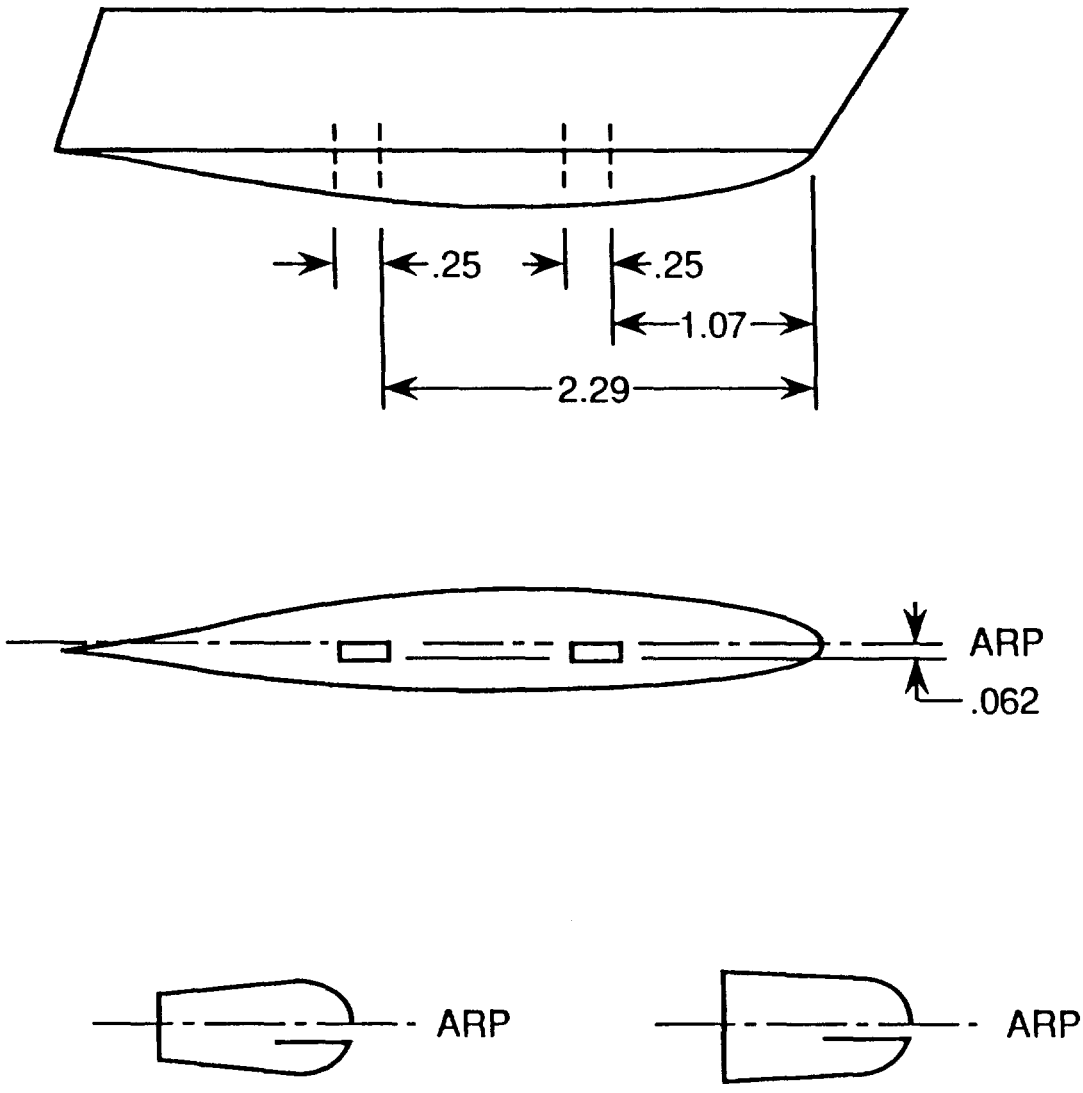

(b) Tip 2.

Figure 23. Continued.

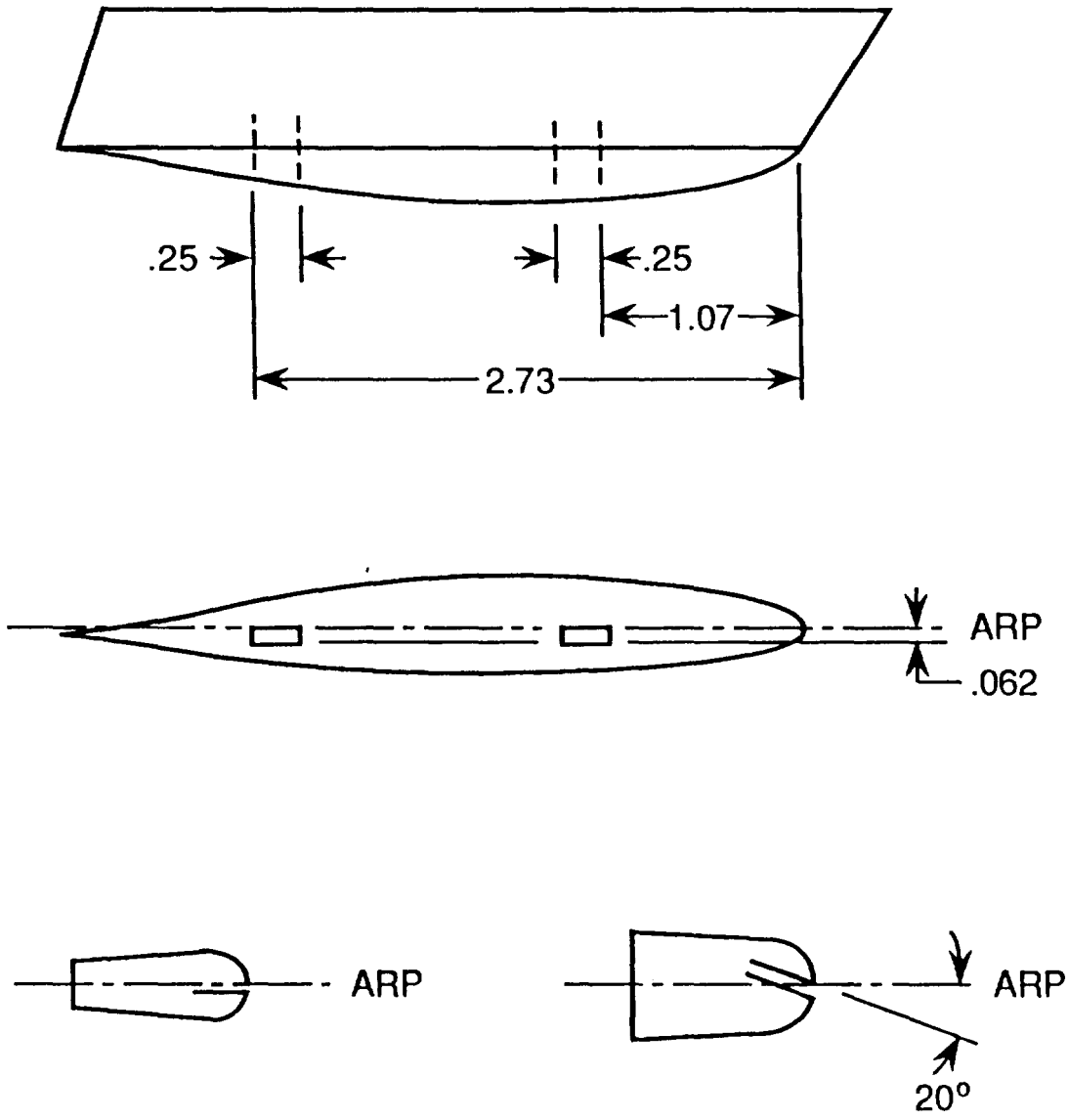

(c) Tip 3.

Figure 23. Continued.

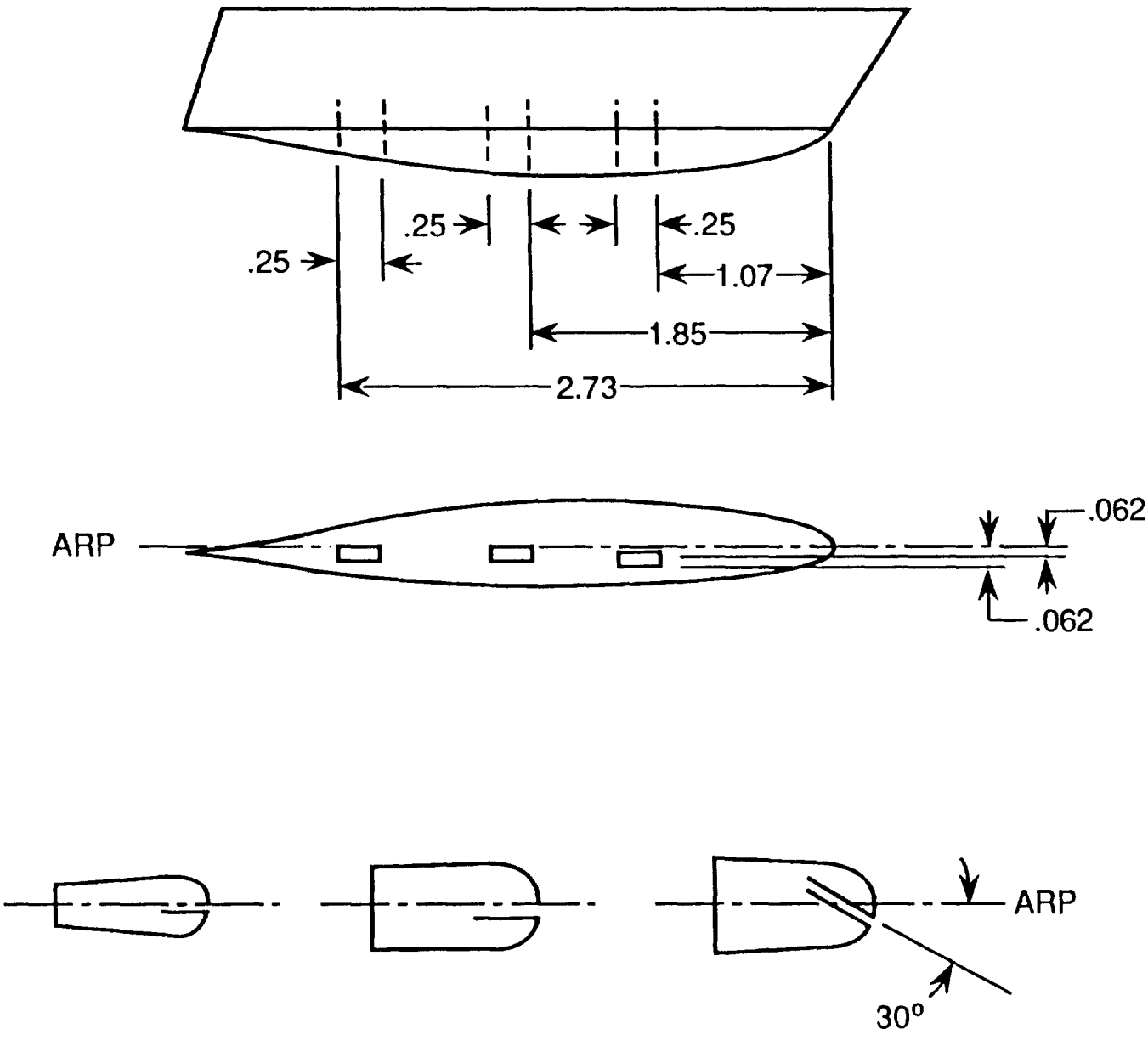

(d) Tip 4.

Figure 23. Continued.

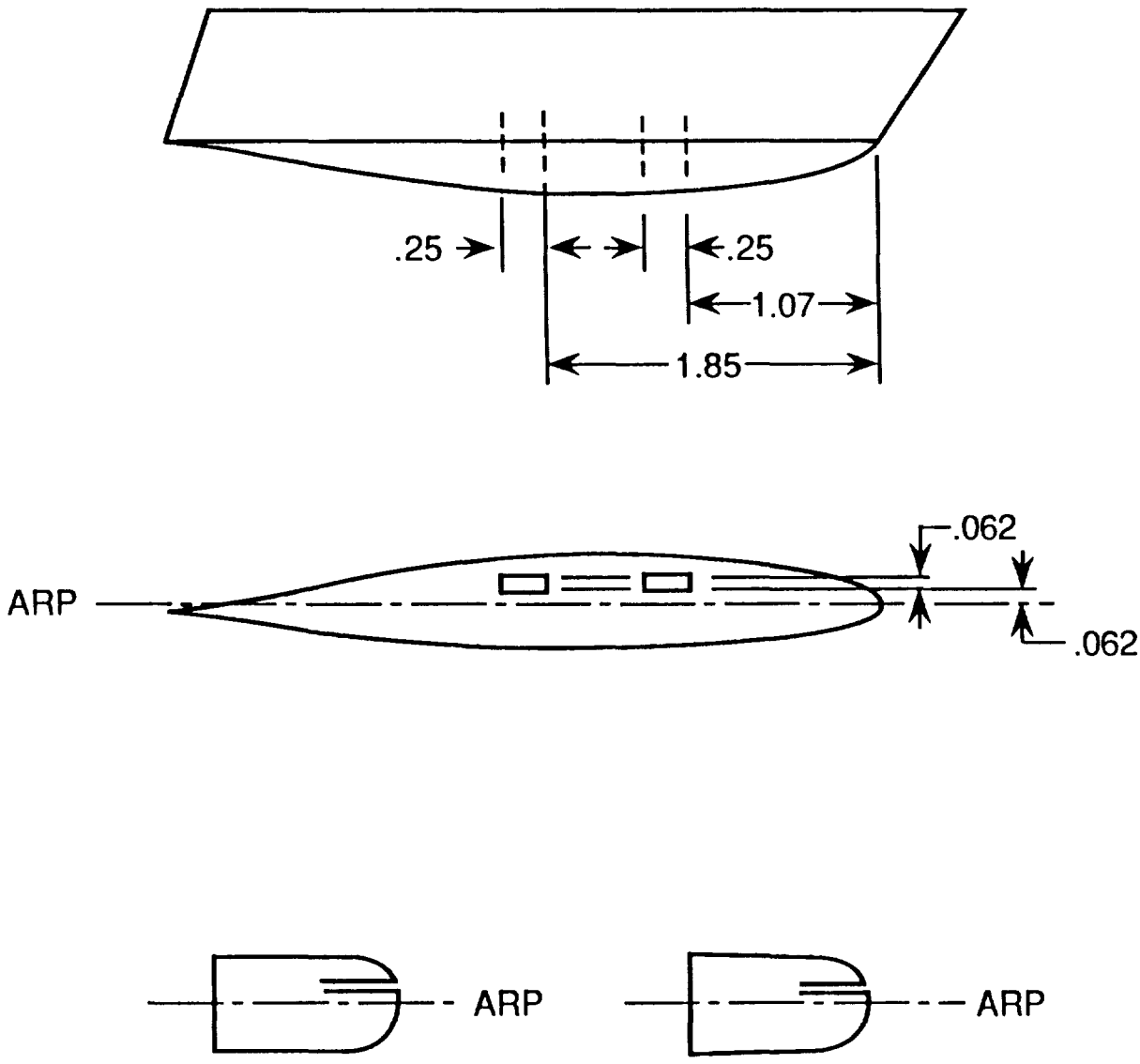

(e) Tip 6.

Figure 23. Continued.

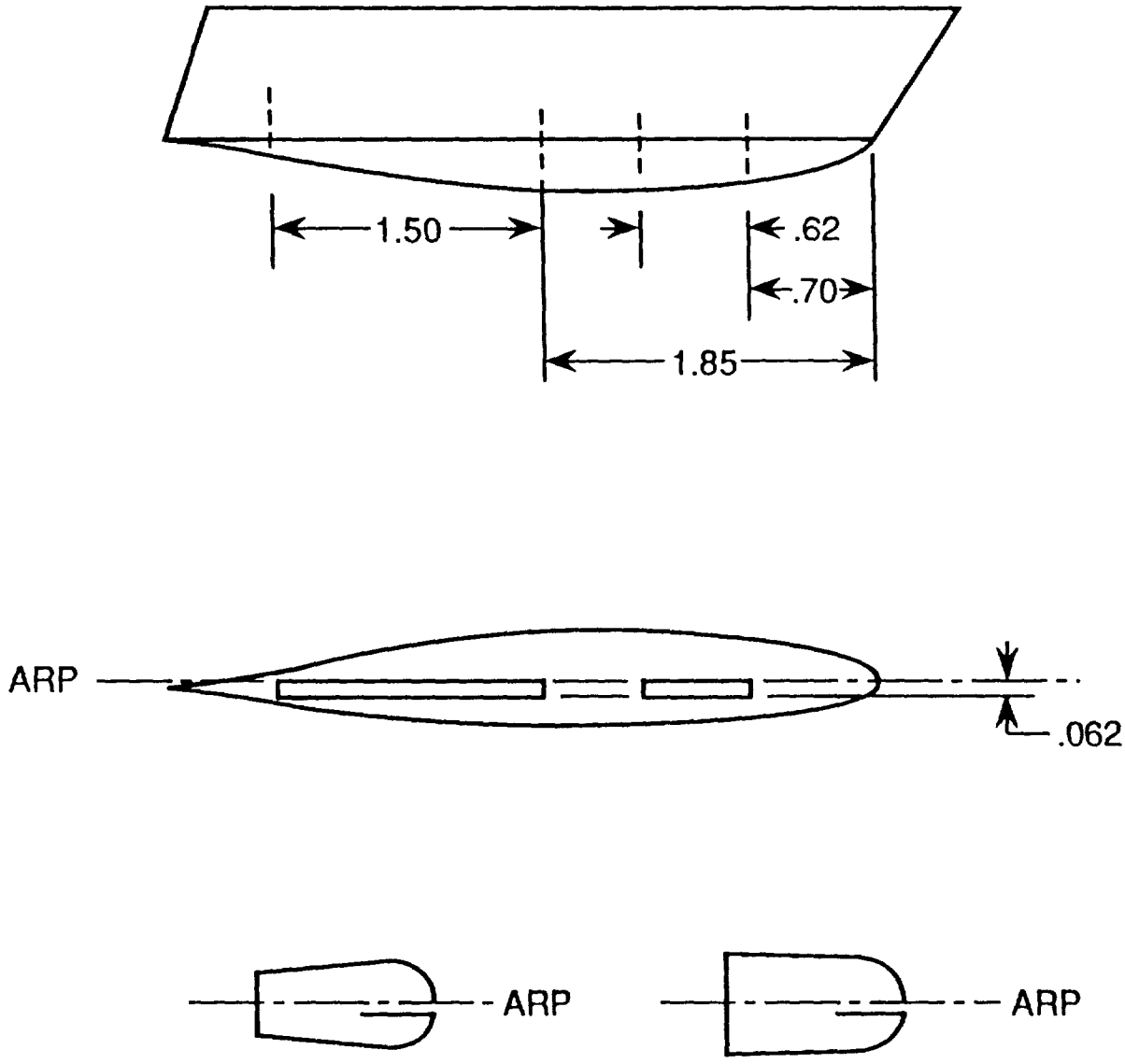

(f) Tip 8.

Figure 23. Continued.

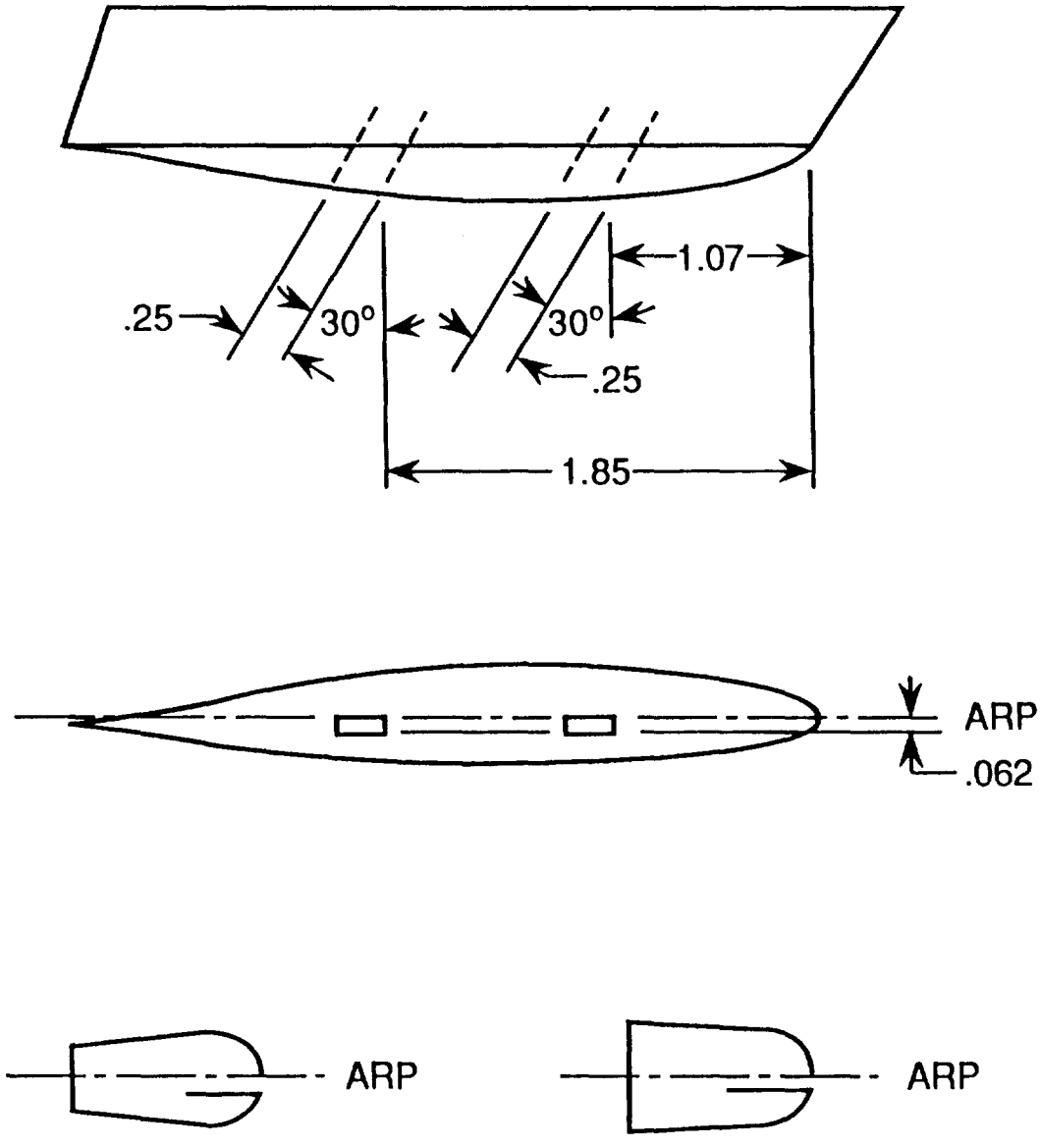

(g) Tip 9.

Figure 23. Concluded.

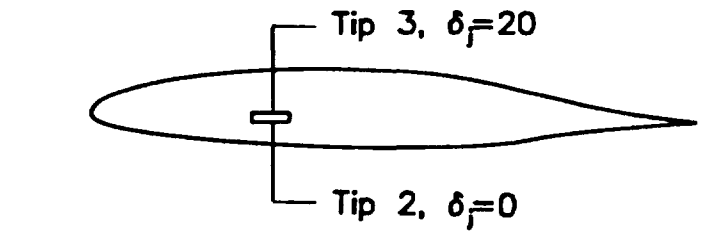

(e) Deflection.

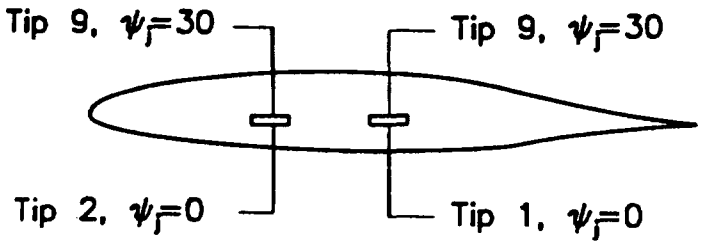

(d) Sweep.

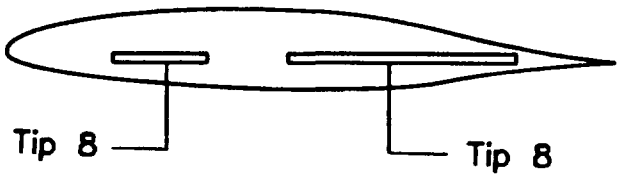

(c) Length.

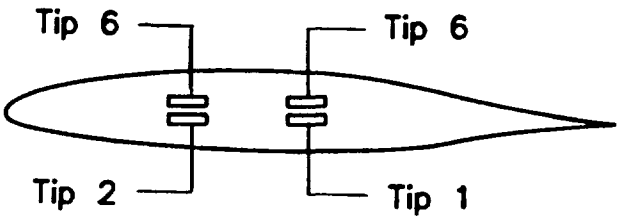

(b) Vertical location.

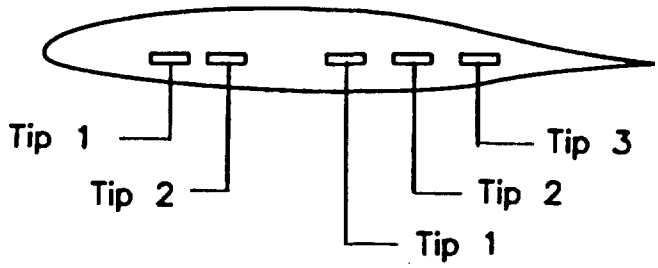

(a) Chordwise location.

Figure 24. Comparison of jet exit locations and exhaust directions.

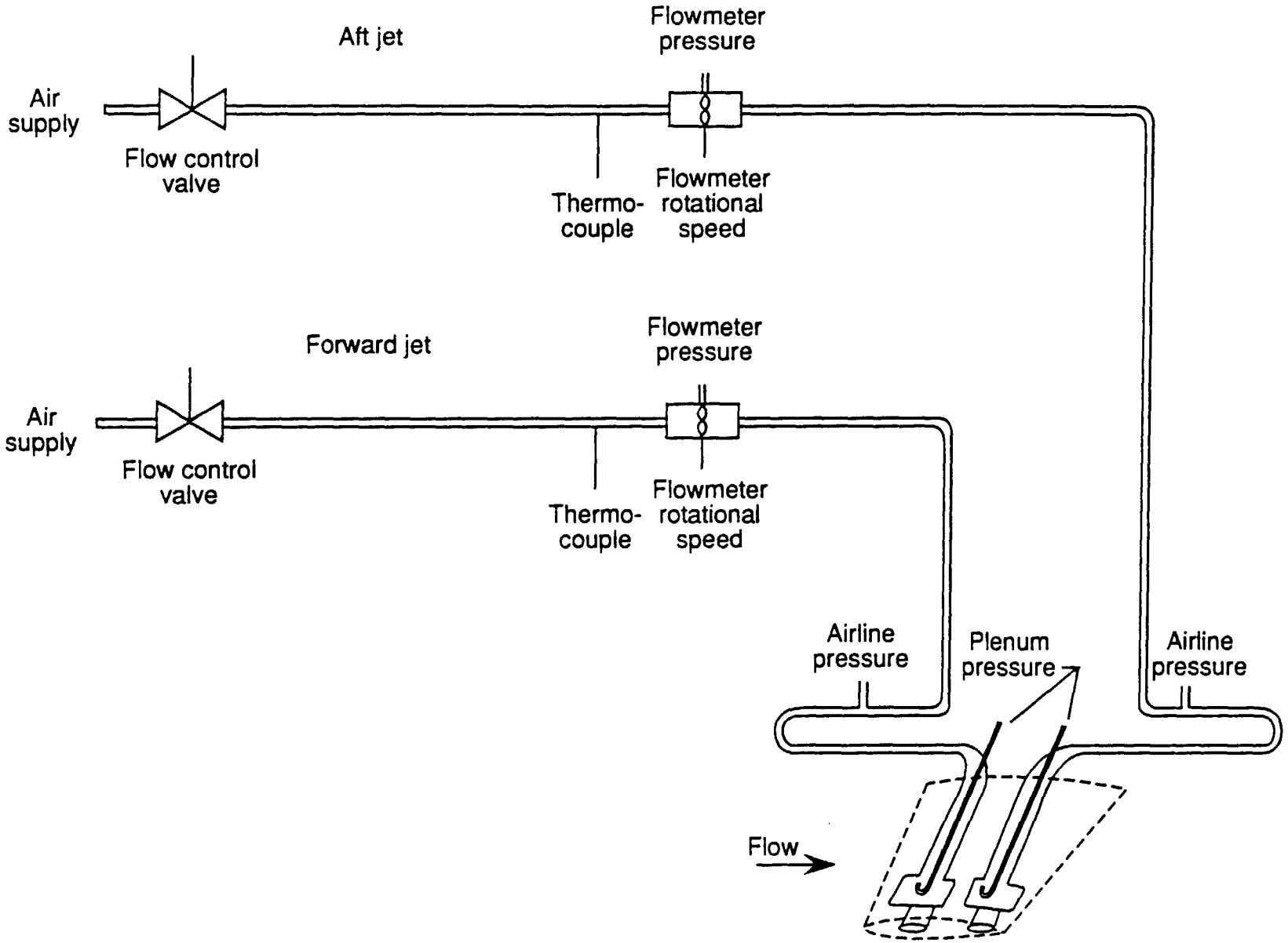

Figure 25. Schematic of the air supply system and the associated instrumentation.

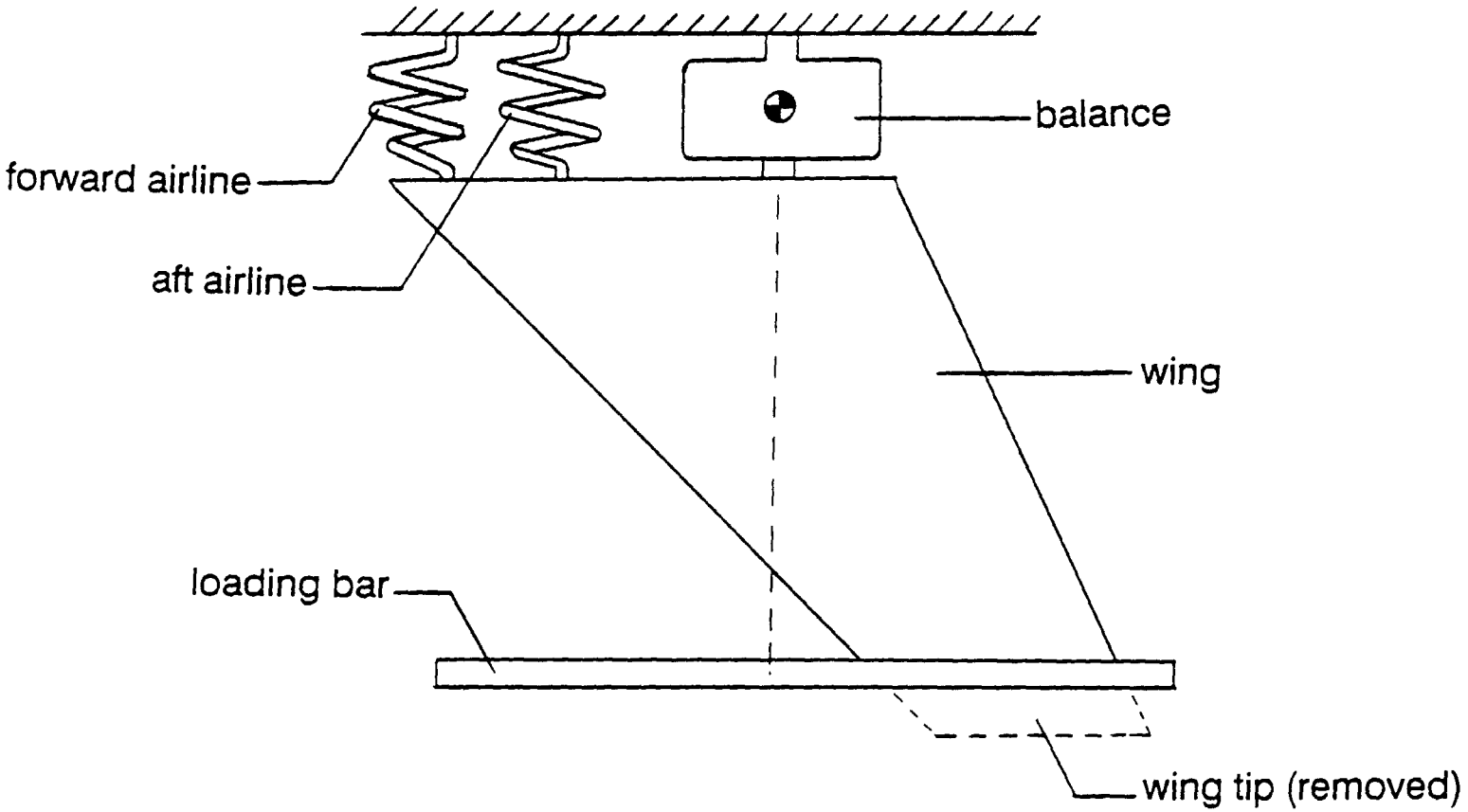

Figure 26. Schematic of the system used to calibrate the balance-airline assembly.

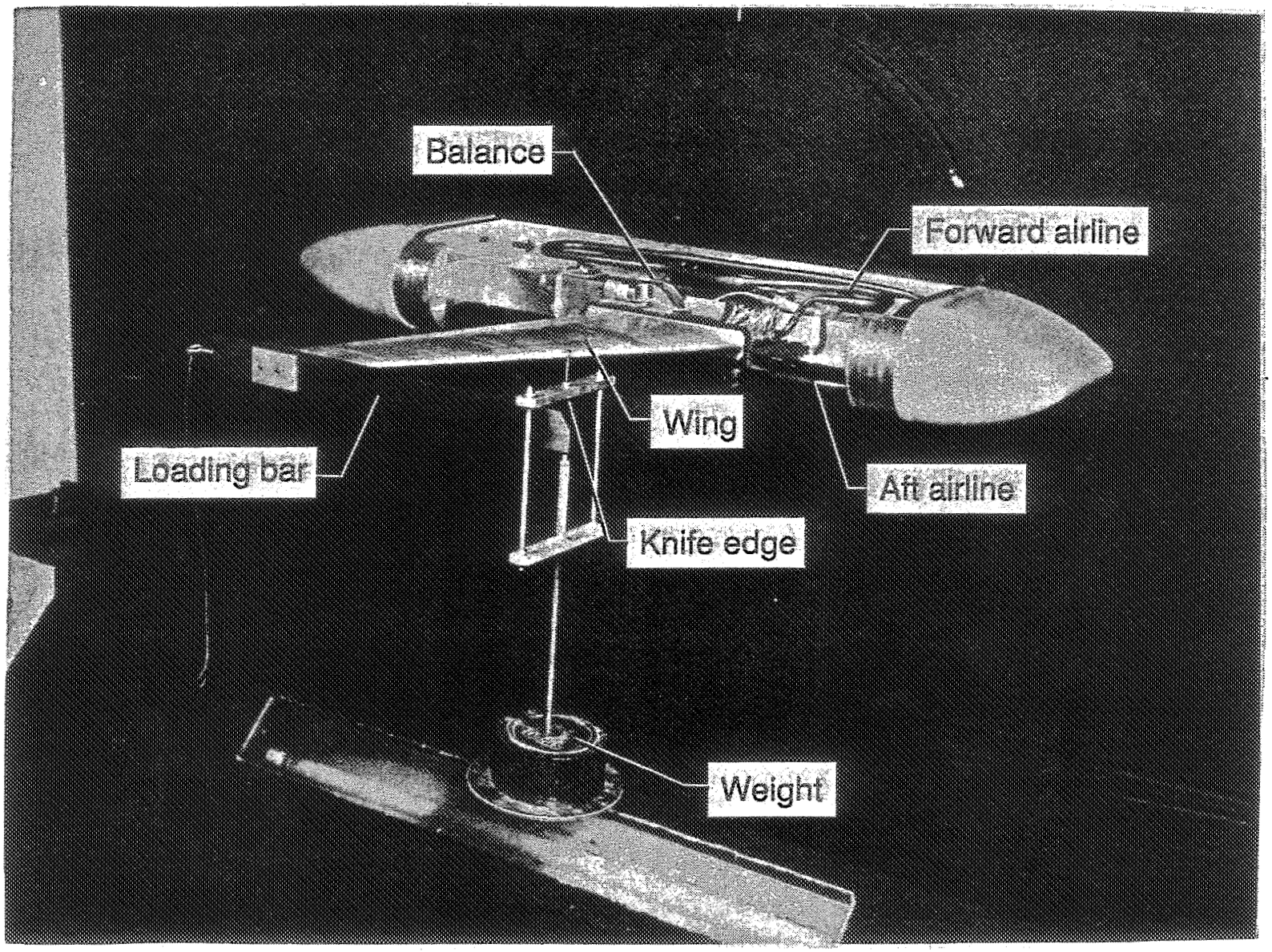

Figure 27. Photograph of the balance-airline assembly undergoing calibration.

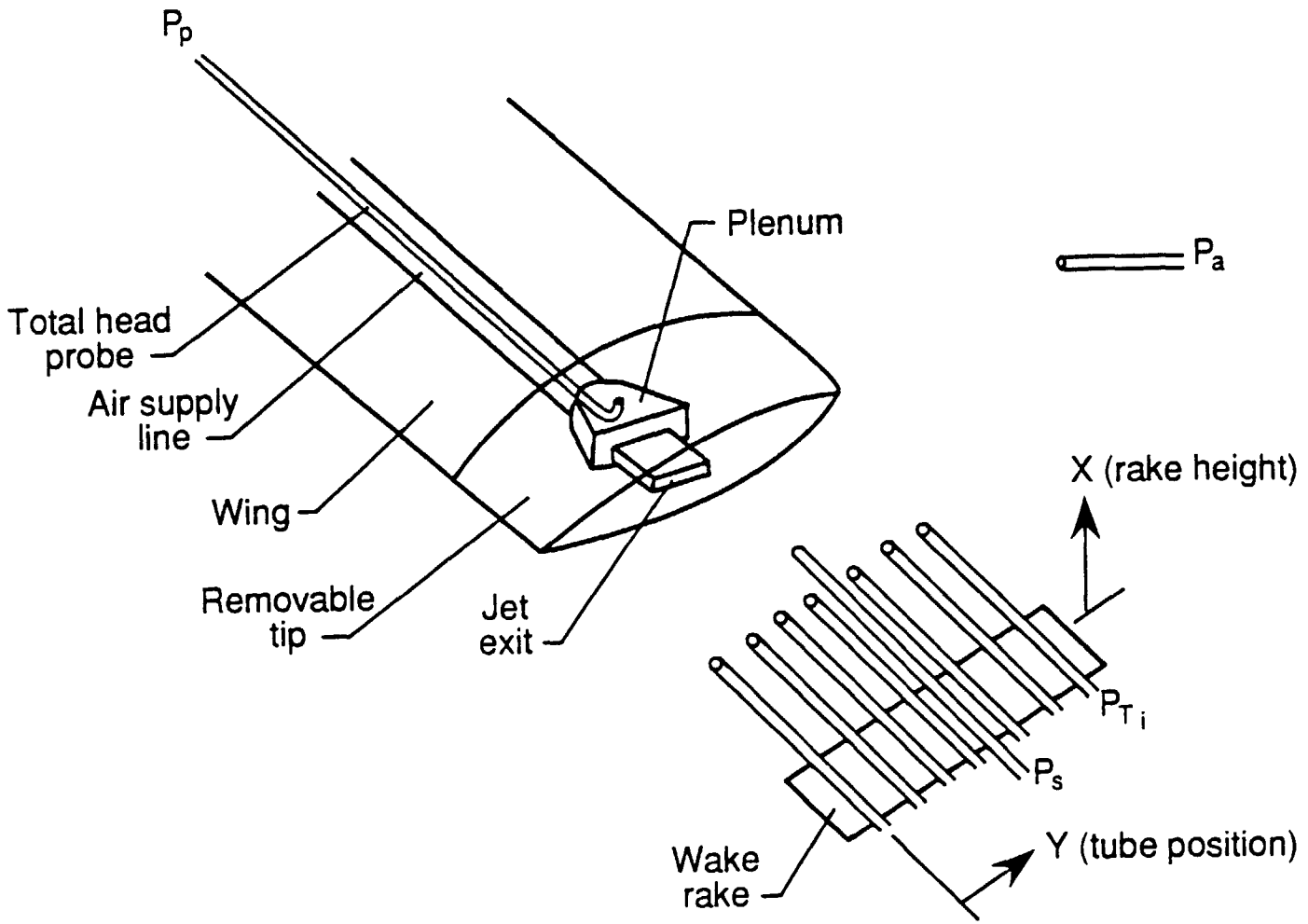

Figure 28. Sketch of the experimental setup for the jet momentum calibration.

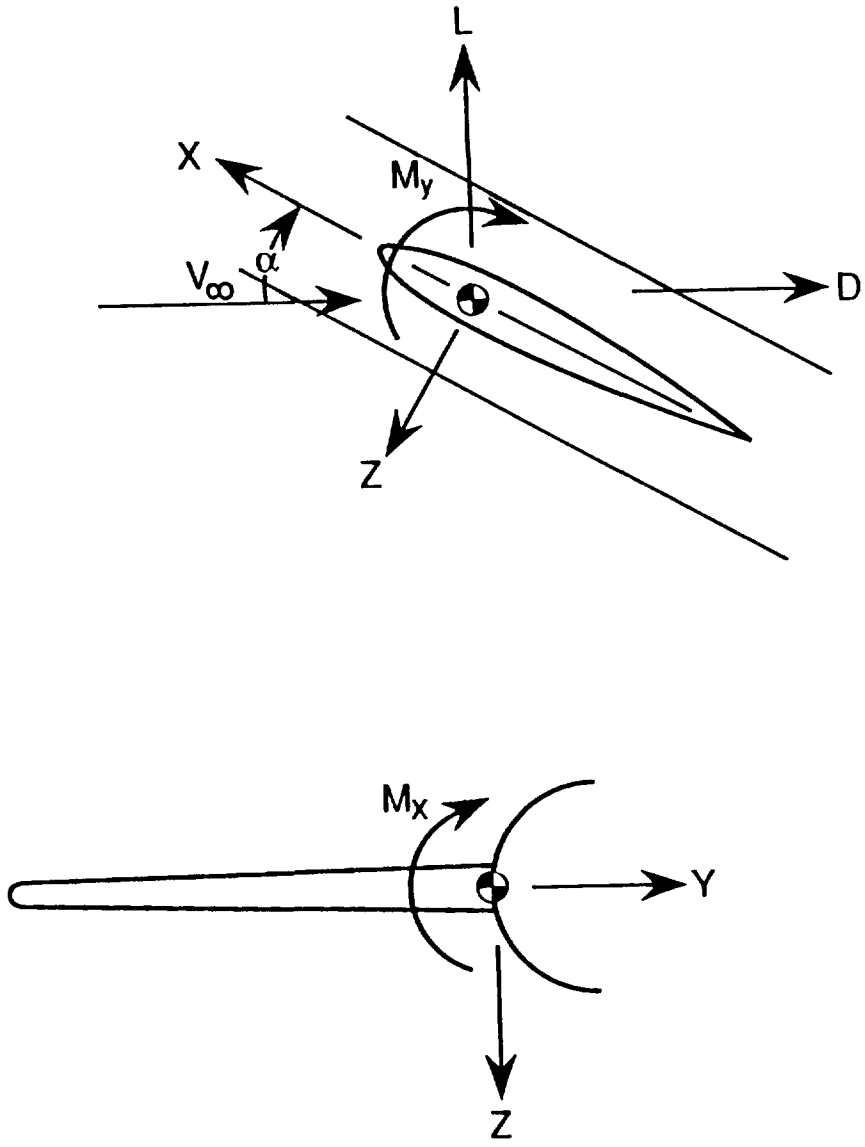

Figure 29. Axis system for balance data.

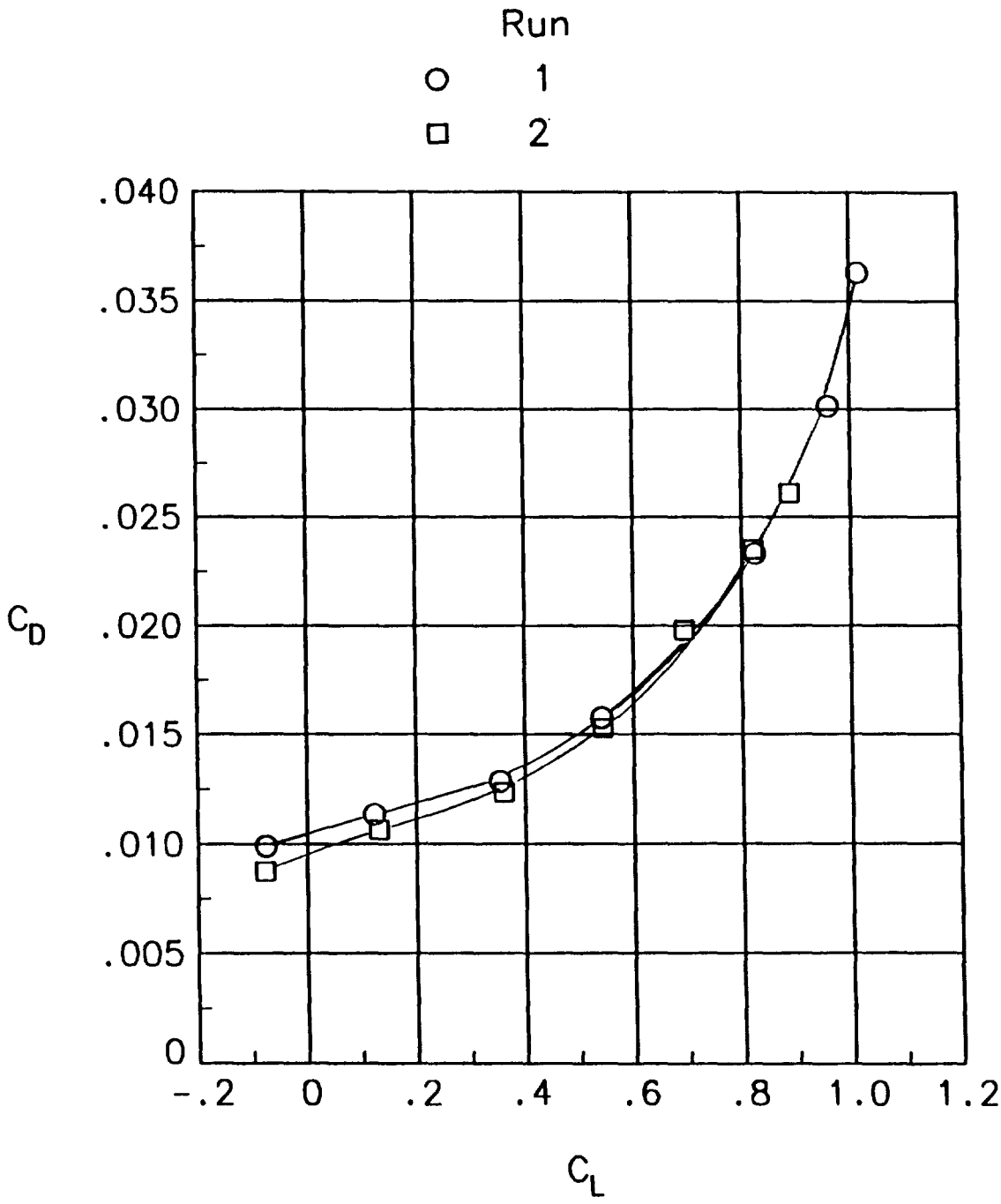

(a) Tip 2.

Figure 30. Repeatability of the drag polars. No blowing. $M_\infty = 0.3$.

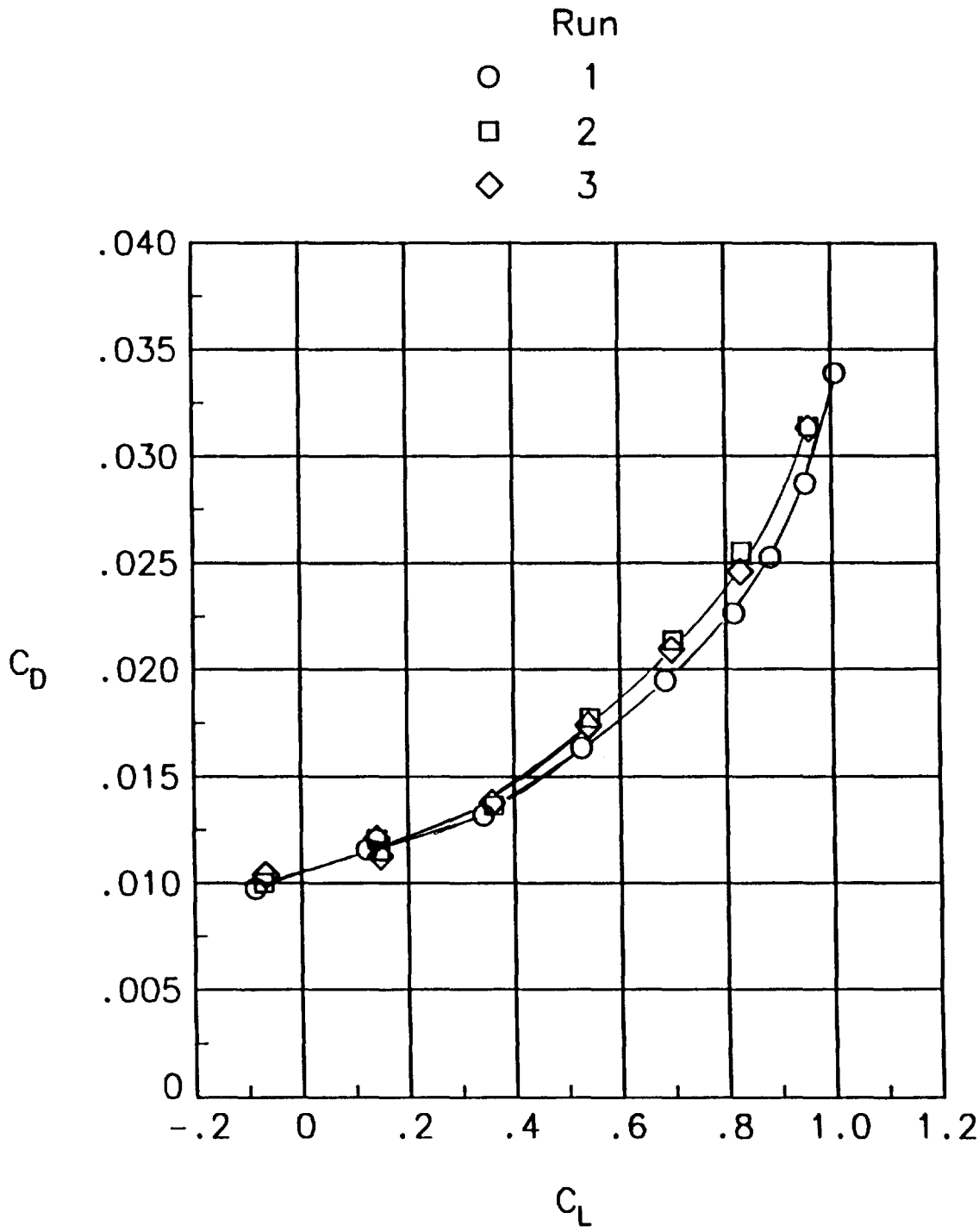

(b) Tip 8.

Figure 30. Concluded.

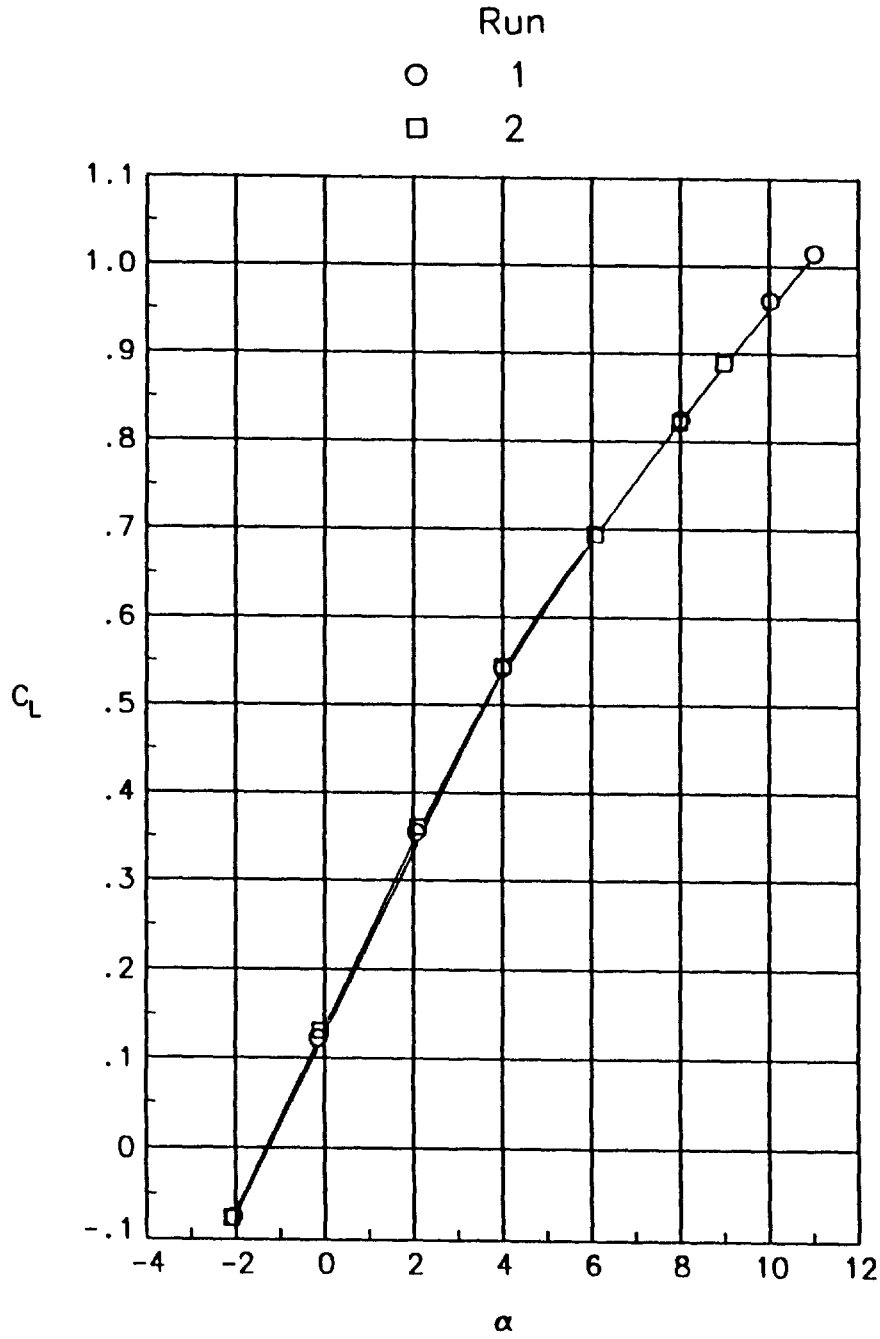

(a) Tip 2.

Figure 31. Repeatability of the lift curves. No blowing. $M_\infty = 0.3$.

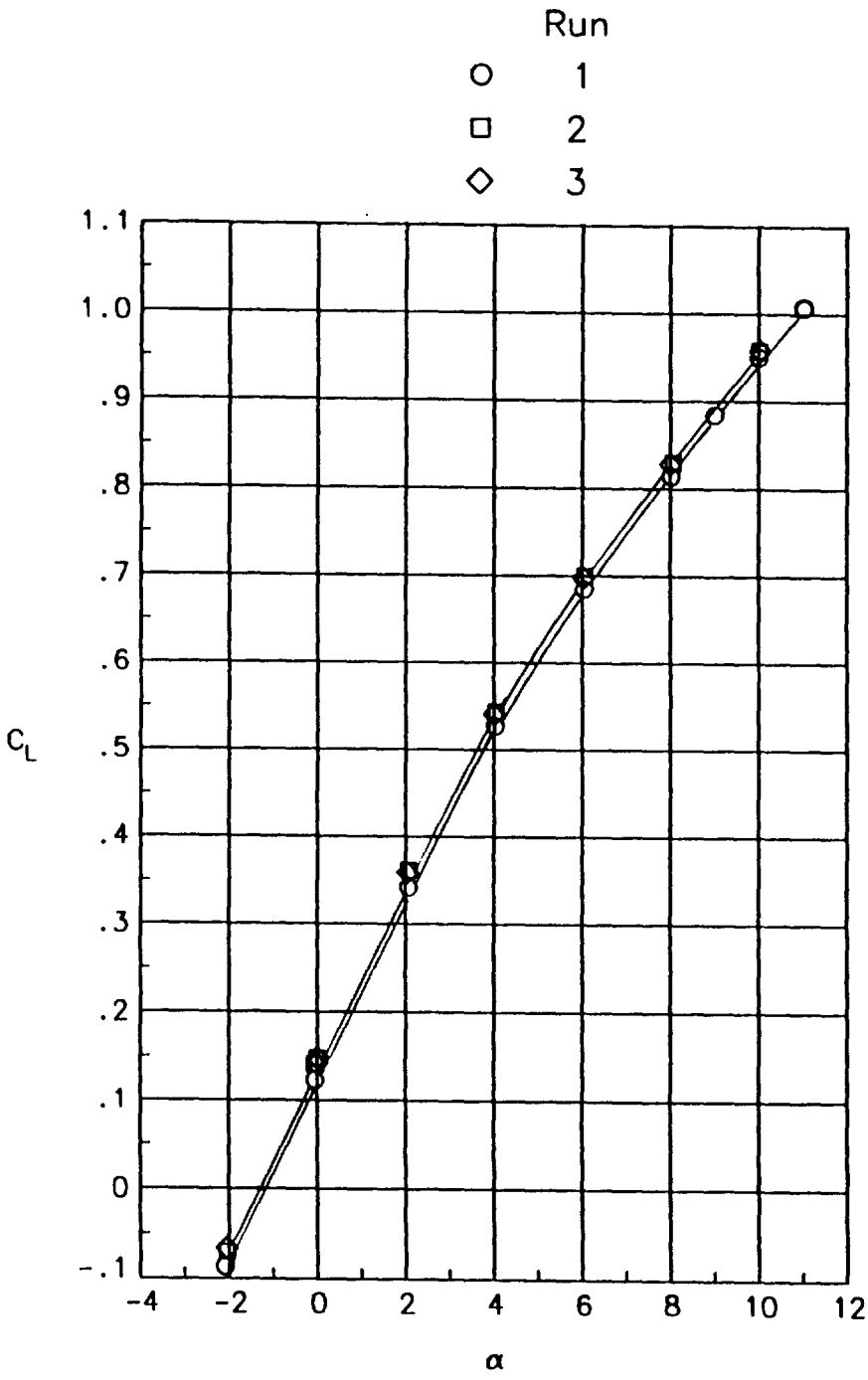

(b) Tip 8.

Figure 31. Concluded.

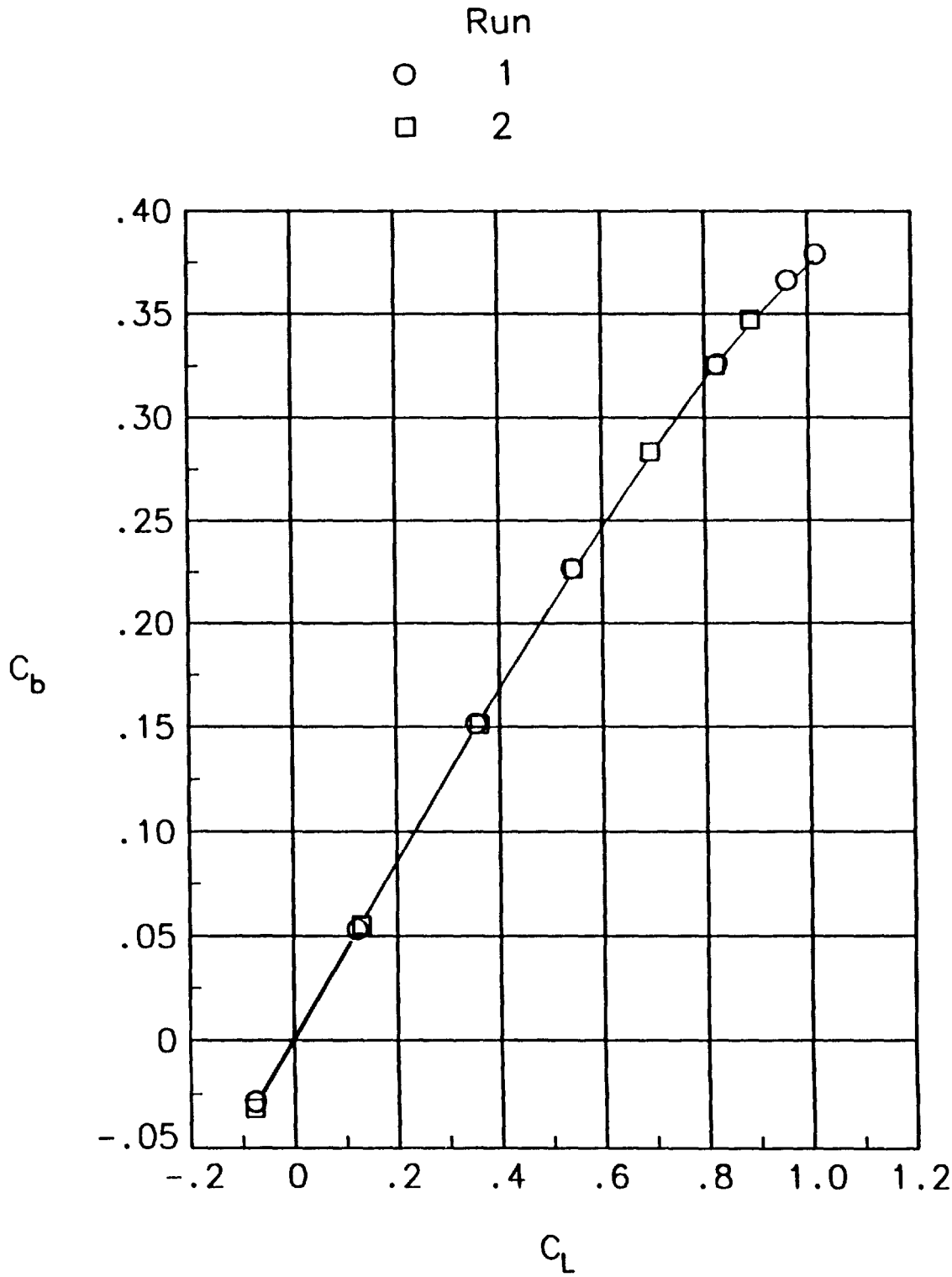

(a) Tip 2.

Figure 32. Repeatability of the wing root bending moment curves.

No blowing. $M_\infty = 0.3$.

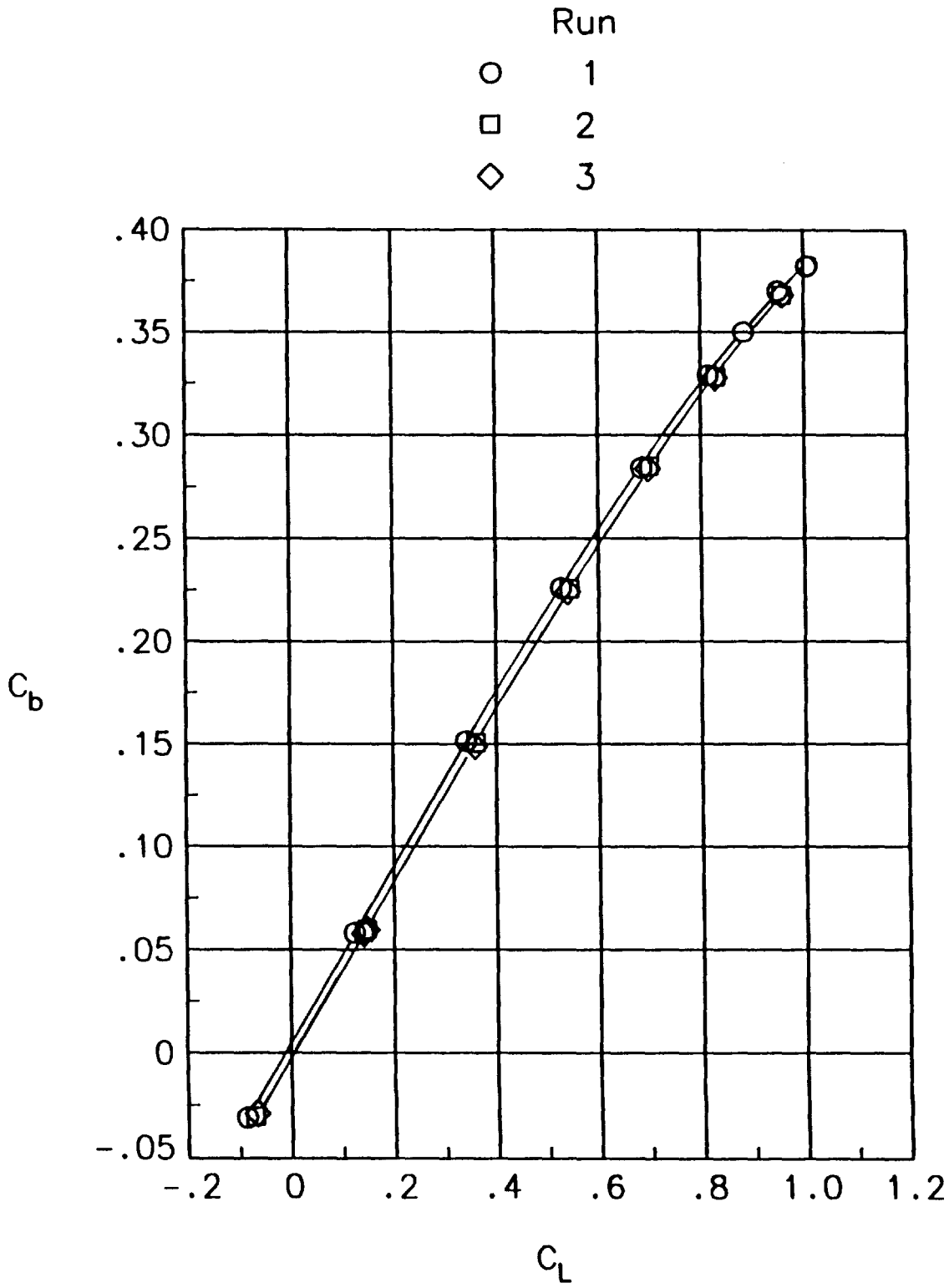

(b) Tip 8.

Figure 32. Concluded.

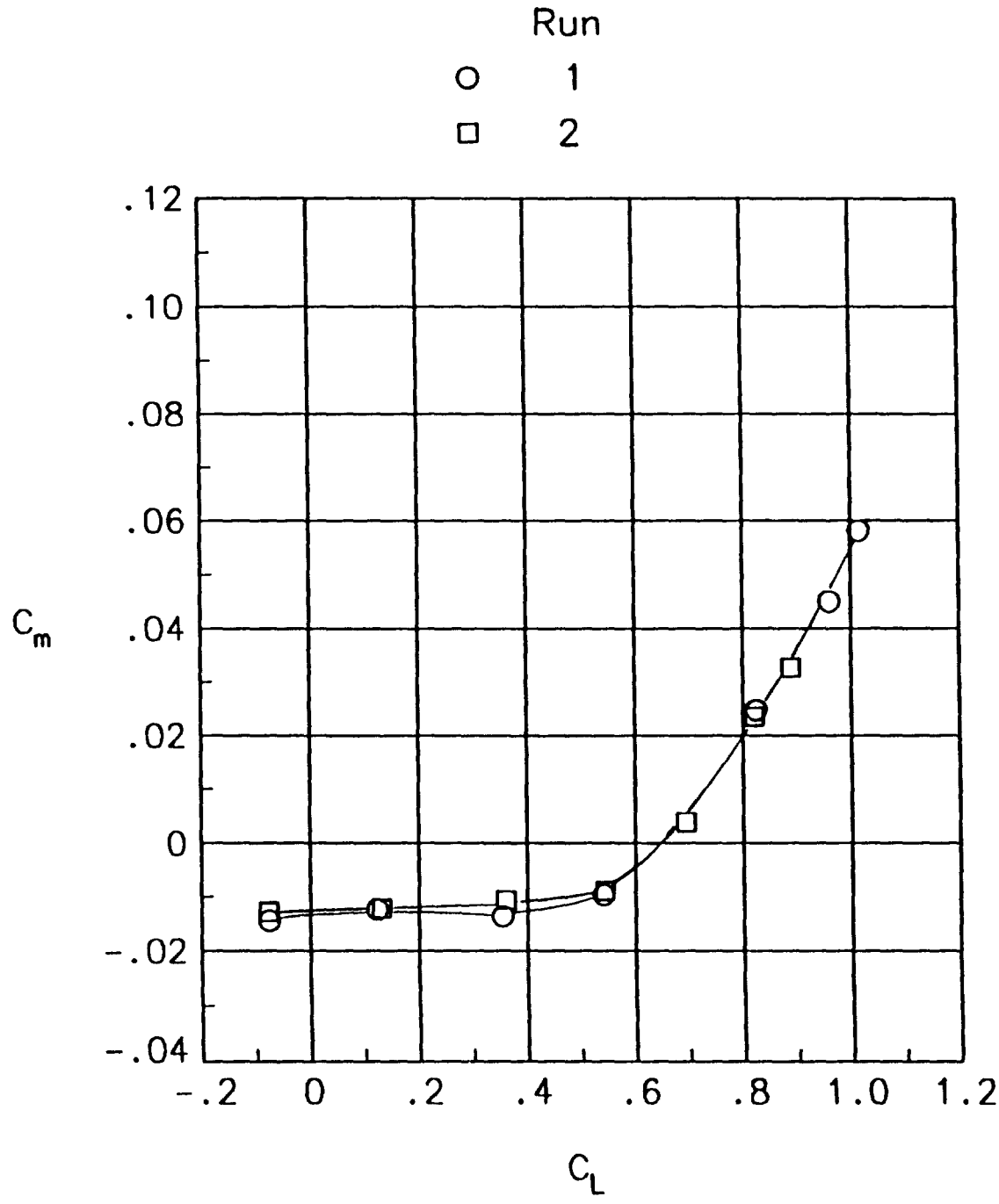

(a) Tip 2.

Figure 33. Repeatability of the wing pitching moment curves.

No blowing. $M_\infty = 0.3$.

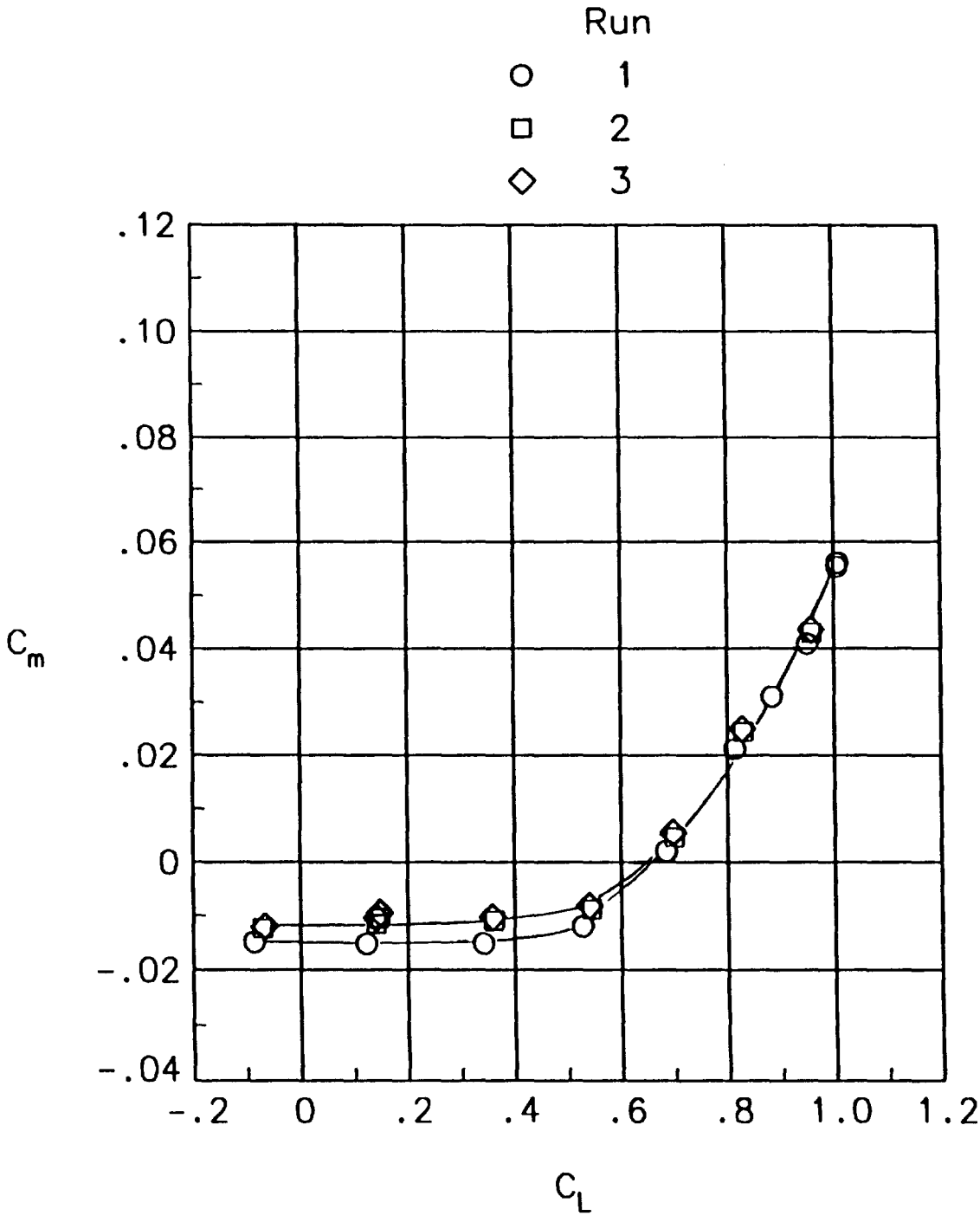

(b) Tip 8.

Figure 33. Concluded.

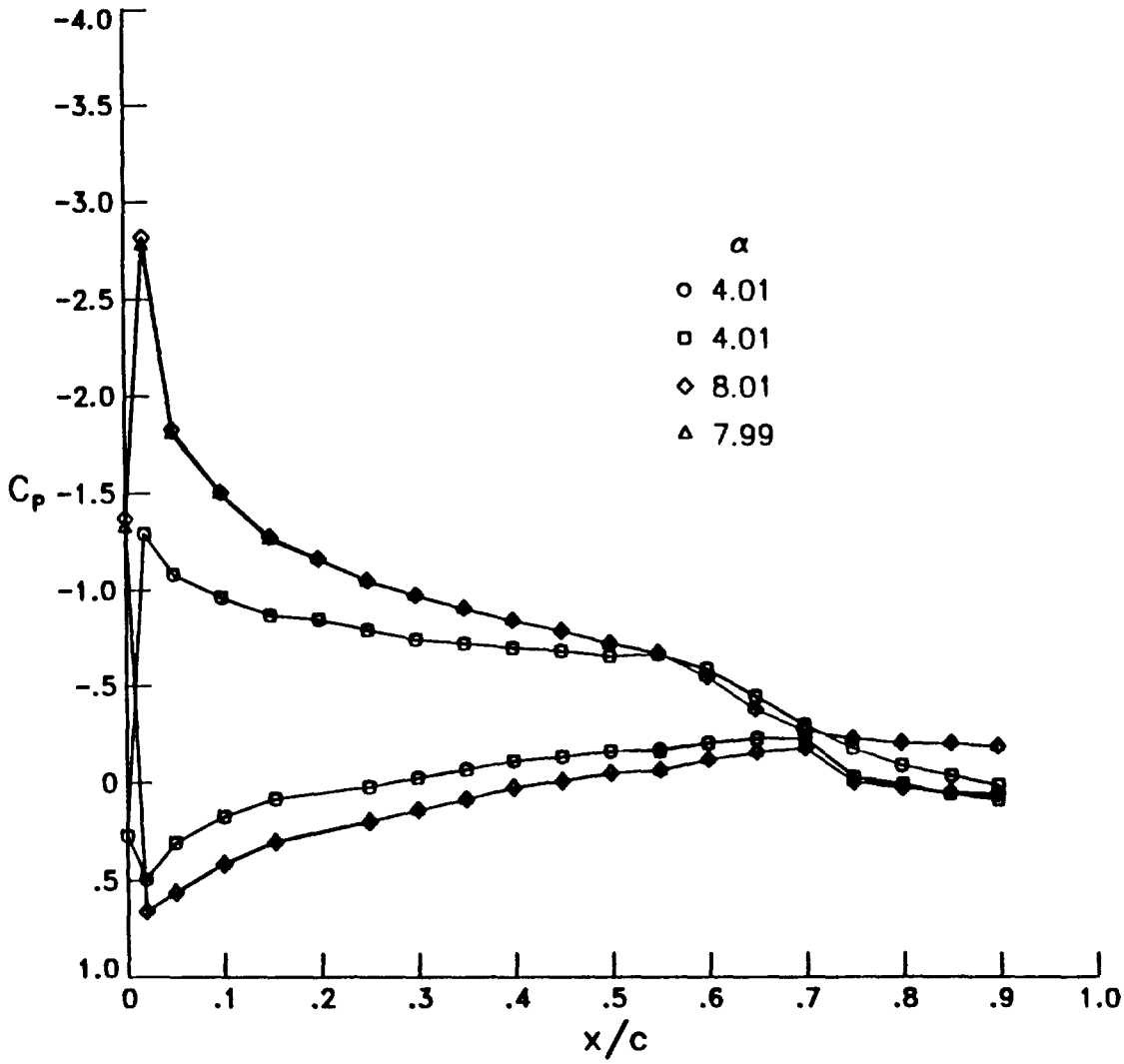

(a) $\eta = 0.25$.

Figure 34. Repeatability of the chordwise pressure distributions.

No blowing. $M_\infty = 0.3$.

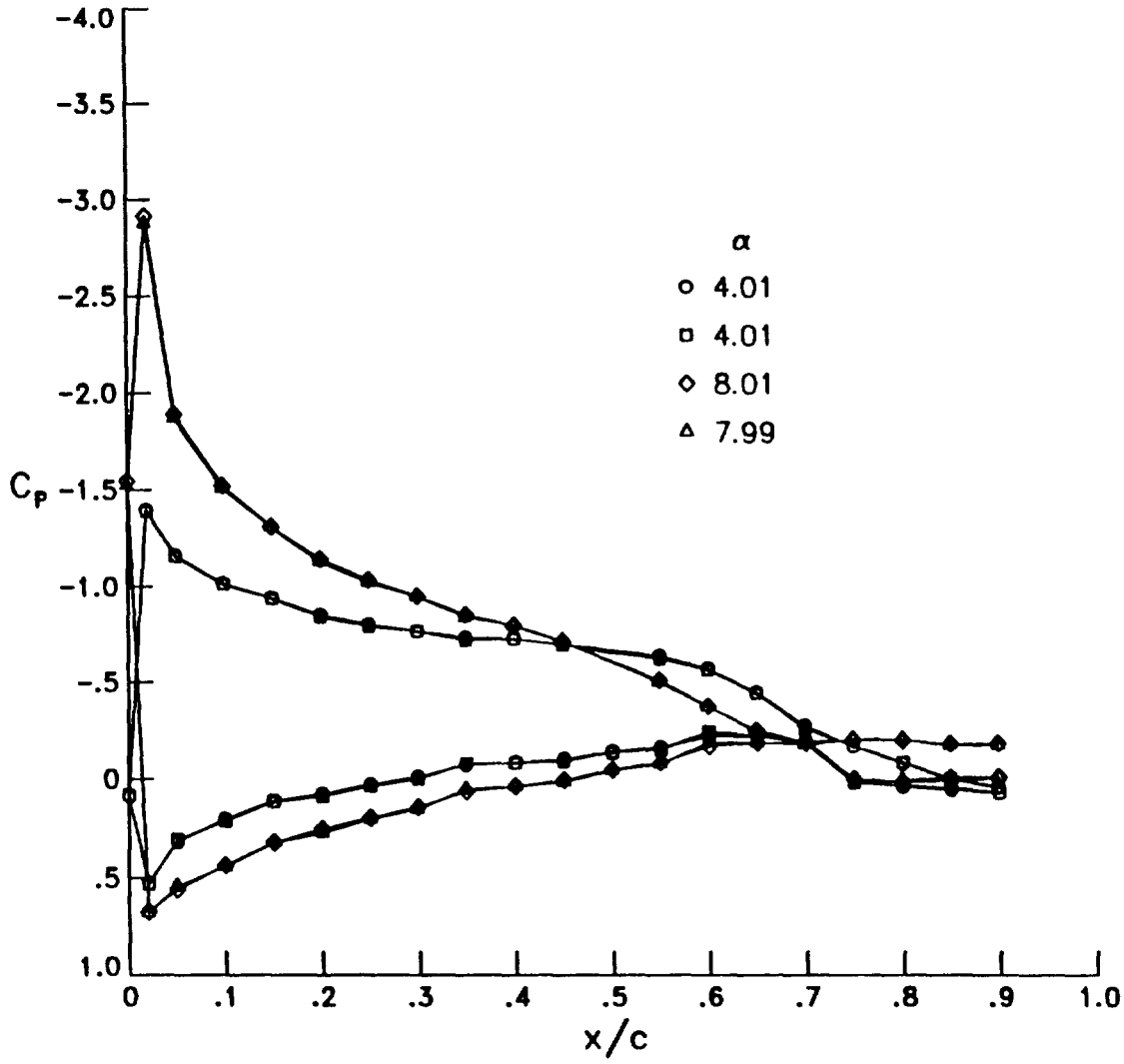

(b) $\eta = 0.50$.

Figure 34. Continued.

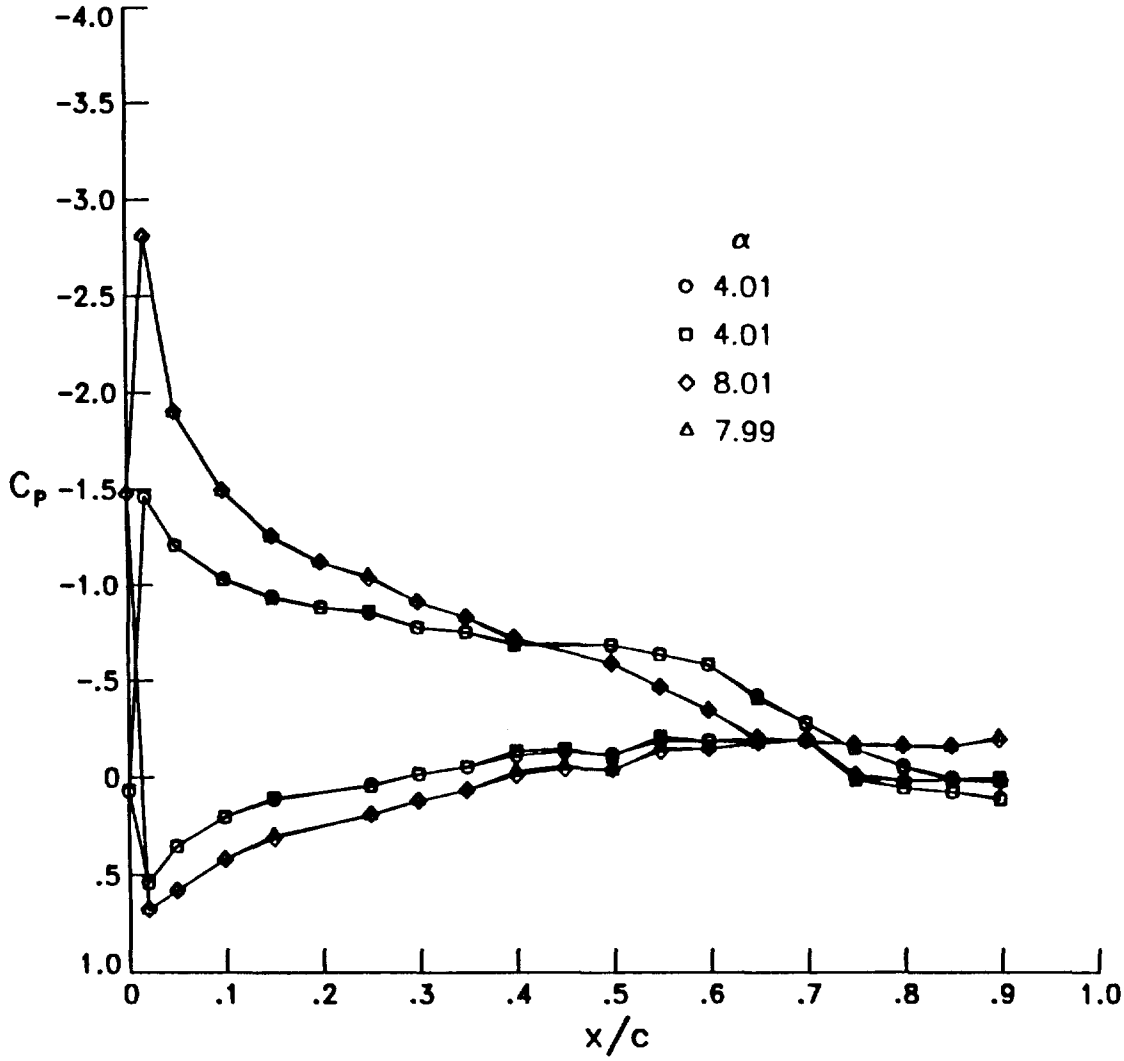

(c) $\eta = 0.70$.

Figure 34. Continued.

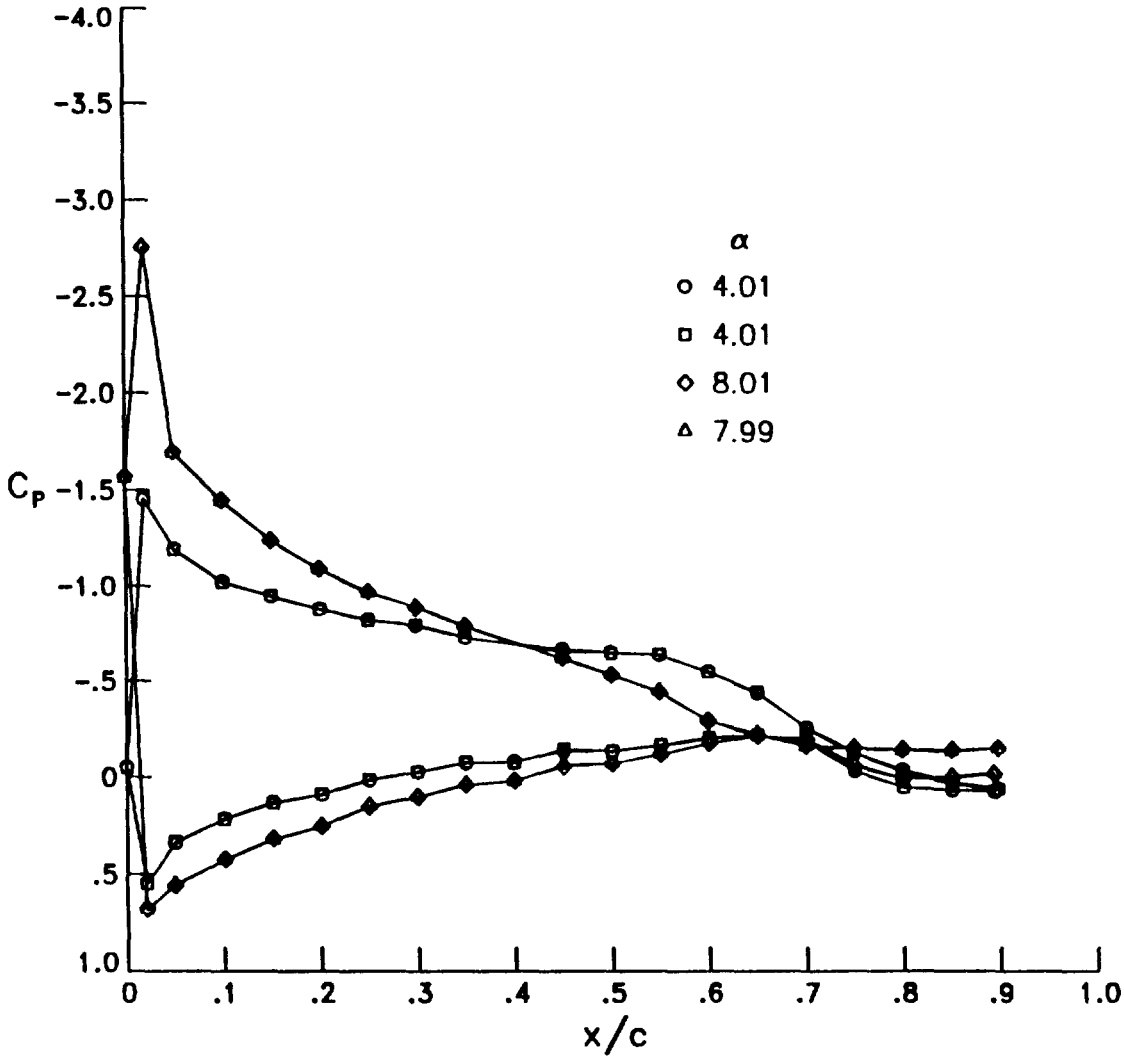

(d) $\eta = 0.80$.

Figure 34. Continued.

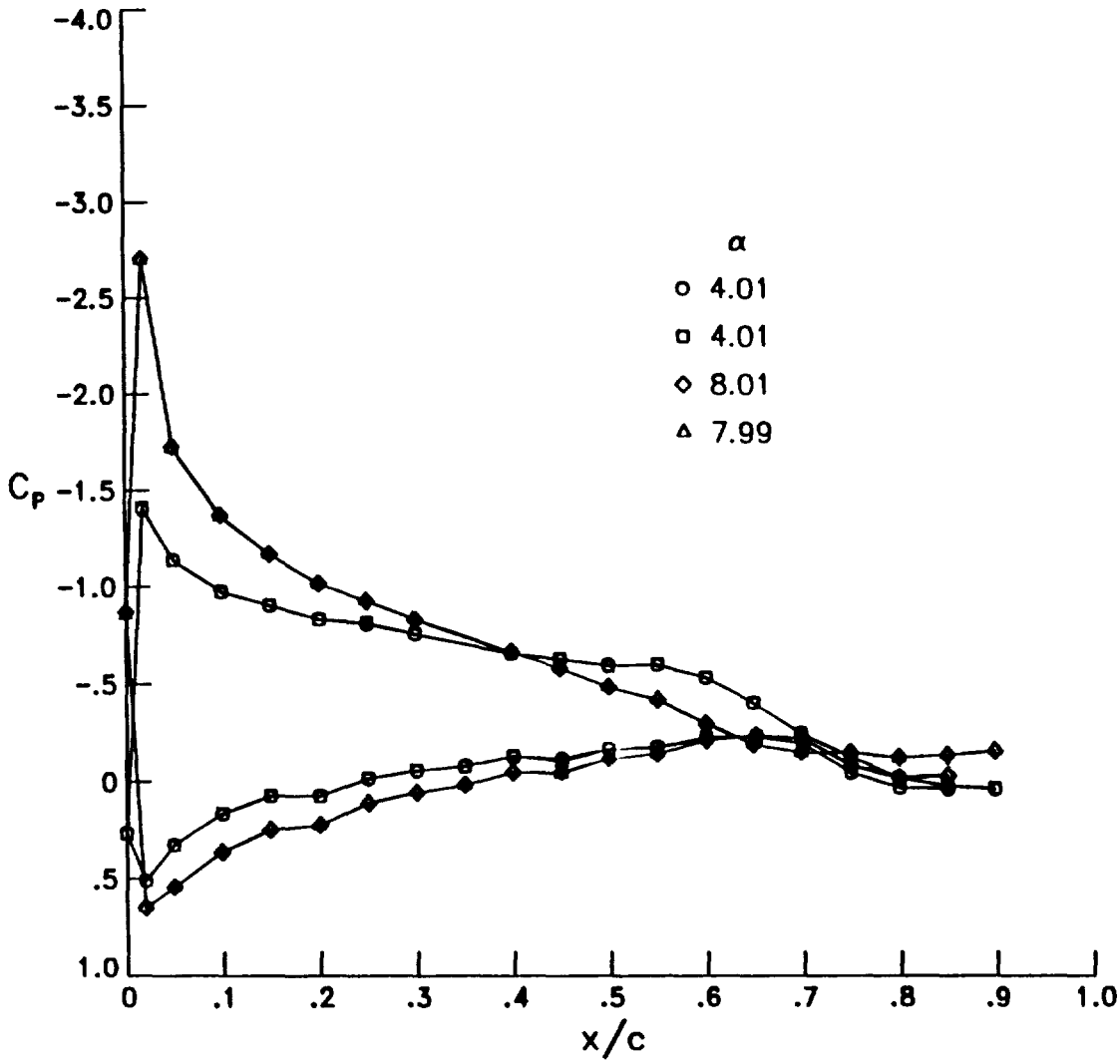

(e) $\eta = 0.90$.

Figure 34. Concluded.

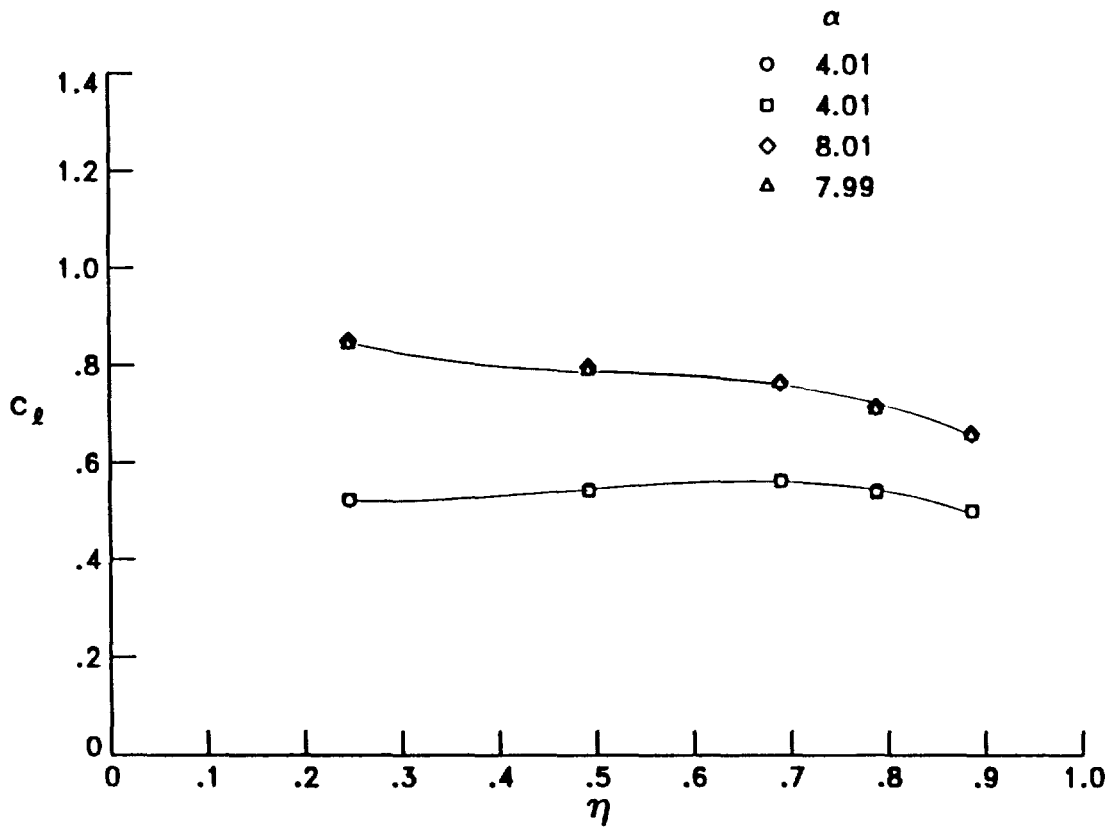

Figure 35. Repeatability of the span load distribution. No blowing. $M_\infty = 0.3$.

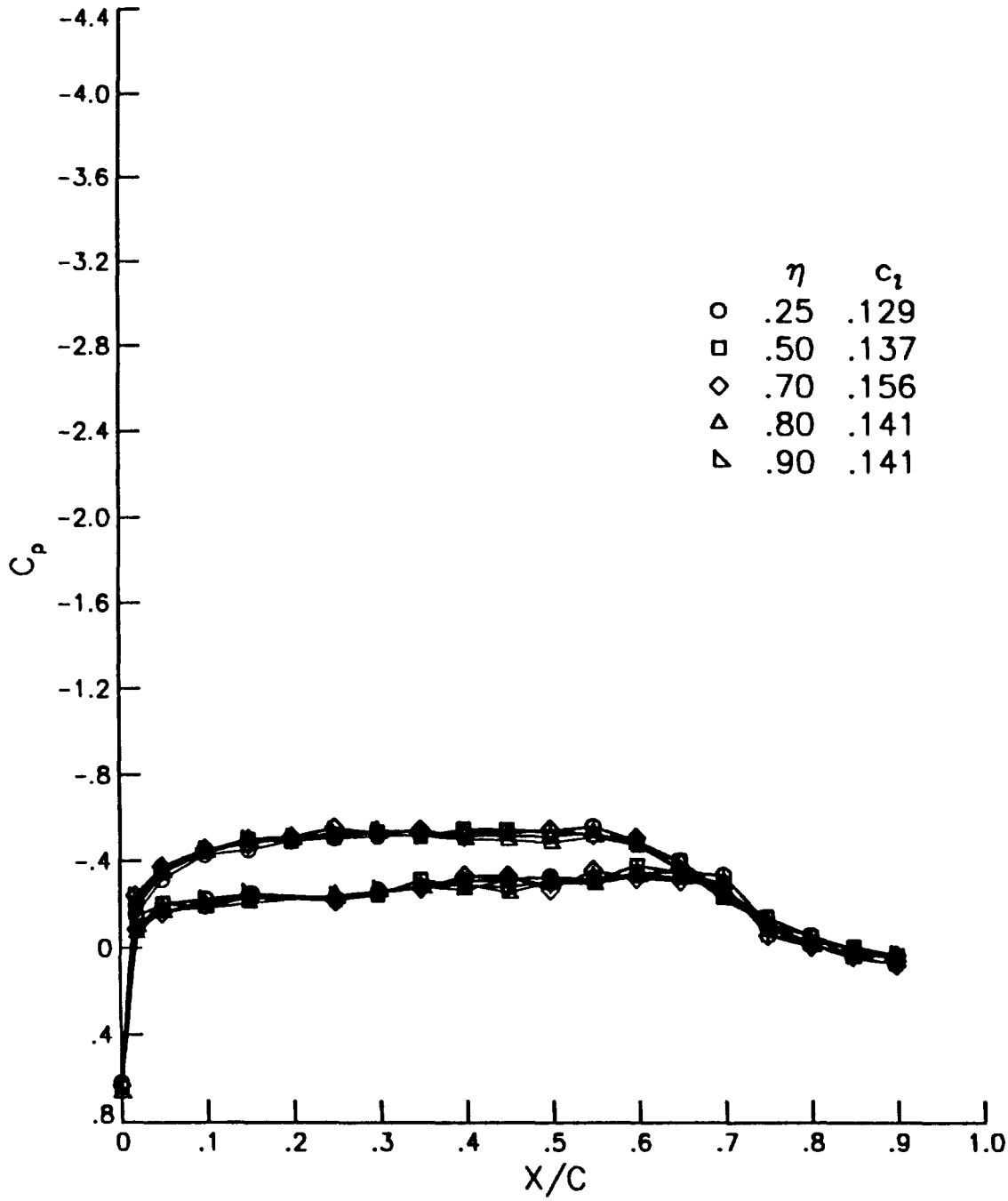

(a) $\alpha = -0.1^{\circ}$.

Figure 36. Effect of angle of attack on the chordwise pressure distributions. No blowing. $M_{\infty} = 0.3$.

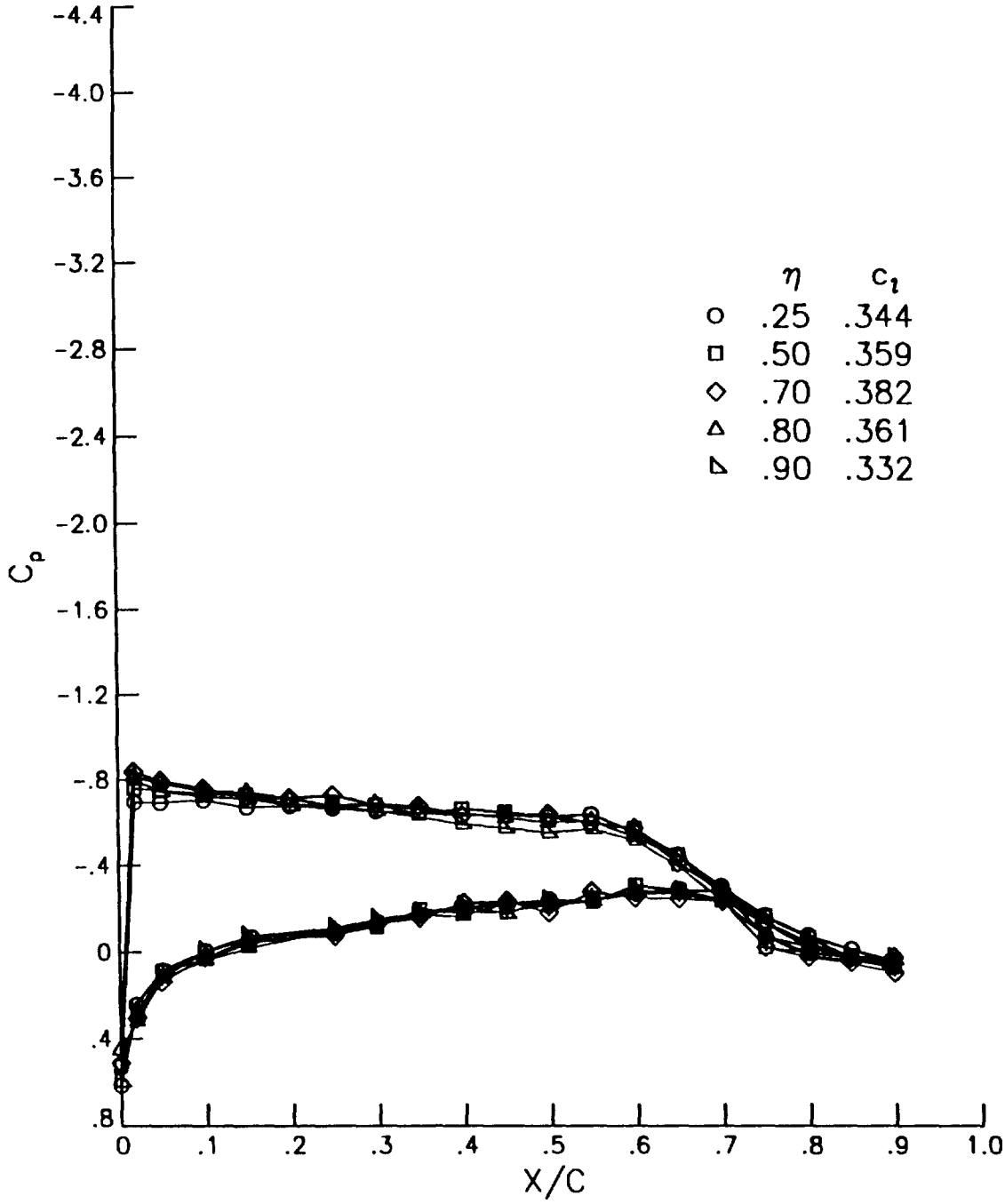

(b) $\alpha = 2.1^{\circ}$.

Figure 36. Continued.

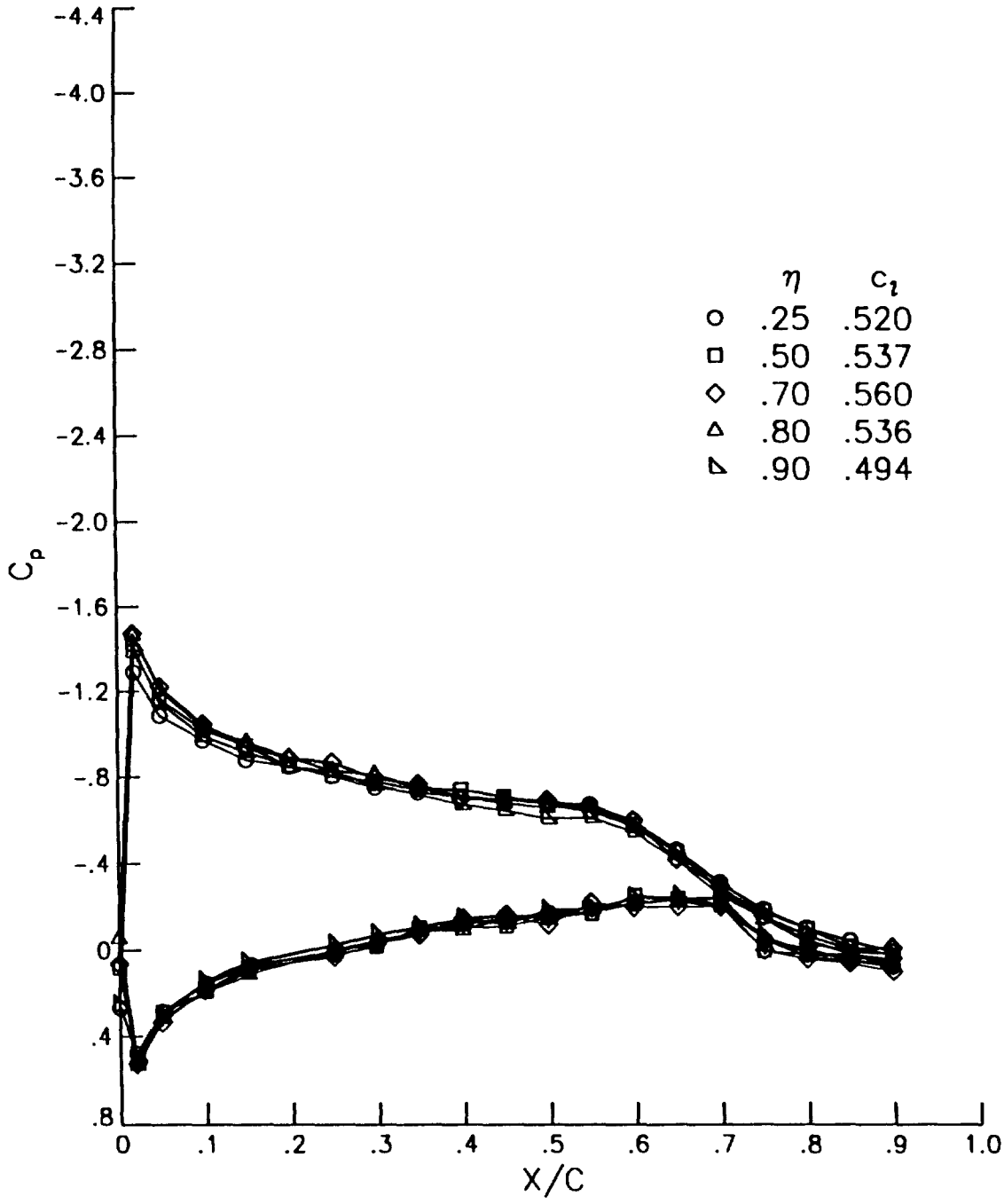

(c) $\alpha = 4.0°$.

Figure 36. Continued.

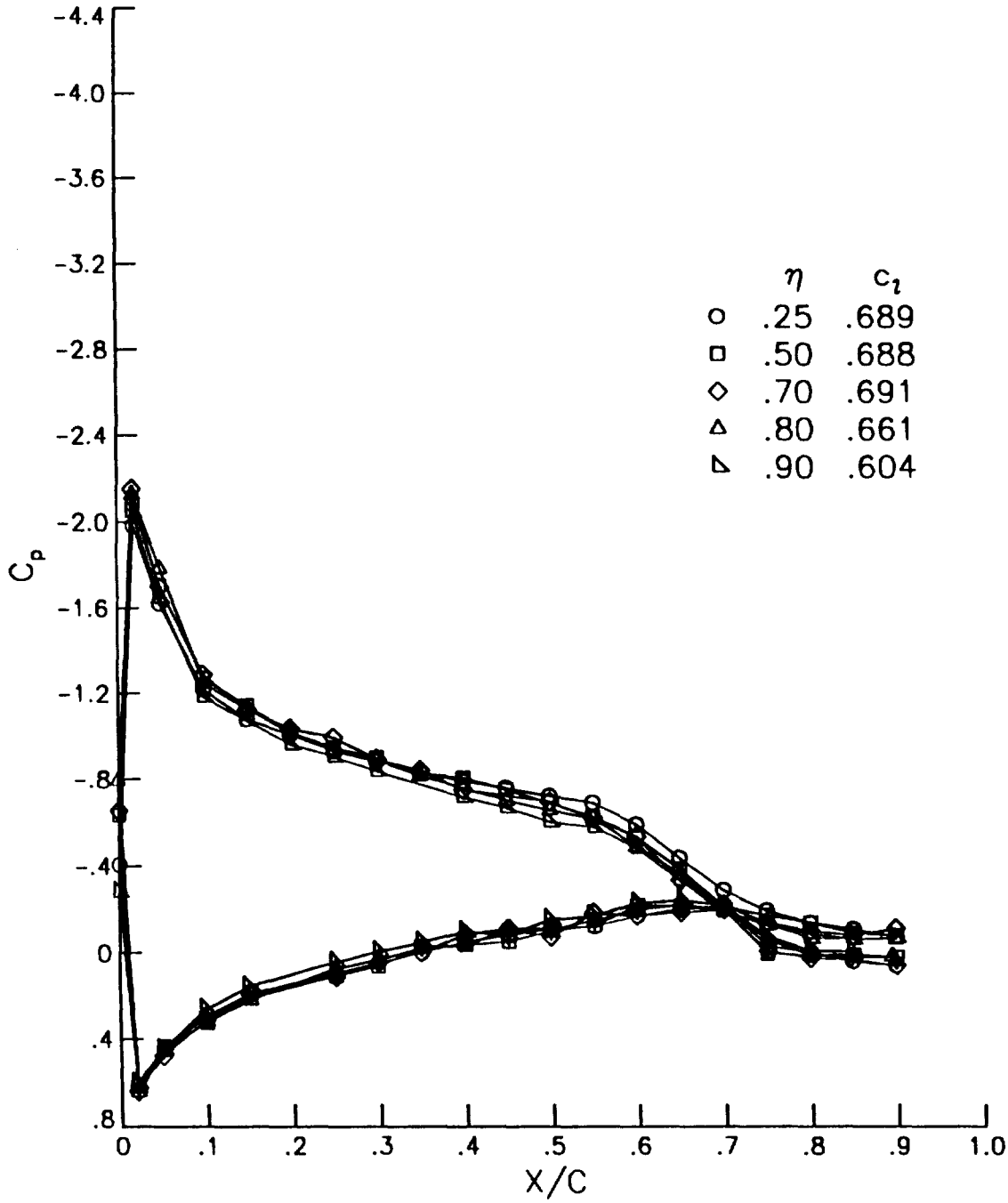

(d) $\alpha = 6.1°$.

Figure 36. Continued.

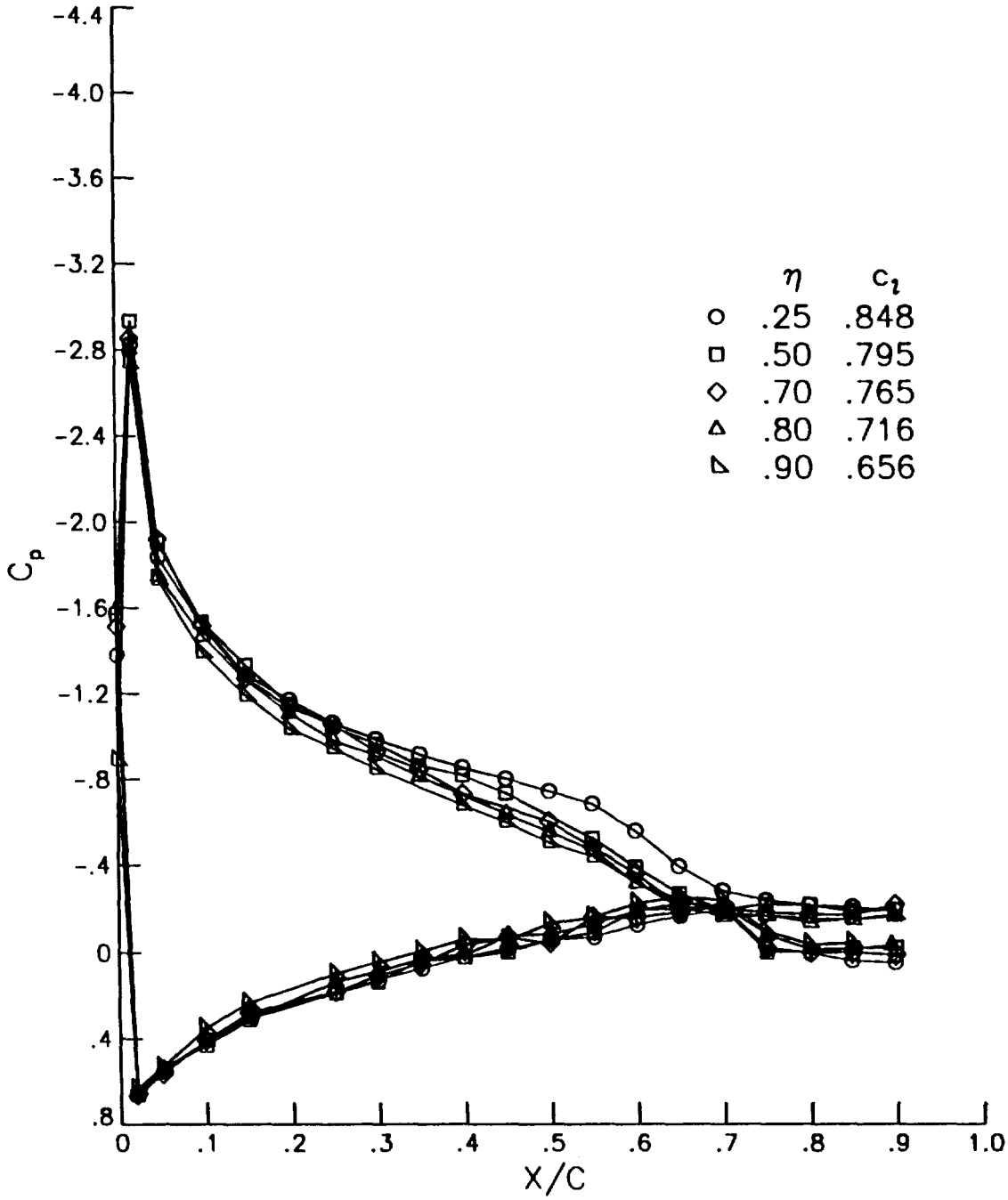

(e) $\alpha = 8.1^{\circ}$.

Figure 36. Continued.

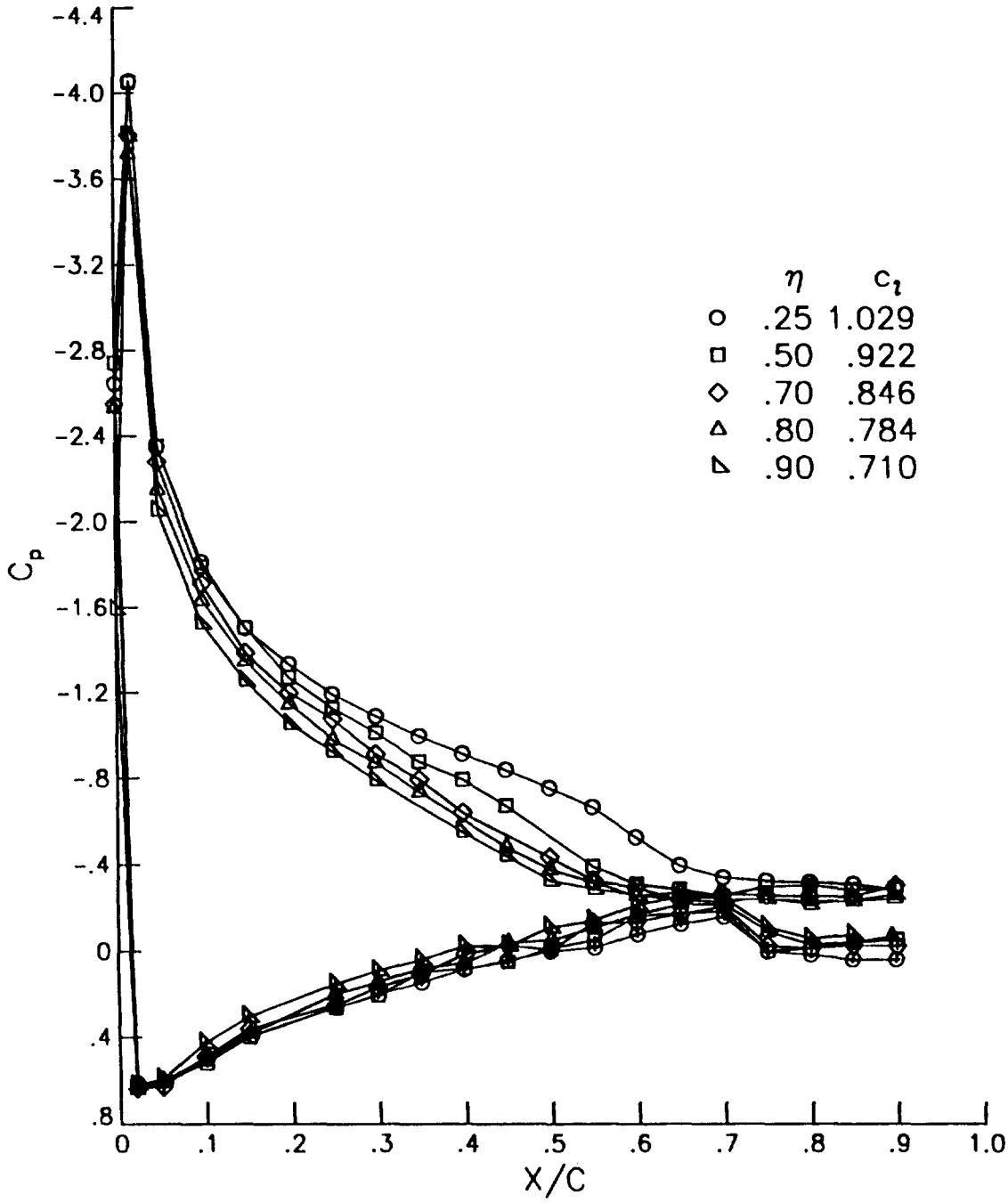

(f) $\alpha = 10.0°$.

Figure 36. Concluded.

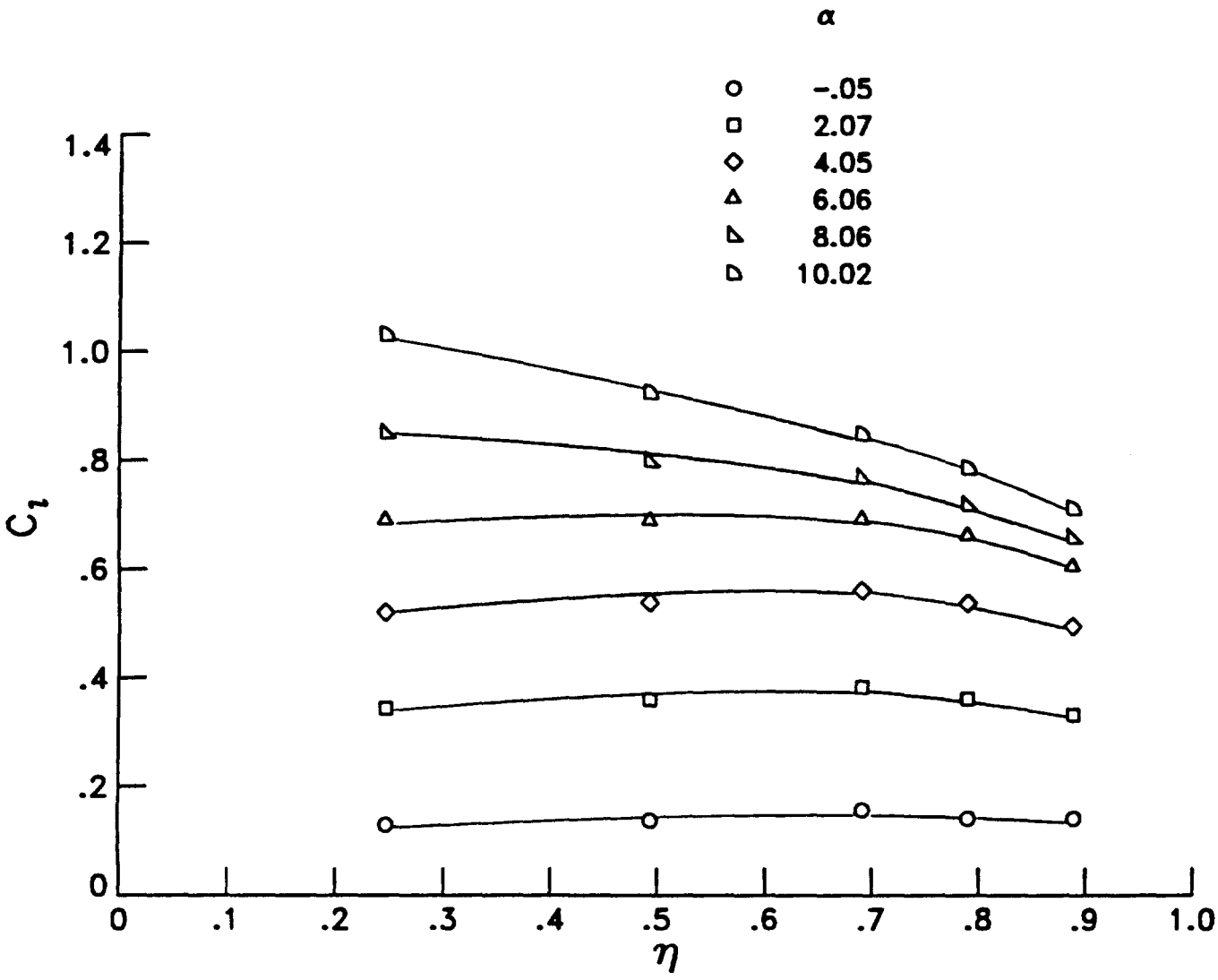

Figure 37. Effect of angle of attack on the span load distribution.

No blowing. $M_\infty = 0.3$.

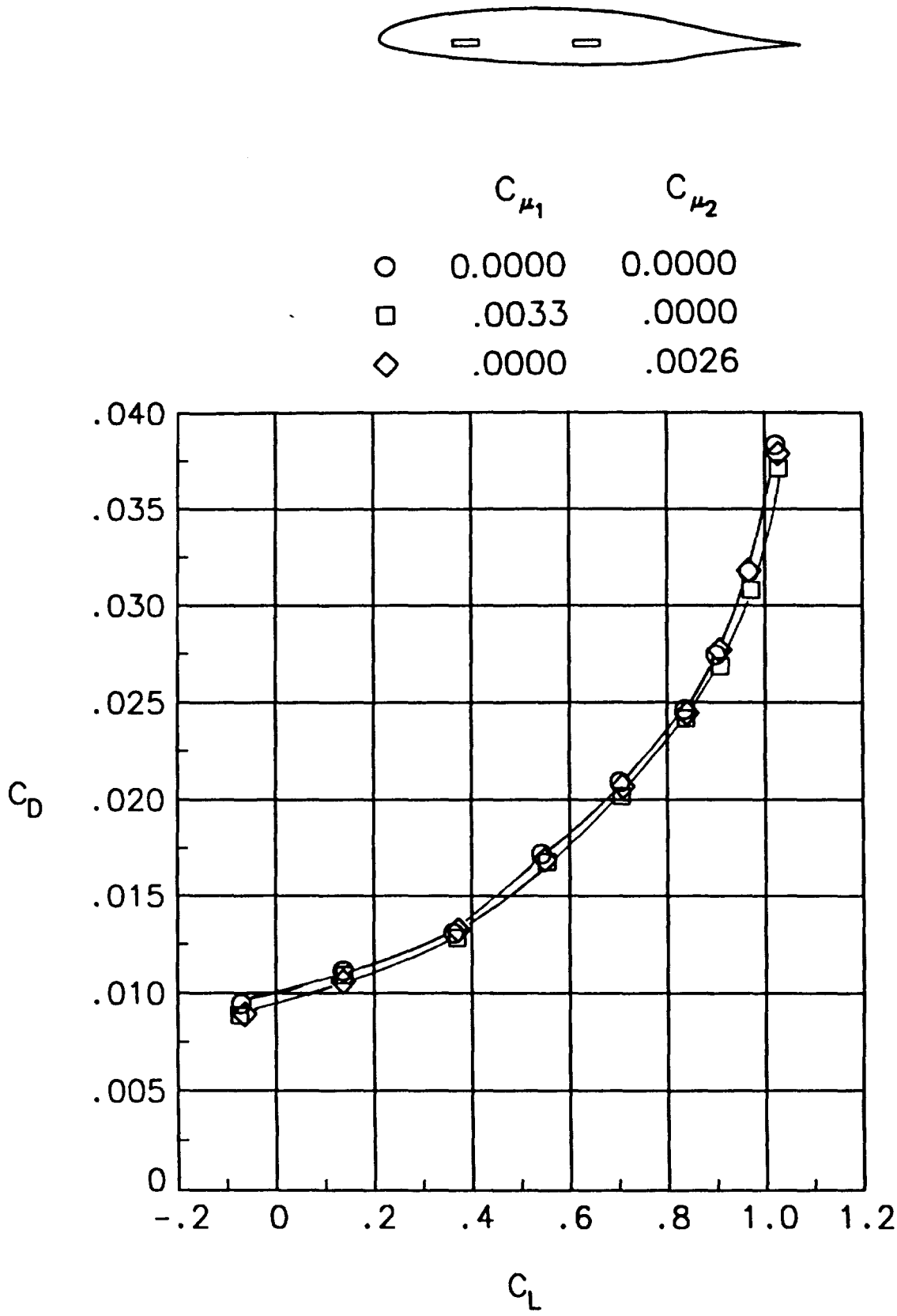

(a) Tip 1.

Figure 38. Effect of spanwise blowing on the drag polars. $M_\infty = 0.3$.

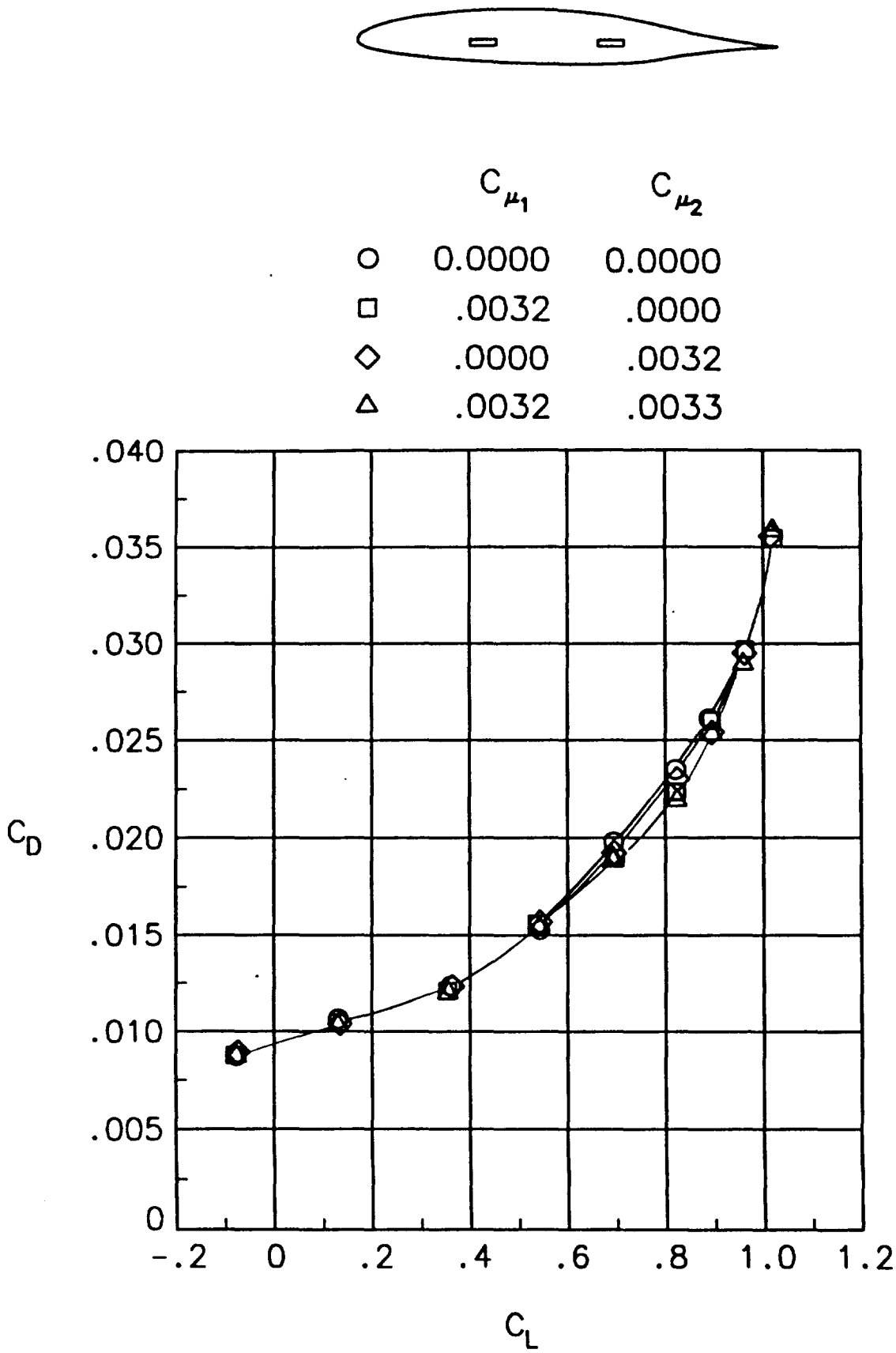

(b) Tip 2.

Figure 38. Continued.

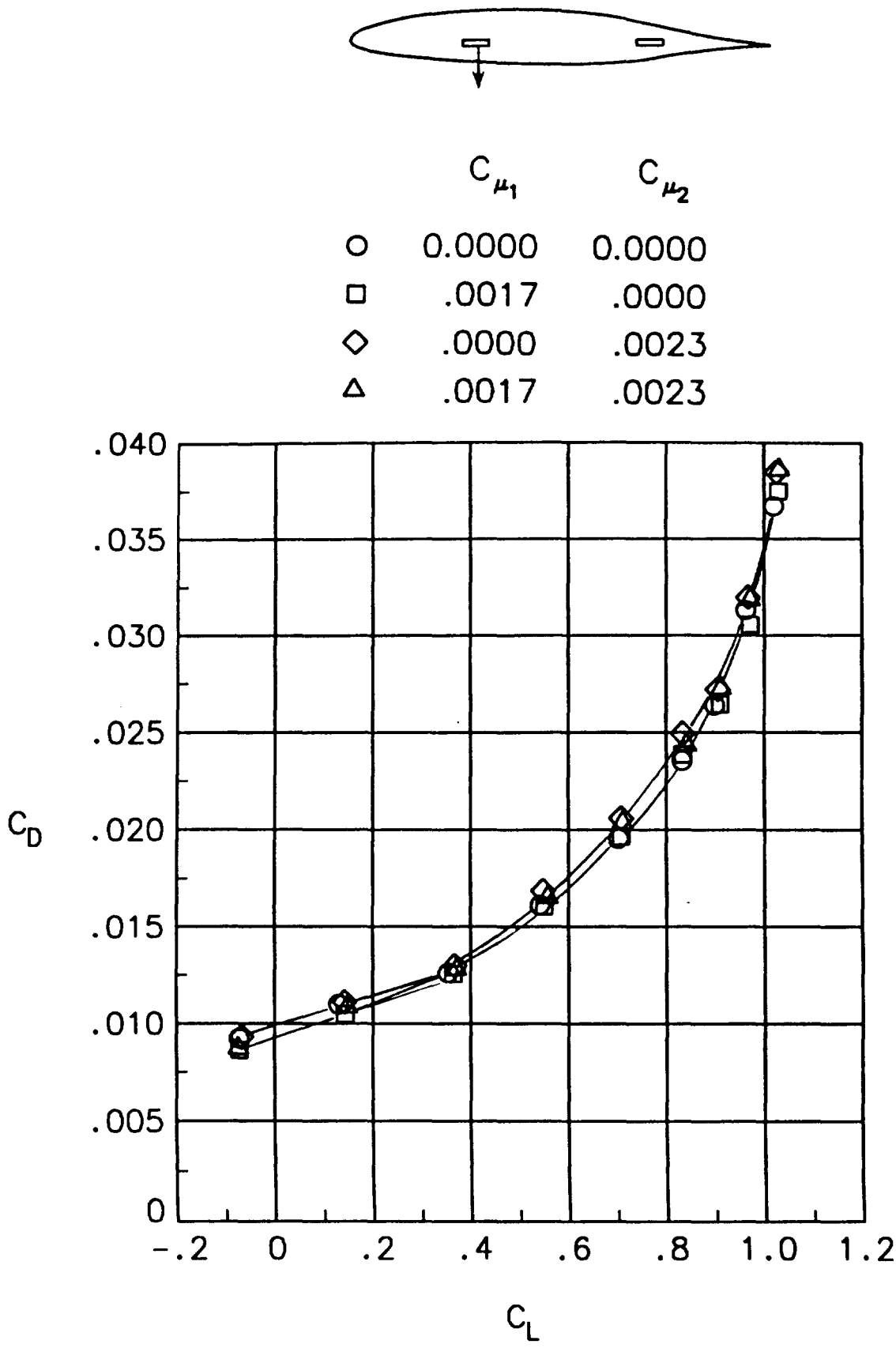

(c) Tip 3.

Figure 38. Continued.

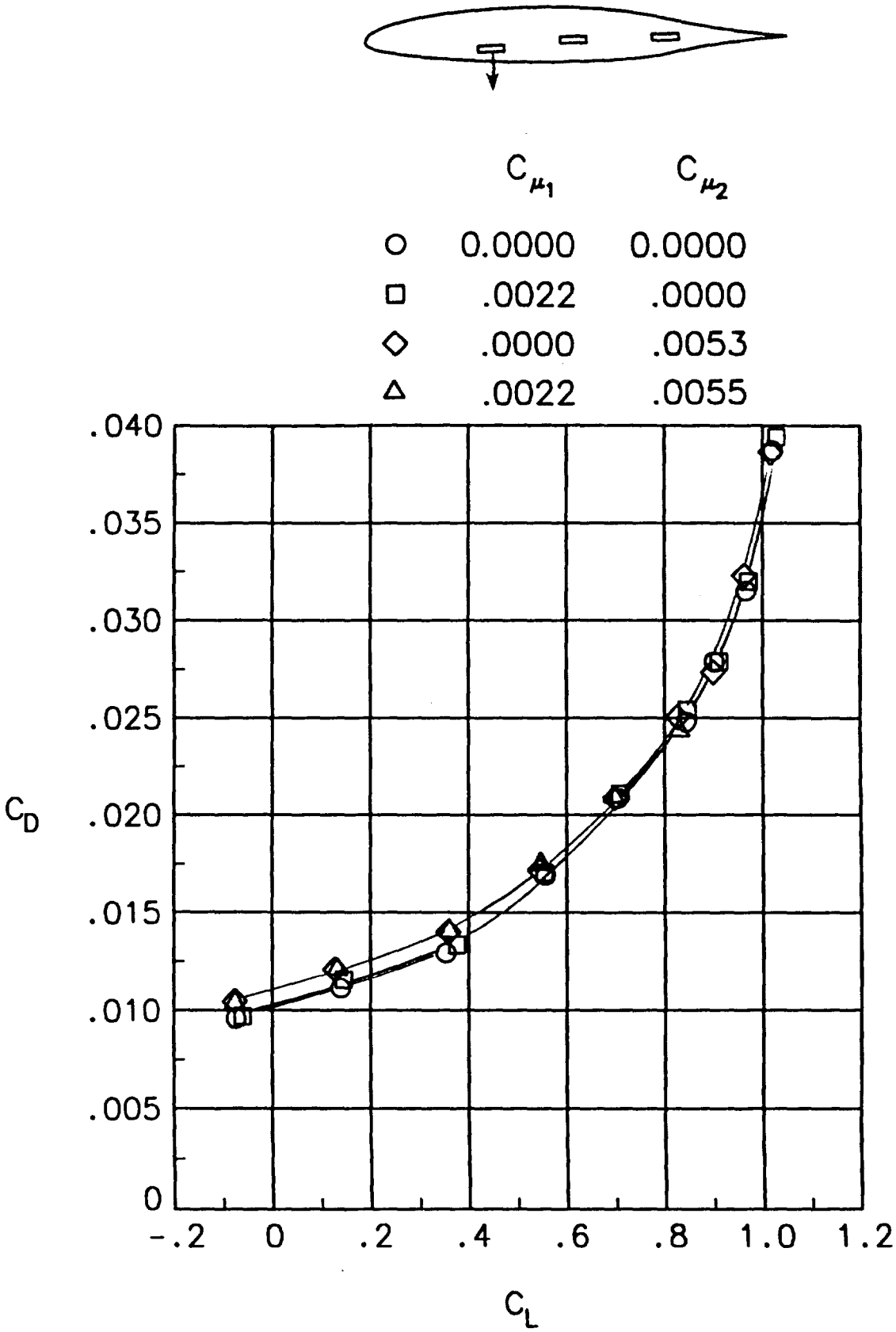

(d) Tip 4.

Figure 38. Continued.

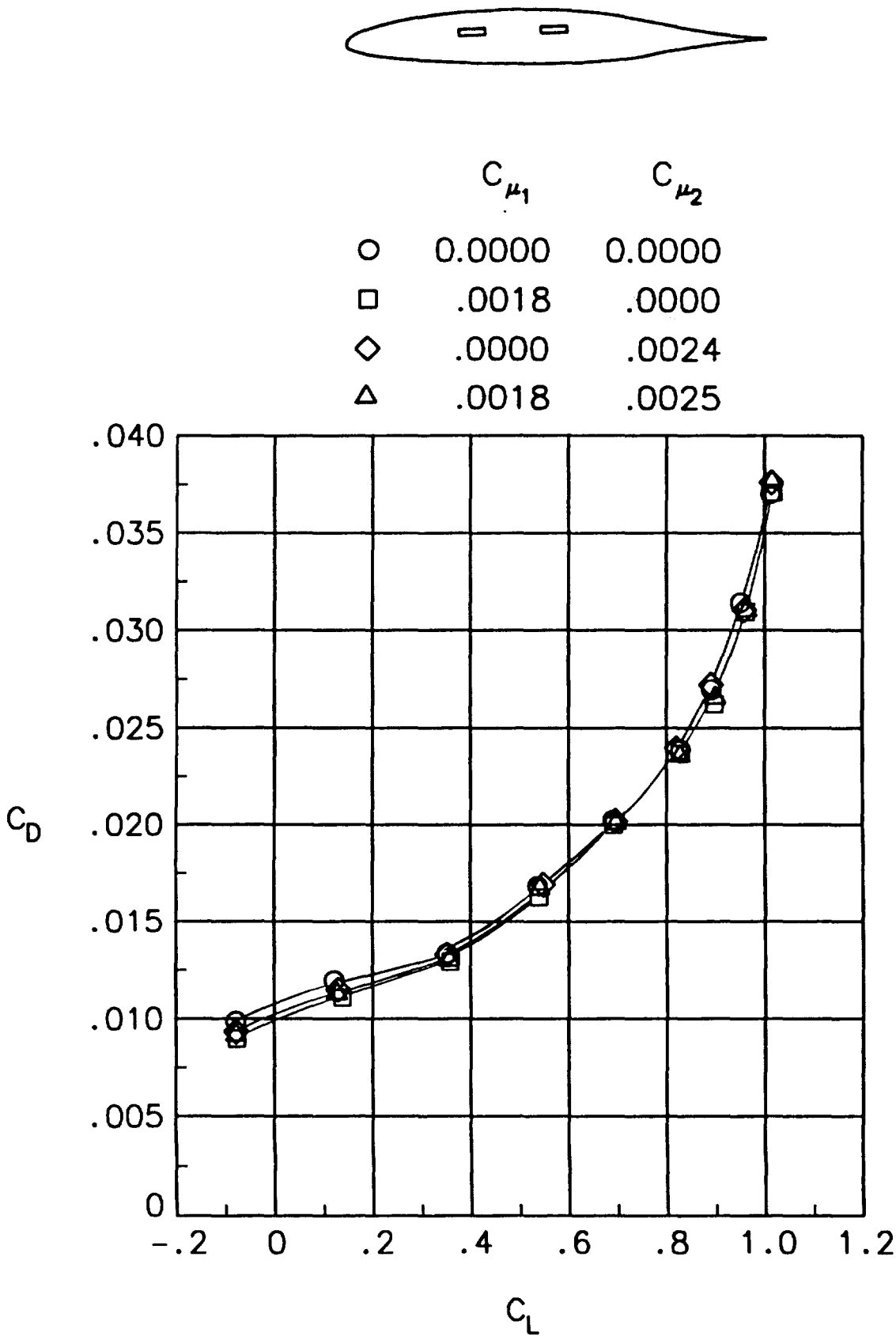

(e) Tip 6.

Figure 38. Continued.

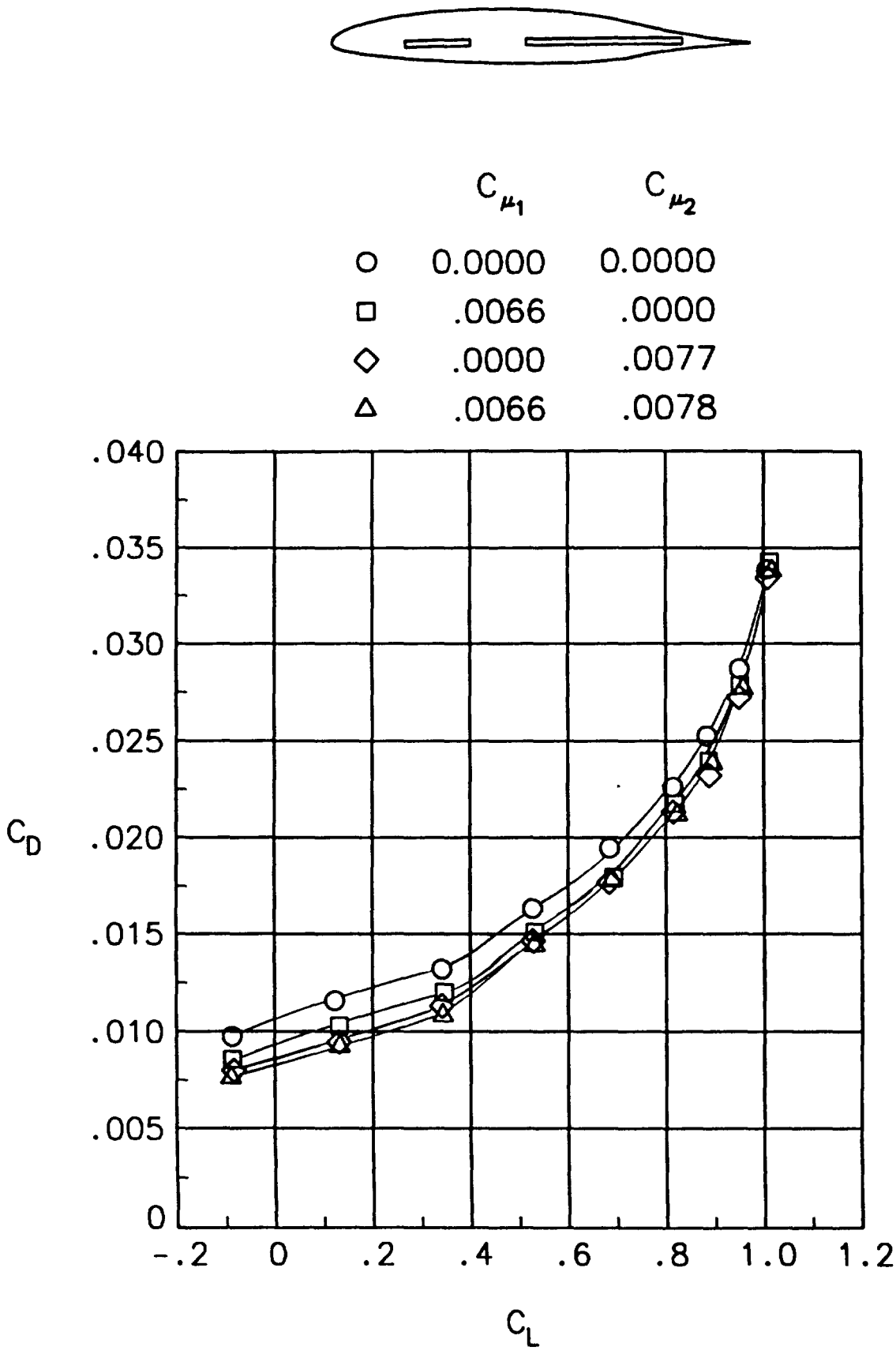

(f) Tip 8.

Figure 38. Continued.

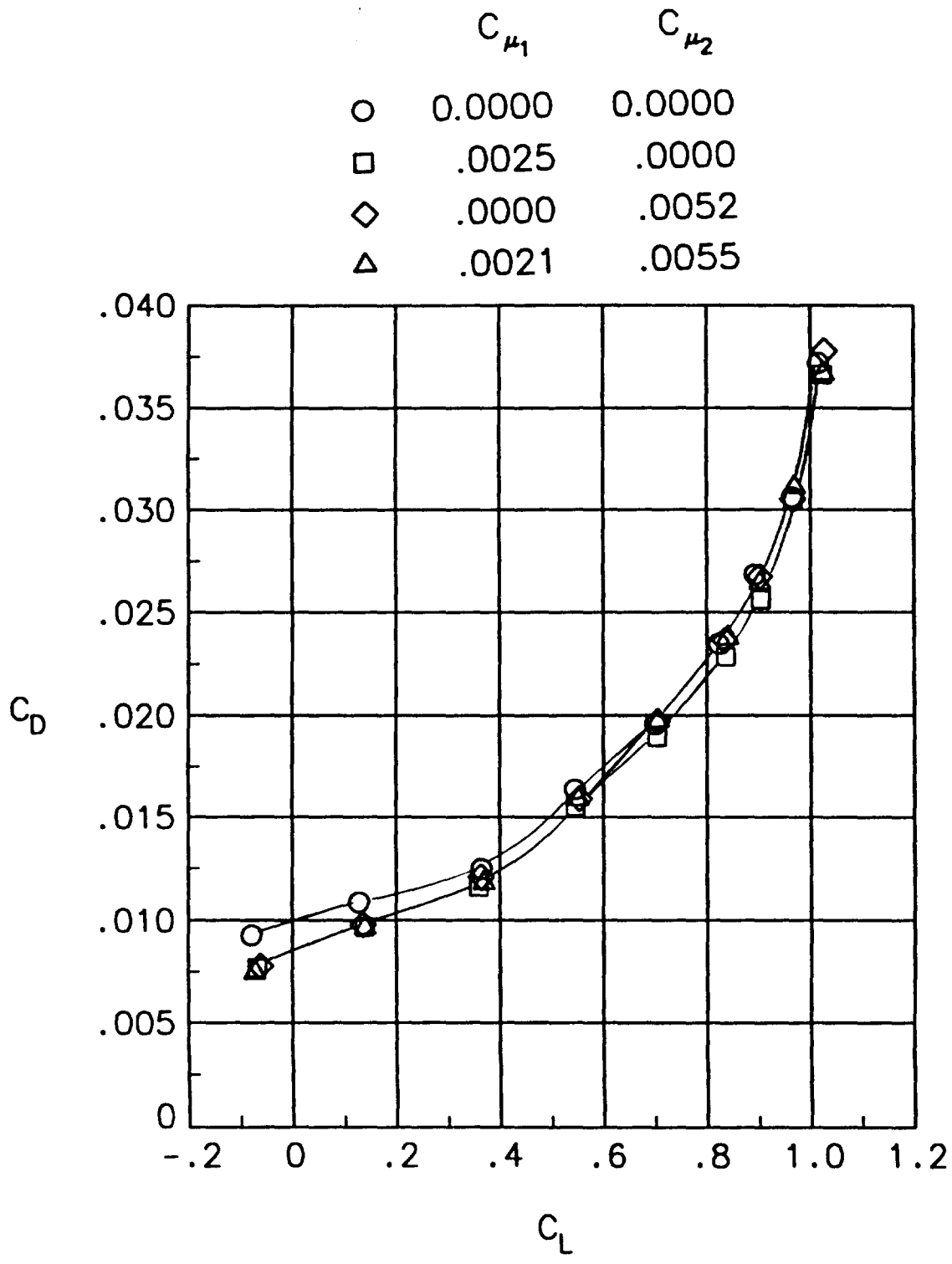

(g) Tip 9.

Figure 38. Concluded.

C-3

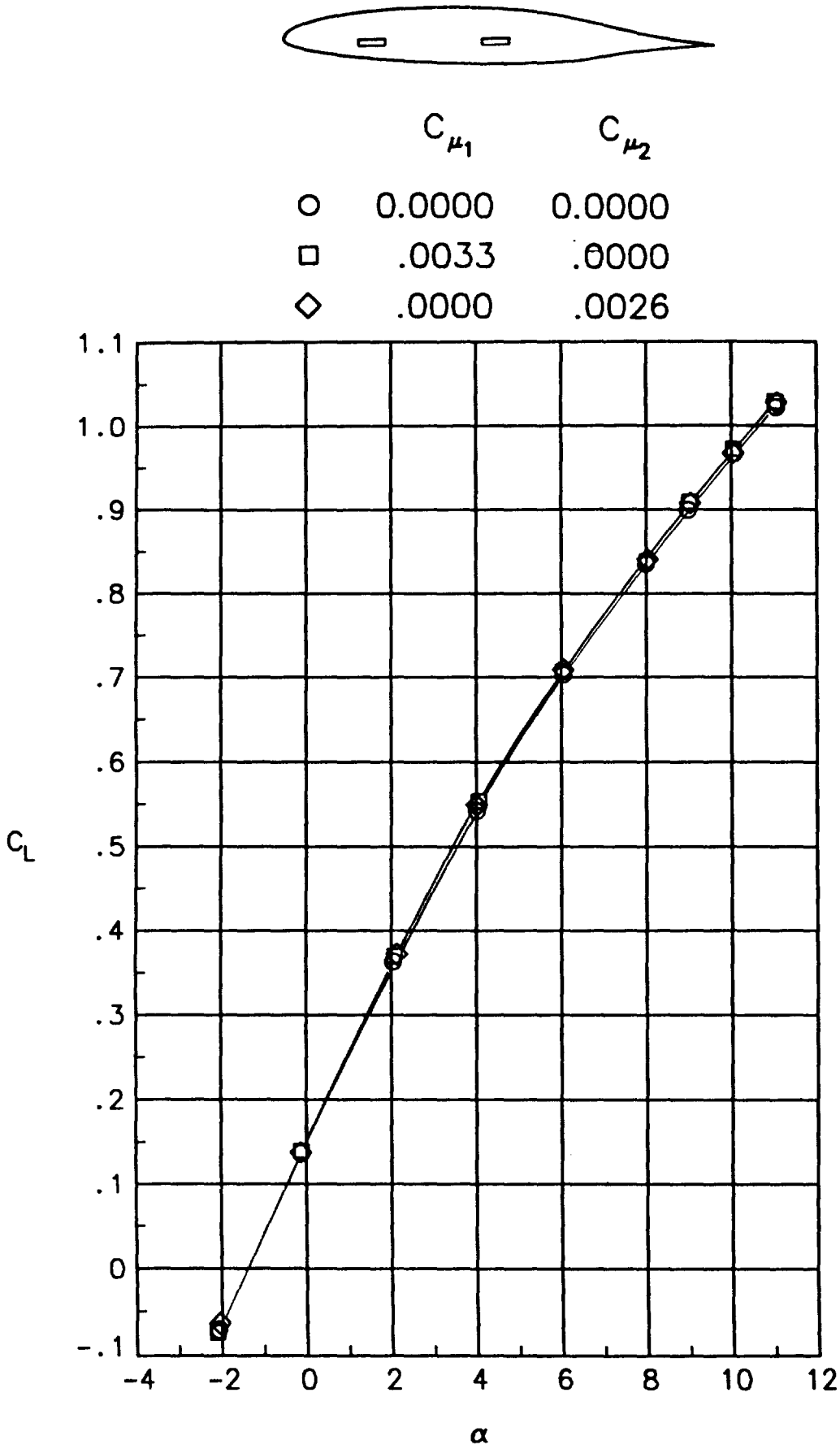

(a) Tip 1.

Figure 39. Effect of spanwise blowing on the lift curves. $M_\infty = 0.3$.

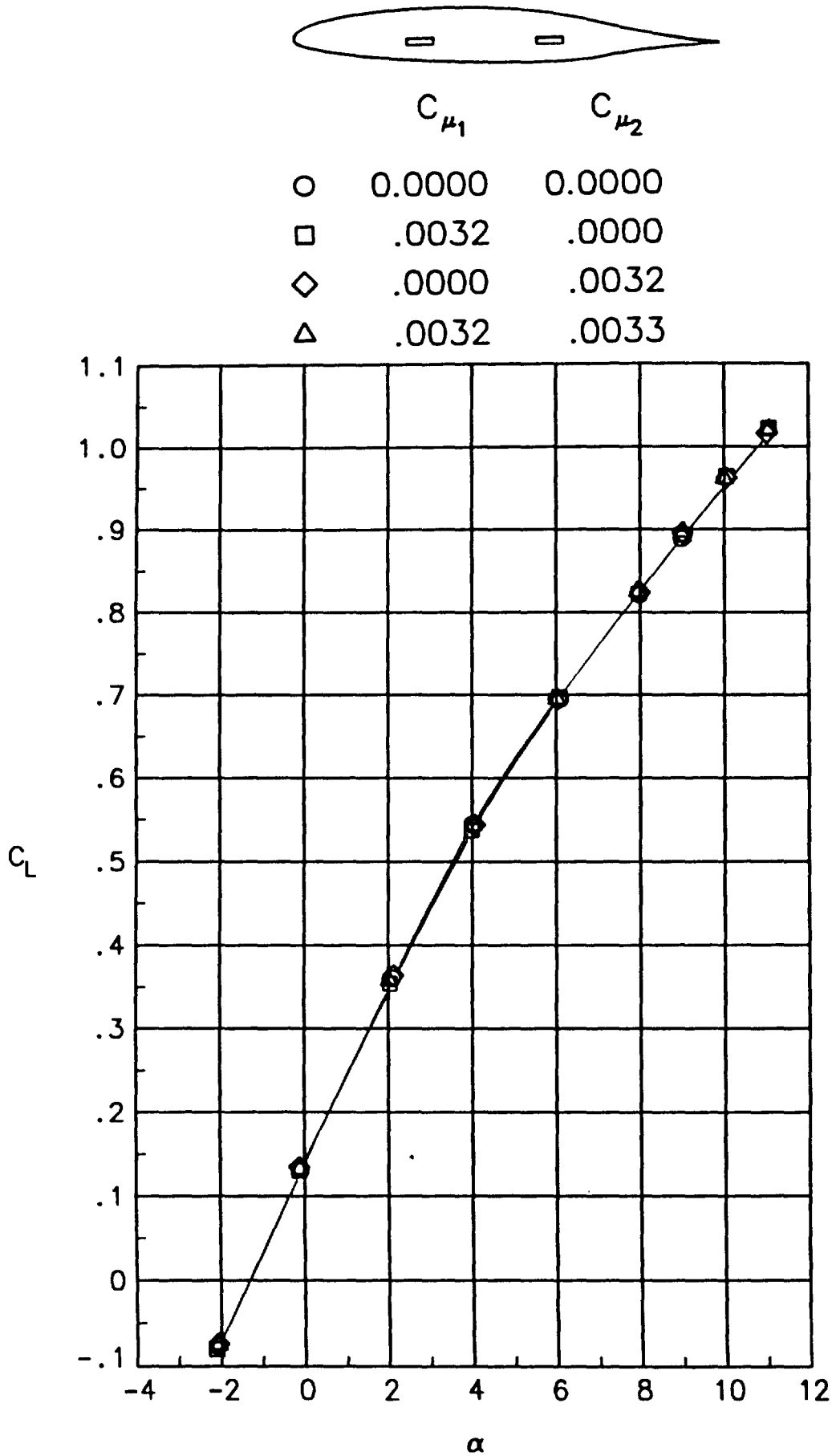

(b) Tip 2.

Figure 39. Continued.

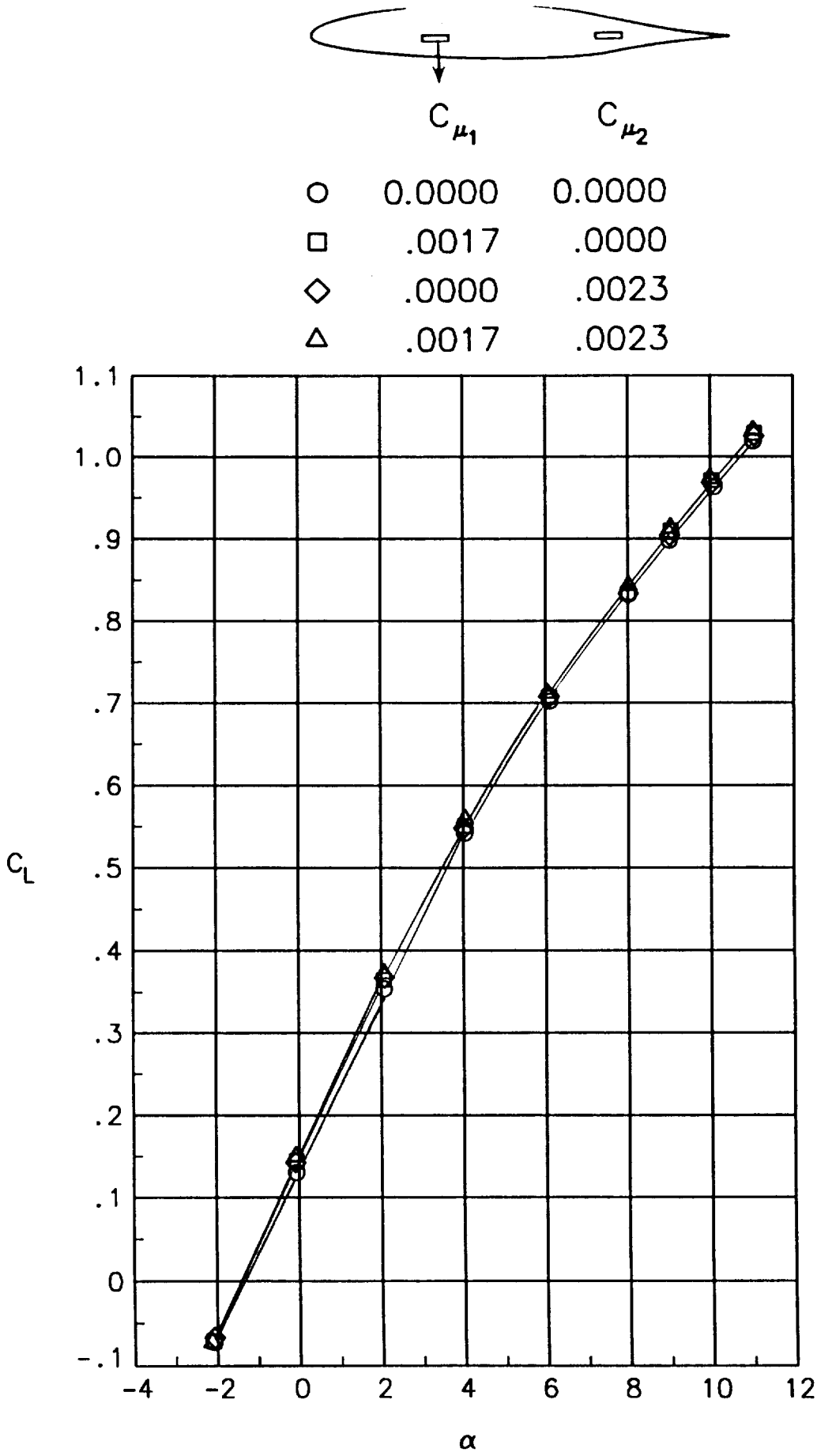

(c) Tip 3.

Figure 39. Continued.

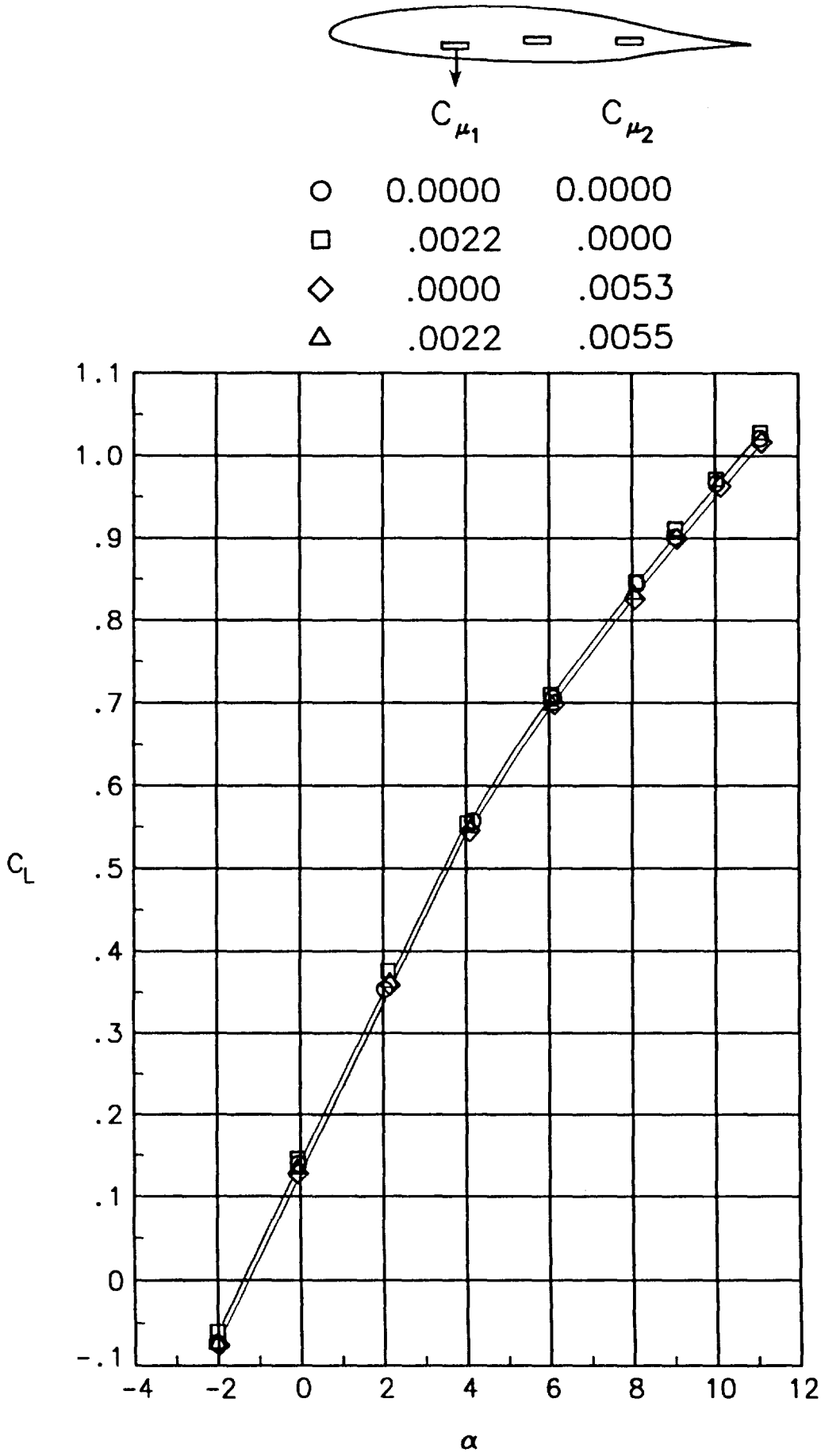

(d) Tip 4.

Figure 39. Continued.

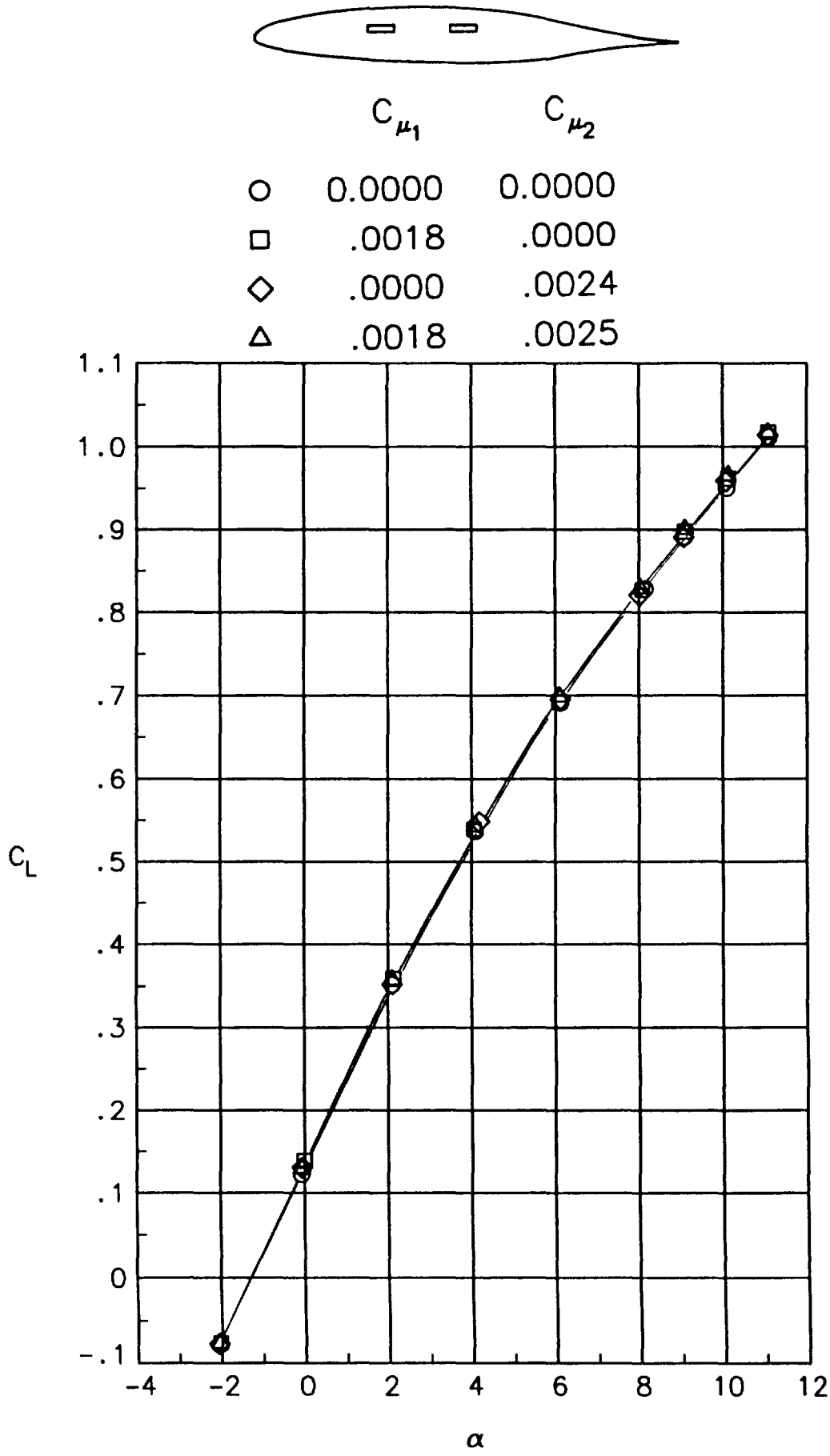

(e) Tip 6.

Figure 39. Continued.

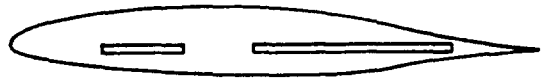

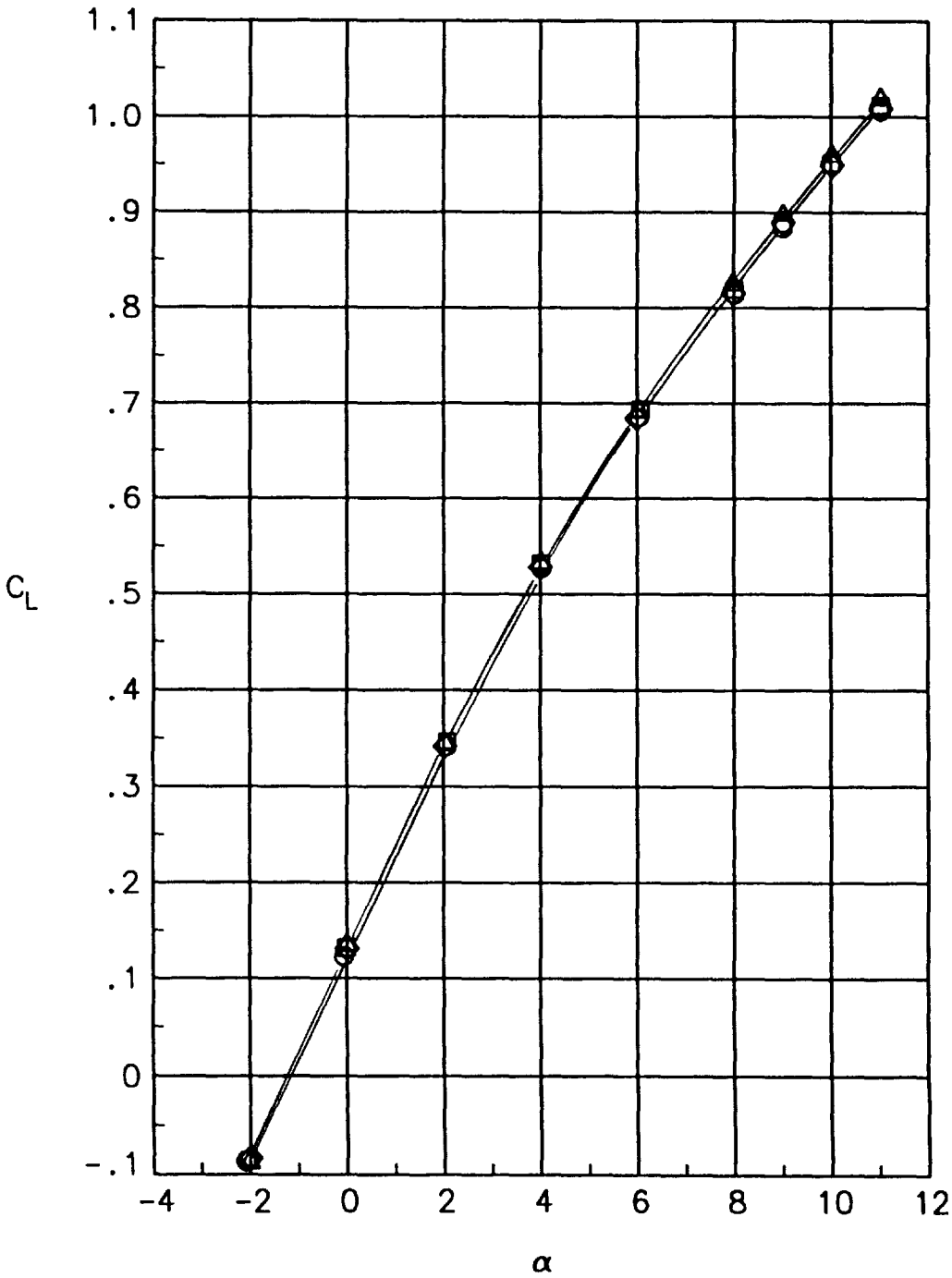

(f) Tip 8.

Figure 39. Continued.

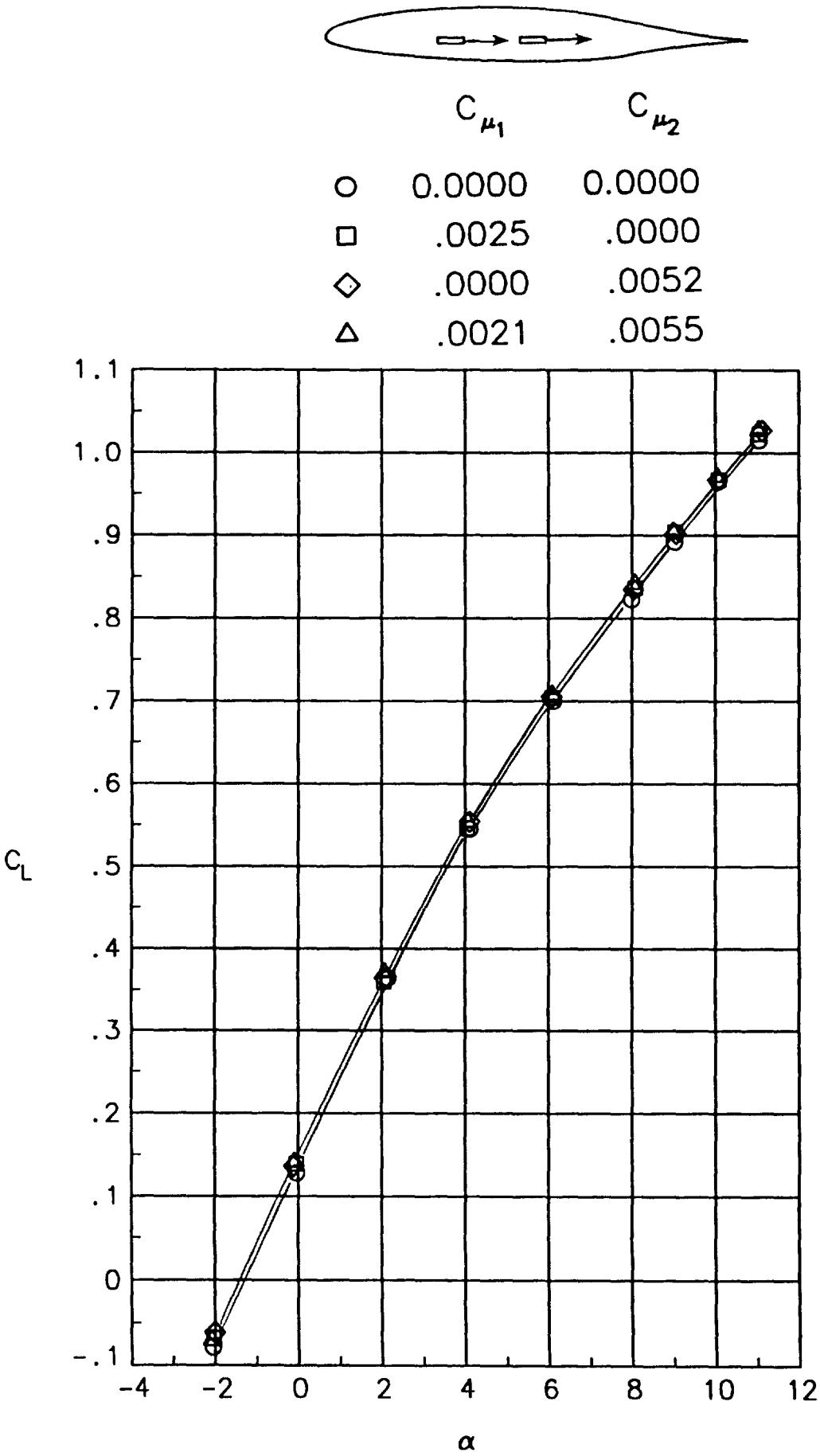

(g) Tip 9.

Figure 39. Concluded.

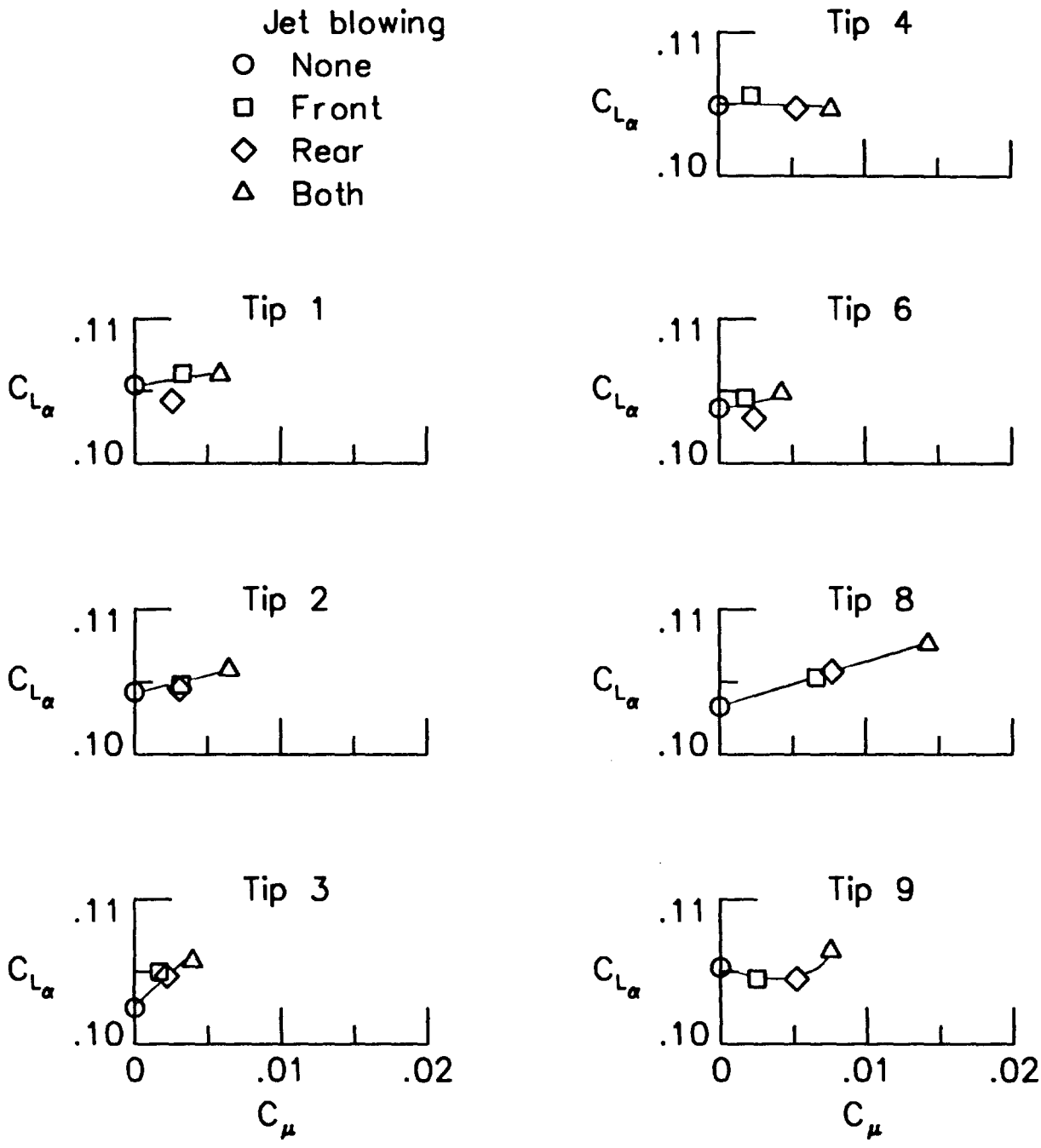

Figure 40. Variation of the lift curve slope with blowing. $M_\infty = 0.3$.

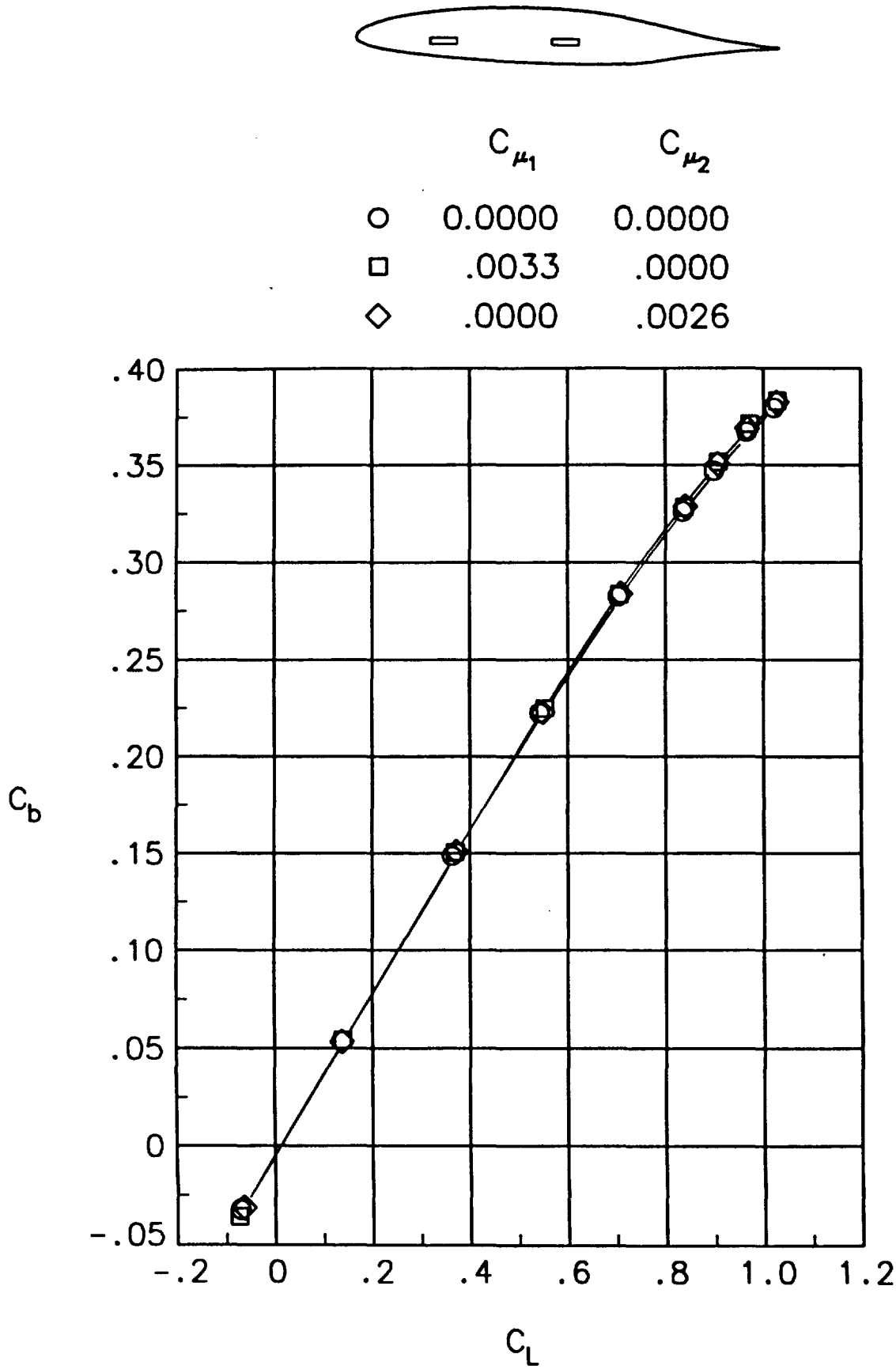

(a) Tip 1.

Figure 41. Effect of spanwise blowing on the wing root bending moment curves. $M_\infty = 0.3$.

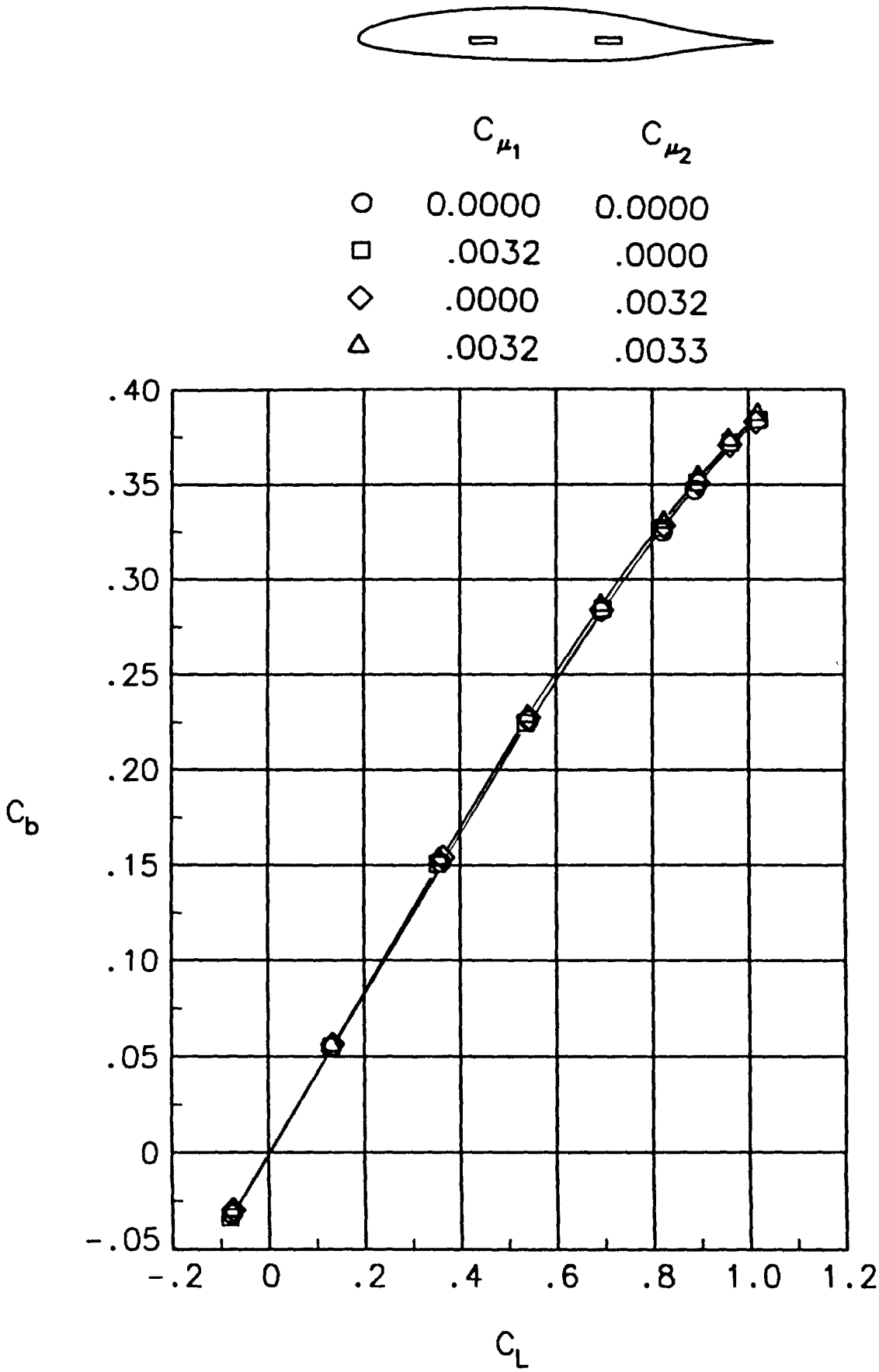

(b) Tip 2.

Figure 41. Continued.

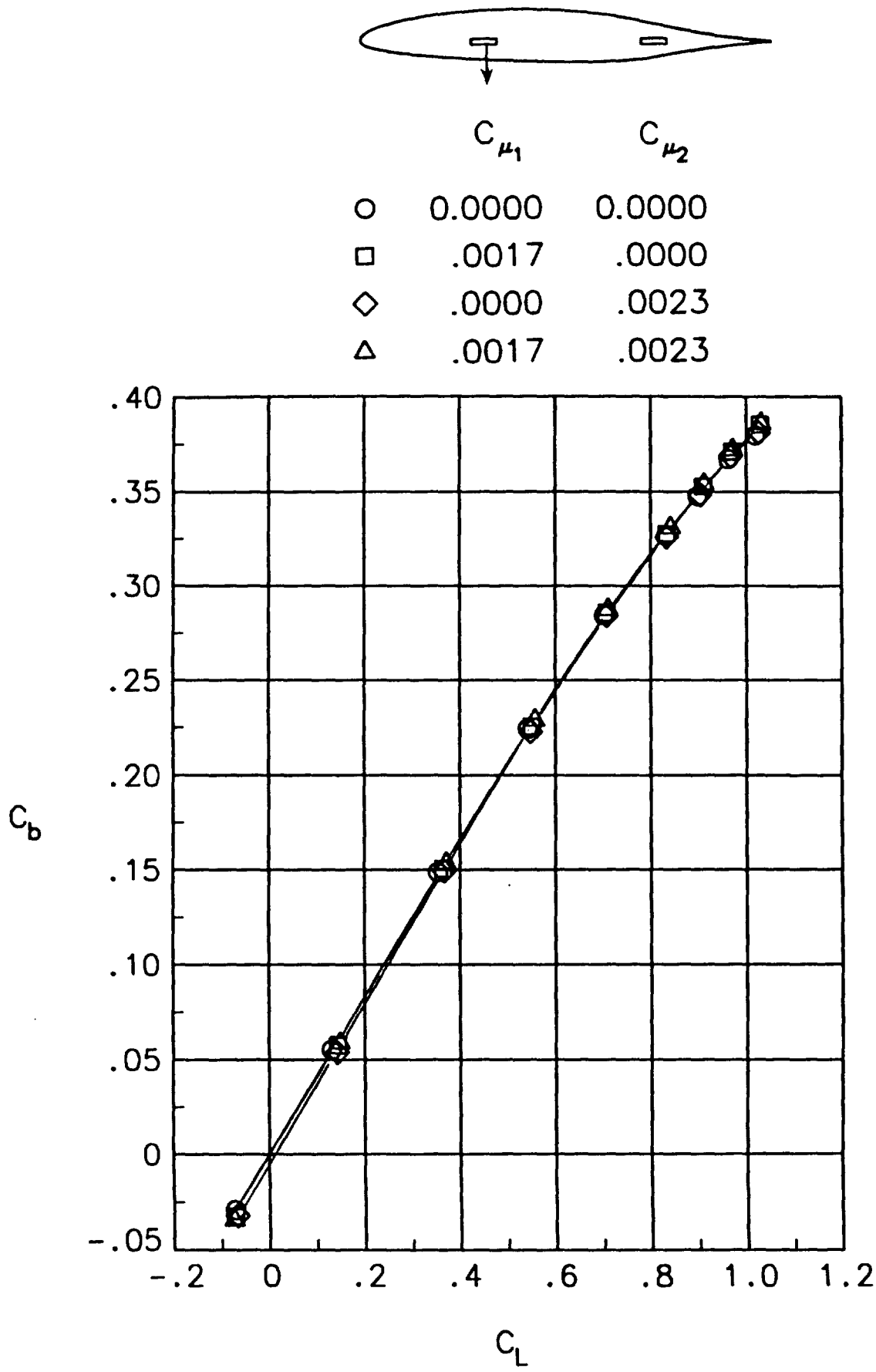

(c) Tip 3.

Figure 41. Continued.

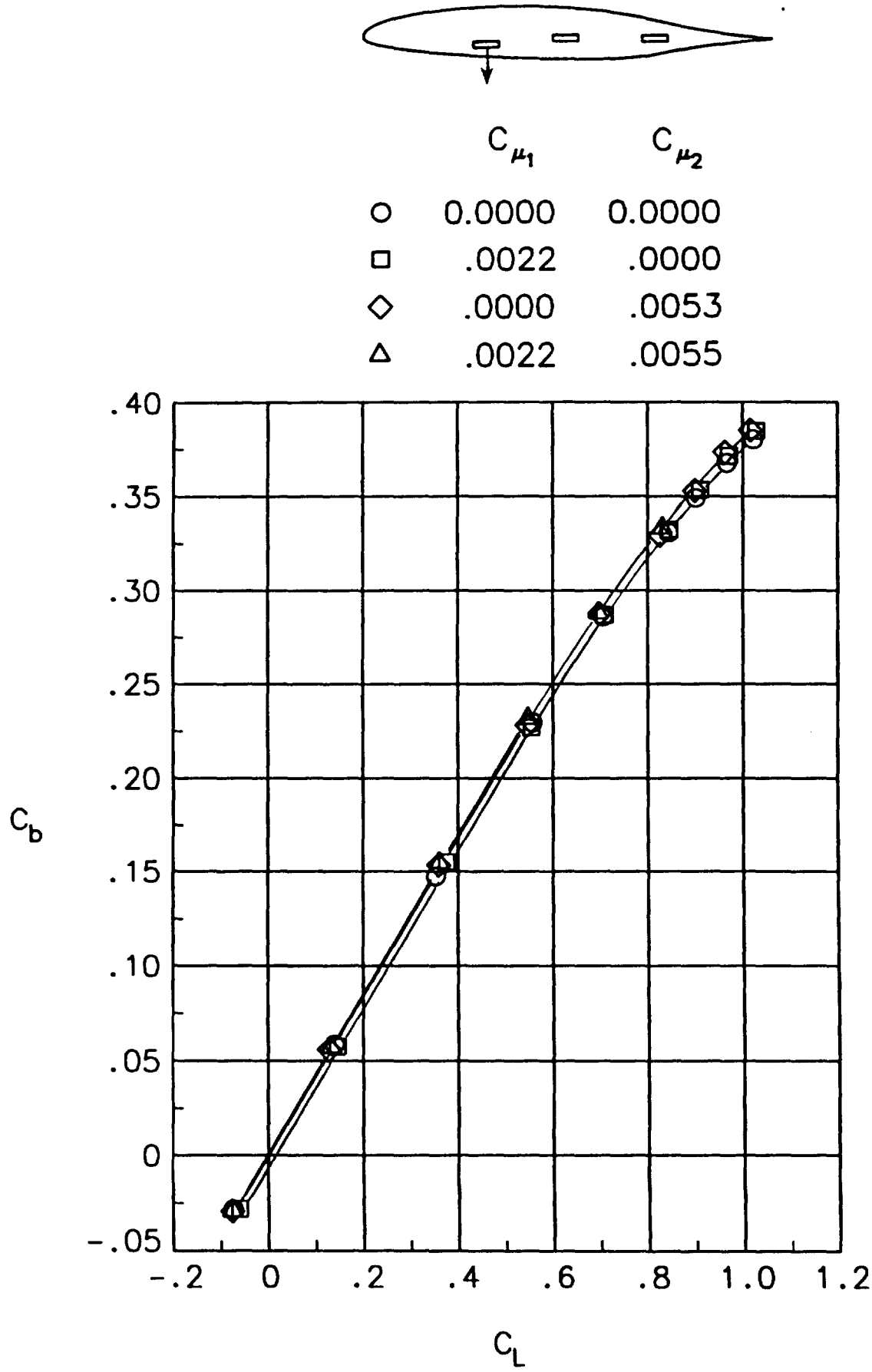

(d) Tip 4.

Figure 41. Continued.

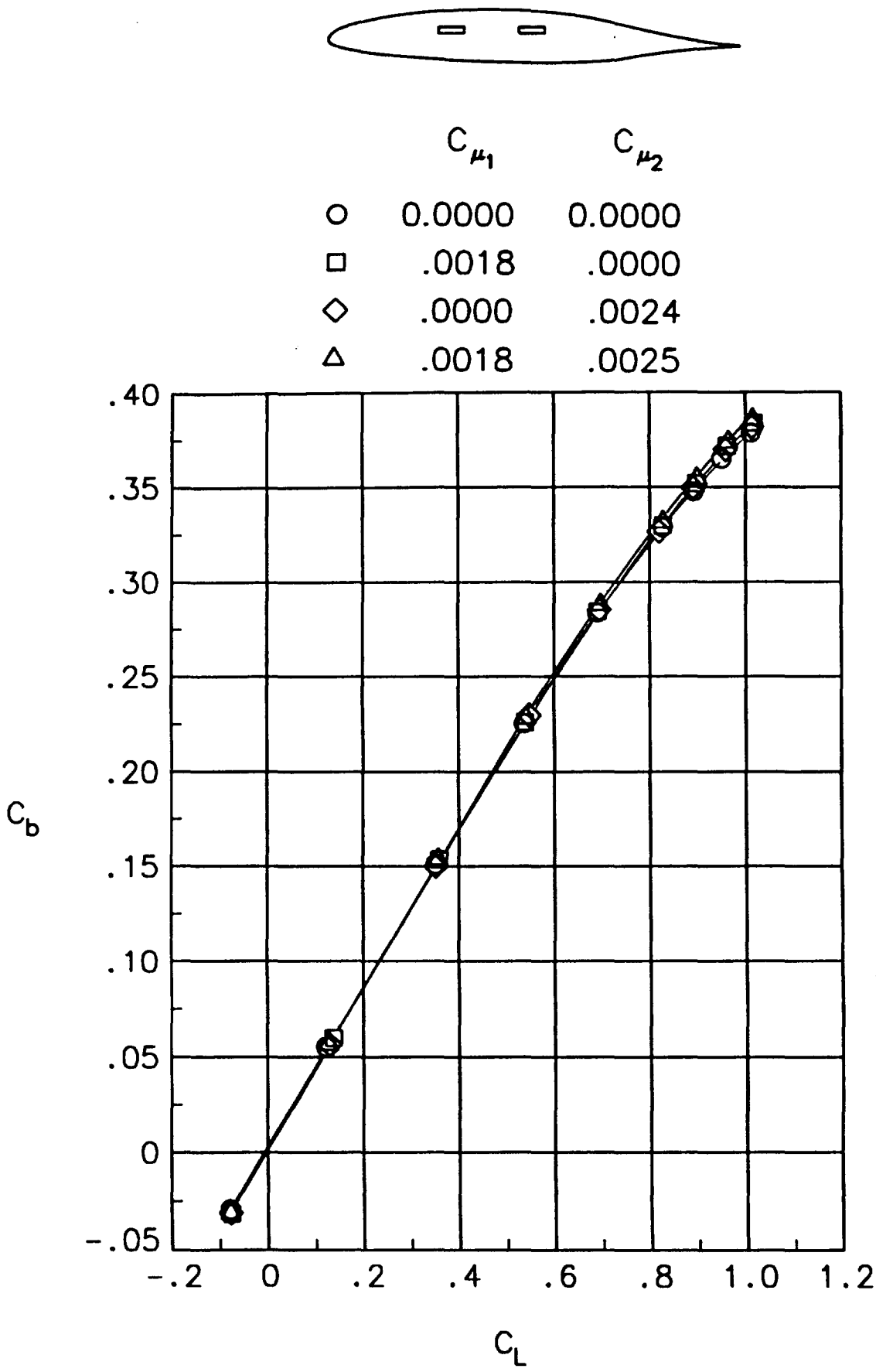

(e) Tip 6.

Figure 41. Continued.

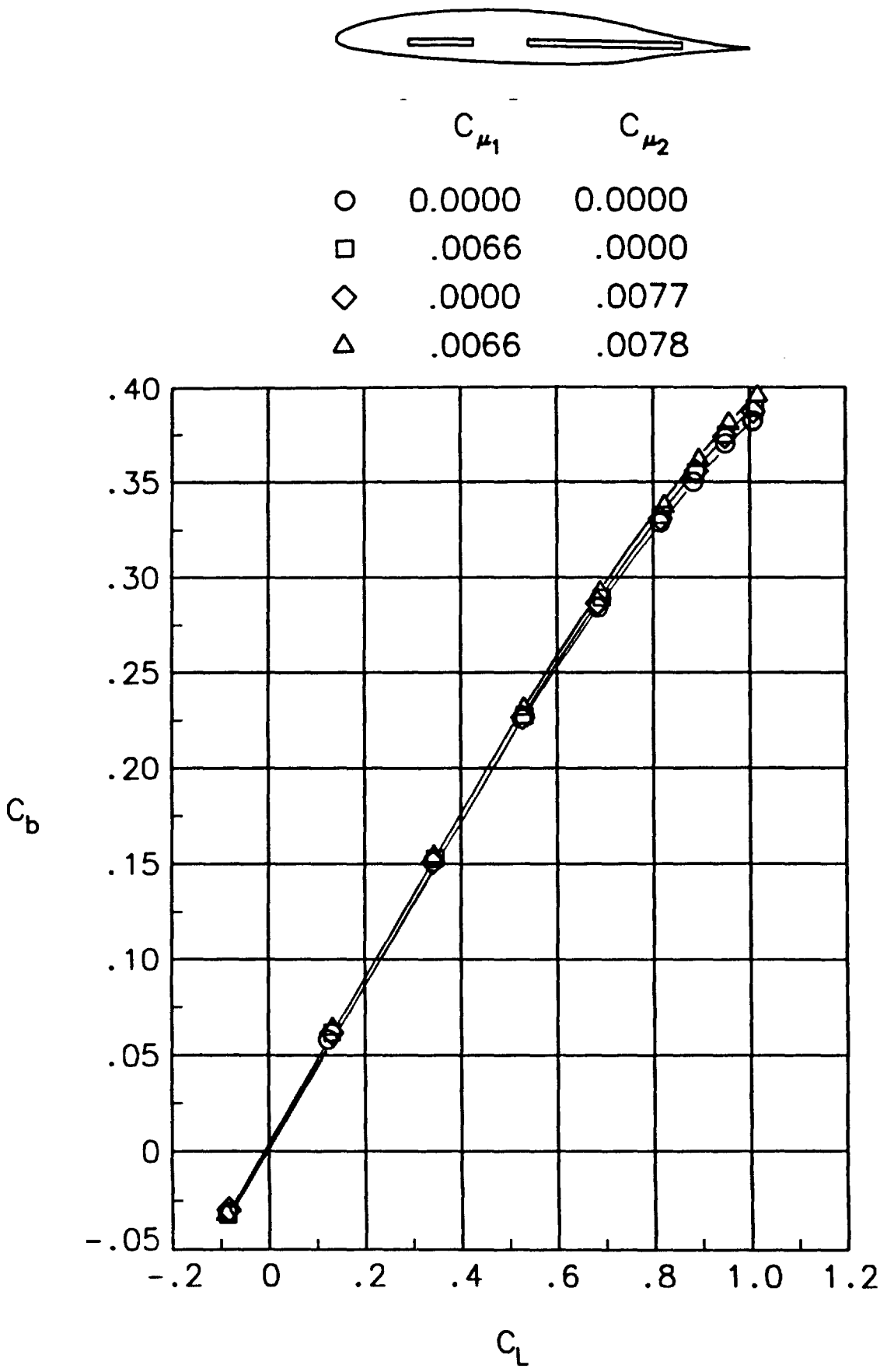

(f) Tip 8.

Figure 41. Continued.

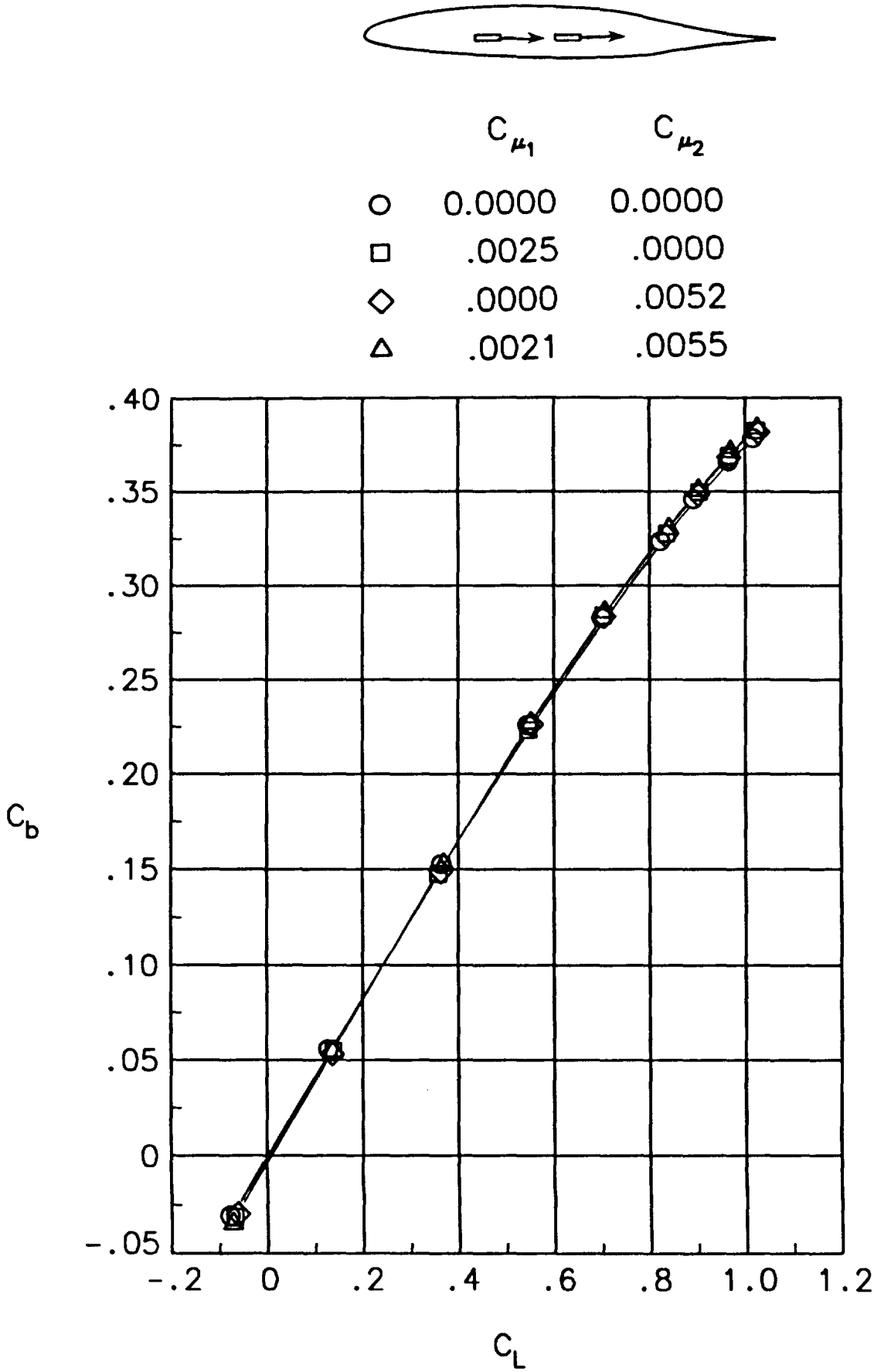

(g) Tip 9.

Figure 41. Concluded.

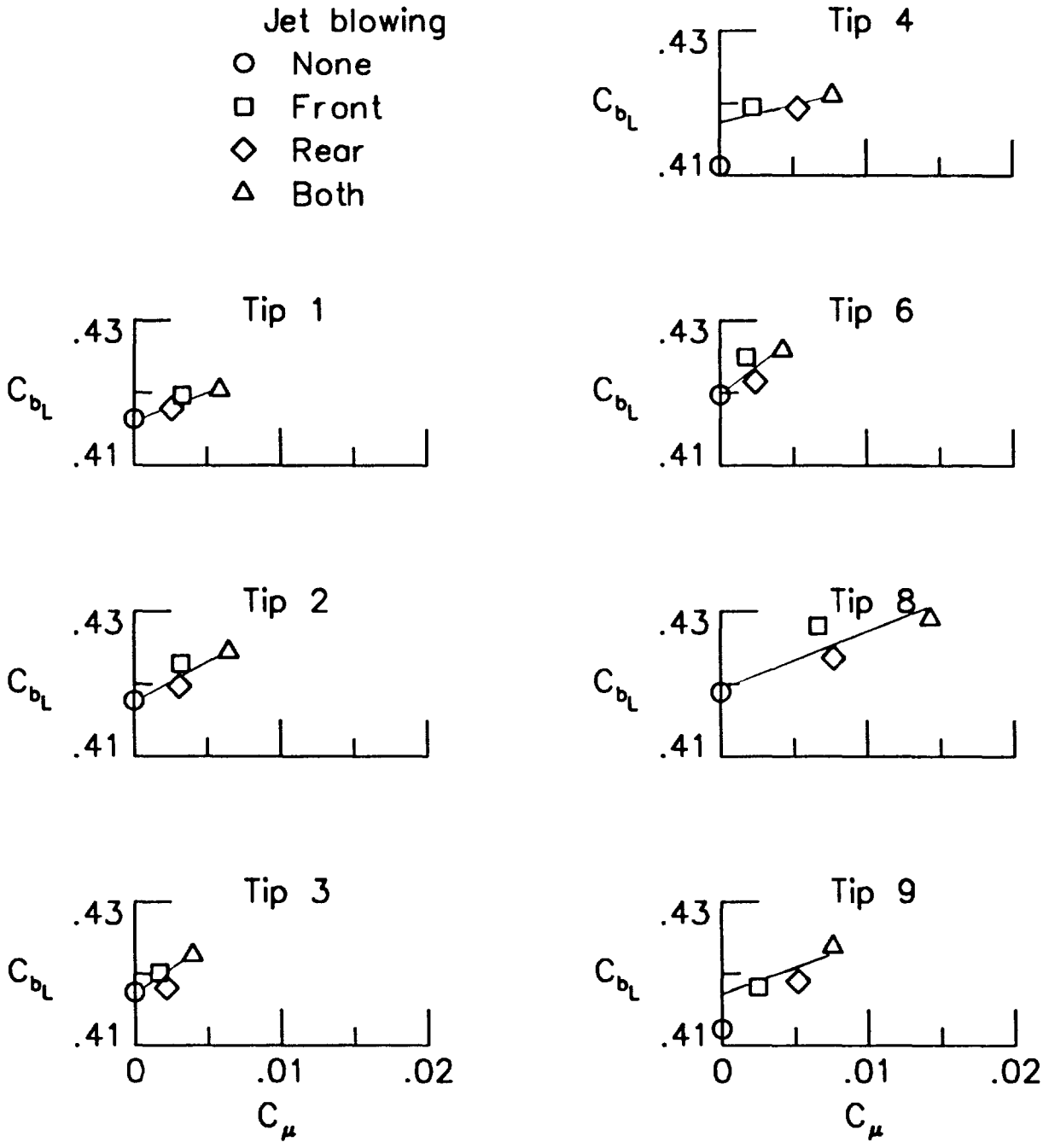

Figure 42. Variation of the slope of the bending moment curve with blowing. $M_\infty = 0.3$.

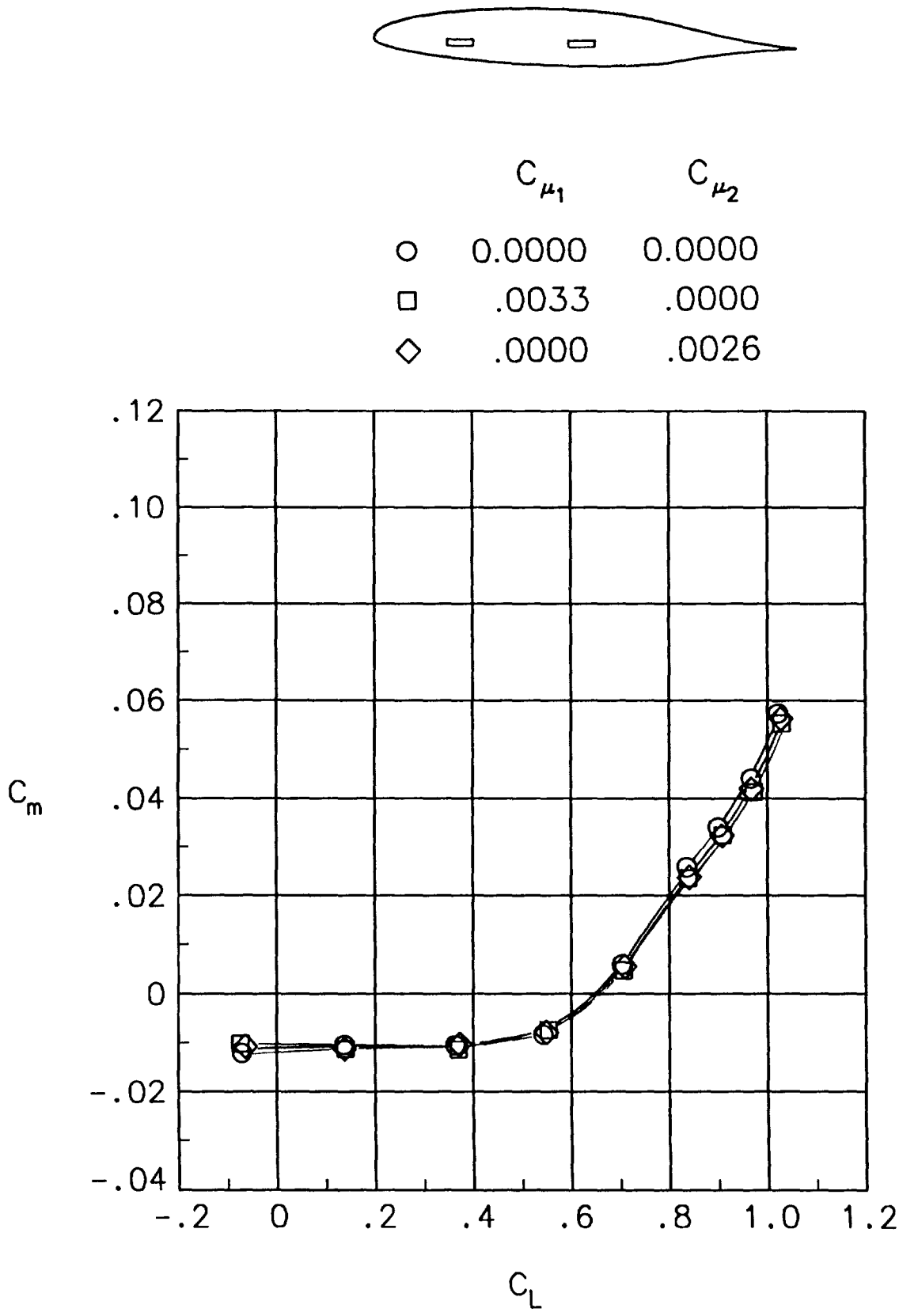

(a) Tip 1.

Figure 43. Effect of spanwise blowing on the wing pitching moment curves. $M_\infty = 0.3$.

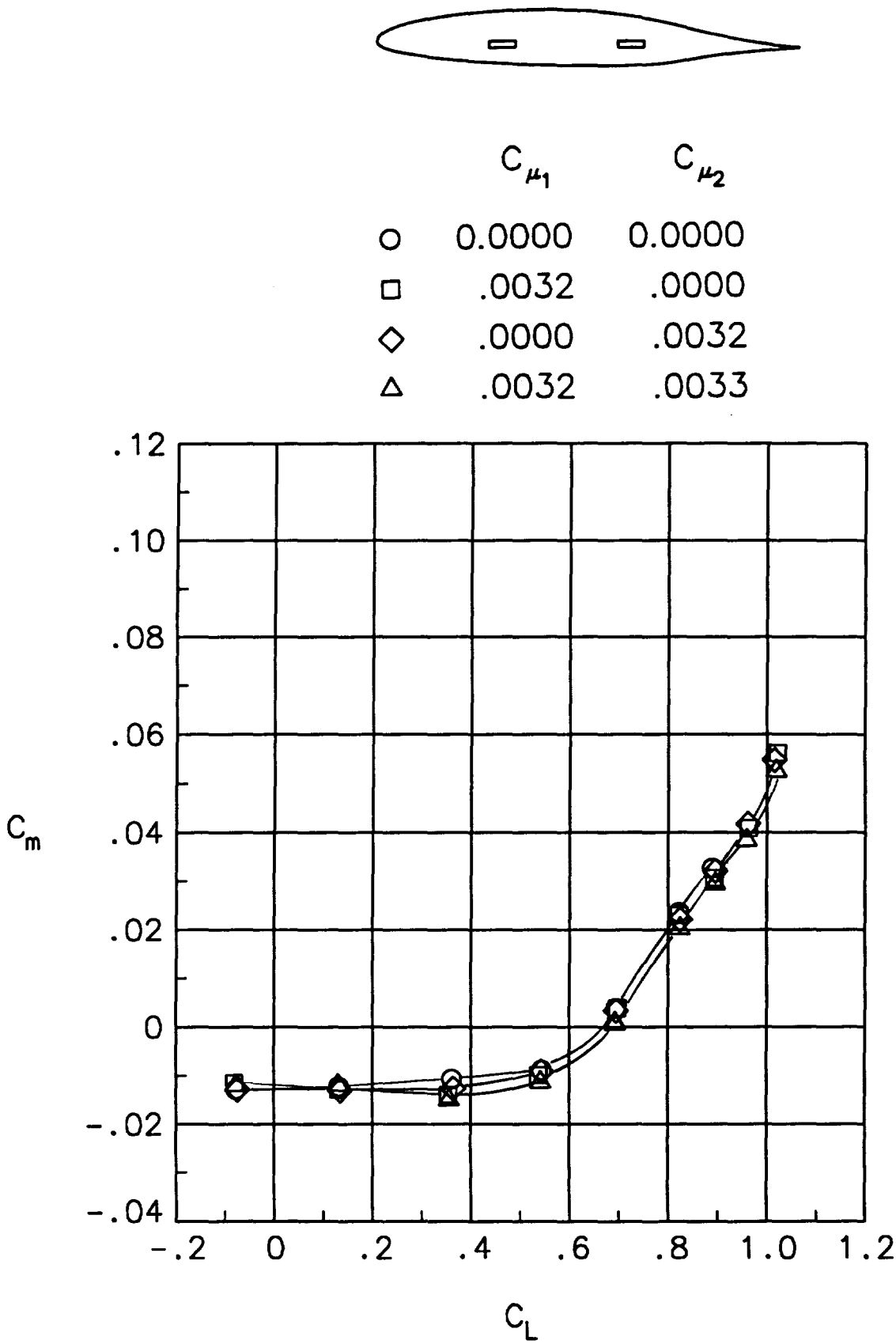

(b) Tip 2.

Figure 43. Continued.

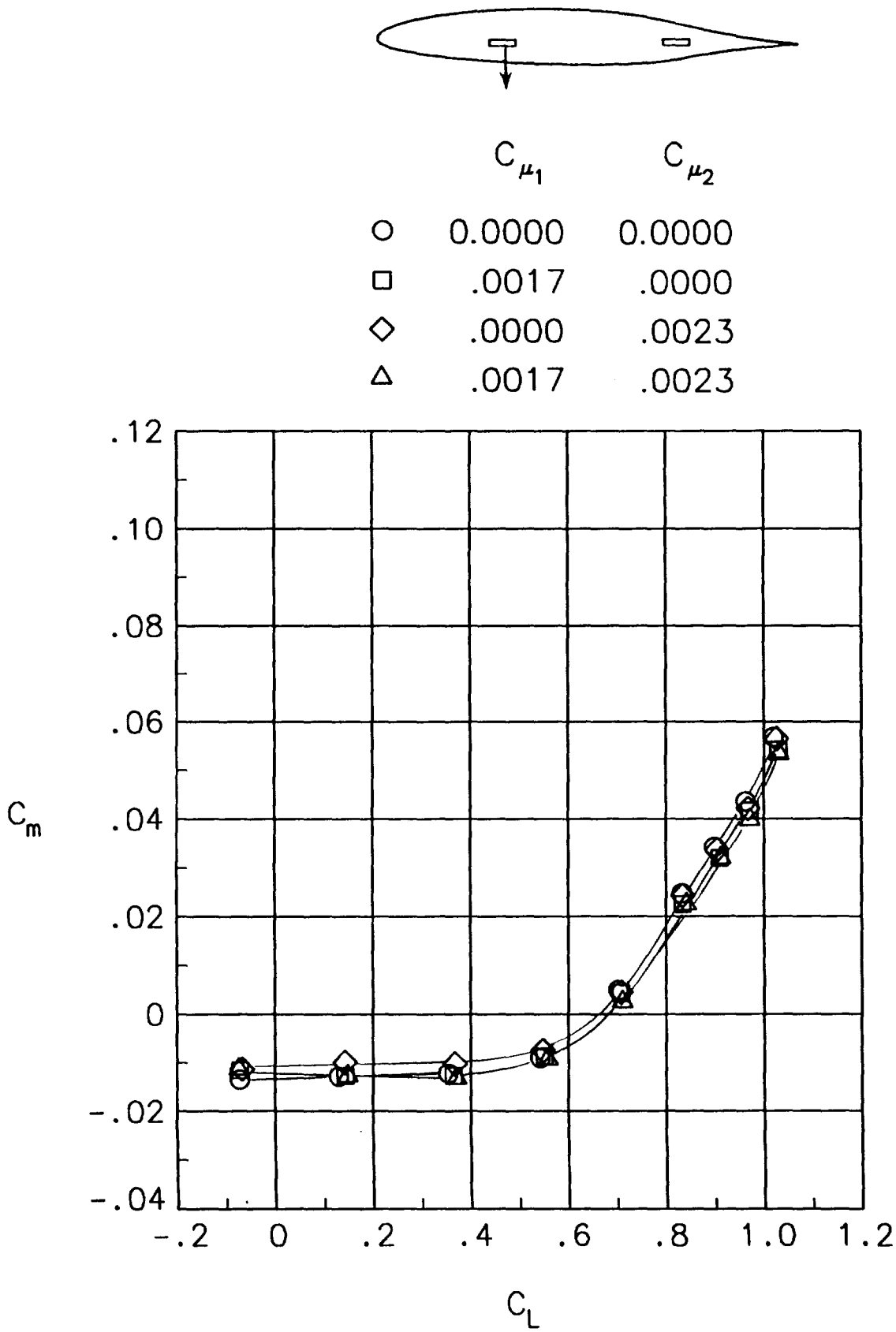

(c) Tip 3.

Figure 43. Continued.

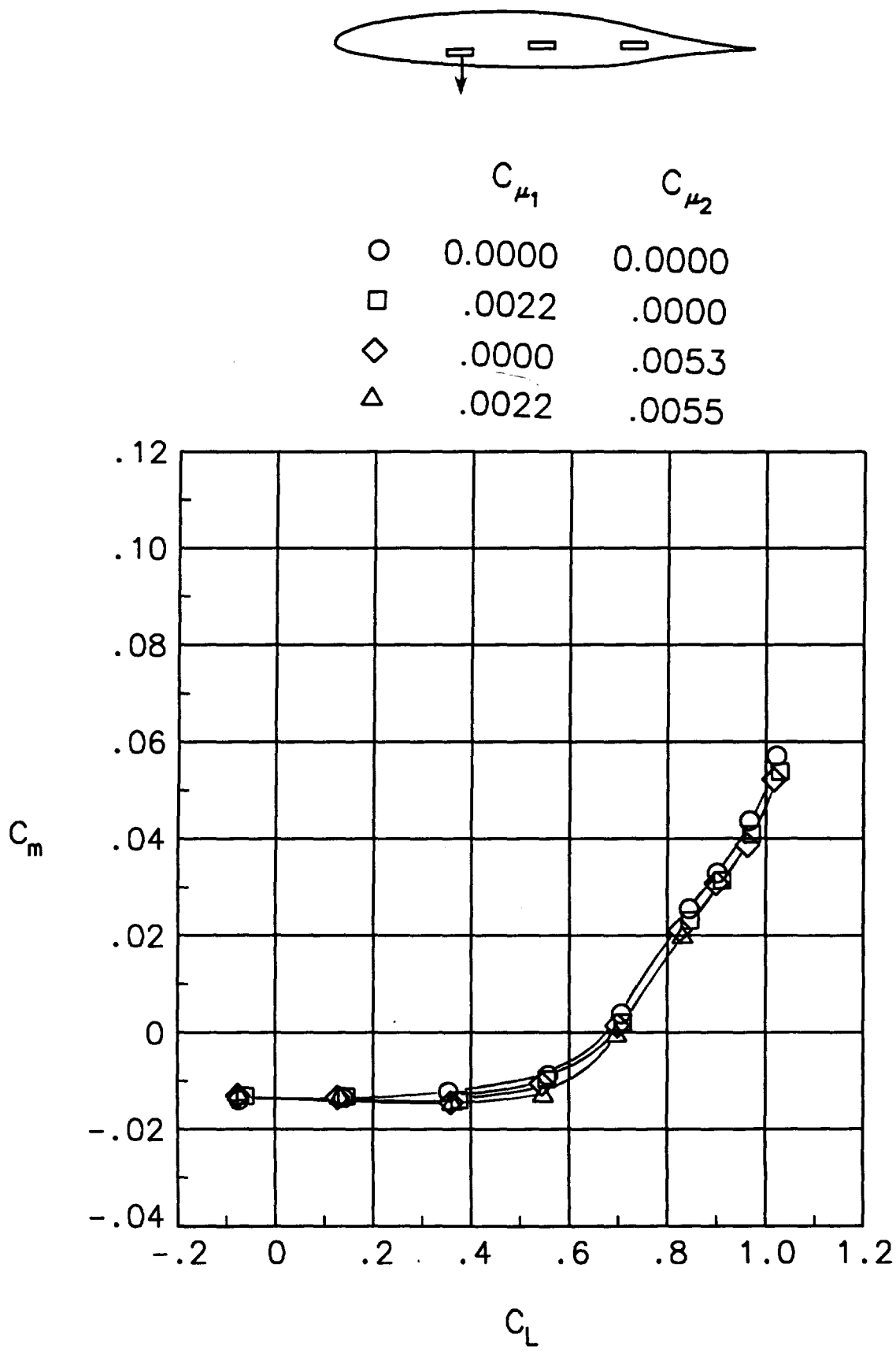

(d) Tip 4.

Figure 43. Continued.

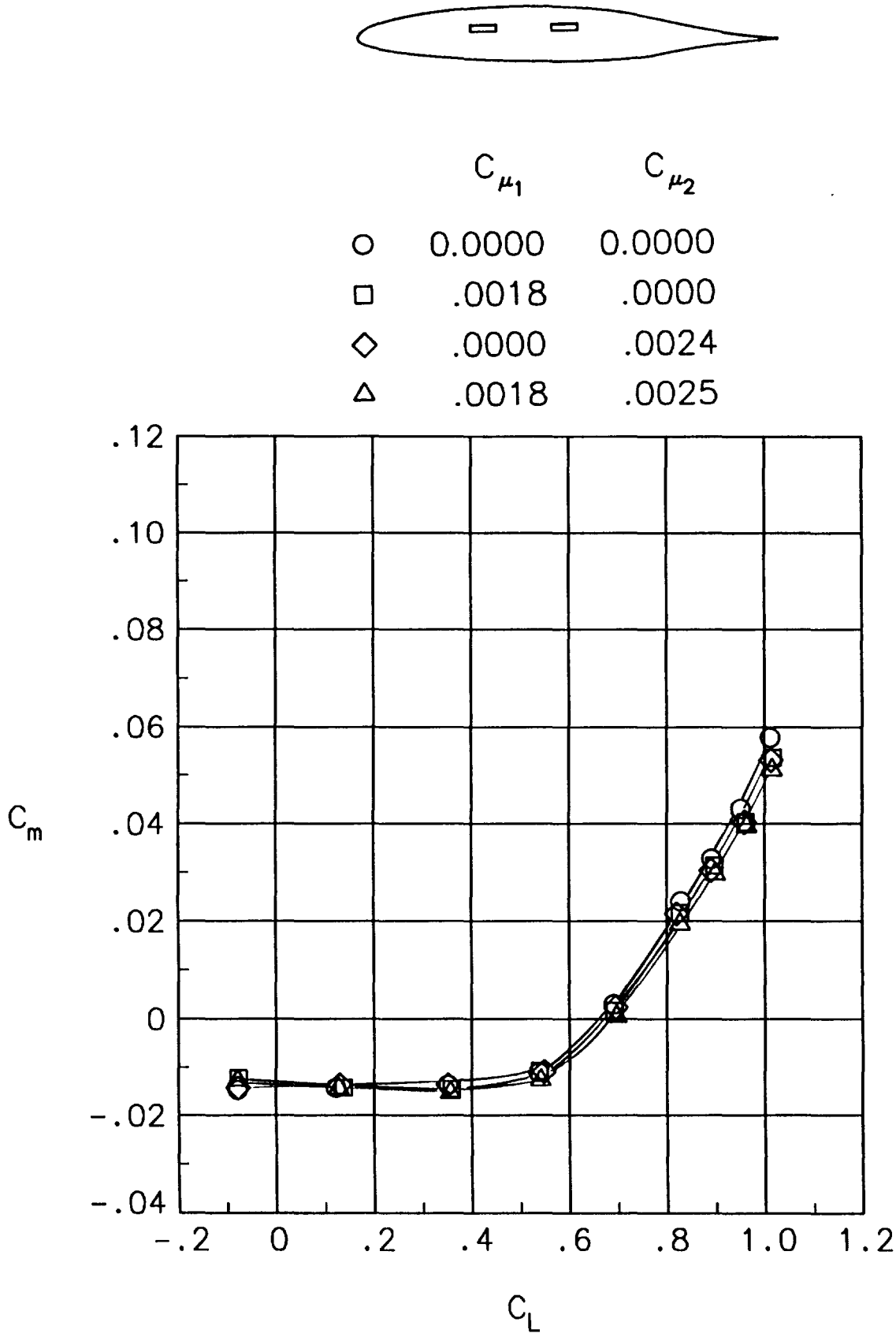

(e) Tip 6.

Figure 43. Continued.

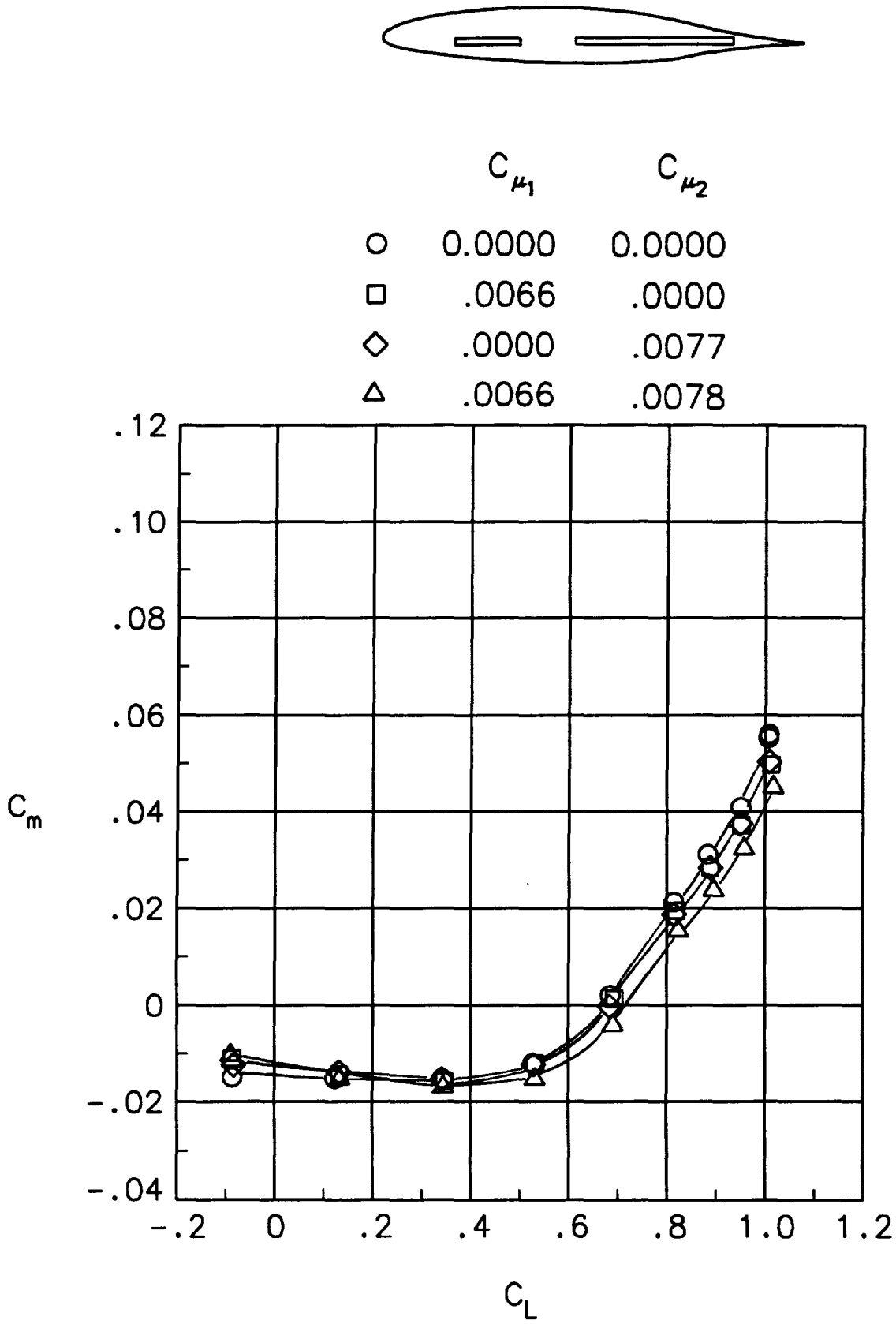

(f) Tip 8.

Figure 43. Continued.

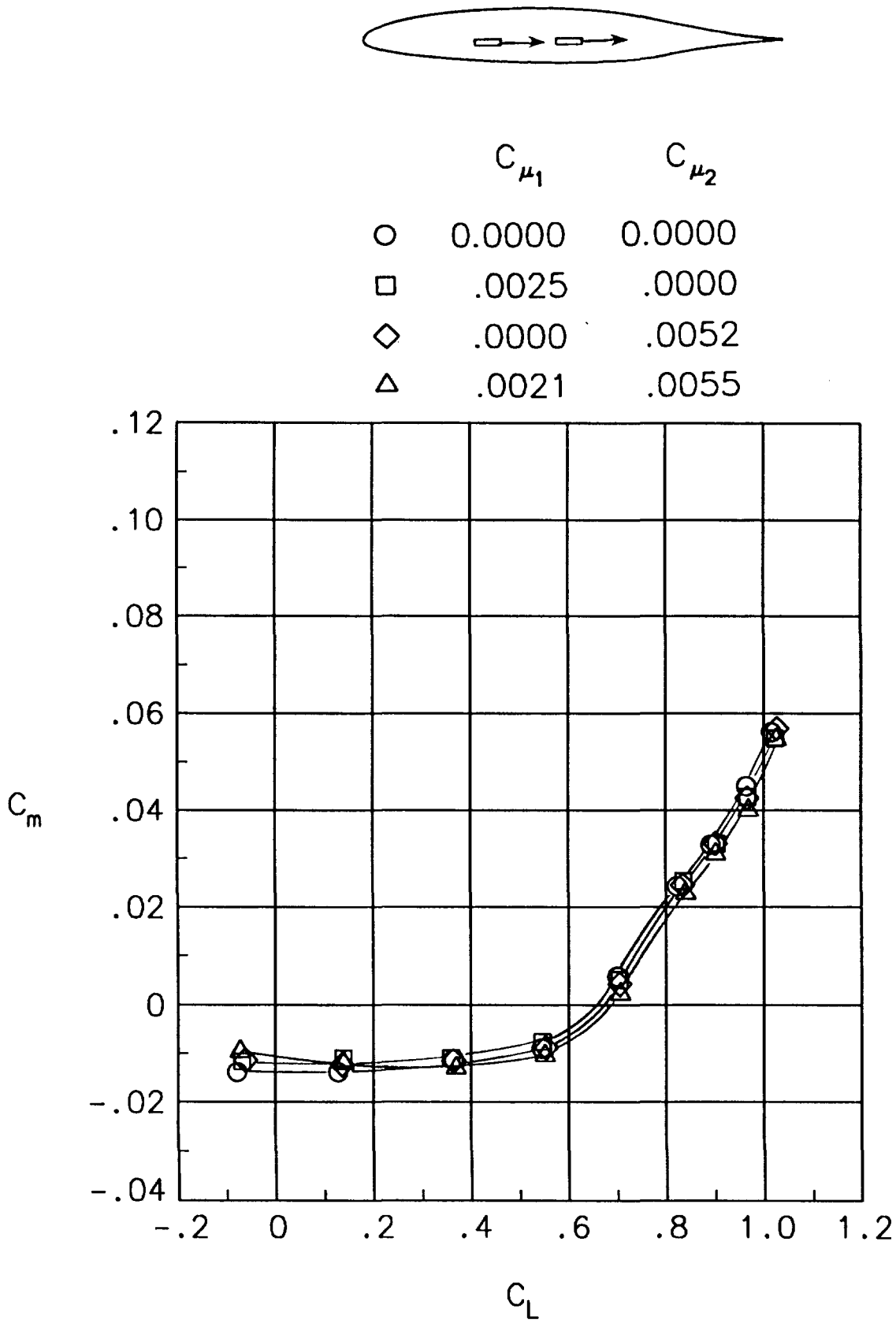

(g) Tip 9.

Figure 43. Concluded.

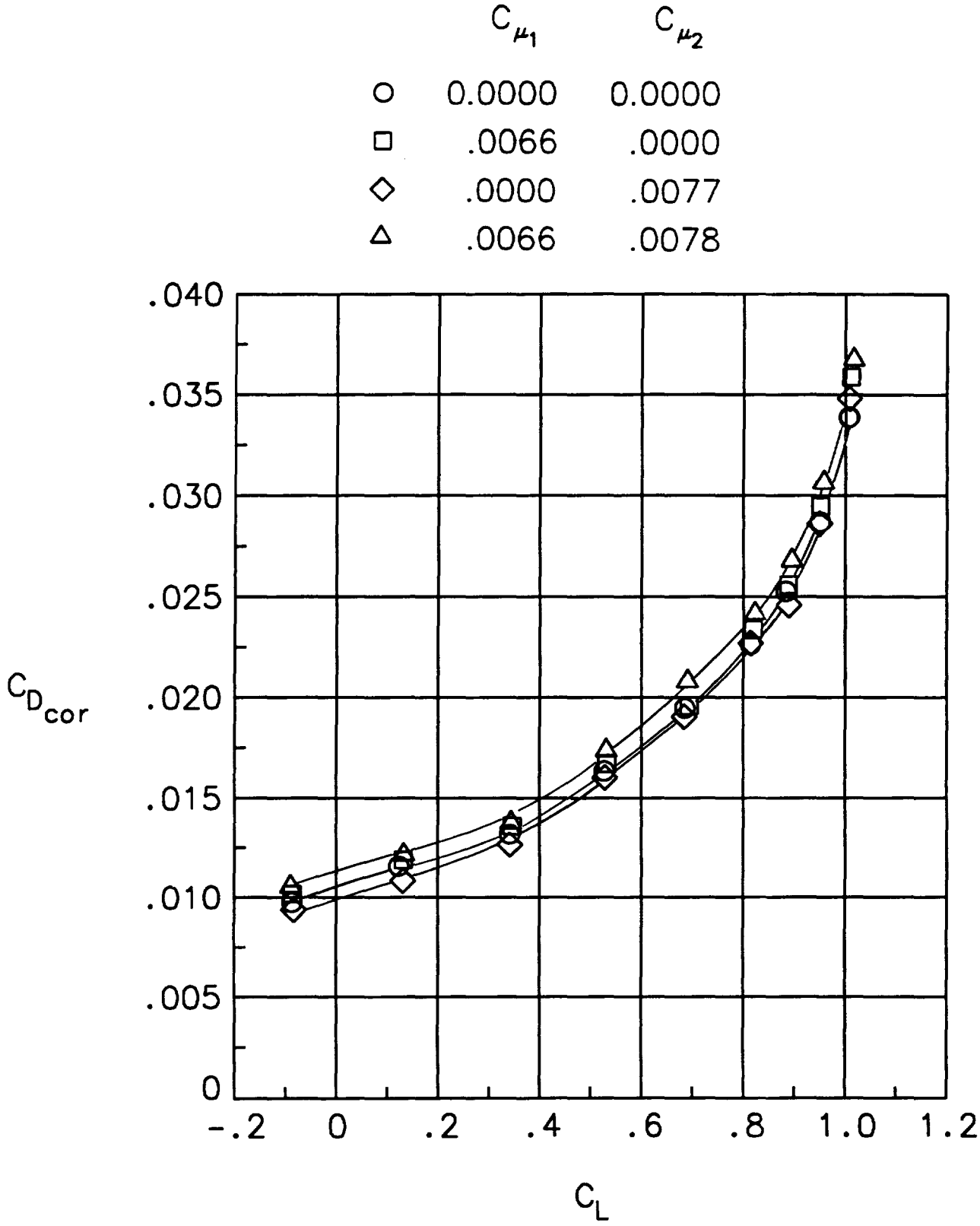

Figure 44. Effect of blowing on the total drag. Tip 8. $M_\infty = 0.3$.

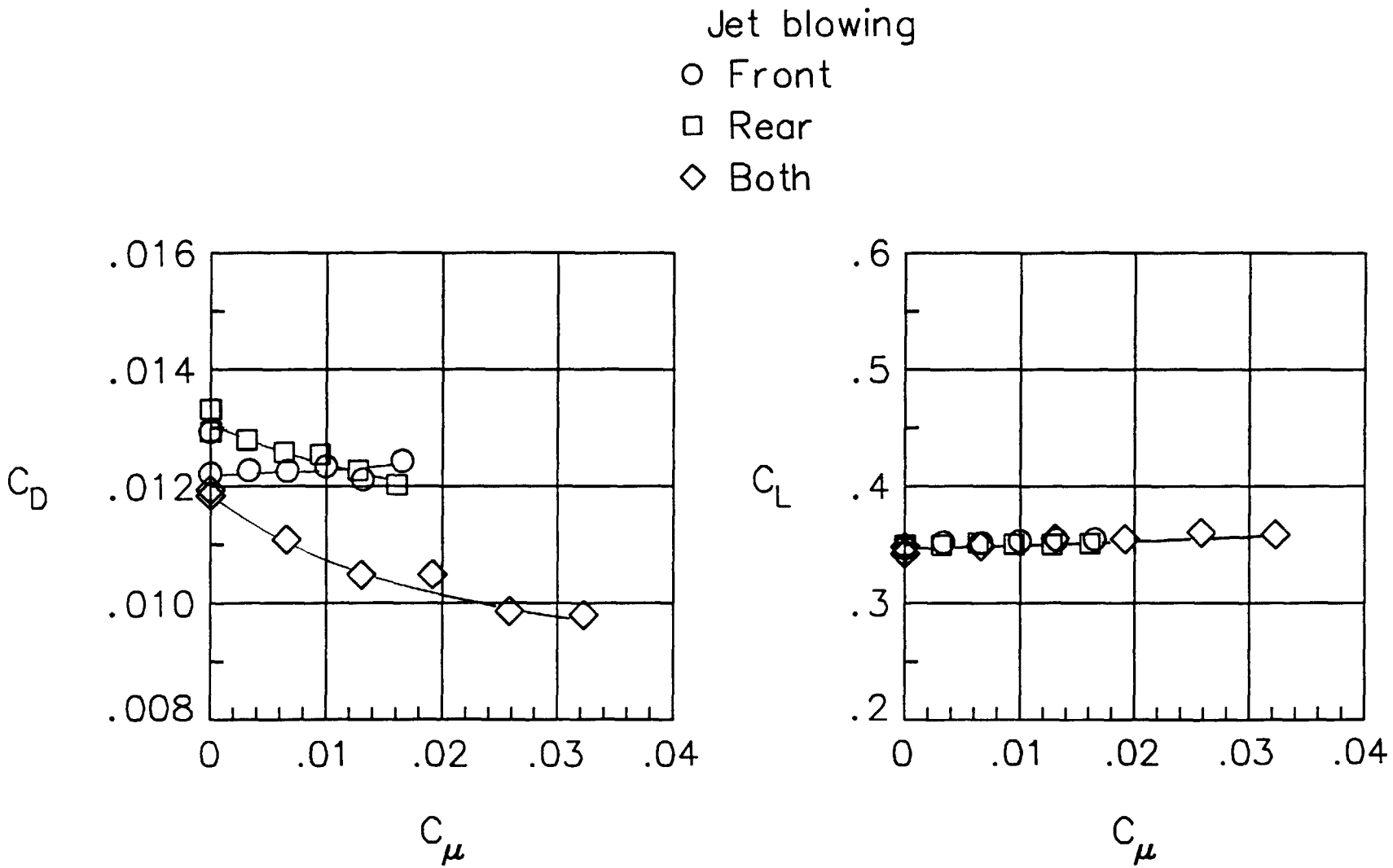

(a) $M_\infty = 0.2$.

Figure 45. Variation of the wing lift and drag coefficients with jet momentum coefficient. $\alpha = 2.1^\circ$.

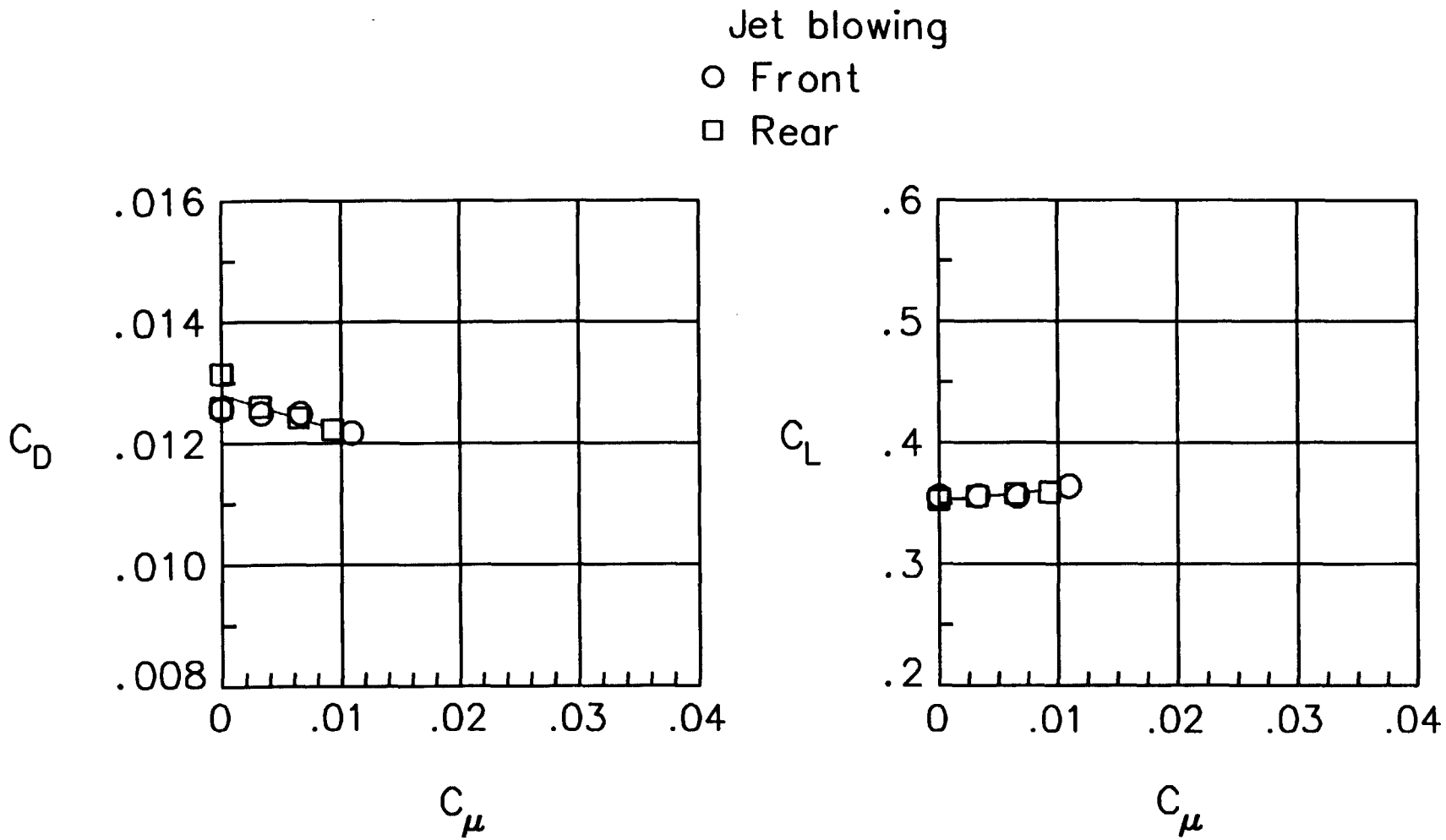

(b) $M_\infty = 0.3$.

Figure 45. Continued.

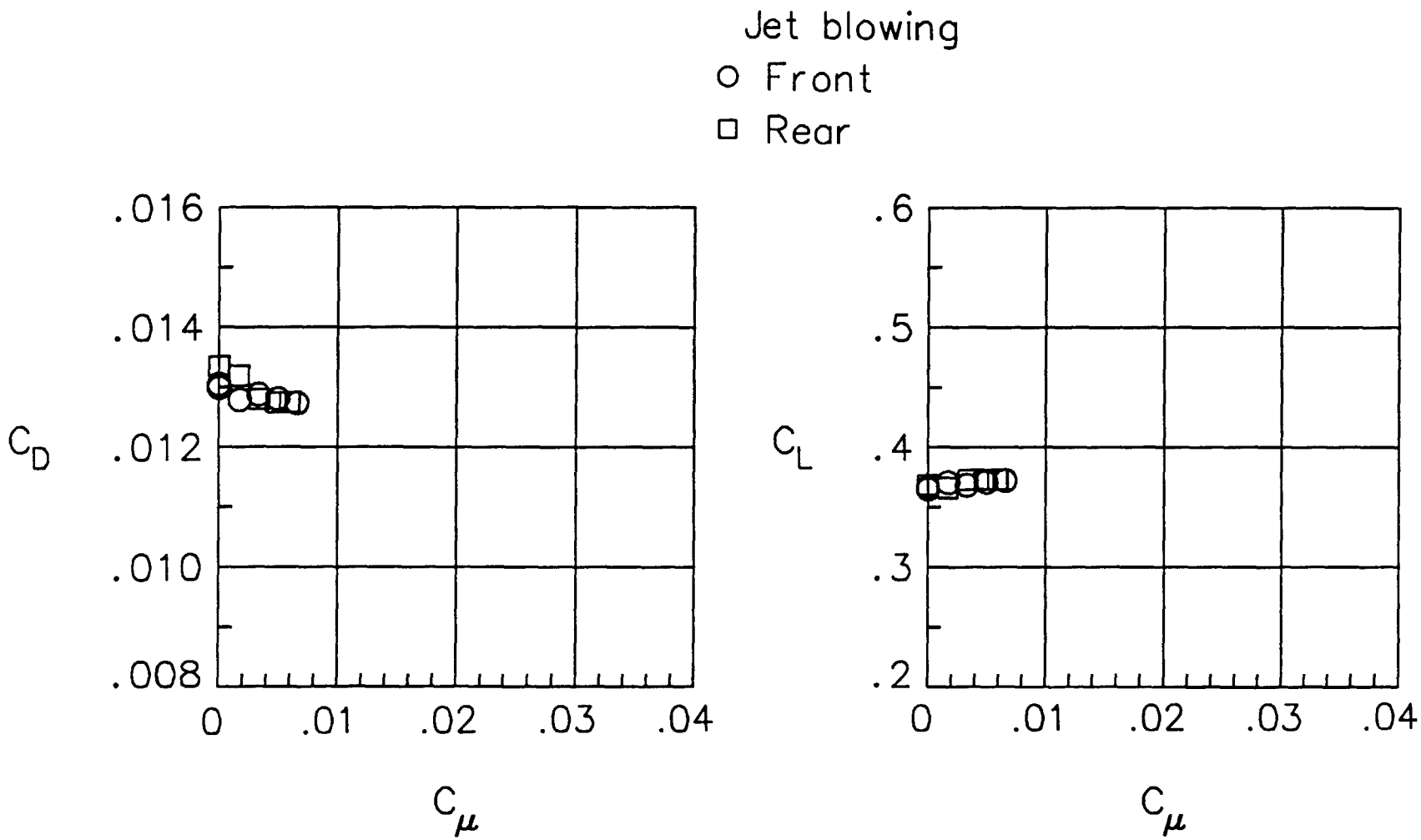

(c) $M_\infty = 0.4$.

Figure 45. Continued.

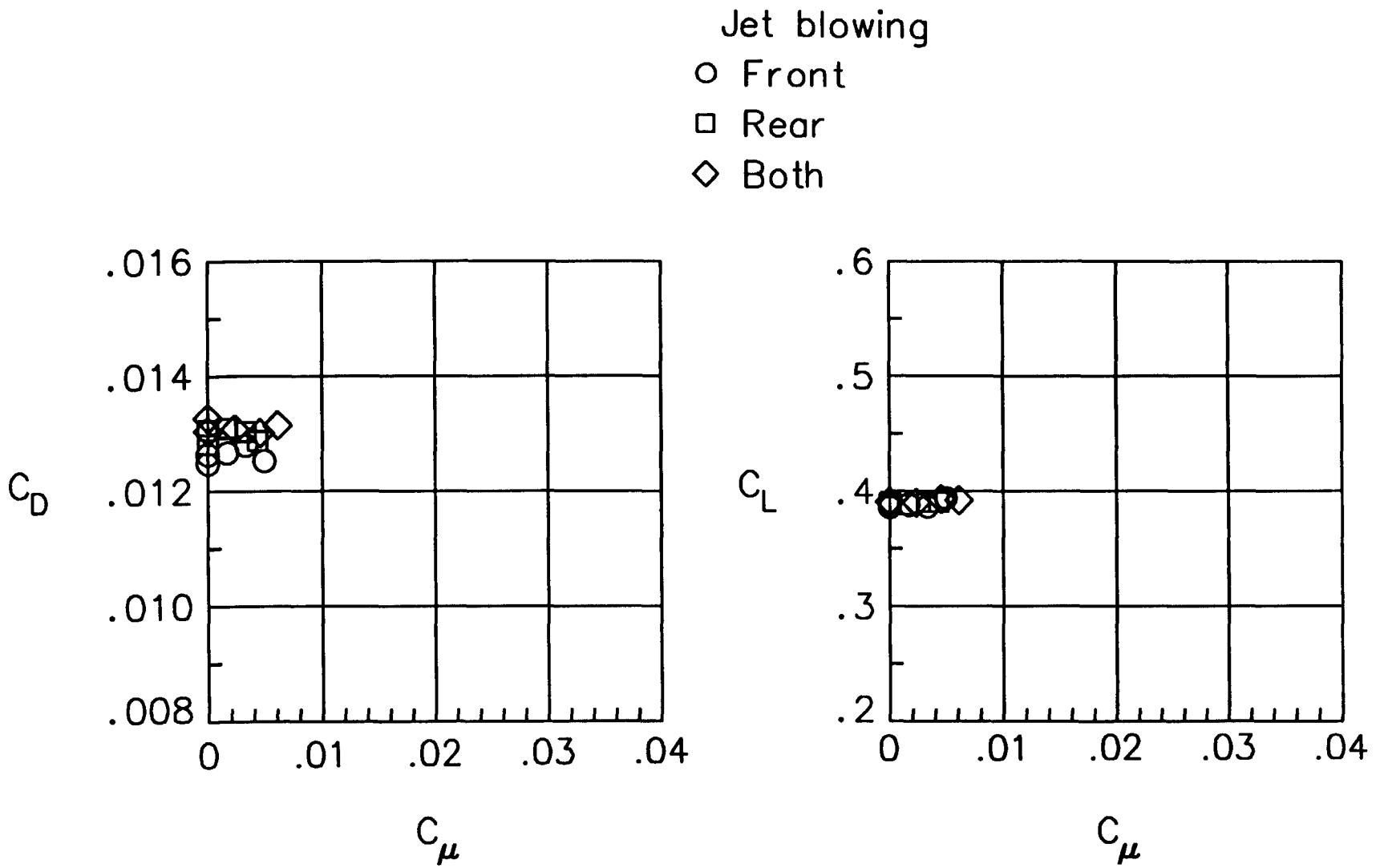

(d) $M_\infty = 0.5$.

Figure 45. Concluded.

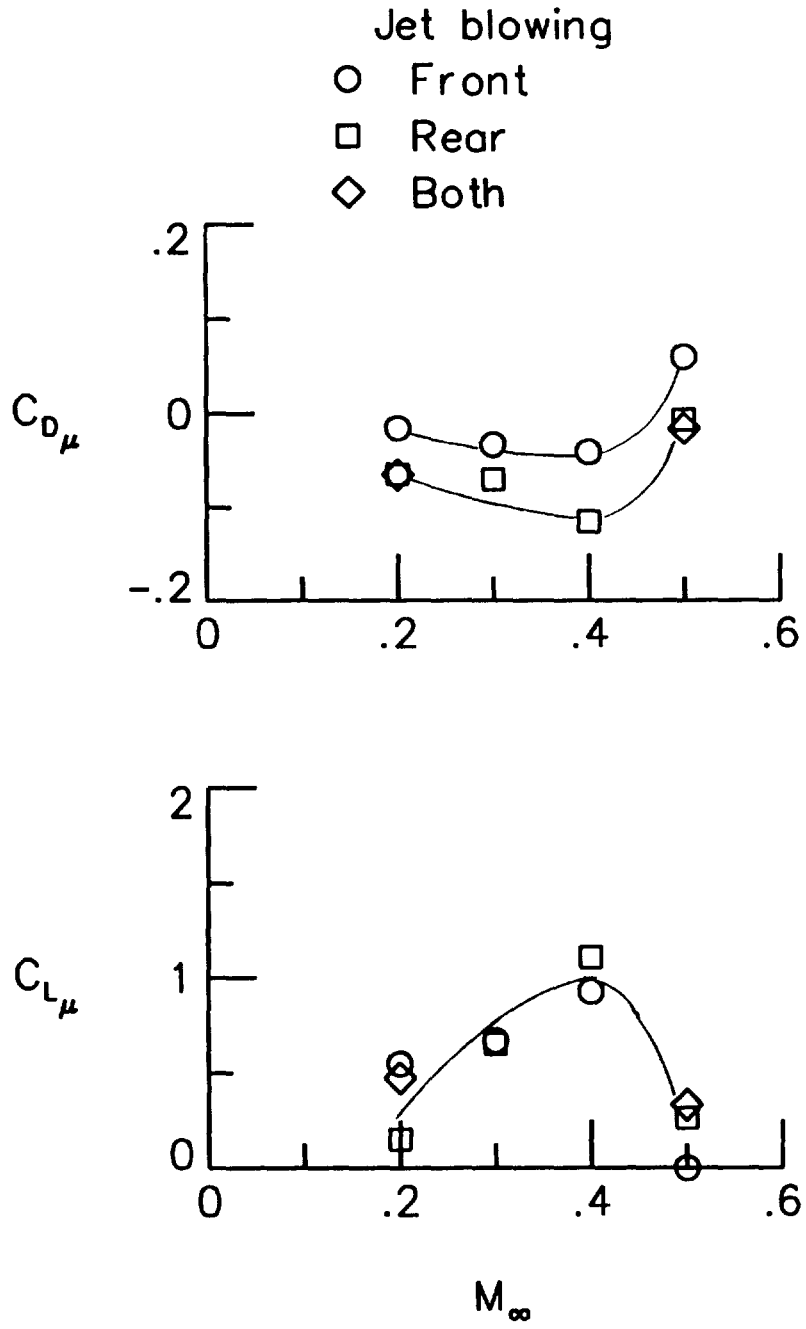

Figure 46. Variation of blowing effectiveness with Mach number for tip 8.

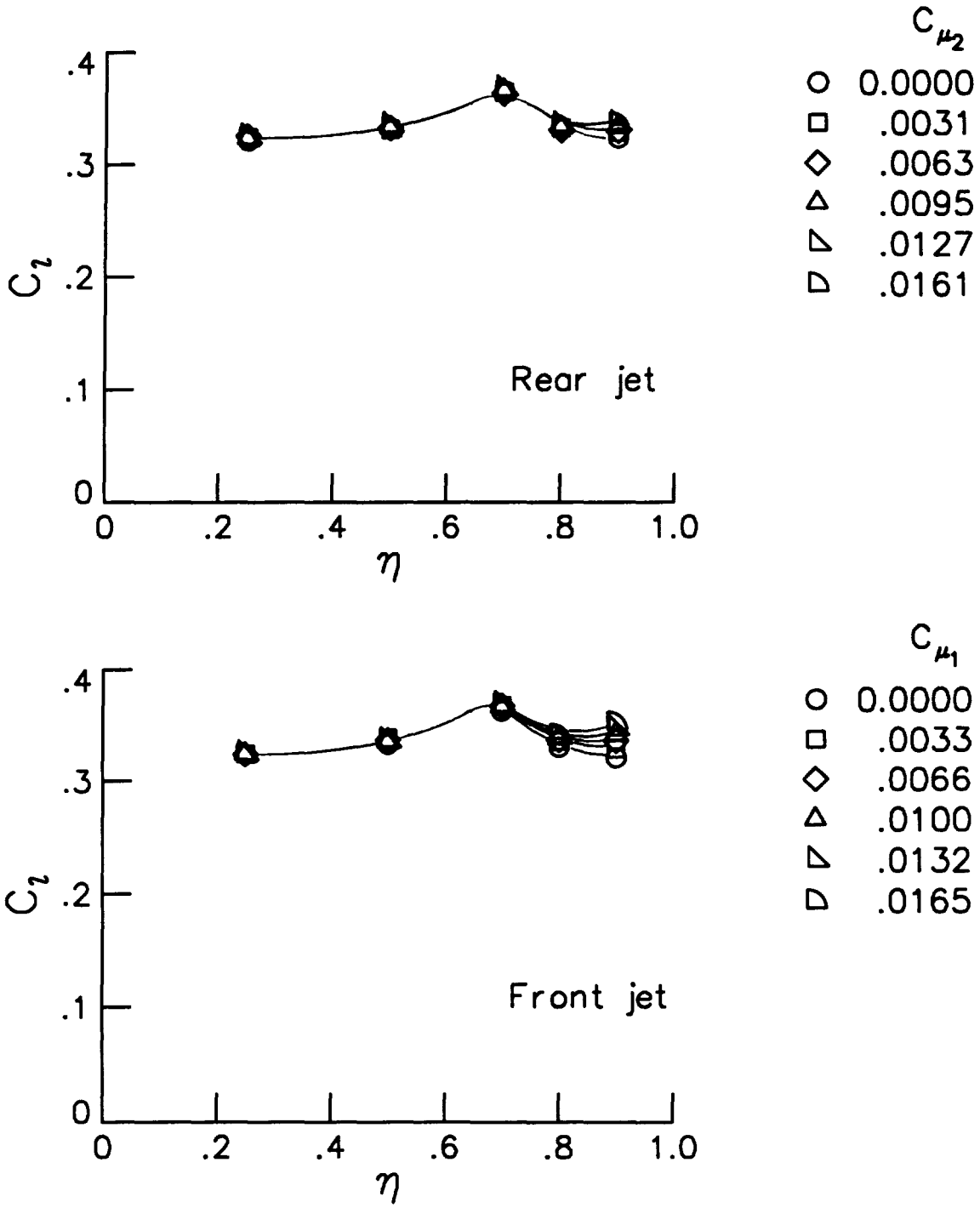

(a) $M_\infty = 0.2$.

Figure 47. Effect of blowing on the span load distribution. Tip 8.

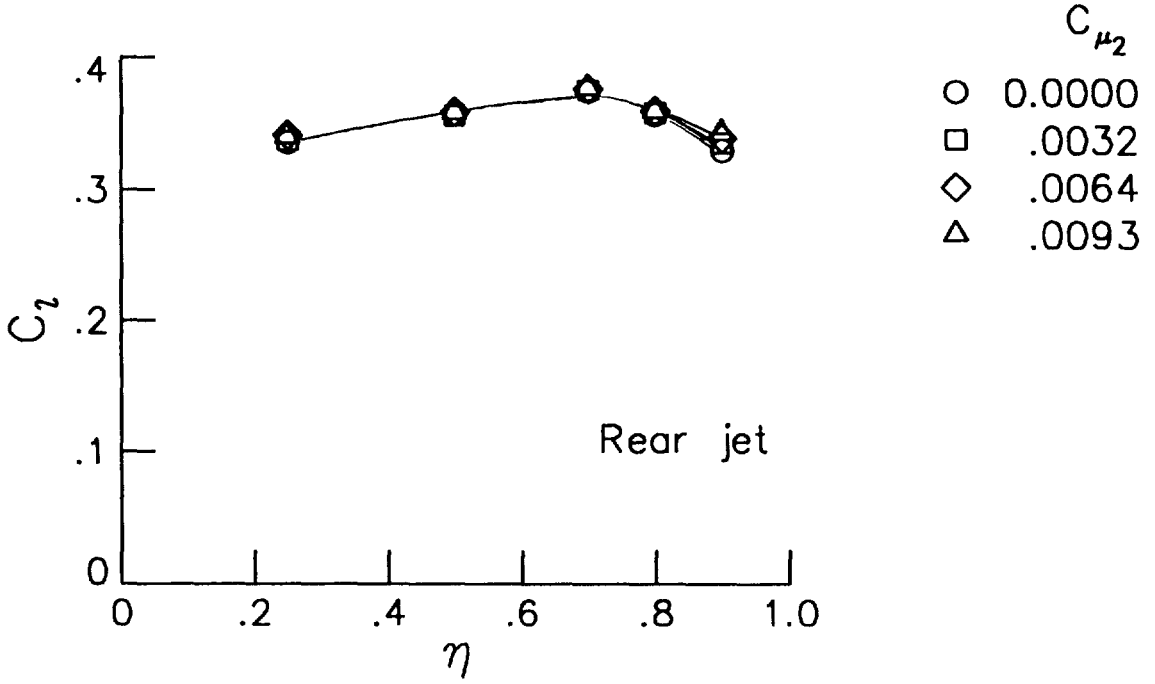

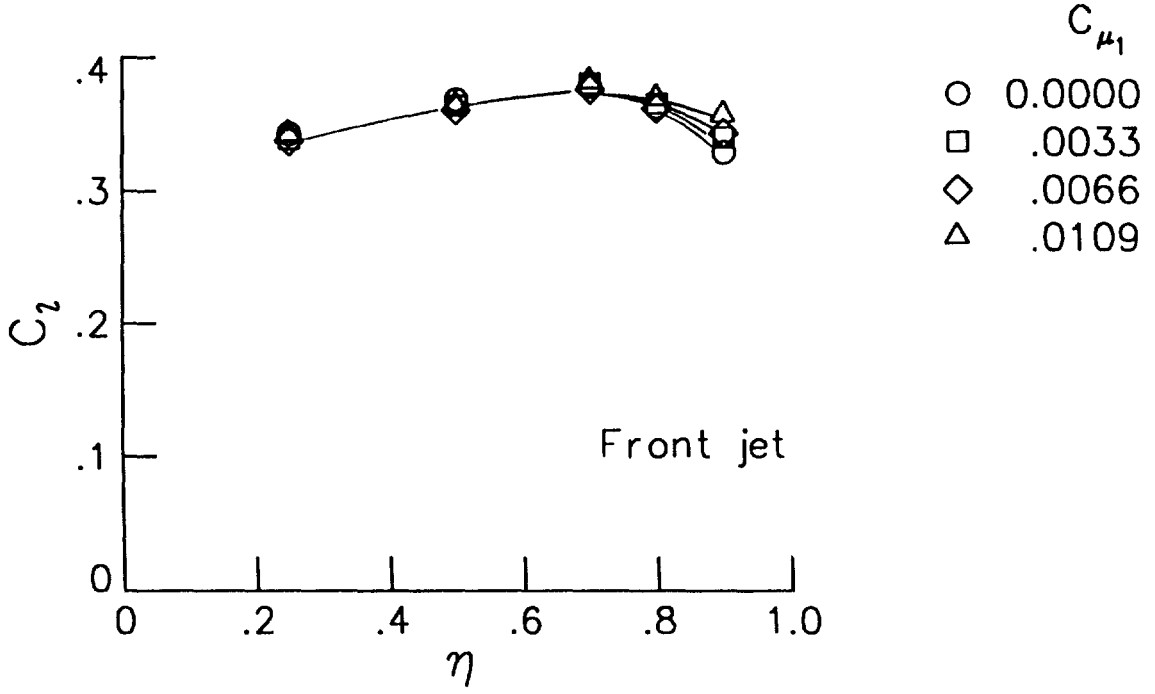

(b) $M_\infty = 0.3$.

Figure 47. Continued.

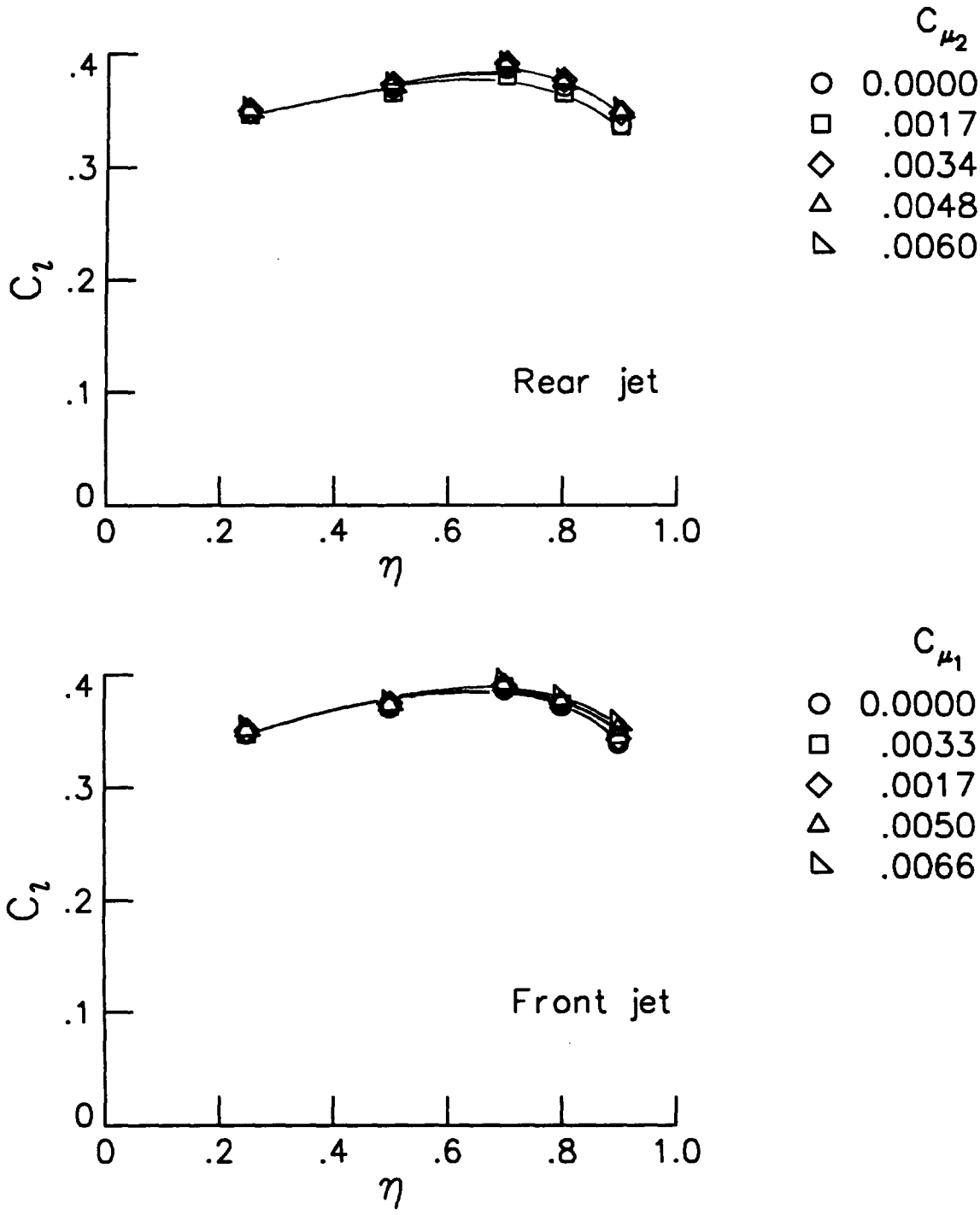

(c) $M_\infty = 0.4$.

Figure 47. Continued.

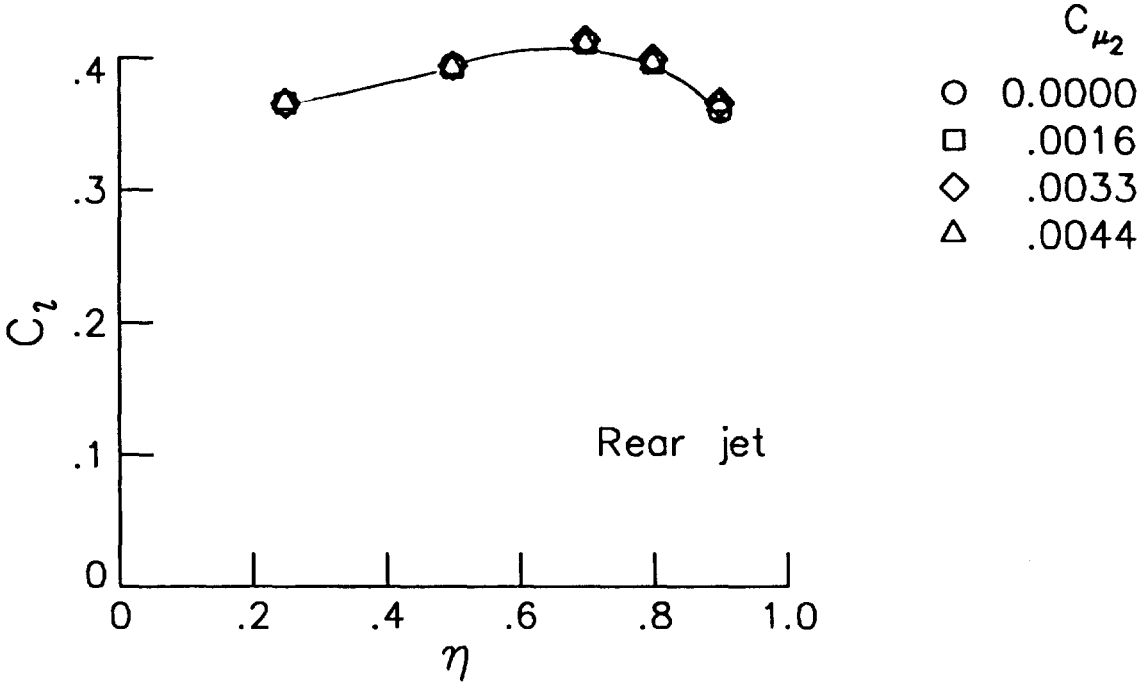

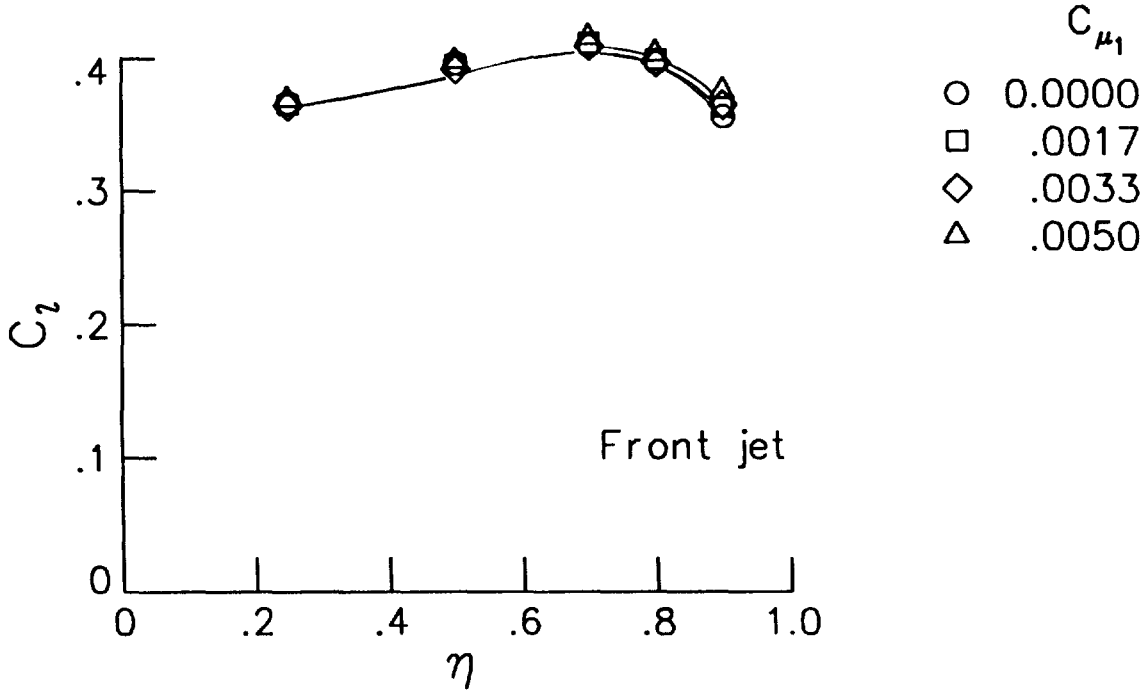

(d) $M_\infty = 0.5$.

Figure 47. Concluded.

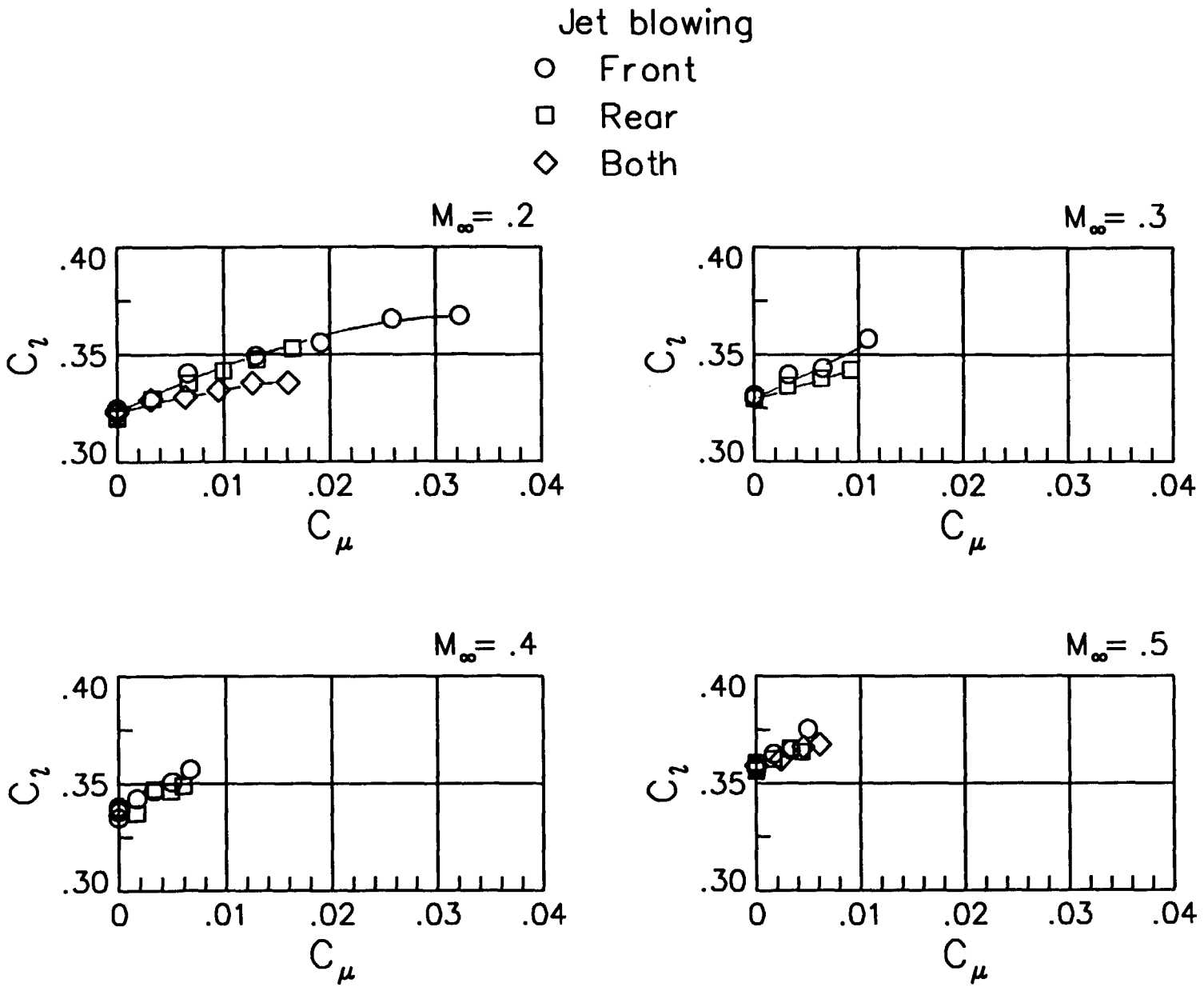

Figure 48. Effect of blowing on the section lift coefficient at the 90 percent semispan location. Tip 8.

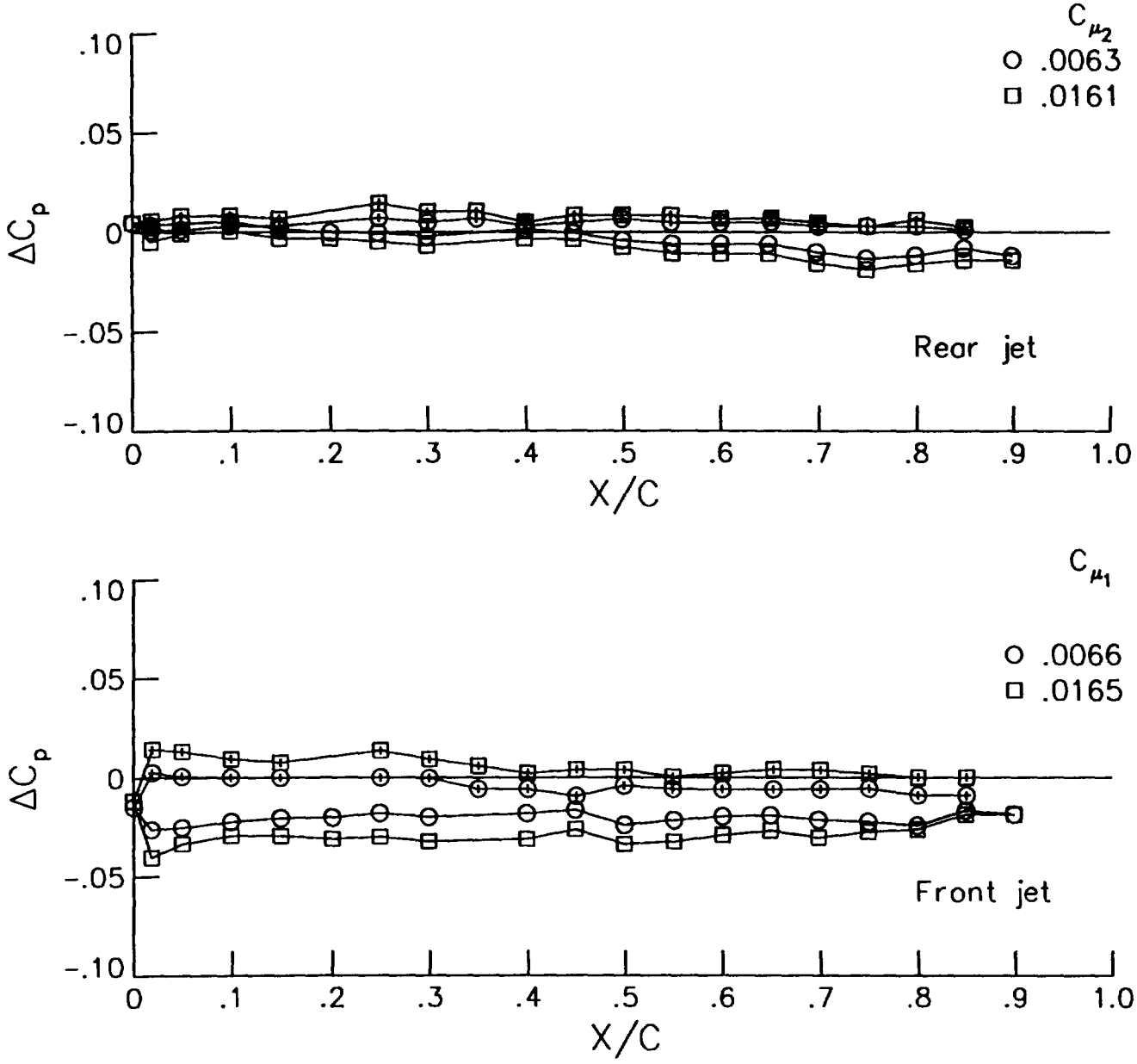

(a) $M_\infty = 0.2$.

Figure 49. Effect of blowing on the chordwise pressure distribution at the 90 percent semispan location. Tip 8.

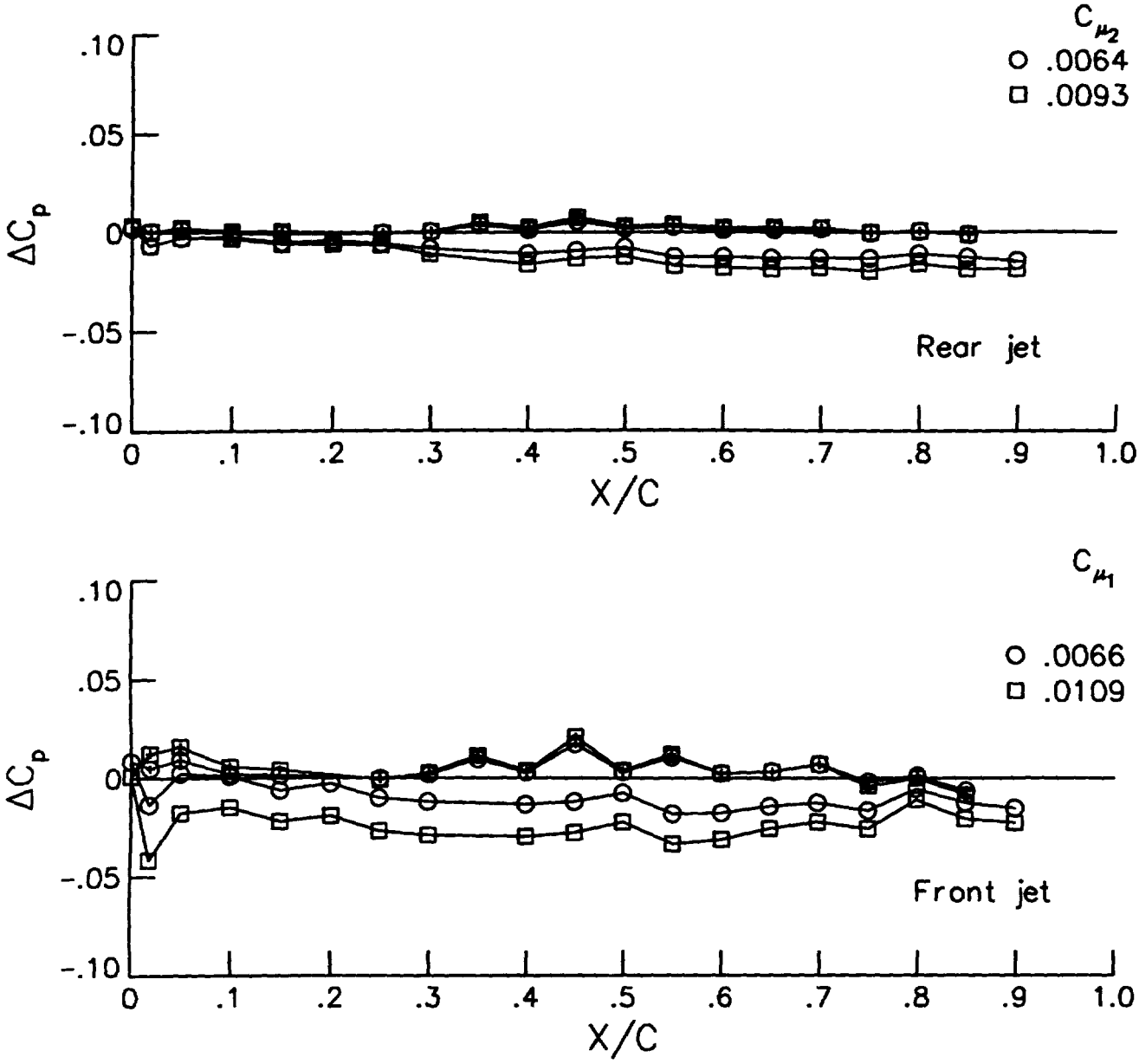

(b) $M_\infty = 0.3$.

Figure 49. Continued.

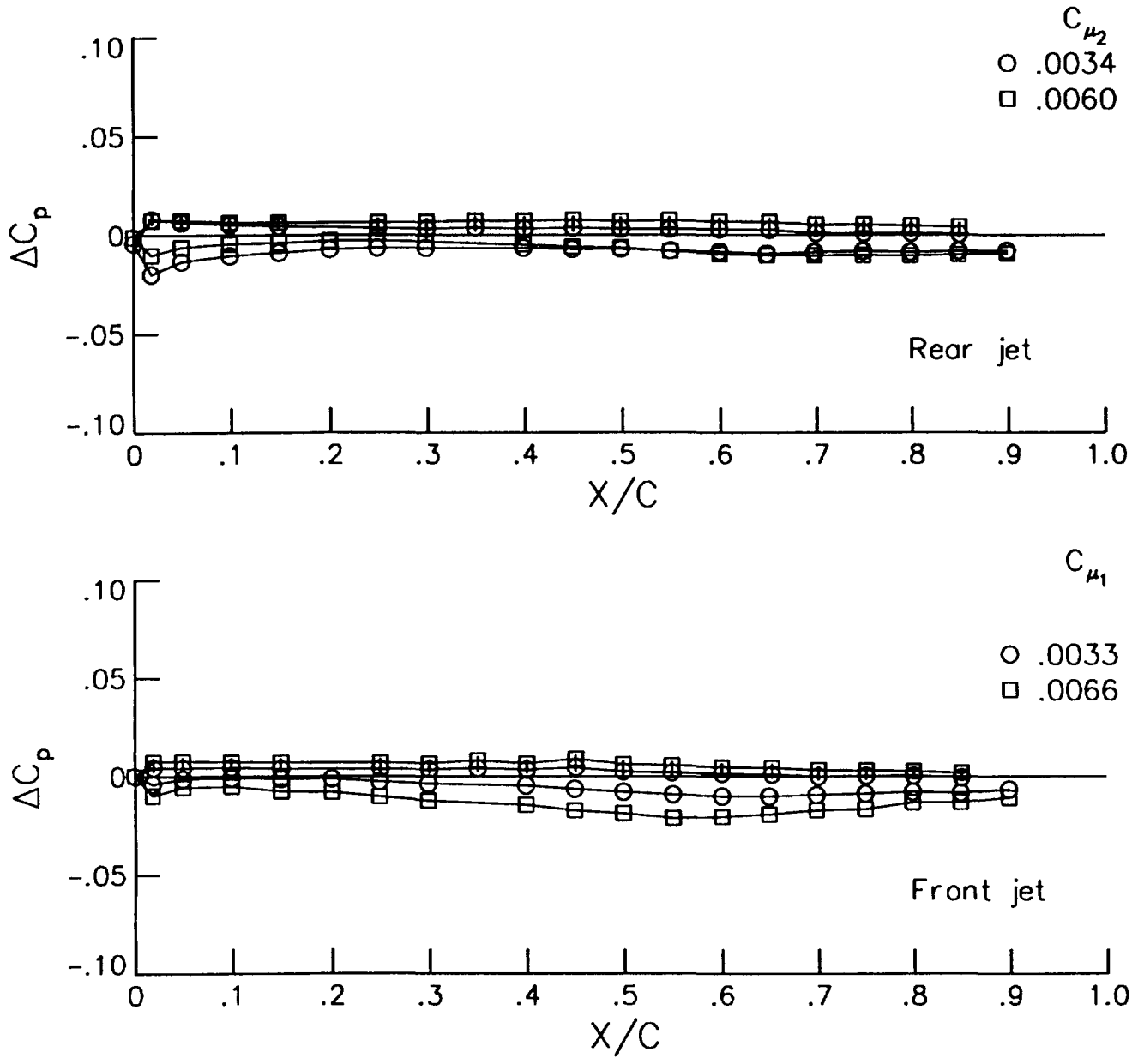

(c) $M_\infty = 0.4$.

Figure 49. Continued.

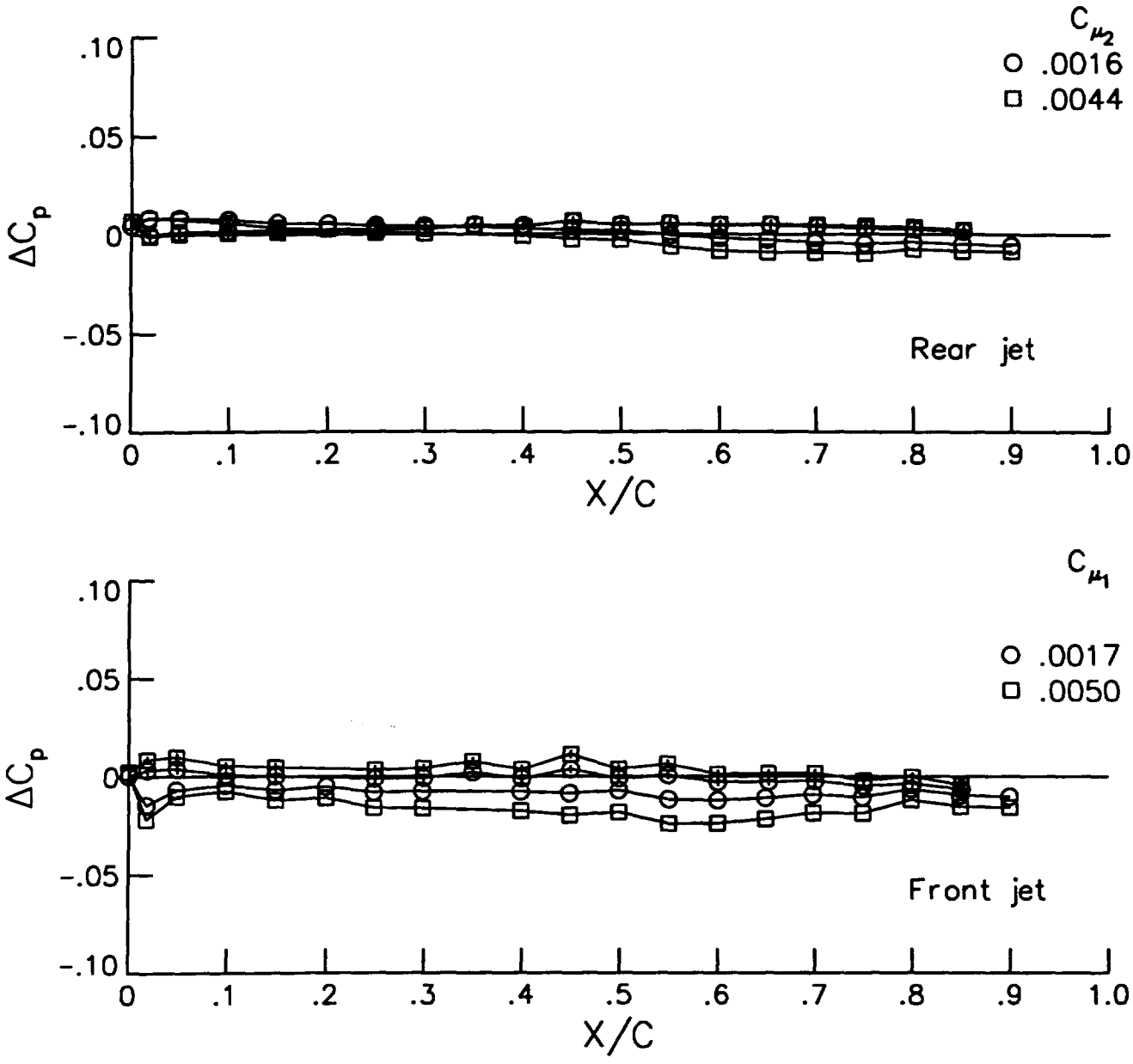

(d) $M_\infty = 0.5$.

Figure 49. Concluded.

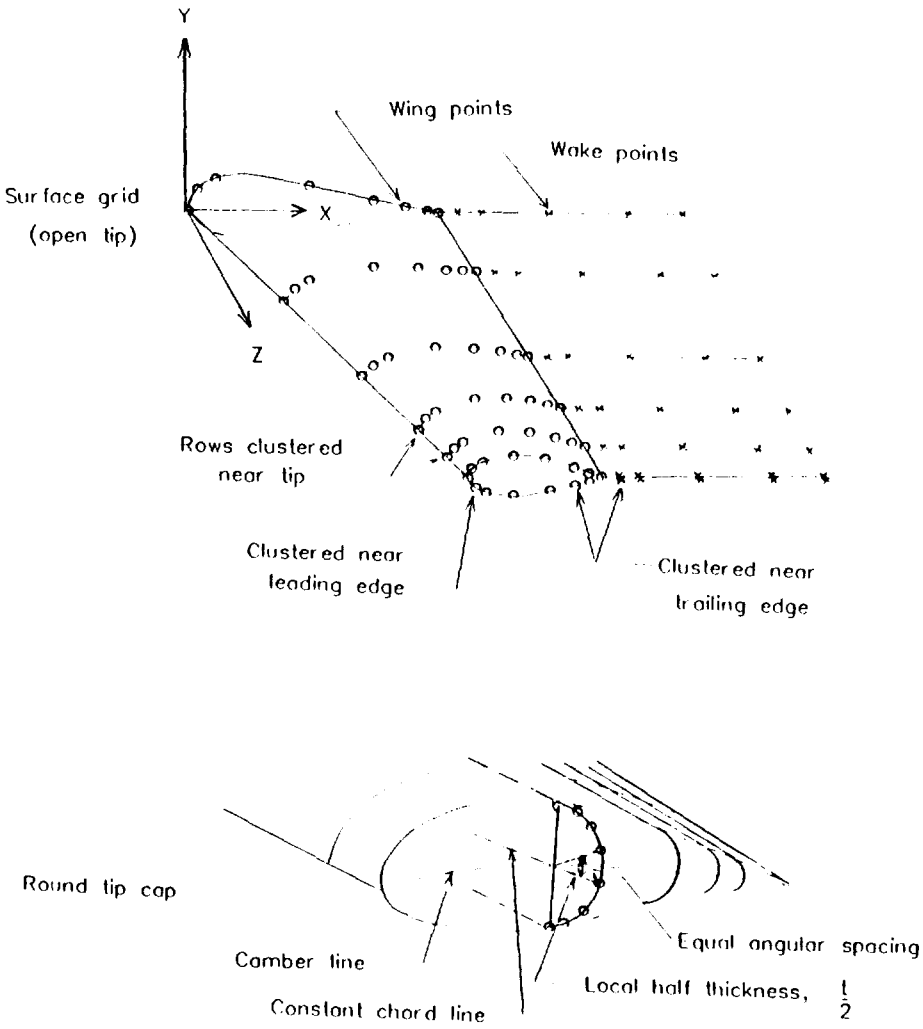

(a) Surface grid.

Figure 50. Sketches of steps used to generate the grid.

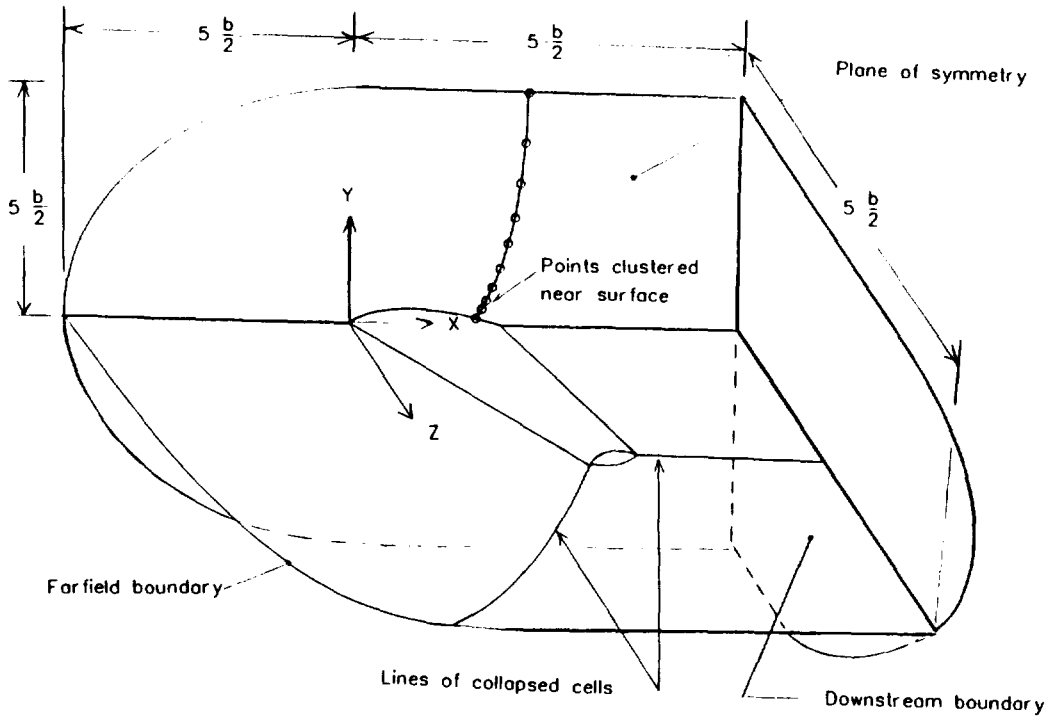

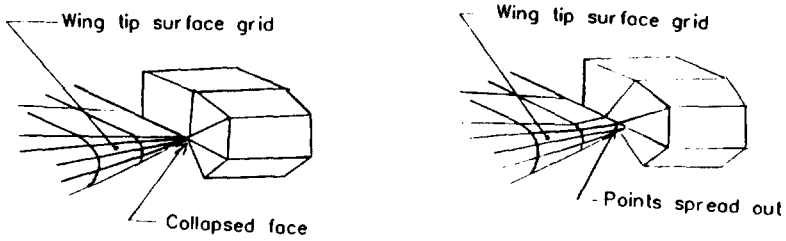

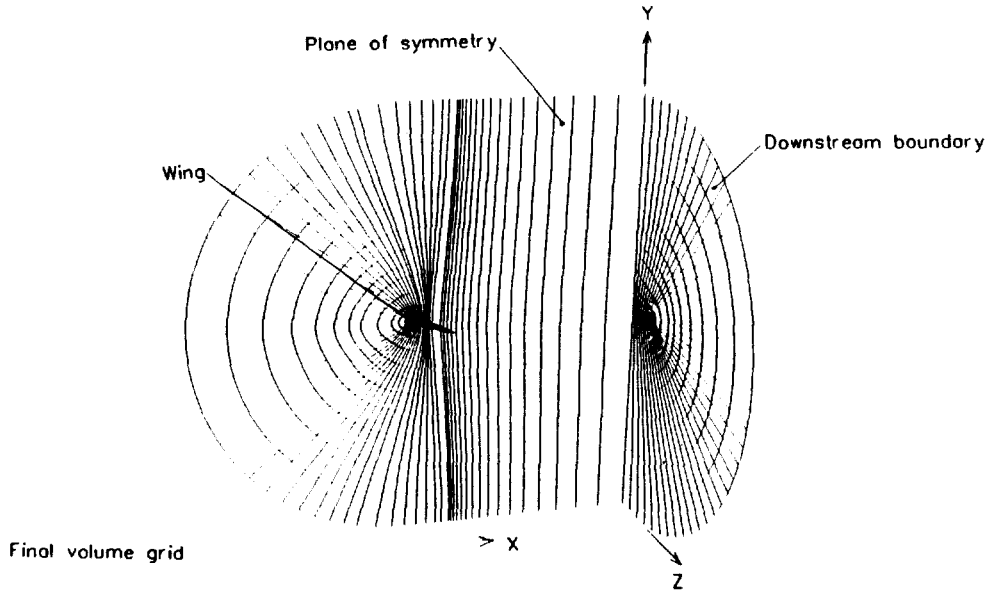

(b) Volume grid.

Figure 50. Concluded.

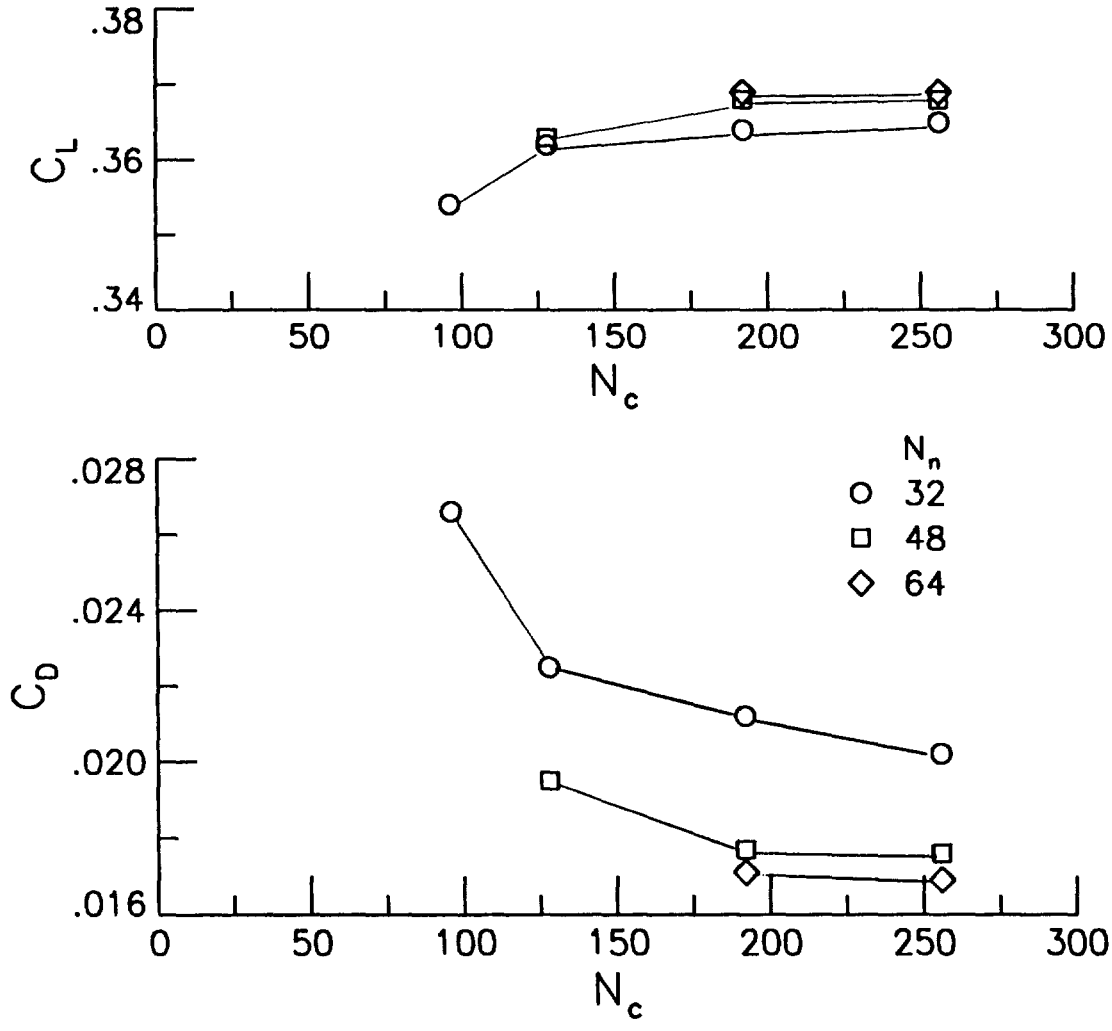

(a) Effect of number of chordwise cells.

Figure 51. Variation of the computed lift and drag with the number of grid cells.

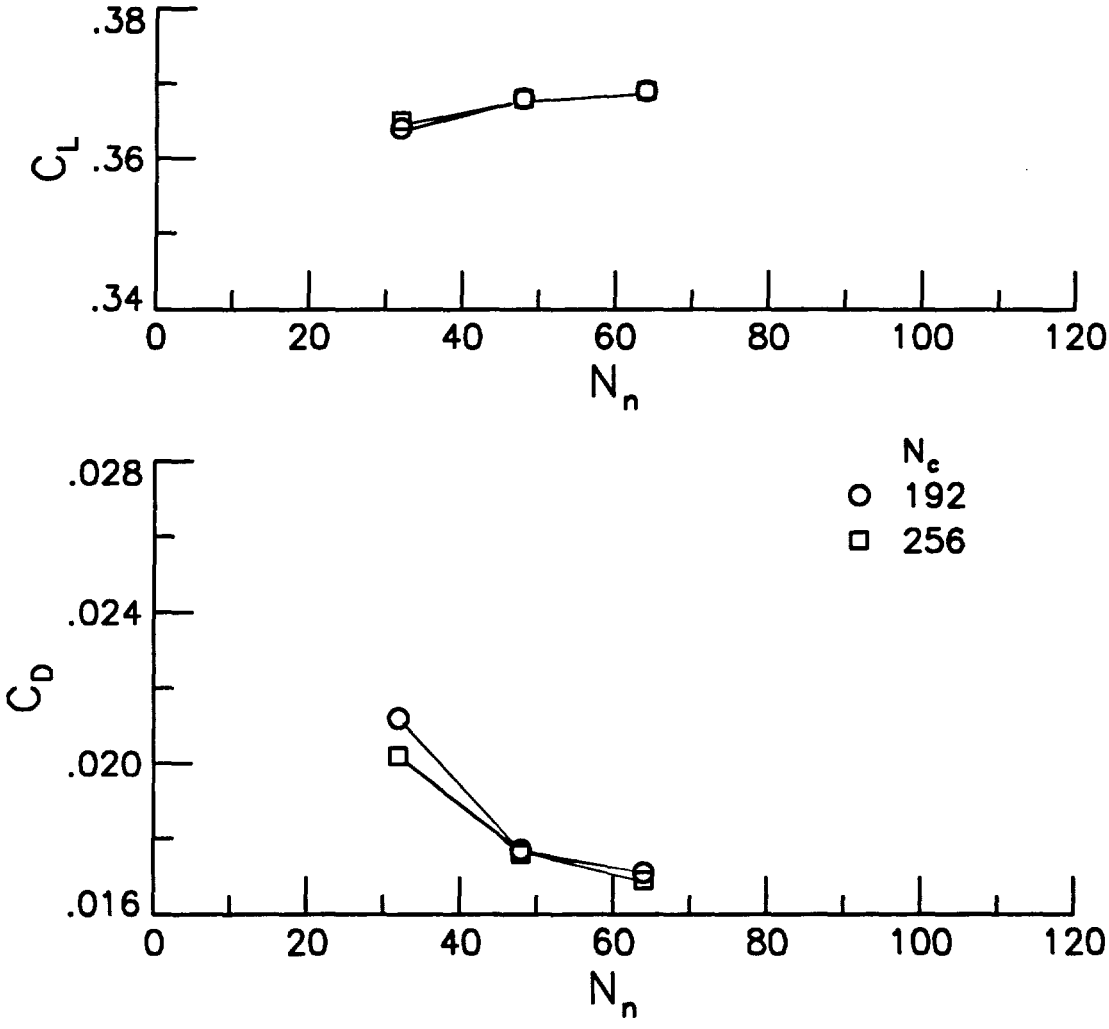

(b) Effect of number of normal cells.

Figure 51. Continued.

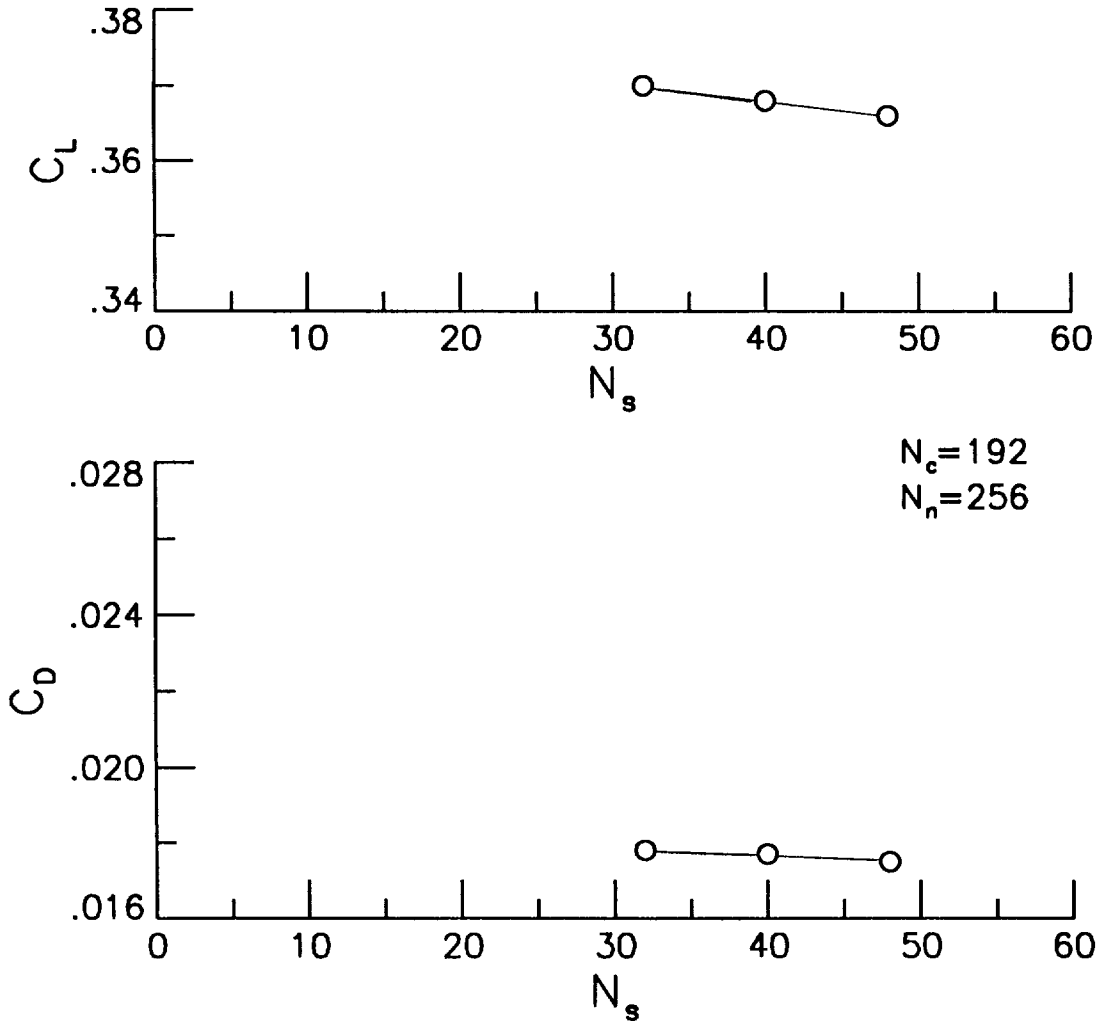

(c) Effect of number of spanwise cells.

Figure 51. Concluded.

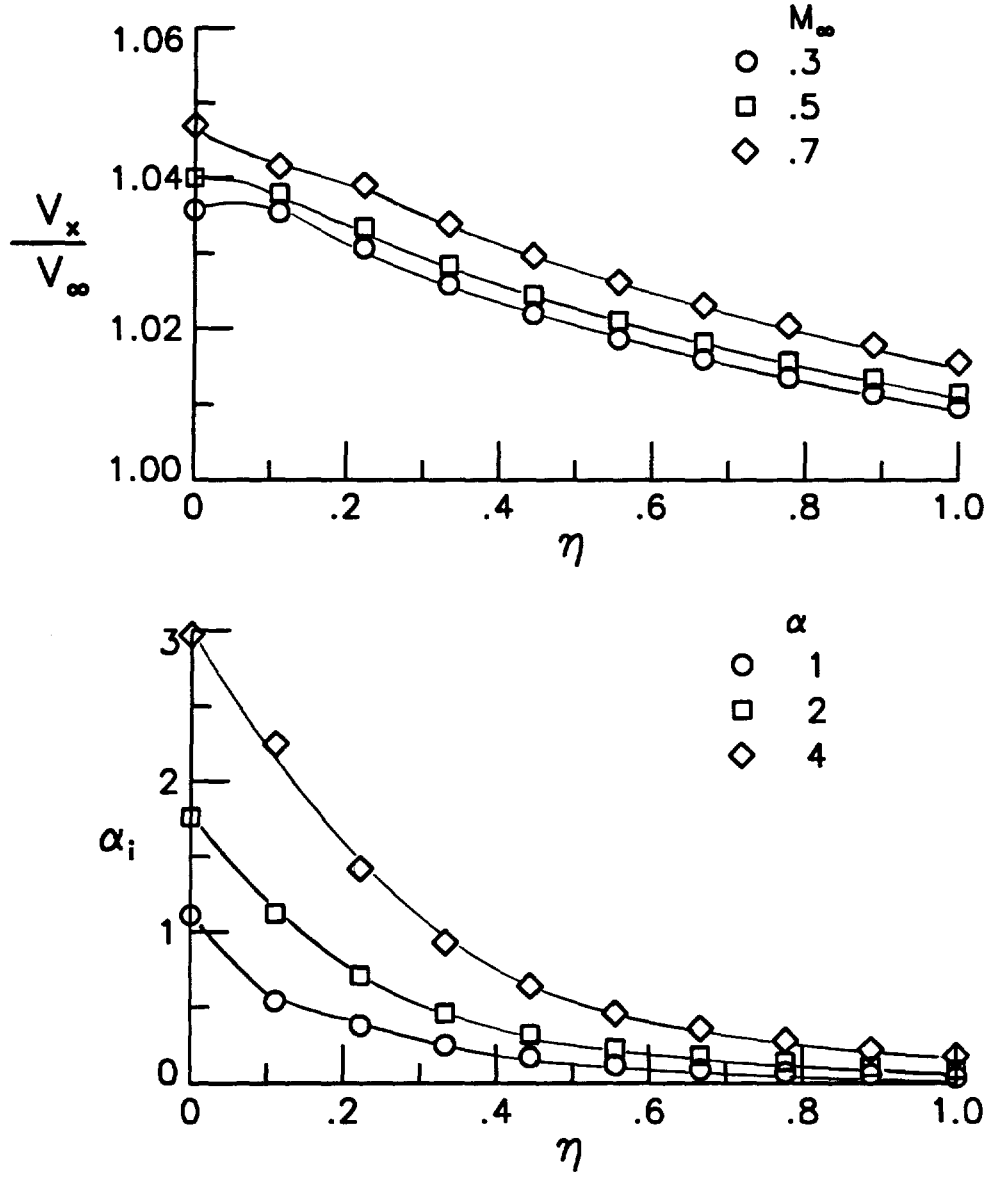

Figure 52. Effect of the body on the flow magnitude and direction along the wing quarter chord line.

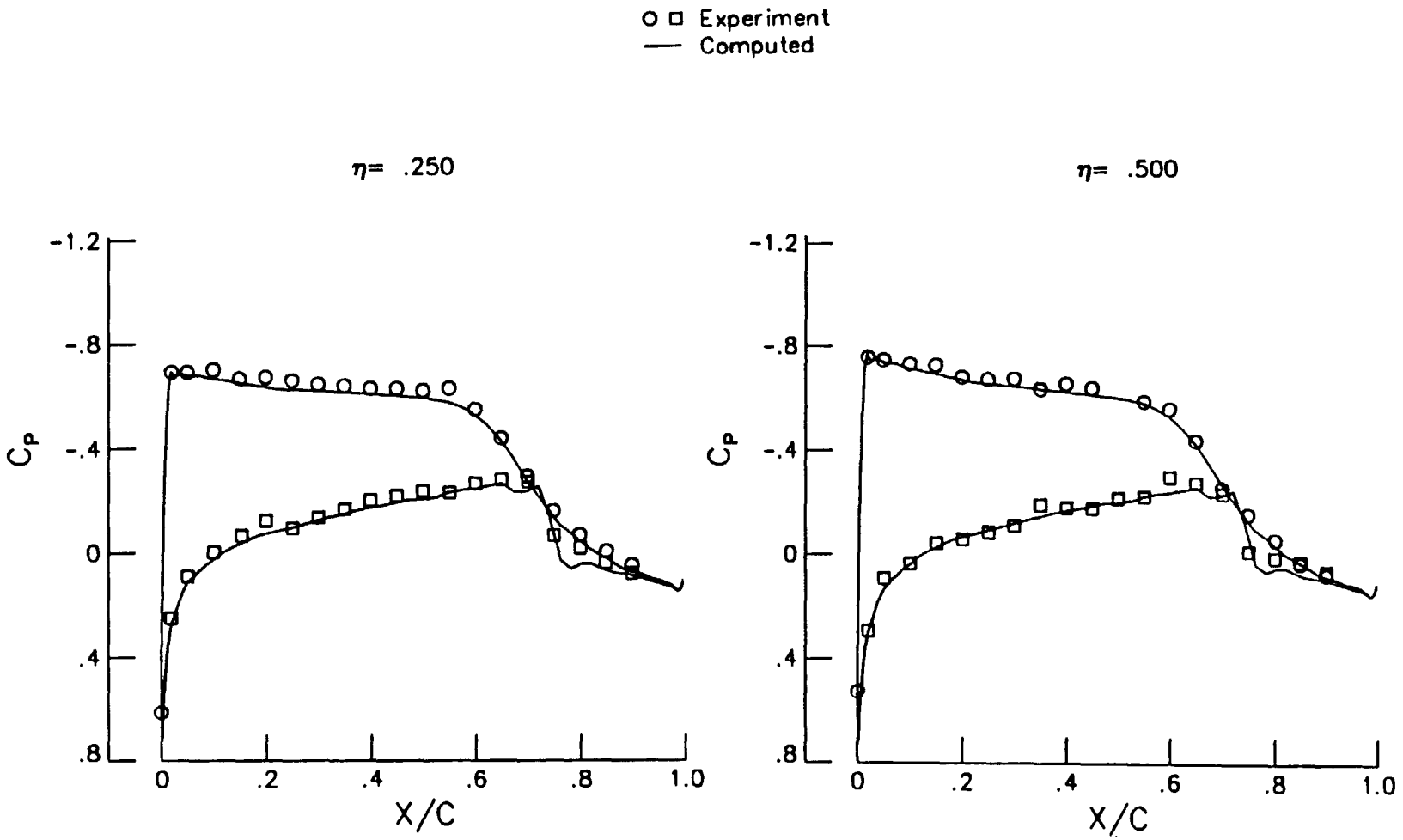

Figure 53. Comparison of experimental and computed chordwise pressure distributions at several spanwise stations. $M_\infty = 0.306$. $\alpha = 2.07°$.

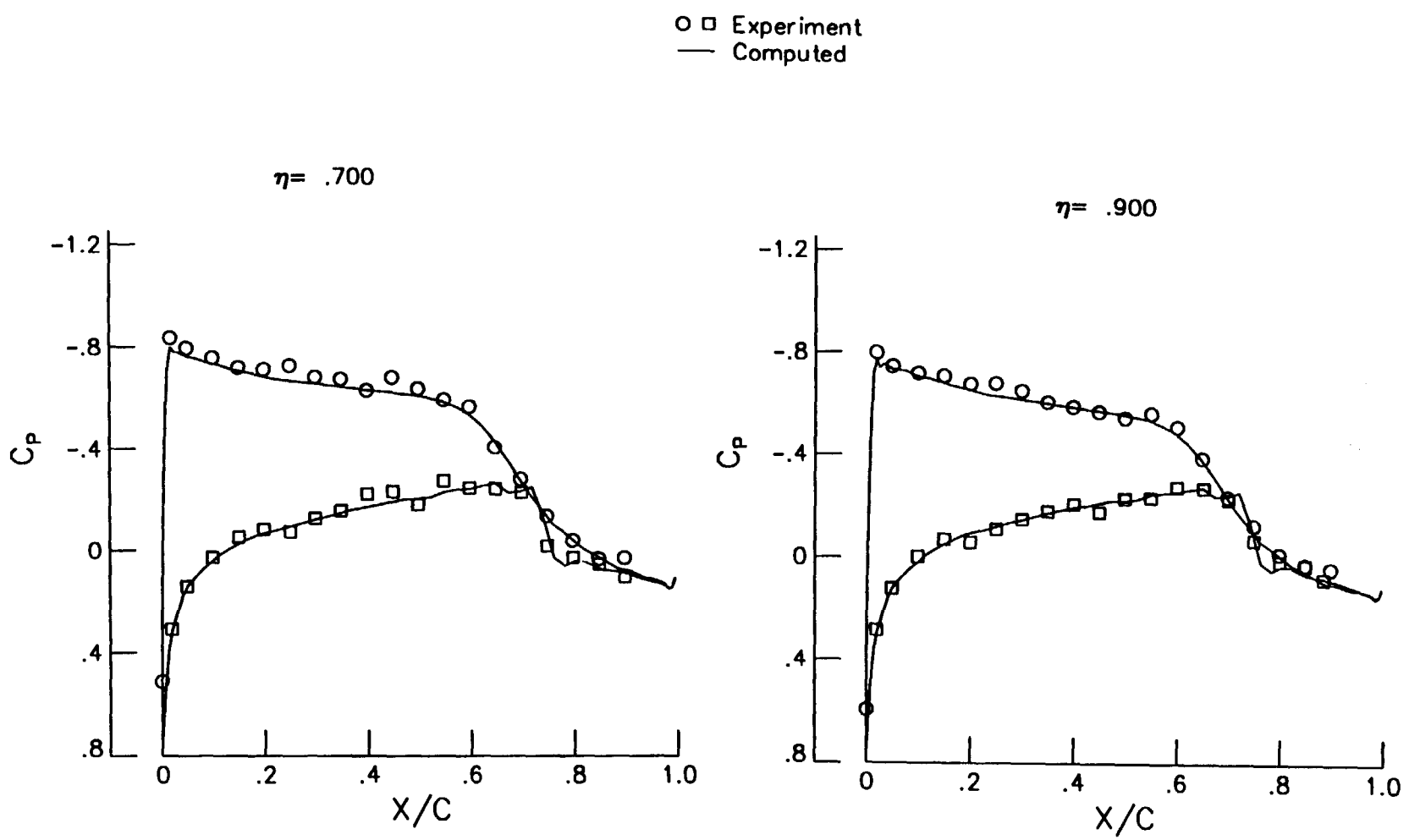

Figure 53. Concluded.

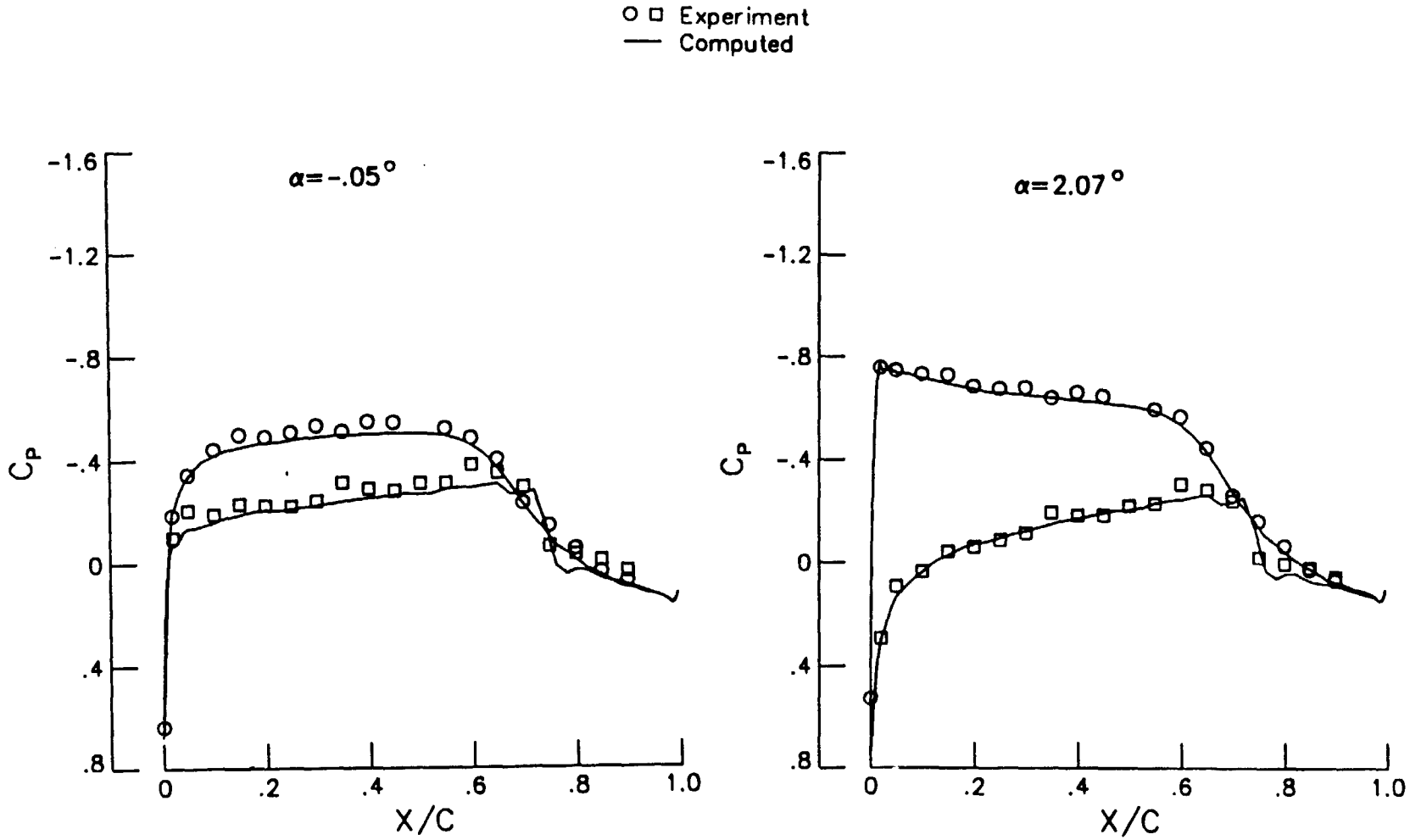

Figure 54. Comparison of experimental and computed chordwise pressure distributions at several angles of attack. $M_\infty = 0.306$. $\eta = 0.50$.

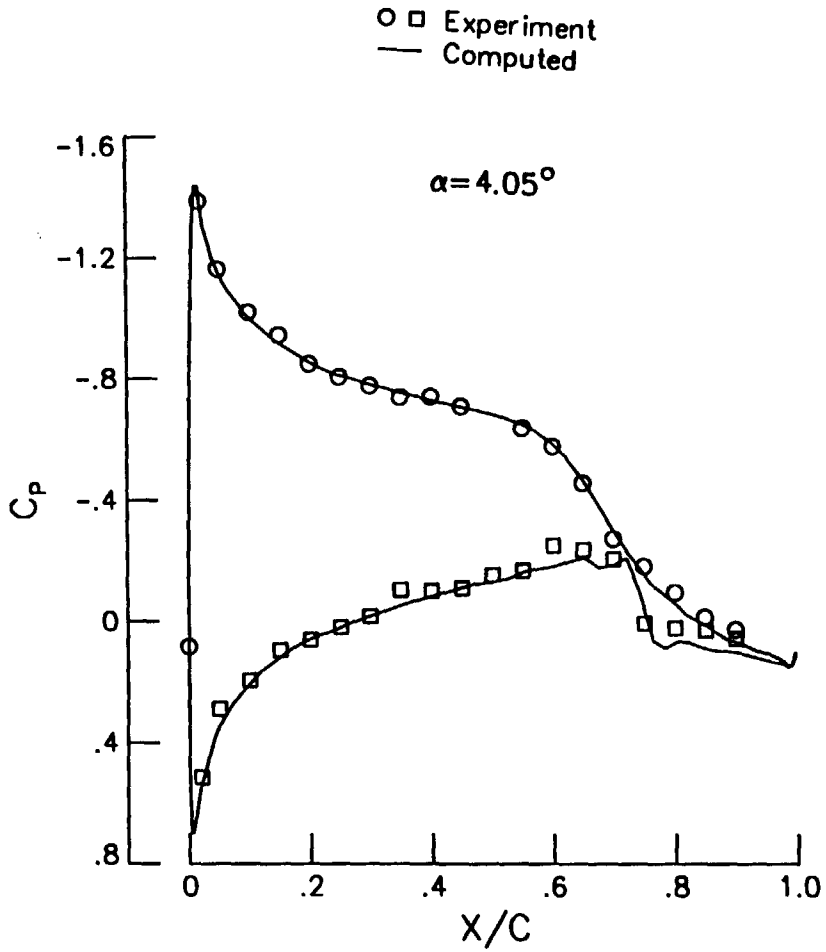

Figure 54. Concluded.

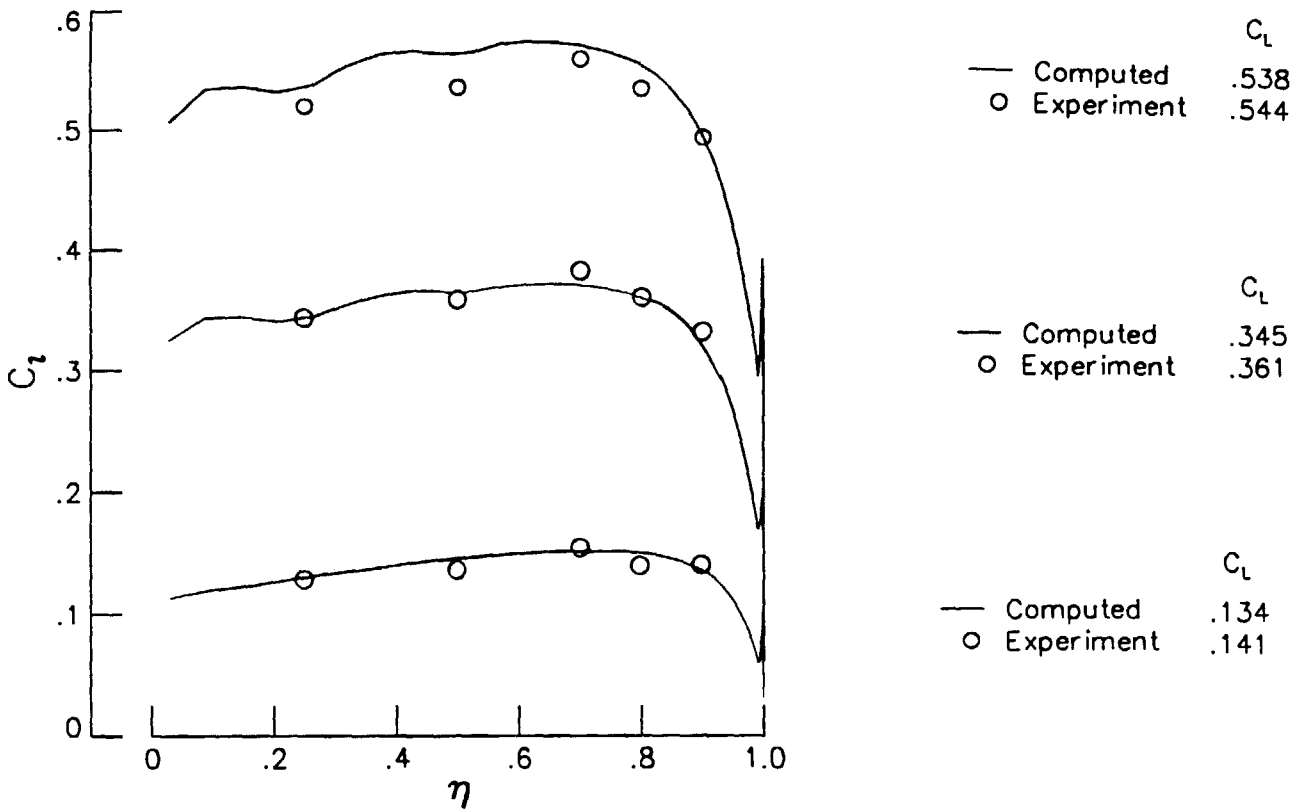

Figure 55. Comparison of experimental and computed spanload distributions at several angles of attack. $M_\infty = 0.306$.

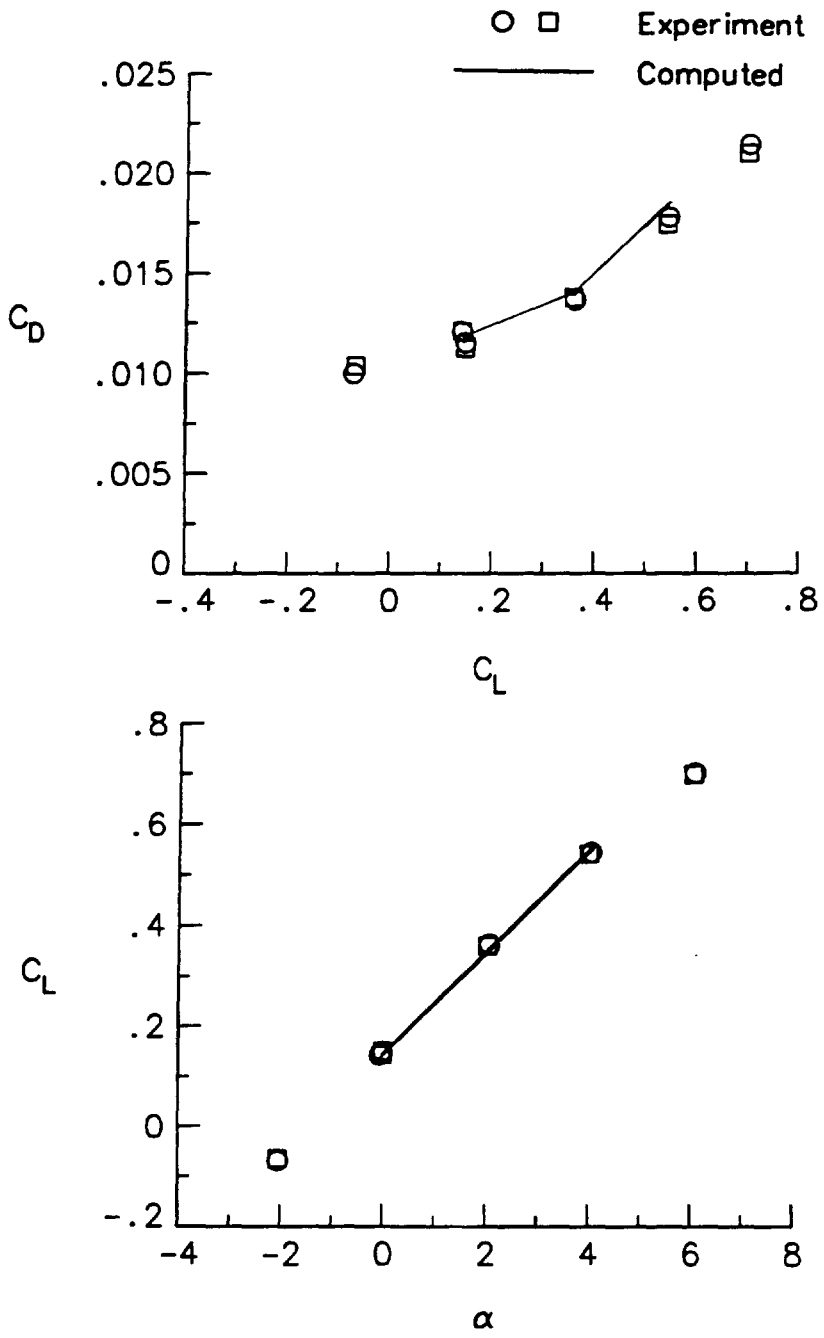

Figure 56. Comparison of experimental and computed lift and drag coefficients. $M_\infty = 0.306$.

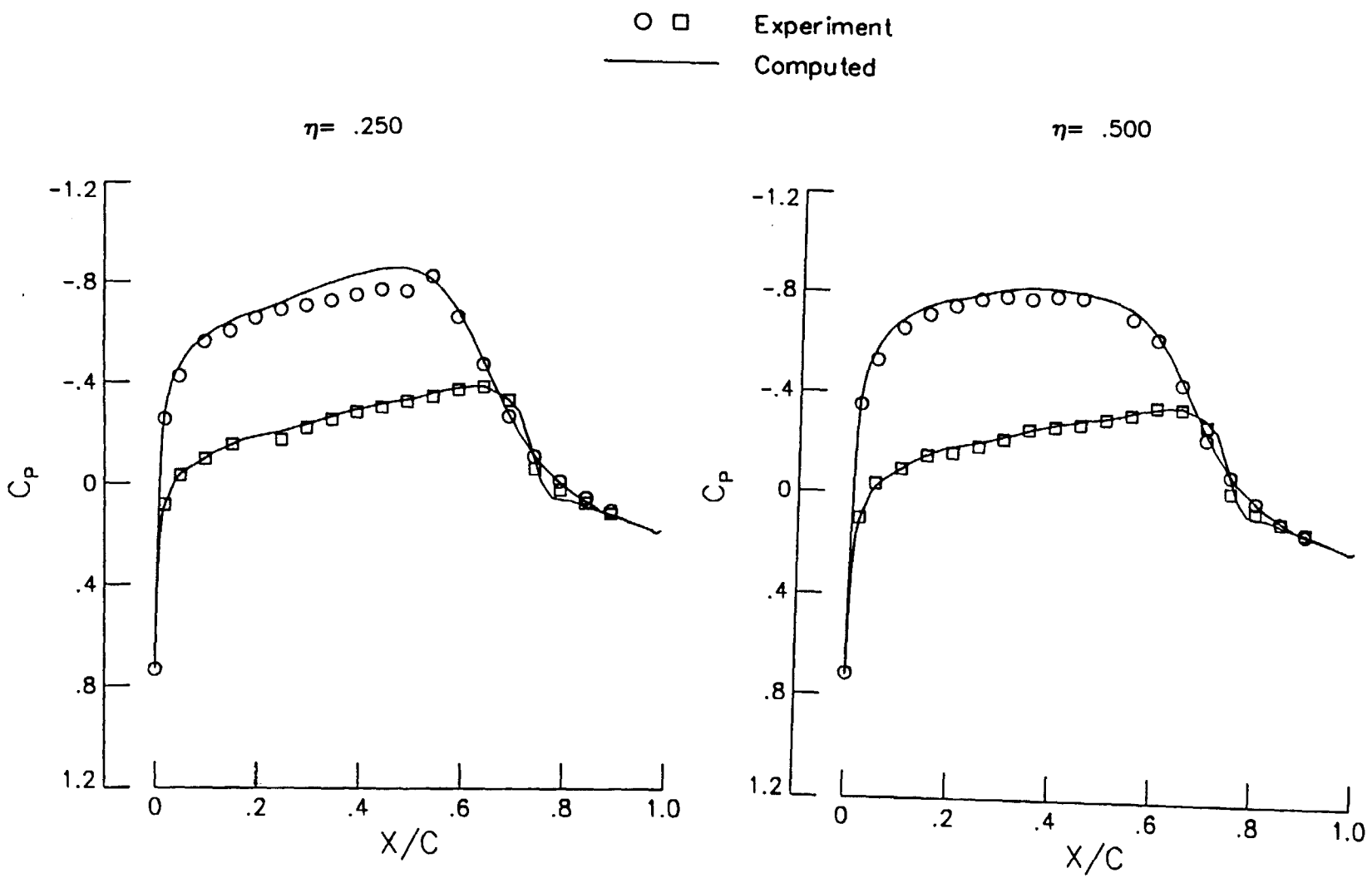

Figure 57. Comparison of experimental and computed chordwise pressure distributions at several spanwise stations. $M_\infty = 0.719$. $\alpha = 0.95°$.

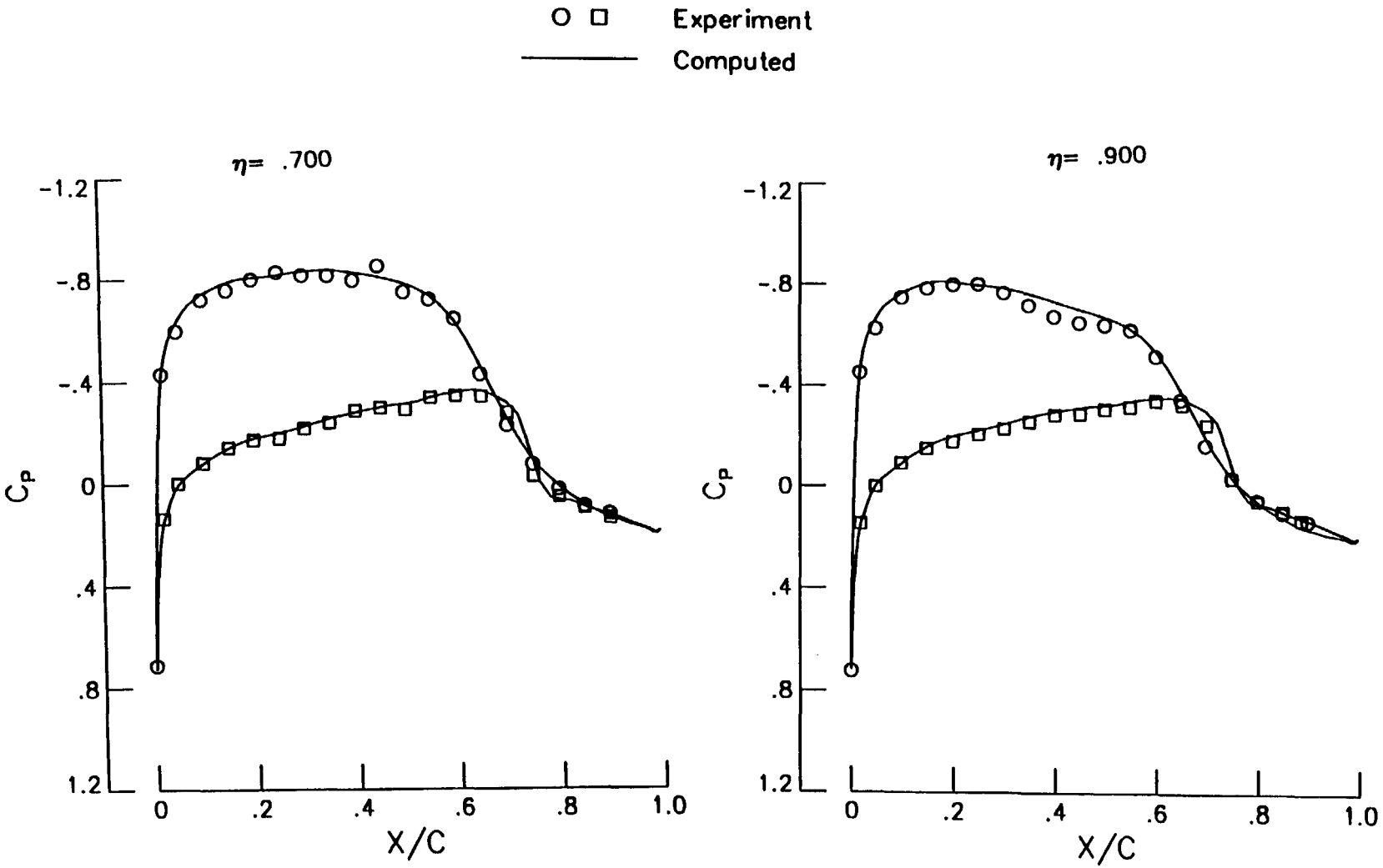

Figure 57. Concluded.

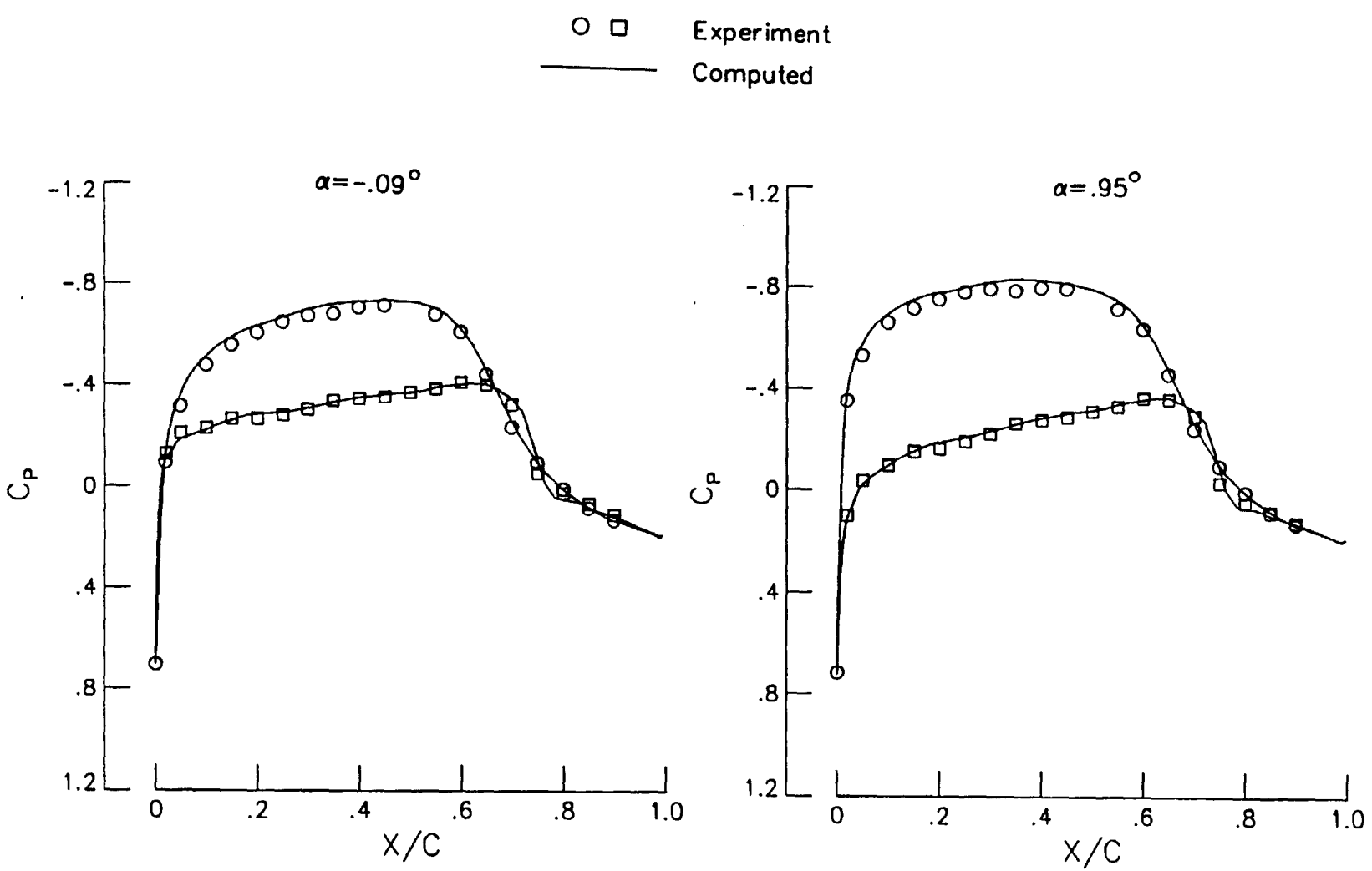

Figure 58. Comparison of experimental and computed chordwise pressure distributions at several angles of attack. $M_\infty = 0.719$. $\eta = 0.50$.

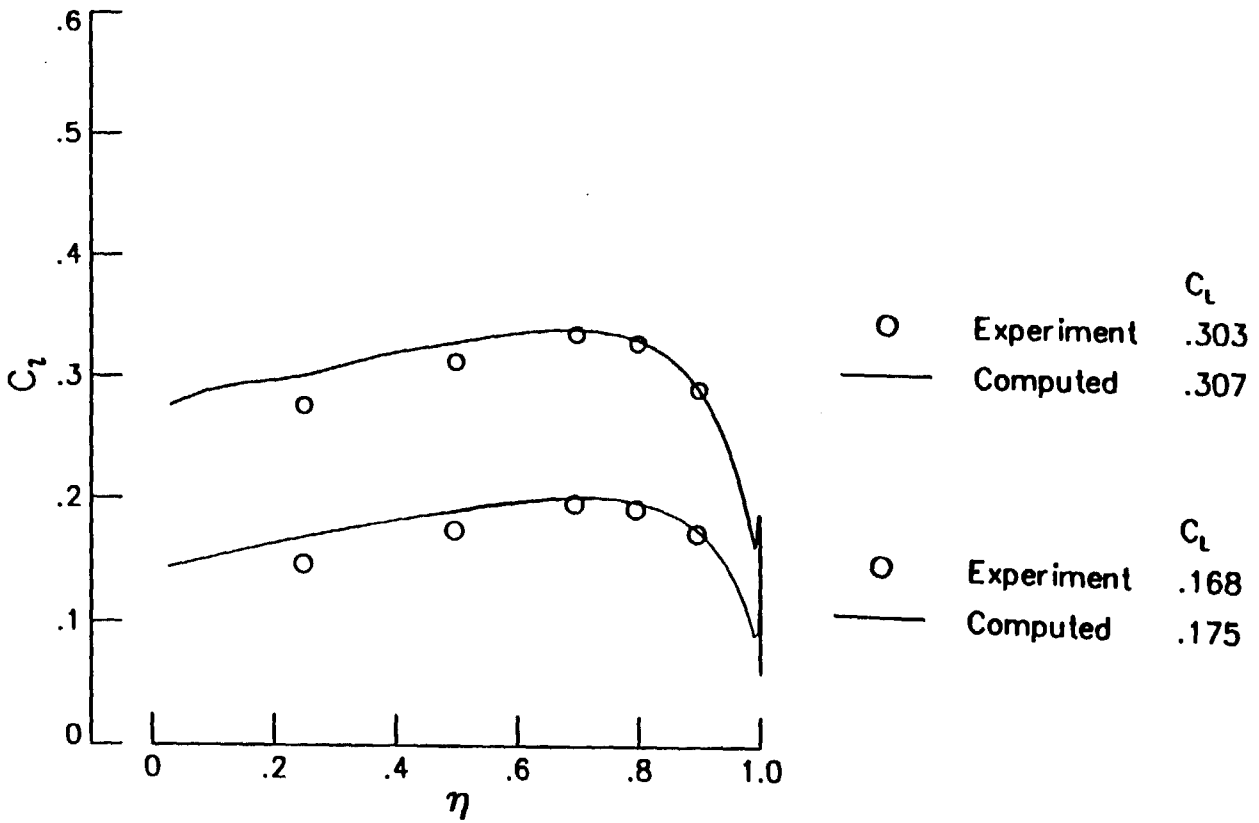

Figure 59. Comparison of experimental and computed spanload distributions at several angles of attack. $M_\infty = 0.719$.

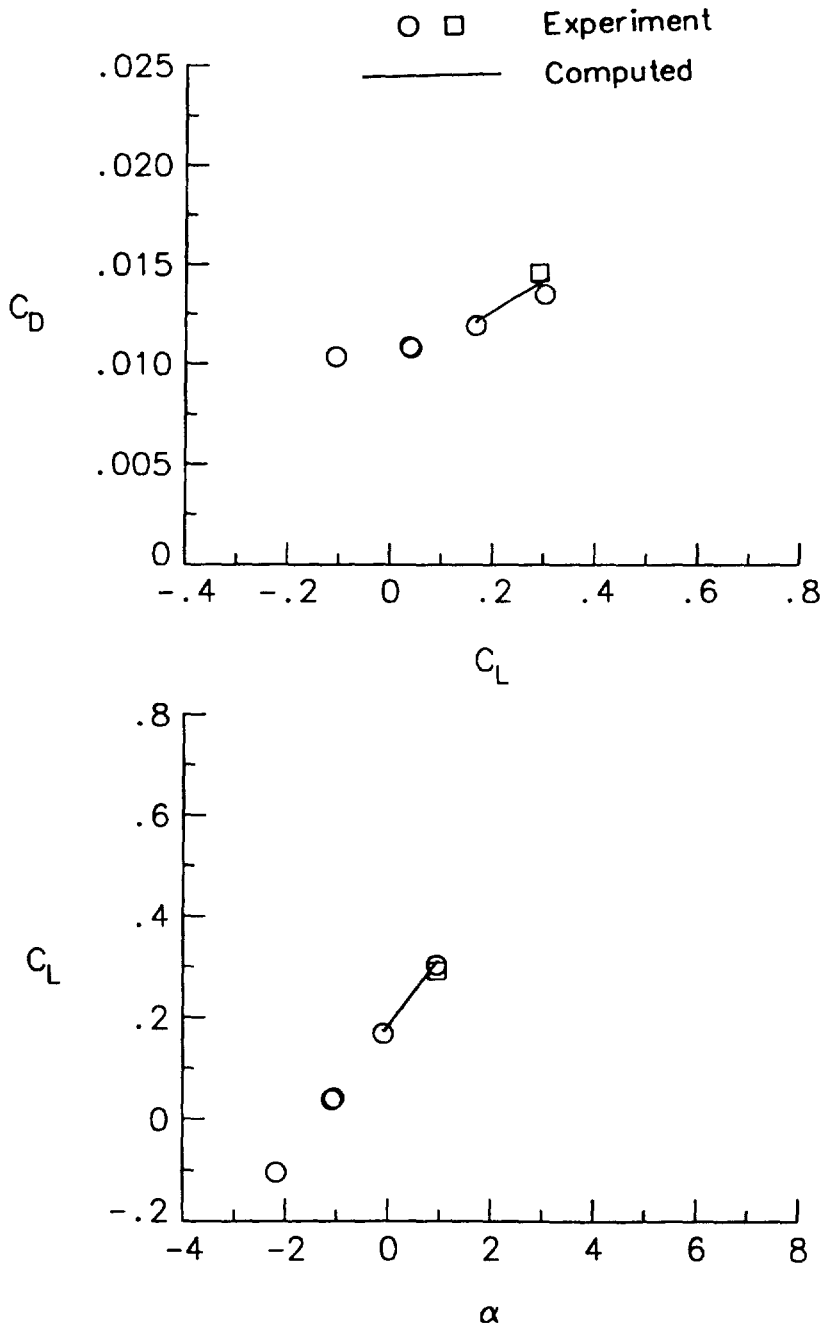

Figure 60. Comparison of experimental and computed lift and drag coefficients. $M_\infty = 0.719$.

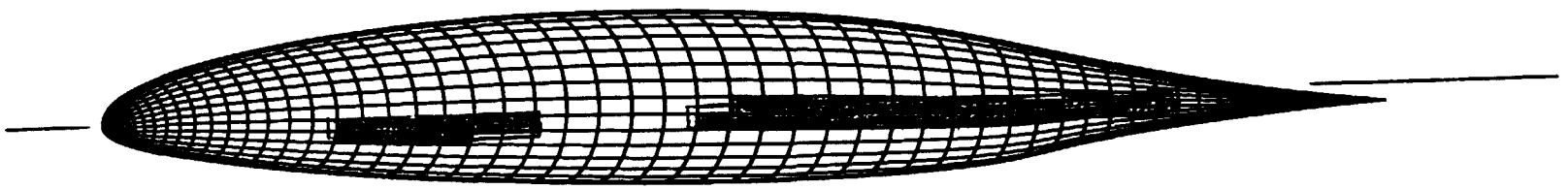

Figure 61. Sketch of the wing tip surface grid.

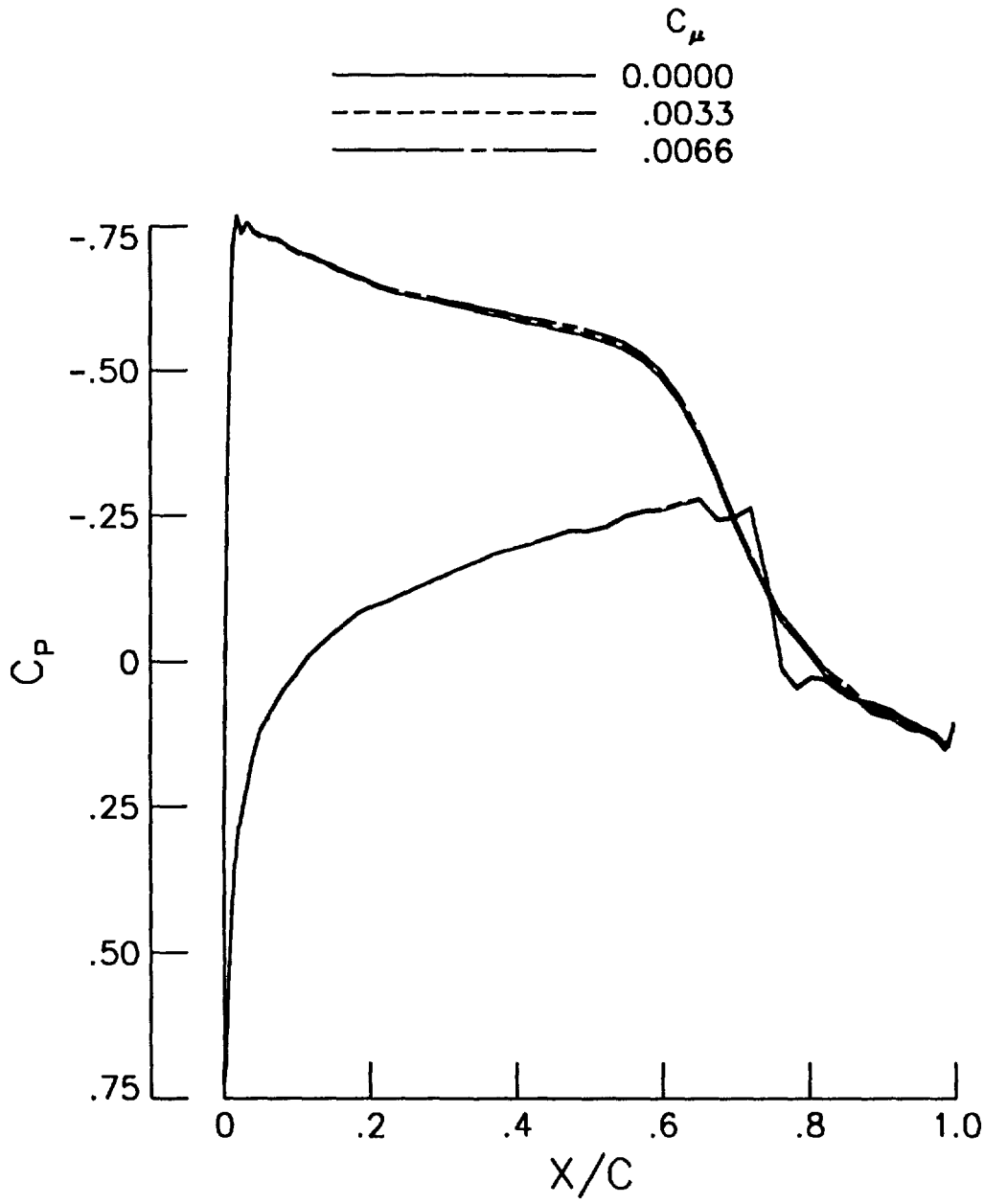

(a) Front jet.

Figure 62. Effect of jet momentum coefficient on the computed chordwise pressure distributions. $M_\infty = 0.307$, $\alpha = 2.07^\circ$, $\eta = 0.90$.

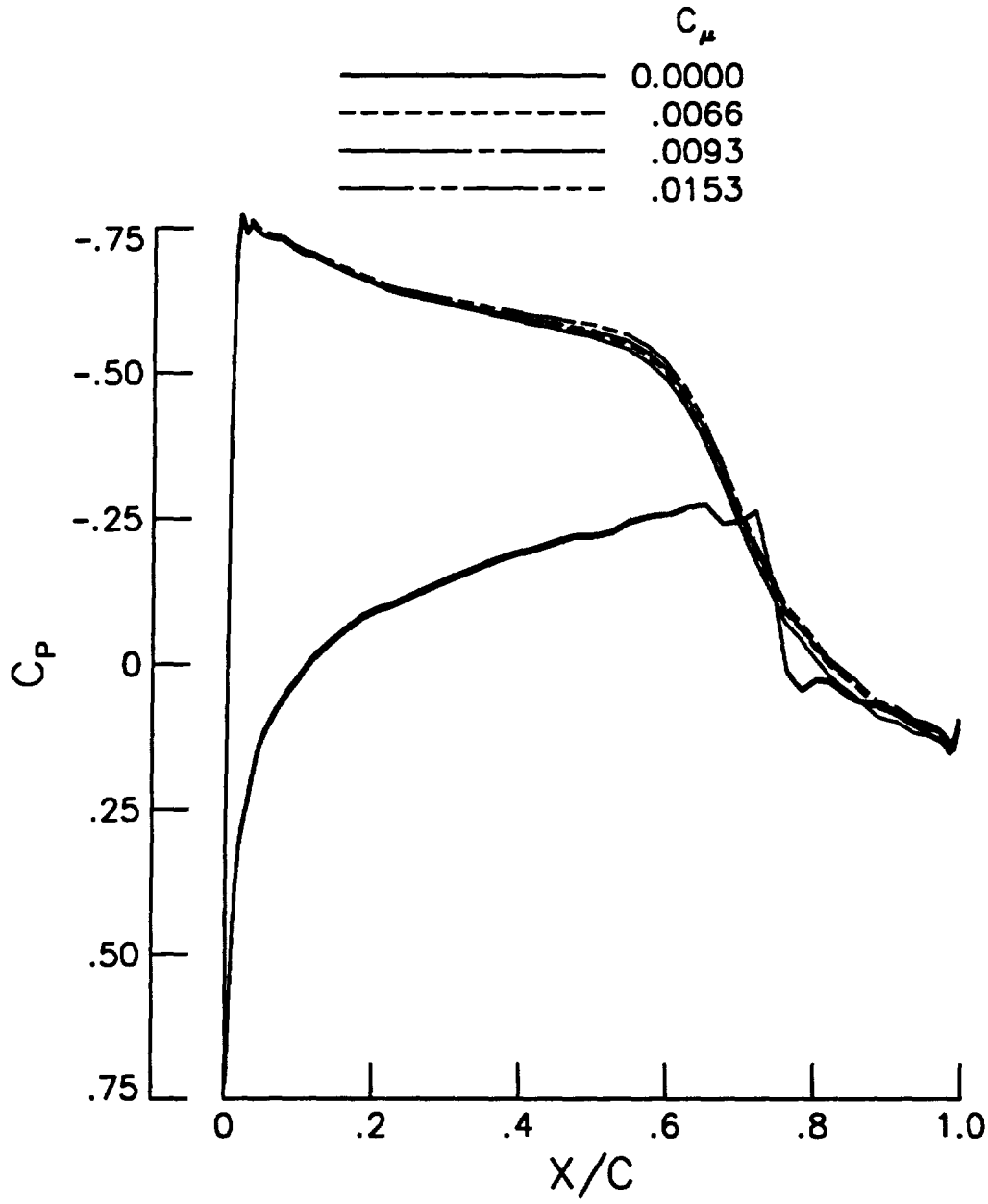

(b) Rear jet.

Figure 62. Concluded.

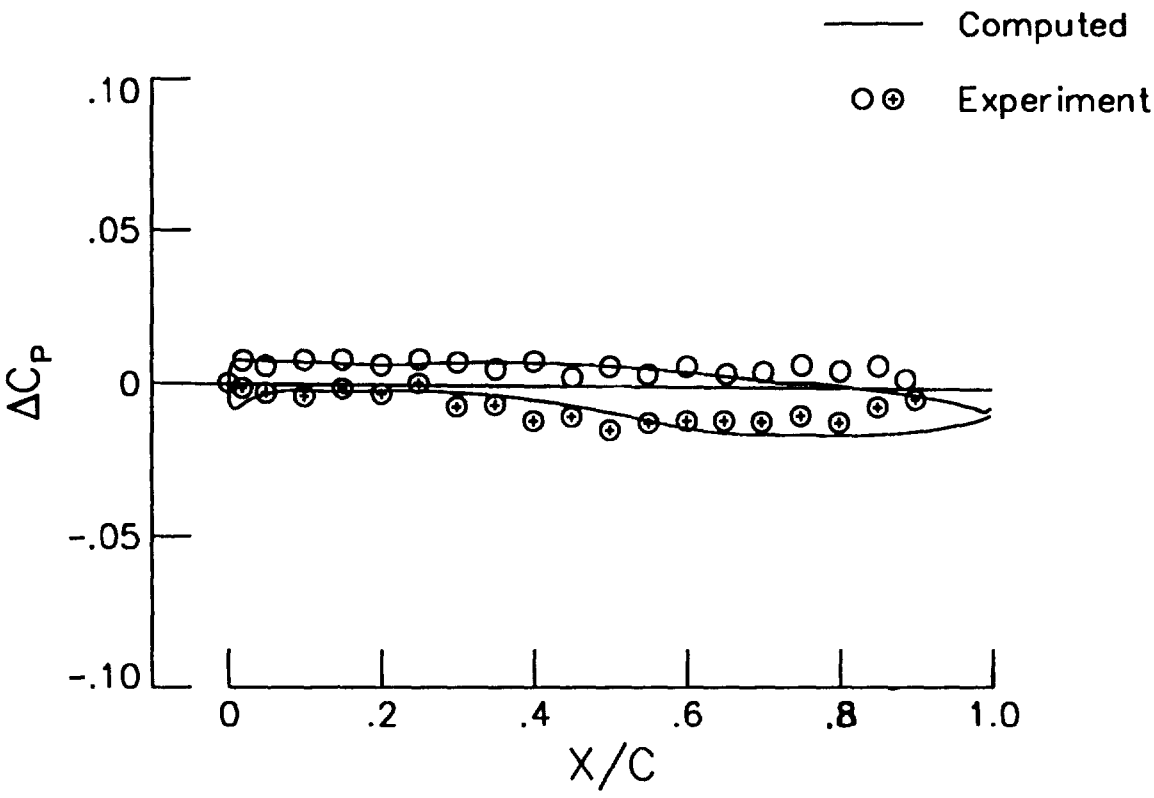

(a) Front jet.

Figure 63. Comparison of experimental and computed changes in the chordwise pressure distributions due to blowing. $M_\infty = 0.307$, $\alpha = 2.07^\circ$, $\eta = 0.90$, $C_\mu = 0.0066$.

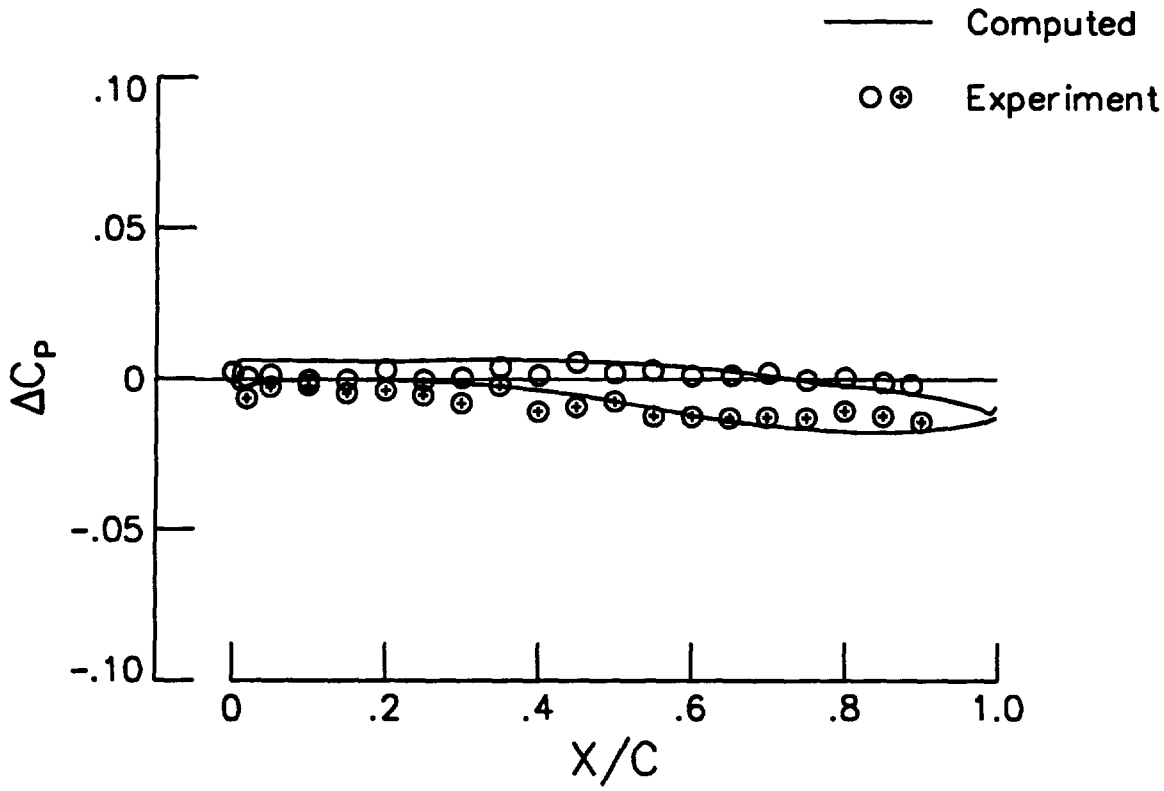

(b) Rear jet.

Figure 63. Concluded.

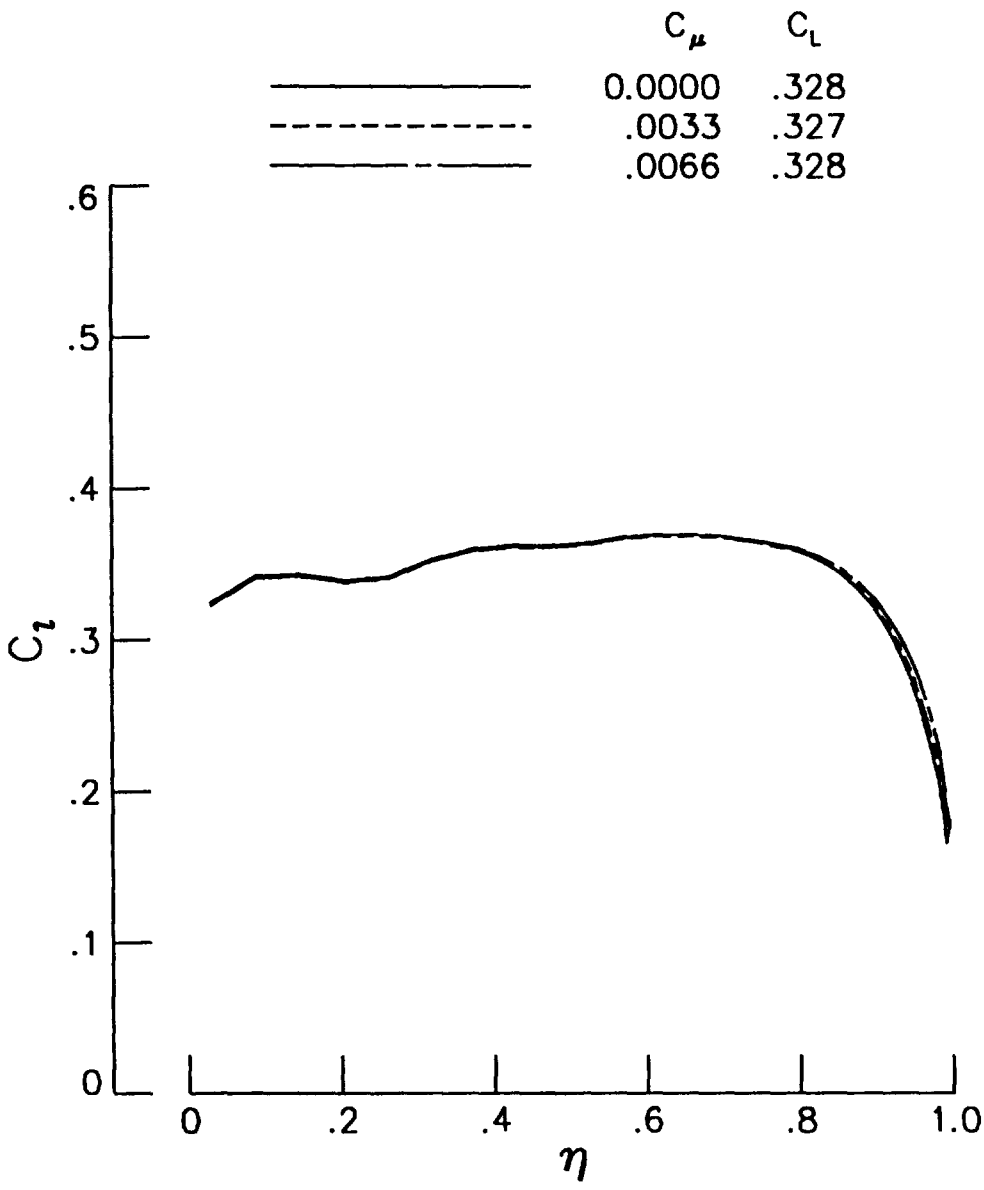

(a) Front jet.

Figure 64. Effect of blowing on the computed span load distributions. M = 0.307, $\alpha = 2.07^{\circ}$.

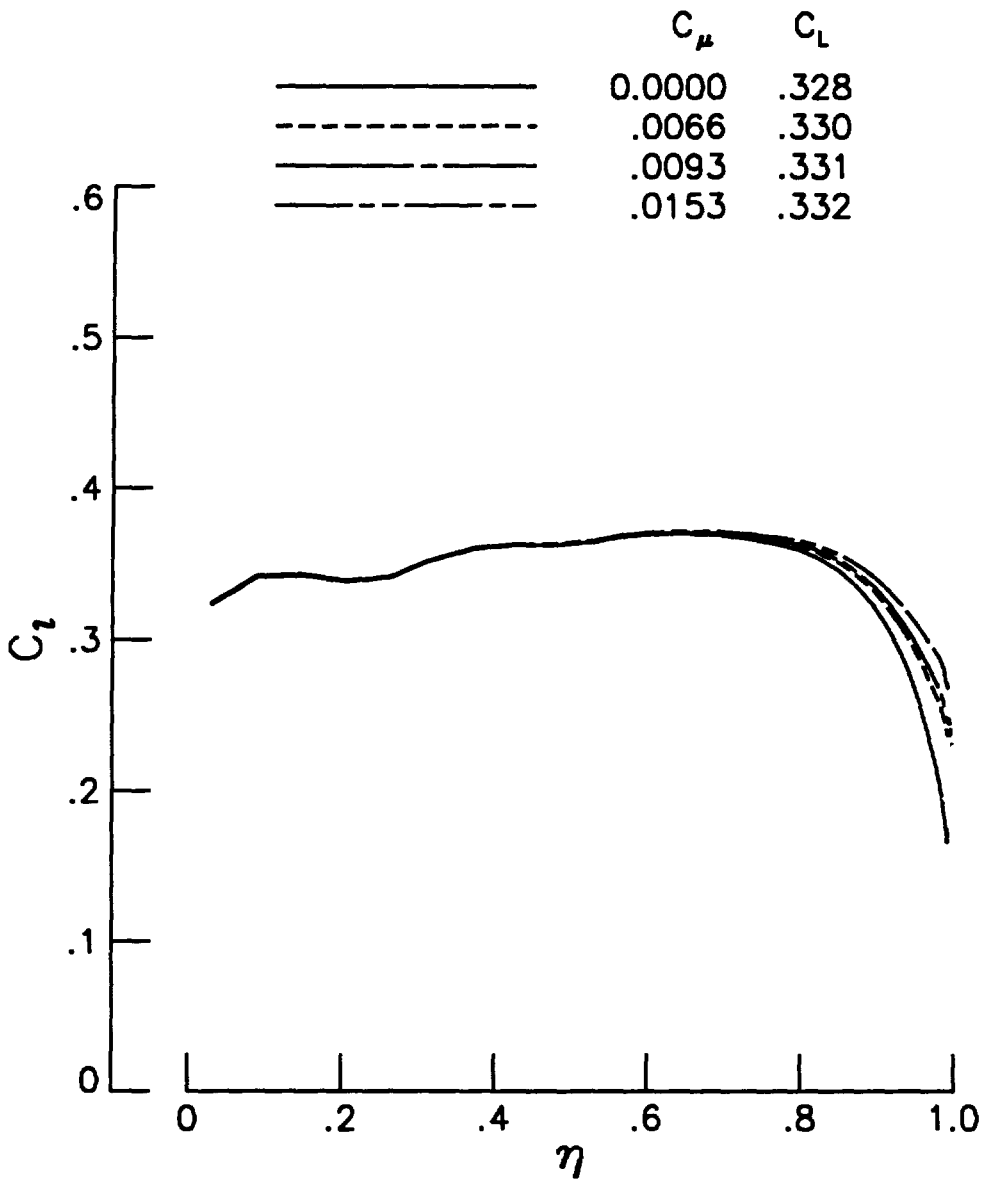

(b) Rear jet.

Figure 64. Concluded.

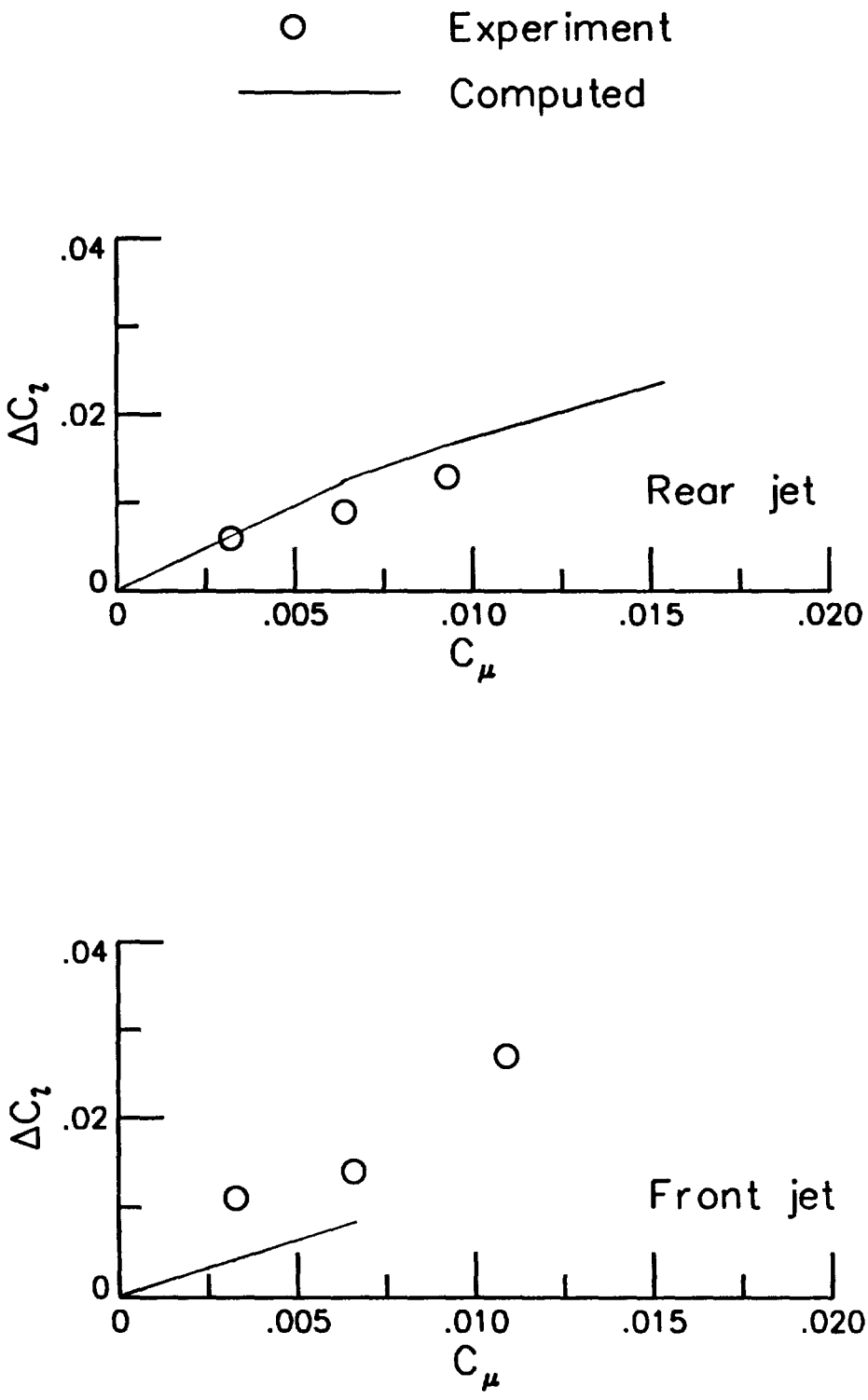

Figure 65. Comparison of the experimental and computed change in the section lift coefficient at $\eta = 0.90$ with blowing. $M_\infty = 0.307$, $\alpha = 2.07^\circ$.

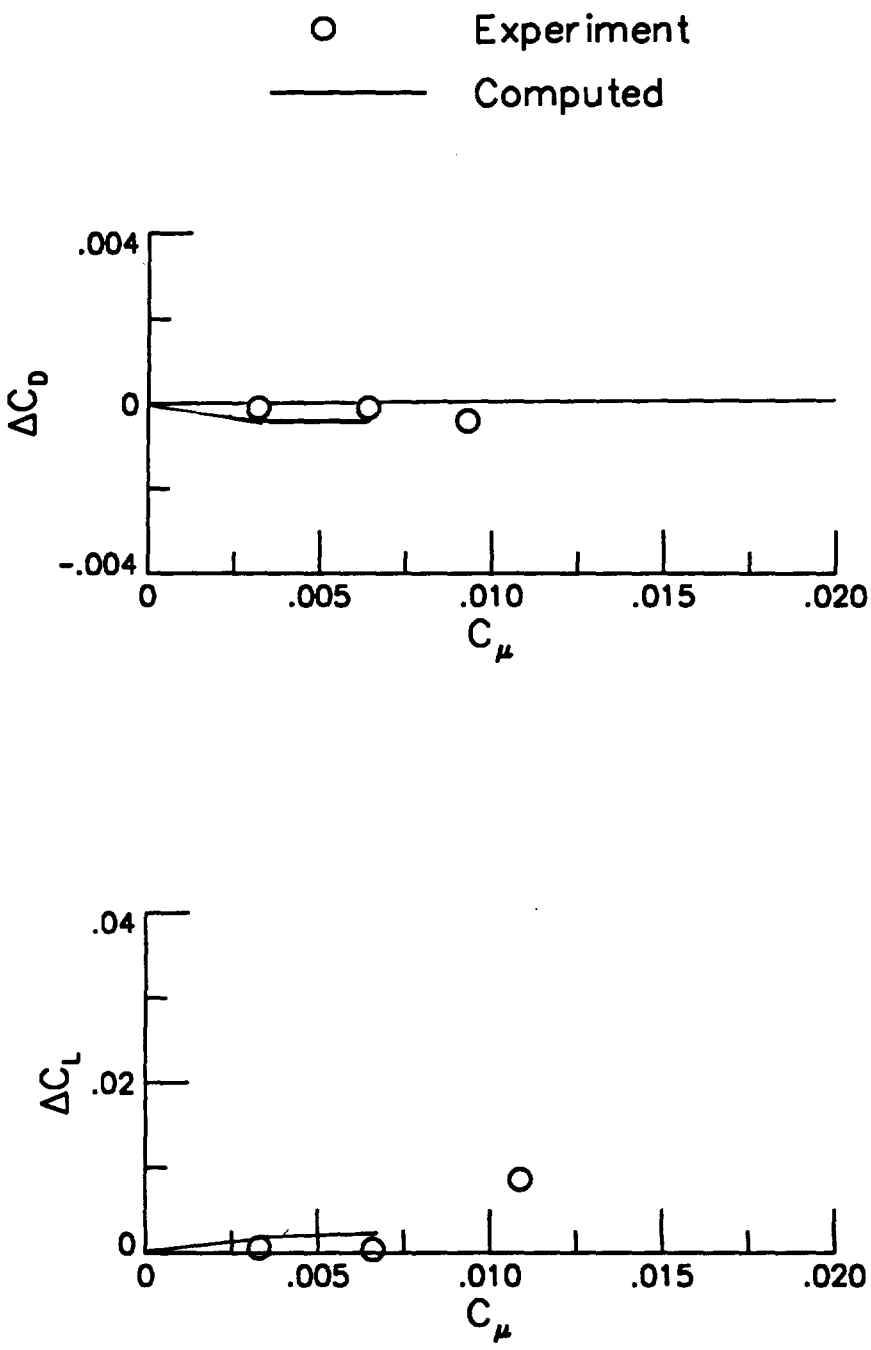

(a) Front jet.

Figure 66. Comparison of the experimental and computed change in wing lift and drag coefficients with blowing. $M_\infty = 0.307$, $\alpha = 2.07°$.

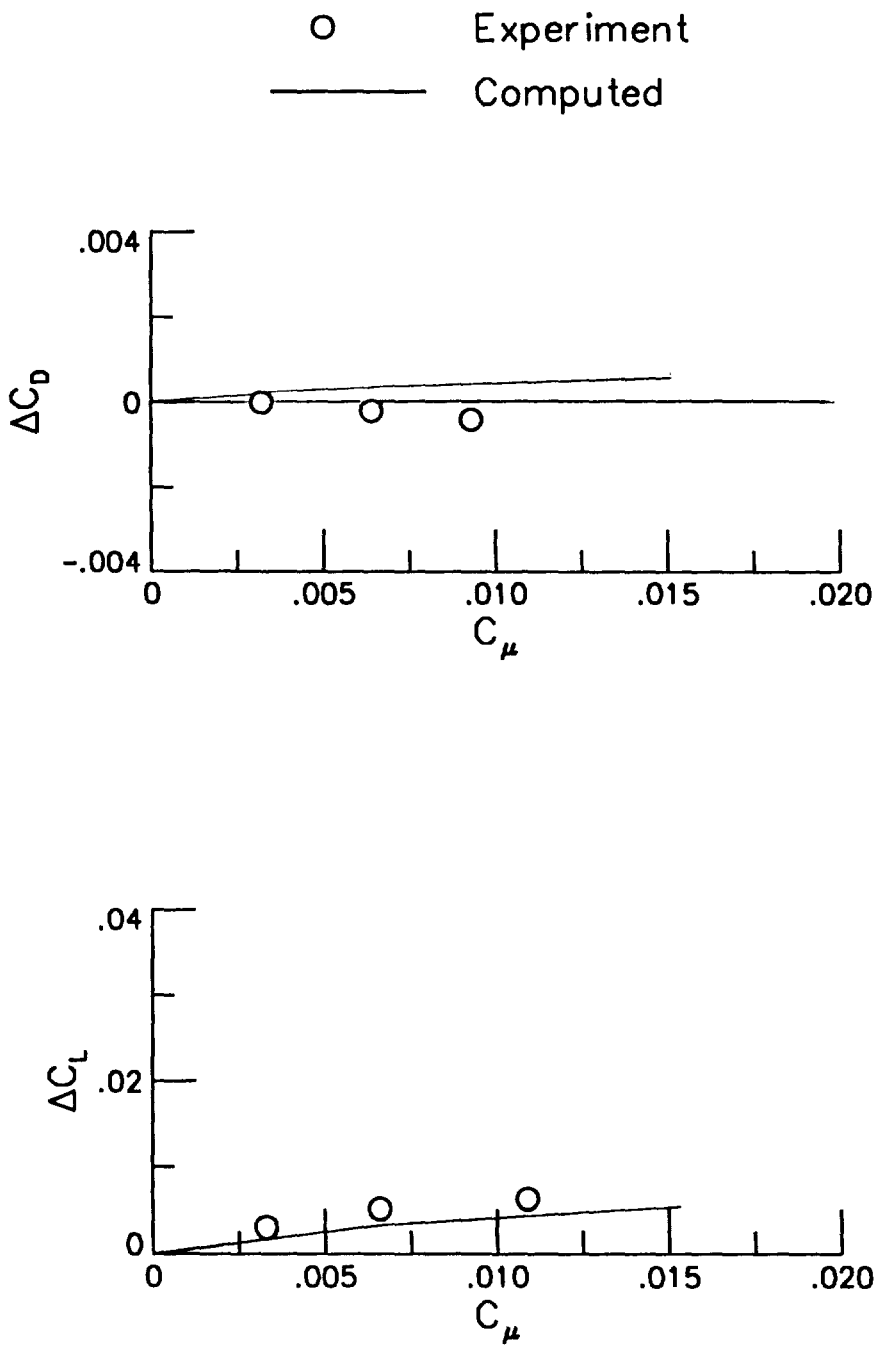

(b) Rear jet.

Figure 66. Concluded.

Water tunnel

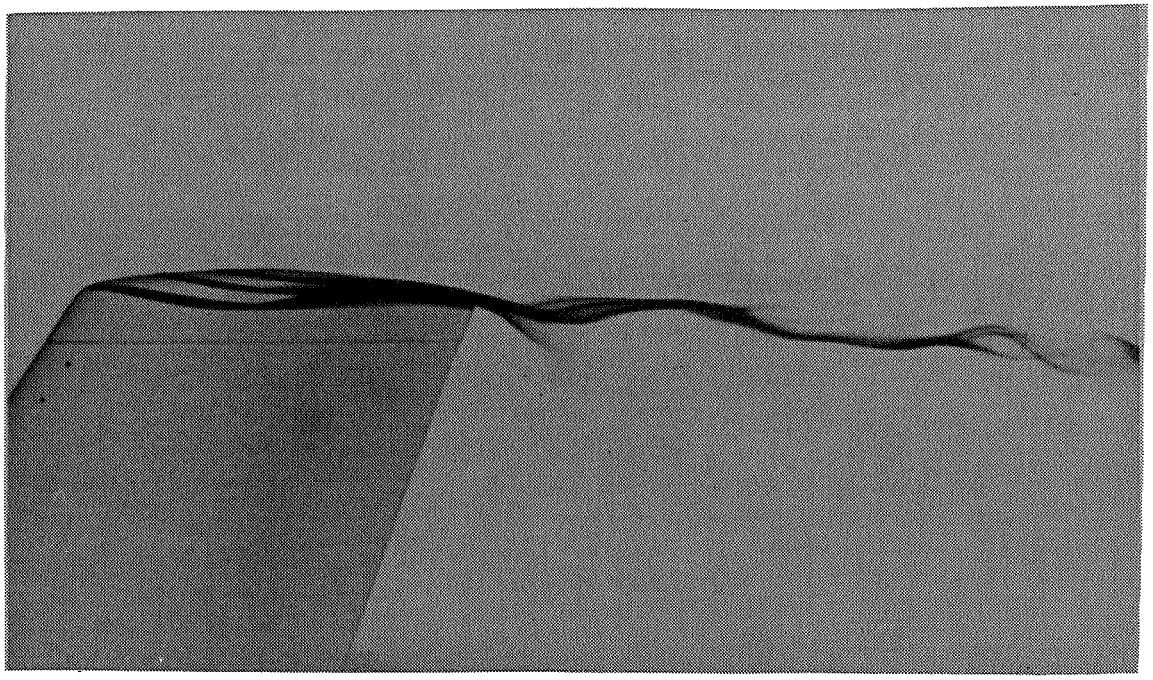

Calculated

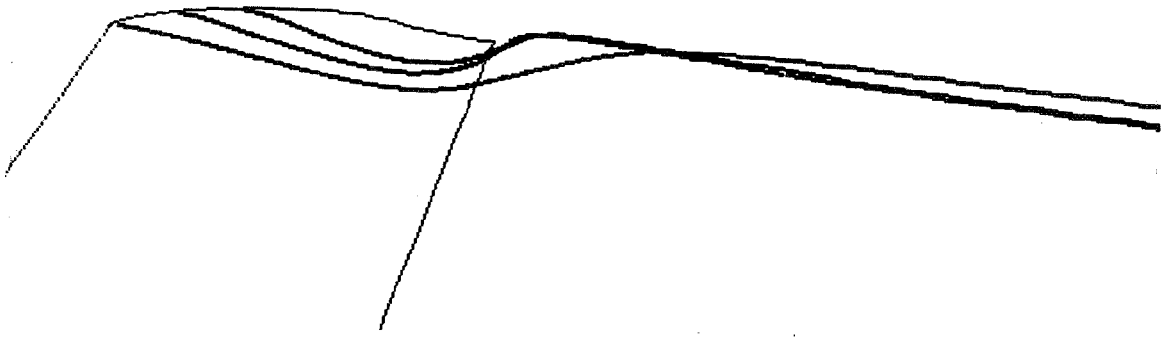

(a) No blowing.

Figure 67. Comparison of water tunnel flow visualization photographs (Reference 35) and computed particle paths. $\alpha = 3.6^{\circ}$

Water tunnel

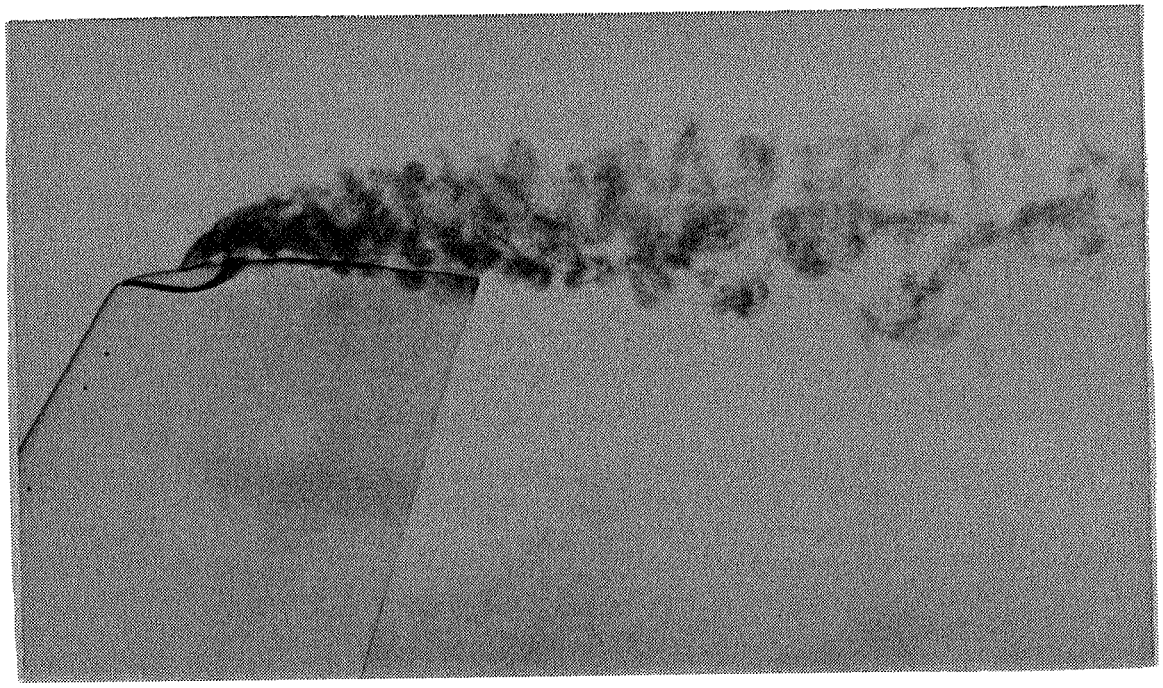

Calculated

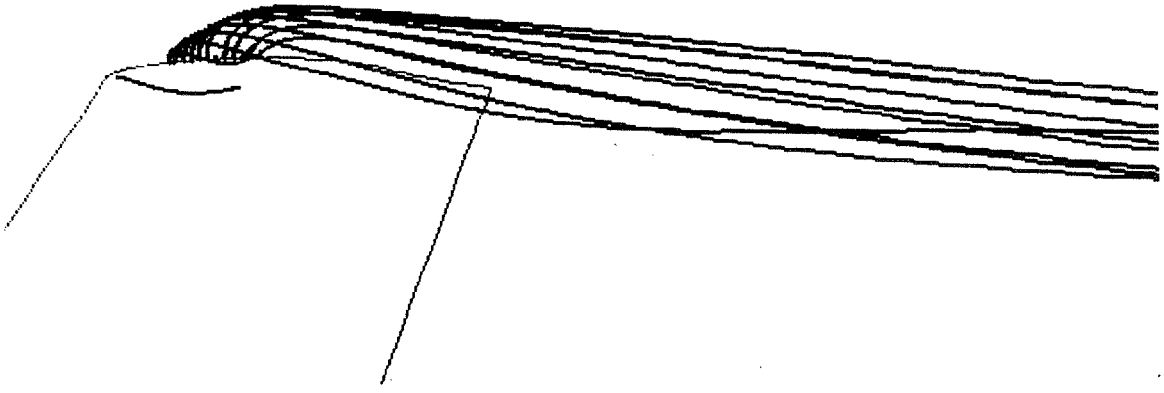

(b) Front jet, $C_\mu = 0.0050$.

Figure 67. Continued.

Water tunnel

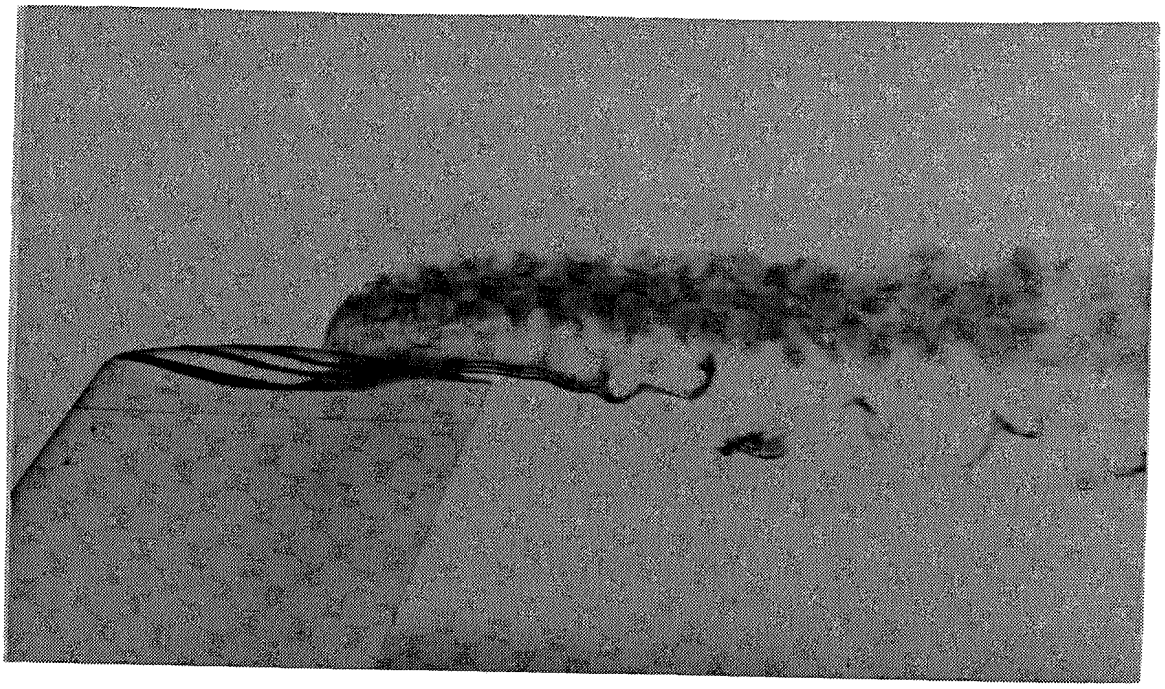

Calculated

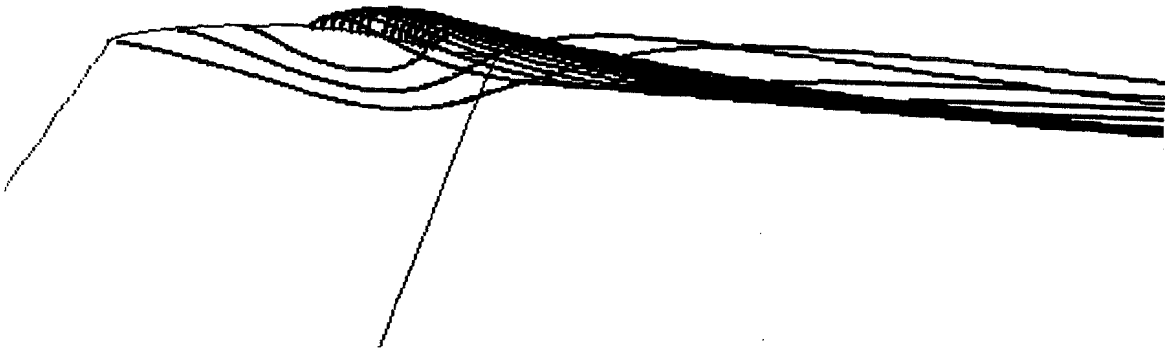

(c) Rear jet, $C_\mu = 0.0018$.

Figure 67. Continued.

Water tunnel

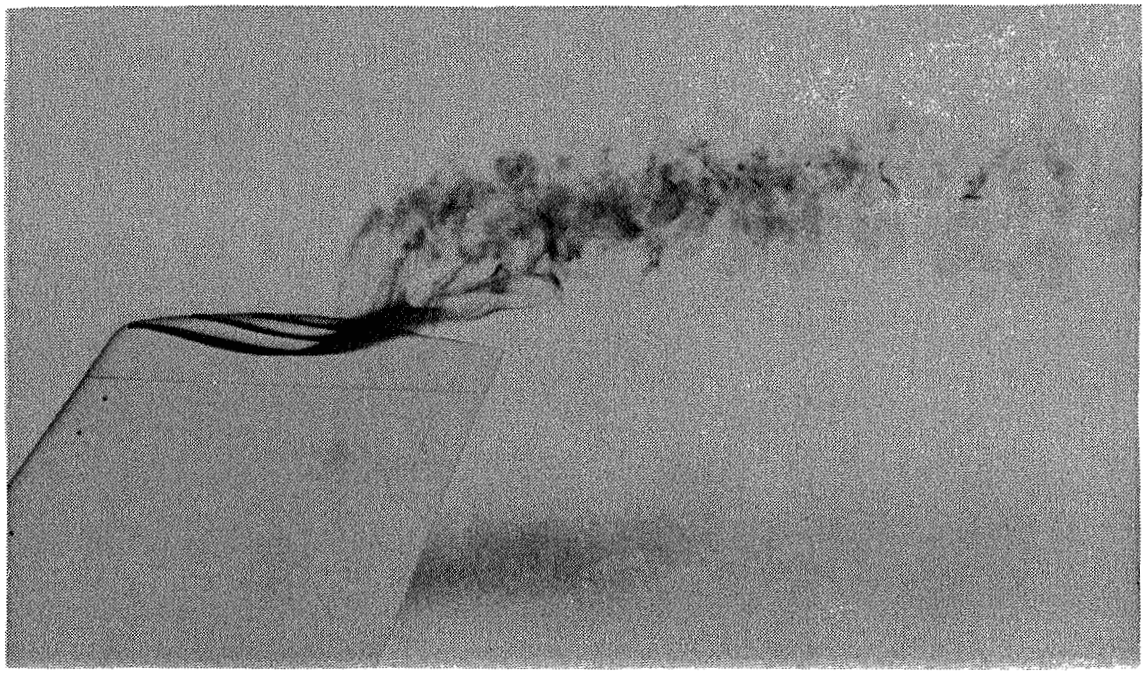

Calculated

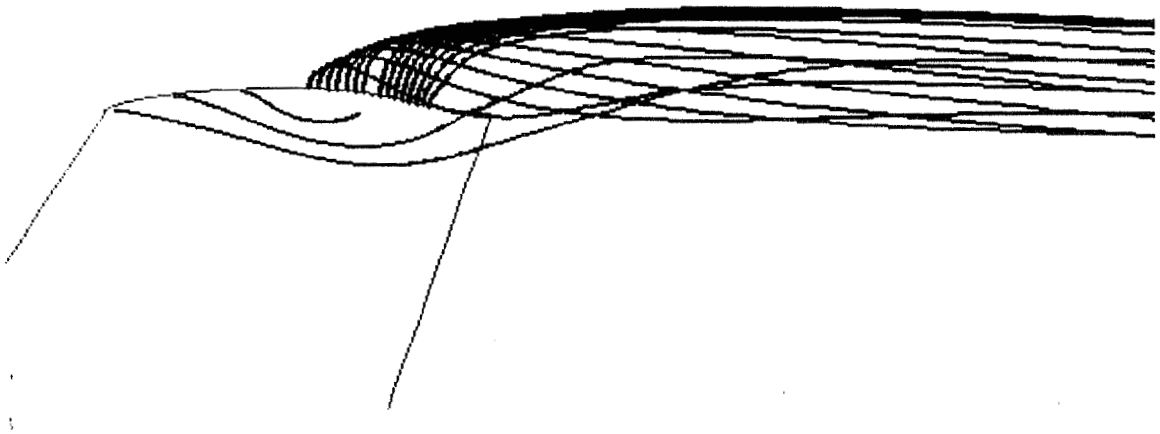

(d) Rear jet, $C_\mu = 0.0073$.

Figure 67. Continued.

Water tunnel

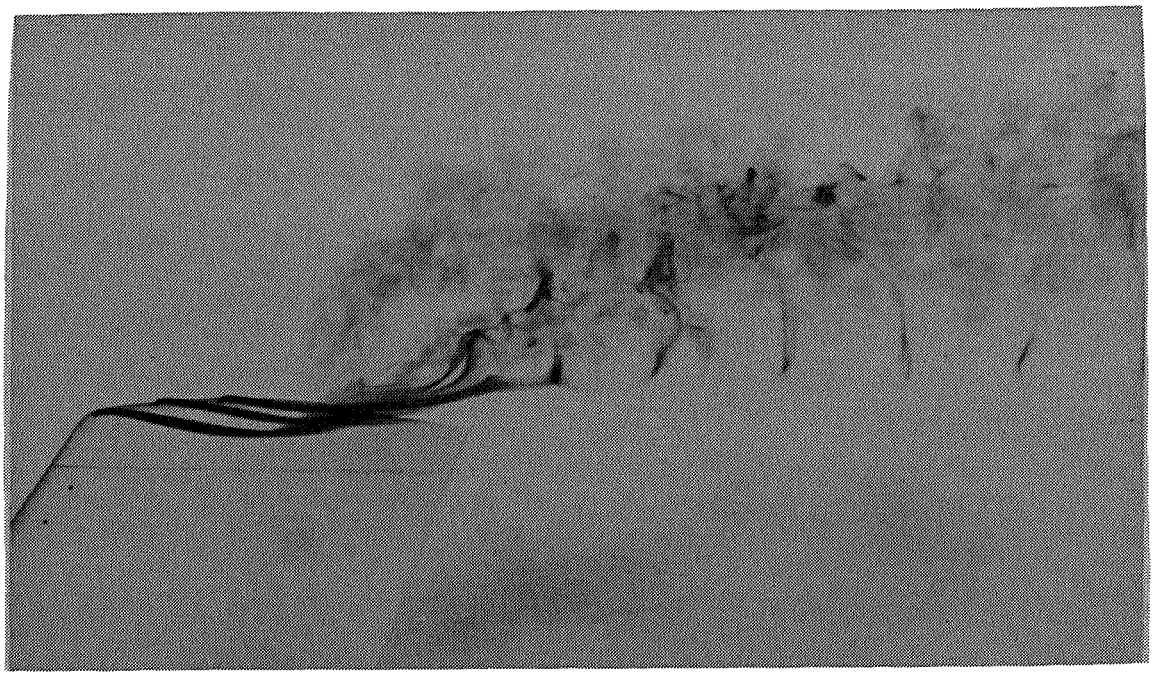

Calculated

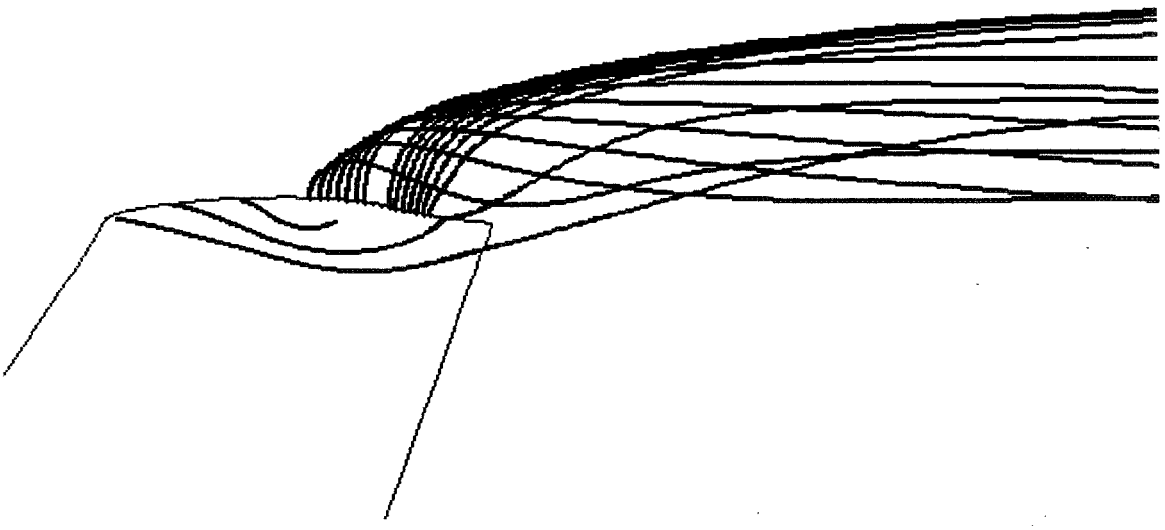

(e) Rear jet, $C_\mu = 0.0165$.

Figure 67. Concluded.

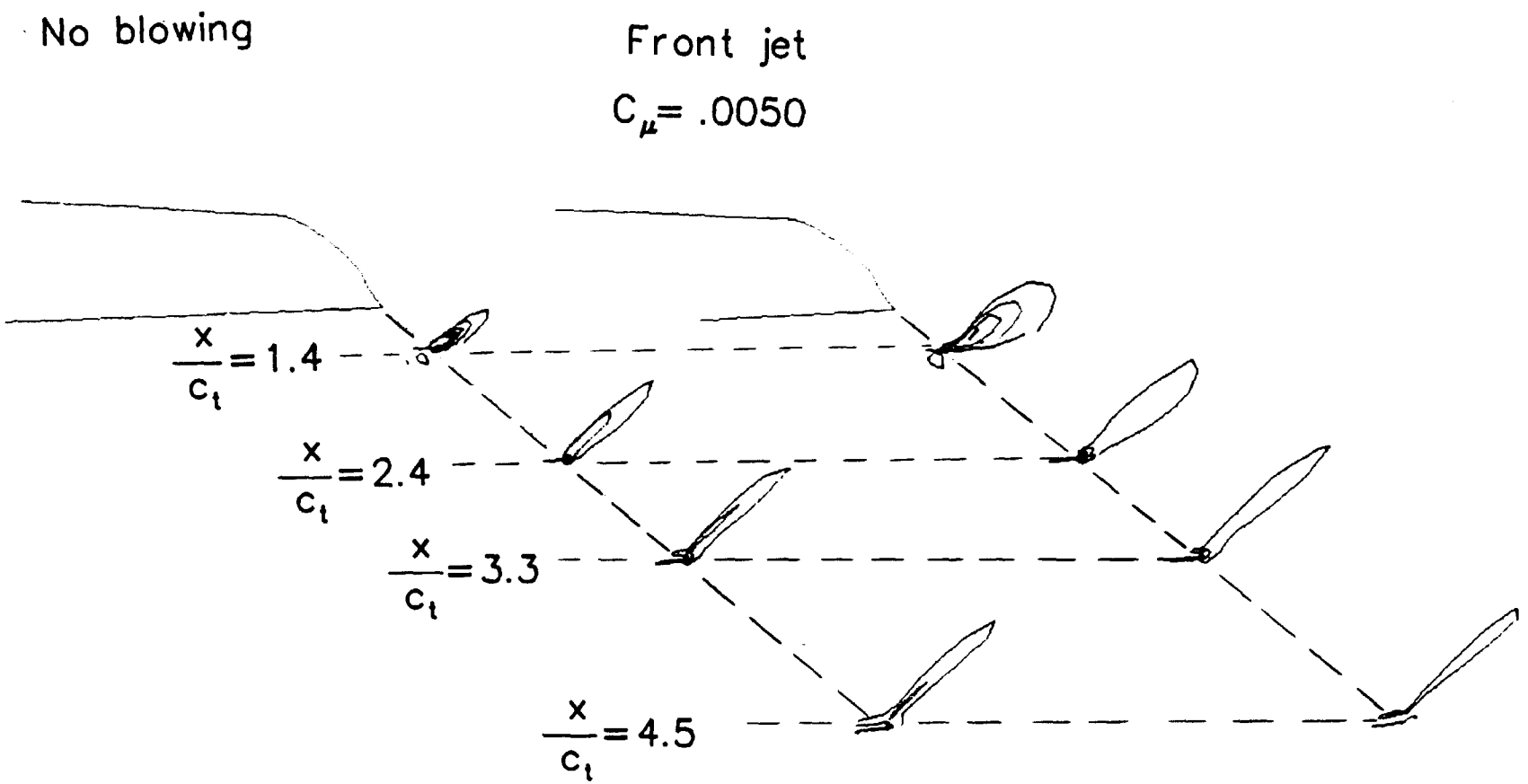

Figure 68. Comparison of the computed streamwise vorticity with and without blowing at several stations downstream of the wing tip. $\alpha = 3.6^\circ$.

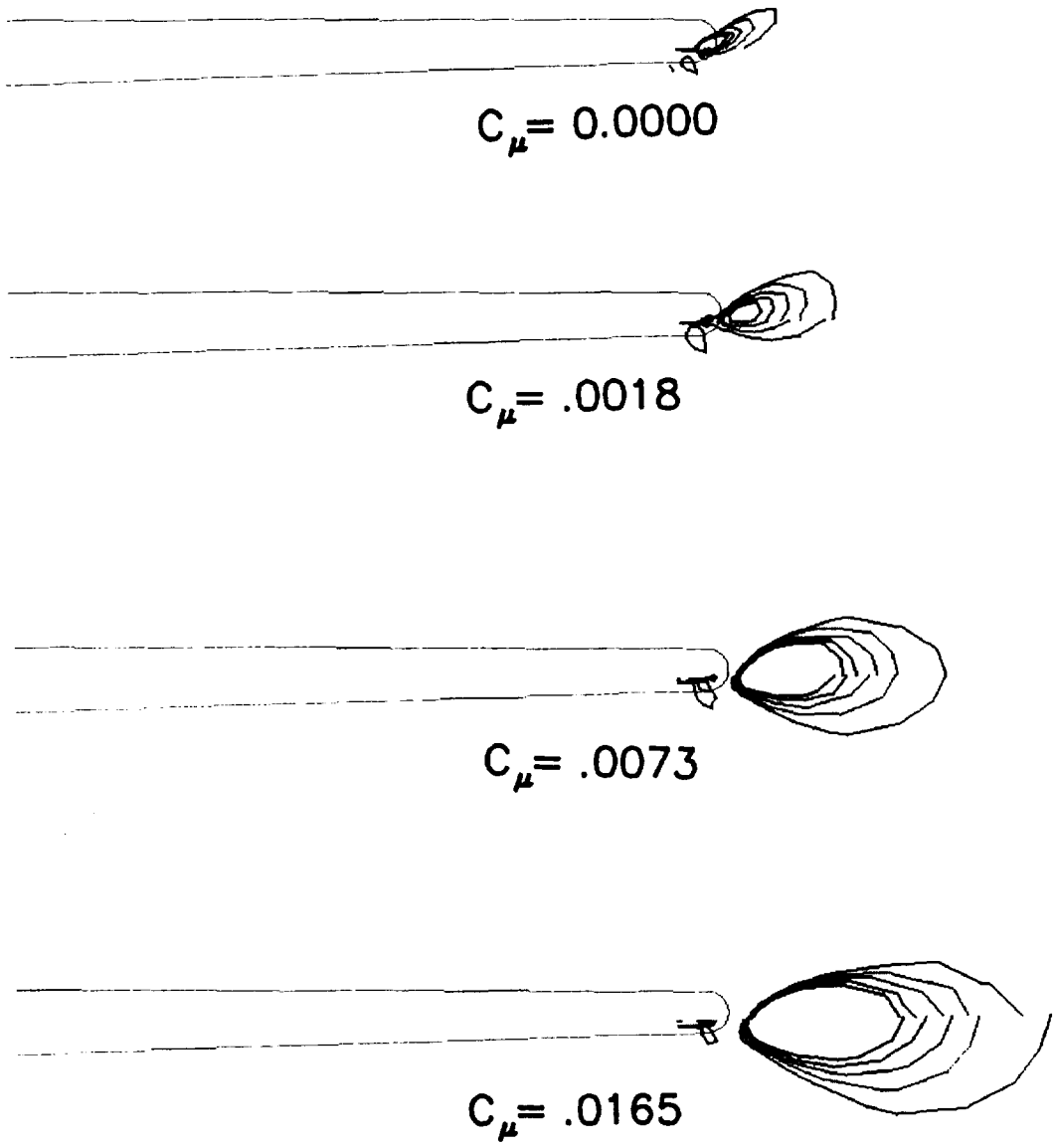

Figure 69. Effect of blowing from the rear jet on the computed streamwise vorticity. $\alpha = 3.6^\circ$, $\frac{x}{c_t} = 1.4$.

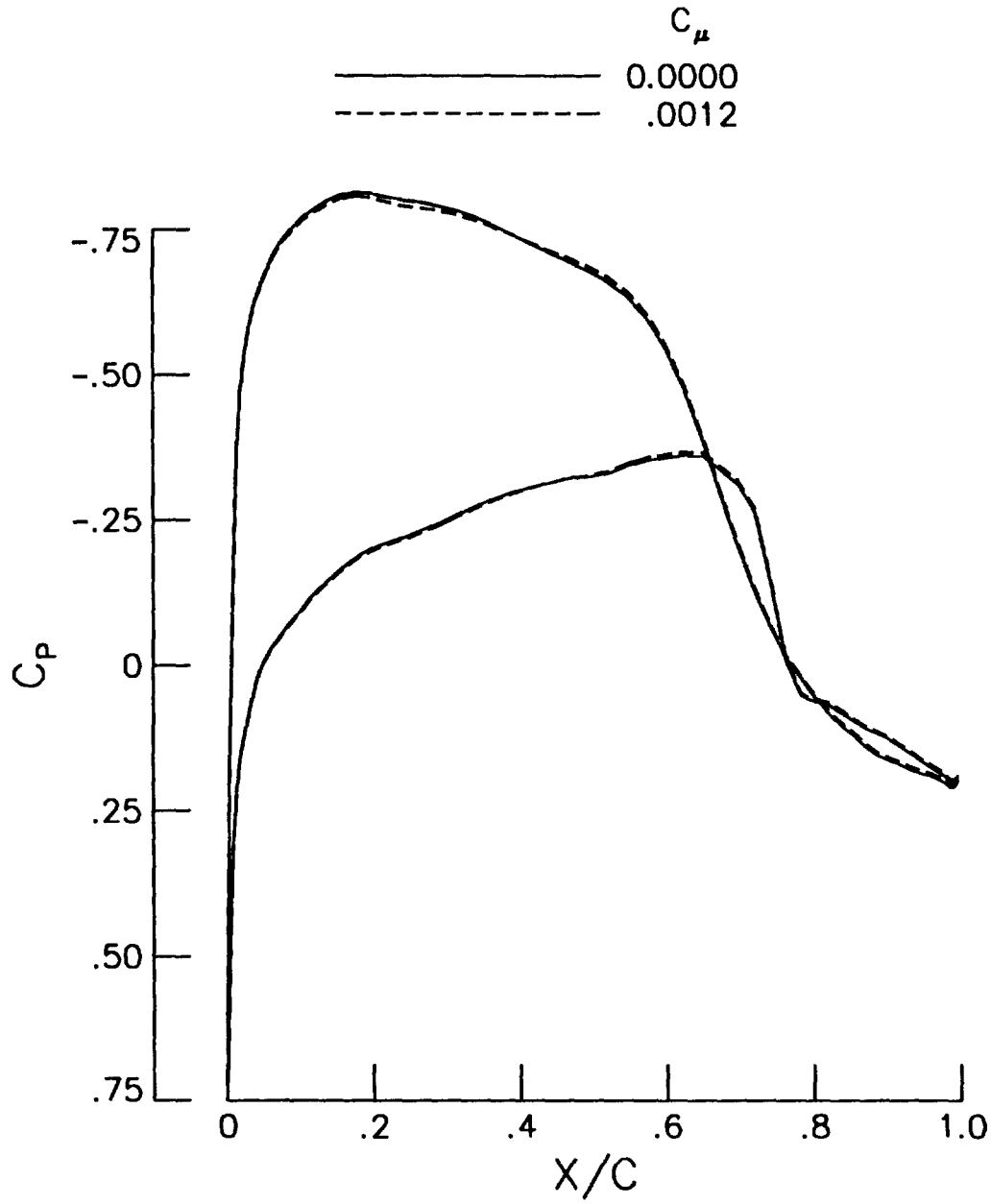

(a) $\eta = 0.90$.

Figure 70. Effect of blowing from the front jet on the computed chordwise pressure distributions. $M_\infty = 0.72$, $\alpha = 1.0°$.

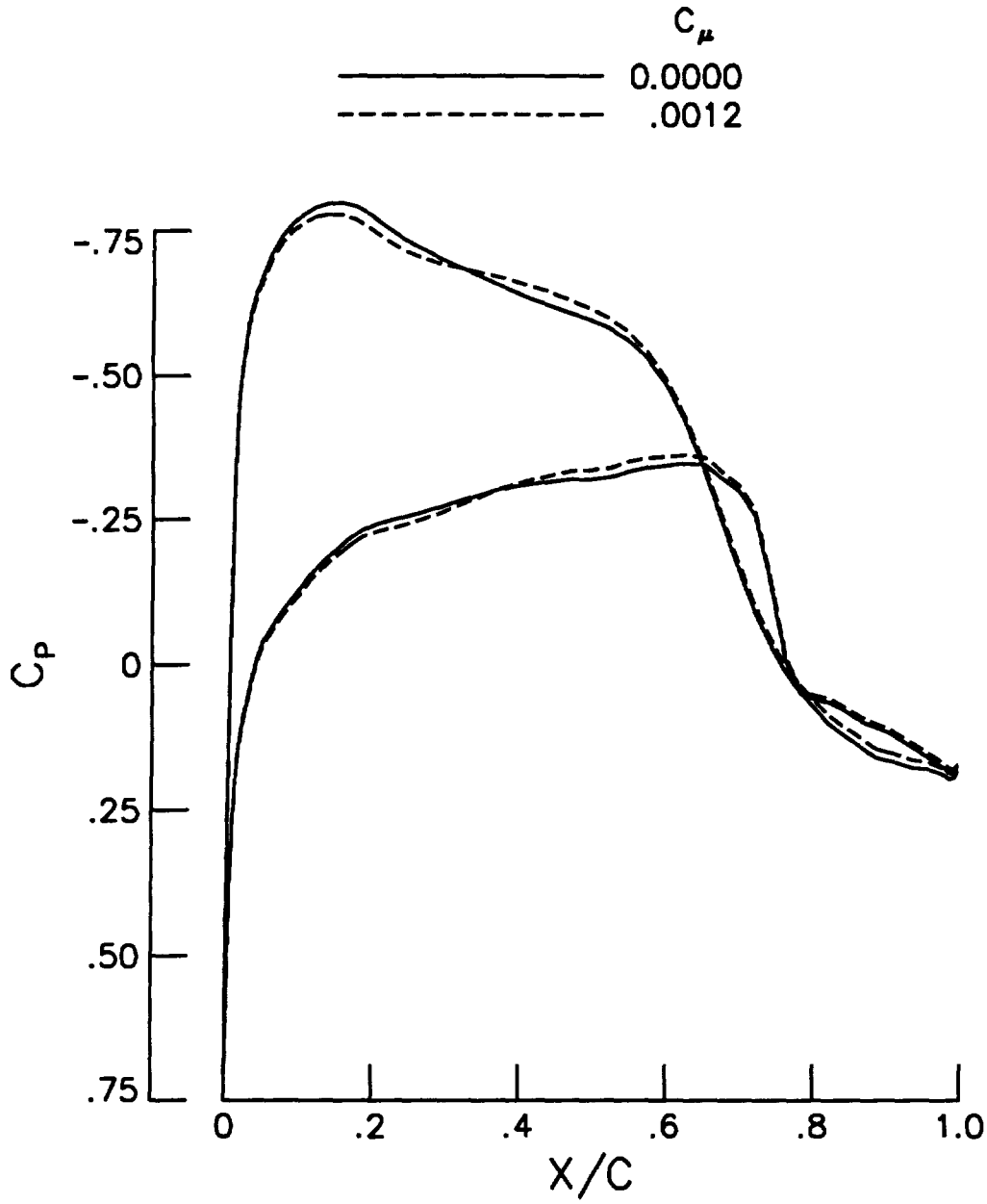

(b) $\eta = 0.95$.

Figure 70. Continued.

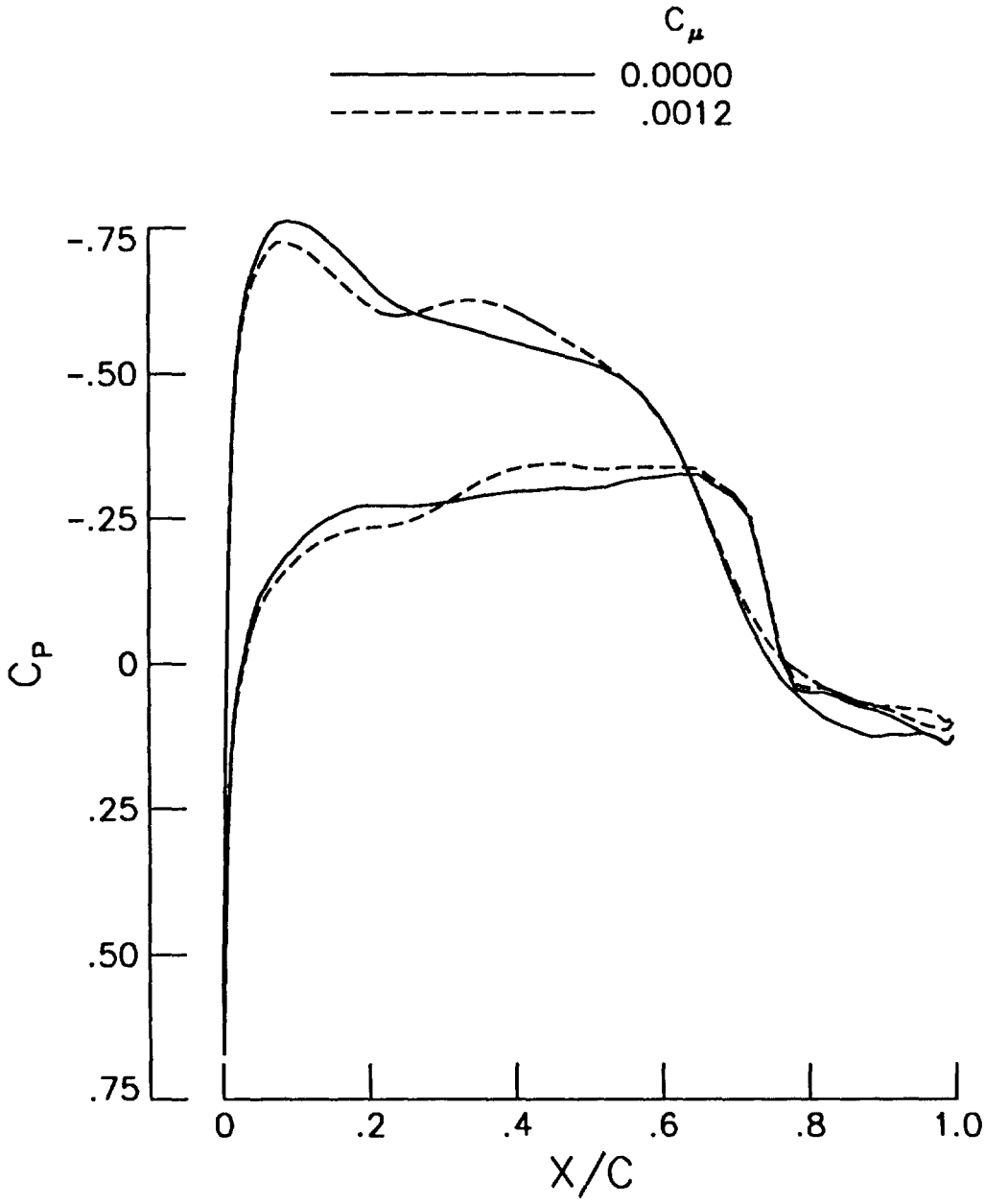

(c) $\eta = 0.98$.

Figure 70. Concluded.

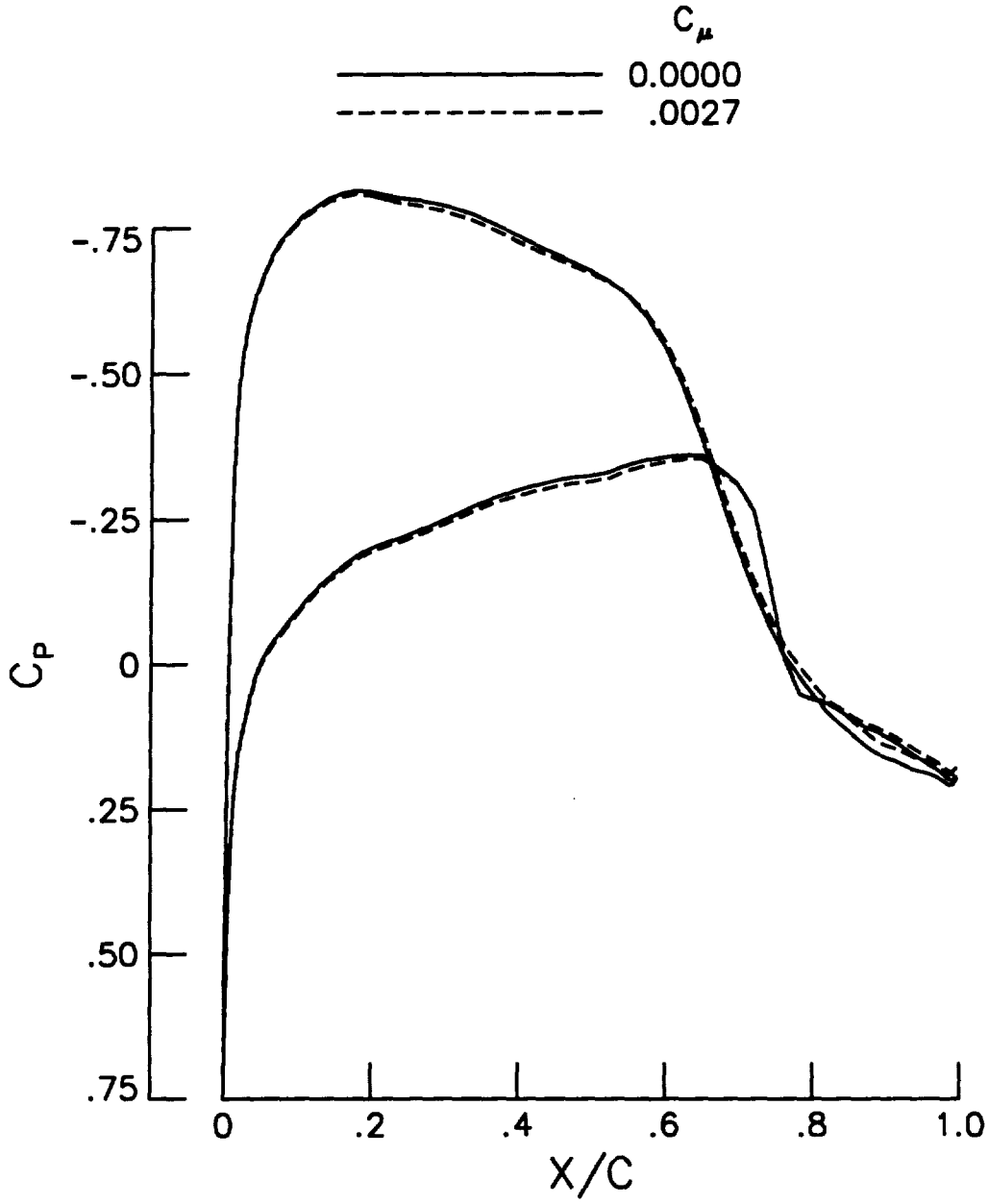

(a) $\eta = 0.90$.

Figure 71. Effect of blowing from the rear jet on the computed chordwise pressure distributions. $M_\infty = 0.72$, $\alpha = 1.0°$.

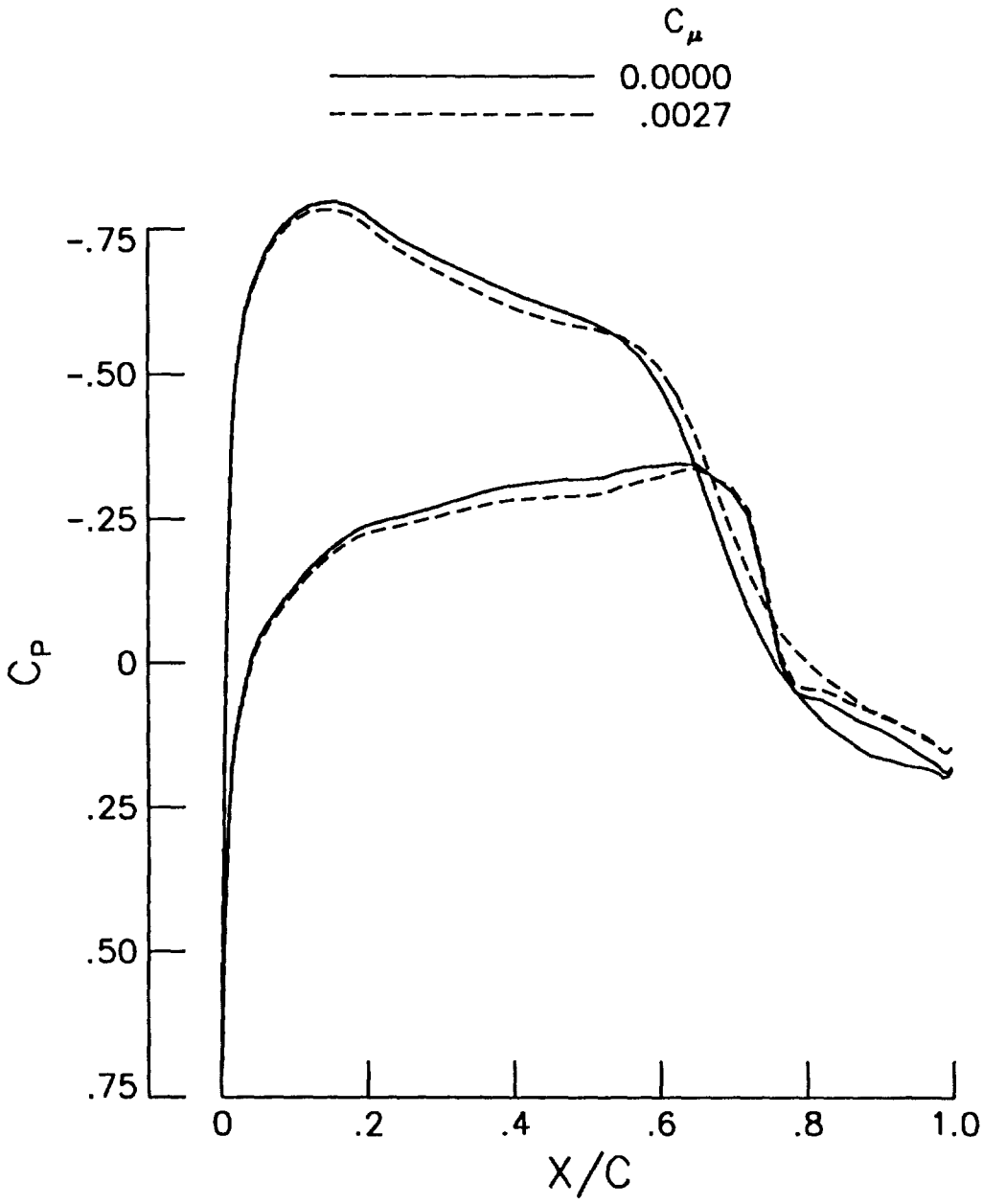

(b) $\eta = 0.95$.

Figure 71. Continued.

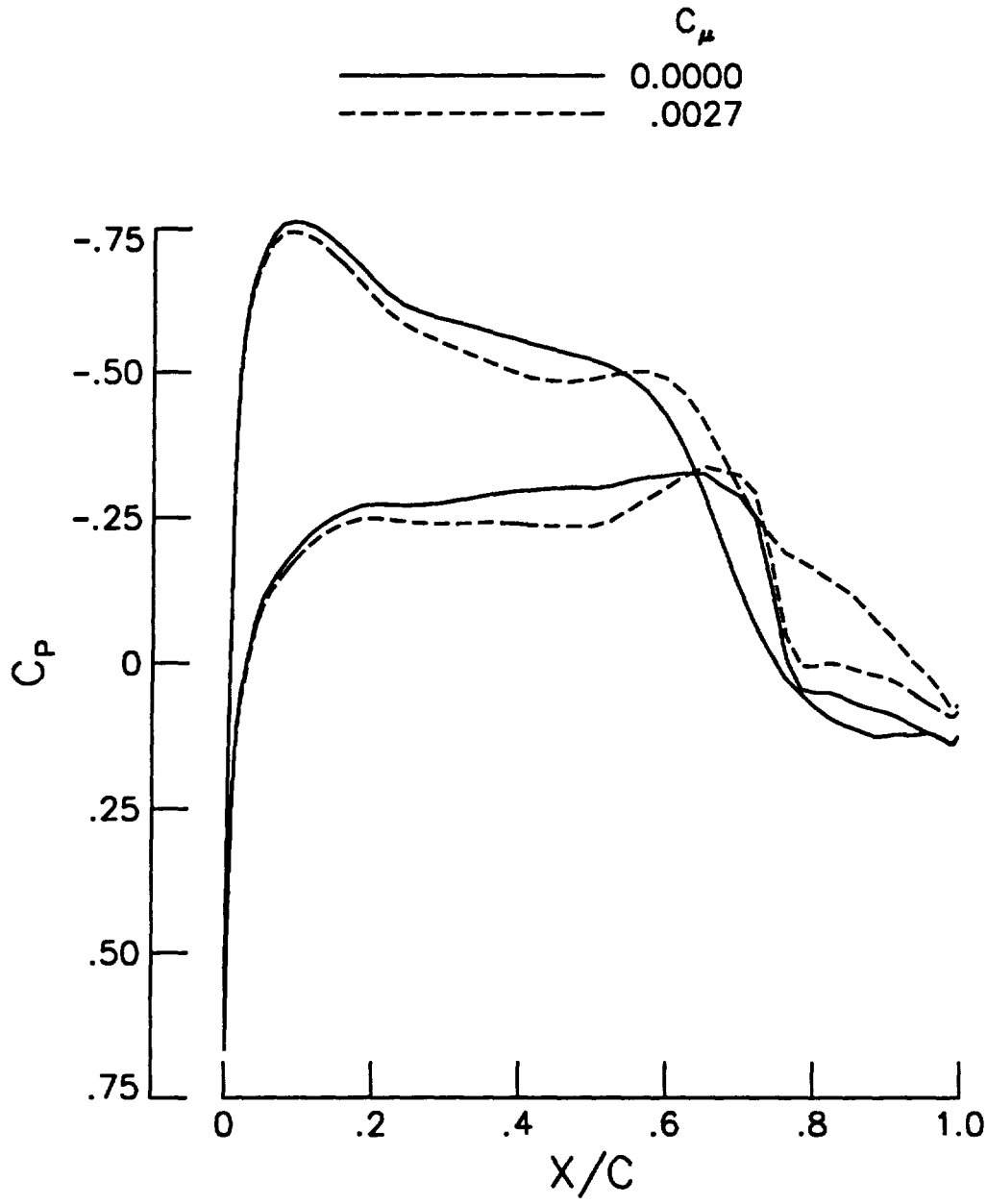

(c) $\eta = 0.98$.

Figure 71. Concluded.

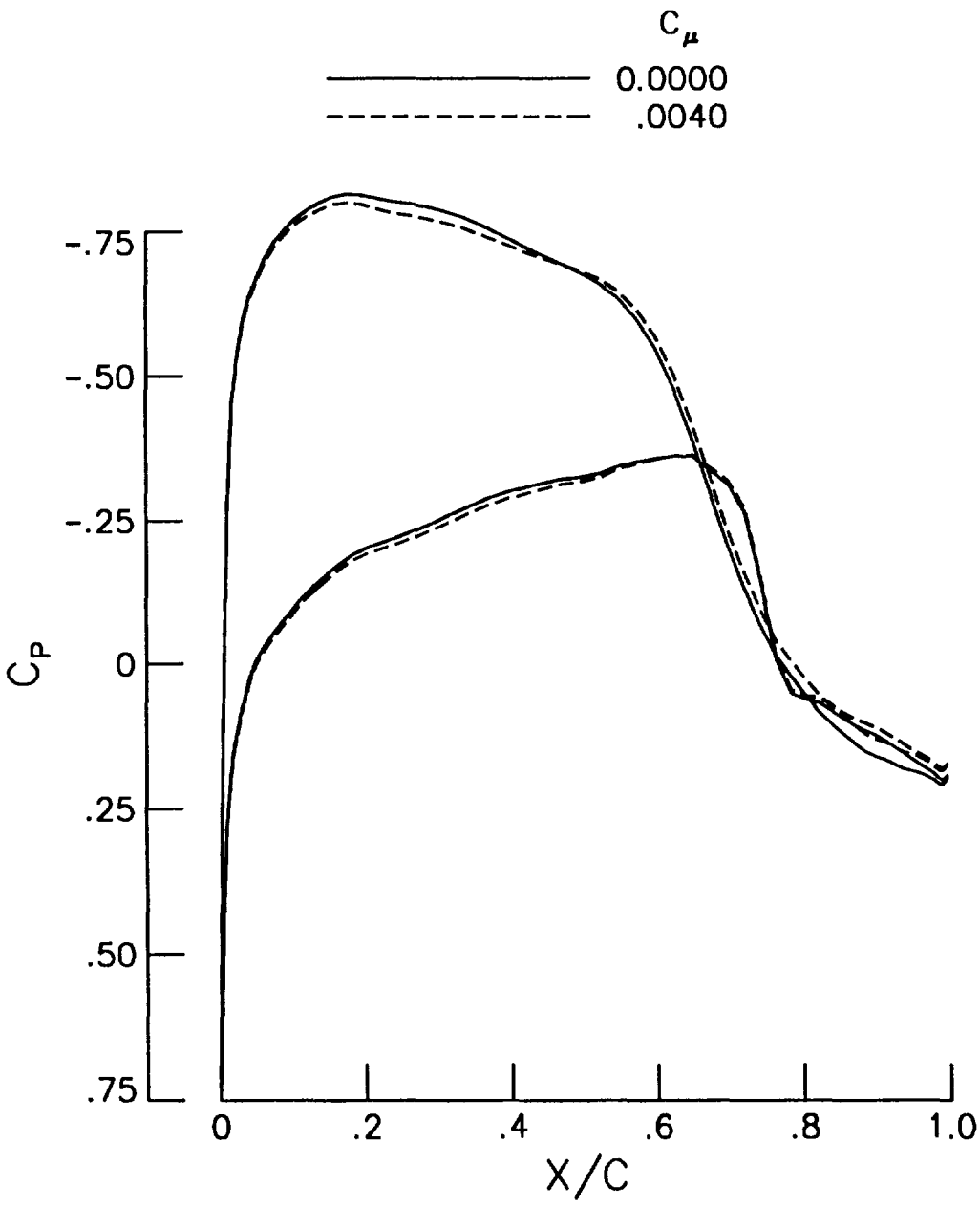

(a) $\eta = 0.90$.

Figure 72. Effect of blowing from both jets on the computed chordwise pressure distributions. $M_\infty = 0.72$, $\alpha = 1.0^\circ$.

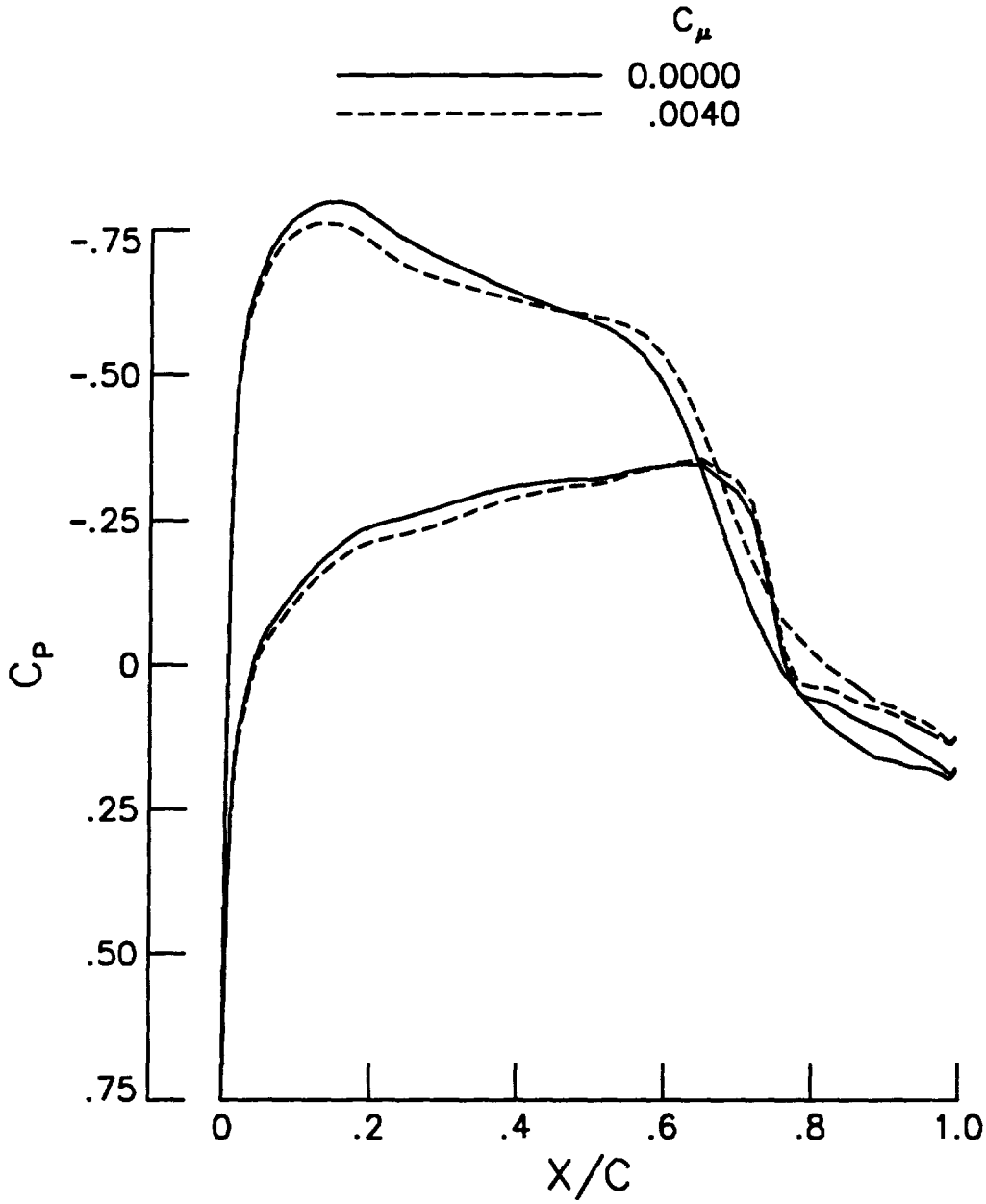

(b) $\eta = 0.95$.

Figure 72. Continued.

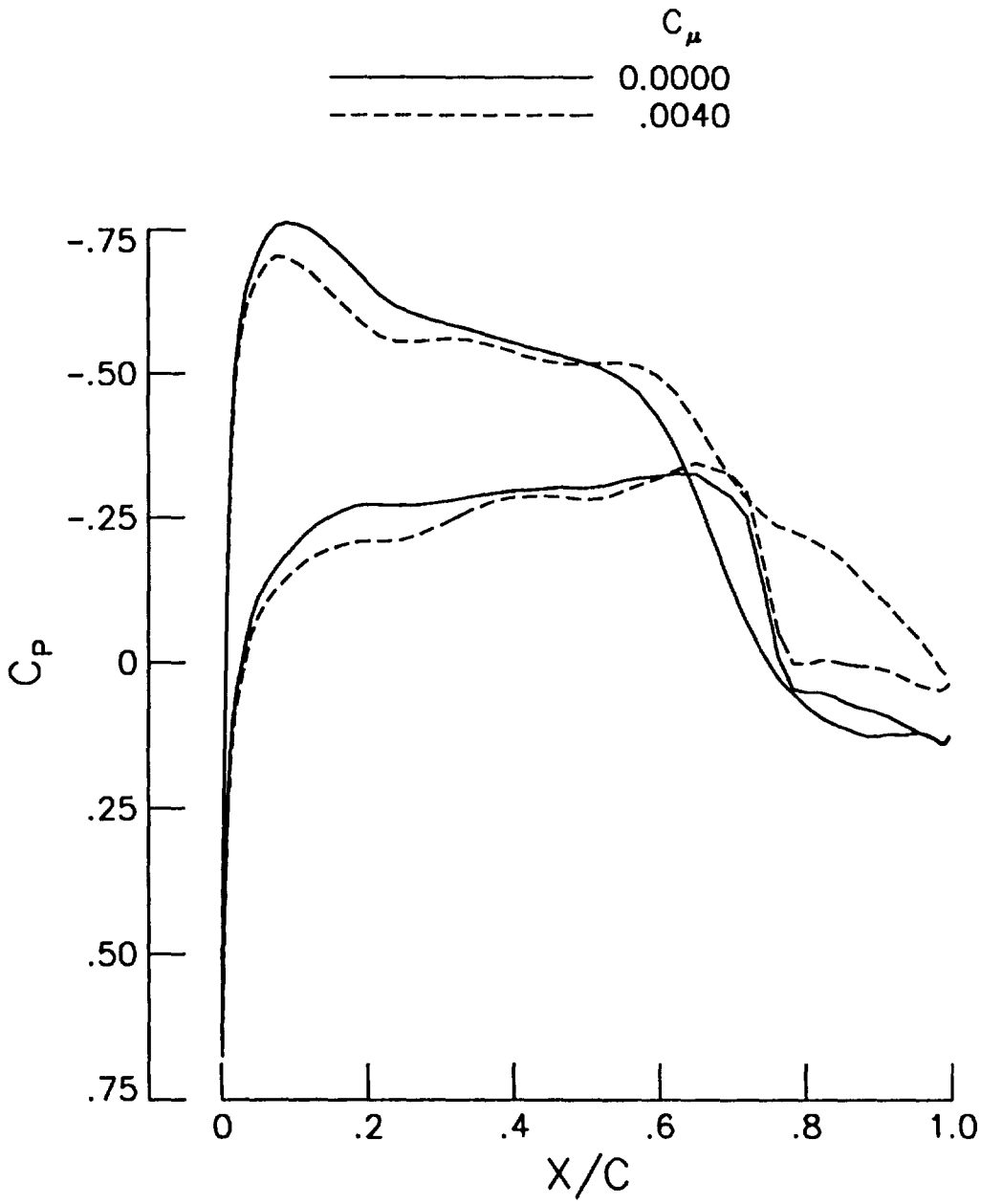

(c) $\eta = 0.98$.

Figure 72. Concluded.

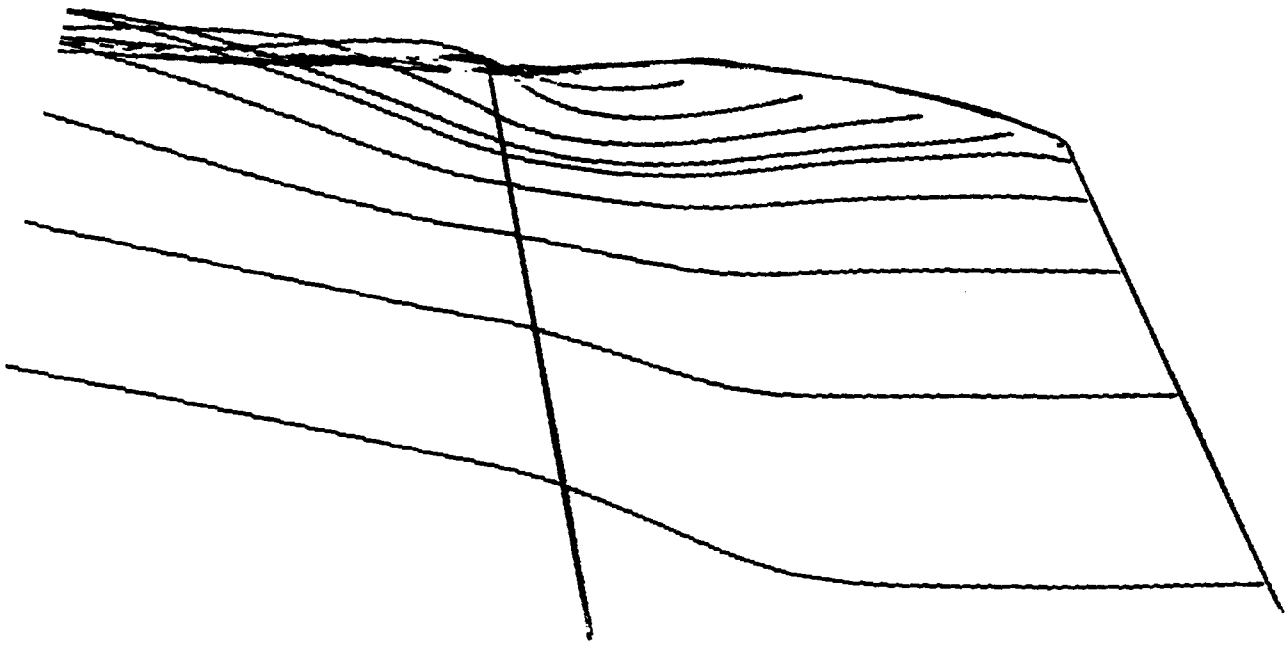

(a) No blowing.

Figure 73. Effect of blowing on the computed particle paths near the wing tip. $M_\infty = 0.72$, $\alpha = 1.0^\circ$.

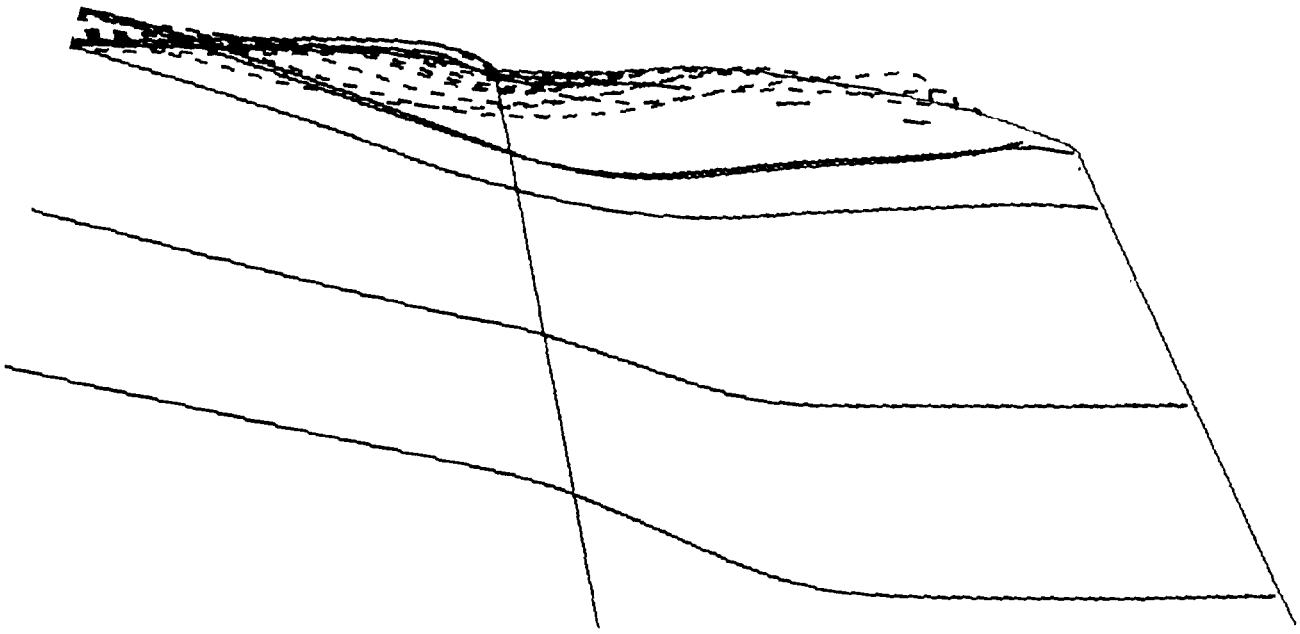

(b) Front jet, $C_\mu = 0.0012$.

Figure 73. Continued.

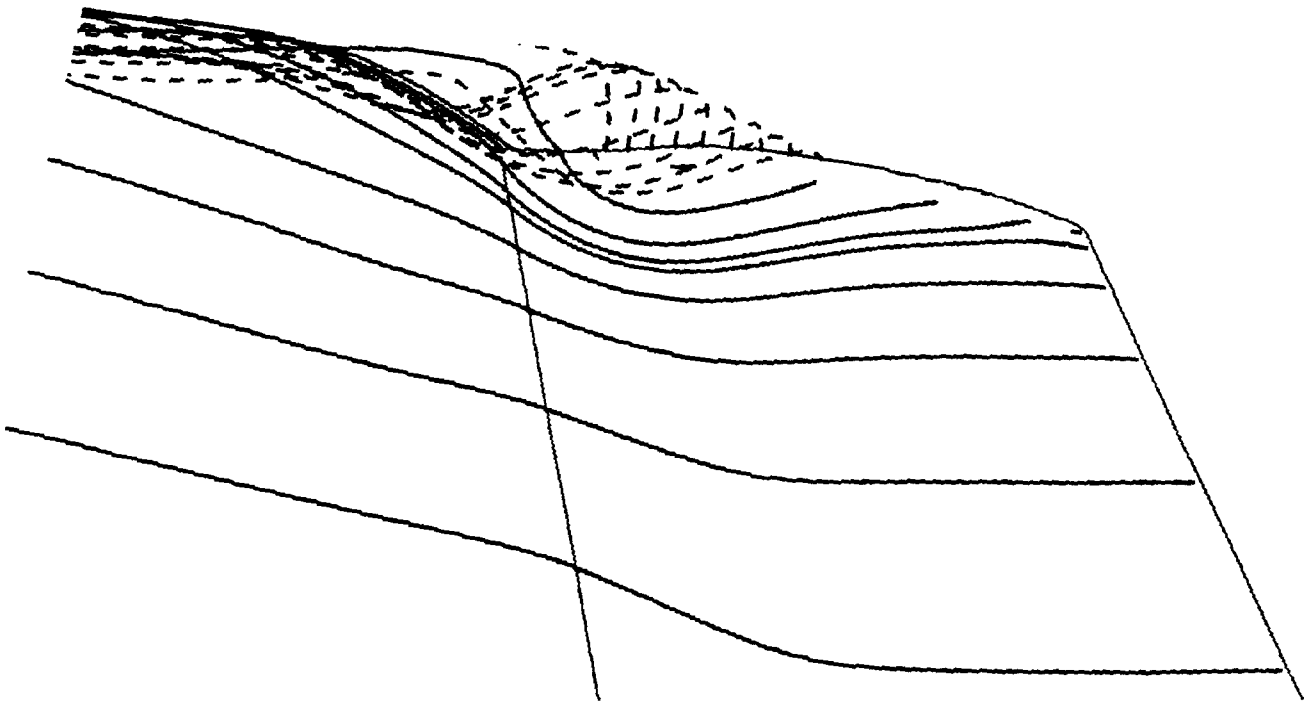

(c) Rear jet, $C_\mu = 0.0027$.

Figure 73. Continued.

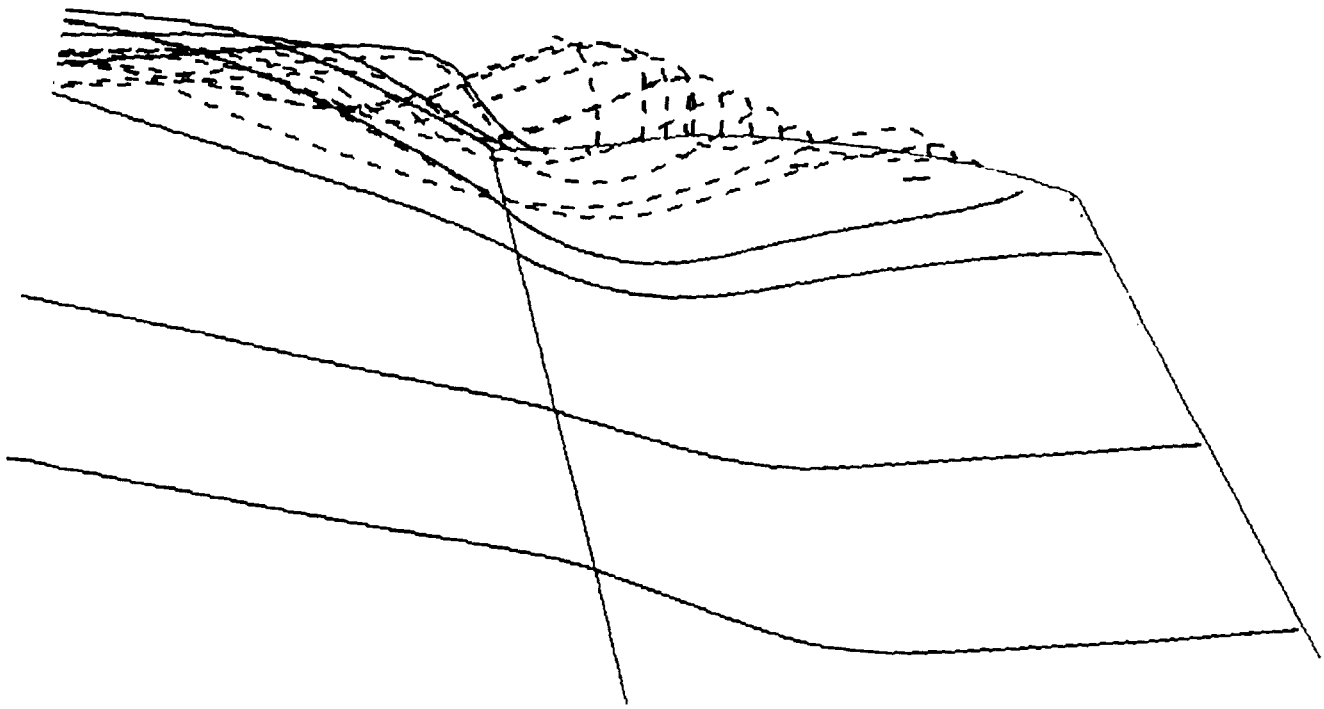

(d) Both jets, $C_\mu = 0.0040$.

Figure 73. Concluded.

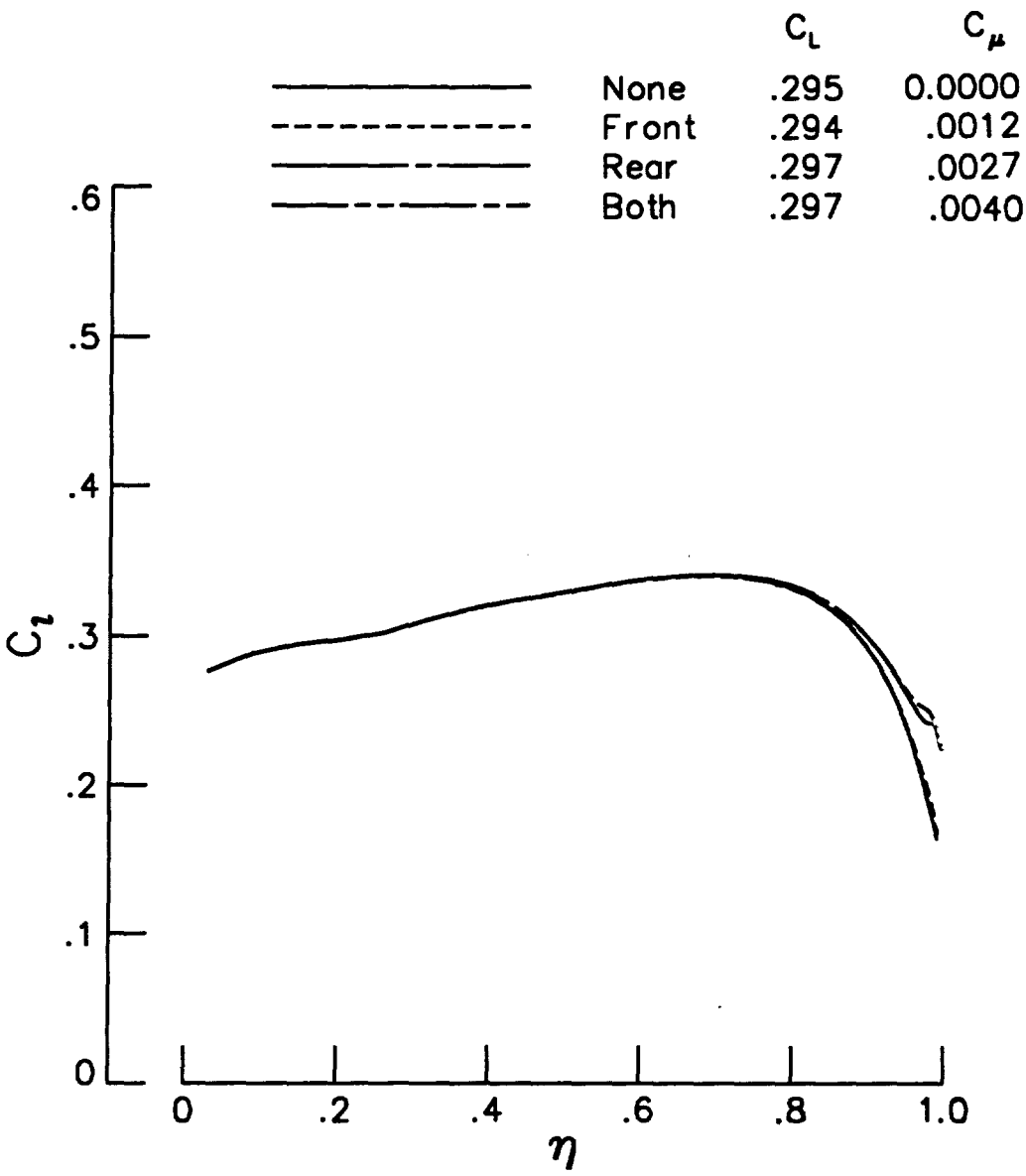

Figure 74. Effect of blowing on the computed span load distributions. $M_\infty = 0.72$, $\alpha = 1.0°$.

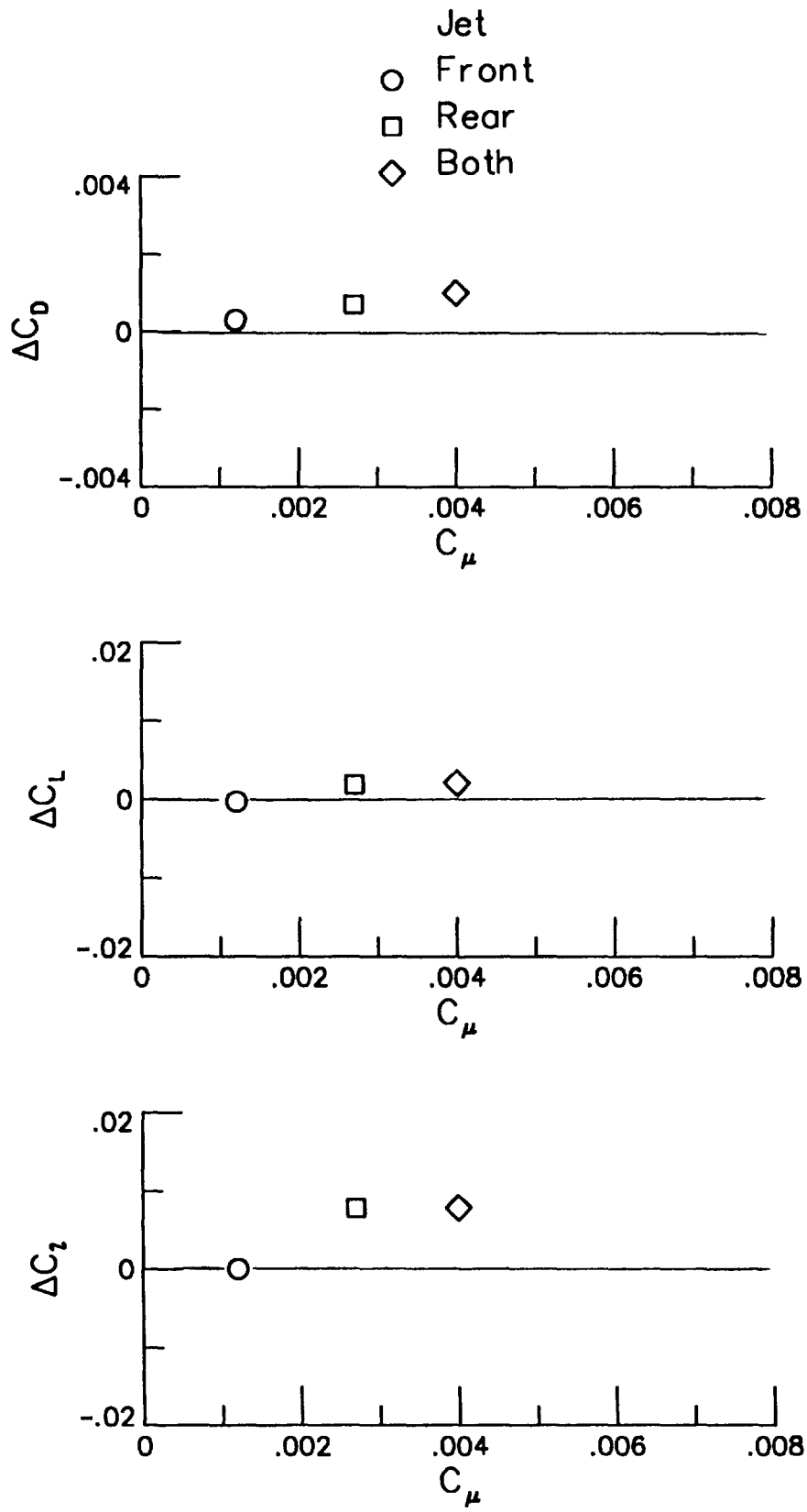

Figure 75. Change in the computed wing loads with blowing. $M_\infty = 0.72$, $\alpha = 1.0°$.

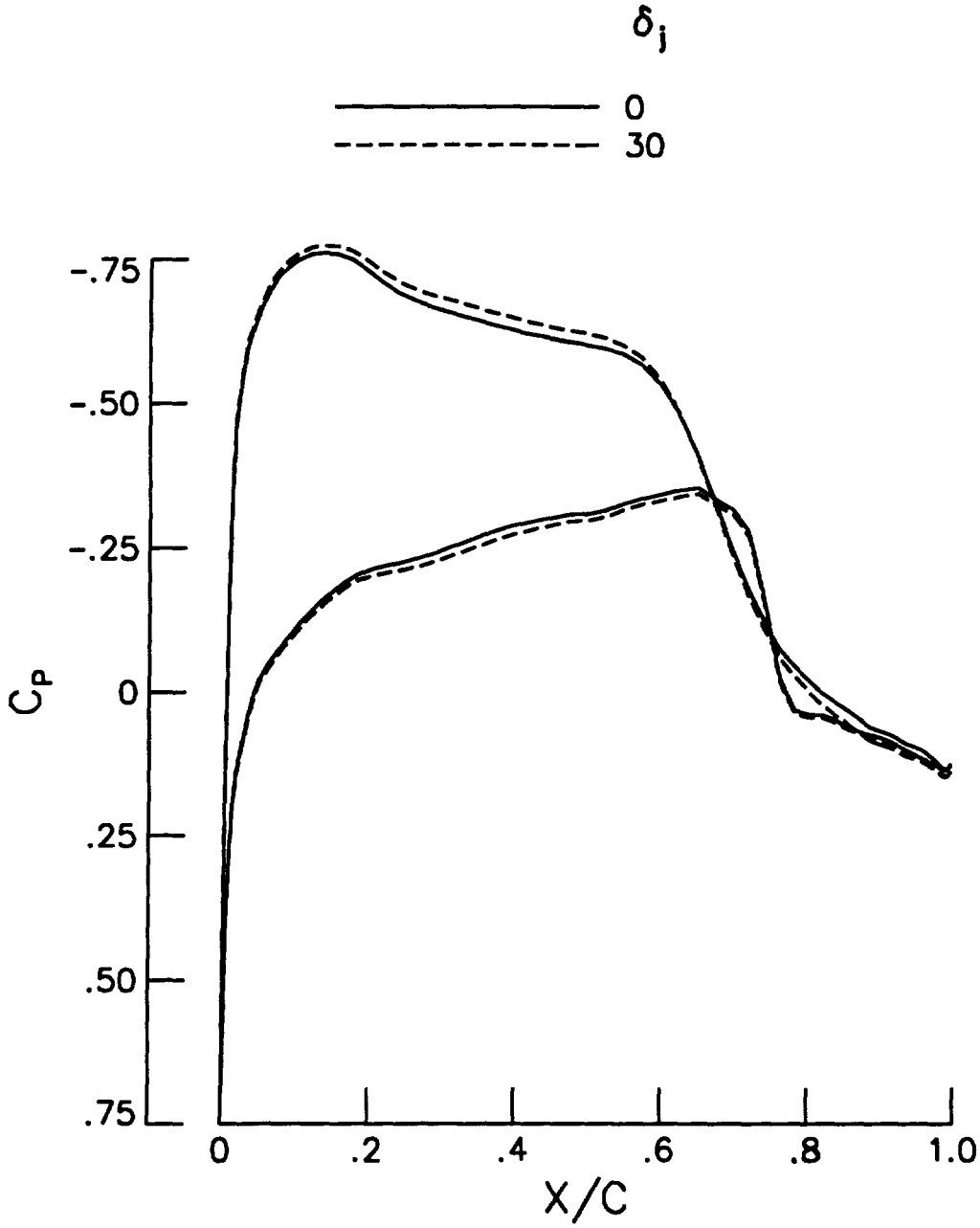

(a) $\eta = 0.95$.

Figure 76. Effect of deflecting the jet exhaust downward on the computed chordwise pressure distributions. $M_\infty = 0.72$, $\alpha = 1.0°$.

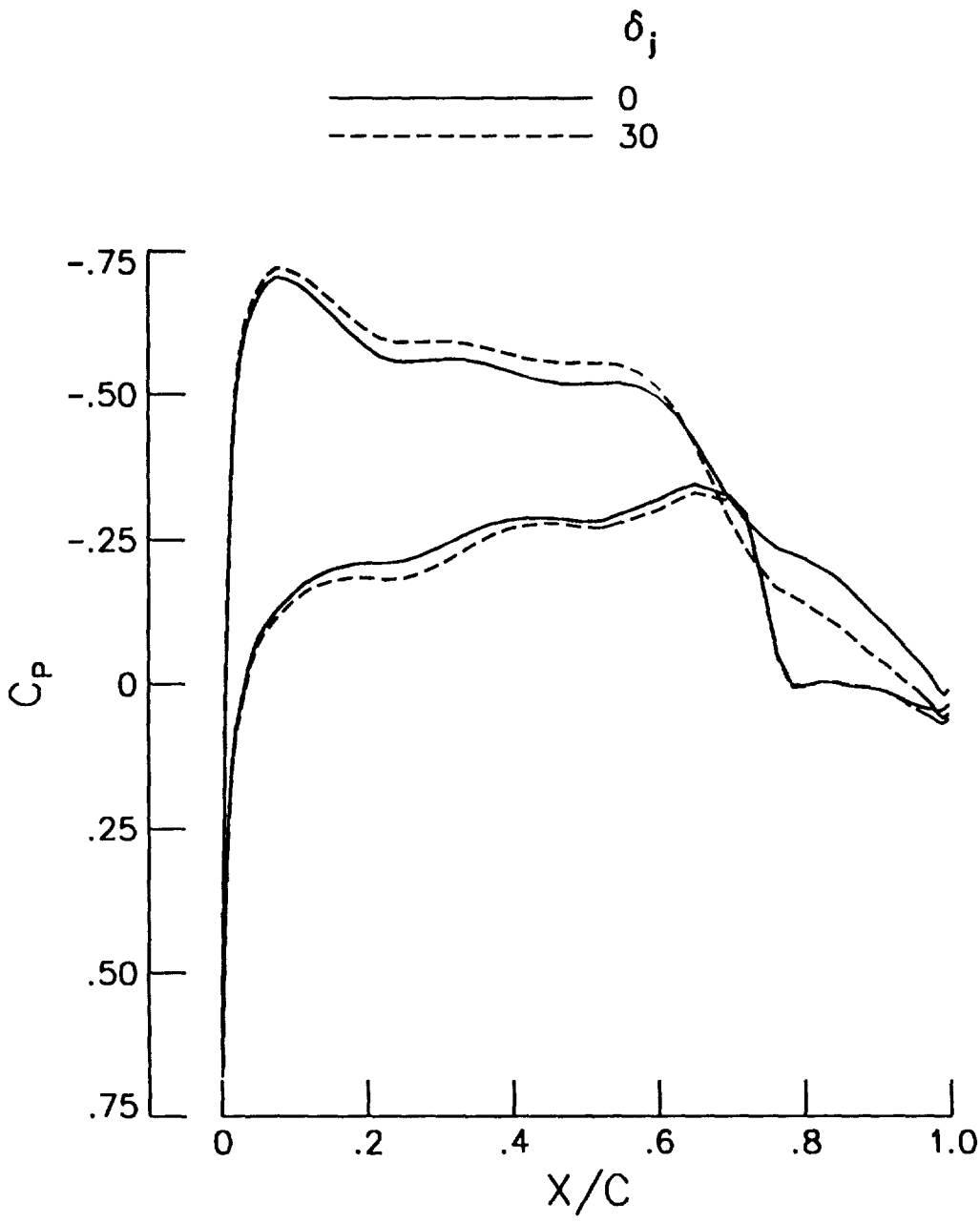

(b) $\eta = 0.98$.

Figure 76. Concluded.

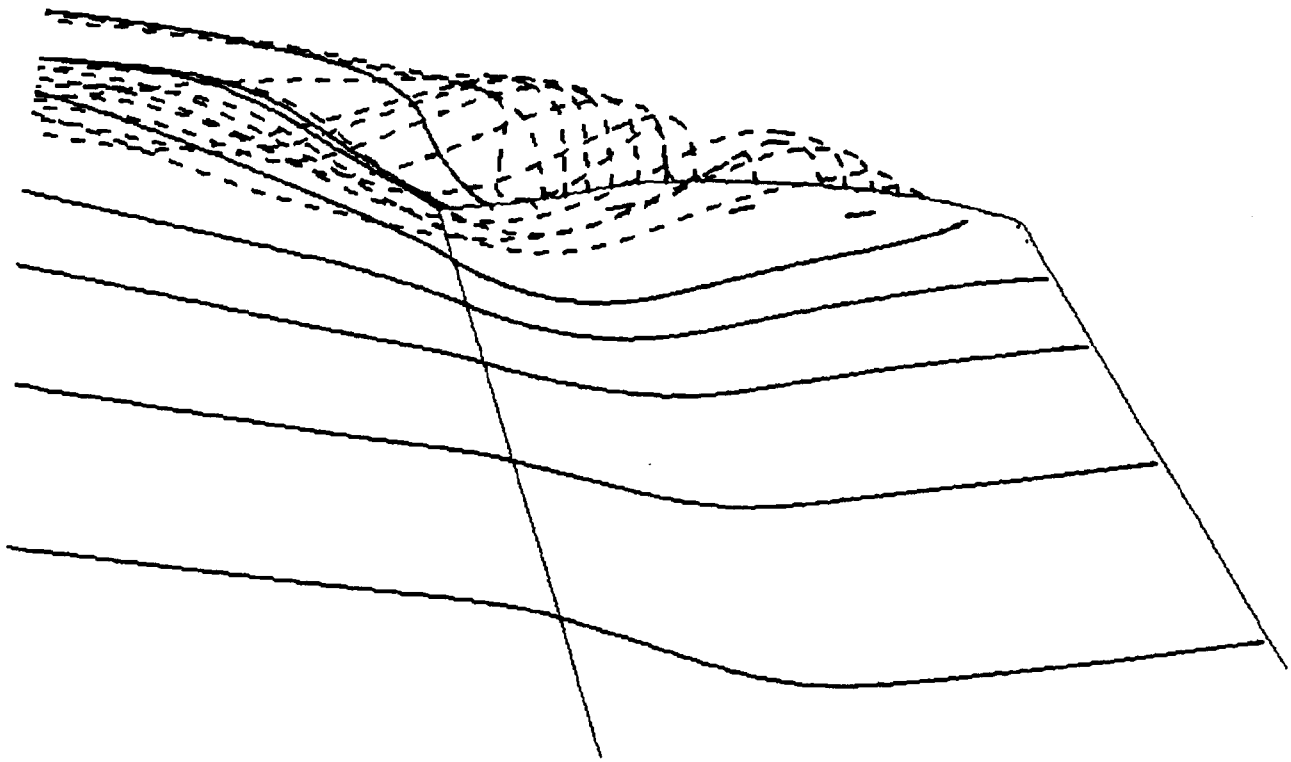

Figure 77. Particle paths near the wing tip for the jet exhaust deflected downward 30°.
$M_\infty = 0.72$, $\alpha = 1.0°$.

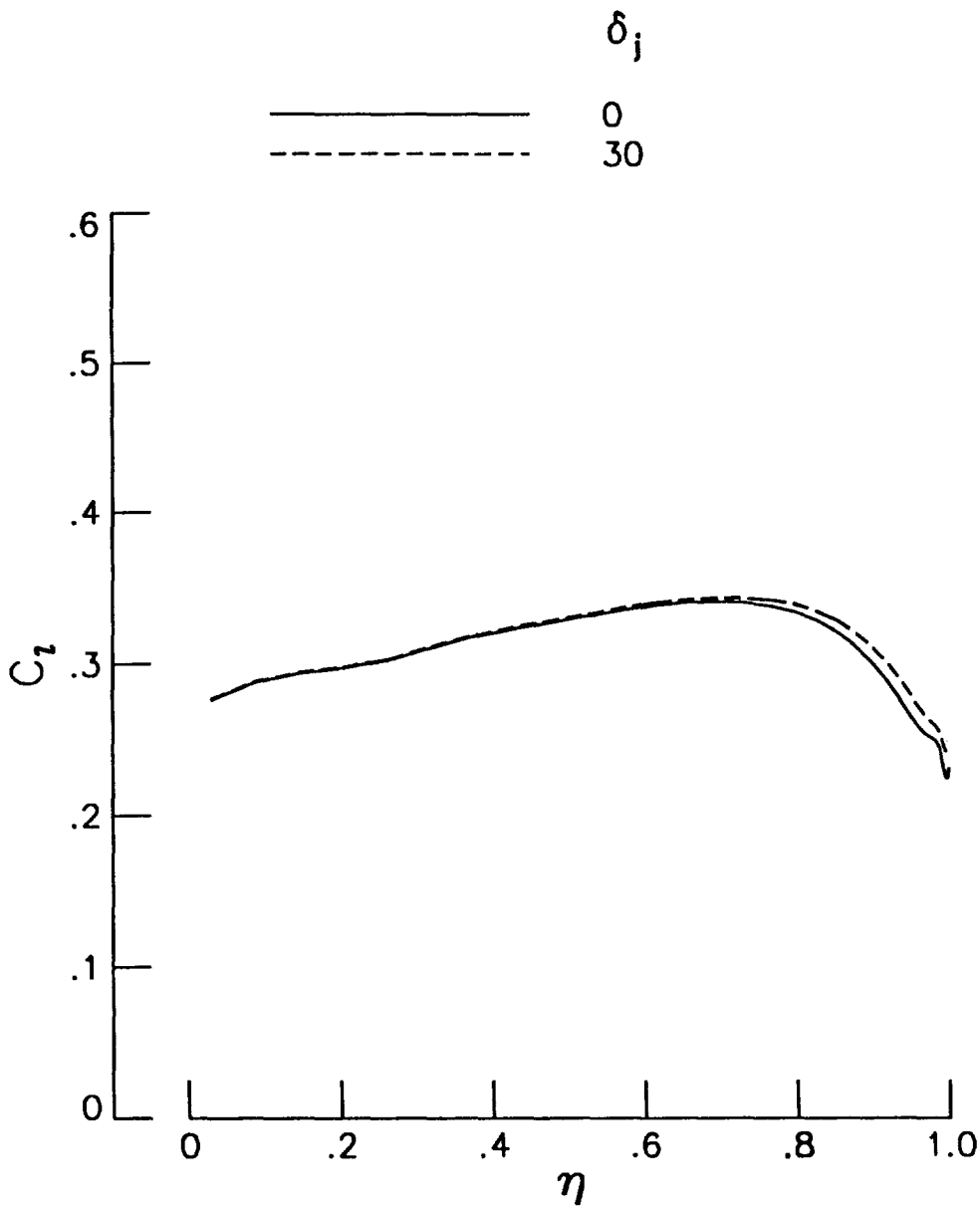

Figure 78. Effect of deflecting the jet downward 30° on the computed span load distributions. $M_\infty = 0.72$, $\alpha = 1.0°$.

APPENDIX A

CALIBRATION OF THE AIRLINES

A strain gage balance was used to measure the wing forces and moments. Under normal circumstances, all of the wing forces and moments pass through the balance. Since air is needed onboard the model, air supply lines must cross from the non-metric to the metric side of the balance. The two airlines used in this investigation provide additional load paths across the balance. This appendix describes the design of the airlines, calibration procedure used to determine the corrections needed for the airlines, and calibration results.

Symbols

AF	axial force, lbf.
NF	normal force, lbf.
PM	pitching moment, in.-lbf.
RM	rolling moment, in.-lbf.
YM	yawing moment, in.-lbf.
P	airline pressure, $\frac{\text{lbf.}}{\text{in.}^2}$
Δ	(measured load without airline) - (measured load with airline)

subscripts

a	applied
m	measured

Design of the Airlines

Design of the airlines should ensure that the airlines do not degrade the balance accuracy or repeatability. Airlines must be flexible so that they do not significantly degrade the sensitivity of each of the balance components. A flexible airline, such as a rubber hose, would have a negligible effect on the sensitivity of the balance measurements. However, experience has shown that the static load from a flexible airline is not repeatable. A "rigid" (for repeatability) but "flexible" (for small changes in balance sensitivity) airline is needed. A long, stiff tube is used to satisfy these conflicting requirements. The airline should be as long as possible to make it as flexible as possible. This is accomplished by looping the airline back and forth within the fuselage. A sketch of the forward airline is shown in figure A1 and a photograph of the airlines and the model in a temporary mounting fixture is presented in figure A2. The airlines were fabricated from copper tubing. Each airline was bolted to the balance support block (or non-metric side of the balance) by using two bridges soldered to the tube as shown in figure A1. The other end of the tube was connected to the air supply fitting on the wing root. Good mechanical connections are needed to ensure that the effect of the airlines on the balance calibration is repeatable.

Calibration Procedure

The balance is first subjected to known loads with the airlines removed. To do this, a steel loading bar was fabricated to replace the removable wing tip section. Weights were suspended from the loading bar using weight pans supported by knife edges. A photograph of the balance-airline assembly undergoing loadings is presented in figure A3. Because the weights were applied at the wing tip, the loads were applied as combinations of axial force and yawing moment, of normal force and rolling moment, and of pitching moment, normal force, and rolling moment. The airlines were then installed and the loadings repeated. The correction to each balance component for the stiffness of the unpressurized airline is the difference between measured loads without and with the airlines attached.

Air pressure within the airline can make the airline stiffer. Each airline was pressurized separately to the maximum available pressure with several different loads applied. The additional correction for each balance component for the increased stiffness due to presure is the difference in the measured loads with and without pressure. Pressure in each airline will try to uncoil the loops in the airline. Each airline was pressurized separately with no applied weight and the change in the measured forces and moments were recorded.

Calibration Results

Effect of airline stiffness on the balance sensitivity is presented in figure A4. The difference between the airline off and airline on load is presented rather than the measured load for clarity. The airline supports part of the load. Thus, the load measured with the airline is less than the load without the airline. The ordinate of each curve represents the increase in load needed to correct for the airline stiffness. Correction factors used to adjust the balance sensitivities for the presence of the unpressurized airline were 1.0 plus the slopes of the curves of the change in load with applied load. Correction factors applied to the balance sensitivity for normal force and axial force were 1.0034 and 1.0042, respectively. Corrections factors for pitching moment, rolling moment, and yawing moment were set to 1.0 since the change in load due to the airline was much smaller than the balance measurement accuracy. The design goal that the airlines not degrade the balance accuracy or sensitivity was achieved.

Effect of pressure on the airline stiffness was checked by increasing the airline pressure to maximum available pressure at several different applied loads. No change was detected in the measured loads when the airline was pressurized to the maximum available pressure. Thus, no additional terms due to airline pressure were included in the correction factor for airline stiffness applied to the balance sensitivity.

The effect of airline pressure on the static loads is presented in figure A5. The two airlines were not anti-symmetric so that increasing pressure can lead to a change in the static load. The only balance component static load that was influenced by airline pressure was axial force. A static load correction of 0.00040 lbf per psi for the forward airline and 0.00045 lbf per psi for the rear airline was applied to the axial force. No corrections for the airline pressure were applied to the other balance components.

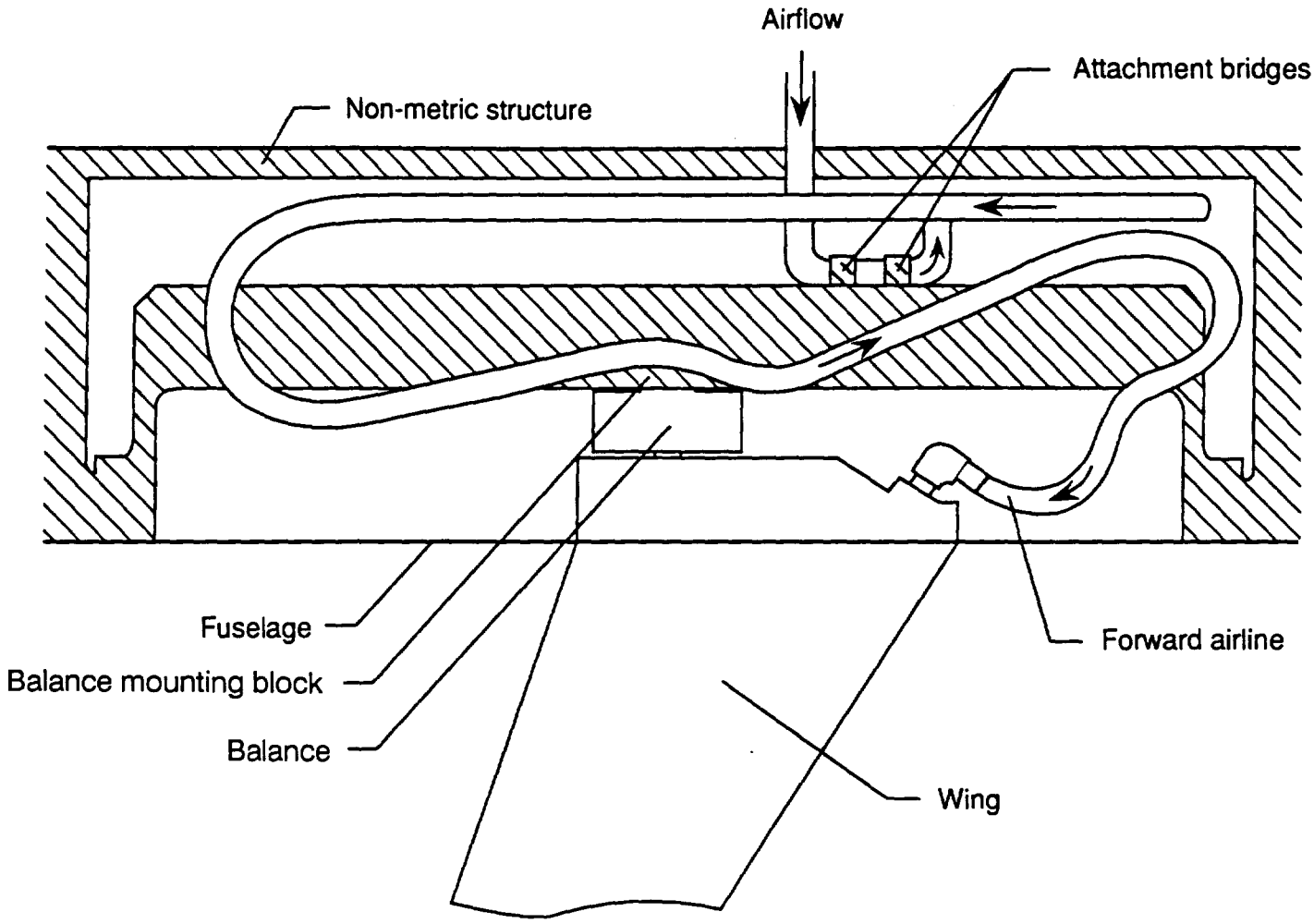

Figure A1. Sketch of the forward jet air supply line.

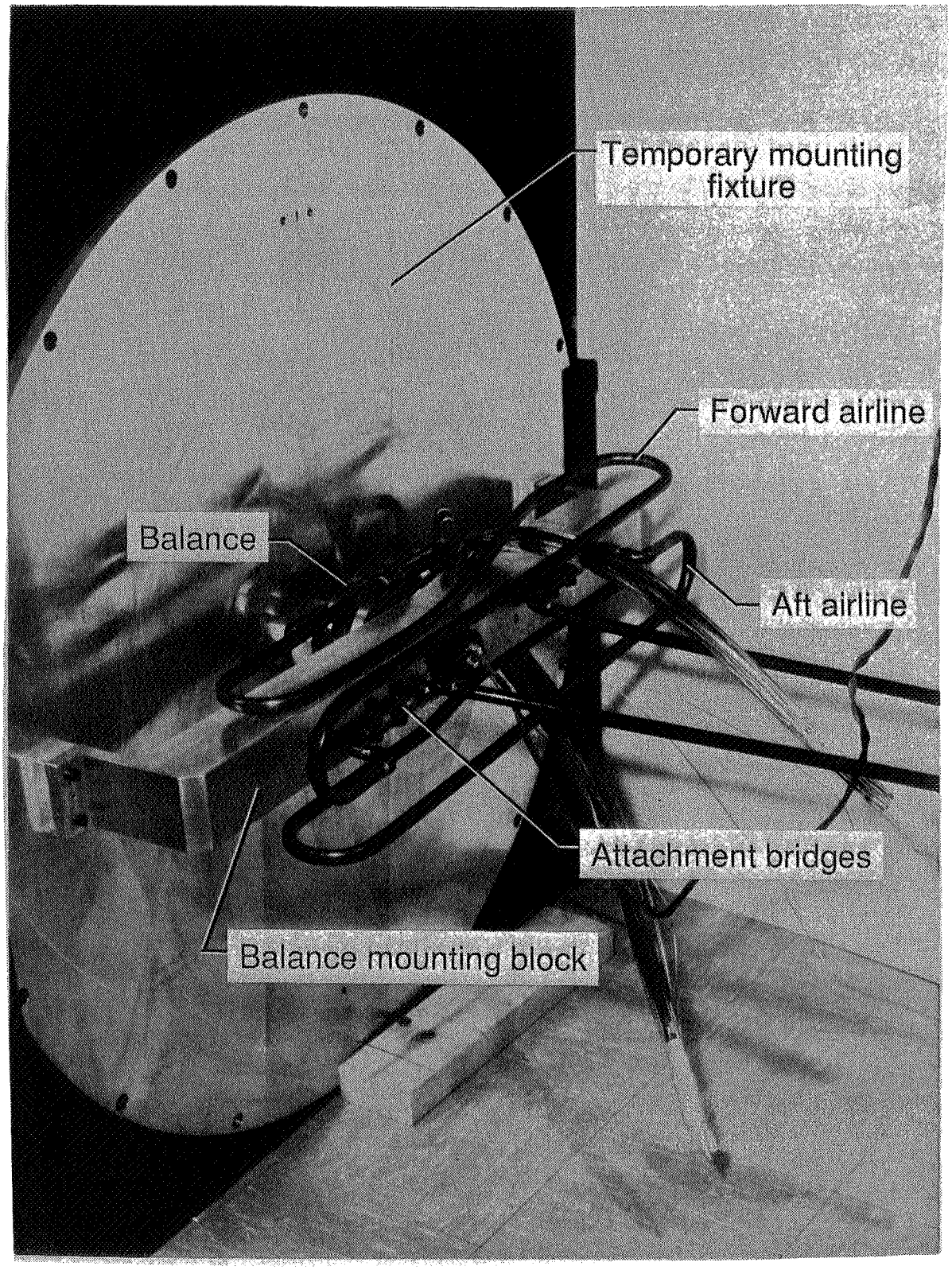

Figure A2. Photograph of the air supply lines with the model in a temporary mounting fixture.

C-4

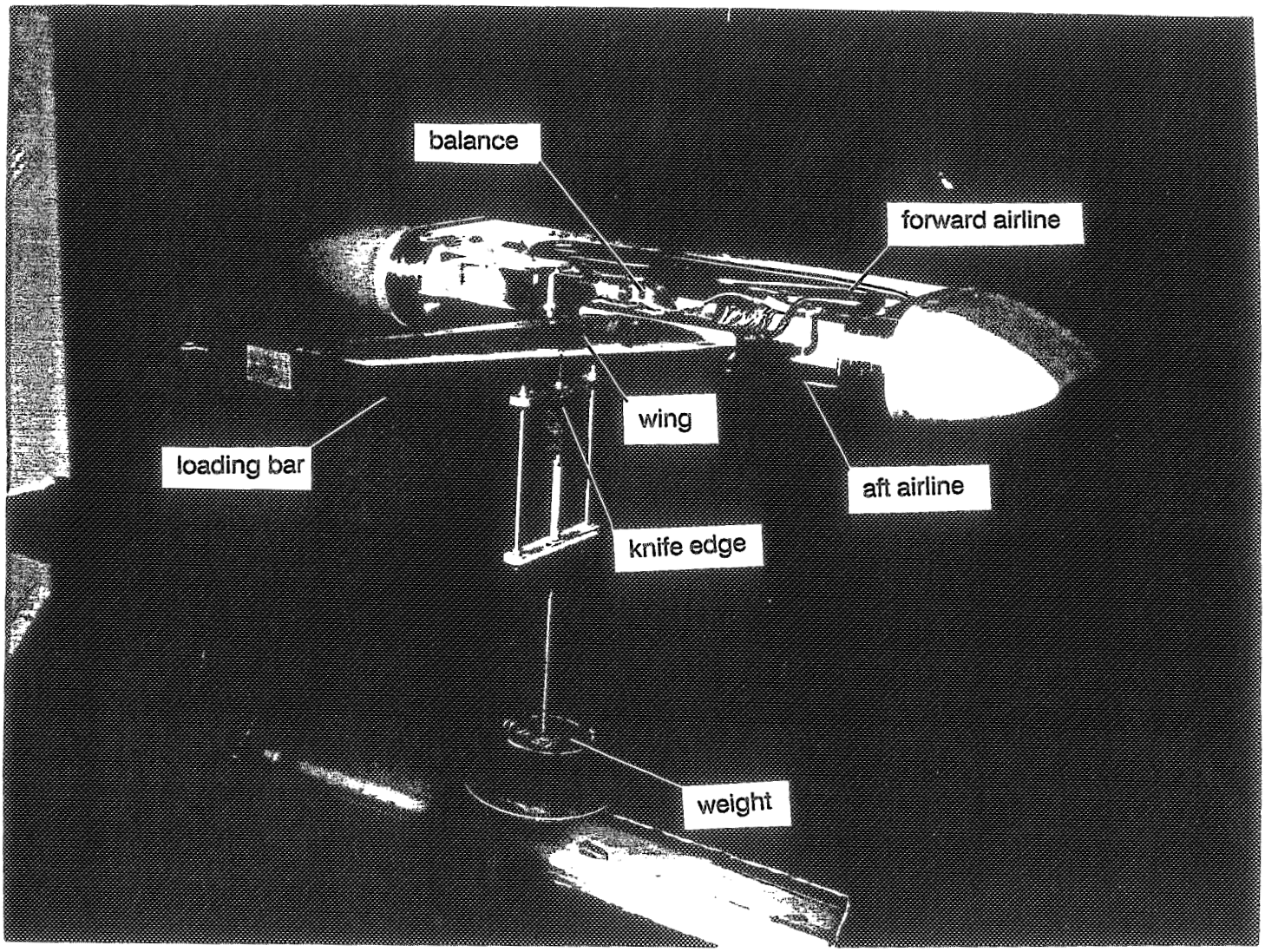

Figure A3. Photograph of the airline balance assembly undergoing calibration in the wind tunnel.

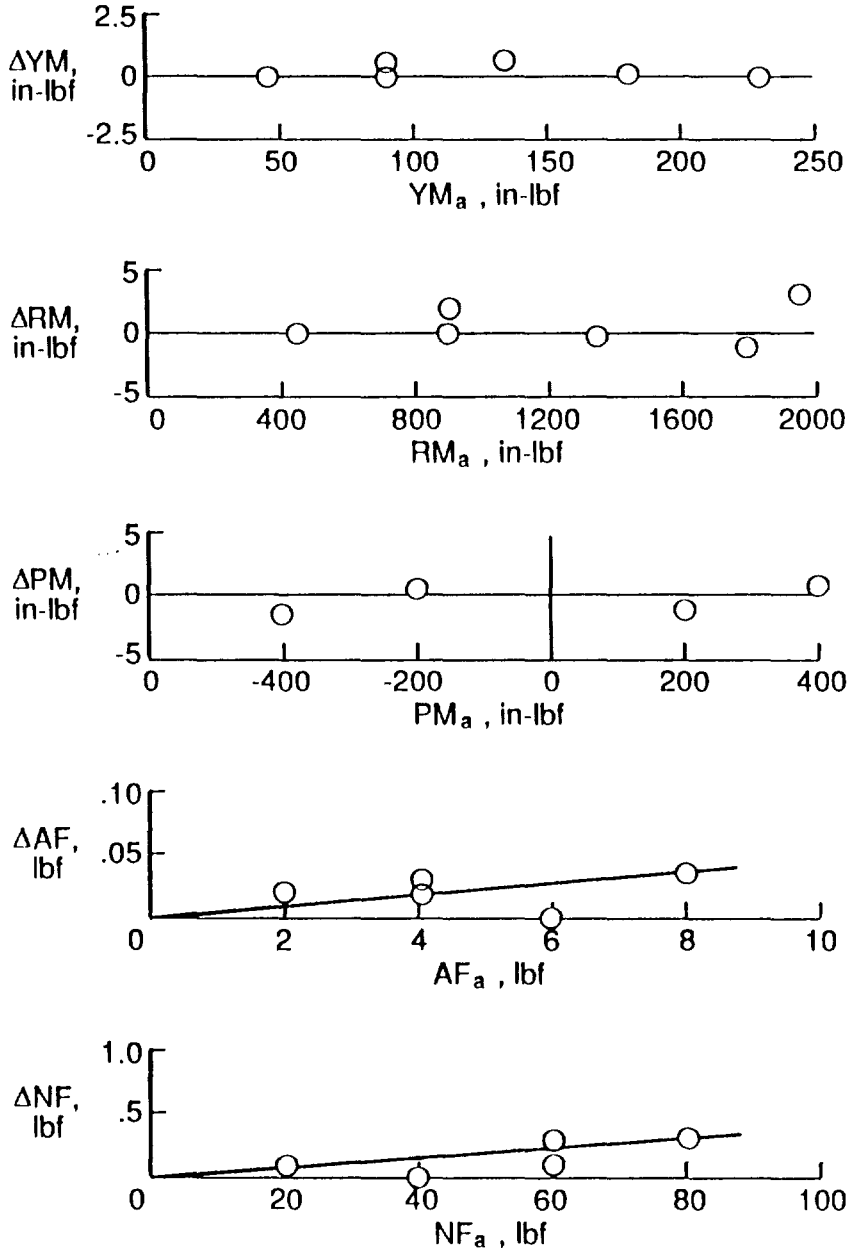

Figure A4. Effect of the airline stiffness on the balance sensitivity.

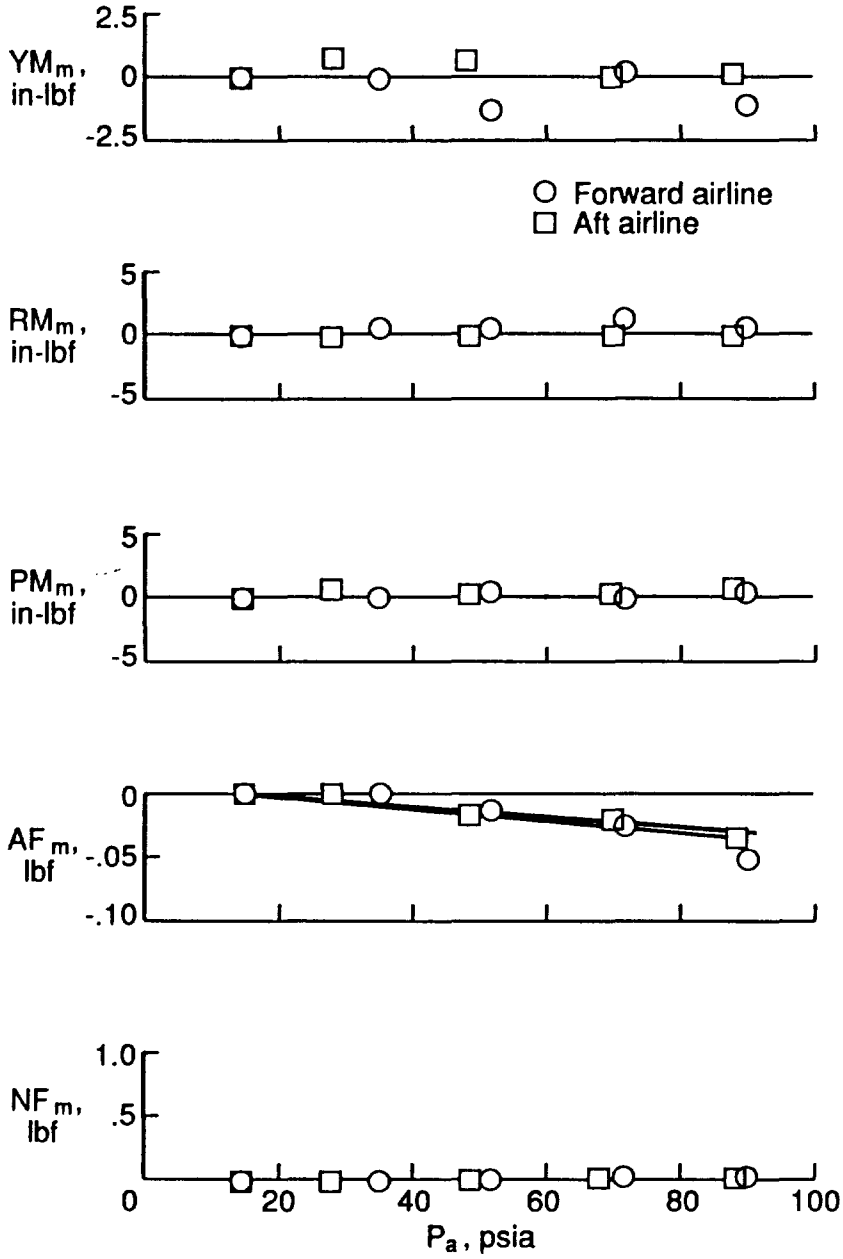

Figure A5. Effect of airline pressure on the balance measurement.

APPENDIX B

CALIBRATION OF THE WINGTIP JETS

Jet momentum could not be measured directly since there was no side force measurement possible with the semispan balance. Momentum was determined by vertically surveying the jet total and static pressure at several chordwise locations of the jet. In this appendix, calibration procedures are defined, equations used to determine the momentum are derived, and calibration results are presented.

Symbols

a	local speed of sound, $\frac{\text{ft.}}{\text{sec.}}$
F	jet momentum, lbf.
f	calibration factor to determine jet momentum from the jet plenum pressure
M	local Mach number
$\dot{m}$	mass flow rate, $\frac{\text{slugs}}{\text{sec.}}$
p	local static pressure, psia
p_a	ambient static pressure, psia
p_{fm}	flowmeter static pressure, psia
p_p	plenum total pressure, psia
p_t	local total pressure, psia
R	gas constant for air, 1715 $\frac{\text{ft. lbf.}}{\text{slug } ^\circ\text{R}}$
T	static temperature, $^\circ$R
T_{fm}	flowmeter static temperature. $^\circ$R
$\dot{V}$	volume flow rate, $\frac{\text{ft.}^3}{\text{sec.}}$

v	local jet velocity, $\frac{ft.}{sec.}$
x	vertical position, inches
y	chordwise position, inches
γ	ratio of specific heats, 1.4
ρ	static density, $\frac{slugs}{ft.^3}$
ρ_{fm}	flowmeter static density, $\frac{slugs}{ft.^3}$

Calibration Procedures

This section defines the procedures that were used to calibrate the front and rear jets on each wing tip section. The front and rear jets were calibrated separately. A sketch of the experimental setup is presented in figure B1(a). Shop air was connected to the airline assembly for the appropriate jet with a valve, regulator, and flexible air hose. A thermocouple and static pressure transducer were used to measure the static temperature and pressure at the flowmeter. The flowmeter measured the volume flow rate in the airline. A tube with a "J" shaped end was installed in the wing tip plenum chamber. The other end of the tube was connected to a pressure transducer, referenced to the ambient pressure, to measure the total pressure in the wing tip plenum. Ambient pressure was measured with an absolute pressure transducer.

A total head tube rake with a static pressure tube was mounted on a traversing mechanism. A sketch of the rake and tip are presented in figure B1(b) and a photograph is presented in figure B2. The rake was positioned so that the total pressure tubes were about 0.5 inches from the jet exit to allow clearance for the static pressure tubes. Five total pressure tubes and the static pressure tube were connected to pressure transducers to measure the total pressure distribution across the width of the jet. Analog output from each piece of instrumentation was connected to a 32 channel data acquisition unit controlled by a personal computer. Total pressure tubes used for the survey were located on either side

of the static pressure tube to ensure that the tube would measure the static pressure within the jet. Spacing of the tubes was selected to include both ends of the jet and cover the entire width of the jet.

The rake was initially positioned either above or below the plane of the jet, the air supply valve opened, and the regulator adjusted to obtain the desired plenum pressure. At each rake position, 128 readings from each channel of the data system were acquired, recorded, and averaged. The rake was repositioned and another set of 128 readings recorded. The process was repeated until the readings indicated that all the total pressure tubes had emerged from the other side of the jet. These surveys were repeated for 2 or 3 plenum pressures. Momentum of the jet at each drive pressure was computed with the equations presented below.

Development of the Calibration Equations

Flow from the jet is assumed to be fully expanded and the ideal gas law is assumed to apply. The flow is assumed to be isentropic from the plenum in the wing tip to the surroundings where the jet is surveyed. Static temperature and pressure are measured at the flowmeter along with the flowmeter volume flow rate. From the ideal gas law and the measured static temperature and pressure, the density of the air at the flowmeter can be determined

$$\rho_{fm} = \frac{144\, p_{fm}}{R\, T_{fm}} \tag{B.1}$$

The mass flow rate is determined from the density and volume flow rate

$$\dot{m} = \rho_{fm} \dot{V} \tag{B.2}$$

A total head rake was positioned about 0.5-inches from the jet exit. Total pressure in the plenum,

static pressure of the jet, ambient static pressure, and total pressures from the rake tubes were recorded at a sufficient number of vertical positions to define the jet exit profile. At each vertical position, the local Mach number in the jet was determined from the measured rake total and static pressure

$$M = \frac{2}{\gamma - 1}\{ (\frac{p}{p_t})^{-\frac{\gamma-1}{\gamma}} - 1\} \tag{B.3}$$

The local speed of sound is

$$a = (\gamma R T)^{1/2} \tag{B.4}$$

From the static temperature and the local static pressure, the local density is

$$\rho = \frac{144\ p}{R\ T} \tag{B.5}$$

The local jet velocity is determined from the local Mach number and speed of sound as follows

$$v = M\ a \tag{B.6}$$

The product of the density and local velocity squared is integrated from the initial to the final rake position to determine the momentum per unit width of the jet

$$\frac{d\ F}{d\ y} = \int_{-\infty}^{+\infty} \rho\ v^2\ dx \tag{B.7}$$

and the total momentum is determined by integrating across the width of the jet

$$F = \int_{-\infty}^{+\infty} \frac{d F}{d y} \, dy \tag{B.8}$$

The jet momentum varied linearly with the plenum pressure. A least squares curve fit of the jet momentum was determined for each jet.

$$F = f (p_p - p_a) \tag{B.9}$$

Calibration Results

Each tip was calibrated separately at 2 or 3 drive pressures. The development of the calibration equations assumed that the jet was fully expanded. The static pressure measured from the static pressure tube on the rake was virtually the same as the ambient pressure indicating that, for the drive pressures used, this assumption is valid. The total pressure distributions for each tip calibration are presented in figures B3. Except for tip 8, the maximum jet Mach number was typically about 0.85 for the highest drive pressure. These total pressure distributions were used to determine the momentum per unit width for each total pressure tube (eq. B.7). These momentum per unit width distributions are presented in figure B4 for each tip. These curves were integrated to determine the jet momentum for each plenum pressure (eq. B.8). The variation of the jet momentum with plenum pressure is presented in figure B5. A linear, least squares fit was applied to the data for each tip to determine the calibration coefficients.

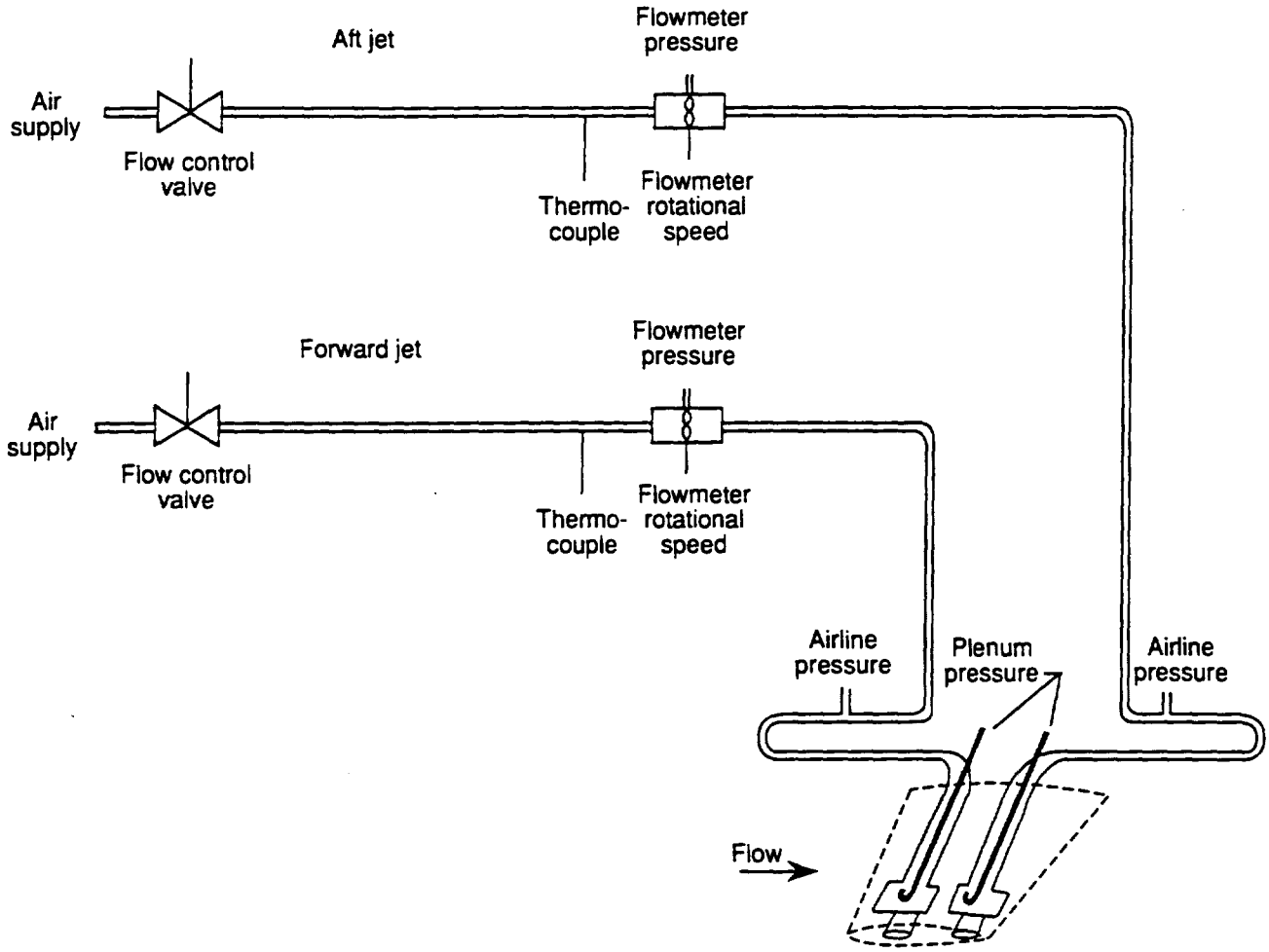

(a) Schematic of the air supply system and associated instrumentation.

Figure B1. Sketch of the experimental setup for the jet calibration.

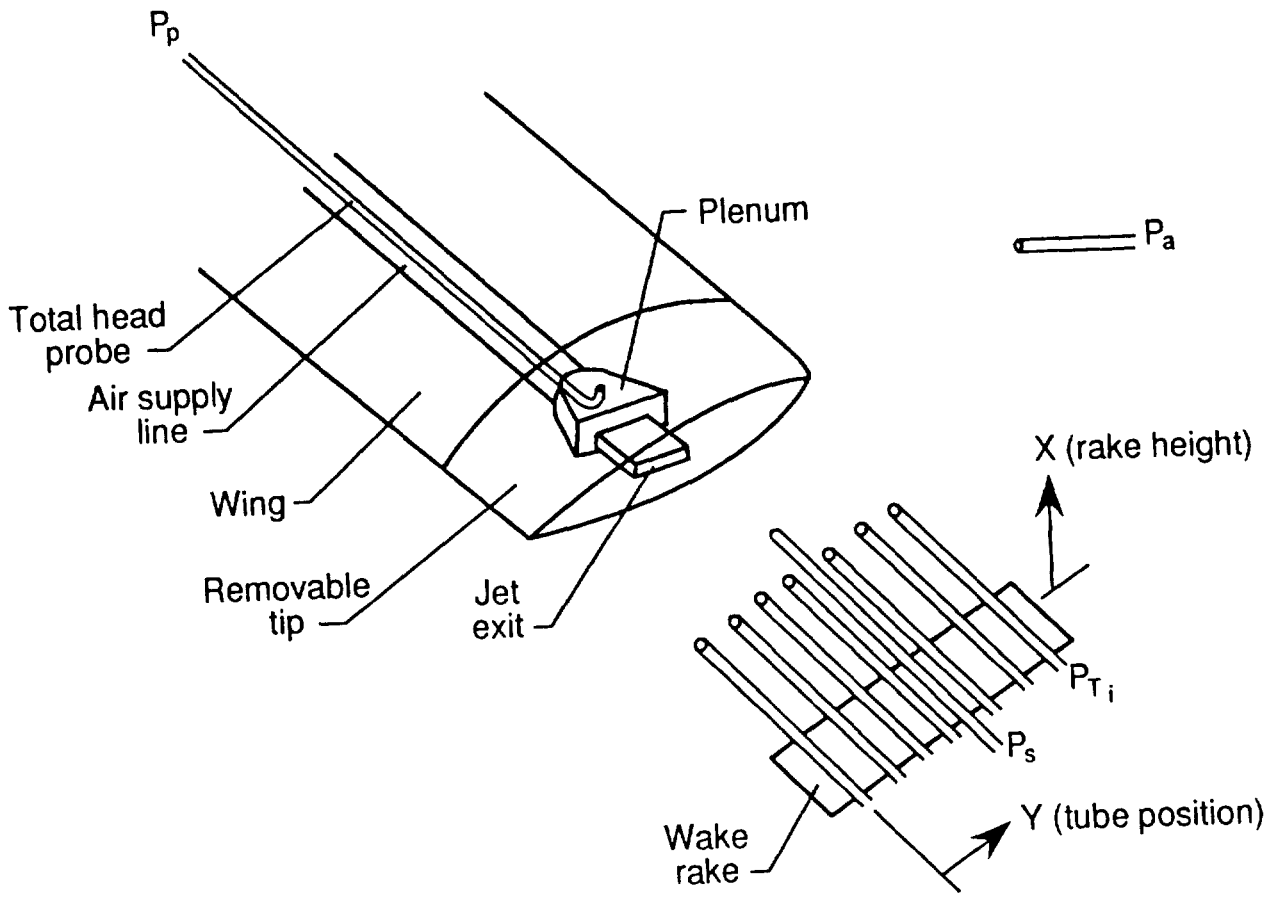

(b) Sketch of the experimental setup for the jet calibrations.

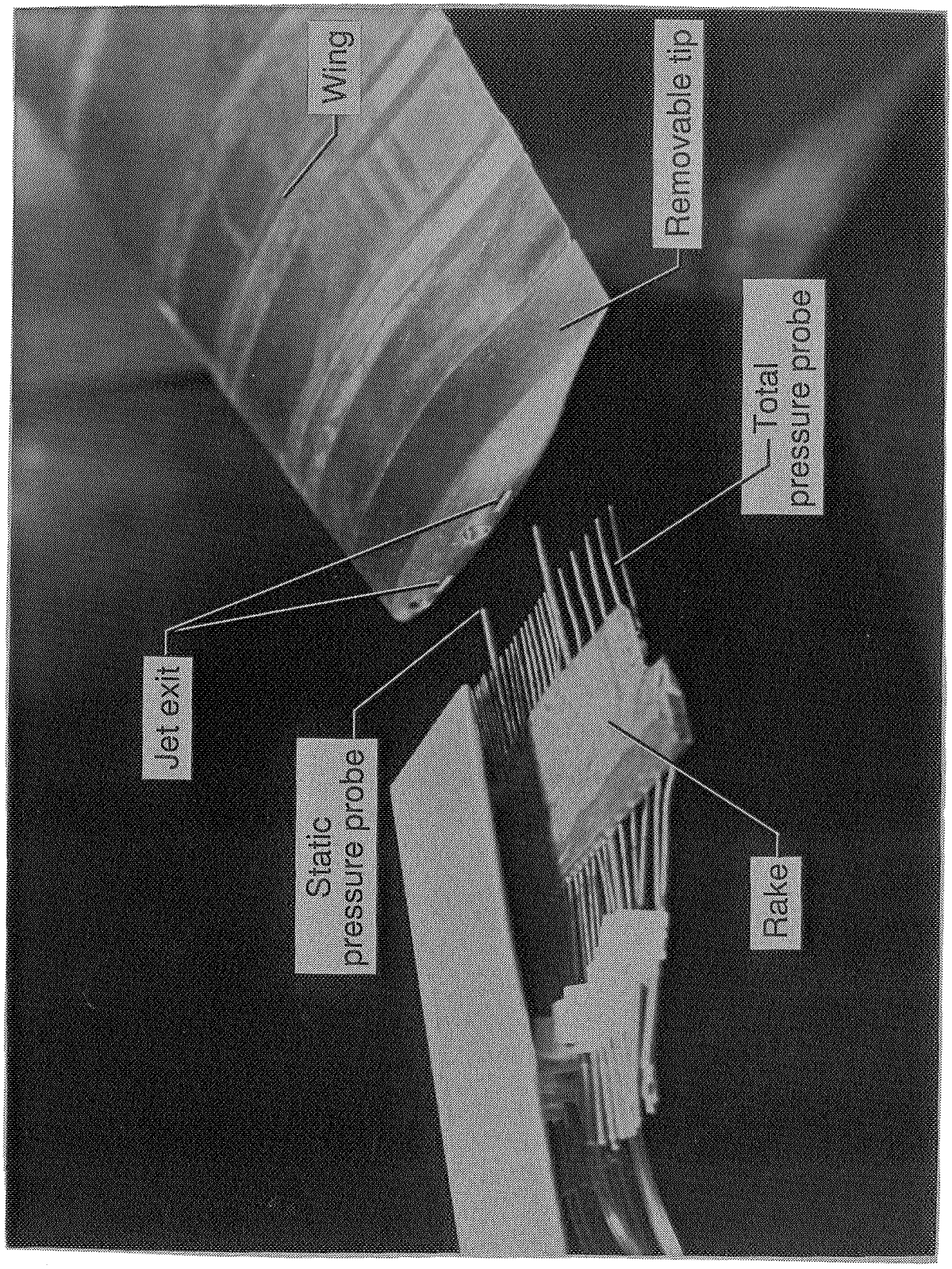

Figure B2. Photograph of the total pressure rake and the wing tip.

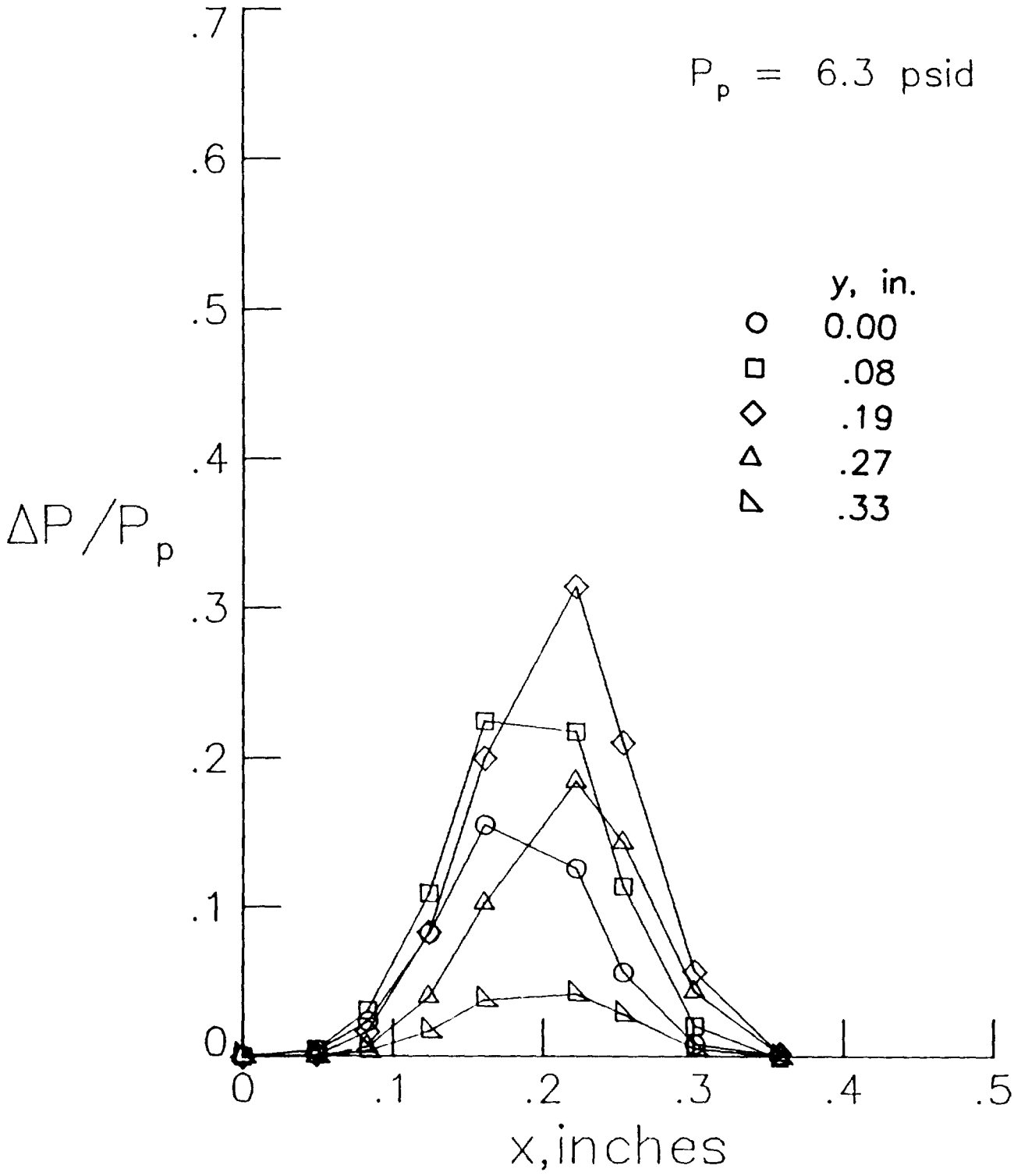

(a) Tip 1, front jet.

Figure B3. Total pressure distribution of the jet exhaust.

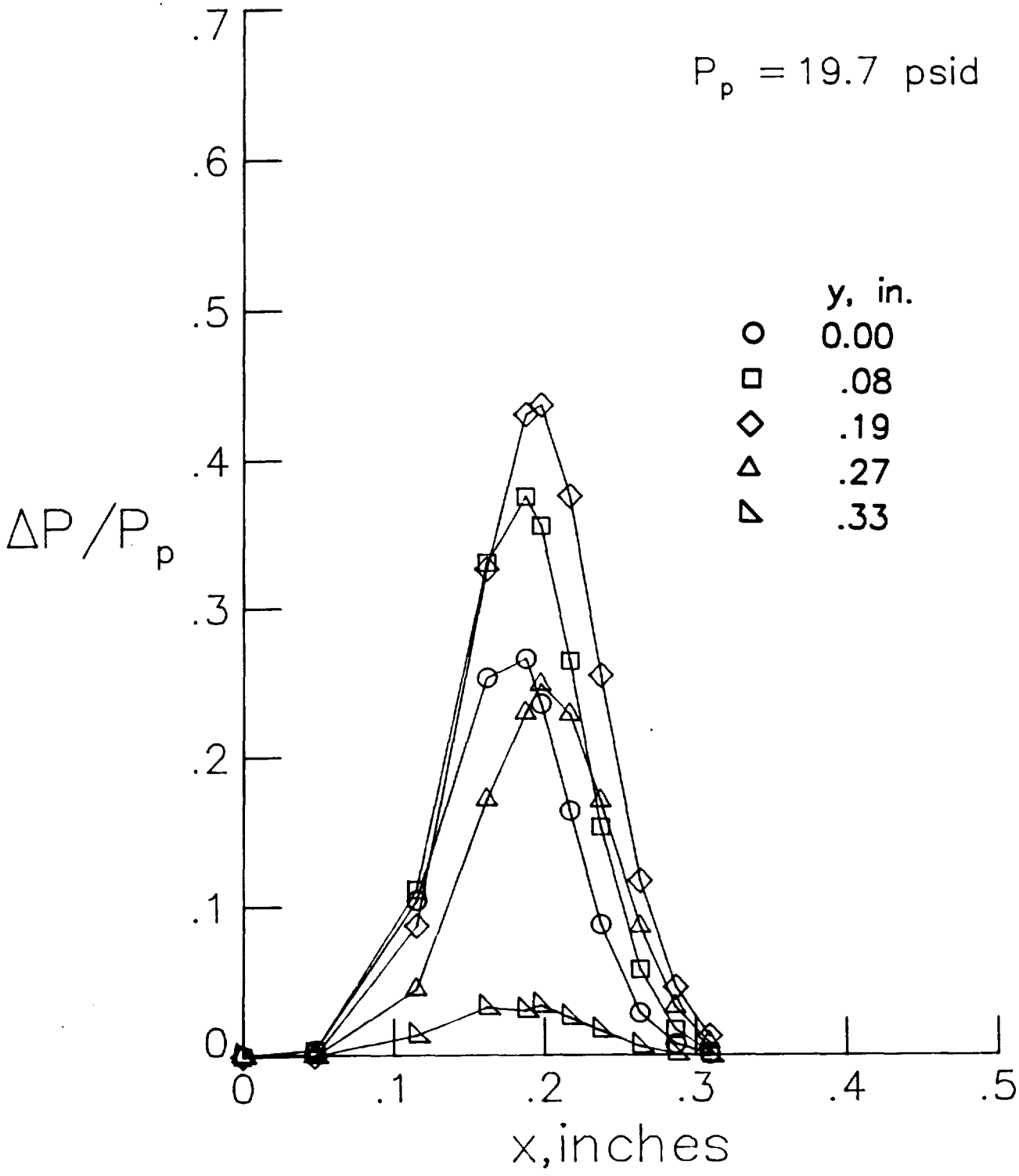

(a) Concluded.

Figure B3. Continued.

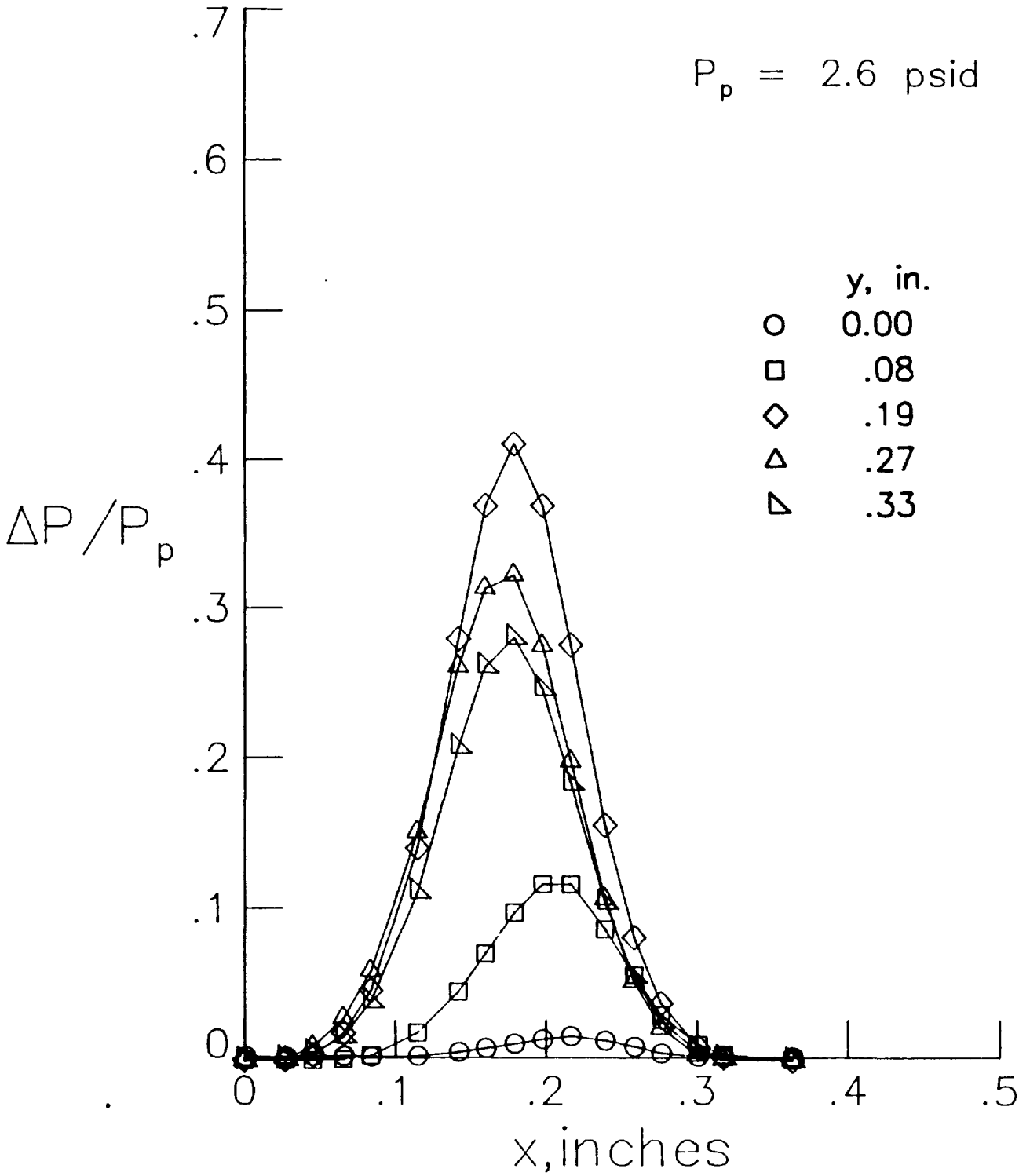

(b) Tip 1, rear jet.

Figure B3. Continued.

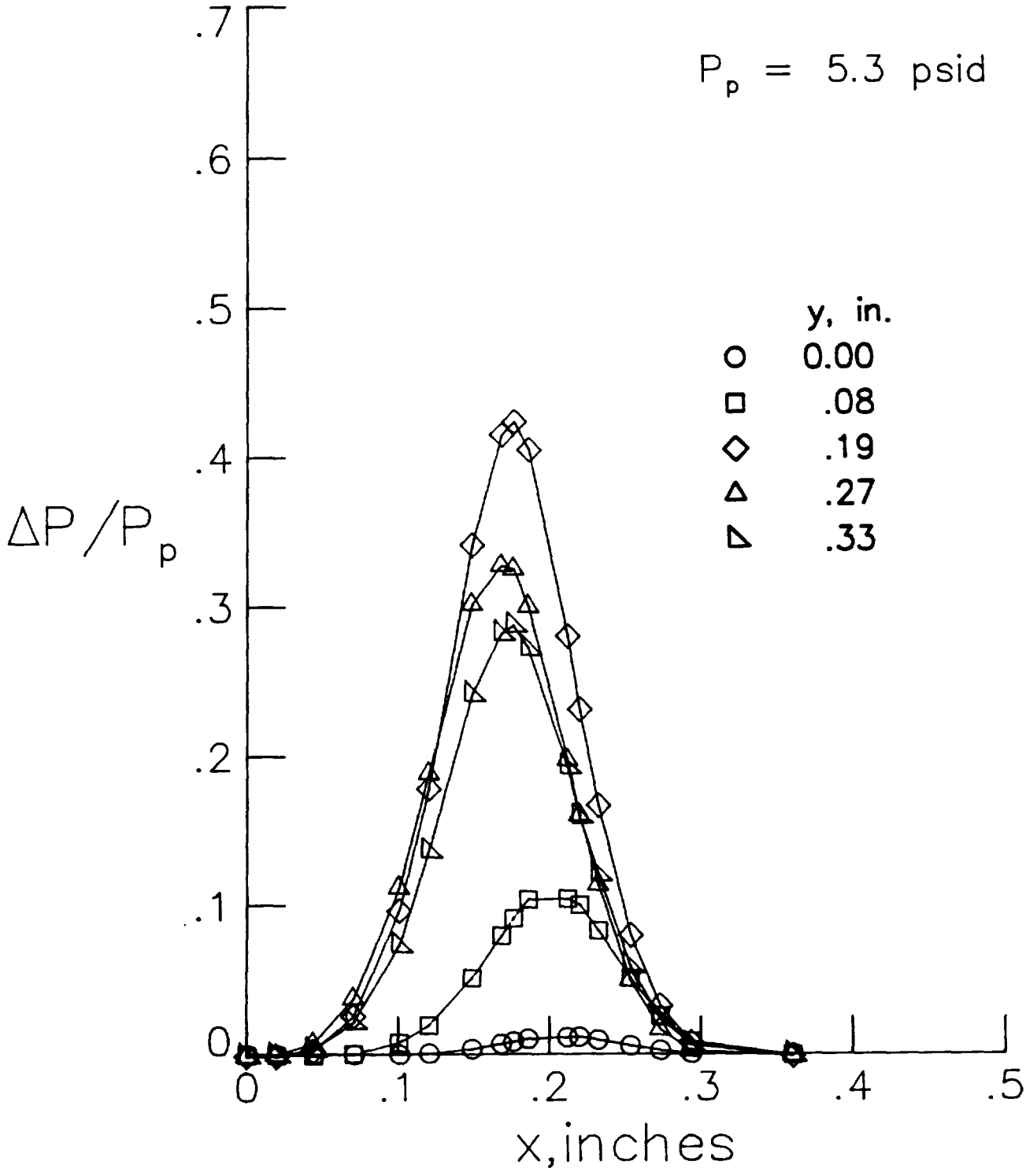

(b) Concluded.

Figure B3. Continued.

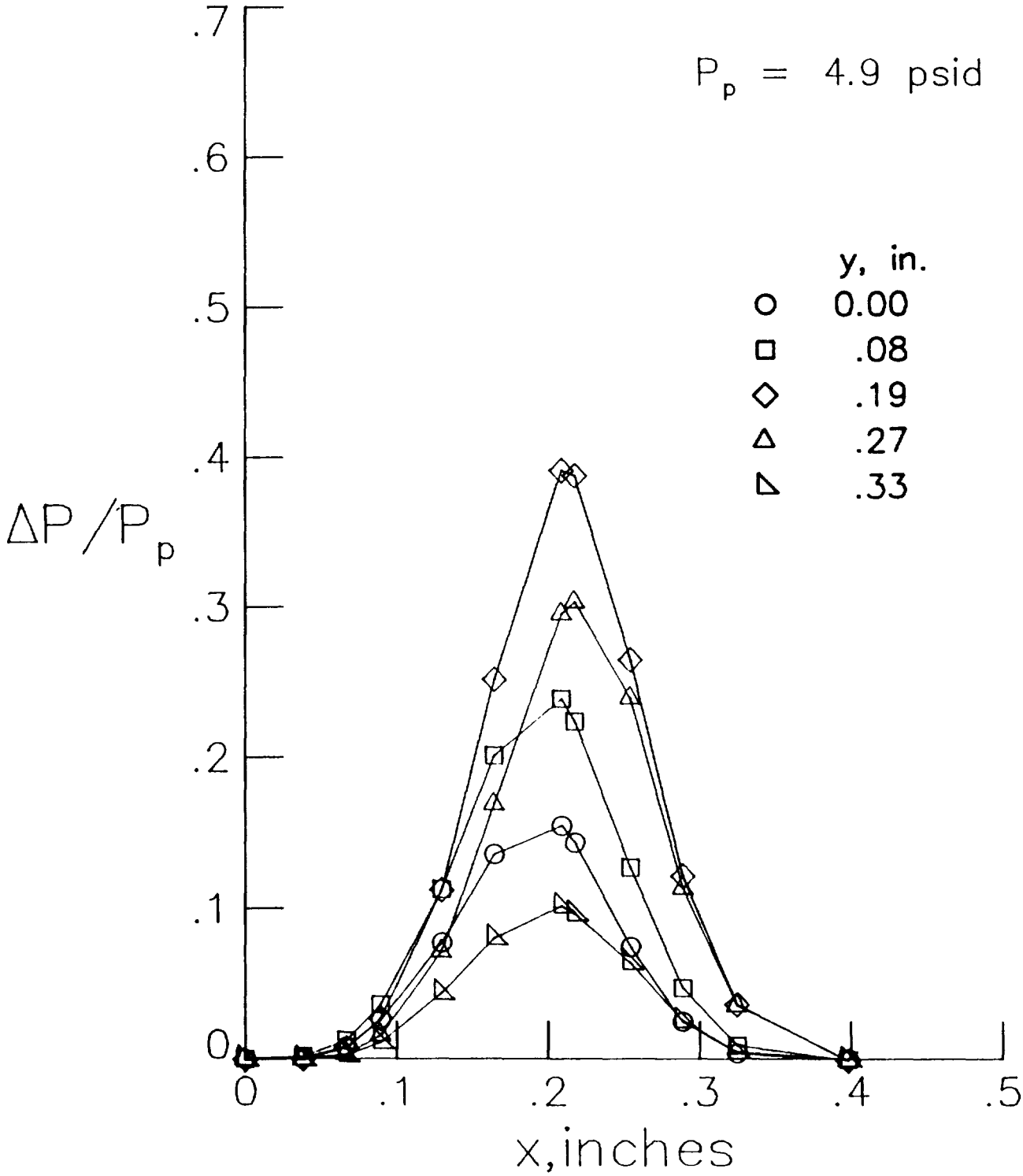

(c) Tip 2, front jet.

Figure B3. Continued.

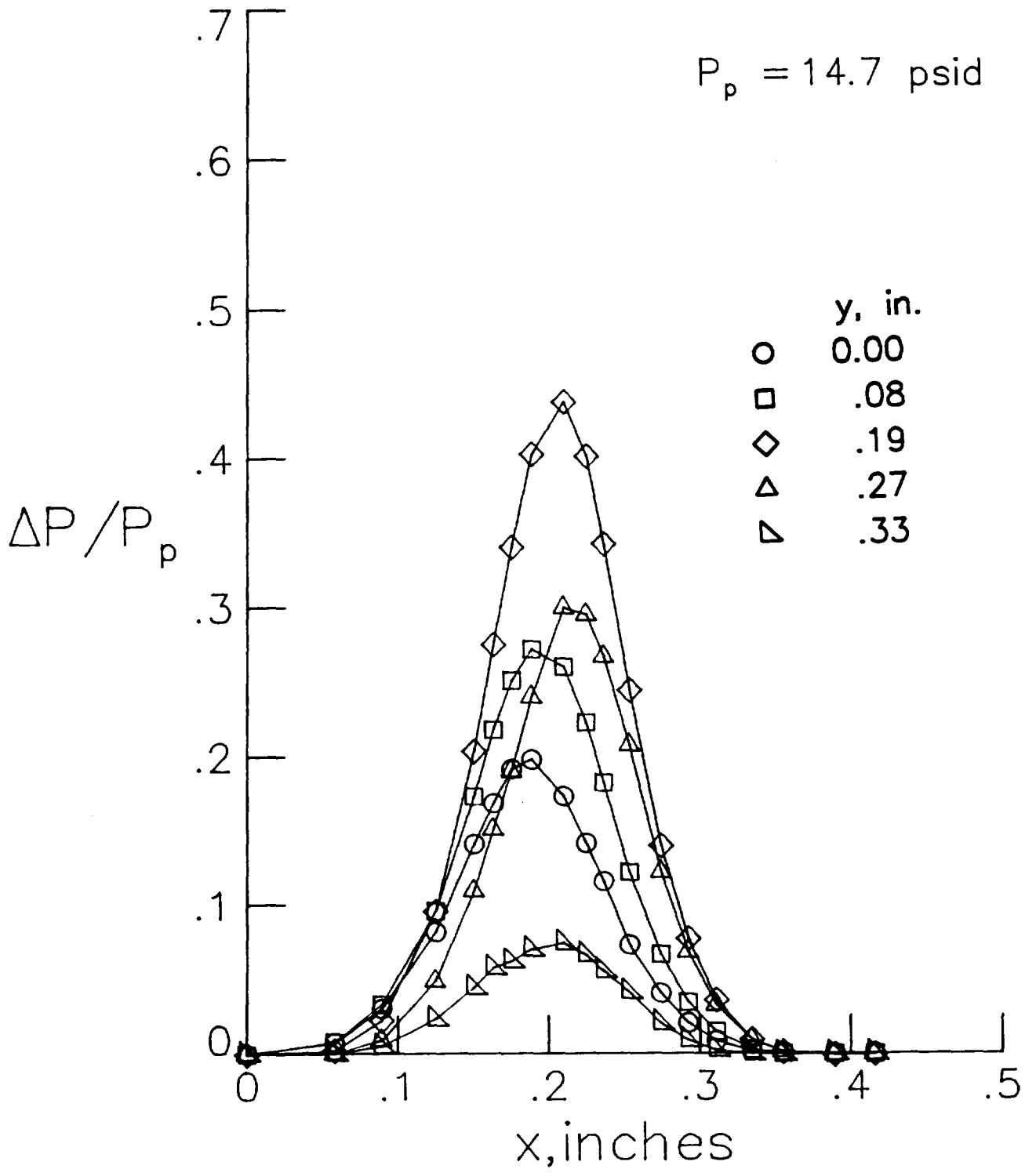

(c) Concluded.

Figure B3. Continued.

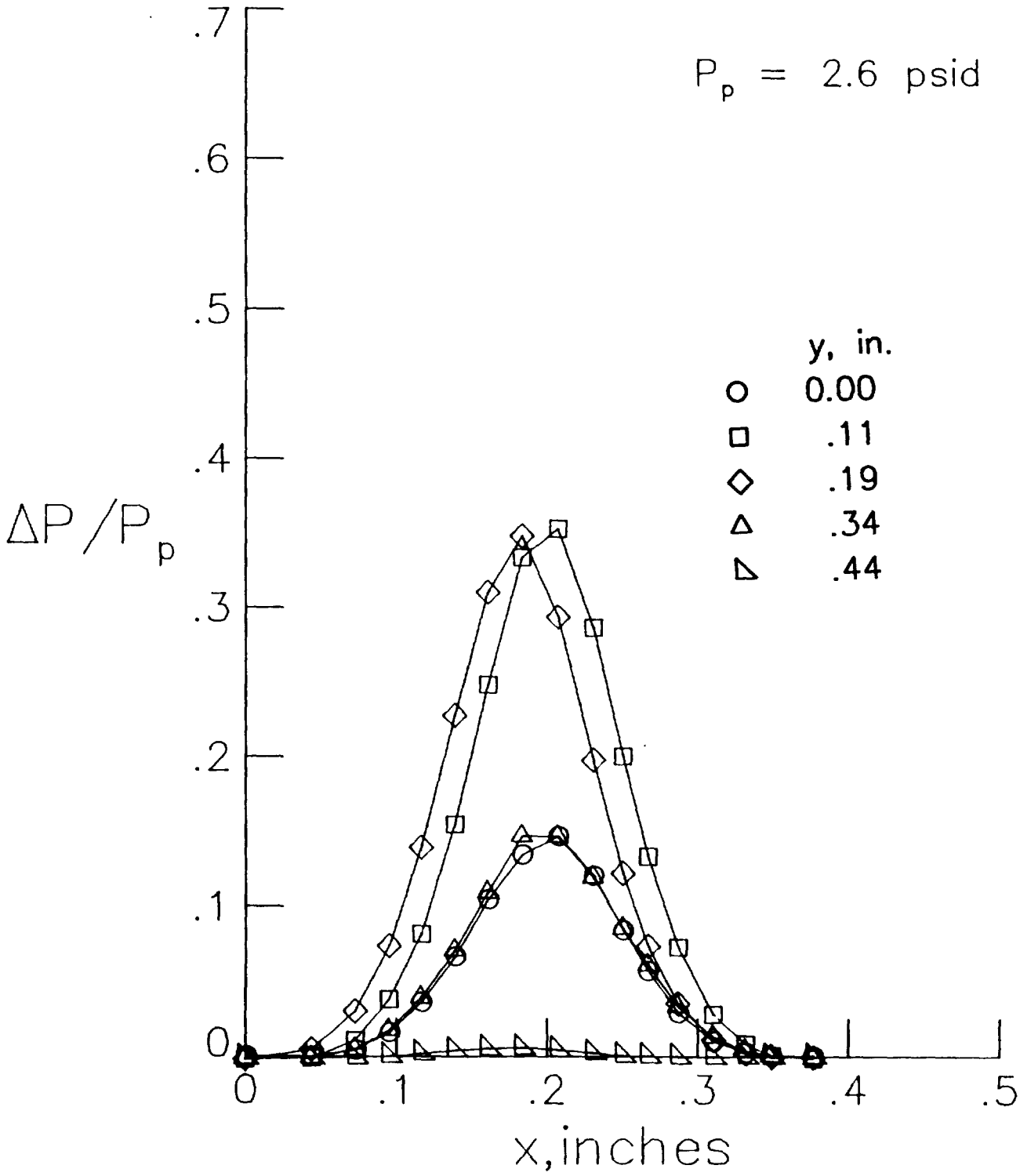

(d) Tip 2, rear jet.

Figure B3. Continued.

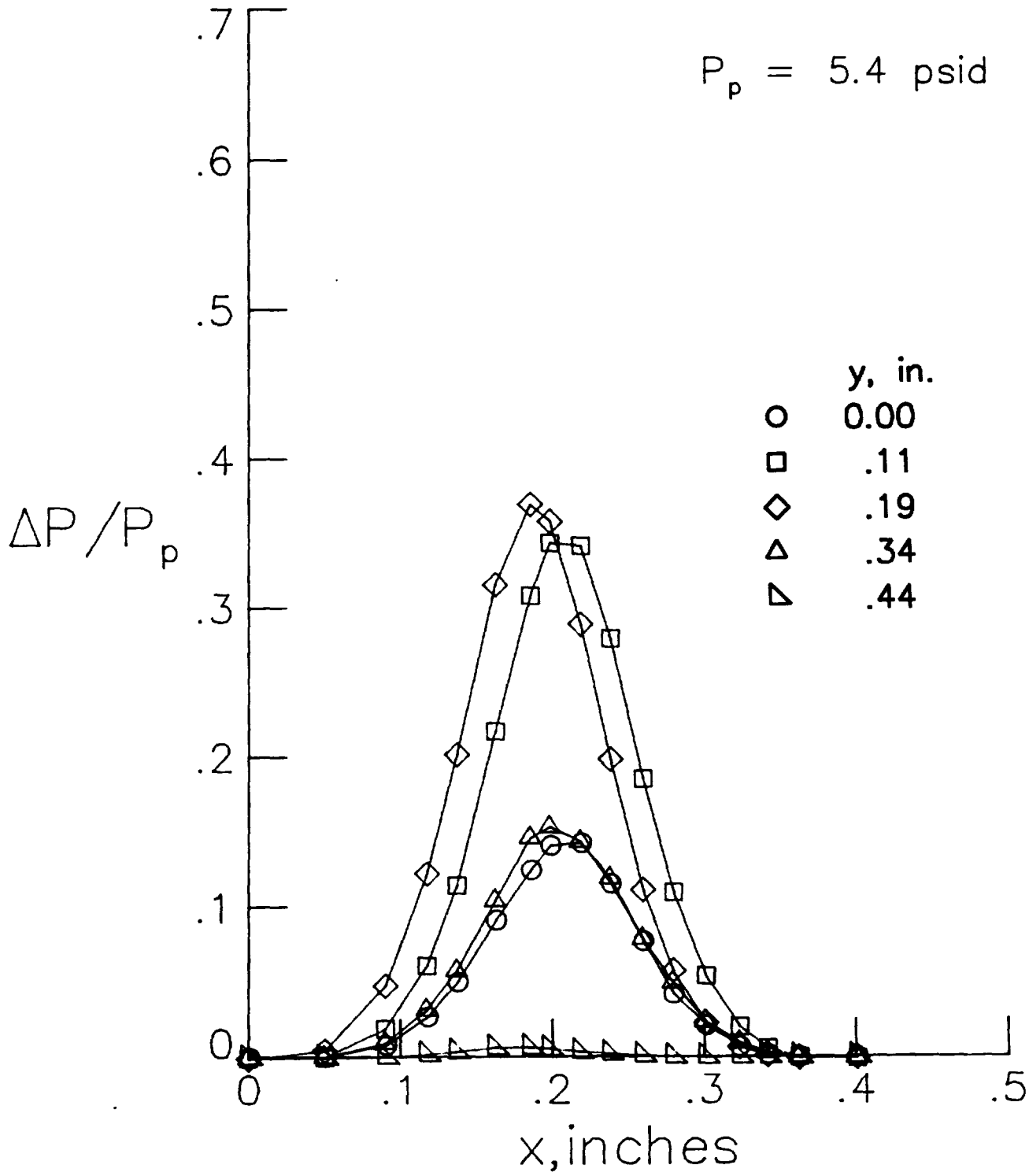

(d) Continued.

Figure B3. Continued.

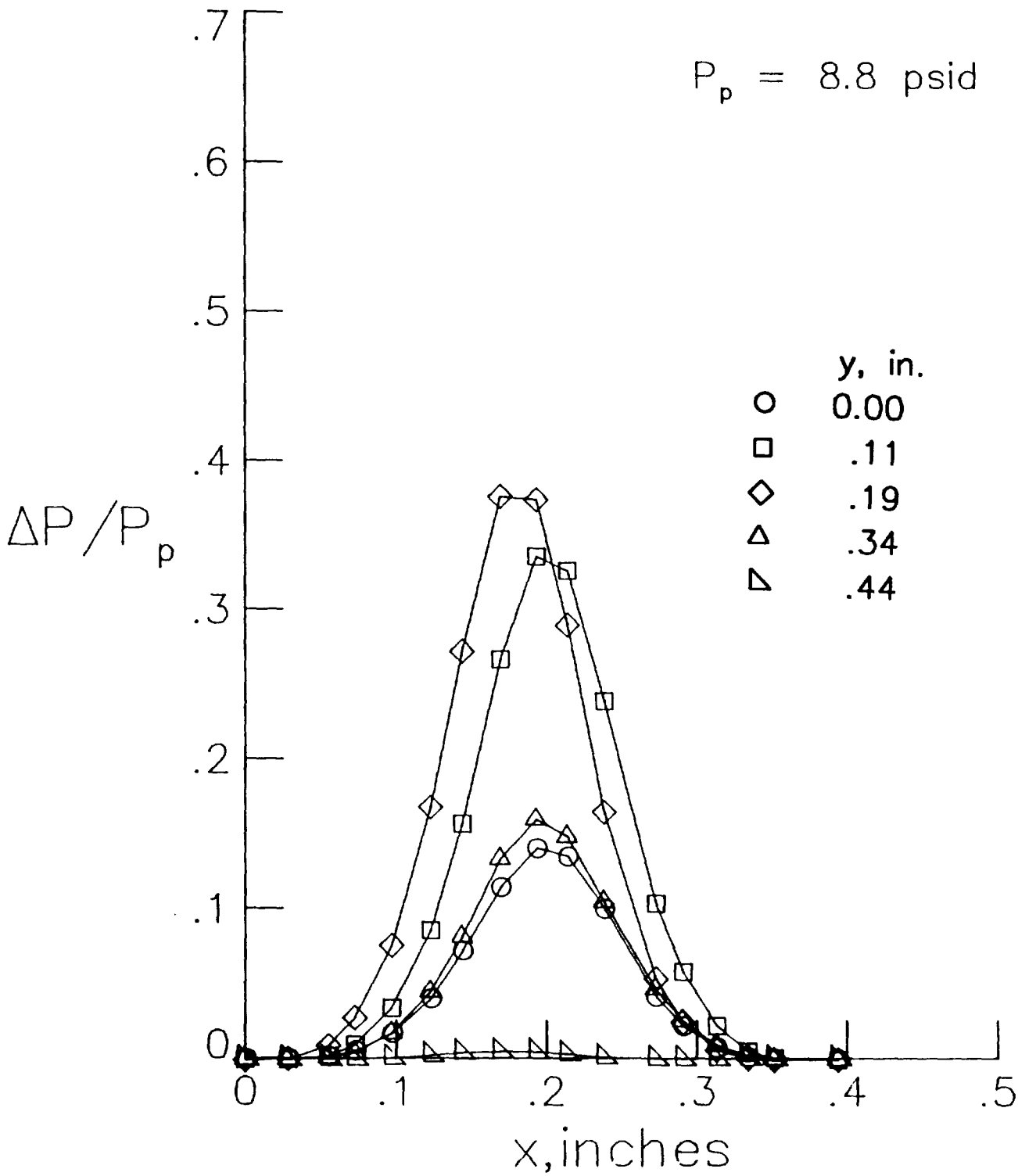

(d) Concluded.

Figure B3. Continued.

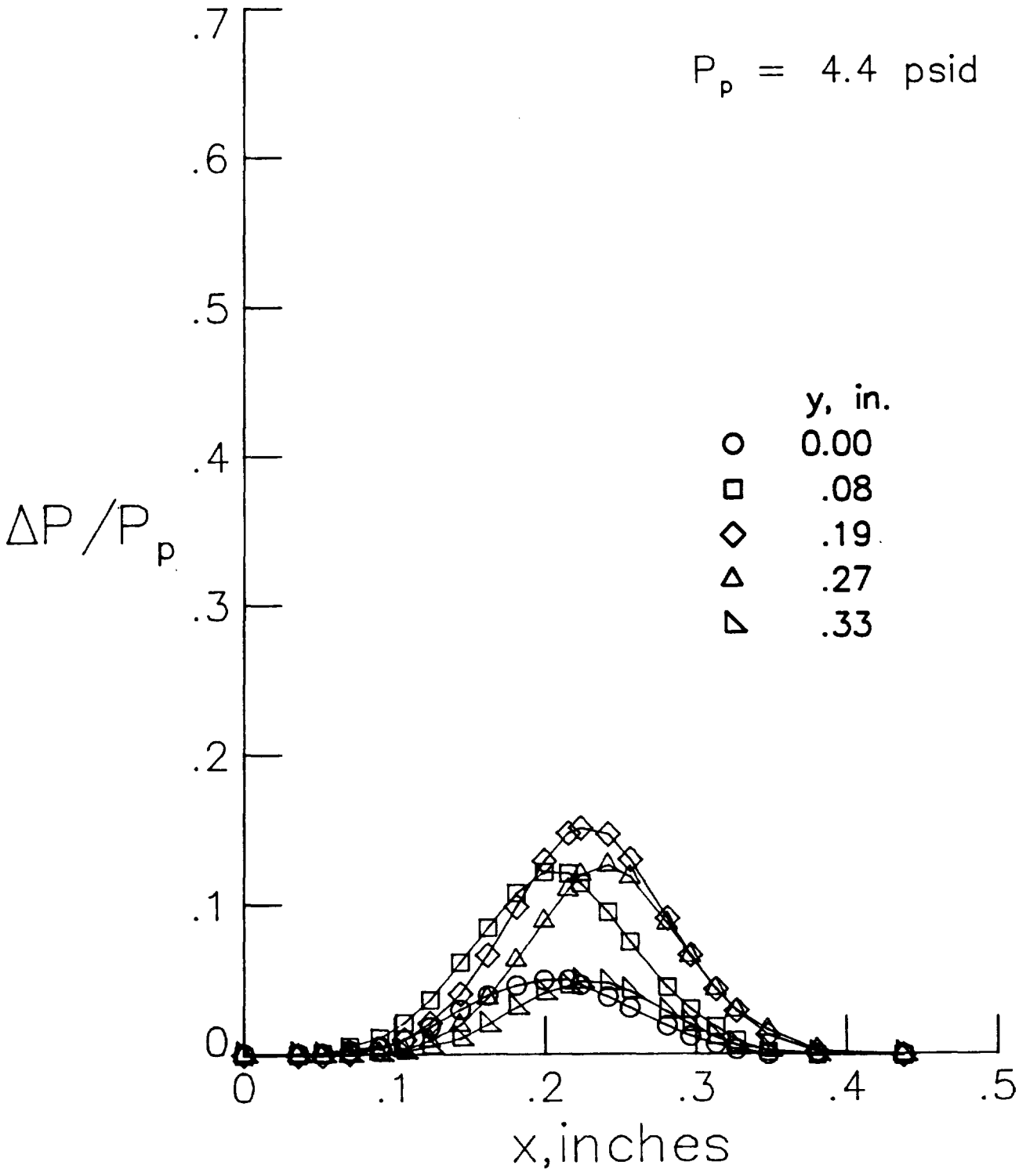

(e) Tip 3, front jet.

Figure B3. Continued.

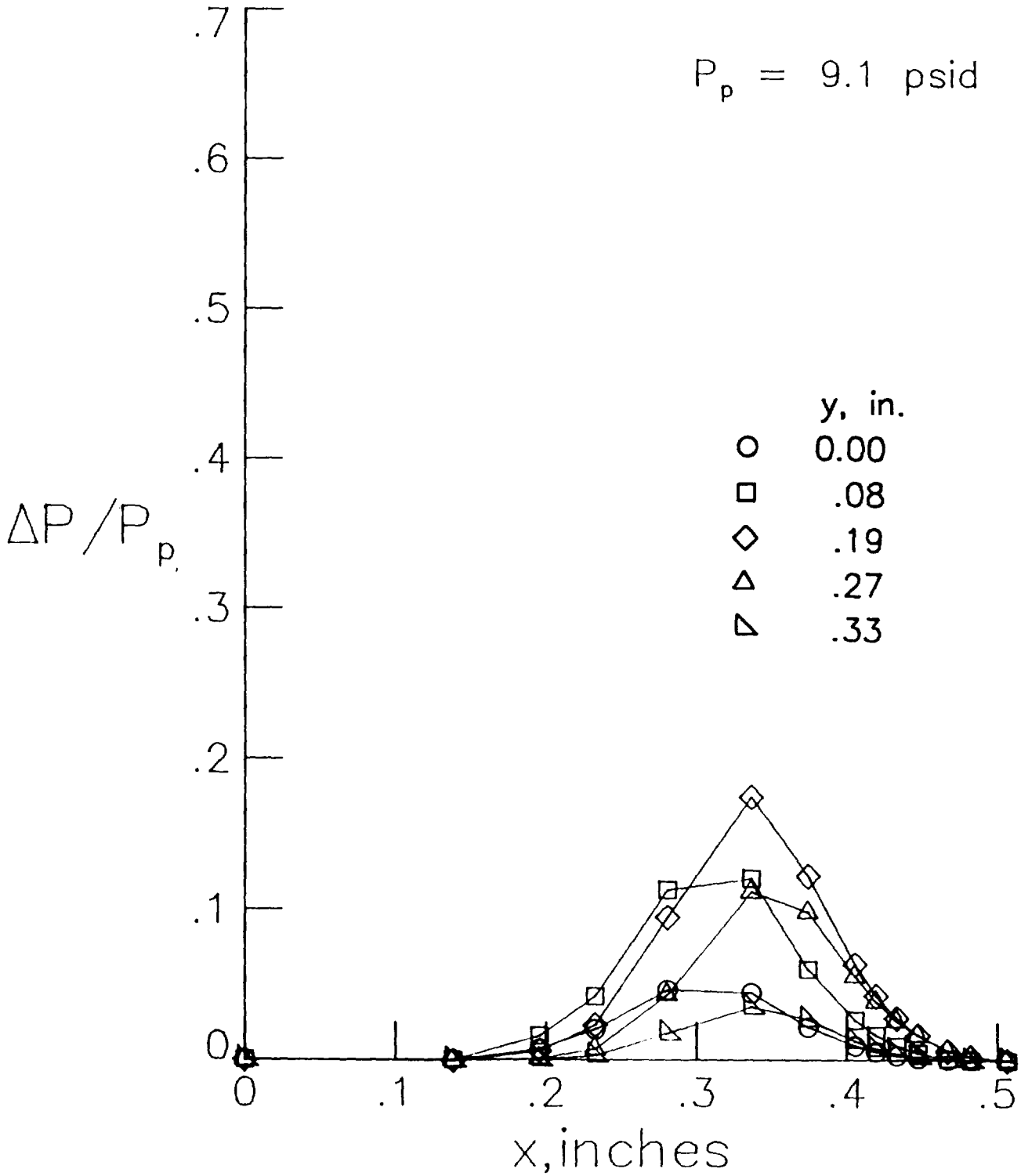

(e) Concluded.

Figure B3. Continued.

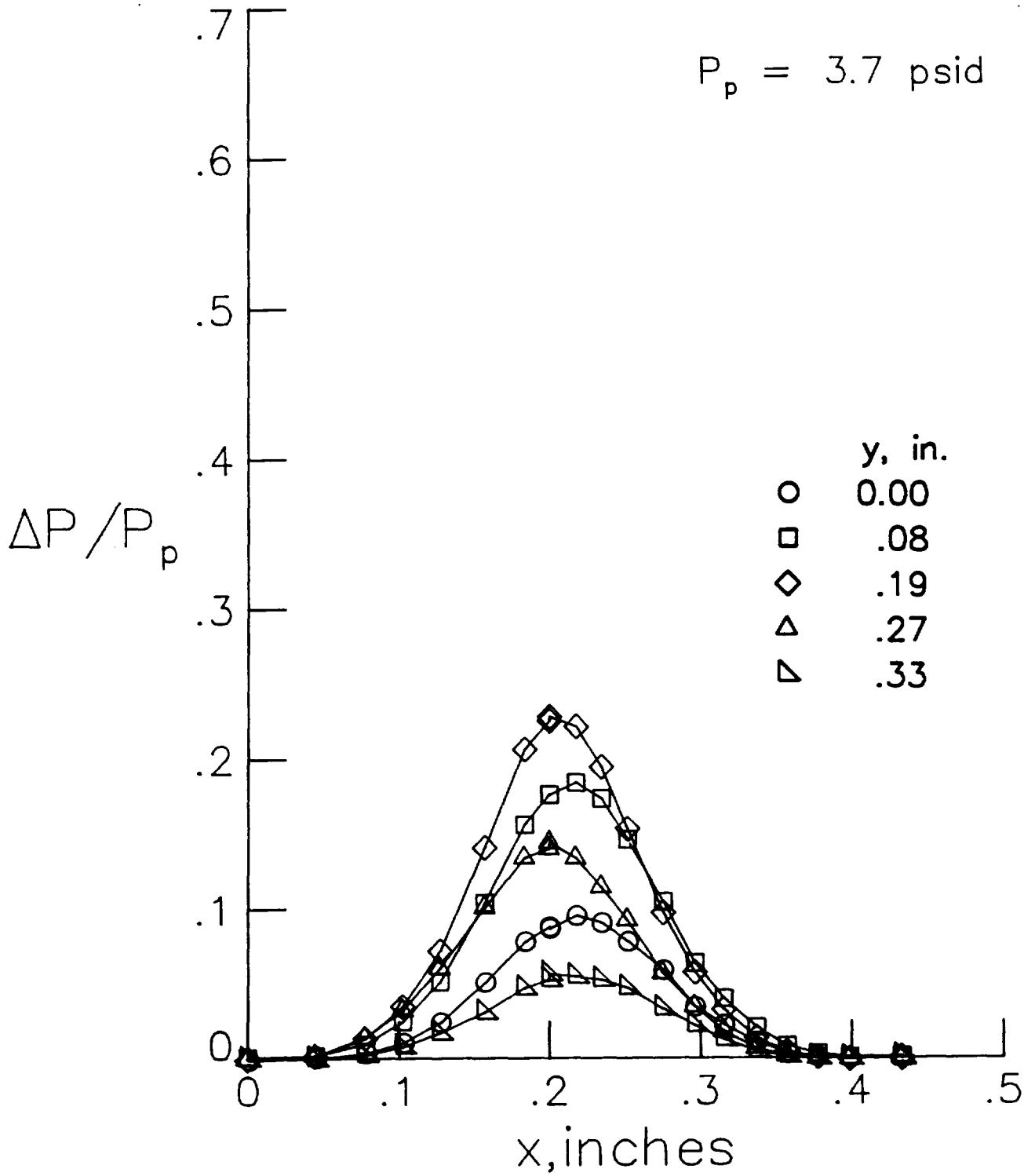

(f) Tip 3, rear jet.

Figure B3. Continued.

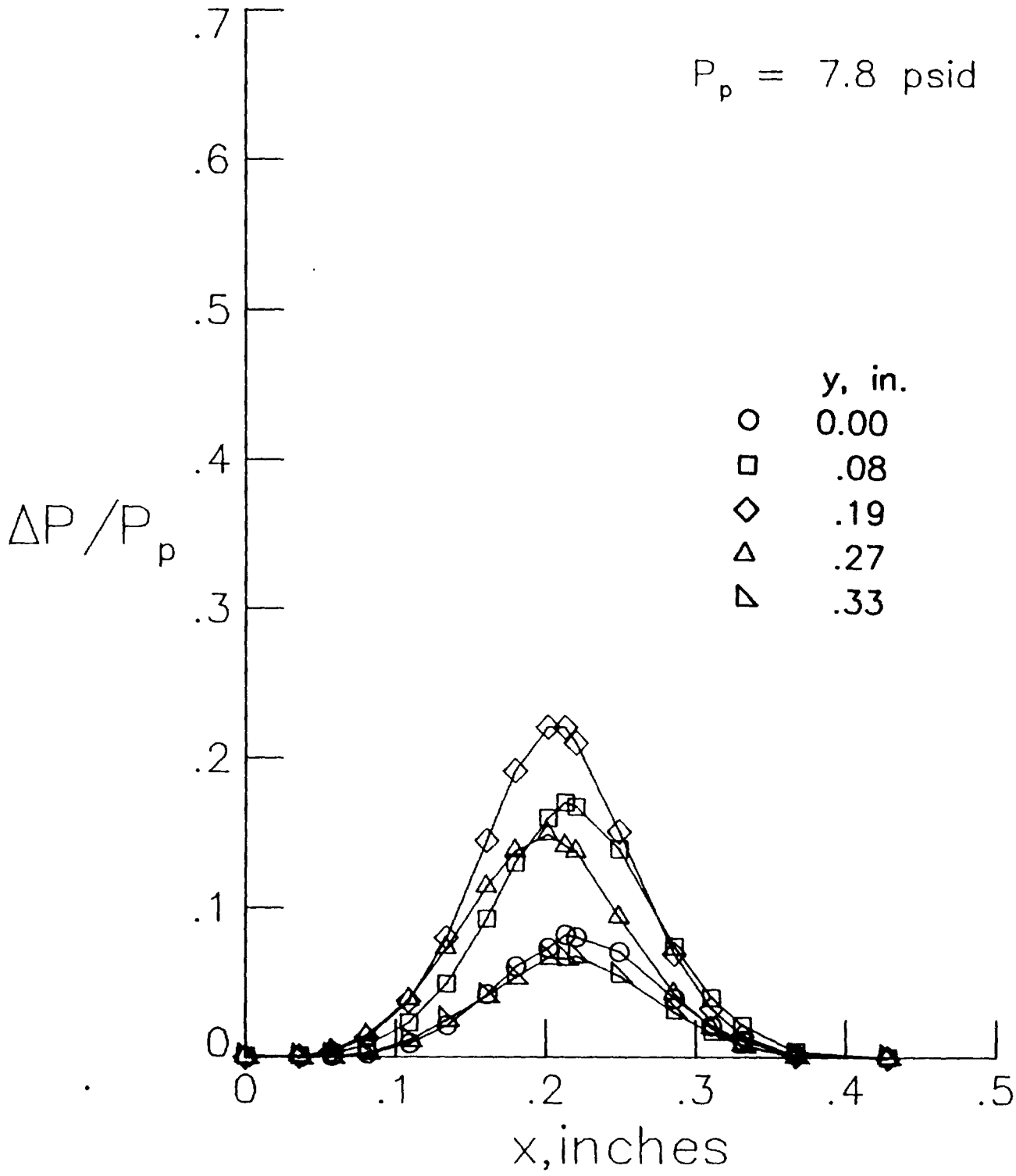

(f) Concluded.

Figure B3. Continued.

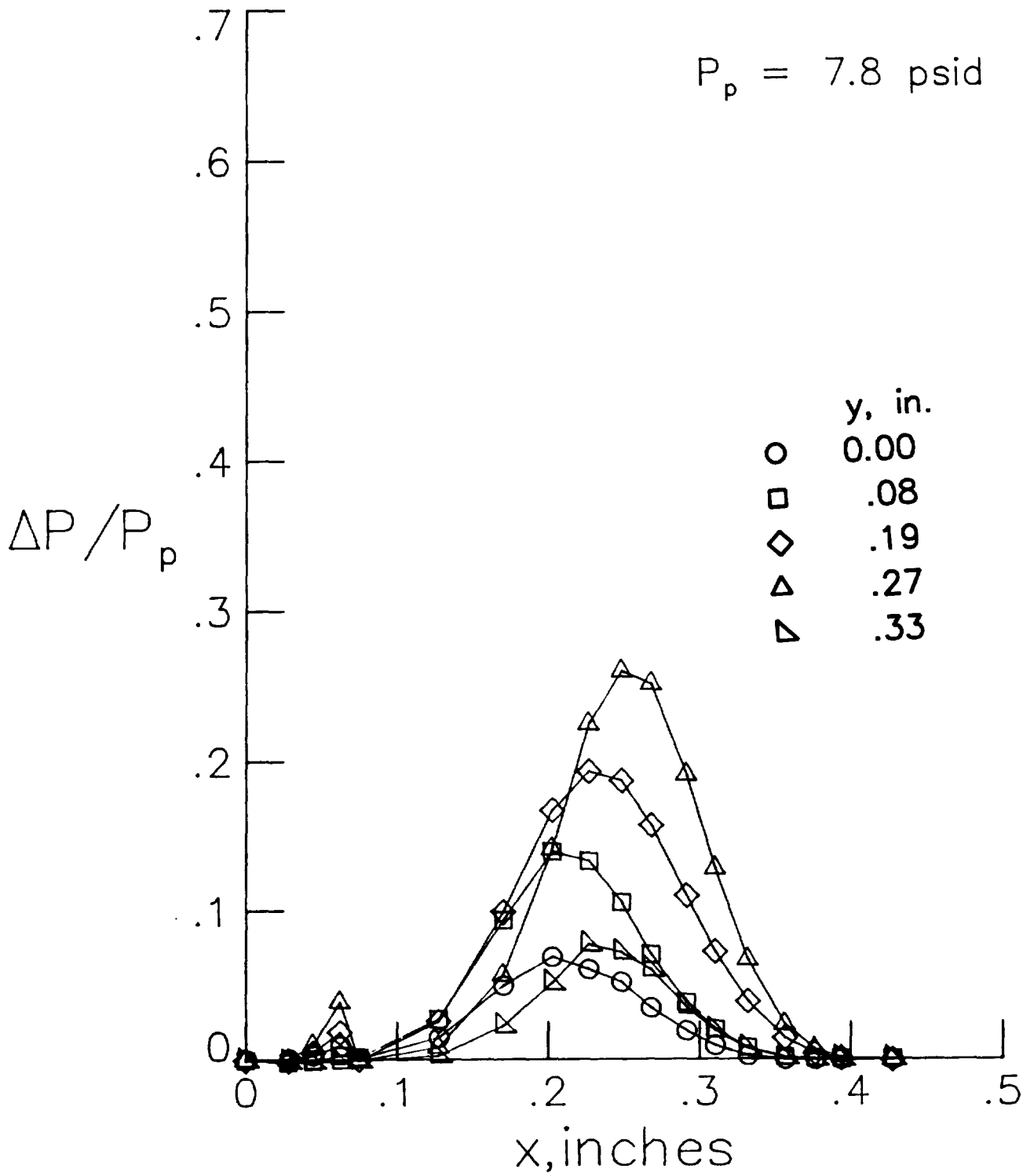

(g) Tip 4, front jet.

Figure B3. Continued.

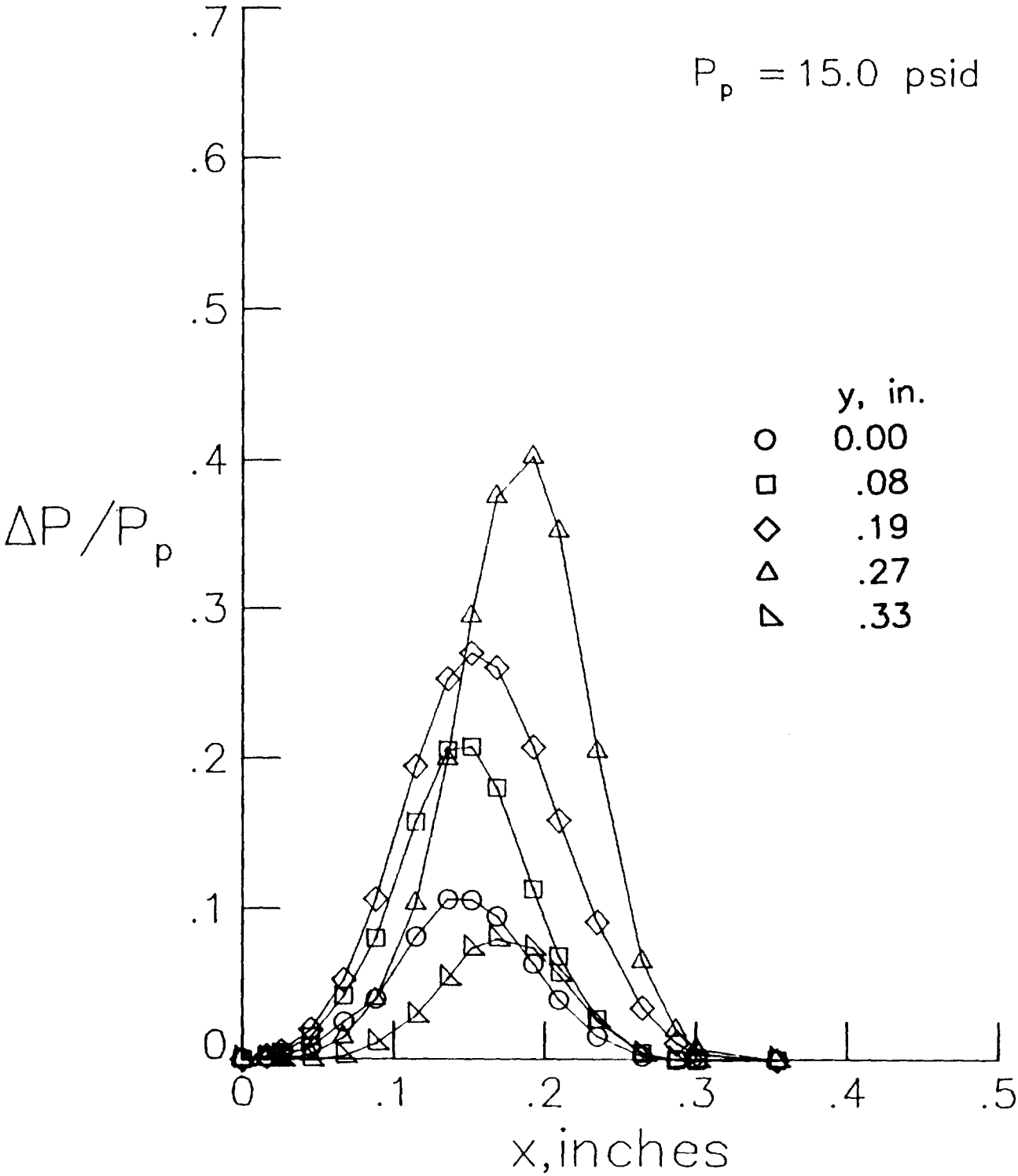

(g) Concluded.

Figure B3. Continued.

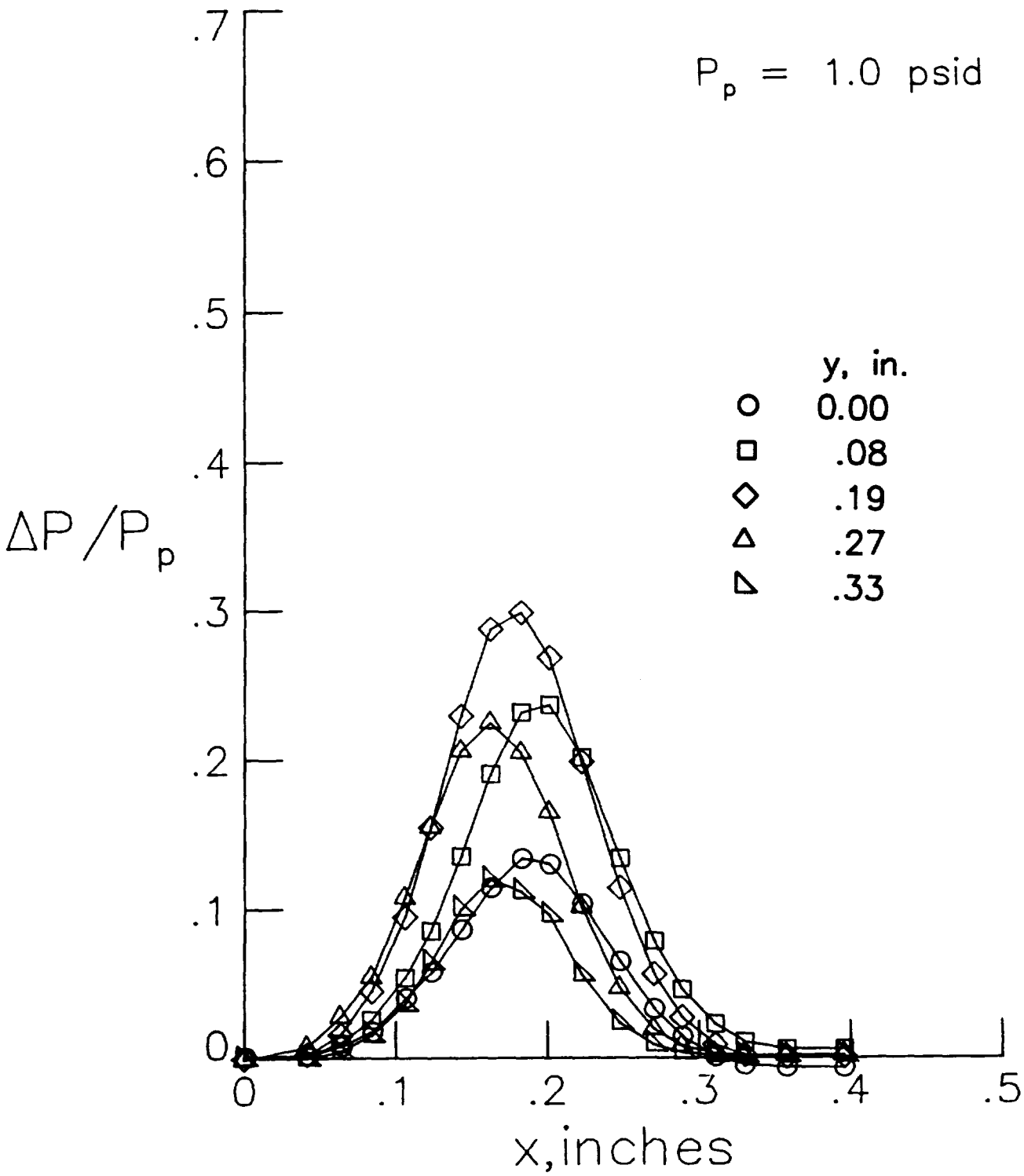

(h) Tip 4, center jet.

Figure B3. Continued.

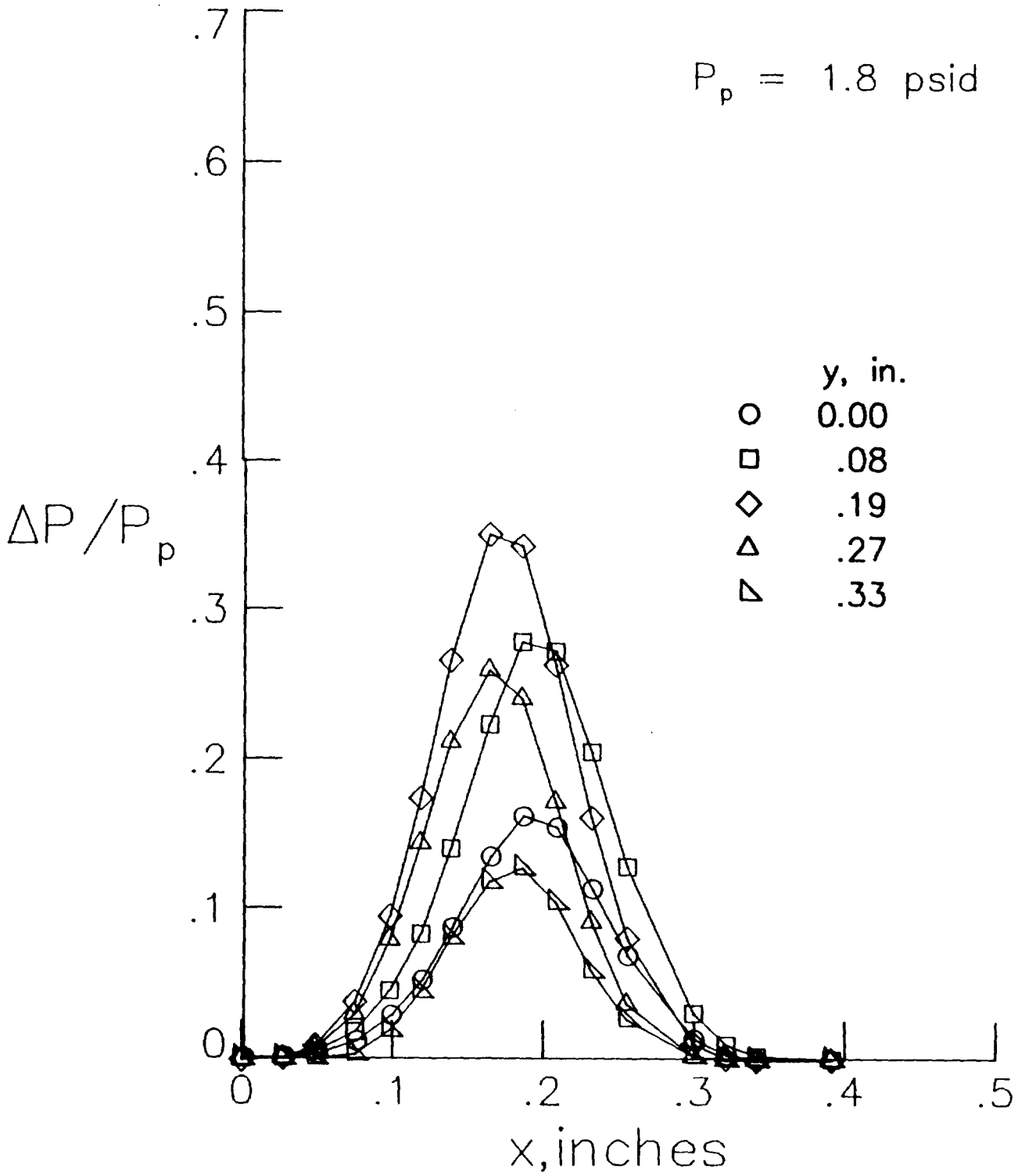

(h) Continued.

Figure B3. Continued.

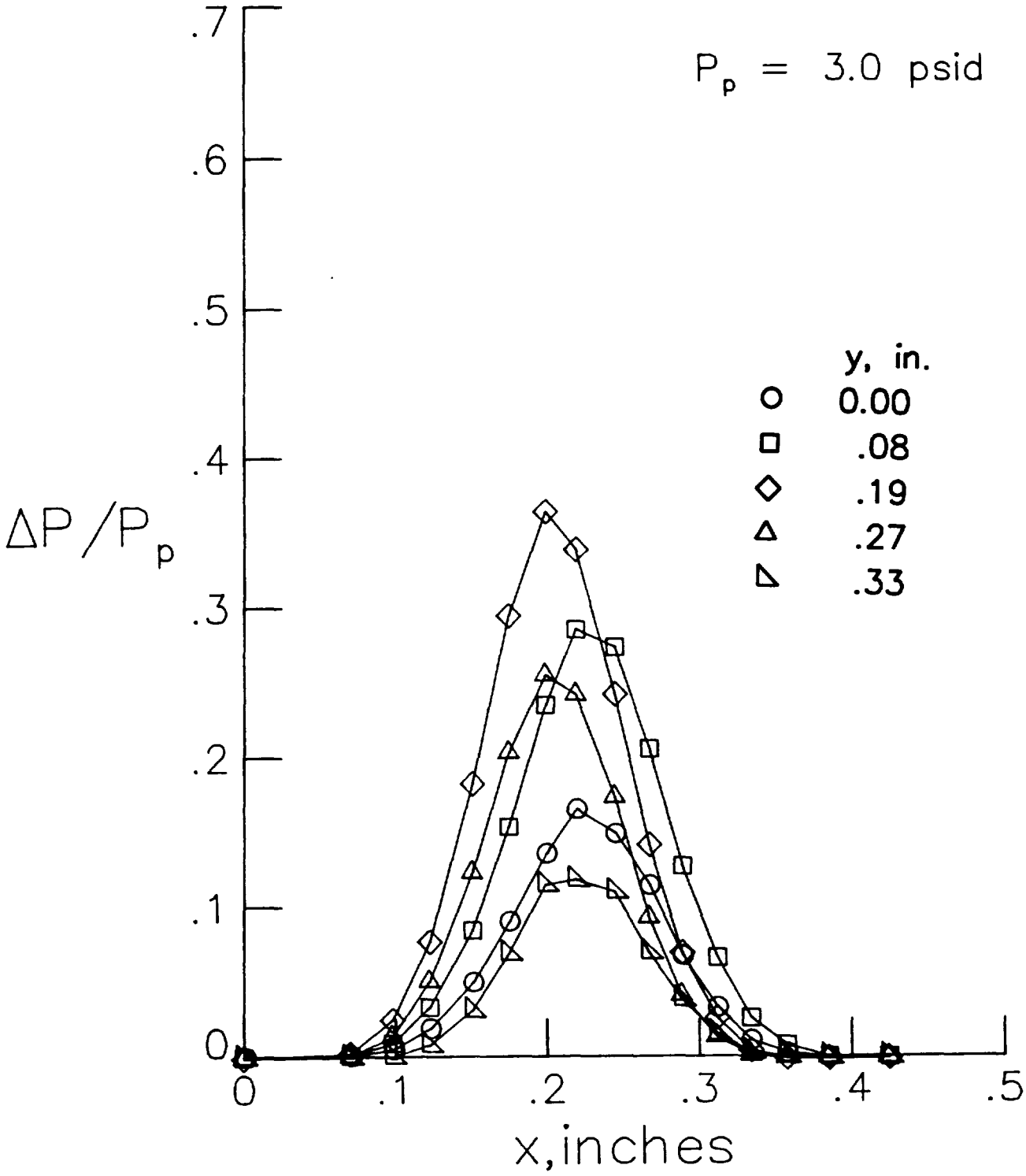

(h) Concluded.

Figure B3. Continued.

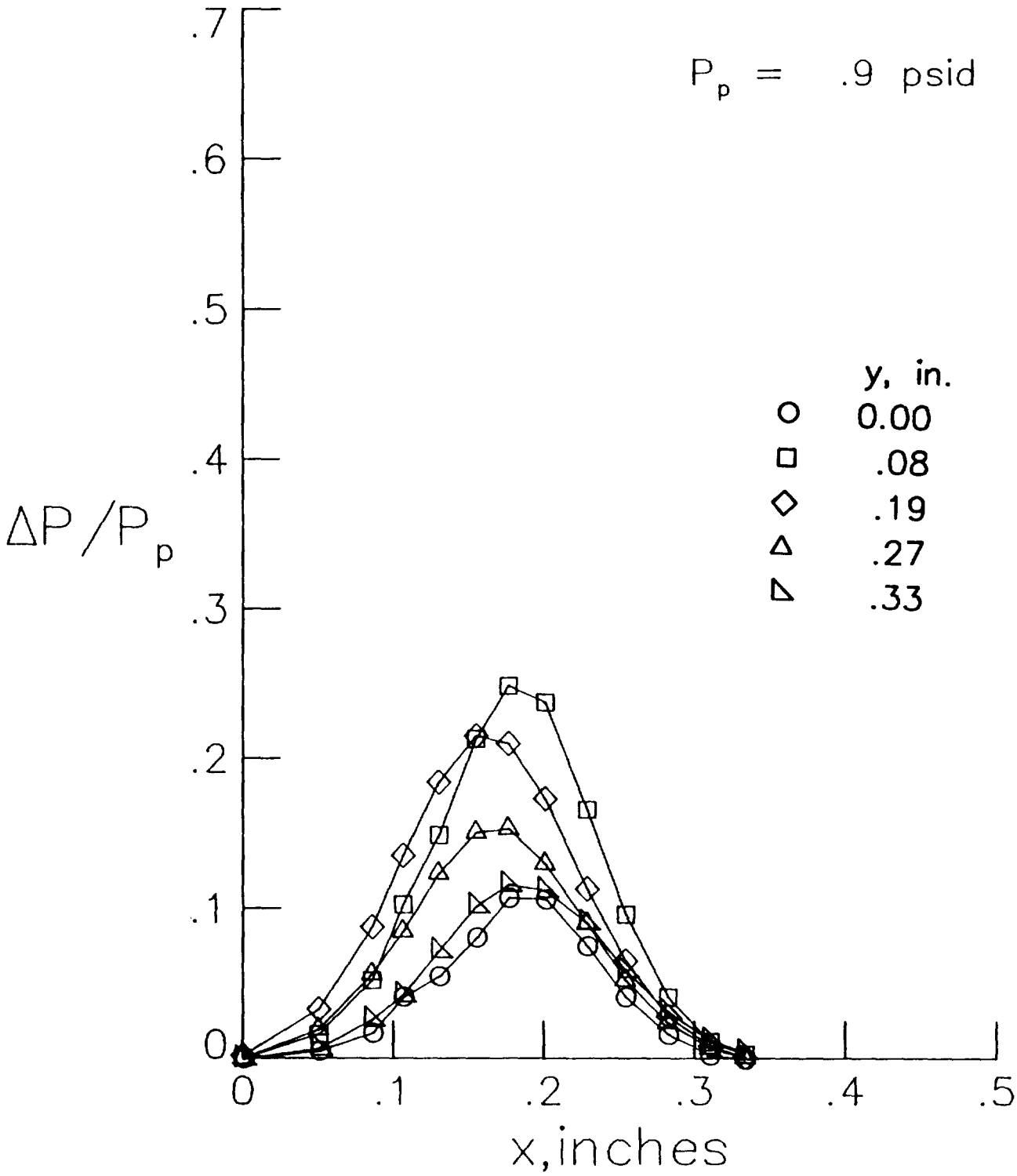

(i) Tip 4, rear jet.

Figure B3. Continued.

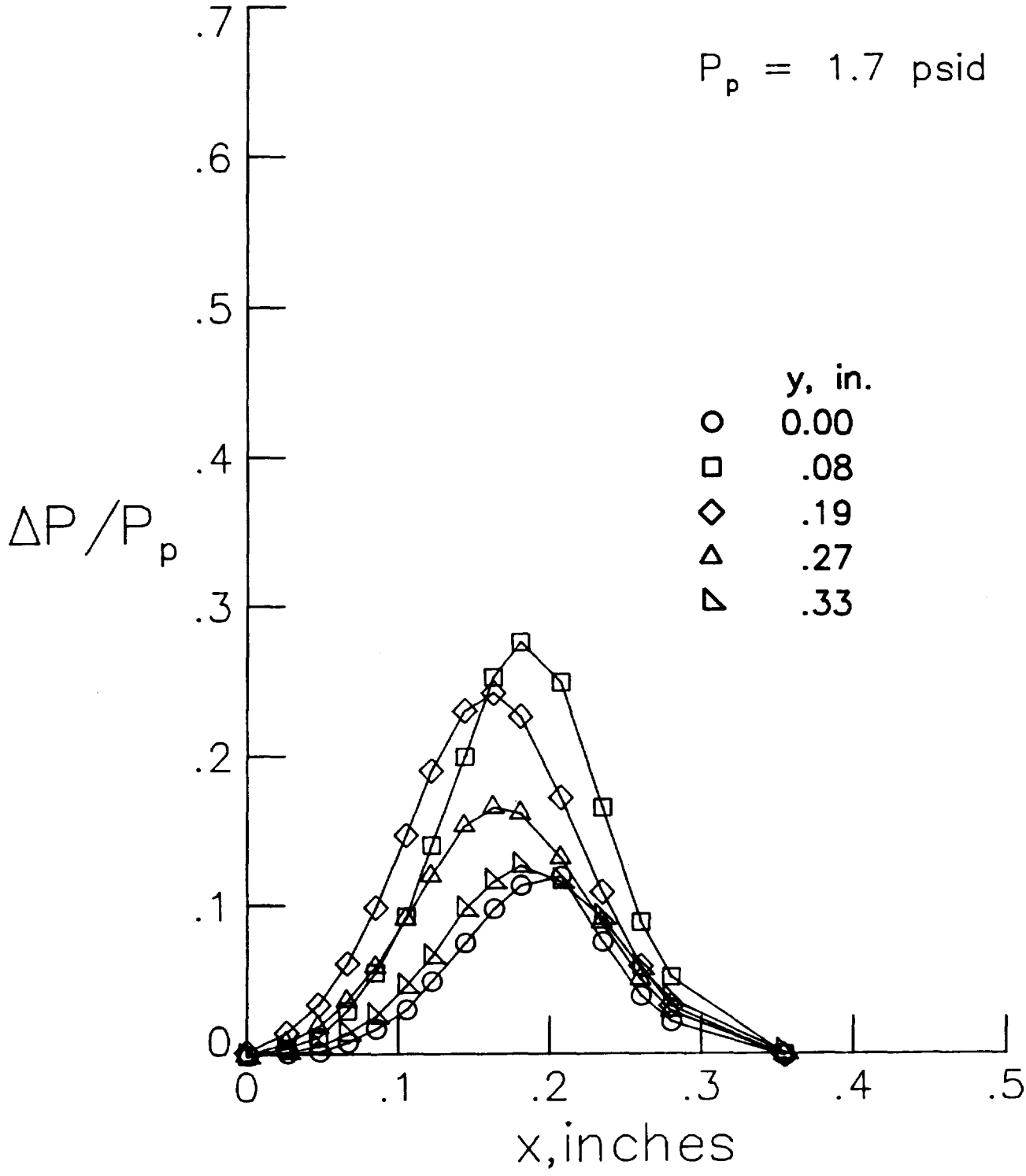

(i) Continued.

Figure B3. Continued.

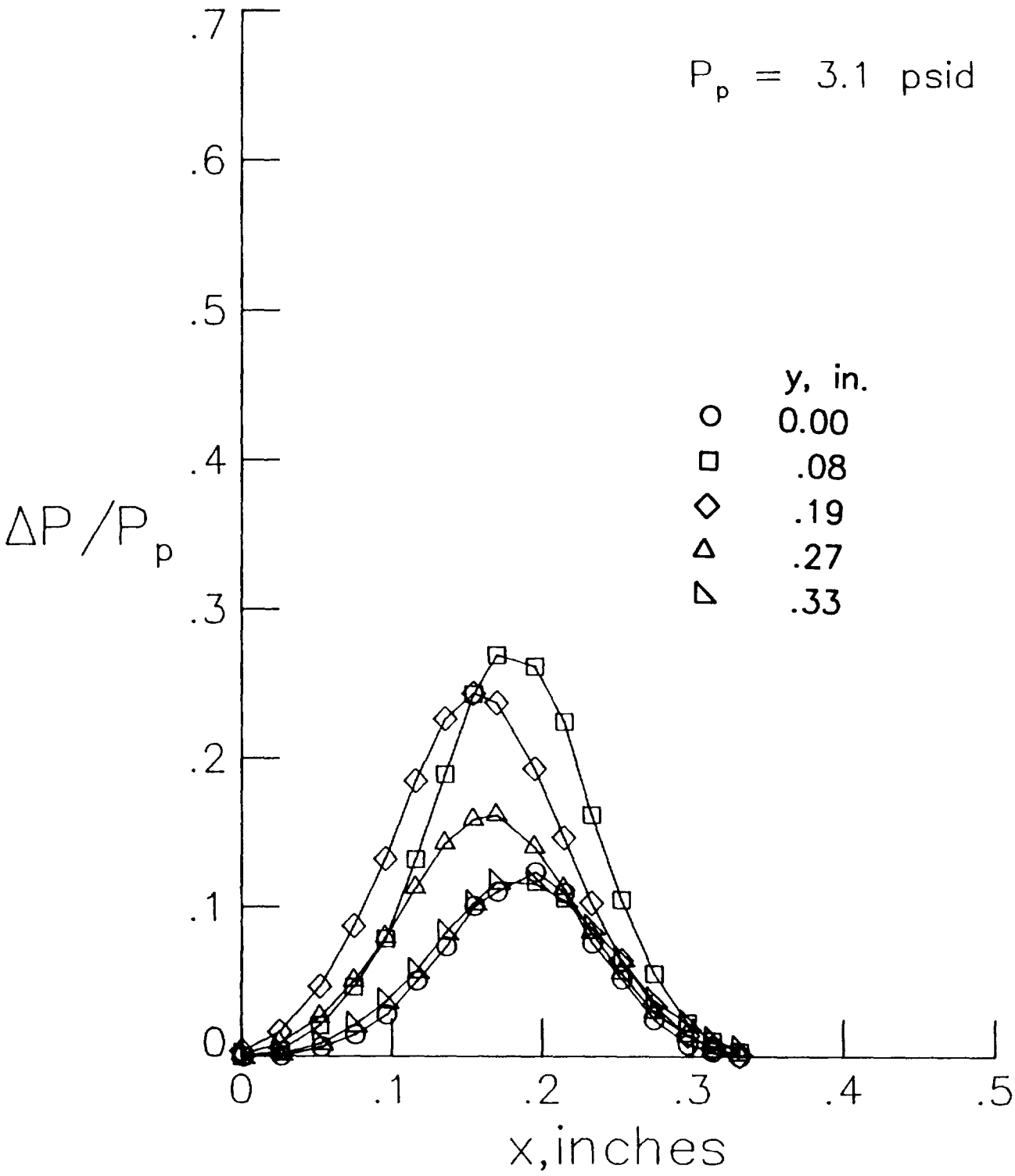

(i) Concluded.

Figure B3. Continued.

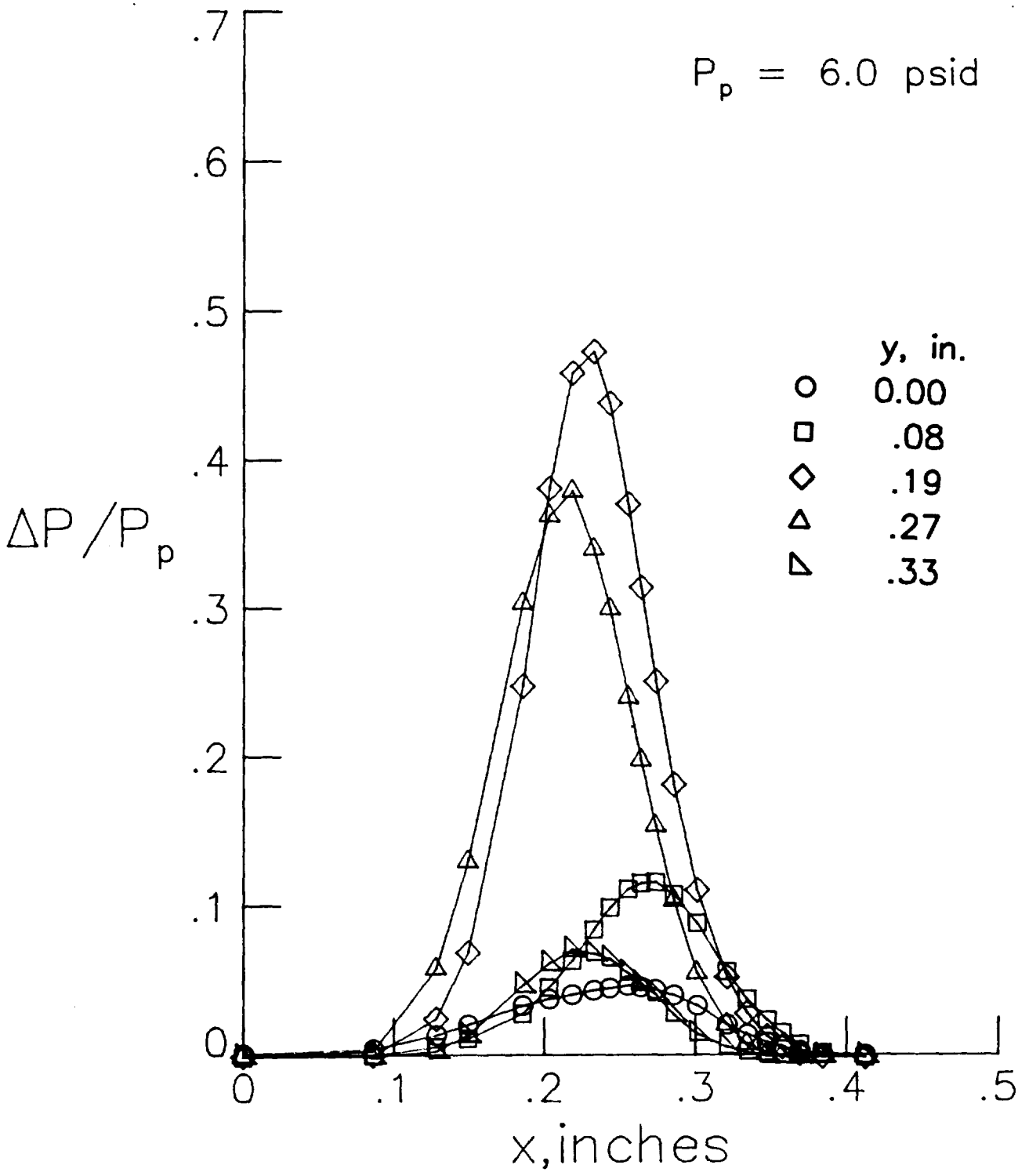

(j) Tip 6, front jet.

Figure B3. Continued.

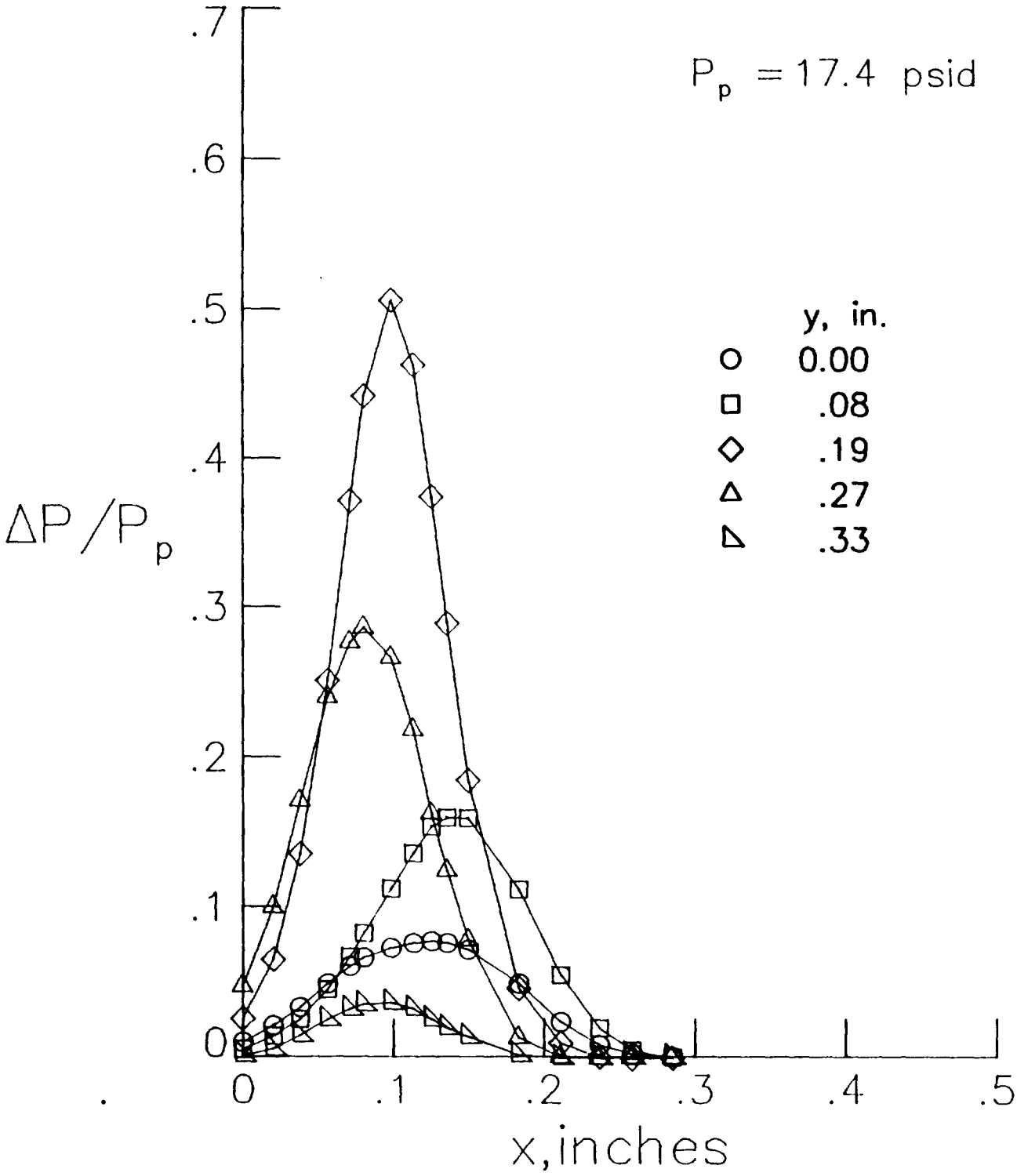

(j) Concluded.

Figure B3. Continued.

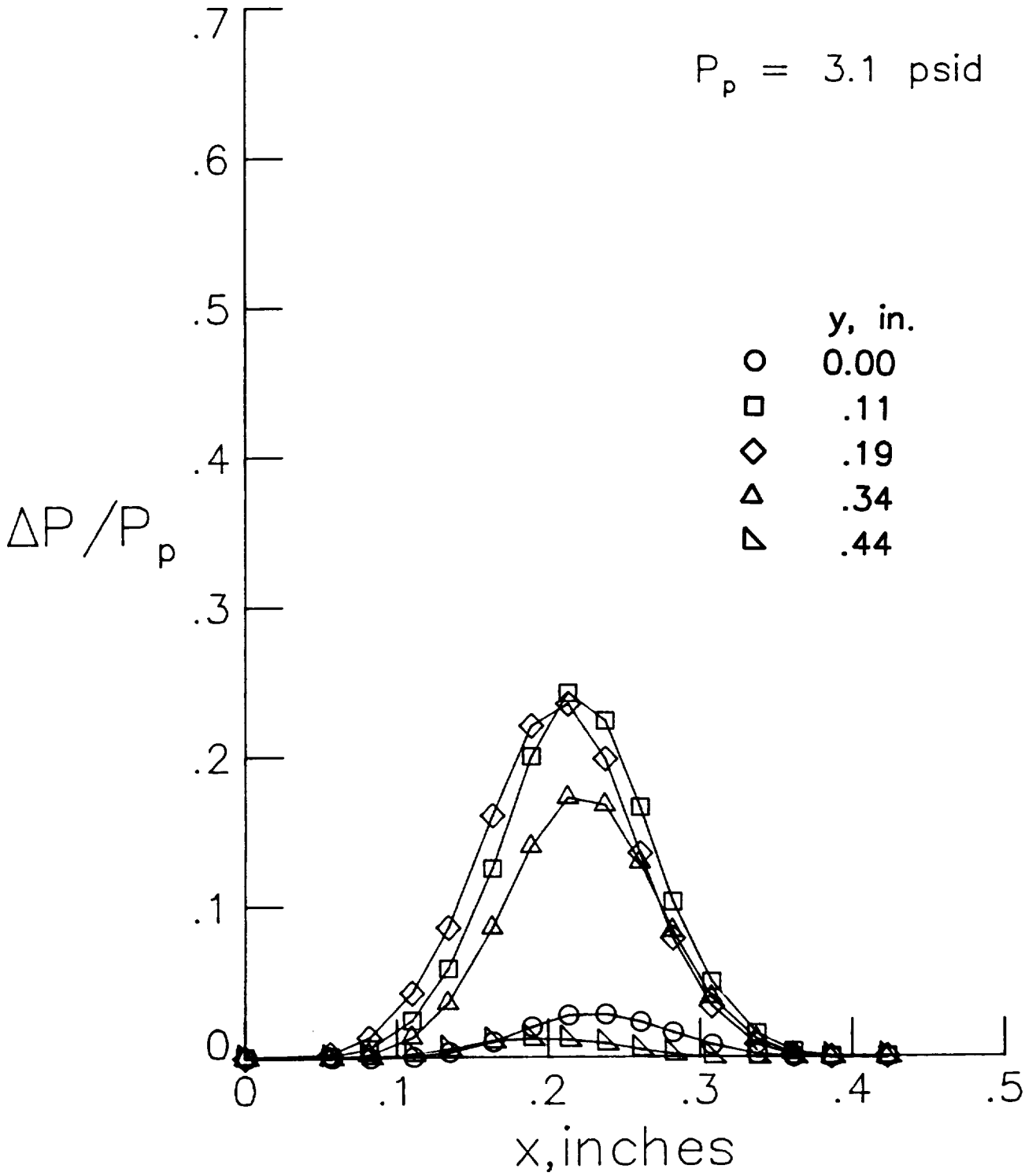

(k) Tip 6, rear jet.

Figure B3. Continued.

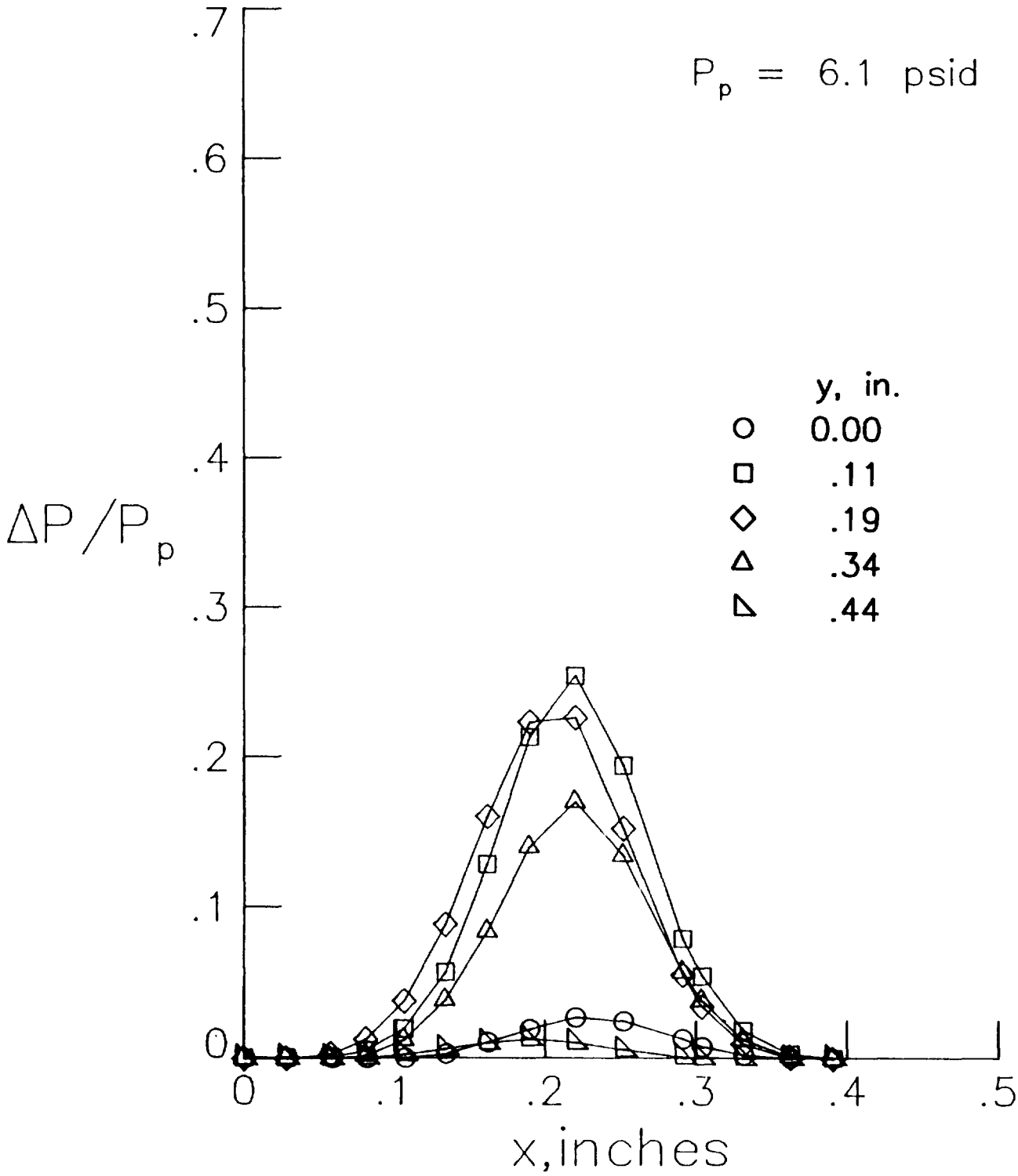

(k) Continued.

Figure B3. Continued.

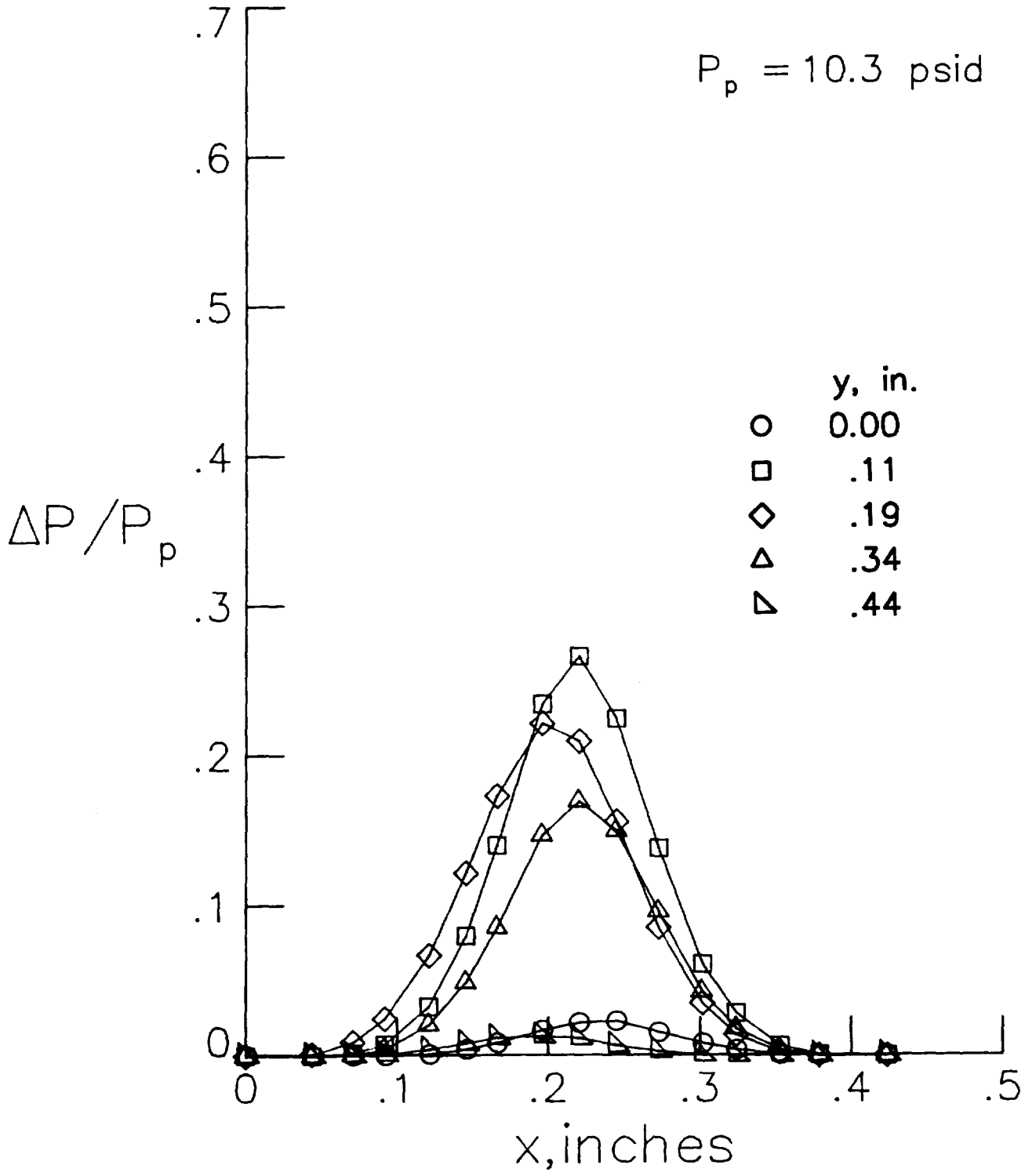

(k) Concluded.

Figure B3. Continued.

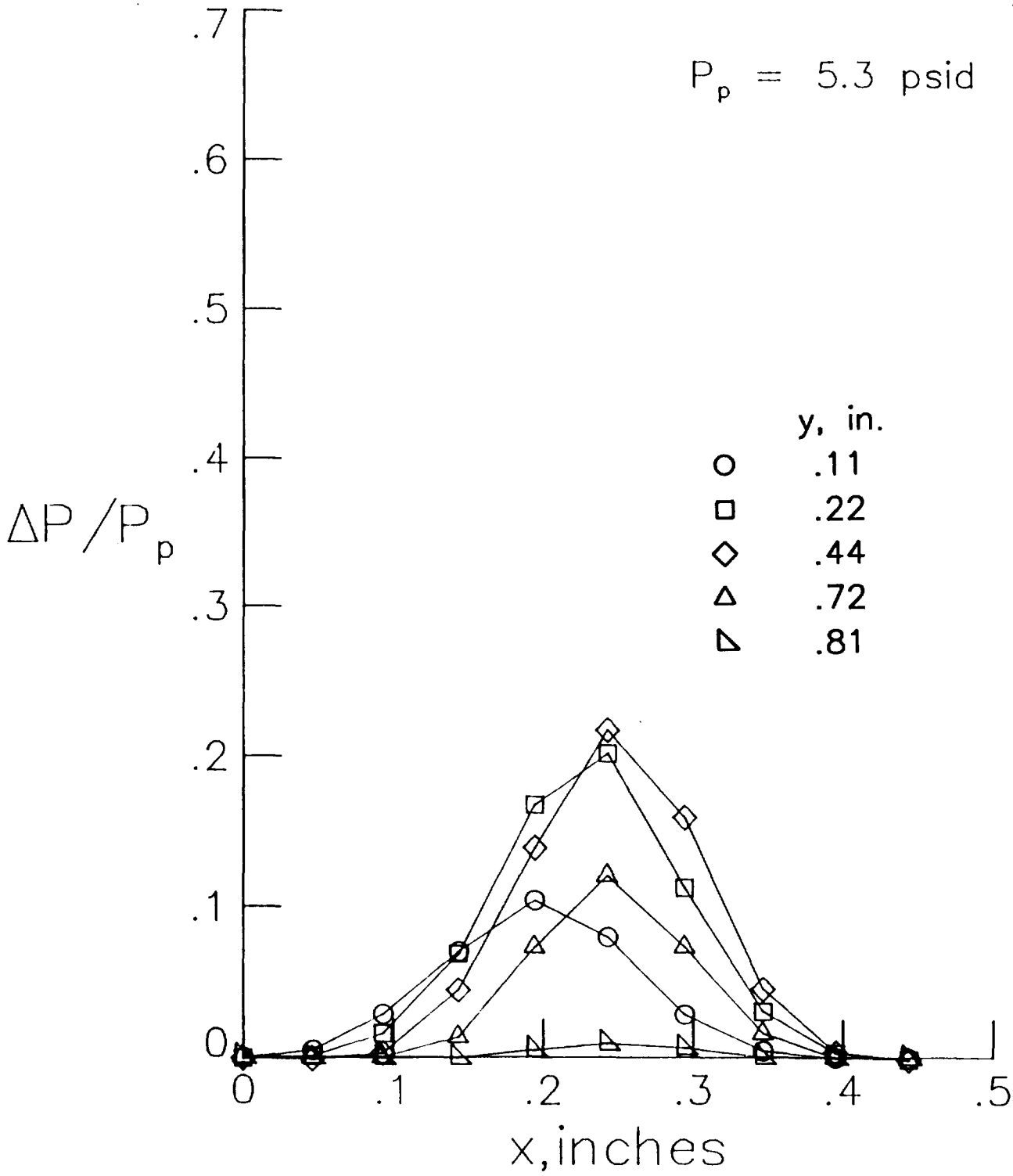

(l) Tip 8, front jet.

Figure B3. Continued.

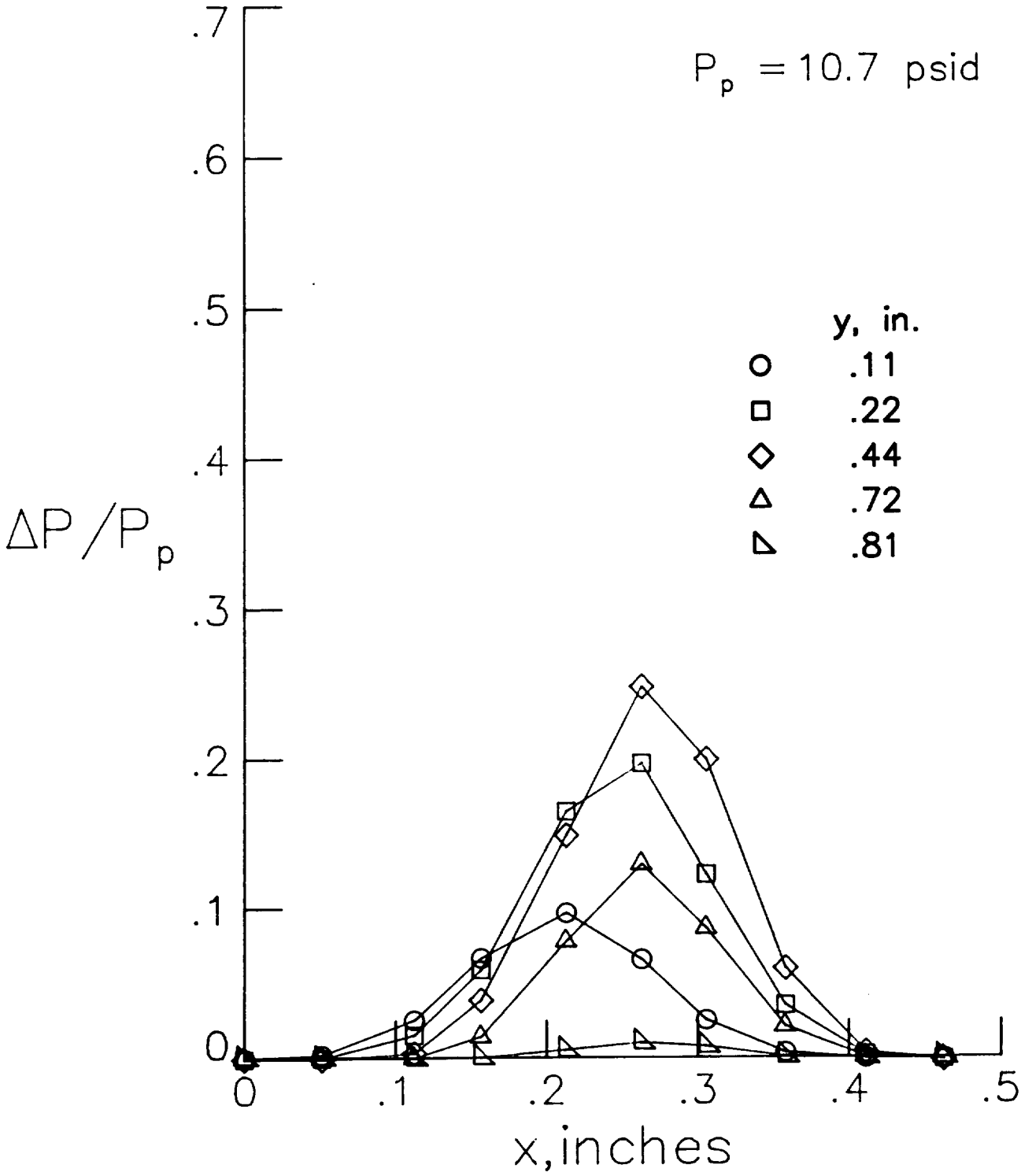

(l) Continued.

Figure B3. Continued.

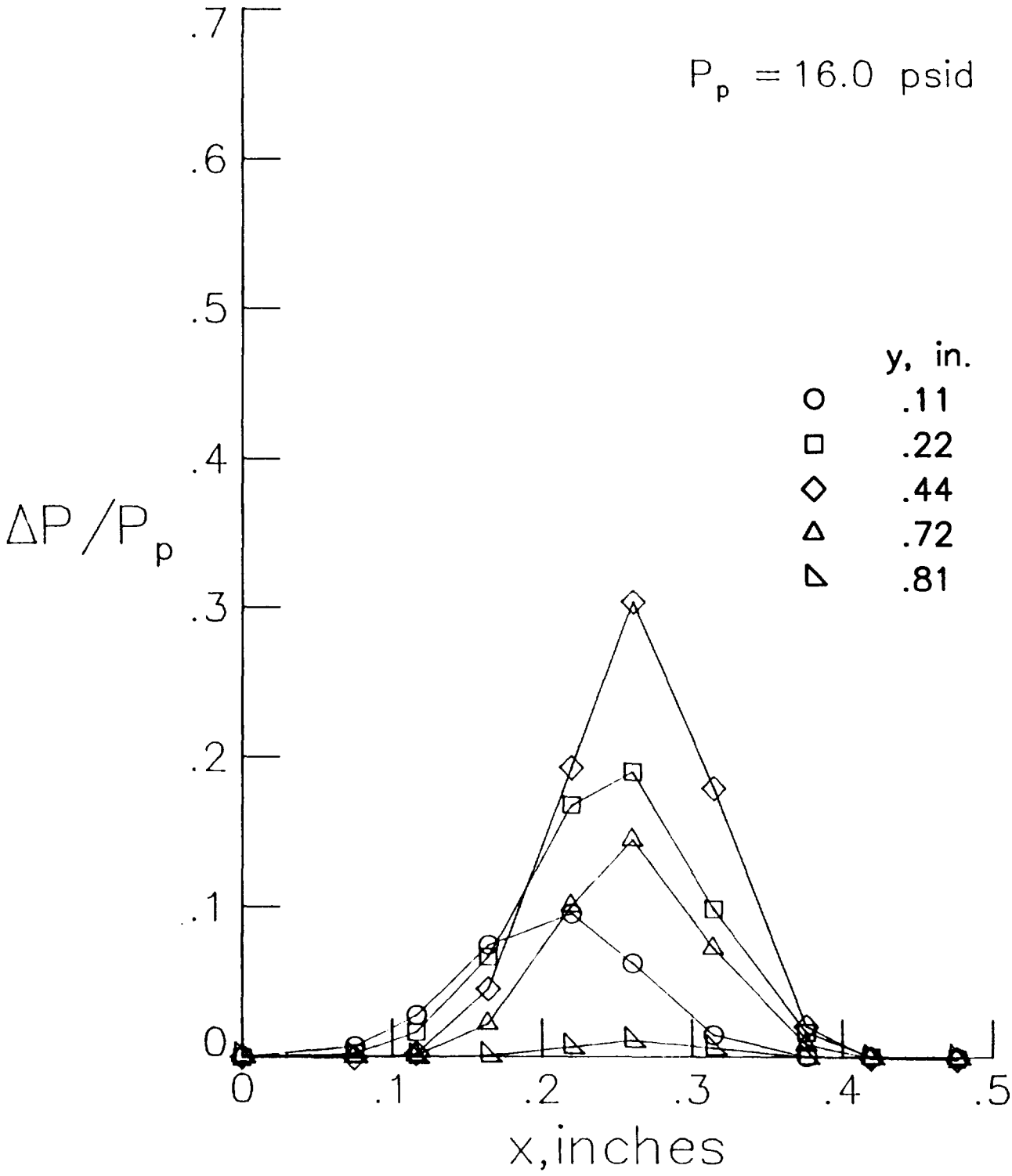

(l) Concluded.

Figure B3. Continued.

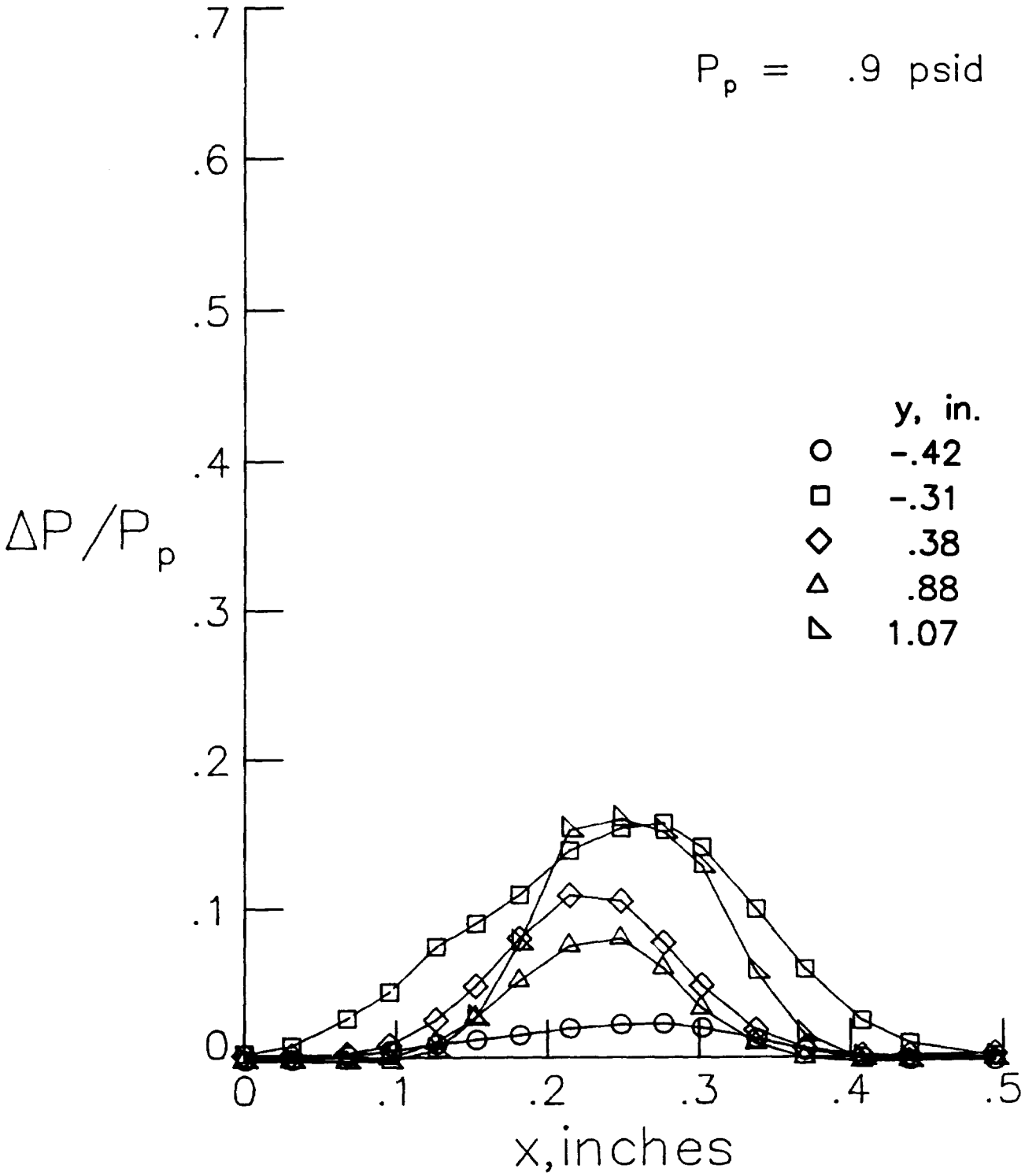

(m) Tip 8, rear jet.

Figure B3. Continued.

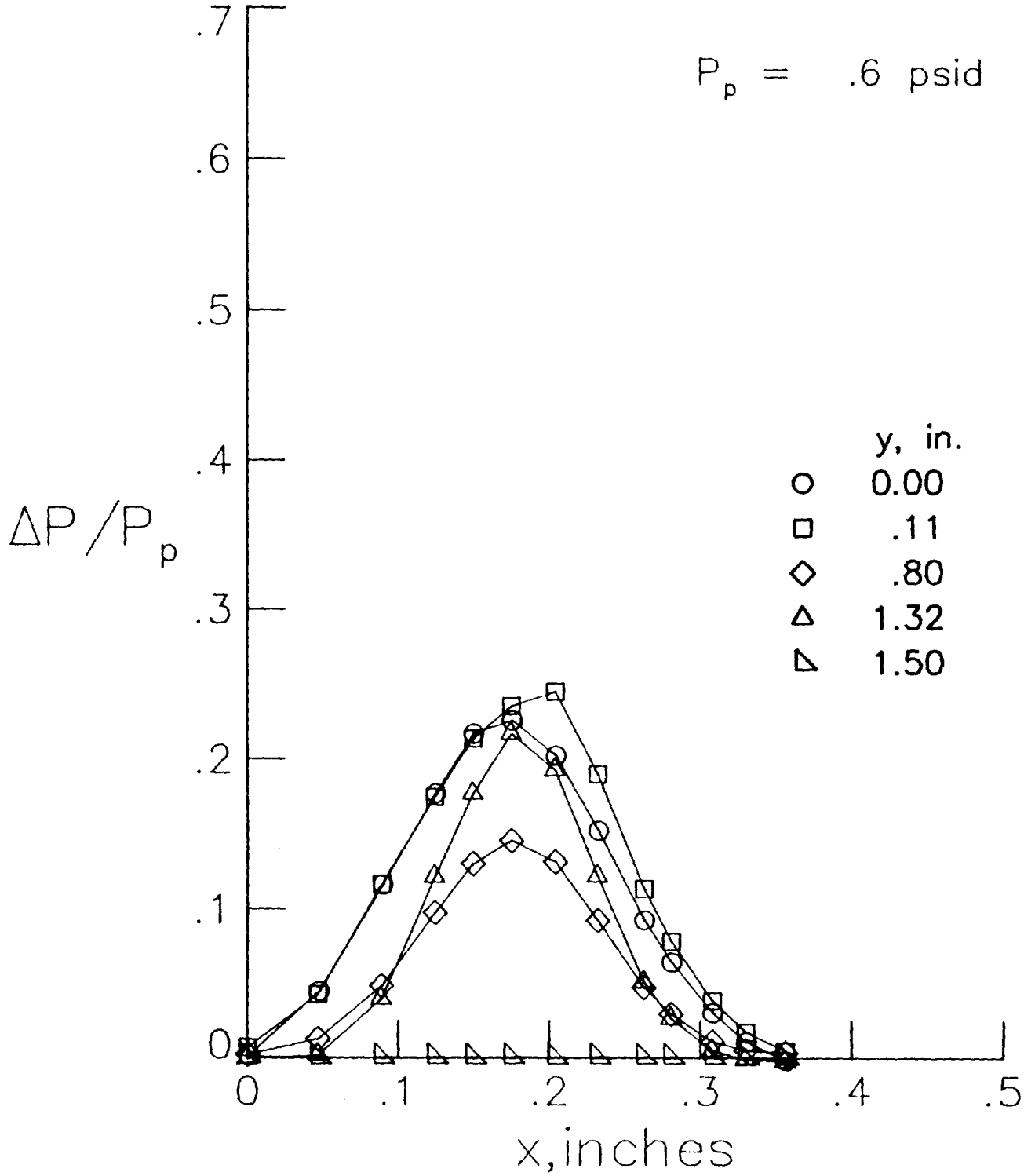

(m) Continued.

Figure B3. Continued.

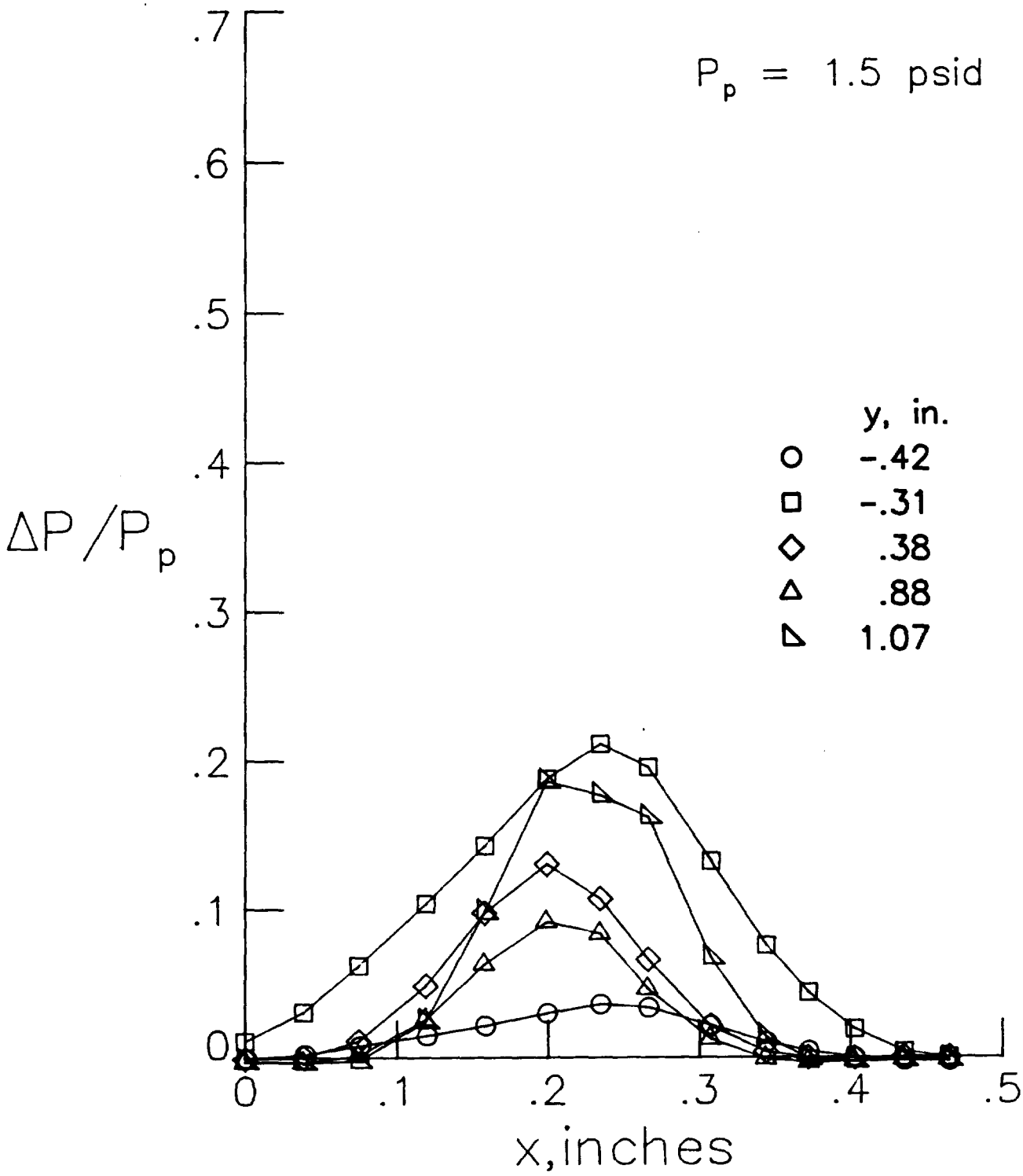

(m) Continued.

Figure B3. Continued.

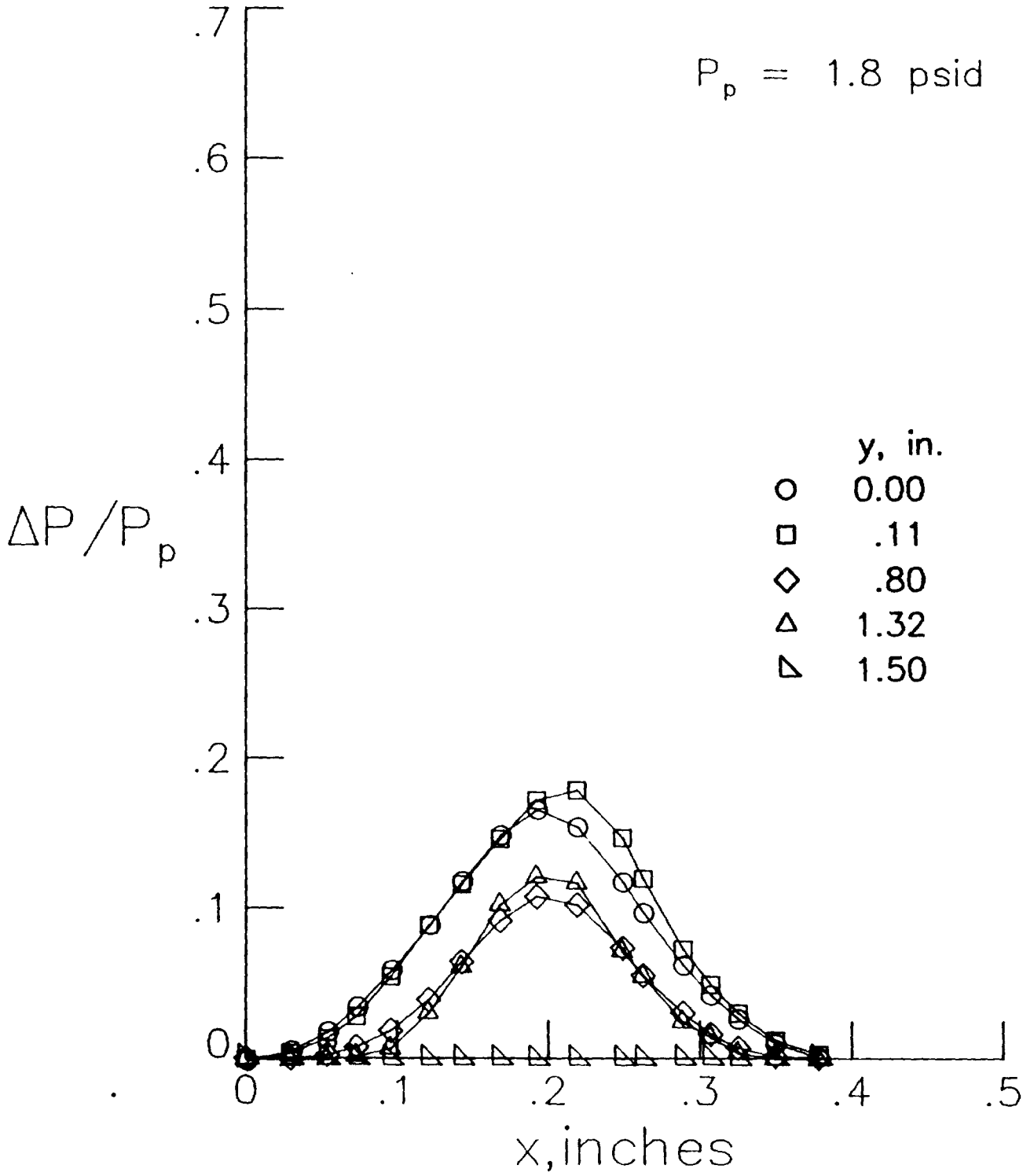

(m) Continued.

Figure B3. Continued.

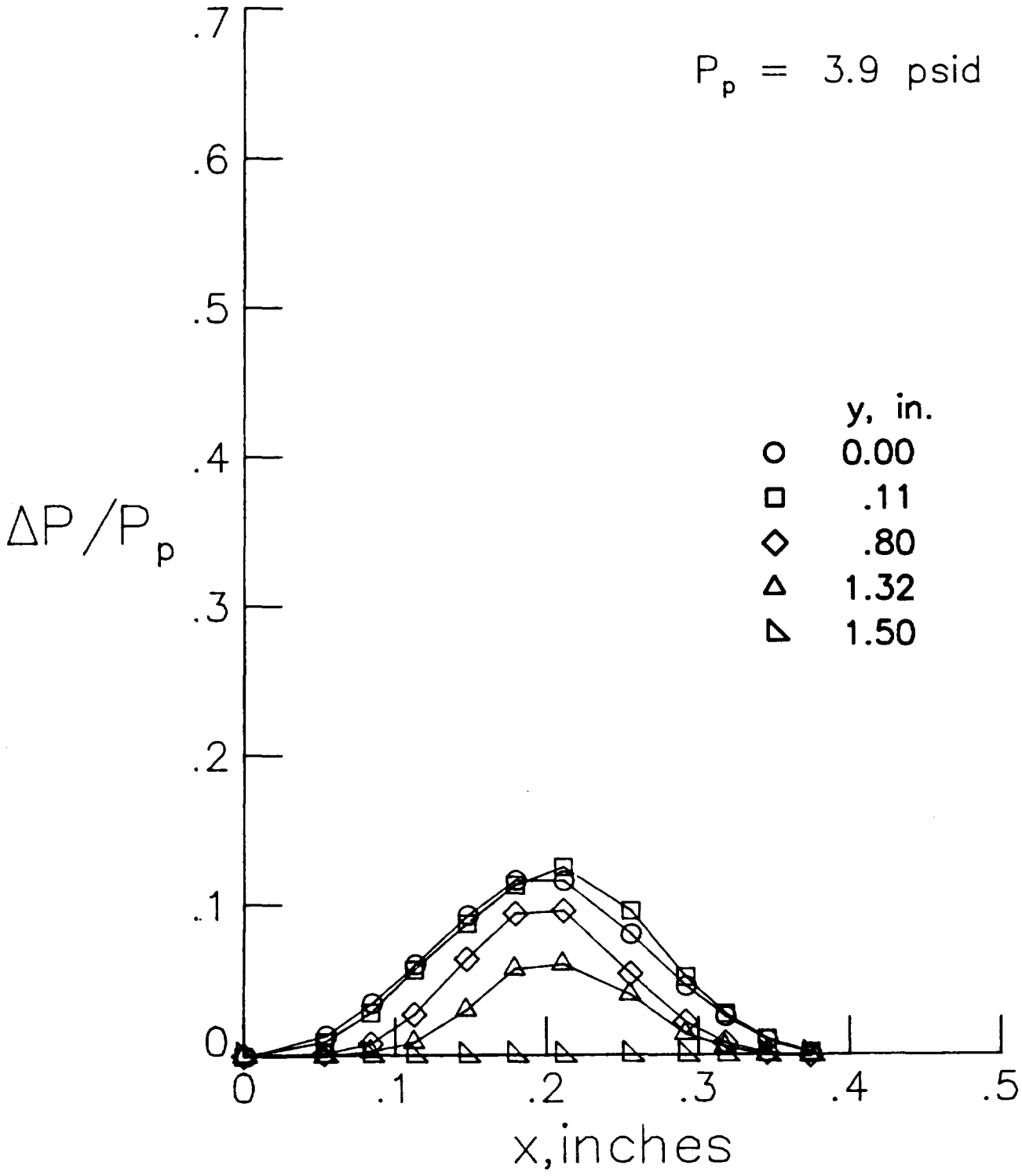

(m) Continued.

Figure B3. Continued.

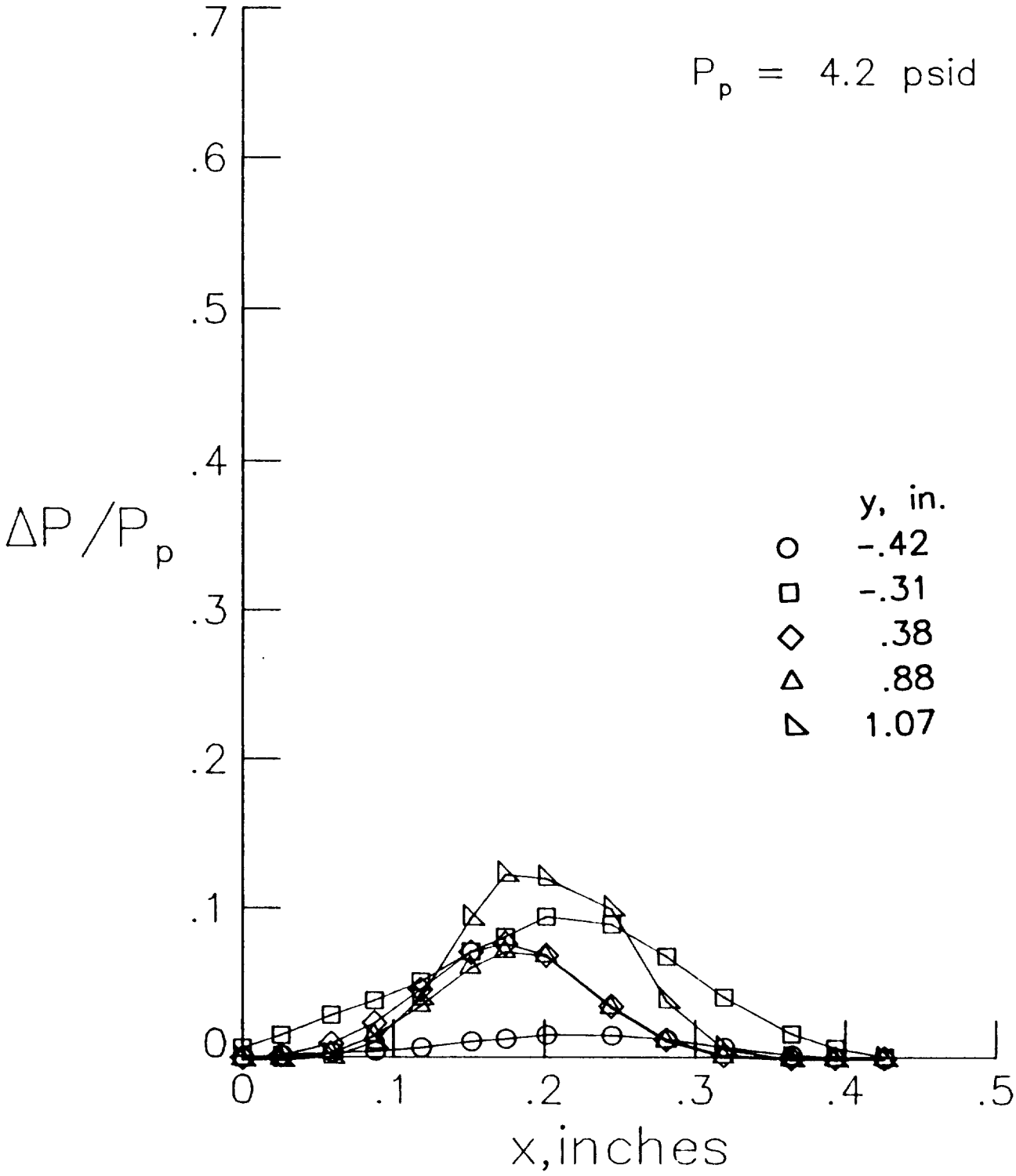

(m) Concluded.

Figure B3. Continued.

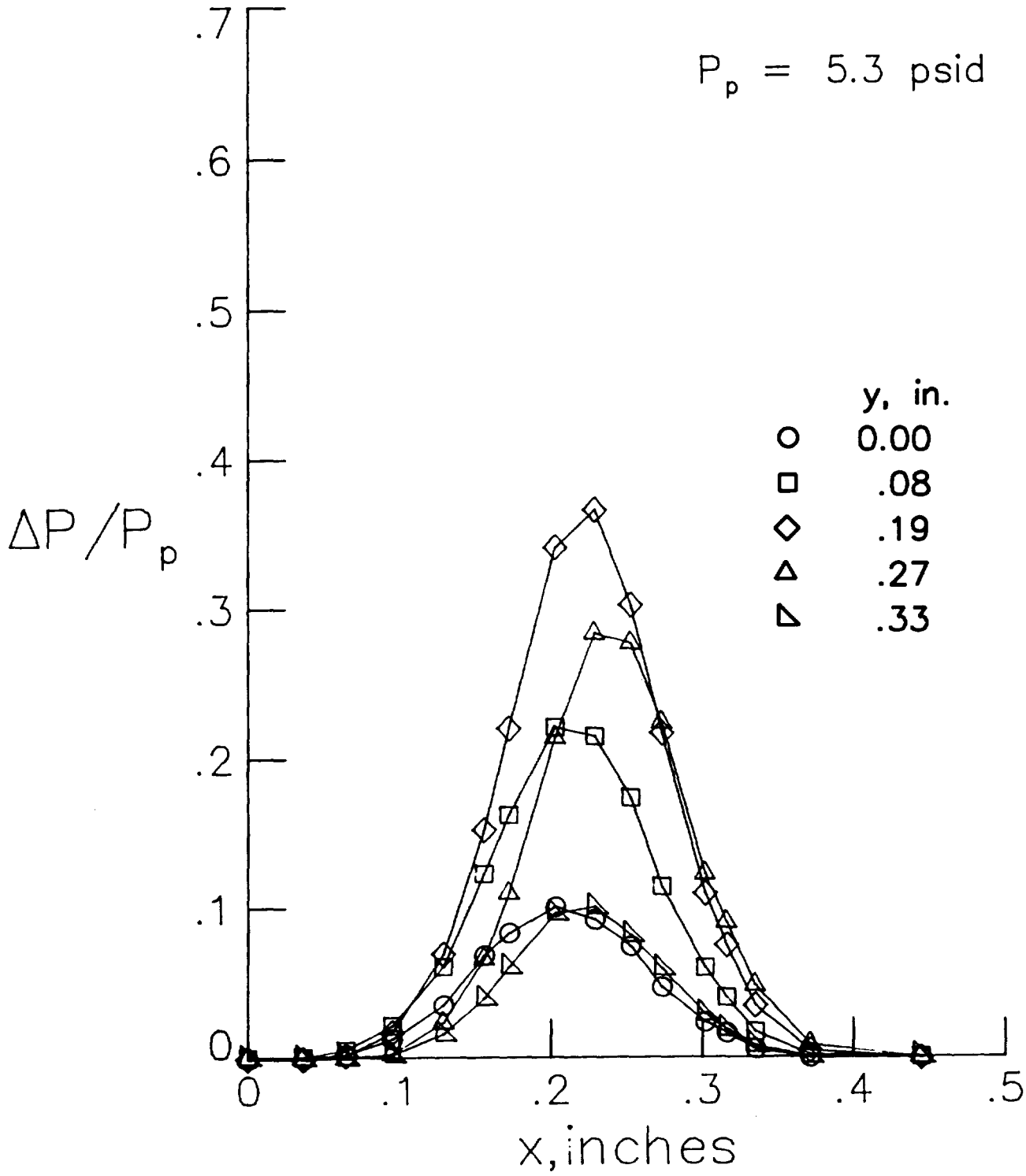

(n) Tip 9, front jet.

Figure B3. Continued.

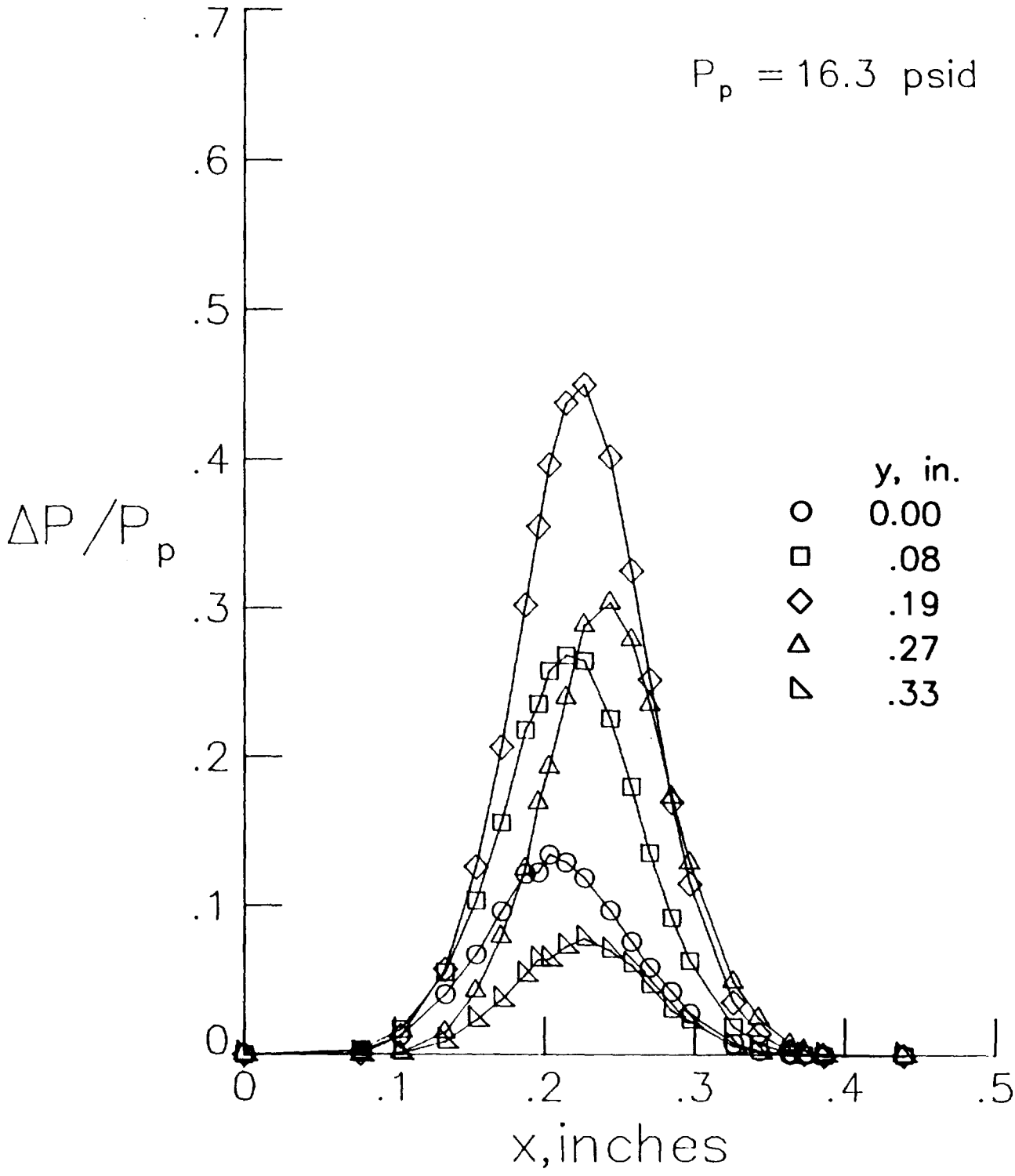

(n) Concluded.

Figure B3. Continued.

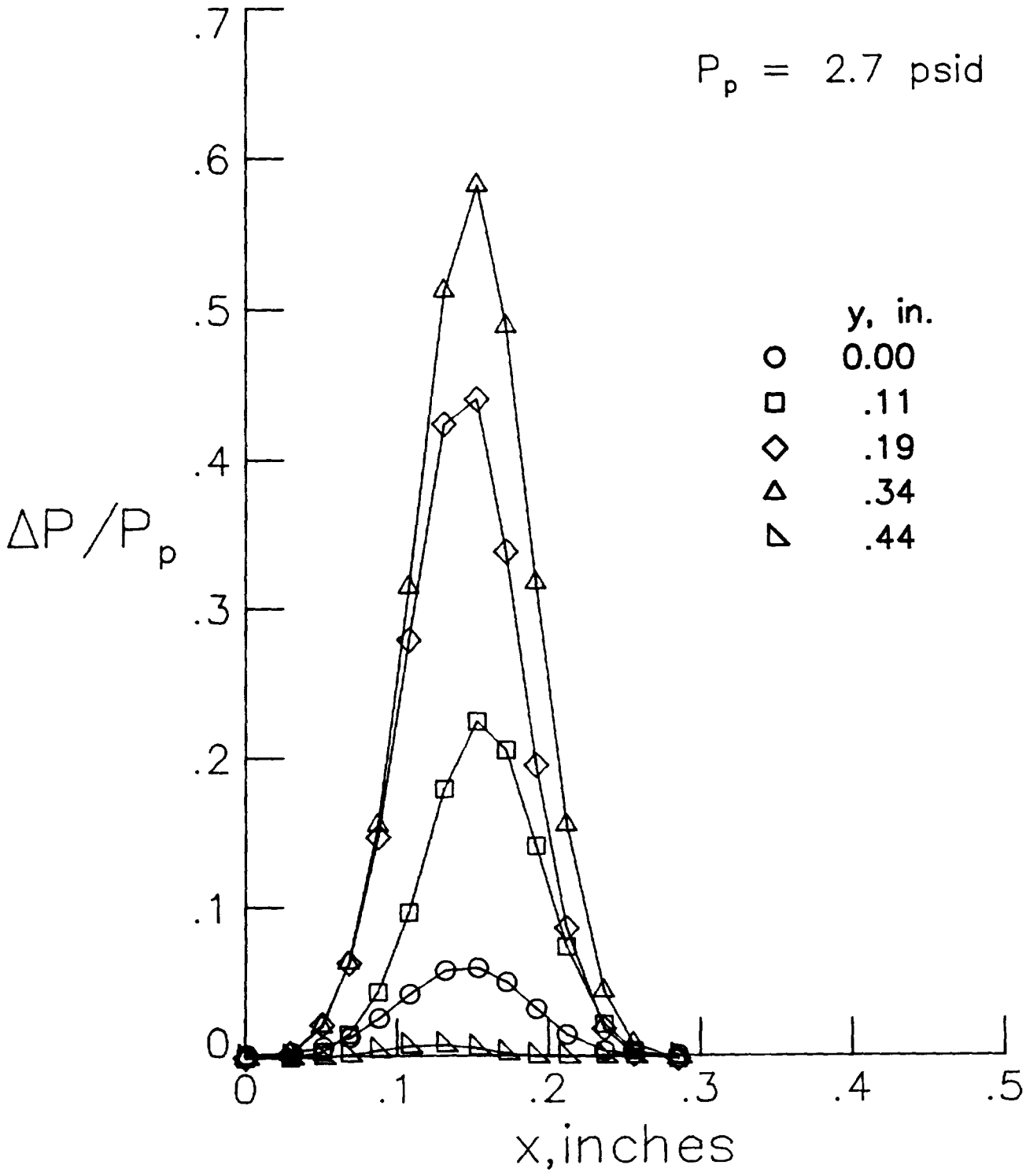

(o) Tip 9, rear jet.

Figure B3. Continued.

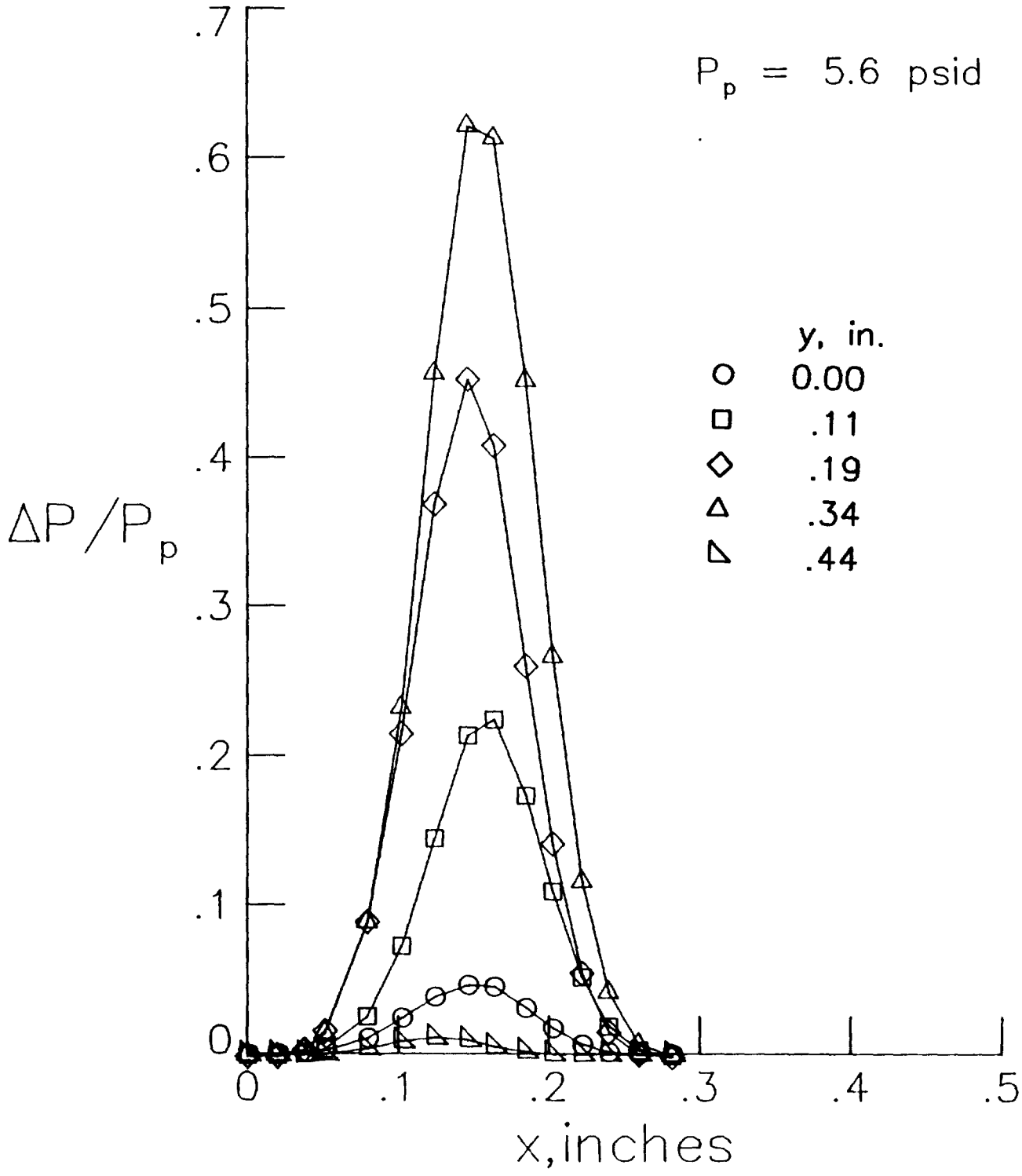

(o) Continued.

Figure B3. Continued.

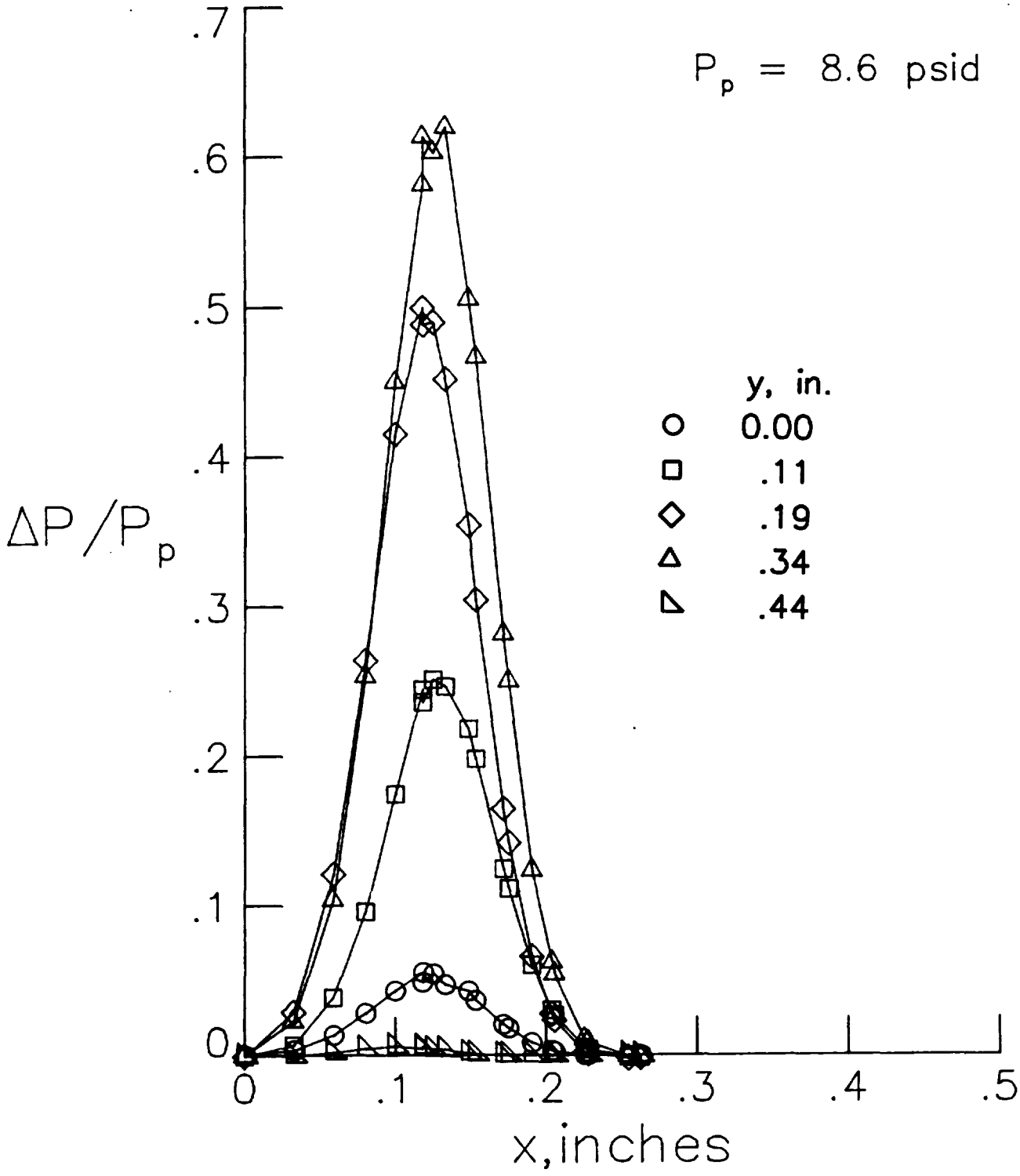

(o) Concluded.

Figure B3. Concluded.

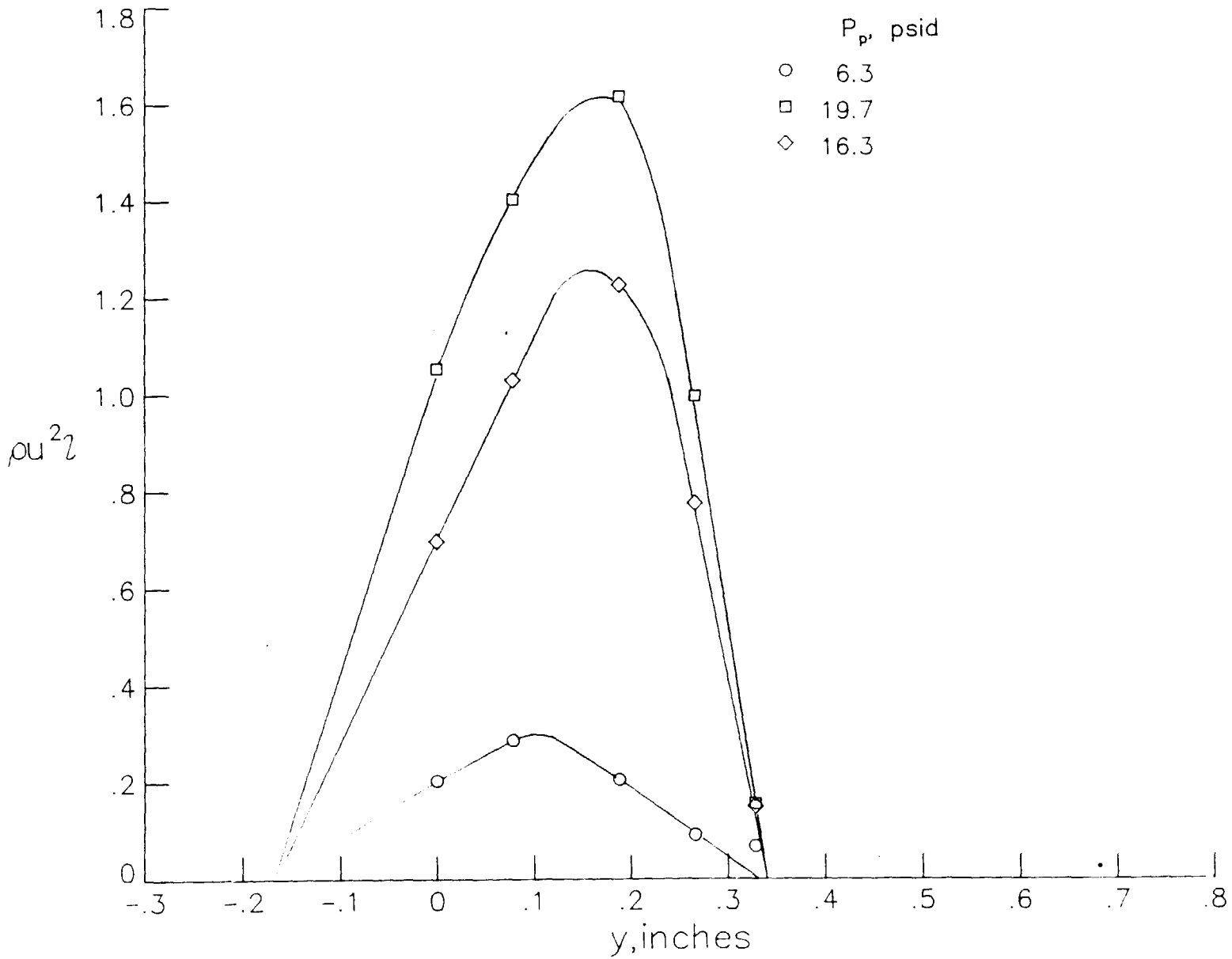

(a) Tip 1, front jet.

Figure B4. Variation of jet section momentum along the length of the jet.

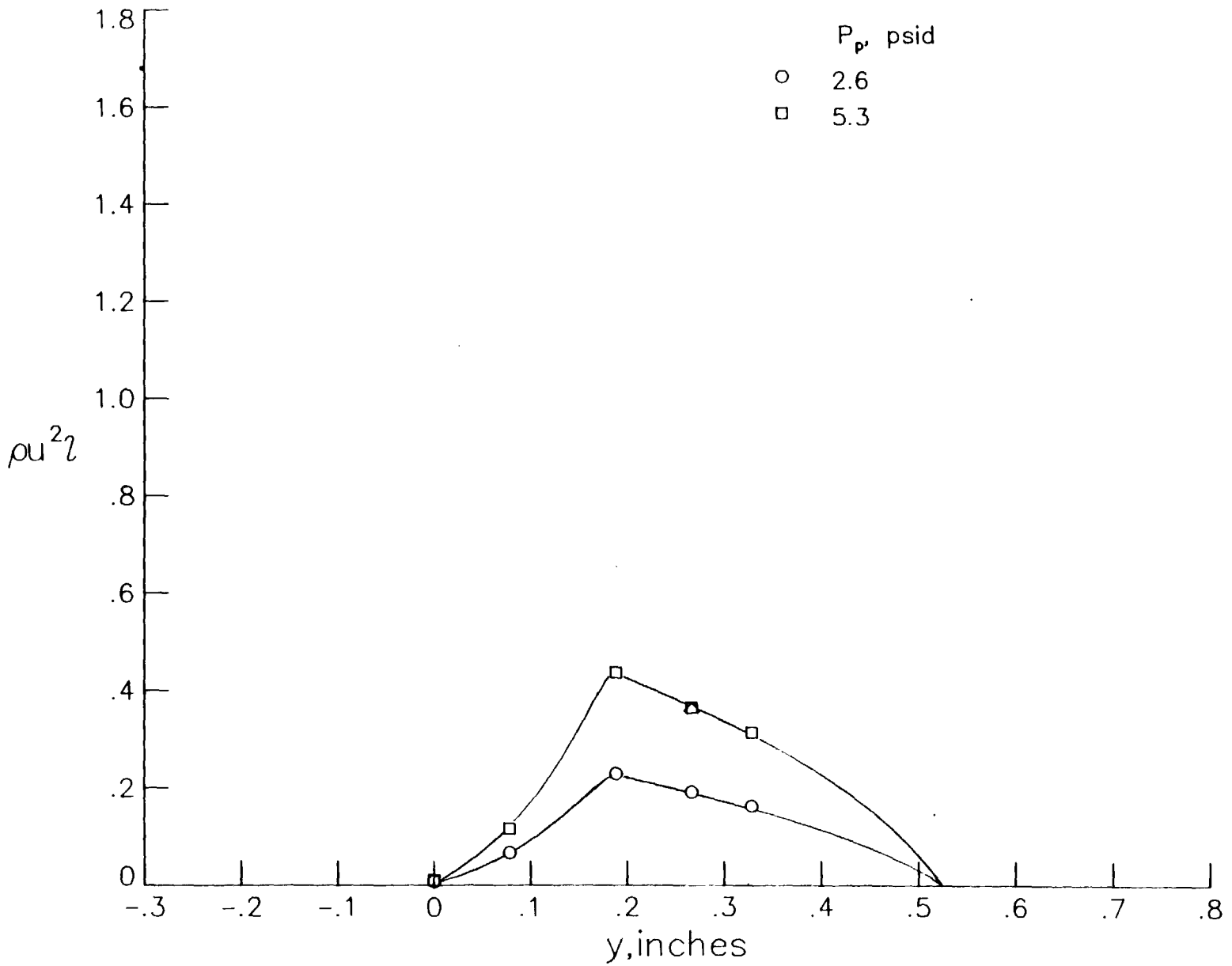

(b) Tip 1, rear jet.

Figure B4. Continued.

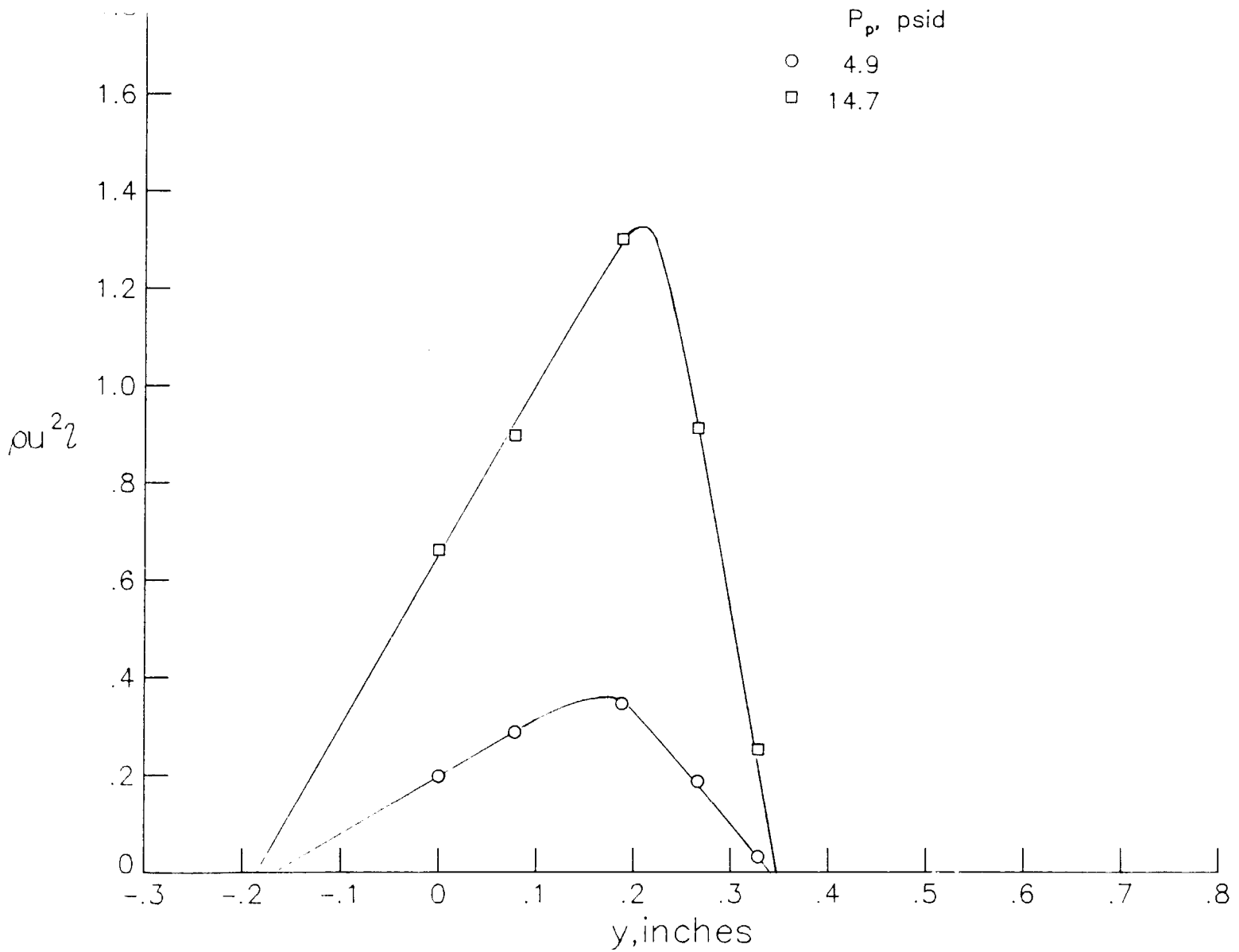

(c) Tip 2, front jet.

Figure B4. Continued.

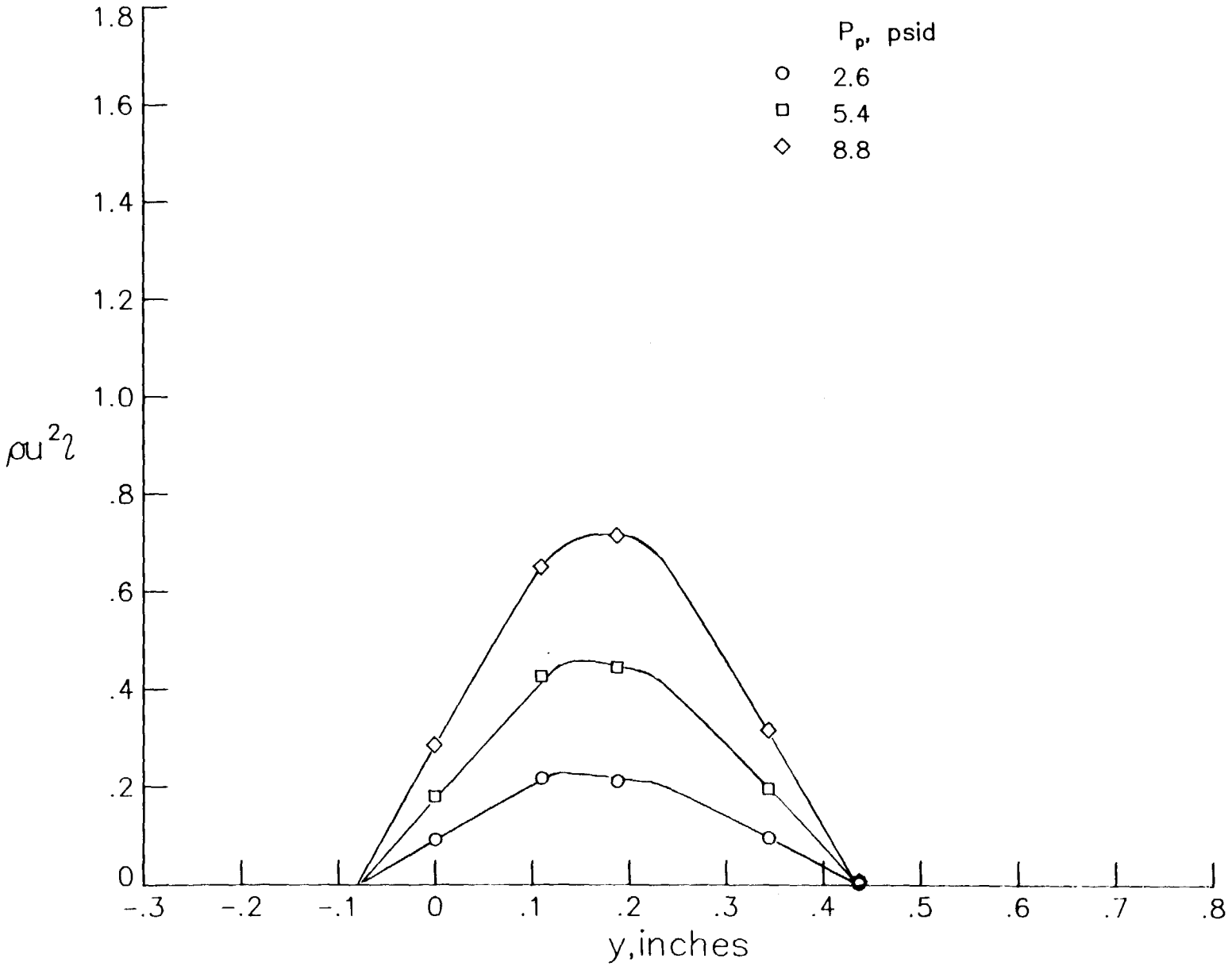

(d) Tip 2, rear jet.

Figure B4. Continued.

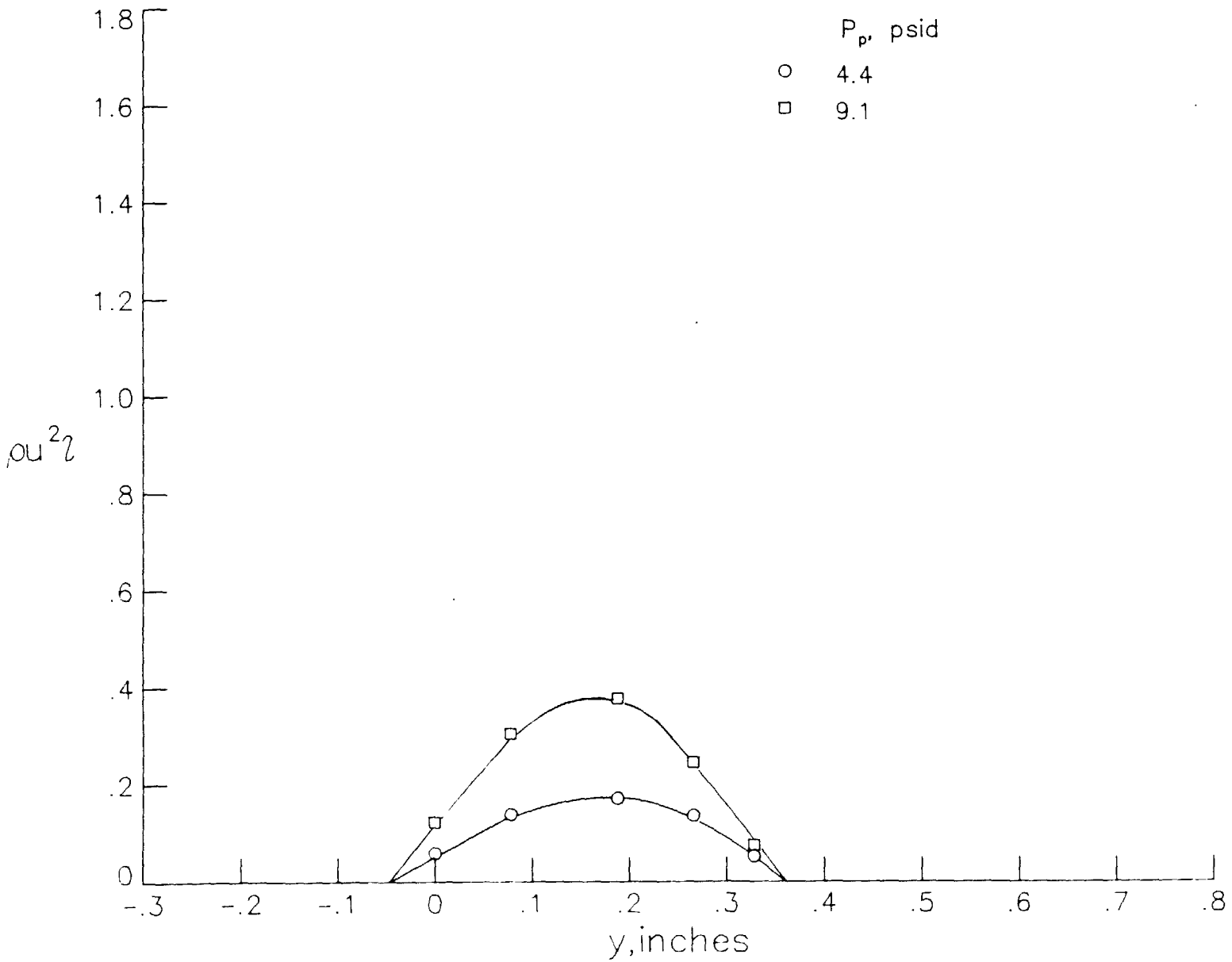

(e) Tip 3, front jet.

Figure B4. Continued.

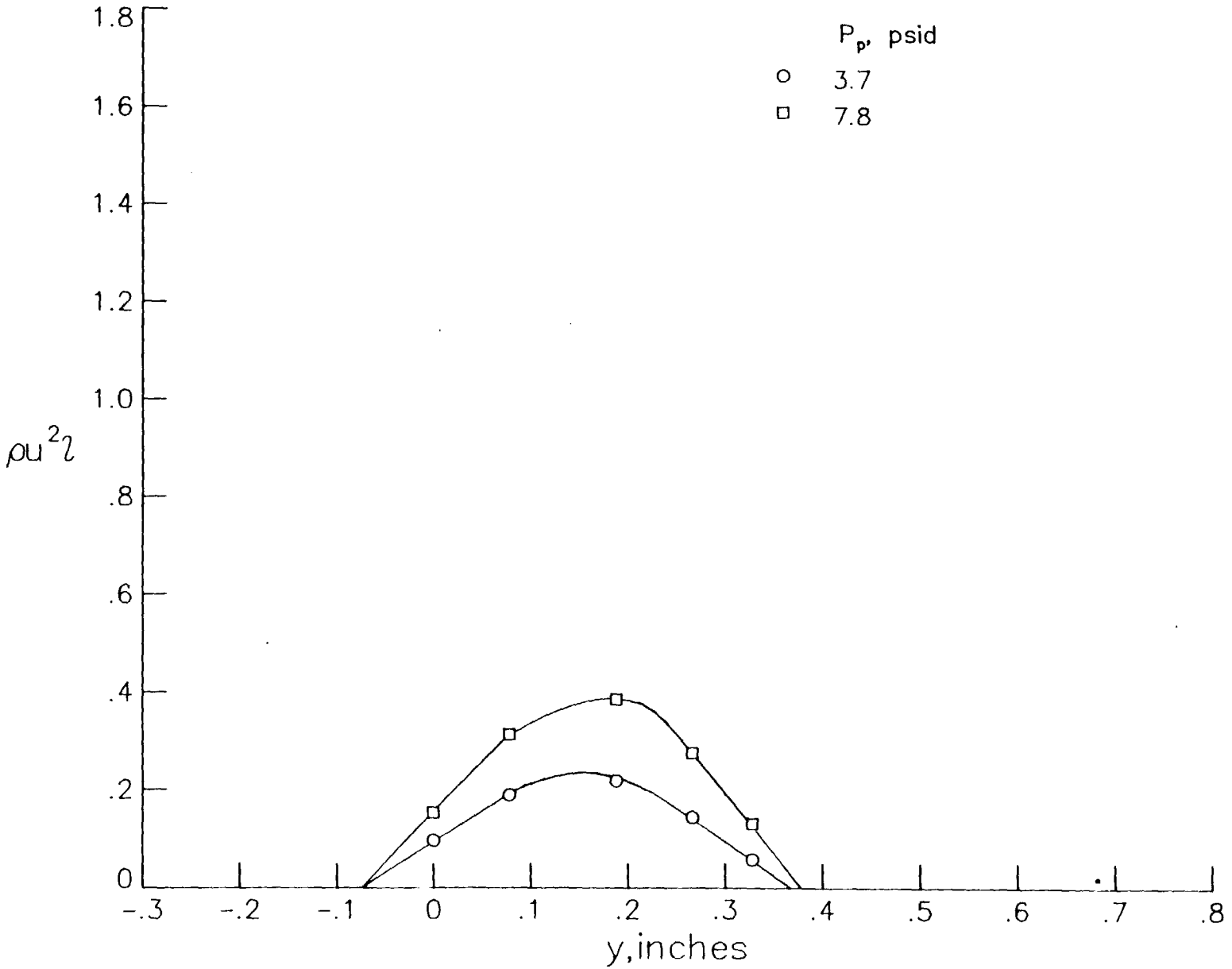

(f) Tip 3, rear jet.

Figure B4. Continued.

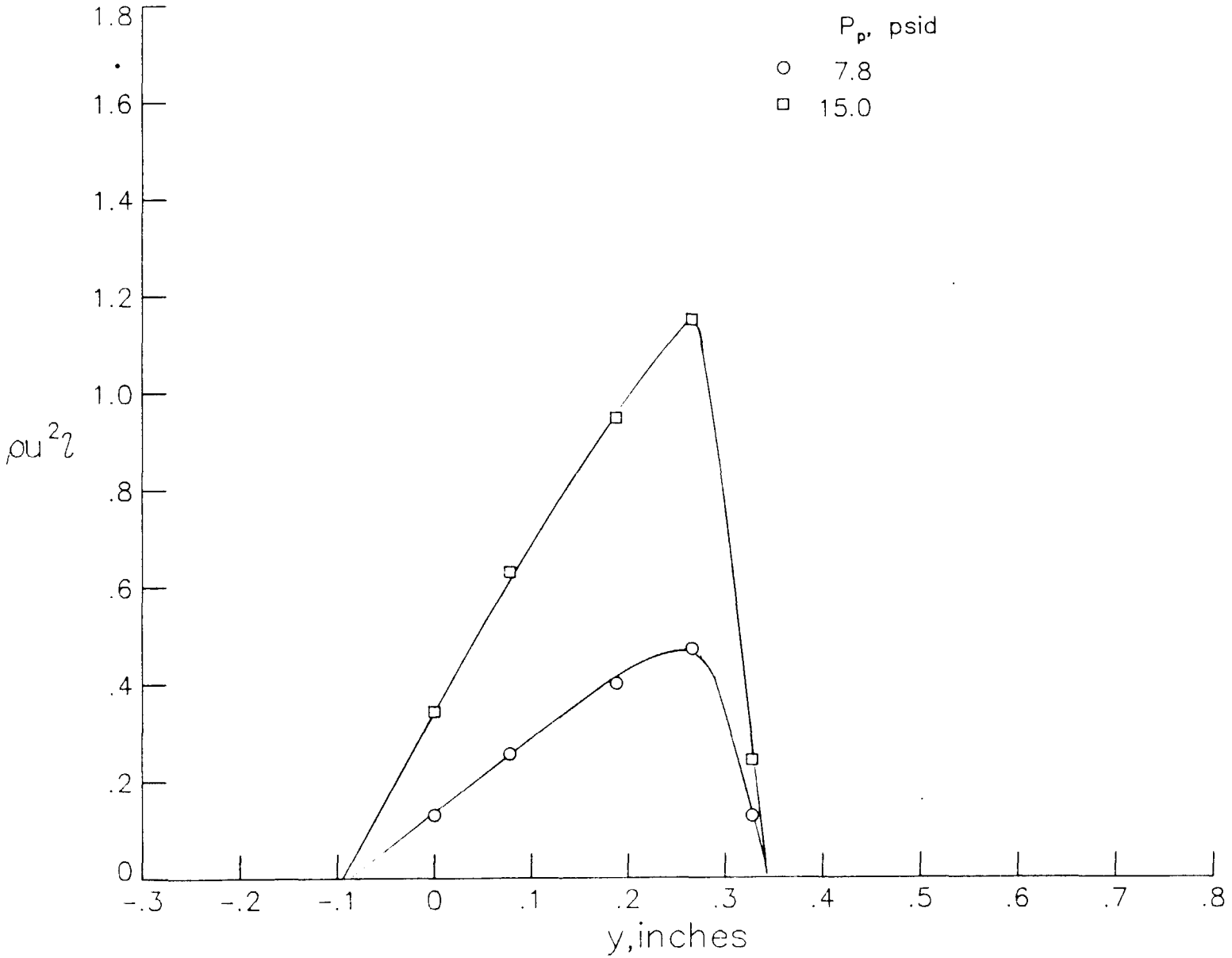

(g) Tip 4, front jet.

Figure B4. Continued.

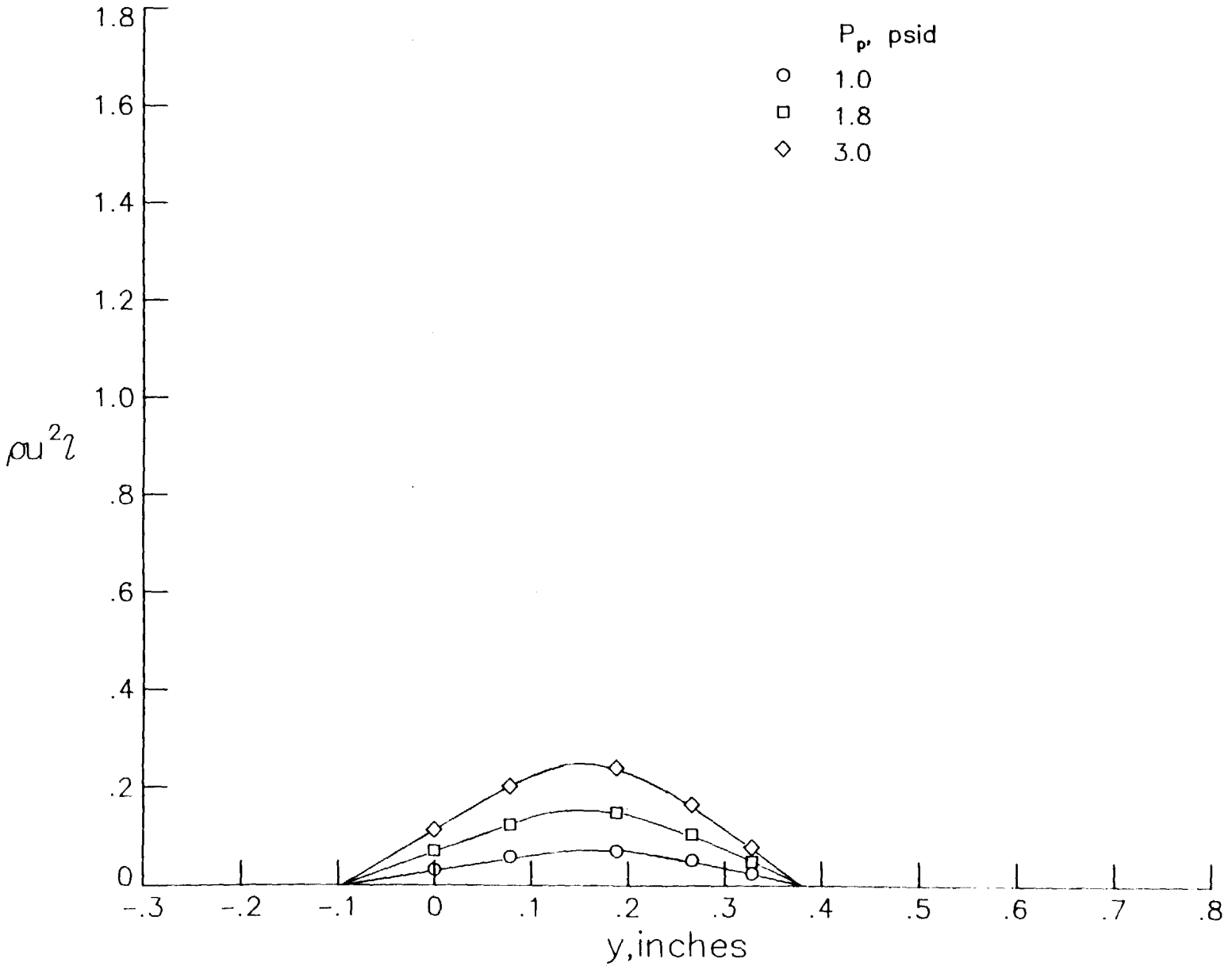

(h) Tip 4, center jet.

Figure B4. Continued.

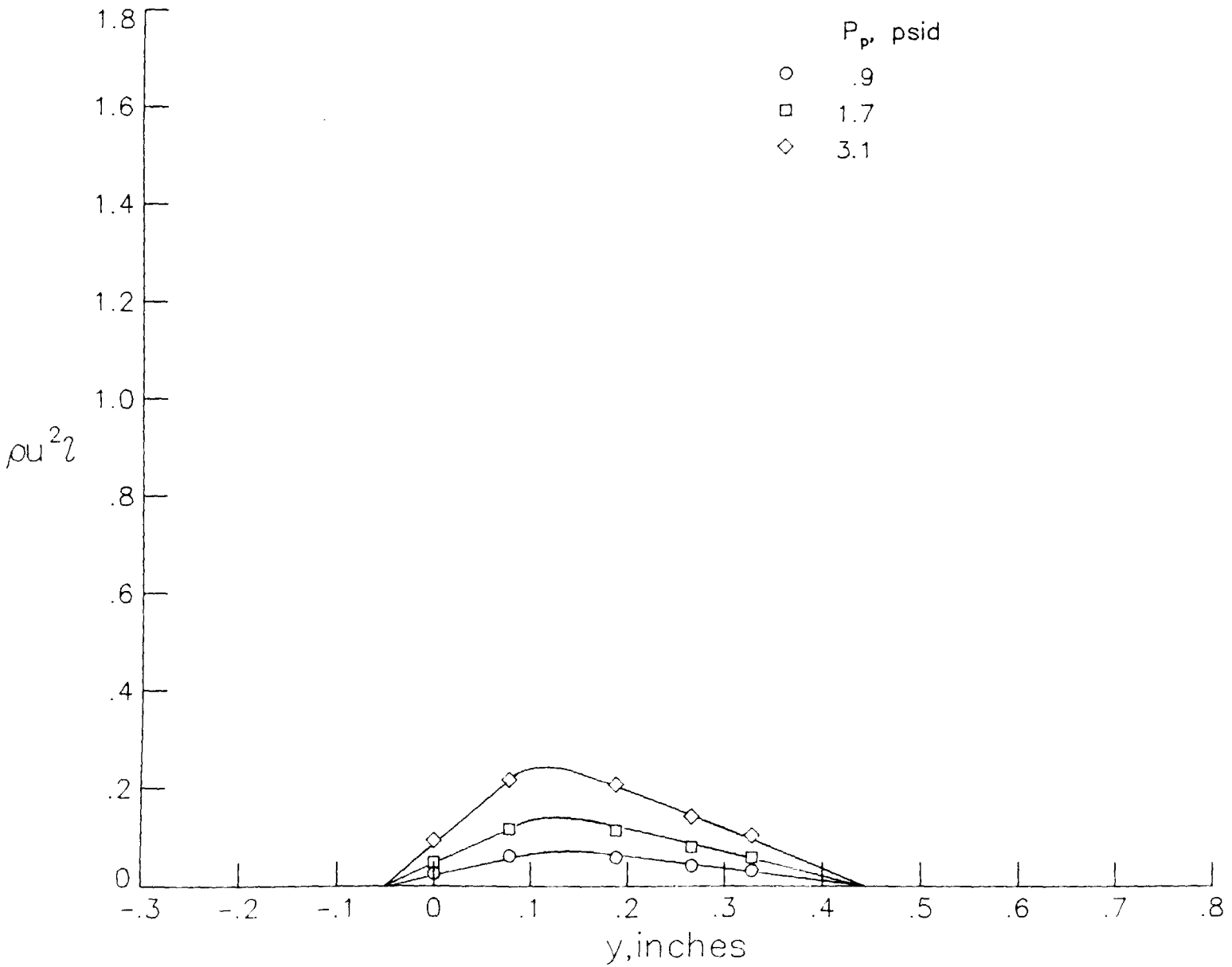

(i) Tip 4, rear jet.

Figure B4. Continued.

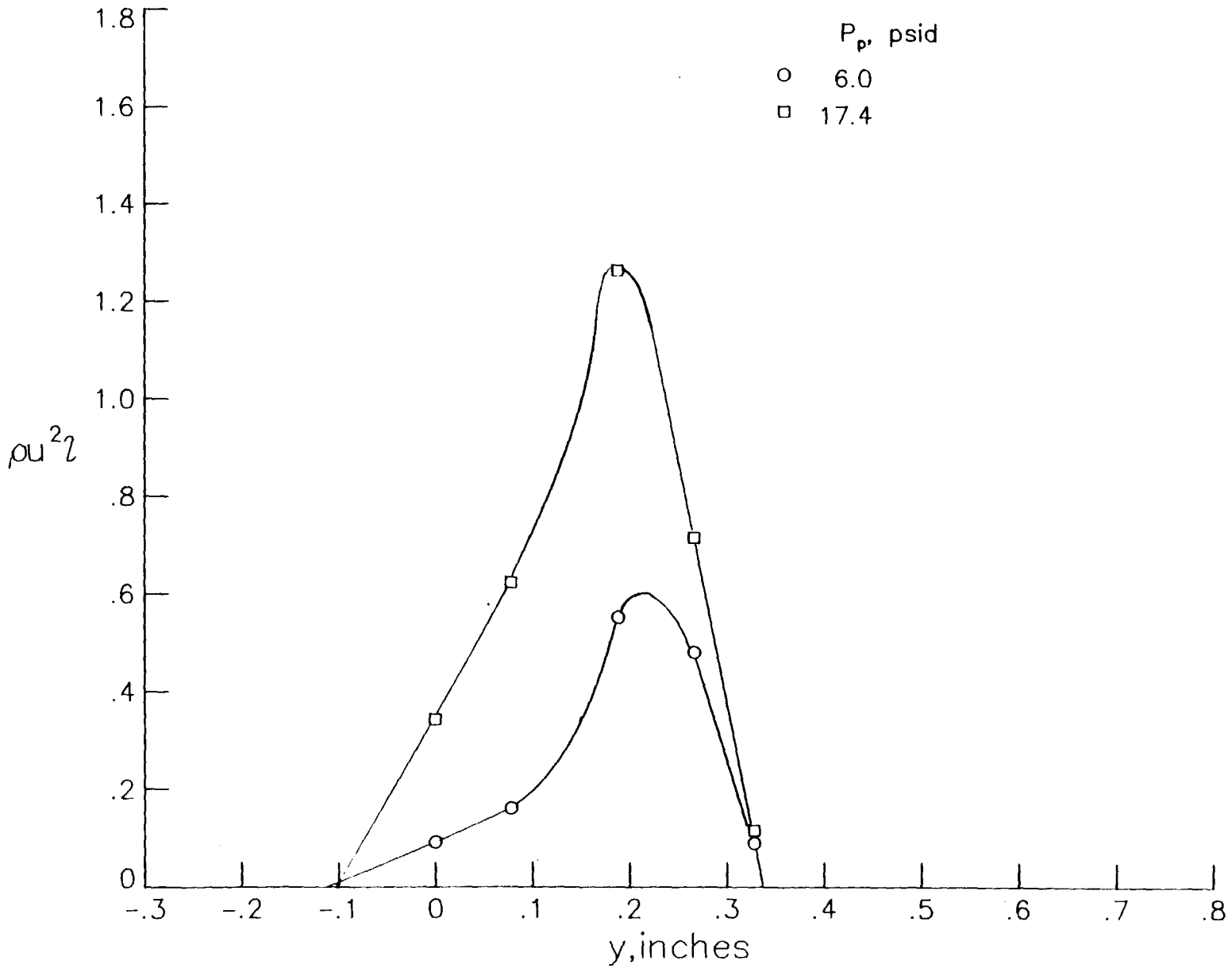

(j) Tip 6, front jet.

Figure B4. Continued.

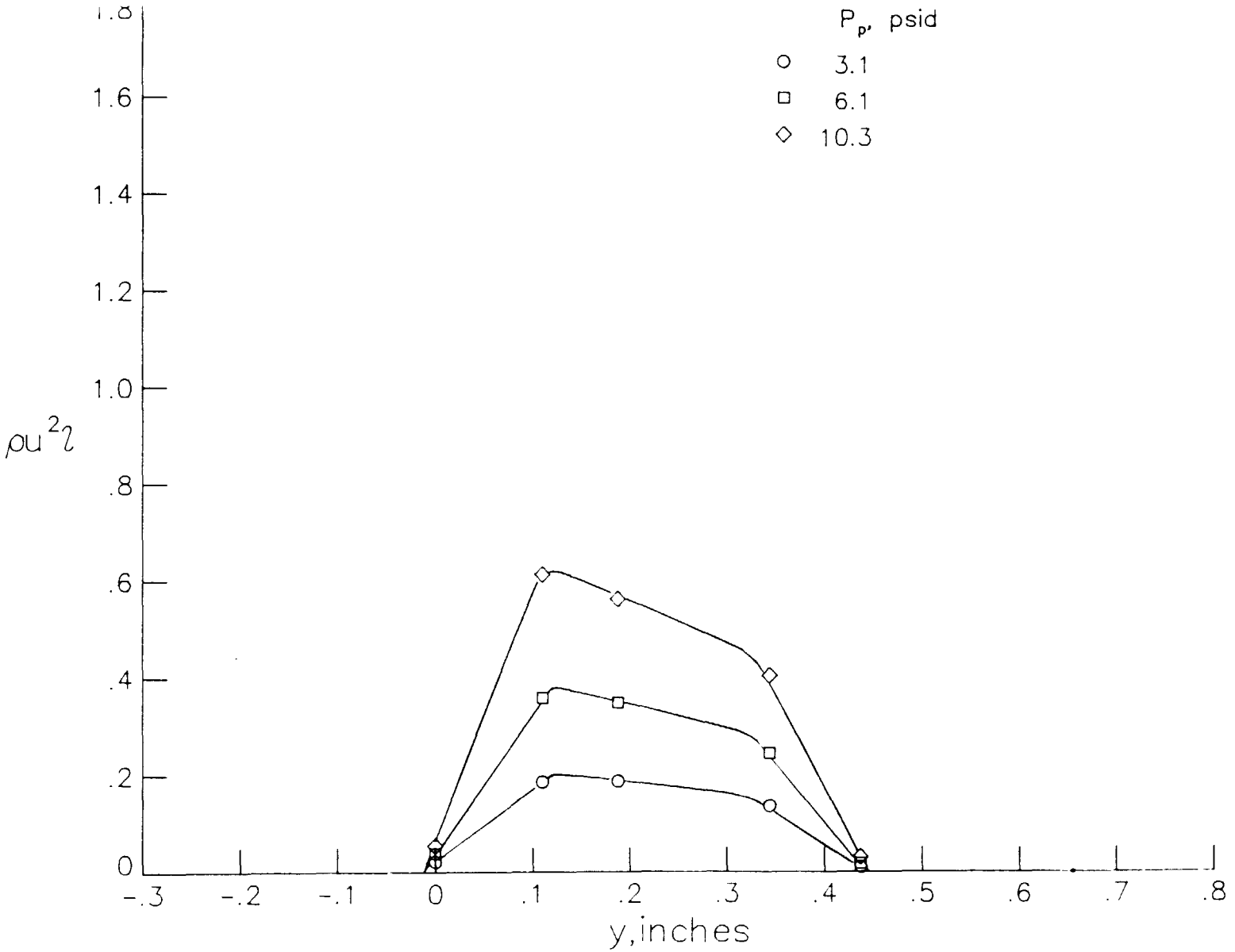

(k) Tip 6, rear jet.

Figure B4. Continued.

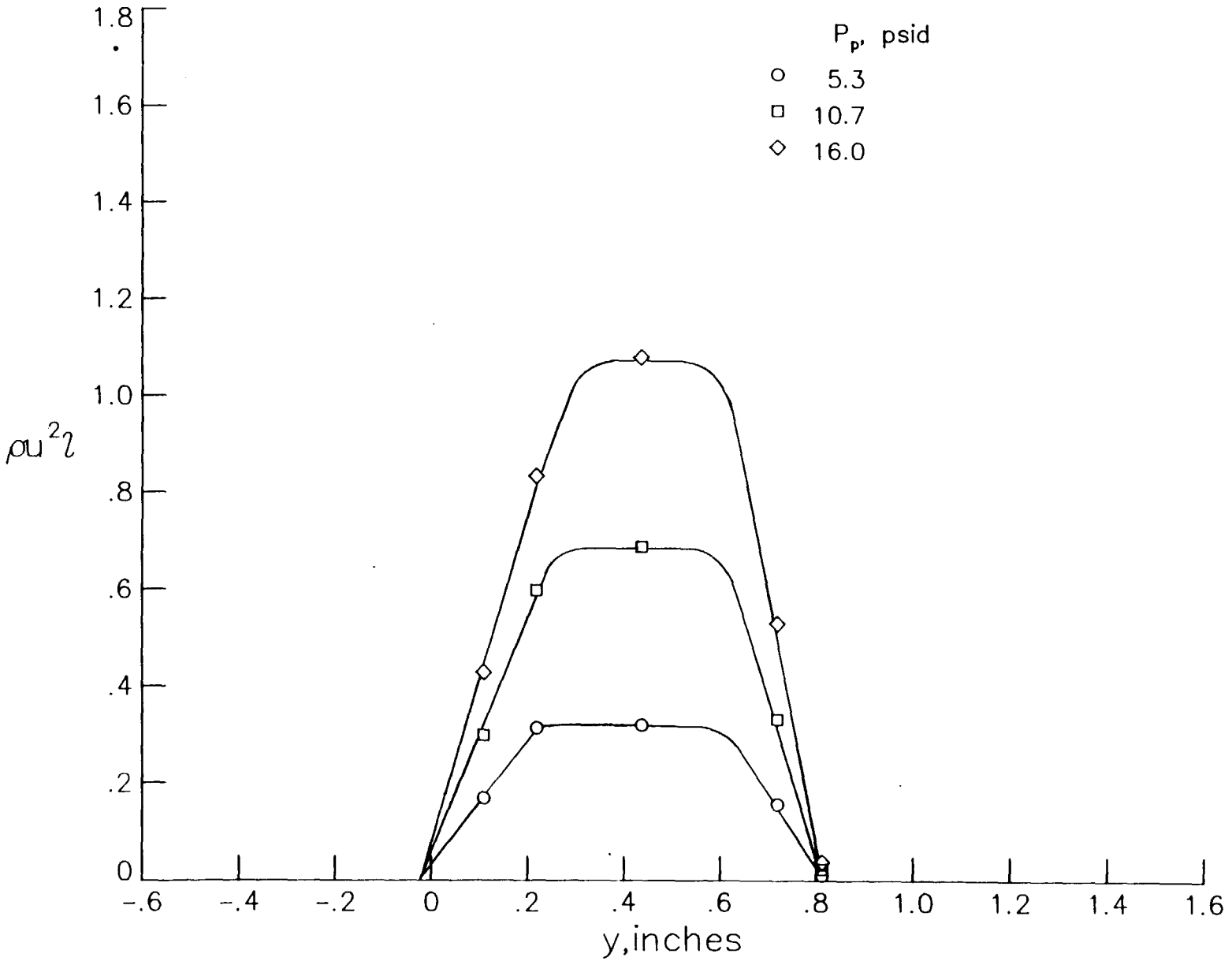

(l) Tip 8, front jet.

Figure B4 Continued

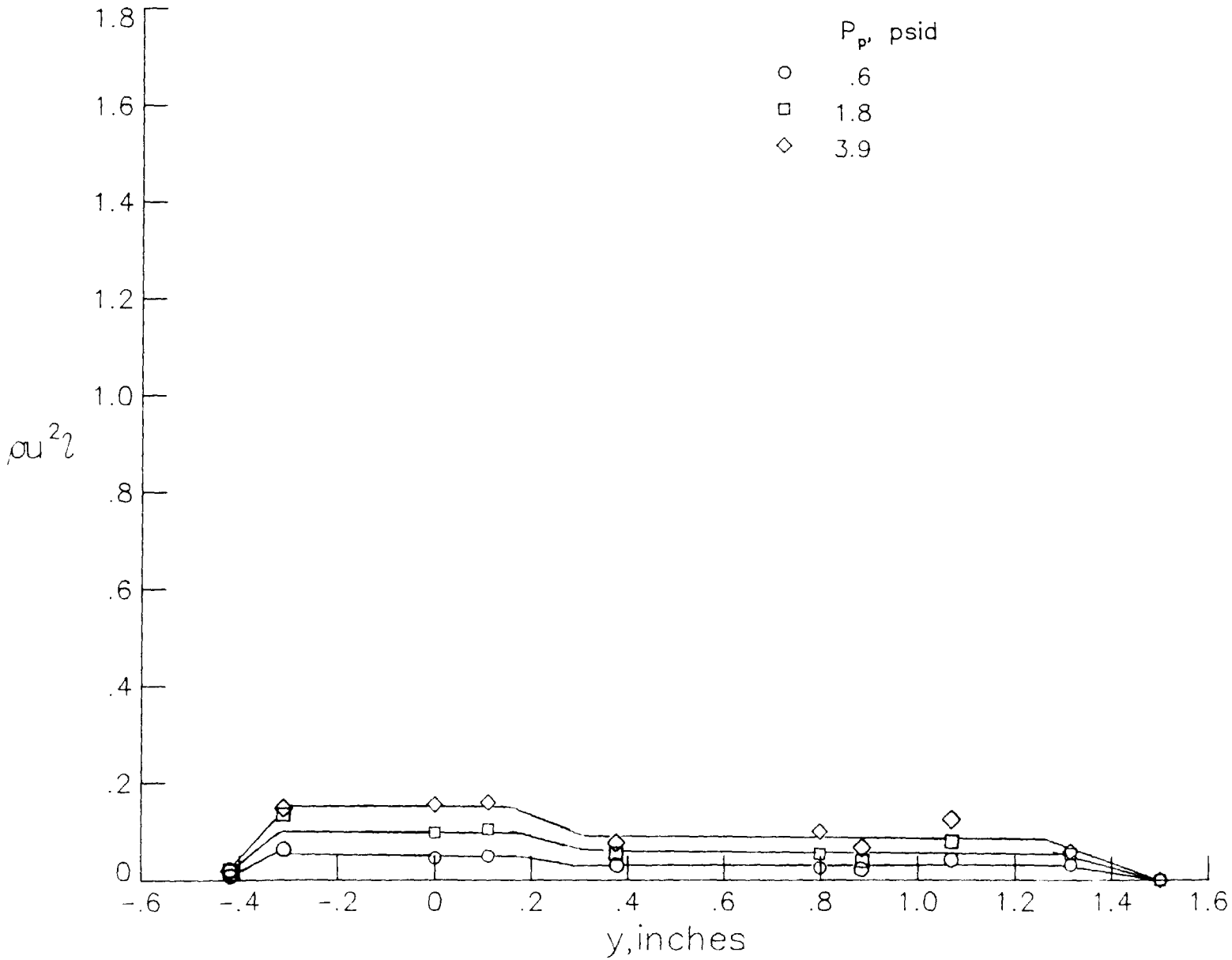

(m) Tip 8, rear jet.

Figure B4. Continued.

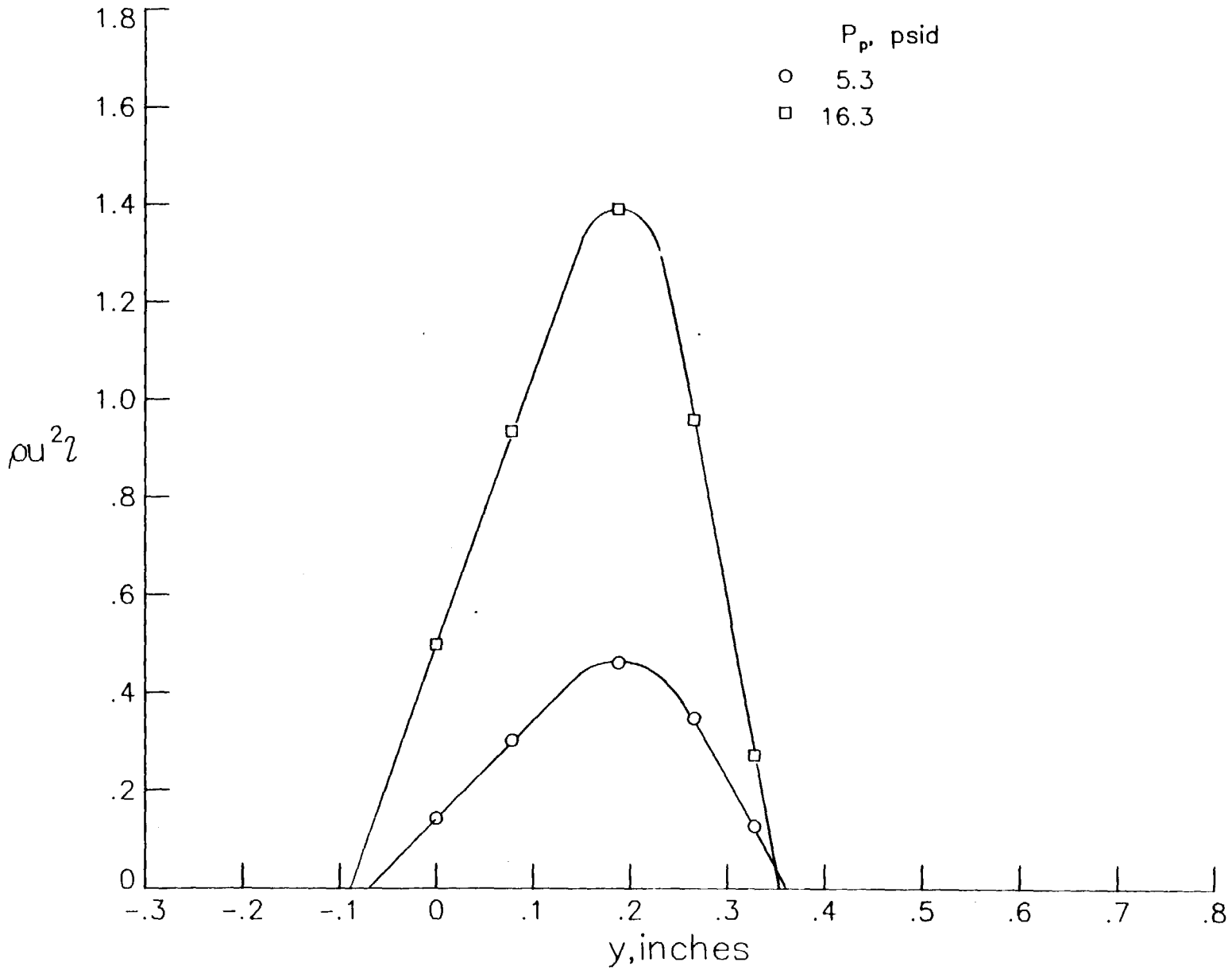

(n) Tip 9, front jet.

Figure B4. Continued.

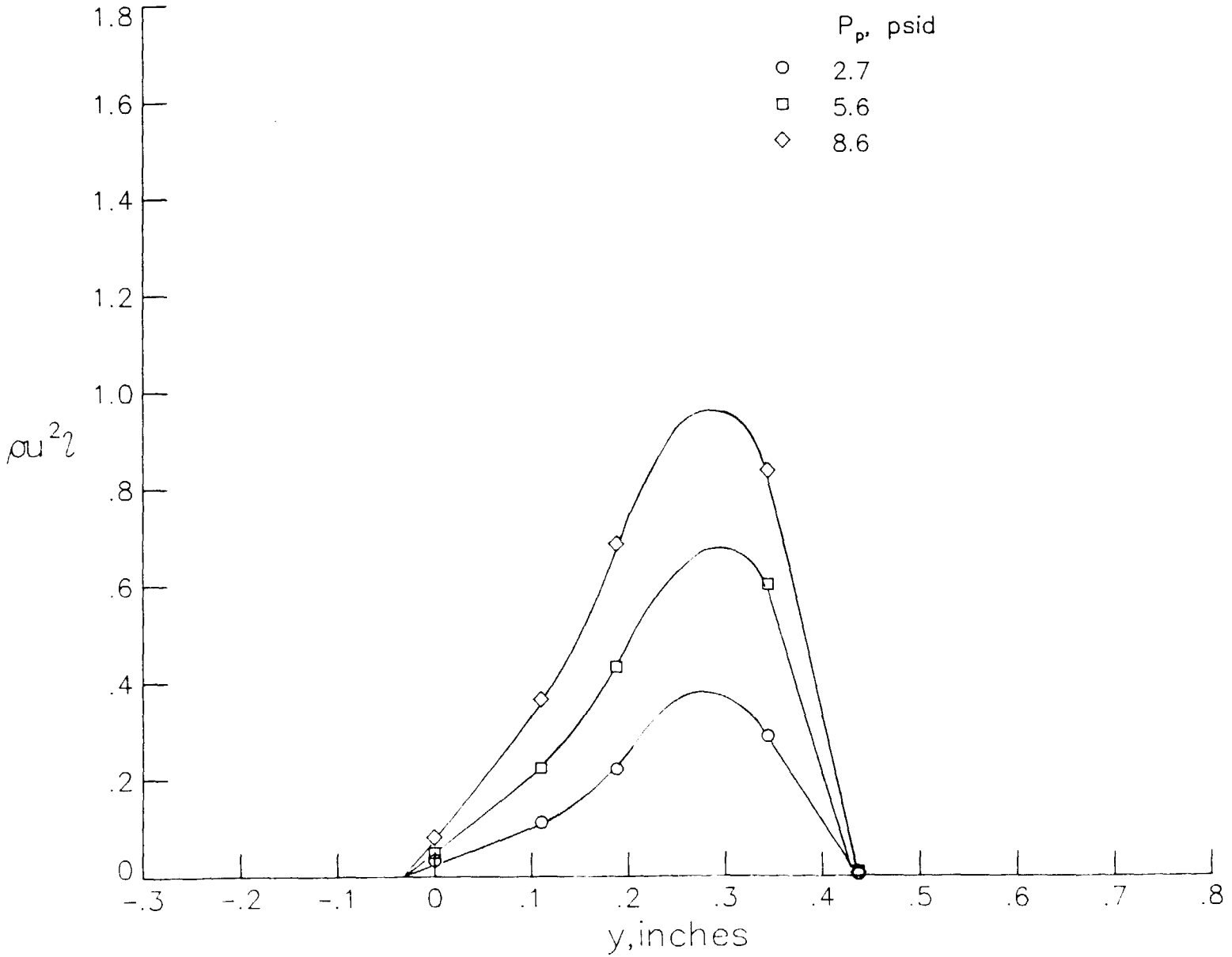

(o) Tip 9, rear jet.

Figure B4. Concluded.

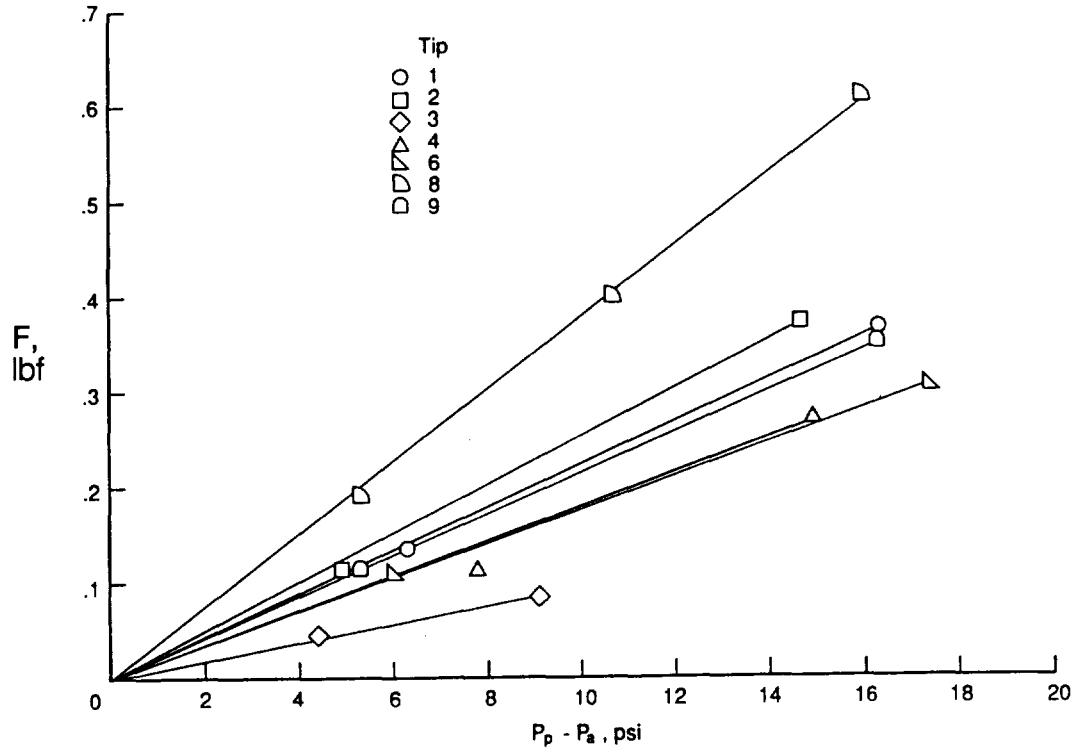

(b) Rear jets.

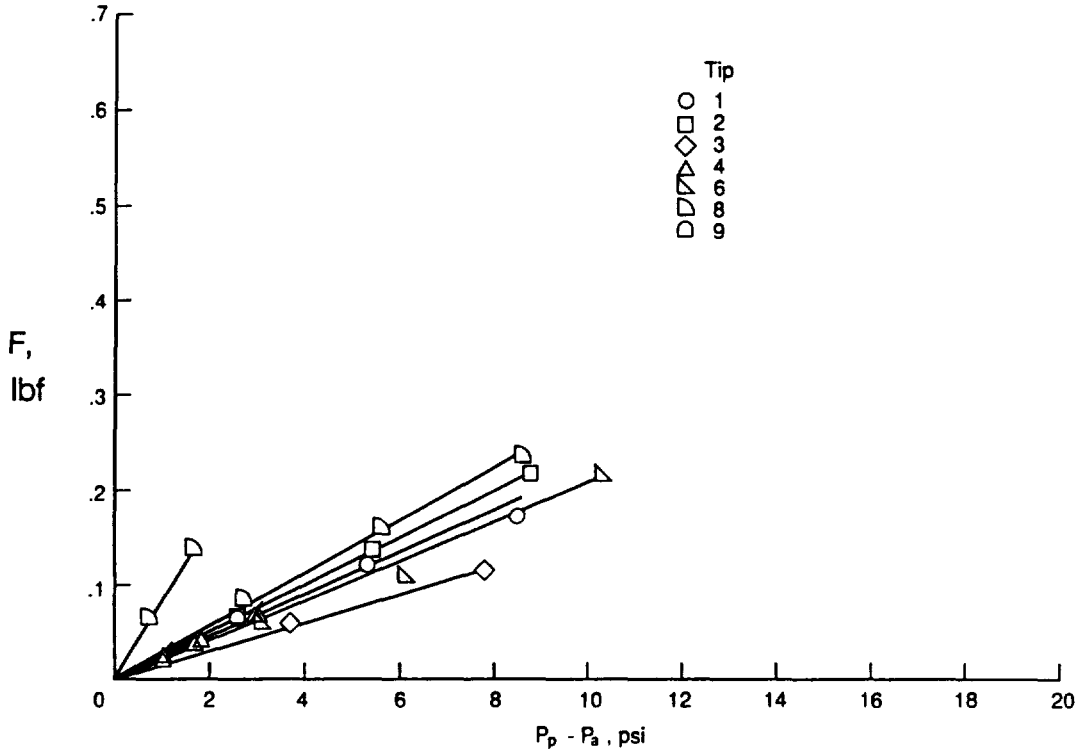

(a) Front jets.

Figure B5. Variation of the jet momentum with jet plenum pressure.

VITA

The author was born in [redacted] on [redacted]. He continued to live in Greenwich, Connecticut while he attended Fairfield College Preparatory School in Fairfield, Connecticut. He graduated from Fairfield College Preparatory School in June, 1966.

In September, 1966, he entered Rensselaer Polytechnic Institute where he received a Bachelor of Science Degree in Aeronautical Engineering in June, 1970. After graduating, he accepted a position on the staff of the NASA Langley Research Center and began work in July, 1970, in the Full Scale Research Division. In September, 1970, he began part-time studies with The George Washington University leading to a Master of Science degree from the department of Civil, Mechanical, and Environmental Engineering with a concentration in Aerodynamics in May, 1975. In September, 1982, he began part time studies the The George Washington University leading to a degree of Doctor of Science.

The author is married and lives with his wife, Linda, and their three children, Jennifer, Christine, and John, in Yorktown, Virginia.